Theoretical Investigations of Group 13 Chlorometallate ionic Liquids

Department of Chemistry - Imperial College London

PhD Thesis

Lennart Heiner Frankemoelle

Febuary 2024

Declaration of Originality

I, Lennart Heiner Frankemoelle, hereby declare that the PhD Thesis titled theoretical investigations into group 13 chlorometallate ionic liqudis, submitted on 30/05/2023, is entirely my original work. I assert that no part of this work has been plagiarized or copied from any other source, and all the ideas, concepts, and materials used are duly acknowledged and properly cited.

I confirm that I have undertaken an extensive review of existing literature, research, and resources to develop a comprehensive understanding of the subject matter. Any sources consulted or referenced in this work have been appropriately cited.

Furthermore, I affirm that I have not previously submitted this work, or any part thereof, for any academic or assessment purposes, nor has it been published in any form. This work represents my independent efforts and reflects my personal thoughts, insights, and analysis.

I take full responsibility for the accuracy and integrity of the information presented in this work. Any errors or omissions are unintentional and do not compromise the overall validity or originality of the work.

I am aware that any form of academic misconduct, including plagiarism or misrepresentation, is a serious offense and may result in severe consequences, including academic penalties or disciplinary actions. I fully understand the ethical and academic standards expected of me, and I have adhered to them throughout the completion of this work.

By signing this declaration, I acknowledge that I am the original author of the work and that I have read and understood the guidelines regarding academic honesty and integrity provided by my institution. I affirm that this work is an authentic representation of my skills, knowledge, and efforts.

Lennart Heiner Frankemoelle, 31.05.2023

Copyright Declaration

The copyright of this thesis rests with the author. Unless otherwise indicated, its contents are licensed under a Creative Commons Attribution-NonCommercial 4.0 International Licence (CC BY-NC).

Under this licence, you may copy and redistribute the material in any medium or format. You may also create and distribute modified versions of the work. This is on the condition that: you credit the author and do not use it, or any derivative works, for a commercial purpose.

When reusing or sharing this work, ensure you make the licence terms clear to others by naming the licence and linking to the licence text. Where a work has been adapted, you should indicate that the work has been changed and describe those changes.

Please seek permission from the copyright holder for uses of this work that are not included in this licence or permitted under UK Copyright Law.

Lennart Heiner Frankemoelle 31.05.2023

Aknowledgements

This thesis is dedicated to my grandparents, Christian and Elizabeth Duester, who passed away during my PhD and have been a cornerstone to my success throughout my life.

I would like to express my deepest gratitude to my family, whose unwavering support and love have been instrumental throughout my academic journey. I am particularly grateful to my wife, Yasmine Faress, for her patience, understanding, and continuous encouragement. Her unwavering belief in me has been a constant source of inspiration.

I would also like to extend my heartfelt appreciation to my parents, Helga and Heiner Frankemoelle, for instilling in me the values of hard work, perseverance, and dedication. Their guidance and sacrifices have played a significant role in shaping my character and fueling my ambitions.

I am indebted to my peers; Sophie Finnigan, Kenn Watson, Rebecca Rowe, Julian Becker, Mikkaila McKeever-Willis, Richard Fogarty, and Frederik D. Philippi, for their camaraderie, insightful discussions, and unwavering support. Our collaborative efforts and shared experiences have enriched my research and personal growth.

I am immensely grateful to my PhD supervisors, Professor Patricia Hunt and Professor Kim Jelfs, for their invaluable guidance, expertise, and mentorship throughout my research journey. Professor Hunts profound knowledge, constructive feedback, and unwavering belief in my abilities have been instrumental in shaping my research and enhancing its quality. I want to thank Professor Jelfs for taking me into her group and allowing me to have a home at the Imperial college London, especially during the tumultuous times of my PhD.

I would also like to extend my appreciation to the staff and faculty members of Imperial College London for their support, resources, and academic environment that fostered my intellectual growth.

This work would not have been possible without the collective support, encouragement, and guidance from these individuals. I am truly fortunate to have them by my side, and I extend my sincere appreciation for their contributions.

Lennart Heiner Frankemoelle, 31.05.2023

Abstract

This study examines group 13 chlorometallate ionic liquids using a hierarchical approach to understand their structures, ion pair interactions, and speciation. It begins with a search for isolated chlorometallate species and cation conformers in both gas and liquid phases. The electronic structures of the most stable configurations are analyzed, revealing nucleophilic and electrophilic sites in anions and cations. Techniques such as Fukui functions, net atomic charge assignments, molecular electrostatic potentials, and reduced density gradient analyses offer insights into the electronic structure and interaction profiles of the ion pairs. The study identifies preferred interaction sites for anions with $[C_2C_1Im]^+$ and ammonium-based cations, showing that maximizing interactions enhances ion pair stability. Self-interactions within anions like $[M_3Cl_{10}]^-$ and linear $[M_4Cl_{13}]^-$ strengthen cation interactions.

Speciation comparisons between mass spectrometry and gas phase analysis reveal discrepancies, suggesting kinetic effects or limited thermodynamic influence in gas phase chlorometallate speciation. The perturbation of anionic speciation impacts chloroaluminate and chlorogallate systems at higher x_{MCl_3} values. The thermodynamic favorability of multimetallic chloroindate complexes above $x_{InCl_3} = 0.5$ remains unexplored, and the absence of pentacoordinate and hexacoordinate chloroindate species at low x_{InCl_3} is plausible. For chloroaluminate and chlorogallate systems, agreement with mass spectrometry is observed below $x_{MCl_3} = 0.67$. This study enhances understanding of group 13 chlorometallate ionic liquids, advancing knowledge of their structures and applications.

Contents

List of Figures **13**

List of Tables **27**

1 Introduction **39**

1.1 The motivation to research halometallate ionic liquids 42

1.1.1 Electrodepostion 43

1.1.2 Battery technology 45

1.1.3 Catalysis 47

1.2 Halometallate Ionic Liquid Chemistry 48

1.2.1 Ionic liquids 48

1.2.2 Deep eutectic solvents 50

1.2.3 Halometallate ionic liquids 53

1.3 Speciation in group 13 halometallate ionic liquids and methods of determining anionic speciation 56

1.3.1 Vibrational spectroscopy 58

1.3.2 NMR Spectroscopy 59

1.3.3 X-ray photoelectron spectroscopy (XPS) 62

1.3.4 X-ray absoroption spectroscopy (XAS) 63

1.3.5 Bulk property measurements 64

1.3.6 Theoretical methods 65

1.3.7 Mass spectrometry (MS) 67

1.3.8 Alternative techniques . . . 68

1.3.9 Speciation methods summery . . . 69

1.4 Current understanding of anionic speciation, relevant properties and potential use in applications 69

1.4.1 Anionic speciation in chloroaluminate, chlorogallate and chloroindate Ionic Liquids in the liquid phase . . . 70

1.4.2 Lewis acidity and basicity in halometallate ionic liquids . . . 71

1.4.3 Redox potential and electrochemical window in halometallate ionic liquids . . . 76

1.5 Chemistry of the halometallate ionic liquids under investigation . . . 77

1.5.1 Group 13 chemistry . . . 78

1.5.2 Cation chemistry . . . 78

1.5.3 Ion - ion interactions . . . 80

1.5.4 Thermodynamics of solvation . . . 89

1.6 Aims of the investigation . . . 90

Bibliography **92**

2 Theoretical Background **103**

2.1 The Schrödinger equation . . . 104

2.1.1 Atomic units . . . 108

2.2 Solving the Schrödinger equation . . . 108

2.2.1 Variational principle . . . 109

2.2.2 Born-Oppenheimer approximation . . . 110

2.2.3 Constructing trial wave functions - linear combination of atomic orbitals basis set approach . . . 113

2.2.4 The secular equation . . . 115

2.3 Many-electron wave functions . . . 117

2.3.1 Hartree products . . . 117

2.3.2 The Hartree hamiltonian . . . 119

2.3.3 Electron spin and antisymmetry . . . 120

2.3.4 Slater determinants . . . 122

2.3.5 Hartree-Fock self-consistent field method . . . 124

2.4 Density functional theory . . . 127

2.4.1 Theoretical motivation . . . 127

2.4.2 Hohenberg - Kohn theorems . . . 130

2.4.3 Kohn - Sham self-consistent field method . . . 133

2.4.4 Exchange-correlation functionals . . . 137

2.5 Basis sets variants . . . 146

2.5.1 Basis set superposition error . . . 150

2.6 Additional approximations . . . 151

2.6.1 Effective core potentials . . . 151

2.6.2 SMD continuum solvation model . . . 157

2.7 Theory of analytical tools . . . 160

2.7.1 Net atomic charge determination methods . . . 161

2.7.2 Molecular electrostatic potential . . . 165

2.7.3 Fukui functions . . . 165

2.7.4 Atoms in molecules . . . 166

2.7.5 Non-covalent interaction plot . . . 167

2.7.6 Interaction region indicator . . . 169

2.7.7 Computing XPS spectra from optimized structures . . . 170

Bibliography **171**

3 Methodology **181**

3.1 Computational methods . . . 182

3.2 Investigation strategy . . . 183

3.2.1 Isolated chlorometallate anion and cation structure searches . . . 184

3.2.2 Optimization . . . 186

3.2.3 Frequency analysis . . . 189

3.2.4 Isolated chlorometallate species . . . 190

3.2.5 Thermodynamic comparison . . . 191

3.2.6 Conformer search and bond dissociation energy via scans . . . 192

3.2.7 Anionic speciation from isolated chlorometallate species . . . 194

3.2.8 Electronic structure evaluation - net atomic charges, molecular electrostatic potential and Fukui functions . . . 195

3.2.9 Ion pair input structure construction . . . 196

3.2.10 Ion pair nomenclature . . . 197

3.2.11 Ion pair convergence evaluation . . . 204

3.2.12 Ion pair structural evaluation . . . 206

Bibliography **208**

4 Isolated Ions **212**

4.1 Isolated group 13 chlorometallate structures in the gas phase and liquid phase 213

4.1.1 Gas phase group 13 chlorometallate structures 214

4.1.2 Liquid phase group 13 chlorometallate structures 221

4.2 Stable cation conformers 242

4.2.1 1-ethyl-3-methyl-imidazolium structural analysis 243

4.2.2 Isolated gas phase [Choline]$^+$, [N_{2110}]$^+$ and [N_{2111}]$^+$ cation structures 244

Bibliography **246**

5 Isolated Ions Electronic Structure **248**

5.1 Liquid phase chlorometallate anion electronic structure evaluation via net atomic charge assignments, molecular electrostatic potentials and Fukui functions 249

5.1.1 Net atomic charges of anionic species species 249

5.1.2 Molecular electrostatic potentials of the chlorometallate anions in the liquid phase . . 257

5.1.3 Fukui Functions of the liquid phase anion structures 265

5.1.4 Liquid phase anion structures charge distribution, MEPs and Fukui function – Key Takeaways 272

5.2 Liquid phase cation electronic structure evaluation 273

5.2.1 1-ethyl-3-methyl-imidazolium electronic structure 274

5.2.2 [Choline]$^+$, [N_{2110}]$^+$ and [N_{2111}]$^+$ cations electronic structure 280

Bibliography **285**

6 Ion Pair Interaction Profiles **286**

6.1 [C_2C_1Im]Cl-MCl_3 ion pair evaluation in the gas phase and liquid phase 287

6.1.1 Gas phase ion pair evaluation 287

6.1.2 Liquid phase ion pair evaluation 309

6.1.3 $[C_2C_1Im]Cl\text{-}MCl_3$ ion pair interaction profile evaluation in the gas phase and liquid phase summery 321

6.1.4 $[C_2C_1Im]Cl\text{-}MCl_3$ ion pair Gas phase and liquid phase ion pair electronic structure evaluation 322

6.2 [Choline][$AlCl_4$], [N_{2110}][$AlCl_4$] and [N_{2111}][$AlCl_4$] ion pair interaction profiles evaluation . . . 327

6.2.1 [Choline][$AlCl_4$], [N_{2110}][$AlCl_4$] and [N_{2111}][$AlCl_4$] ion pair interaction profiles 327

Bibliography **332**

7 Anionic speciation **333**

7.1 Chlorometallate gas phase speciation through thermodynamic comparisons from isolated anions 334

7.1.1 Gas phase chlorometallate speciation at $x_{MCl_3} = 0.25$, 0.33 and 0.5 334

7.1.2 Gas phase chlorometallate speciation at $x_{MCl_3} = 0.67$ 336

7.1.3 Gas phase chlorometallate speciation at $x_{MCl_3} = 0.75$ 338

7.1.4 Gas phase chlorometallate speciation at $x_{MCl_3} = 0.8$ 339

7.1.5 Gas phase chlorometallate speciation summery 341

7.2 Chlorometallate liquid phase speciation through thermodynamic comparisons from isolated anions 342

7.2.1 Liquid phase chlorometallate speciation at $x_{MCl_3} = 0.25$, 0.33 and 0.5 342

7.2.2 Liquid phase chlorometallate speciation at $x_{MCl_3} = 0.67$ 344

7.2.3 Liquid phase chlorometallate speciation at $x_{MCl_3} = 0.75$ 346

7.2.4 Liquid phase chlorometallate speciation at $x_{MCl_3} = 0.8$ 348

7.3 Speciation evaluation from isolated anions summary 349

7.3.1 Monometallic chlorometallate system speciation discrepancies . . . 353

7.4 Chlorometallate liquid phase speciation through thermodynamic comparisons of ion pair structures . . . 355

7.4.1 Liquid phase chloroindate speciation at $x_{MCl_3} = 0.25$, 0.33 and 0.5 with explicit solvations 356

7.4.2 Liquid phase chloroaluminate and chlorogallate speciation at $x_{MCl_3} = 0.67$ with explicit solvations . . . 357

7.4.3 Liquid phase chloroaluminate and chlorogallate speciation at $x_{MCl_3} = 0.75$ with explicit solvations . . . 358

7.4.4 Liquid phase chloroaluminate and chlorogallate speciation at $x_{MCl_3} = 0.8$ with explicit solvations . . . 360

7.4.5 Liquid phase ion pair speciation summery . . . 361

7.5 XPS spectra . . . 362

7.6 Speciation summery . . . 363

Bibliography **365**

8 Conclusion **367**

A appendix **370**

A.1 Anion Structure Data . . . 372

A.1.1 Optimized Gas Phase Anion Structures . . . 372

A.1.2 Gas Phase structure Gibbs Free Energy Comparisons . . . 383

A.1.3 selected Gas Phase Structures Structural Data . . . 387

A.1.4 Optimized Liquid Phase Anion Structures . . . 393

A.1.5 Gas Phase structure Gibbs Free Energy Comparisons . . . 403

A.1.6 selected Liquid Phase Structures Structural Data . . . 408

A.1.7 Condensed Fukui Functions 414

A.2 $[C_2C_1Im][M_xCl_y]$ Ion pair Data 425

A.2.1 $[C_2C_1Im][M_xCl_y]$ Gas Ion pair structures 425

A.2.2 $[C_2C_1Im][M_xCl_y]$ liquid phase Ion pair structures 438

A.2.3 $[C_2C_1Im][M_xCl_y]$ AIM analysis 447

A.2.4 $[C_2C_1Im][AlCl_4]$ Molecular orbitals 465

A.2.5 Ion Pair XPS spectra 473

A.2.6 $[Choline][M_xCl_y]$ Gas Ion pair structures 477

A.2.7 $[N_{2110}][M_xCl_y]$ Gas Ion pair structures 491

A.2.8 $[N_{2111}][M_xCl_y]$ Gas Ion pair structures 500

List of Figures

1.1 Examples of an ionic liquid ([C_2C_1Im]Cl) and a hydrogen bond acceptor ([Choline]Cl) and the resulting Halometallate ionic liquids ([Cat]Cl-$AlCl_3$) upon the addition of equimolar amount of metal halide ($AlCl_3$) 40

1.2 Thesis structure schematic highlighting key topics in each chapter 42

1.3 Diagrammatic representation of the electrodeposition of Zinc onto a screw (cathode) using a zinc anode in an aqueous zinc chloride solution[2] 44

1.4 Diagrammatic representation of charge and discharge in an electrical Battery[3] 46

1.5 Diagrammatic representation of the effect of a catalyst on the activation energy of a reaction[1] 47

1.6 selected IL cations (top); Dialkylpyrrolidinium, Alkylammonium, Alkylmethylimidazoilium and anions (bottom); Tetrafluoroborane, Nitrate, Alkyl sulfate and Halides 49

1.7 Selected halide salts and hydrogen bond donors 51

1.8 The eutectic behavior of the mixture of compounds A and B described with respect to the temperature (Y axis) and the composition of the mixture (X axis) 51

1.9 Different $[M_nCl_{3n-1}]^-$ structures that form at different x_{MCl_3} 54

1.10 [C_2C_1Im]Cl-$AlCl_3$ anionic speciation with respect to x_{MCl_3}[56] 55

1.11 Schematic representation of the effects of x_{AlCl_3} on various HMIL attributes 57

1.12 Chloroaluminate ^{27}Al $\Delta v_{1/2}$ (Hz)[y-axis] at various x_{AlCl_3} [x-axis] in the [C_4py]Cl-$AlCl_3$ system[1] 60

1.13 [C_2C_1Im]Cl-$AlCl_3$ Melting points versus x_{AlCl_3} measured by DSC 65

1.14 Schematic representation of the effects of speciation on Lewis acidity and electrochemical potential in the chloroalluminate, chlorogallate and chloroindate ionic liquids 70

1.15 The formation of tetrachloroalluminate, $[AlCl_4]^-$, through the creation of a dative covalent bond between aluminum chloride, $AlCl_3$, and a chloride ion, Cl^- 71

1.16 [C_4Py]Cl-$AlCl_3$, [C_2C_1Im]Cl-$AlCl_3$, [C_8C_1Im]Cl-$AlCl_3$, [C_8C_1Im]Cl-$GaCl_3$ and [C_8C_1Im]Cl-$InCl_3$ ^{31}P chemical shift (left y-axis) and the Guttman acceptor number [AN] (right y-axis) with respect to x_{MCl_3} (x-axis) 74

1.17 Electrochemical windows of [BuPy]Cl-$AlCl_3$ and [C_2C_1Im]Cl-$AlCl_3$ in the neutral (black), Acidic (red) and Basic (blue) regions[2] 76

1.18 Group 13 atomic number, atomic mass, electronic configuration, accessible oxidation states and electronegativity (Pauling scale) 78

1.19 1-ethyl-3-methylimidazolium atomic numbering 78

1.20 1-ethyl-3-methylimidazolium resonance structures 79

1.21 Ammonium analog cation structures: choline, trimethyl-ethyl-ammonium dimethyl-ethyl-ammonium 80

1.22 Attractive and repulsive coulombic interactions 81

1.23 Permanent dipole - permanent dipole interactions (Keesom Forces) (A) example and (B) diagrammatic representation 82

1.24 Permanent dipole - permanent dipole interactions (Keesom Forces) alternative orientation diagrammatic representation 83

1.25 Permanent dipole - induced dipole interactions (Debye forces) example 84

1.26 Induced dipole - induced dipole interactions (London dispersion forces) between two butane molecules 84

1.27 Hydrogen bonding between two water molecules 85

1.28 Hydrogen bonding molecular orbitals 86

1.29 Representation of a σ-hole in $[AlCl_4]^-$ via the visualization of the molecular electrostatic potential 87

1.30 C_6H_6 2d charge distribution visualization 87

1.31 Repulsive face stacked (left), attractive Y & T shaped (center) and parallel displaced (right) aromatic interactions 88

1.32 Aromatic Interactions with non-aromatic species; aromatic-cation, aromatic-anion and aromatic-permanent dipole interactions 88

2.1 Schematic representation of a vectors present in a dihydrogen, (H_2) system; The positions of Hydrogen nuclei A and B and electrons i and j are given by r_1 represented by dashed blue lines and distances between two species, r_{12}, are shown in dashed orange lines 105

2.2 Schematic representations of a (A) one reaction coordinate dependant and (B) two reaction coordinate dependant potential energy surfaces 112

2.3 Basis function which can be used to represent a σ-bond; s functions on the left and combinations of s and p functions on the right 115

2.4 HF SCF procedure flow chart 127

2.5 KS SCF procedure flow chart 137

2.6 2D representation of 1s STOs and 3 GTOs 147

2.7 Schematic representation of LCGTO 148

2.8 Diagrammatic representation of effective core potential components alongside the ECP equation 154

2.9 3 RNA Base Pairs showing various NCIs represented in 3D and 2D 169

3.1 Monometallic guess structures where M=Al, Ga or In 185

3.2 Three $[M_2Cl_7]^-$ starting structures with different numbers of bridging halides 186

3.3 $[M_2Cl_8]^{2-}$ stereo isomeric starting structures example 186

3.4 Optimization flowchart with possibilities in white, actions in light blue, error messages in grey and results in green 187

3.5 Error L716 flowchart with possibilities in white, actions in light blue, error messages in grey and results in green or orange 188

3.6 L9999 and L502 flowchart with possibilities in white, actions in light blue, error messages in grey and results in green or orange 189

3.7 Frequency flowchart with possibilities in white, actions in light blue, possible errors in grey and results in green 190

3.8 Depiction of the terminal Al - terminal Al distance scan coordinate (turquoise) of the $[Al_4Cl_{13}]^-$ anion 193

3.9 SCF energy change versus the terminal Al- terminal Al distance of the $[Al_4Cl_{13}]^-$ anion . . . 193

3.10 Depiction of the $[C_2C_1Im]^+$ ethyl arm rotation via the dihedral angle scan coordinate (turquoise) 194

3.11 $[AlCl_4]^-$ Total electron density, electrostatic potential and overlap contours 195

3.12 Stable positions of Cl^- around the $[C_nC_1Im]^+$ cation 197

3.13 Geometric elements of the MCl_4 tetrahedron which can face the cations 197

3.14 $[C_2C_1Im]^+$ dihedreal angle 198

3.15 $[C_2C_1Im][AlCl_4]$ C_2 - Al distance 198

3.16 $[Al_2Cl_7]^-$, $[Al_3Cl_{10}]^-$, linear $[Al_4Cl_{13}]^-$ and branched $[Al_4Cl_{13}]^-$ anions central atoms 199

3.17 $[C_2C_1Im][AlCl_4]$ and $[C_2C_1Im][Al_2Cl_7]$ ion pairs 'plane - angle' 199

3.18 $[C_2C_1Im]^+$ angle information 200

3.19 $[C_2C_1Im][AlCl_4]$ and $[C_2C_1Im][Al_2Cl_7]$ ion pairs 'plane - dihedral angle' 201

3.20 $[C_2C_1Im]^+$ Dihedral angle information 201

3.21 $[C_2C_1Im][AlCl_4]$_-58_3.7_122_87 202

3.22 Ammonium based cation - anion distance 203

3.23 Amonium based cation - anion angle 203

3.24 Ammonium based cation - anion dihedral angle 204

3.25 $[Choline]^+$ internal dihedral angle 204

3.26 $[C_2C_1Im][AlCl_4]$ low frequency rotational and translational motion vibration examples 206

4.1 The colour scheme of chlorine, aluminium, gallium and indium atoms in this chapter 213

4.2 Optimized monometallic chlorometallate species in the gas phase 214

4.3 Stable $[M_2Cl_4]^{2+}$, M_2Cl_6, $[M_2Cl_7]^-$, $[M_2Cl_9]^{3-}$, and $[M_2Cl_{10}]^{4-}$ species in the gas phase, SD = structure dissociates 215

4.4 Stable $[M_2Cl_3]^{3+}$ species in the gas phase, relative Gibbs free energy in kJ mol^{-1}, TS structure = transition state structure 216

4.5 Stable dimetallic $[M_2Cl_5]^+$ species in the gas phase, relative Gibbs free energy in kJ mol^{-1}, converges to XX = converges to an alternative conformational isomer which can be found in the appendix 217

4.6 Stable trimetallic species in the gas phase, relative Gibbs free energy in kJ mol^{-1} 218

4.7 Stable tetrametallic species in the gas phase, relative Gibbs free energy in kJ mol^{-1} where [Low X] indicates X imaginary frequencies smaller than 50 cm^{-1} and MHF indicates the structures did not converge due to the structures featuring multiple high frequencies 220

4.8 Stable square pyramidal $[InCl_5]^{2-}$ species in the liquid phase and the relative Gibbs free energy in kJ mol^{-1} 222

4.9 Stable $[M_2Cl_4]^{2+}$, $[M_2Cl_7]^-$, $[M_2Cl_9]^{3-}$, $[M_2Cl_{10}]^{4-}$, $[M_2Cl_{11}]^{5-}$ species in the liquid phase . 223

4.10 Stable $[M_2Cl_3]^{3+}$ species in the liquid phase and their relative Gibbs energy in kJ mol^{-1} . . . 224

4.11 Stable $[M_2Cl_5]^+$ species in the liquid phase and their relative Gibbs energy in kJ mol^{-1} . . . 225

4.12 Stable M_2Cl_6 species in the liquid phase and their relative Gibbs energy in kJ mol^{-1} 226

4.13 Additional Stable $[In_2Cl_9]^{3-}$ species in the liquid phase and their relative Gibbs energy in kJ mol^{-1} 226

4.14 liquid phase $[M_2Cl_7]^-$ contortion scans and scan coordinate (M(1)-M(2) distance) with respect to SCF energy where M=Al, Ga or In 227

4.15 $[M_2Cl_7]^-$ rotational scans and scan coordinates (Cl(1)-M(2)-M(3)-Cl(4) dihedral angle) with respect to SCF energy where M = Al, Ga or In 228

4.16 Structural features contributing to high energy in the $[Al_2Cl_7]^-$ structure at scan coordinate -90 (right) and 0 (left) from a side and front view 229

4.17 Stable linear $[M_3Cl_{10}]^-$ conformers in the liquid phase, terminal indium - terminal indium distance in Angstrom and relative Gibbs free energies (kJ mol^{-1}) 230

4.18 Stable non-linear $[M_3Cl_{10}]^-$ species in the liquid phase and their relative Gibbs energy in kJ mol^{-1} 232

4.19 Stable M_3Cl_9 species in the liquid phase 233

4.20 Liquid phase $[M_3Cl_{10}]^-$ contortion scans and scan coordinate (M(1)-M(2) distance) with respect to SCF energy where M=Al, Ga or In 234

4.21 $[M_3Cl_{10}]^-$ rotation scans and scan coordinates (Cl(1)-M(2)-M(3)-Cl(4) dihedral angle) with respect to SCF energy where M=Al, Ga or In 235

4.22 Stable linear $[Al_4Cl_{13}]^-$ conformers, terminal aluminum - terminal aluminum distance in Angstrom and relative Gibbs free energies in kJ mol^{-1} 236

4.23 Stable linear $[Ga_4Cl_{13}]^-$ conformers, terminal gallium - terminal gallium distance in Angstrom and relative Gibbs free energies in kJ mol^{-1} 236

4.24 Stable linear $[In_4Cl_{13}]^-$ conformers, terminal indium - terminal indium distance in Angstrom and relative Gibbs free energies in kJ mol^{-1} 237

4.25 Branched $[M_4Cl_{13}]^-$ chlorometallate structures in the liquid phase and their relative Gibbs energy in kJ mol^{-1} 238

4.26 Branched $[M_4Cl_{13}]^-$ chlorometallate structures in the liquid phase and their relative Gibbs energy in kJ mol^{-1} 239

4.27 Liquid phase linear $[M_4Cl_{13}]^-$ contortion scans and scan coordinate (M(1)-M(2) distance) with respect to SCF energy where M=Al, Ga or In 240

4.28 Linear $[Al_4Cl_{13}]^-$ scan $AlCl_3$ rearrangement conformers, aluminium - aluminium distance scan coordinate (Angstrom) and relative SCF energies (kJ mol^{-1}) 241

4.29 Linear $[M_4Cl_{13}]^-$ twisting Scans and scan coordinates (Cl(1)-M(2)-M(3)-Cl(4) dihedral angle) with respect to SCF energy where M = Al, Ga or In 242

4.30 Stable conformers of the $[C_2C_1Im]^+$ cation, the relative Gibbs free energy and dihedral angle of the ethyl arm in the gas phase and liquid 243

4.31 Stable conformers of the $[Choline]^+$ and their relative Gibbs free energies in the gas phase . . 244

4.32 Stable conformers of the $[N_{2110}]^+$ and $[N_{2111}]^+$ cations in the gas phase 244

5.1 $[MCl_4]^-$ net atomic ADCH charges and chemical environments; ● chlorides (Cl) and ● metals; Al, Ga and In 250

5.2 $[InCl_5]^{2-}$ and $[InCl_6]^{3-}$ net atomic ADCH charges 251

5.3 $[M_2Cl_7]^-$ net atomic ADCH charges and chemical environments; ● terminal chlorides (Cl(T)), ● bridging chlorides (Cl(B)) and ● metals; Al and Ga 252

5.4 $[M_3Cl_{10}]^-$ net atomic ADCH charges and chemical environments; ● terminal metal (M(T)), ● bridging metals (M(B)), ● bridging chlorides, ● terminal chlorides attached to bridging metals (Cl(T-BM)) and ● terminal chlorides attached to terminal metals (Cl(T)) where M = Al or Ga 253

5.5 Linear $[M_4Cl_{13}]^-$ net atomic ADCH charges and chemical environments; ● terminal metals (M(T)), ● bridging metals (M(B)), ● outter bridging chlorides (Cl(B-out)), ● inner bridging chloride (Cl(B-in)), ● terminal chlorides attached to bridging metals (Cl(T-BM)) and ● terminal chlorides attached to terminal metals (Cl(T)) where M = Al or Ga 254

5.6 Branched $[M_4Cl_{13}]^-$ net atomic ADCH charges and charge environments; ● terminal metal of the linear segment (M(T-Lin)), ● terminal metal of the branched segment (M(T-Bra)), ● bridging metal (M(B)), ● bridging chloride of the linear segment (Cl(B-Lin)), ● bridging chloride of the branched segment (Cl(B-Bra)), ● terminal chloride attached to the bridging metal (Cl(T-BM), ● terminal chloride attached to the terminal metal of the linear segment (Cl(T-Lin)), ● terminal chloride attached to the terminal metal of the branched segment (Cl(T-Lin)) where M = Al or Ga 256

5.7 $[MCl_4]^-$ molecular electrostatic potentials projected onto the $[MCl_4]^-$ total density at an isovalue of 0.0008 258

5.8 $[InCl_5]^{2-}$ and $[InCl_6]^{3-}$ molecular electrostatic potentials projected onto the $[InCl_5]^{2-}$ and $[InCl_6]^{3-}$ total densities at an isovalue of 0.0008 259

5.9 $[M_2Cl_7]^-$ molecular electrostatic potentials projected onto the $[M_2Cl_7]^-$ total densities at an isovalue of 0.0008 260

5.10 $[M_3Cl_{10}]^-$ molecular electrostatic potentials projected onto the $[M_3Cl_{10}]^-$ total densities at an isovalue of 0.0008 261

5.11 Linear $[M_4Cl_{13}]^-$ molecular electrostatic potentials projected onto the linear $[M_4Cl_{13}]^-$ total densities at an isovalue of 0.0008 262

5.12 Branched $[M_4Cl_{13}]^-$ molecular electrostatic potentials projected onto the branched $[M_4Cl_{13}]^-$ total densities at an isovalue of 0.0008 264

5.13 $[MCl_4]^- \rightarrow MCl_4$ Fukui functions projected onto the $[MCl_4]^-$ total density at an isovalue of 0.008 265

5.14 The three degenerate HOMOs of each $[MCl_4]^-$ species at an isovalue of 0.02 267

5.15 $[InCl_5]^{2-} \rightarrow [InCl_5]^-$ Fukui Function projected onto the $[InCl_5]^{2-}$ total density at an isovalue of 0.008 and $[InCl_6]^{3-} \rightarrow [InCl_6]^{2-}$ Fukui functions projected onto the $[InCl_6]^{3-}$ total density at an isovalue of 0.008 268

5.16 $[M_2Cl_7]^- \rightarrow M_2Cl_7$ Fukui functions projected onto the $[M_2Cl_7]^-$ total density at an isovalue of 0.008 269

5.17 $[M_3Cl_{10}]^- \rightarrow M_3Cl_{10}$ Fukui functions projected onto the $[M_3Cl_{10}]^-$ total density at an isovalue of 0.008 270

5.18 Linear $[M_4Cl_{13}]^- \rightarrow M_4Cl_{13}$ Fukui functions projected onto the linear $[M_4Cl_{13}]^-$ total density at an isovalue of 0.008 271

5.19 Branched $[M_4Cl_{13}]^- \rightarrow M_4Cl_{13}$ Fukui functions projected onto the branched $[M_4Cl_{13}]^-$ total density at an isovalue of 0.008 272

5.20 $[C_2C_1Im]^+$ atomic numbering 274

5.21 $[C_2C_1Im]^+$ in plane net atomic charges computed in NPA, ChelpG and ADCH 274

5.22 $[C_2C_1Im]^+$ out of plane net atomic charges computed in NPA, ChelpG and ADCH 275

5.23 $[C_2C_1Im]^+$ molecular electrostatic potential projected onto the $[C_2C_1Im]^+$ total density at an isovalue of 0.0008 278

5.24 In plane $[C_2C_1Im]^+ \rightarrow C_2C_1Im$ Fukui function projected onto the $[C_2C_1Im]^+$ total density at an isovalue of 0.0004 279

5.25 Out of plane $[C_2C_1Im]^+ \rightarrow C_2C_1Im$ Fukui function projected onto the $[C_2C_1Im]^+$ total density at an isovalue of 0.0004 279

5.26 $[Choline]^+$ molecular electrostatic potential projected onto the $[Choline]^+$ total density at an isovalue of 0.0008 281

5.27 $[N_{2110}]^+$ and $[N_{2111}]^+$ molecular electrostatic potentials projected onto the $[N_{2110}]^+$ and $[N_{2111}]^+$ total densities at an isovalue of 0.0008 282

5.28 Gauche $[Choline]^+ \rightarrow$ Choline and $[N_{2110}]^+ \rightarrow N_{2110}$ Fukui functions projected onto the $[Choline]^+$ and $[N_{2110}]^+$ total densities at an isovalue of 0.01 283

5.29 $[N_{2111}]^+ \rightarrow N_{2111}$ Fukui function projected onto the N_{2111} total density at an isovalue of 0.01 284

6.1 $[C_2C_1Im][MCl_4]$, $[C_2C_1Im][InCl_5]^-$ and $[C_2C_1Im][InCl_6]^{2-}$ lowest energy gas phase structures 290

6.2 $[C_2C_1Im][AlCl_4]$_-58_3.7_122_87 (0) interaction profile 291

6.3 $[C_2C_1Im][AlCl_4]$_-112_4_113_82 (16) [1] interaction profile (showing interactions shorter than 3.4 Å) in the gas phase 293

6.4 $[C_2C_1Im][AlCl_4]$ interaction profiles (showing interactions shorter than 3.4 Å) in the gas phase 294

6.5 $[C_2C_1Im][M_2Cl_7]$ lowest energy gas phase structures 296

6.6 $[C_2C_1Im][Al_2Cl_7]$ interaction profiles (showing interactions shorter than 3.4 Å) in the gas phase297

6.7 $[C_2C_1Im][Al_2Cl_7]$ interaction profiles (showing interactions shorter than 3.4 Å) in the gas phase298

6.8 $[C_2C_1Im][M_3Cl_{10}]$ lowest energy gas phase structures 299

6.9 $[C_2C_1Im][Al_3Cl_{10}]$ interaction profiles (showing interactions shorter than 3.4 Å) in the gas phase300

6.10 $[C_2C_1Im][Al_3Cl_{10}]$ interaction profiles (showing interactions shorter than 3.4 Å) in the gas phase301

6.11 branched $[C_2C_1Im][M_4Cl_{13}]$ lowest energy gas phase structures 302

6.12 Branched $[C_2C_1Im][Al_4Cl_{13}]$ lowest energy gas phase structure interaction profiles (showing interactions shorter than 3.4 Å) 303

6.13 Linear $[C_2C_1Im][M_4Cl_{13}]$ lowest energy gas phase structures 304

6.14 Linear $[C_2C_1Im][Al_4Cl_{13}]$ lowest energy structures interaction profiles (showing interactions shorter than 3.4 Å) 305

6.15 Linear $[C_2C_1Im][Al_4Cl_{13}]$ highest energy gas phase structure interaction profile (showing interactions shorter than 3.4 Å) 306

6.16 Dissociated $[C_2C_1Im][InCl_6]^{2-}$ gas phase ion pair structures 308

6.17 $[C_2C_1Im][MCl_4]$, $[C_2C_1Im][InCl_5]^-$ and $[C_2C_1Im][InCl_6]^{2-}$ lowest energy liquid phase structures 311

6.18 Selected $[C_2C_1Im][AlCl_4]$ ion pair structure interaction profiles in the liquid phase 313

6.19 $[C_2C_1Im][AlCl_4]$ ion pair structure interaction profiles (showing interactions shorter than 4.0 Å) in the liquid phase 314

6.20 $[C_2C_1Im][M_2Cl_7]$ lowest energy liquid phase structures 315

6.21 $[C_2C_1Im][Al_2Cl_7]$ interaction profiles (showing interactions shorter than 3.6 Å) in the liquid phase 316

6.22 $[C_2C_1Im][Al_2Cl_7]$ interaction profiles (showing interactions shorter than 3.6 Å) in the liquid phase 317

6.23 $[C_2C_1Im][M_3Cl_{10}]$ lowest energy liquid phase structures 318

6.24 $[C_2C_1Im][Ga_3Cl_{10}]$ self interactions between 3.7 and 3.9 Åin length 318

6.25 Linear $[C_2C_1Im][M_4Cl_{13}]$ lowest energy liquid phase structures 319

6.26 $[C_2C_1Im][InCl_6]^{2-}$_56_4.3_156_-108 (-15) Ion pair structure 320

6.27 $[C_2C_1Im][AlCl_4]$ gas phase and liquid phase AIM topology 323

6.28 $[C_2C_1Im][AlCl_4]$ gas phase and liquid phase AIM topology 325

6.29 $[C_2C_1Im][AlCl_4]$ gas phase and liquid phase IRIs 326

6.30 $[C_2C_1Im][AlCl_4]$ gas phase and liquid phase IRIs 327

6.31 Gauche [Choline][$AlCl_4$] interaction profiles (showing interactions shorter than 3.4 Å) in the gas phase 328

6.32 Trans [Choline][$AlCl_4$] Interaction profiles (showing interactions shorter than 3.4 Å(in the gas phase 329

6.33 [N_{2110}][$AlCl_4$] Interaction profiles (showing interactions shorter than 3.4 Å) in the gas phase . 330

6.34 [N_{2111}][$AlCl_4$] Interaction profiles (showing interactions shorter than 3.4 Å) in the gas phase . 330

7.1 Gibbs free energy differences in kJ mol^{-1} of possible anionic speciations at $x_{MCl_3} = 0.25$ in the gas phase 334

7.2 Gibbs free energy differences in kJ mol^{-1} of possible anionic speciations at $x_{MCl_3} = 0.67$ in the gas phase 337

7.3 Gibbs free energy differences in kJ mol^{-1} of possible anionic speciations at $x_{MCl_3} = 0.75$ in the gas phase 338

7.4 Gibbs free energy differences in kJ mol^{-1} of possible anionic speciations at $x_{MCl_3} = 0.8$ in the gas phase 340

7.5 Gibbs free energy differences in kJ mol^{-1} of possible anionic speciations at $x_{MCl_3} = 0.25$ in the liquid phase 343

7.6 Gibbs free energy differences in kJ mol^{-1} of possible anionic speciations at $x_{MCl_3} = 0.67$ in the liquid phase 345

7.7 Gibbs free energy differences in kJ mol^{-1} of possible anionic speciations at $x_{MCl_3} = 0.75$ in the liqud phase 346

7.8 Gibbs free energy differences in kJ mol^{-1} of possible anionic speciations at $x_{MCl_3} = 0.8$ in the liquid phase 348

7.9 $[MCl_4]^-$, $[InCl_5]^{2-}$ and $[InCl_6]^{3-}$ dissociation scan coordinates - M(2)-Cl(1) distance where M=Al, Ga or In 353

7.10 Gibbs free energy differences in kJ mol^{-1} of possible anionic speciations at $x_{InCl_3} = 0.25$ in the liquid phase 356

7.11 Gibbs free energy differences in kJ mol^{-1} of possible anionic speciations at x_{AlCl_3} and x_{GaCl_3} = 0.67 in the liquid phase 358

7.12 Gibbs free energy differences in kJ mol^{-1} of possible anionic speciations at x_{AlCl_3} and x$_{GaCl_3}$ = 0.75 in the liquid phase 359

7.13 Gibbs free energy differences in kJ mol^{-1} of possible anionic speciations at x_{AlCl_3} and x$_{GaCl_3}$ = 0.8 in the liquid phase 360

7.14 $[C_2C_1Im][Al_xCl_y]$ IP Simulated XPS Spectra 362

7.15 Simulated $[InCl_4]^-$ XPS Spectra vs experimental $[InCl_4]^-$ XPS spectra[10] 363

A.1 $[AlCl_4]^-$ Condensed Fukui functions 414

A.2 $[Al_2Cl_7]^-$ Condensed Fukui functions 414

A.3 $[Al_3Cl_{10}]^-$ Condensed Fukui functions 415

A.4 Branched $[Al_4Cl_{13}]^-$ Condensed Fukui functions 416

A.5 Linear $[Al_4Cl_{13}]^-$ Condensed Fukui functions 417

A.6 $[GaCl_4]^-$ Condensed Fukui functions 418

A.7 $[Ga_2Cl_7]^-$ Condensed Fukui functions 418

A.8 $[Ga_3Cl_{10}]^-$ Condensed Fukui functions 419

A.9 Branched $[Ga_4Cl_{13}]^-$ Condensed Fukui functions 420

A.10 Linear $[Ga_4Cl_{13}]^-$ Condensed Fukui functions 420

A.11 $[InCl_4]^-$ Condensed Fukui functions 421

A.12 $[InCl_5]^{2-}$ Condensed Fukui functions 421

A.13 $[InCl_6]^{3-}$ Condensed Fukui functions 422

A.14 $Inplane[c_2c_1Im]^+$ Condensed Fukui functions 423

A.15 Out of Plane $[c_2c_1Im]^+$ Condensed Fukui functions 424

A.16 $[C_2C_1Im][AlCl_4]$ IP AIM Critical points 447

A.17 $[C_2C_1Im][Al_2Cl_7]$ IP AIM Critical points 448

A.18 $[C_2C_1Im][Al_3Cl_{10}]$ IP AIM Critical points 449

A.19 $[C_2C_1Im][Al_3Cl_{10}]$ IP AIM Critical points continued 450

A.20 $[C_2C_1Im][Al_4Cl_{13}]_Bra$ IP AIM Critical points 451

A.21 $[C_2C_1Im][Al_4Cl_{13}]_Bra$ IP AIM Critical points continued 452

A.22 $[C_2C_1Im][GaCl_4]$ IP AIM Critical points 453

A.23 $[C_2C_1Im][Ga_2Cl_7]$ IP AIM Critical points 454

A.24 $[C_2C_1Im][Ga_2Cl_7]$ IP AIM Critical points continued 455

A.25 $[C_2C_1Im][Ga_3Cl_{10}]$ IP AIM Critical points 456

A.26 $[C_2C_1Im][Ga_3Cl_{10}]$ IP AIM Critical points continued 457

A.27 $[C_2C_1Im][Ga_4Cl_{13}]_Bra$ IP AIM Critical points 458

A.28 $[C_2C_1Im][Ga_4Cl_{13}]_Bra$ IP AIM Critical points continued 459

A.29 $[C_2C_1Im][InCl_4]$ IP AIM Critical points 460

A.30 $[C_2C_1Im][InCl_5]^-$ IP AIM Critical points 461

A.31 $[C_2C_1Im][InCl_5]^-$ IP AIM Critical points continued 462

A.32 $[C_2C_1Im][InCl_6]^{2-}$ IP AIM Critical points 463

A.33 $[C_2C_1Im][InCl_6]^{2-}$ IP AIM Critical points continued 464

A.34 $[C_2C_1Im][AlCl_4]_ - 58_3.7_122_87$ IP MOs I 465

A.35 $[C_2C_1Im][AlCl_4]_ - 58_3.7_122_87$ IP MOs II 466

A.36 $[C_2C_1Im][AlCl_4]_ - 60_3.9_109_86_LP$ IP MOs I 467

A.37 $[C_2C_1Im][AlCl_4]_ - 60_3.9_109_86_LP$ IP MOs II 468

A.38 $[C_2C_1Im][AlCl_4]_ - 71_4.6_58_ - 97_LP$ IP MOs I 469

A.39 $[C_2C_1Im][AlCl_4]_ - 71_4.6_58_ - 97_LP$ IP MOs II 470

A.40 $[C_2C_1Im][AlCl_4]_- - 78_4.3_64_81$ IP MOs I 471

A.41 $[C_2C_1Im][AlCl_4]_- - 78_4.3_64_81$ IP MOs II 472

List of Tables

1.1 Types of deep eutectic solvents 52

1.2 Equilibriums and speciation of chloroaluminate ionic liquids at $x_{AlCl_3} = 0.5$, 0.67, 0.75 and 0.8 54

1.3 $\Delta v_{1/2}$ in selected chloroaluminate, chlorogallate and chloroindate ionic liquids at $x_{MCl_3} = 0.5$ 61

1.4 Predominant liquid phase speciation of group 13 chlorometallate Ionic liquids at selected x_{MCl_3} 70

1.5 Properties of hard and soft acids and bases 72

1.6 Investigated group 13 chlorometallate ionic liquids 77

3.1 Mol fraction of metal halide introduced, x_{MCl_3}, the corresponding empirical formula of the anions and selected speciations of the anions 192

3.2 Frequency calculation convergence criteria example 205

5.1 $[MCl_4]^-$ net atomic charges and ratios with respect to absolute values of NACs according to the NPA, ChelpG and ADCH NAC assignment methods 250

6.1 Number of IP structures grouped by relative Gibbs free energy with respect to the lowest energy structure of each IP in the ranges of ≤ 10, $10 \leq 20$, $20 \leq 30$, $30 \leq 40$, $40 \leq 50$ and $50 <$ kJ mol^{-1} of each $[C_2C_1Im][M_xCl_y]^{z-}$ IP in the gas phase and the appendix table where the structures can be found 288

6.2 $[C_2C_1Im][MCl_4]$ lowest energy structures interactions distances in Å 292

6.3 Number of IP structures divided into relative Gibbs free energy with respect to the lowest energy structure of each IP in the ranges of ≤ 10, $10 \leq 20$, $20 \leq 30$ and $30 \leq 40$ in kJ mol^{-1} of each $[C_2C_1Im][M_xCl_{3y}]^{z-}$ IP in the liquid phase and the appendix table where the structures can be found 310

6.4 $[C_2C_1Im][MCl_4]$ gas phase and liquid Phase lowest energy structures thermodynamics 312

6.5 The most stable $[C_2C_1Im][AlCl_4]$ gas phase structure and corresponding liquid phase structure interaction distances and differences in Å 313

6.6 $[C_2C_1Im][AlCl_4]$_-58_3.7_122_87 (0) BCP electron density and interaction strength 324

6.7 $[C_2C_1Im][AlCl_4]$_-60_3.9_109_86_LP (11) BCP electron density and interaction strength 324

6.8 $[C_2C_1Im][AlCl_4]$_-78_4.3_64_81 (8) BCP electron density and interaction strength 325

6.9 $[C_2C_1Im][AlCl_4]$_-71_4.6_58_-97_LP (0) BCP electron density and interaction strength 326

7.1 Dominant specation in the gas phase speciation in the group 13 chlorometallate ionic liquids with at $x_{MCl_3} = 0.25$, 0.33 and 0.5 350

7.2 Dominant specation in the gas phase speciation in the group 13 chlorometallate ionic liquids with at $x_{MCl_3} = 0.67$, 0.75 and 0.8 350

7.3 Dominant specation in the liquid phase speciation in the group 13 chlorometallate ionic liquids with at $x_{MCl_3} = 0.25$, 0.33 and 0.5 351

7.4 Dominant specation in the liquid phase speciation in the group 13 chlorometallate ionic liquids with at $x_{MCl_3} = 0.67$, 0.75 and 0.8 352

7.5 Monometallic species dissociation $\Delta G_{dissociation}$, $\Delta SCF_{dissociation}$, $\Delta SCF^{Scan}_{dissociation}$ and difference between the two computed SCF energies in kJ mol^{-1} 354

A.1 Evaluated monometallic chlorometallate species 372

A.2 Evaluated monometallic chlorometallate species continued 373

A.3 Evaluated dimetallic chlorometallate species 374

A.4 Evaluated dimetallic chlorometallate species continued I 375

A.5 Evaluated dimetallic chlorometallate species continued II 376

A.6 Evaluated dimetallic chlorometallate species continued III 377

A.7 Evaluated dimetallic chlorometallate species continued IV 378

A.8 Evaluated dimetallic chlorometallate species continued V 379

A.9 Evaluated dimetallic chlorometallate species continued VI 380

A.10 Evaluated trimetallic chlorometallate species 381

A.11 Evaluated tetrametallic chlorometallate species 382

A.12 $[M_4Cl_{13}]^-$ comparison I 383

A.13 $[M_4Cl_{13}]^-$ comparison II 383

A.14 $[M_4Cl_{13}]^-$ comparison III 383

A.15 M_4Cl_{12} comparison I 383

A.16 M_4Cl_{12} comparison II 384

A.17 M_4Cl_{11} comparison I 384

A.18 M_4Cl_{11} comparison II 384

A.19 M_3Cl_{10} comparison I 384

A.20 M_3Cl_{10} comparison II 384

A.21 M_3Cl_9 comparison I 385

A.22 M_3Cl_9 comparison II 385

A.23 M_2Cl_{10} comparison I 385

A.24 M_2Cl_{10} comparison II 385

A.25 M_2Cl_9 comparison 385

A.26 M_2Cl_8 comparison 386

A.27 M_2Cl_7 comparison 386

A.28 M_2Cl_6 comparison 386

A.29 M_2Cl_5 comparison 386

A.30 M_2Cl_4 comparison 386

A.31 M_2Cl_3 comparison 387

A.32 MCl_6 comparison I 387

A.33 MCl_6 comparison II 387

A.34 $[AlCl_4]^-$ Gas Phase Distances and Angles 387

A.35 $[GaCl_4]^-$ Gas Phase Distances and Angles 387

A.36 $[InCl_4]^-$ Gas Phase Distances and Angles 388

A.37 $[InCl_5]^{2-}$ Gas Phase Distances and Angles 388

A.38 $[InCl_6]^{3-}$ Gas Phase Distances and Angles 388

A.39 $[Al_2Cl_7]^-$ Gas Phase Distances and Angles 388

A.40 $[Ga_2Cl_7]^-$ Gas Phase Distances and Angles 389

A.41 $[Al_3Cl_{10}]^-$ Gas Phase Distances and Angles 389

A.42 $[Ga_3Cl_{10}]^-$ Gas Phase Distances and Angles 390

A.43 Branched $[Al_4Cl_{13}]^-$ Gas Phase Distances and Angles 390

A.44 Branched $[Ga_4Cl_{13}]^-$ Gas Phase Distances and Angles 391

A.45 Linear $[Al_4Cl_{13}]^-$ Gas Phase Distances and Angles 392

A.46 Linear $[Ga_4Cl_{13}]^-$ Gas Phase Distances and Angles 392

A.47 Evaluated monometallic chlorometallate species in solution 393

A.48 Evaluated monometallic chlorometallate species in solution continued 394

A.49 Evaluated dimetallic chlorometallate species in solution 395

A.50 Evaluated dimetallic chlorometallate species in solution continued I 396

A.51 Evaluated dimetallic chlorometallate species in solution continued II 397

A.52 Evaluated dimetallic chlorometallate species in solution continued III 398

A.53 Evaluated dimetallic chlorometallate species in solution continued IV 399

A.54 Evaluated dimetallic chlorometallate species in solution continued V 400

A.55 Evaluated dimetallic chlorometallate species in solution continued VI 401

A.56 Evaluated trimetallic chlorometallate species in solution 402

A.57 Evaluated Tetrametallic chlorometallate species in solution 403

A.58 $[M_4Cl_{13}]^-$ comparison I 403

A.59 $[M_4Cl_{13}]^-$ comparison II 404

A.60 $[M_4Cl_{13}]^-$ comparison III 404

A.61 M_4Cl_{12} comparison I 404

A.62 M_4Cl_{12} comparison II 404

A.63 M_4Cl_{11} comparison I 404

A.64 M_4Cl_{11} comparison II 405

A.65 M_3Cl_{10} comparison I 405

A.66 M_3Cl_{10} comparison II 405

A.67 M_3Cl_9 comparison I 405

A.68 M_3Cl_9 comparison II 405

A.69 M_2Cl_{10} comparison I 406

A.70 M_2Cl_{10} comparison II 406

A.71 M_2Cl_9 comparison 406

A.72 M_2Cl_8 comparison 406

A.73 M_2Cl_7 comparison 406

A.74 M_2Cl_6 comparison 407

A.75 M_2Cl_5 comparison 407

A.76 M_2Cl_4 comparison 407

A.77 M_2Cl_3 comparison 407

A.78 M_3Cl_9 comparison I 407

A.79 M_3Cl_9 comparison II 408

A.80 $[AlCl_4]^-$ Liquid Phase Distances and Angles 408

A.81 $[GaCl_4]^-$ Liquid Phase Distances and Angles 408

A.82 $[InCl_4]^-$ Liquid Phase Distances and Angles 408

A.83 $[InCl_5]^{2-}$ Liquid Phase Distances and Angles 408

A.84 $[InCl_6]^{3-}$ Liquid Phase Distances and Angles 409

A.85 $[Al_2Cl_7]^-$ Liquid Phase Distances and Angles 409

A.86 $[Ga_2Cl_7]^-$ Liquid Phase Distances and Angles 409

A.87 $[Al_3Cl_{10}]^-$ Liquid Phase Distances and Angles 410

A.88 $[Ga_3Cl_{10}]^-$ Liquid Phase Distances and Angles 410

A.89 Branched $[Al_4Cl_{13}]^-$ Liquid Phase Distances and Angles 411

A.90 Branched $[Ga_4Cl_{13}]^-$ Liquid Phase Distances and Angles 412

A.91 Linear $[Al_4Cl_{13}]^-$ Liquid Phase Distances and Angles 413

A.92 Linear $[Ga_4Cl_{13}]^-$ Liquid Phase Distances and Angles 413

A.93 $[C_2C_1Im][AlCl_4]$ Gas Phase Ion Pair Structures 425

A.94 $[C_2C_1Im][Al_2Cl_7]$ Gas Phase Ion Pair Structures 426

A.95 $[C_2C_1Im][Al_3Cl_{10}]$ Gas Phase Ion Pair Structures 427

A.96 $[C_2C_1Im][Al_4Cl_{13}]_Bra$ Gas Phase Ion Pair Structures 428

A.97 $[C_2C_1Im][Al_4Cl_{13}]_Lin$ Gas Phase Ion Pair Structures 429

A.98 $[C_2C_1Im][GaCl_4]$ Gas Phase Ion Pair Structures 430

A.99 $[C_2C_1Im][Ga_2Cl_7]$ Gas Phase Ion Pair Structures 431

A.100 $[C_2C_1Im][Ga_3Cl_{10}]$ Gas Phase Ion Pair Structures 432

A.101 $[C_2C_1Im][Ga_4Cl_{13}]_Bra$ Gas Phase Ion Pair Structures 433

A.102 $[C_2C_1Im][Ga_4Cl_{13}]_Lin$ Gas Phase Ion Pair Structures 434

A.103 $[C_2C_1Im][InCl_4]$ Gas Phase Ion Pair Structures 435

A.104 $[C_2C_1Im][InCl_5]^-$ Gas Phase Ion Pair Structures 436

A.105 $[C_2C_1Im][InCl_6]^{2-}$ Gas Phase Ion Pair Structures 437

A.106 $[C_2C_1Im][AlCl_4]$ Liquid Phase Ion pair structures 438

A.107 $[C_2C_1Im][Al_2Cl_7]$ Liquid Phase Ion pair structures 439

A.108 $[C_2C_1Im][Al_3Cl_{10}]$ Liquid Phase Ion pair structures 440

A.109 $[C_2C_1Im][Al_4Cl_{13}]_Bra$ Liquid Phase Ion pair structures 440

A.110 $[C_2C_1Im][Al_4Cl_{13}]_Lin$ Liquid Phase Ion pair structures 441

A.111 $[C_2C_1Im][GaCl_4]$ Liquid Phase Ion pair structures 441

A.112 $[C_2C_1Im][Ga_2Cl_7]$ Liquid Phase Ion pair structures 442

A.113 $[C_2C_1Im][Ga_3Cl_{10}]$ Liquid Phase Ion pair structures 442

A.114 $[C_2C_1Im][Ga_4Cl_{13}]_Bra$ Liquid Phase Ion pair structures 443

A.115 $[C_2C_1Im][Ga_4Cl_{13}]_Lin$ Liquid Phase Ion pair structures 443

A.116 $[C_2C_1Im][InCl_4]$ Liquid Phase Ion pair structures 444

A.117 $[C_2C_1Im][InCl_5]^-$ Liquid Phase Ion pair structures 445

A.118 $[C_2C_1Im][InCl_6]^{2-}$ Liquid Phase Ion pair structures 446

A.119 $[C_2C_1Im][M_xCl_y]$ IP Simulated XPS Spectra 473

A.120 $[Choline][M_xCl_y]$ IP Simulated XPS Spectra 474

A.121 $[N_{2110}][M_xCl_y]$ IP Simulated XPS Spectra 475

A.122 $[N_{2111}][M_xCl_y]$ IP Simulated XPS Spectra 476

A.123 Number of IP structures divided into relative Gibbs free energy with respect to the lowest energy structure of each IP in the ranges of ≤ 10, $10 \leq 20$, $20 \leq 30$, $30 \leq 40$, $40 \leq 50$ and $50 <$ in $kJ\ mol^{-1}$ of each $[Choline][M_xCl_{3y}]^{z-}$ IP in the Gas Phase 477

A.124 $[Choline][AlCl_4]$ Gas Phase Ion Pair Structures 478

A.125 $[Choline][Al_2Cl_7]$ Gas Phase Ion Pair Structures 479

A.126 $[Choline][Al_3Cl_{10}]$ Gas Phase Ion Pair Structures 480

A.127 $[Choline][Al_4Cl_{13}]$ Branched Gas Phase Ion Pair Structures 481

A.128 $[Choline][Al_4Cl_{13}]$ Linear Gas Phase Ion Pair Structures 482

A.129 $[Choline][GaCl_4]$ Gas Phase Ion Pair Structures 483

A.130 $[Choline][Ga_2Cl_7]$ Gas Phase Ion Pair Structures 484

A.131 $[Choline][Ga_3Cl_{10}]$ Gas Phase Ion Pair Structures 485

A.132 $[Choline][Ga_4Cl_{13}]$ Branched Gas Phase Ion Pair Structures 486

A.133 $[Choline][Ga_4Cl_{13}]$ Linear Gas Phase Ion Pair Structures 487

A.134 $[Choline][InCl_4]$ Gas Phase Ion Pair Structures 488

A.135 $[Choline][InCl_5]^-$ Gas Phase Ion Pair Structures 489

A.136 $[Choline][InCl_6]^{2-}$ Gas Phase Ion Pair Structures 490

A.137 Number of IP structures divided into relative Gibbs free energy with respect to the lowest energy structure of each IP in the ranges of ≤ 10, $10 \leq 20$, $20 \leq 30$, $30 \leq 40$, $40 \leq 50$ and $50 <$ in $kJ\ mol^{-1}$ of each $[N_{2110}][M_xCl_{3y}]^{z-}$ IP in the Gas Phase 491

A.138 $[N_{2110}][AlCl_4]$ Gas Phase Ion Pair Structures 491

A.139 $[N_{2110}][Al_2Cl_7]$ Gas Phase Ion Pair Structures 492

A.140 $[N_{2110}][Al_3Cl_{10}]$ Gas Phase Ion Pair Structures 492

A.141 $[N_{2110}][Al_4Cl_{13}]$ Branched Gas Phase Ion Pair Structures 493

A.142 $[N_{2110}][Al_4Cl_{13}]$ Linear Gas Phase Ion Pair Structures 494

A.143 $[N_{2110}][GaCl_4]$ Gas Phase Ion Pair Structures 494

A.144 $[N_{2110}][Ga_2Cl_7]$ Gas Phase Ion Pair Structures 495

A.145 $[N_{2110}][Ga_3Cl_{10}]$ Gas Phase Ion Pair Structures 496

A.146 $[N_{2110}][Ga_4Cl_{13}]$ Branched Gas Phase Ion Pair Structures 497

A.147 $[N_{2110}][Ga_4Cl_{13}]$ Linear Gas Phase Ion Pair Structures 498

A.148 $[N_{2110}][InCl_4]$ Gas Phase Ion Pair Structures 498

A.149 $[N_{2110}][InCl_5]^-$ Gas Phase Ion Pair Structures 499

A.150 $[N_{2110}][InCl_6]^{2-}$ Gas Phase Ion Pair Structures 499

A.151 Number of IP structures divided into relative Gibbs free energy with respect to the lowest energy structure of each IP in the ranges of ≤ 10, $10 \leq 20$, $20 \leq 30$, $30 \leq 40$, $40 \leq 50$ and $50 <$ in $kJ\ mol^{-1}$ of each $[N_{2111}][M_xCl_{3y}]^{z-}$ IP in the Gas Phase 500

A.152 $[N_{2111}][AlCl_4]$ Gas Phase Ion Pair Structures 501

A.153 $[N_{2111}][Al_2Cl_7]$ Gas Phase Ion Pair Structures 501

A.154 $[N_{2111}][Al_3Cl_{10}]$ Gas Phase Ion Pair Structures 502

A.155 $[N_{2111}][Al_4Cl_{13}]$ Branched Gas Phase Ion Pair Structures 502

A.156 $[N_{2111}][Al_4Cl_{13}]$ Linear Gas Phase Ion Pair Structures 503

A.157 $[N_{2111}][GaCl_4]$ Gas Phase Ion Pair Structures 503

A.158 $[N_{2111}][Ga_2Cl_7]$ Gas Phase Ion Pair Structures 504

A.159 $[N_{2111}][Ga_3Cl_{10}]$ Gas Phase Ion Pair Structures 504

A.160 $[N_{2111}][Ga_4Cl_{13}]$ Branched Gas Phase Ion Pair Structures 505

A.161 $[N_{2111}][Ga_4Cl_{13}]$ Linear Gas Phase Ion Pair Structures 505

A.162 $[N_{2111}][InCl_4]$ Gas Phase Ion Pair Structures 506

A.163 $[N_{2111}][InCl_5]^-$ Gas Phase Ion Pair Structures 506

A.164 $[N_{2111}][InCl_6]^{2-}$ Gas Phase Ion Pair Structures 507

Abbreviations

1. **HMILs** Halometallate ionic liquids
2. **DES** Deep eutectic solvents
3. **ILs** Ionic liquids
4. **HBA** Hydrogen bond acceptor
5. **HBD** Hydrogen bond donor
6. **IP** Ion pair
7. **GP** Gas phase
8. **LP** Liquid phase
9. **CVD** Chemical vapor depositon
10. **PVD** Plasma vapor deposition
11. **REACH** Registration, evaluation, authoriztion and restriction of chemical substances
12. **RTILs** Room temperature ionic liquids
13. **LTILs** Low temperature ionic liquids
14. **TSILs** Task specific ionic liquids
15. **DFT** Density functional theory
16. **HF** Hartree-Fock
17. **MNDO** Modified neglect of differential overlap
18. **MD** Molecular dynamics
19. **QM** Quantum mechanics
20. **DSC** differential scanning calorimetry
21. **FAB** Fast atom bombardment
22. **ESI** Electrospray ionization
23. **gLA** Global Lewis acidity
24. **eLA** Effective Lewis acidity
25. **iLA** Intrinsic Lewis acidity
26. **AN** Acceptor number
27. **LUMO** Lowest unoccupied molecular orbital
28. **HOMO** Highest occupied molecular orbital
29. **HSAB** Hard and soft acids and bases
30. **TEPO** triethyl phosphine oxide
31. **EW** Electrochemical window
32. **AO** Atomic orbital

33. **LCAO** Linear combination of atomic orbitals
34. **MO** Molecular orbital
35. **KS** Kohn-Sham
36. **SCF** Self-consistnet Field
37. **LDA** Local density approximation
38. **LSDA** Local spin density approximation
39. **GGA** Generalized gradient approximation
40. **mGGA** meta-generalized gradient approximation
41. **SIE** Self interactione error
42. **GH** Global hybrid
43. **CBS** Complete basis set
44. **BSSE** Basis set superposition error
45. **RSH** range-separated hybrid
46. **GTO** Gaussian-type orbital
47. **STO** Slater-type orbital
48. **ECPs** Effective core potential
49. **CCP** core-polarization potential
50. **MPs** Model potentials
51. **PPs** Pseudopotentials
52. **NAC** Net atomic charge
53. **NPA** Natural population analysis
54. **ADCH** Atomic dipole corrected Hirshfield charges
55. **ChelpG** Charges from electrostatic potentials using a grid based method
56. **MEP** Molecular electrostatic potential
57. **QTAIM** Quantum theory of atoms in molecules
58. **AIM** Atoms in molecules
59. **CP** critcal point
60. **BCP** Bond critical point
61. **NCI** Non-covalent interaction
62. **IRI** Interaction region indicator

Chapter 1

Introduction

HMILs (Halometallate Ionic Liquids) are an exciting class of highly tunable solvents which are being explored for novel applications and as greener alternatives to conventional solvents in specific contexts.[1] Research into HMILs has steadily increased over the past 40 years, with a predominant focus on their utilization as mediums for electrochemistry[2], catalysis[1], and as electrolytes in batteries.[3]

HMILs are a subclass of ILs (ionic liquids) and DESs (deep eutectic solvents). ILs are salts composed of discrete anions and cations which are liquid below 373 K.[4] DES are eutectic mixtures of Brønsted or Lewis acids and bases. The acids can function as hydrogen bond donors (HBDs) and the bases can function as hydrogen bond acceptors (HBAs).[5,6] HMILs have been described as both ILs and DES due to the intersectionality between the definitions of the ions of ionic liquids and HBAs in DES precursors, as shown in figure 1.1.[7]

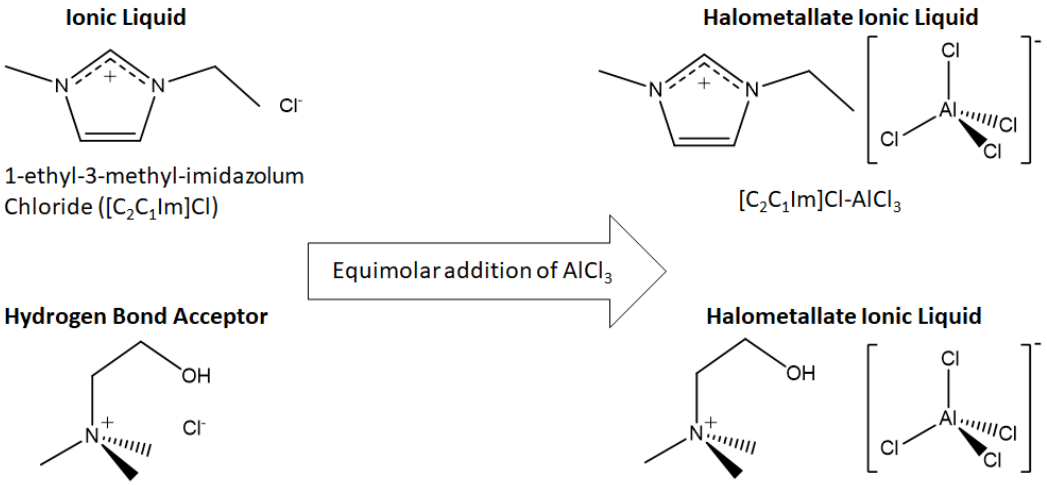


Figure 1.1: Examples of an ionic liquid ($[C_2C_1Im]Cl$) and a hydrogen bond acceptor ([Choline]Cl) and the resulting Halometallate ionic liquids ($[Cat]Cl\text{-}AlCl_3$) upon the addition of equimolar amount of metal halide ($AlCl_3$)

Physio-chemical properties of HMILs can be tuned by altering their anionic speciation. Anionic speciation, the distribution of anionic species that form under defined conditions, is predominantly controlled through the ratio of chloro-organic salt to metal halide. Understanding the correlation of anionic speciation and the physio-chemical properties is the key to unlocking the technological potential of HMILs.[1]

HMILs have proven advantages which are exemplified by their use in industry and technological potential showcased by the many studies on HMILs. Electrodeposition from HMILs is appealing as the deposition morphology of metals and alloys can be controlled through anionic speciation. Additionally metals which are

conventionally hard to deposit from aqueous mixtures like aluminum can be readily deposited from HMILs without the need for a mixture of organic solvents and toxic complexing agents.[2] Industrially HMILs have prominently been used as catalysts in the Dimersol process developed by the Institute Francais Petrol.[8] The Dimersol process uses $[C_2C_1im]Cl–NiCl_2–AlEtCl_2$ to catalyze the dimerization of alkenes; propene and butene to hexene and octene. The high abundance and redox properties of aluminum have made it one of the candidates to supplant lithium for the use in modern batteries. Chloroaluminate ILs function as electrolytes in second generation aluminum dual-ion batteries which are currently under development.[3]

The research presented in this thesis is of a computational investigation into chlorometallate ILs featuring the group 13 metals; aluminum, gallium and indium. The anionic speciation and the corresponding properties are initially studied in the system featuring the $[C_2C_1Im]^+$ (1-Ethyl-3-Methyl-Imidazolium) cation and is then extended to a comparison with the $[Choline]^+$, $[N_{2110}]^+$ (Ethyl-Dimethyl-Ammonium) and $[N_{2111}]^+$ (Ethyl-Trimethyl-Ammonium) cations.

The thesis is subdivided into eight chapters as outlined in figure 1.2. The introduction aims to give a comprehensive overview of the research in the field while highlighting challenges in the development of technologies and understanding. The current state of understanding of HMILs; HMIL speciation, corresponding chemical properties, techniques of speciation, relevant chemistry and applications are discussed.

In the second chapter the theoretical background of the computational techniques employed in this investigation are examined. The aim is to describe density functional theory (DFT) and the analytical techniques which are used to evaluate chemical interactions such as AIM analysis and a variety of reduced density gradient analyses. The third chapter describes the details of the specific methods used in this investigation; how calculations were set up, the selection of structures for further analysis and workflows to achieve the desired goals.

Chapters four through seven are the results chapters composed of the original contributions. Chapter four encompasses the exploration of structure, focusing on the search for stable conformers among the isolated group 13 chlorometallate species and cations, alongside an in-depth discussion concerning the chemical structure of these identified stable conformers. Chapter five discusses the electronic structure of the chlorometallate anion and cation conformers which were found to be stable. Chapter six presents an evaluation of the ion pair (IP) structures of group 13 chlorometallates paired with the $[C_2C_1Im]^+$, $[Choline]^+$, $[N_{2110}]^+$ and $[N_{2111}]^+$ cations. The intermolecular interactions between the chlorometallate anions and the $[C_2C_1Im]^+$, $[Choline]^+$, $[N_{2110}]^+$ and $[N_{2111}]^+$ cations is discussed. Chapter seven discusses the anionic speciation based on the thermochemistry of the isolated anions and the IP structures. Chapter

eight summarizes the key findings from the original contributions and suggests further investigations to carry out.

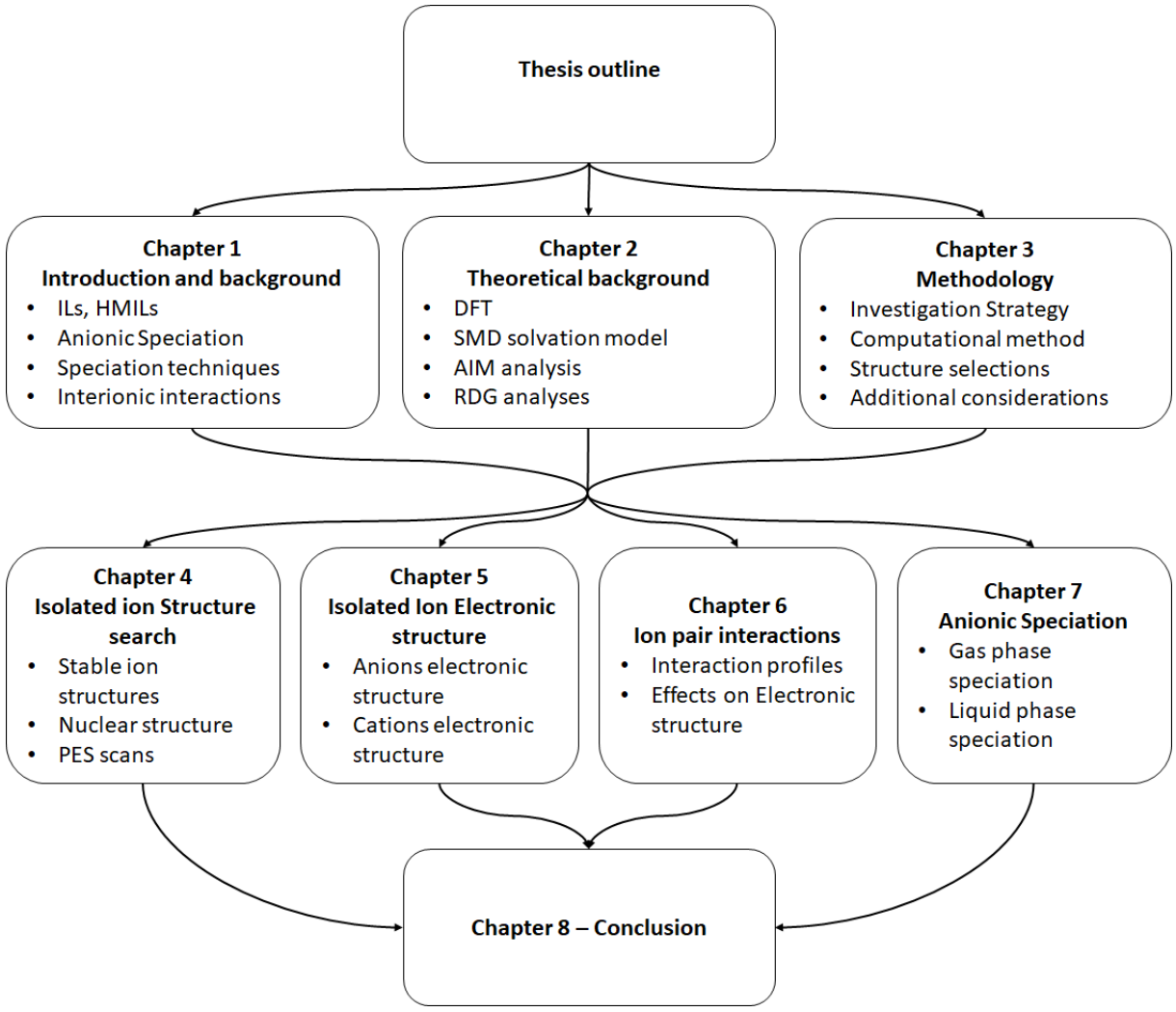


Figure 1.2: Thesis structure schematic highlighting key topics in each chapter

1.1 The motivation to research halometallate ionic liquids

The objective of this section is to elucidate the significance of studying HMILs. To achieve this, the advantages of utilizing HMILs in the context of sustainability and the fundamental concepts associated with the industrial applications of HMILs are discussed. An overview of the industrial standards in electrodeposition, catalysis and electrochemical batteries is introduced and compared to the current state of HMIL research in each field. The sections on each application discuss the advantages and shortcomings

of competitive technologies for each application. The technological benefit of using HMILs and the challenges in the development of new technologies are highlighted for each application.

Since the early 1990s research into sustainable solutions has experienced amplified growth due to a growing societal awareness of the depletion of natural resources and the impact of environmental degradation associated with industrialization.[9] In the chemical industry solvents play a crucial role in many processes accounting for 85-90% of the mass used and between 80-85% of the waste produced by the chemical industry.[10] Hence the development of novel solvents, and understanding the associated chemistry and environmental impact, is important in developing sustainable alternatives for chemical industry. HMILs are novel solvents which could also replace conventional volatile and hazardous solvents.[1]

There are multiple advantages to using HMILs for different applications which go beyond their use as a solvent. HMILs are attributed with several attractive properties for both electrochemistry and catalysis, namely low vapor pressure, thermal stability, a tunable electrochemical window, and tunable acidity. The previously mentioned properties should not be assumed and every newly synthesized IL should be evaluated for properties of interest. In electrochemical processes HMILs can be used as electrolytes.[2] In catalytic processes HMILs function as solvents and catalysts and can be used to separate reactants from products through phase separation of the HMIL liquid phase and the product liquid phase.[1]

1.1.1 Electrodepostion

Electrodeposition is the process of depositing of metals onto a substrate cathode through the reduction of metal cations in a solution through the application of an electrical current (figure 1.3). A positive erodible anode composed of the metal to be electroplated, an electrolyte solution or fluid with analogous metal ions and counter ions, a cathode onto which the metal will be coated, a container and an electrical current are the components required for electrodeposition. Electrodeposition is primarily used to modify the surface properties of an object to make it corrosion resistant, wear resistant or more aesthetic.[2] Commercial electroplating commonly includes toxic complexing agents which allow for control over the surface morphology of the deposit. Al, Cr, Ni, Cu, Au, Ag, Zn, Cd, Ti metals as well as various zinc and copper alloys are commercially plated.[11]

Industrial electrodeposition has to compete with alternative coating technologies such as plasma vapor deposition (PVD)[12,13] and chemical vapor deposition (CVD).[14,15] PVD and CVD allow for the deposition onto various substrates (ceramic, plastic, glass, metals and others) and are not limited to the deposition of metals and alloys. Organic moieties like oxides, nitrides and carbides can be deposited onto a surface matrix.

PVD and CVD are technically interesting but are limited by the requirement for high capital investment and the difficulty of applying thick coatings, confining their application to high value niche products.[2]

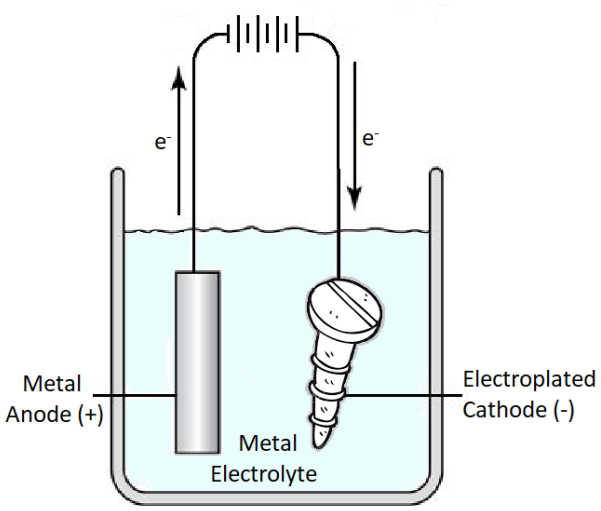


Figure 1.3: Diagrammatic representation of the electrodeposition of Zinc onto a screw (cathode) using a zinc anode in an aqueous zinc chloride solution[2]

Electroplating using aqueous solutions has been successfully commercialized because of; low cost, non-flammability, high solubility of metal salts and electrolytes, high conductivities, and high rates of mass transfer of water.[11] However, there are several limitations to using aqueous solutions for electrodeposition. The limited potential window of water limits the range of metals that can be deposited. Incorrect handling of gas evolution can lead to hydrogen embrittlement of electrodes. Passivation of metals can occur at both electrodes rendering them useless through the formation of an oxide layer. Toxic complexing agents like cyanide are often required and water used in the electroplating process has to be chemically treated before discharge.[2]

Environmental directives such as Registration, evaluation, Authorization and Restriction of Chemical substances (REACH) in the European union are key drivers for the development of alternative coating technologies.[16] Commercially employed technologies can be adversely impacted by some REACH directives and hence there is a need for modern alternatives based on cleaner, less toxic and more environmentally friendly electrolytes. The limited number of metals which can be deposited from aqueous solutions motivate research into alternative solvents, in addition to the desire to deposit more exotic metals and alloys.[2]

A variety of alternatives to aqueous solutions can be used for electrodeposition but they must satisfy several

prerequisites. A non-aqueous medium has to be an electrolyte solution composed of polar solvent molecules, preferably of low molecular weight and volume to maximize fluidity in order to optimize mass transfer.[17] A larger potential is required for the reduction of complexes in polar organic solvents which makes most electrodeposition from polar organic solvents unviable for commercial applications. A number of metals have been deposited from polar organic solutions but no advantages over aqueous solutions have been determined, with one exception.[2]

Aluminum, which cannot be deposited from aqueous solvents, can be deposited from polar organic solvents because of the high reduction potential of aluminum, 1.67 V vs SHE. The wide electrochemical window of aromatic hydrocarbon solutions allows for the deposition of Ti and Al.[2] The SIGAL Process uses toluene as a solvent and is the only process used to electroplate Al commercially.[18–20]

Another alternative to aqueous and organic solvents for electrodeposition are ionic fluids or molten salts.[2] In the electrowinning industry the extraction of metals from ores or alloys makes use of the electrodeposition process. After a chemical reagent is used to leach a metal from the ore, it is purified by deposition onto a cathode. Electrowinning is commonly carried out in high temperature molten salts in order to extract Li, Na, Ti and Al.[21–23] Molten salts have a number of attractive properties for electrodeposition; high conductivity, metal salts are highly soluble, and molten salts feature a wide electrochemical window. However, molten salts as a medium require high operating temperatures which are expensive to maintain and limit the substrate choice.[2]

ILs offer an opportunity to utilize a fluid with the advantages of a molten salt, while negating the problems associated with high temperature operating conditions.[2] The possibilities to work with water sensitive metals for deposition or the deposition on water sensitive substrates, like depositing Al onto Zn opens up possibilities for new materials for conduction and surface plating.[24] The controlled deposition of semiconductors by depositing mixtures of group III, IV and V metals from ILs, provides a more efficient route for the generation of super fine tuned semi-conductor structures.[2] The ability to deposit Si[25,26], Ge[26], Ga[27] and In[28] and variations of Alloys such as Si_xGe_{1-x}[26], Sb-Te[29,30] and CdS[31] from ILs has been shown. The tunable deposition of nanostructures via ILs has also been explored for the generation of catalytic surfaces and sensors.[32–34]

1.1.2 Battery technology

Electrical batteries are composed of one or multiple conjoint electrochemical cells. Each electrical cell is composed of a positive cathode and a negative anode separated by an electrolyte as depicted in figure

1.4. Charging and discharging of an electrical battery relies on the electronic potential generated by the oxidation and reduction of the energy carrier.[35] Lithium-ion batteries are currently the industry standard in electrochemical energy storage.[36]

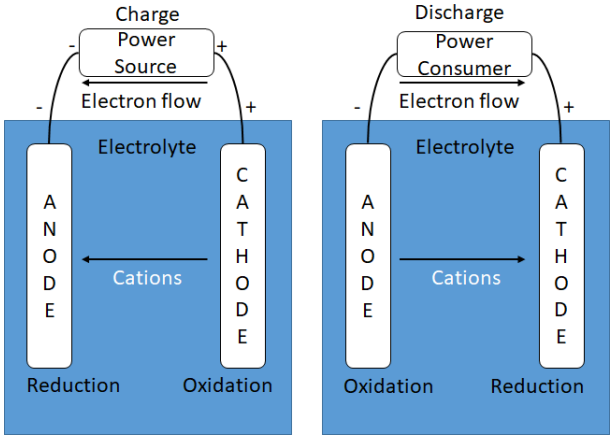


Figure 1.4: Diagrammatic representation of charge and discharge in an electrical Battery[3]

In a lithium-ion battery the high standard electrode potential of -3.04 V is leveraged to store potential energy.[36] During charging lithium is oxidized at the cathode to Li^+ cations, which move to the anode through the electrolyte, and an electrons (e^-) move through the external circuit. The Li^+ cations and free electrons are stabilized at the anode through intercalating into a graphite matrix. Upon connection to an external circuit discharge takes place in which lithium cations move back to the cathode through the electrolyte and spontaneously reduce to lithium metal while the electrons move through the external circuit providing power. Modern lithium-ion batteries feature additional technological nuances to make them work more effectively which are covered in a comprehensive review by Yi-Chun et al.[37]

The industrial scale production of lithium ion-batteries are limited by the scarcity of lithium.[38] Thus the development of battery technologies utilizing more abundant resources such as aluminum is desirable. Aluminum is the third most abundant element in the earth's crust, making up roughly 8.3% of it. Al also has a high energy density (13.36Wh cm^{-3})[39] and high theoretical volumetric capacity (8.05 Ah cm^{-3}).[39] The high theoretical energy density and theoretical volumetric capacity even outperform lithium which has values of 6.20Wh cm^{-3} and 2.04 Ah cm^{-3}, respectively. Research into aluminum based batteries has been invigorated as a sustainable alternative to lithium-ion batteries because of the abundance and favorable attributes of aluminum.[39]

Batteries utilizing chloroaluminate ILs as an electrolyte in conjunction with an aluminum electrode are

second generation aluminum batteries. Chloroaluminate ILs are aprotic solvents, non-corrosive and have a high resilience against oxidation and reduction and can be used to dissolve and deposit aluminum which make them appealing to use as battery electrolytes.[39] In 2015 a breakthrough was made in which an aluminum metal electrode in conjunction with a three dimensional graphitic foam and a chloroaluminate electrolyte was used.[40] The voltage of the aluminum-chloride-graphite battery, referred to as dual-ion battery, is determined by the chloroaluminate electrolyte as it participates in the electrochemical reaction. The redox reaction mechanism involves the deposition and stripping of Aluminum at the anode and the interchelation of $[AlCl_4]^-$ into the cathode highlighted in equations 1.2.1 and 1.2.2.[38]

$$Al + 7[AlCl_4]^- \longleftrightarrow 4[Al_2Cl_7]^- + 3e^-(anode) \tag{1.1.1}$$

$$C_n[AlCl_4] + e^- \longleftrightarrow C_n[AlCl_4]^-(cathode) \tag{1.1.2}$$

The dual-ion cells feature novel ideas but do not leverage the full potential of the aluminum redox process due to the monovalency of the species involved. Consequentially only low capacity electrodes could be achieved (<100 mAh g^{-1}).[38] Due to the tetrahedral $[AlCl_4]^-$ anion being relatively bulky the interchelating process at the anode has an adverse effect on the energy density capping the cells at 70 mAh g^{-1} versus aluminum batteries potential 2.98 Ah g^{-1}.[38] The issue is prominent in many examples featuring chloroaluminate electrolytes and requires the development of a matrix which can stabilize Al^{3+} in the cathode.[38,39]

1.1.3 Catalysis

Catalysis is the process in which the activation energy, E_A, of a chemical reaction is lowered by introducing a suitable catalyst as shown in figure 1.5.[41]

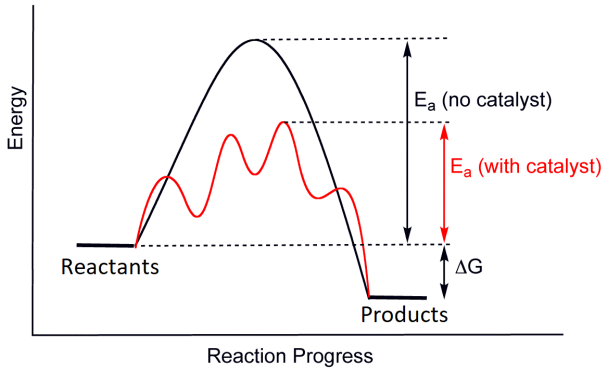


Figure 1.5: Diagrammatic representation of the effect of a catalyst on the activation energy of a reaction[1]

Catalysts are widely used, being involved in the production of approximately 80% of all consumer goods and 90% of all chemical transformations on the industrial level.[42] Broadly speaking catalysts fall into two categories; homogeneous and heterogeneous catalysts. Homogeneous catalysts are usually small organic molecules or inorganic complexes that are in the same phase as the chemical reaction which they are catalyzing while heterogeneous catalysts are in a different phase from the reaction.[41] Familiar homogeneous catalysis processes include Friedel-crafts alkylation and acelyatios which use $AlCl_3$ as a homogeneous catalyst.[43] The most famous heterogeneous catalytic process is the Haber-Bosch process which uses a promoted iron catalyst to convert hydrogen and nitrogen into ammonia.[44]

HMILs can be utilized for catalysis and have several beneficial attributes. The acidity of HMILs is controllable and adjustable during chemical reactions. The tunable acidity can be leverages to facilitate successive reactions in the same environment. Metal complexes have a high solubility in HMILs and the medium can hence function as a co-catalyst or as ligands to enable alternative reaction pathways.[1] Non-polar hydrocarbons are generally less soluble in HMILs and hence a synthesis method can be designed which separates the product from the reaction phase allowing for simple separation methods. The afore mentioned dimersol process is the most prominent catalytic method using HMILs.[8]

1.2 Halometallate Ionic Liquid Chemistry

The next section aims to give a clearer understanding of what HMILs are and how HMIL chemistry underpins their useful characteristics and makes them tunable. Two prerequisite concepts, ILs and DESs, are discussed first to give insight into the nuances of HMIL chemistry.

1.2.1 Ionic liquids

Ionic liquids (ILs) are a subclass of molten salts that are typically liquid below 373 K of which a large subclass are room temperature ionic liquids (RTILs) which are liquid at 298 K. Another subclass are low temperature Ionic liquids (LTILs) which are liquid below 133 K. In contrast to salts like sodium chloride (NaCl), which are made up of distinct spherical ions that arrange into a crystal lattice, ILs are composed of bulkier ions, as depicted in figure 1.6, which frustrate the formation of a crystal lattice. Typically, one ion present is a bulky organic or inorganic ion and one or both ions have a delocalized charge. The bulky ions and charge delocalization lower the coulombic interaction between ions which leads to small lattice enthalpies. The ILs constituent ion size variation and conformational flexibility leads to significant entropy which also favors the

liquid phase. The small lattice enthalpy and liquid phase entropy contributions give rise to the low melting point of ILs. The thermodynamic preference for the liquid state, arising from the enthalpic and entropic contributions, is expressed by the Gibbs free energy of fusion $\Delta_{fus}\mathrm{G}^o$ $(IL_{(S)} \rightarrow \mathrm{IL}_{(L)})$ being negative below 373 K for ILs.[4]

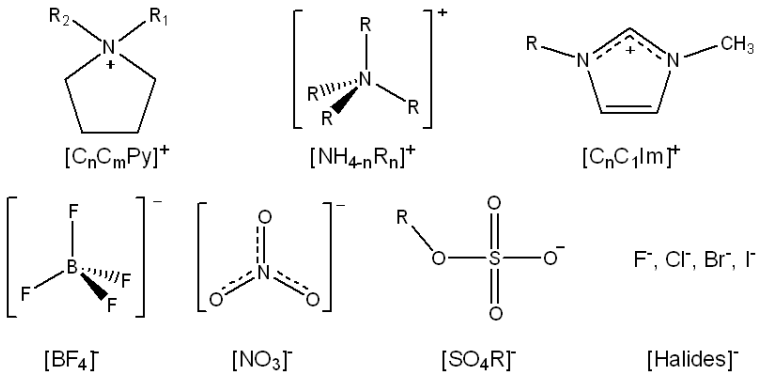


Figure 1.6: selected IL cations (top); Dialkylpyrrolidinium, Alkylammonium, Alkylmethylimidazoilium and anions (bottom); Tetrafluoroborane, Nitrate, Alkyl sulfate and Halides

ILs are generally attributed with non-flammability, non-volatility and are said to be stable when exposed to air and water, however these properties should not be inherently assumed when synthesizing a new IL. Properties of ILs can be tailored to a particular task through the choice of anion or cation. the constituent anions and cations of ILs can be amended with a particular functional group to incorporate a particular property or reactivity. Task-specific ILs (TSILs) are ILs embedded with a particular functional group which allows them to interact with a specific target analyte.[45,46] ILs have been touted as 'designer solvents' and 'solvents of the future' because their tunable properties via the choice from a multitude of anions and cations as well as the ability to functionalize ILs. In principle every application could have a tailor made IL.[47]

ILs have wide electrochemical windows and coordinating anions with a high activity, analogous to molten salts, with the additional benefit of being usable at low operating temperatures. Similarly to molecular solvents various chemical interactions can be facilitated between an IL and a solute which allows for more control over the solvation environment if understood and leveraged correctly.[4] The variety of chemical interactions occurring in ILs such as H-bonding, van der Waals interactions and aromatic interactions in addition to the ionic interactions add additional nuance to the chemistry of ILs. The interactions in ILs become apparent when comparing IL chemistry to molten salt chemistry. The variety of chemical interactions in ILs can enhance ILs tunability.[47]

ILs have been studied extensively and the history[4] and synthesis[48,49] of ILs is covered in popular reviews.

ILs have been industrially employed, with BASFs BASIL process being the most well-known industrial utilization of ILs.[50] In the BASIL process Imidazole acts as a proton scavenger while phenyl-chlorophosphines and alcohols produce phosphines. In the commercialized Dimersol process a Lewis acid catalyst dimerizes butene to produce C_8 olefins which are further converted to C_9 alcohols used in plasticizer manufacture.[8] Other applications of ILs include electrolytes in batteries, supercapacitors, dye-sensitized solar cells, and as engineering liquids for gas storage, actuators and lubrication. A more comprehensive and detailed list of applications is covered in numerous reviews.[50–52] Electrodeposition using ILs has not been commercialized but successful electroplating using ILs has been carried out beyond lab scale.[2]

1.2.2 Deep eutectic solvents

DESs are eutectic mixtures of Lewis or Brønsted acids and bases. A eutectic mixture is a mixture of two compounds which has a melting point that is lower than that of the constituent compounds. The mixture of A and B in figure 1.8 represents a DES with a single eutectic point but some DES are known to have more than one eutectic point.[5] One differentiating factor between DESs and ILs is the diversity of species which form upon the mixing of the individual compounds. ILs are composed of a discrete anion and a discrete cation. In contrast to an IL, the composition of a DES can include various anions and/or cations. Literature distinguishes between a DES and an IL depending on the capacity of the constituents to function as HBD and HBA (DES) or not (ILs).[53]

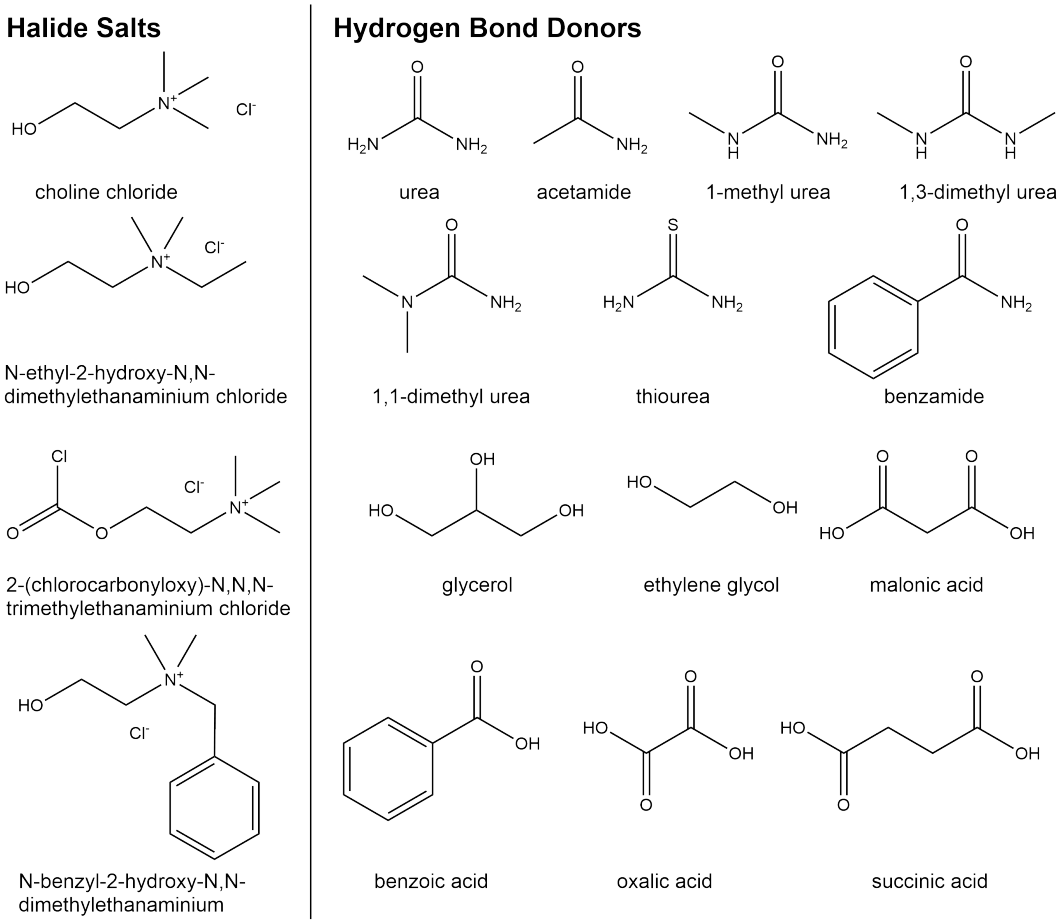


Figure 1.7: Selected halide salts and hydrogen bond donors

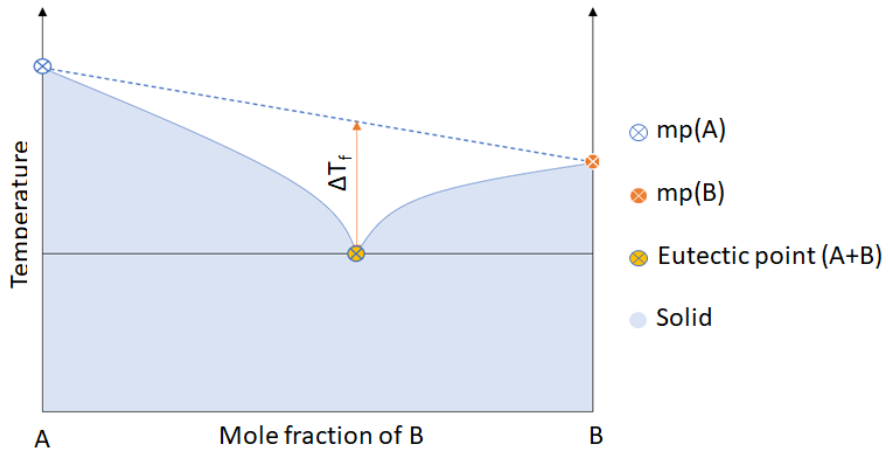


Figure 1.8: The eutectic behavior of the mixture of compounds A and B described with respect to the temperature (Y axis) and the composition of the mixture (X axis)

DESs, like ILs, are composed of large, unsymmetrical ions that frustrate the formation of a crystal lattice. DES are generated upon mixing an organic halide salt, acting as a Lewis base, with a metal salt or a hydrogen bond donor (HBD) functioning as a Lewis acid (figure 1.7).[53] The classical understanding is that the charge delocalization upon complexation of the Lewis acid and base leads to a lowered melting point of the mixture relative to the melting points of the constituent components. More recent investigations have found that the variety of H-bonds engaging in competitive interactions impacts the entropy of the systems which in turn contributes to the eutectic nature of DES.[54]

Generally, DES are described through the formula:

$$Cat^+X^-zY \tag{1.2.1}$$

where Cat^+X^- is the salt composed of the cation, Cat^+, which is commonly a quaternary ammonium, phosphonium or sulfonium cation and X^- which is commonly a halide anion or an alternative Lewis base functioning as HBA. Y is commonly a metal chloride or a HBD, functioning as a Lewis or Brønsted acid and z quantifies the relative number of acidic molecules interacting with one base molecule on average.[5]

DES can be further subdivided into five different classes summarized in table 1.1[5]

Table 1.1: Types of deep eutectic solvents

Type	Composition	General formula	Species:
I	Lewis basic salt + metal halide	$Cat^+X^-zMY_x$	M = Zn, Sn, Fe, Al, Ga, In
II	Lewis basic salt + metal halide hydrate	$Cat^+X^-zMY_x.yH_2O$	M = Cr, Co, Cu, Ni, Fe
III	Lewis basic salt + HBD	Cat^+X^-zRZ	Z = CONH2, COOH, OH
IV	metal halide hydrate + HBD	$MY_x + RZ = MY^+_{x-1} \cdot RZ + MY_{x+1}$	M = Zn & Z = $CONH_2$, OH
V	non ionic HBD + non ionic HBA	R_1-OH + R_2	R_1-OH = Thymol R_2 = CH_3OH

Type I DES are conceptually the simplest DESs made up of a Lewis base containing salt which complexes with a metal chloride according to equation 1.2.1 in the presence of a cation. Depending on the ratio of

metal halide to Lewis basic salt the anionic speciation of Type I DESs is a discrete anion or multiple anions in equilibrium. The chemistry of type I DESs are defined by the different halometallate anions which can form.[5]

Type II DES expand the variety of eutectics by using hydrated metal chloride salts. Type II DES are particularly interesting because of low cost and stability with respect to air and water, making type II DES compelling for industrial employment.[5]

Type III eutectics are composed of a HBD and a Lewis base containing salt. Type III DESs have been studied with a wide range of HBDs but typically choline chloride is used as a Lewis base containing salt. Type III eutectics are good solvents for transition metal complexes but have a smaller electrochemical window which limits the types of metals which can be deposited. The large variety of HBDs as illustrated in figure 1.7 can be modulated in their organic structure adding more versatility to type III DES. Type III eutectics have been explored for synthesis of cellulose derivatives, metal oxide processing and the removal of glycerol from biodiesel.[5]

Type IV DES are composed of a HBD and a metal chloride. Type IV DES have been explored sparingly with known type IV species being limited to $ZnCl_2$ in conjunction with urea, acetamide, ethylene glycol and 1,6-hexadiol. Furthermore no notable applications have yet been explored.[5]

Type V DESs are the newest class of DESs. Type V DESs are mixtures of nonionic HBDs and HBAs which are currently being explored. The most prominent examples are mixtures of thymol with lidocaine and methanol.[55]

The synthesis of DESs is simple, usually only requiring the mixing of two chemicals under mild heat. The simple synthesis is a huge benefit of DESs for any application.[6] DESs also do not have to be registered as new chemicals as DESs are simply a composition of two already registered chemicals making them legislatively easier to employ. DES water insensitivity also make them industrially viable as the water content can also help modulate the deposition process favorably.[2] Another benefit of using DESs for electrodeposition is the control of deposition morphology and the electrodeposition process through the ionic speciation, anionic for Types I-III and cationic for type IV eutectics.[2]

1.2.3 Halometallate ionic liquids

Halometallate Ionic liquids (HMILs) are considered as both type I DES and ILs as they can be synthesized from halo-organic salts and metal halides or HBAs and metal chlorides, respectively. HMILs are generated

through mixing metal halides and halo-organic salts. The ratio of the metal halide to halo-organic salt determines the anionic speciation. A number of chemical properties of a HMIL are in turn determined by the anionic speciation.[1]

For example, upon mixing aluminum chloride, $AlCl_3$, and the chloro-organic salt 1-ethyl-3-methyl-imidazolium chloride, $[C_2C_1Im]Cl$, the system formed is denoted $[C_2C_1Im]Cl$-$AlCl_3$. The ratio of $[C_2C_1Im]Cl$ to $AlCl_3$ is the primary variable which determines anionic speciation. The ratio between metal halide and halo-organic salt is expressed a mole fraction of the metal halide, x_{MX_n} in the system, i.e. x_{AlCl_3} for a chloroaluminate system. At an equimolar ratio of $[C_2C_1Im]Cl$ to $AlCl_3$ the mole fraction of $AlCl_3$ is $x_{AlCl_3} = 0.5$. The anionic speciation in the chloroalluminate system is controlled by equilibriums between monometallic, dimetallic, trimetallic and tetrametallic chloroalluminate species. Table 1.2 summarizes the anionic species which form in the $[C_2C_1Im]Cl$-$AlCl_3$ system upon increasing x_{AlCl_3}.[1]

Table 1.2: Equilibriums and speciation of chloroaluminate ionic liquids at $x_{AlCl_3} = 0.5$, 0.67, 0.75 and 0.8

Formula	$[C_2C_1Im]Cl$: $AlCl_3$ ratio	x_{AlCl_3}
$[C_2C_1Im][Cl] + AlCl_3 \rightleftharpoons [C_2C_1Im][AlCl_4]$	1:1	0.5
$[C_2C_1Im][AlCl_4] + AlCl_3 \rightleftharpoons [C_2C_1Im][Al_2Cl_7]$	1:2	0.67
$[C_2C_1Im][Al_2Cl_7] + AlCl_3 \rightleftharpoons [C_2C_1Im][Al_3Cl_{10}]$	1:3	0.75
$[C_2C_1Im][Al_3Cl_{10}] + AlCl_3 \rightleftharpoons [C_2C_1Im][Al_4Cl_{13}]$	1:4	0.8

Three of the four chloroaluminate structures which form upon oligomerization are shown in figure 1.9 below.

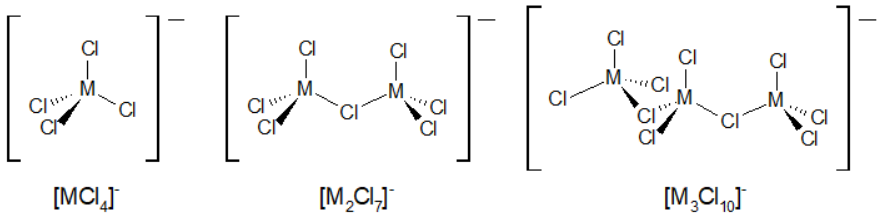


Figure 1.9: Different $[M_nCl_{3n-1}]^-$ structures that form at different x_{MCl_3}

The description of the chloroaluminate species which form via the formulas expressed in table 1.2 are instructive but the description of the system is incomplete as the species are usually in equilibrium with one another. The two exceptions are when $AlCl_3$ is equimolar to $[C_2C_1Im]Cl$ and when no $AlCl_3$ has been introduced. The anionic speciation of the $[C_2C_1Im]Cl$-$AlCl_3$ system has been characterized with respect to

different x_{AlCl_3} which can be seen in the figure 1.10. figure 1.10 shows the systems anionic speciation upon changing x_{AlCl_3}.[56]

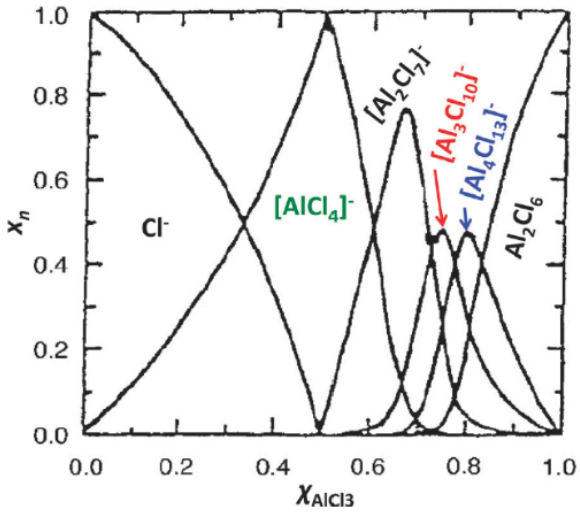


Figure 1.10: $[C_2C_1Im]Cl\text{-}AlCl_3$ anionic speciation with respect to x_{MCl_3}[56]

Up to $x_{AlCl_3} = 0.5$ only $[AlCl_4]^-$ and Cl^- are in equilibrium with the chloride ions being consumed as more $AlCl_3$ is introduced into the system. At exactly $x_{AlCl_3} = 0.5$, $[AlCl_4]^-$ is the only anionic species present. Between $x_{AlCl_3} = 0.5$ and $x_{AlCl_3} = 0.67$, $[Al_2Cl_7]^-$ starts forming and becomes the predominant species around $x_{AlCl_3} = 0.6$. However $[Al_2Cl_7]^-$ is never the sole species in the system is always in an equilibrium with other anions. Low amounts of $[Al_3Cl_{10}]^-$ start forming around $x_{AlCl_3} = 0.55$ while $[Al_4Cl_{13}]^-$ starts to form around $x_{AlCl_3} = 0.65$. Insoluble Al_2Cl_6 starts to precipitate above $x_{AlCl_3} = 0.67$ and thereby regulates the amount of aluminum chloride dissolved in the system.[1]

The anionic speciation of a HMIL, such as the one described for the $[C_2C_1im]Cl\text{-}AlCl_3$ system, is determined by the metal coordination number and anionic oligomerization which in turn depends on the mol fraction of metal halide introduced, x_{AlCl_3}, the halide already present in the halide salt/IL, the metal center coordination chemistry and the metal center oxidation state. Hence, each system has a unique anionic speciation profile with respect to x_{MX_n}.[1]

The physical and chemical properties of HMILs relate directly to the anionic speciation which in turn depends on x_{MX_n}. Lewis acidity, the susceptibility to react with water (hydrophilicity), electrical conductivity, viscosity and melting point all depend on the anionic speciation. A full understanding of the electrochemical and catalytic process which can occur in HMILs requires an understanding of the anionic speciation and the corresponding properties. In electrochemical processes ligands binding to a metal alter the redox potential,

electrode kinetics, structure of the solid-liquid interface among other parameters. The design of industrially competitive electrochemical and catalytic applications requires an understanding of the effects of speciation on redox properties and acidity.[1,2]

1.3 Speciation in group 13 halometallate ionic liquids and methods of determining anionic speciation

Controlled speciation is a highly desirable attribute in solvents for electrochemical and catalytic processes. For example, aqueous solvents suffer from requiring strong ligands and consequentially undesirable reagents such as cyanides or high concentrations of ligands to facilitate controlled speciation. ILs can incorporate desired ligands into their chemical matrix while allowing rigorous control over water content and activity.[1] The relationship between speciation and various properties is illustrated in the figure 1.11.

Chloroalluminate anionic speciation profiles, as depicted in figure 1.10 for $[C_2C_1im]Cl\text{-}AlCl_3$, have been rigorously elucidated and facilitate a solid basis upon which application focused studies are carried out.[56] The anionic speciation of most HMILs is not understood as well as the speciation in chloroalluminate systems, hence further investigation is required to attain an understanding on par with that of chloroalluminate speciation for all HMILs.

The experimental study of anionic speciation can be carried out in all phases. However, liquid phase speciation analysis is preferable as phase changes can perturb the anionic speciation and the applications of ILs require the speciation to be understood precisely in the liquid phase.[1] The analysis of liquid phase anionic speciation can be carried out using Raman[57] or infrared spectroscopy (IR)[58] , Nuclear magnetic resonance (NMR)[59,60] , electron paramagnetic resonance (EPR)[61–63], x-ray photoelectron spectroscopy (XPS)[64], x-ray absorption spectroscopy (XAS)[65], ultra violet/visual spectroscopy[1], bulk property measurements[1] and neutron scattering.[66,67] Analytical techniques used to determine anionic equilibria can simultaneously interrogate bulk properties and macromolecular arrangements of HMILs. The simultaneous interrogation of anionic speciation and the HMILs properties at a given speciation gives insight into the relation between properties and anionic speciation.[1]

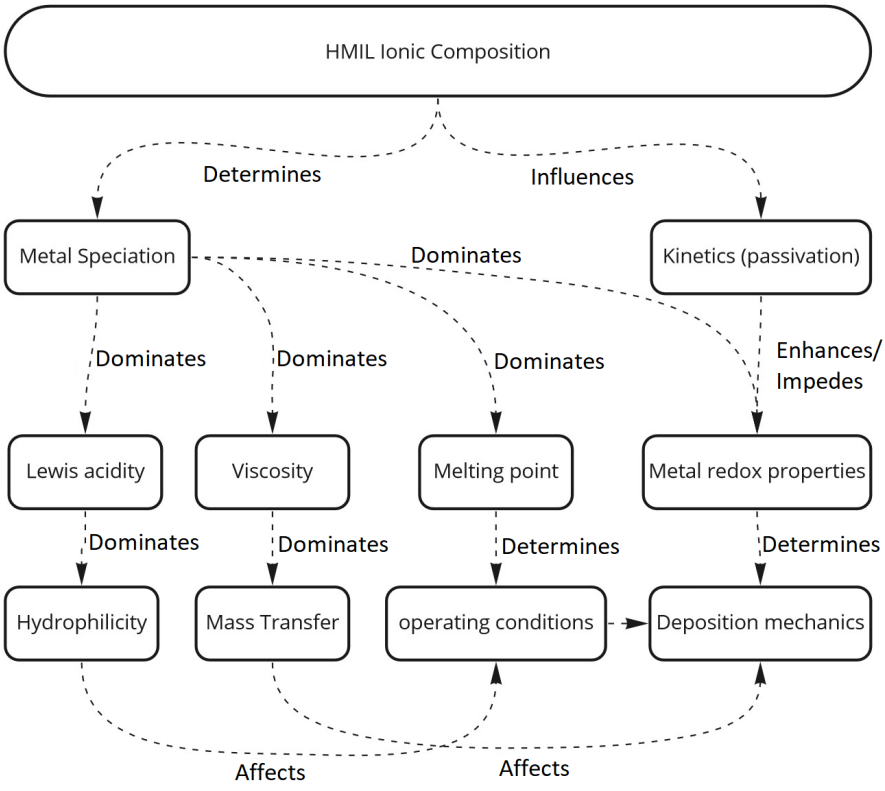


Figure 1.11: Schematic representation of the effects of x_{AlCl_3} on various HMIL attributes

Investigation into anionic speciation is often hampered by the number of different anionic species present at a particular x_{MX_n}.[1] Complex anionic equilibria investigated through vibrational spectroscopy have indistinguishable spectral peaks which result in spectra which cannot be interpreted to give conclusive results about the anion speciation. Improved theoretical methods and growing computational capacities allow density functional theory (DFT) and *ab initio* techniques to generating precise comparative data which make the task of interpreting complex spectra more surmountable.[68]

The following sections will highlight selected analytical techniques and methods used to determine anionic speciation. The techniques used to determine anionic speciation using each method are presented and substantiated with examples. The benefits and limitations of using each analytical method and techniques are discussed. The role of computational methods which can be used to support and expand on experimental results are discussed. The overall aim is to give justification as to why a computational investigation of anionic speciation is invaluable in developing further understanding of HMIL chemistry.

1.3.1 Vibrational spectroscopy

Raman and IR spectroscopy are the 'go to' analytical techniques for the initial examination of the anionic speciation in HMIL systems. The interrogation of bonds of anions and cations allows for a reasonable speciation if adequate comparative literature or *ab initio* data is available. The lack of vibrational data for larger oligomeric halometallate anions make the generation of their spectra through computational techniques invaluable.[1]

Precise anionic speciation using Raman spectroscopy requires accurate vibrational band assignments of metal halide bonds (M-X), usually situated between 600 – 650 cm^{-1}, and well resolved vibrational spectra.[58] Solid and liquid state samples can be investigated while water and air sensitive samples may be examined in a sealed environment. Successful determination of the anionic speciation of Au (I), Cu (I), Zn (II), Al (III), Ga (III), In (III), Fe (III) and Ti (IV) anions has been carried out using Raman spectroscopy.[57]

Accurate vibrational band assignments can be attained through studying solid state metal halide structures or high temperature molten metal halides. The presence of $[AlCl_4]^-$ at $x_{AlCl_3} = 0.5$ and $[Al_2Cl_7]^-$ at $x_{AlCl_3} = 0.67$ were identified by comparing medium resolution Raman spectra of $[C_4py]Cl$-$AlCl_3$ to Raman spectra of molten aluminum chloride salts.[69]

Polarization-dependent Raman spectroscopy is used to determine the symmetry of Raman-active nodes. The comparison of horizontally and vertically polarized Raman spectra gives insight into the symmetry of a species being evaluated. The interrogation of chlorogallate(III) anionic speciation using a vertical and horizontal polarization determined the presence of $[Ga_2Cl_7]^-$ at $x_{GaCl_3} > 0.50$. A vibrational mode at 414 cm^{-1} could be representative of either Ga_2Cl_6 if polarized and $[Ga_2Cl_7]^-$ when if not polarized. The polarization which was reported for Ga_2Cl_6 in literature could not be observed and hence the presence of $[Ga_2Cl_7]^-$ could be confirmed. Species like $[Ga_3Cl_{10}]^-$ and $[C_2C_1Im][GaCl_3]^+$ could only hypothesized as no distinct vibrational modes could be identified at any x_{GaCl_3}.[70]

A study compared well resolved Raman spectra of $[C_2C_1Im]Cl$-$AlCl_3$ with spectra predicted through *ab initio* methods. Hartree-Fock (HF) in conjunction with a polarized split valence Pople basis set 6-31G* and the semi empirical modified neglect of differential overlap (MNDO) method were used to generate the Raman spectra computationally. The theoretical calculations were carried out exclusively on the anions and hence neglected any effects which the cation might have had. The overlap between the computationally generated and experimental Raman spectra confirmed that $[Al_2Cl_7]^-$ had a C_2 symmetry with a 123^o Al-Cl-Al bond angle.[71]

Chlorocuprate(I) IL speciation was investigated through Raman and IR spectroscopy, however, the lack of Raman and IR band assignments for species present at $x_{CuCl_2} = 0.50$ hampered further investigations. $[Cu_2Cl_3]^-$ could not be identified due to the lack of comparable vibrational bands from molten salts or computational investigations. Comparable vibrational band assignments of oligomeric species is rare in literature as the oligomerization of anionic species is more common in HMILs than in molten salts.[1]

The interrogation of anionic speciation of $[C_4C_1Im]Cl$-$NbCl_4$ and $[C_4C_1Im]Cl$-$ZnCl_2$ systems revealed that the formation of different anions can be monitored through the evaluation of C_2-H stretching frequencies of the $[C_4C_1Im]^-$ cation. In $[C_4C_1Im]Cl$ a chloride ion is commonly found H-bonded to the C_2 hydrogen, consequentially weakening the C_2-H bond which resulted in lower frequency vibrations. Upon introducing metal halides the C_2-H frequencies compared to $[C_4C_1Im]Cl$ were more intense in both the $[C_4C_1Im]Cl$-$NbCl_4$ and $[C_4C_1Im]Cl$-$ZnCl_2$ systems. $[NbCl_6]^-$ was identified in the $[C_4C_1Im]Cl$-$NbCl_4$ system by observing the increase in C_2-H frequency and the observed deformation of the symmetrical O_h symmetry of $[NbCl_6]^-$. Within the $[C_4C_1Im]Cl$-$ZnCl_2$ system the presence of $[ZnCl_4]^{2-}$ (T_d) at $x_{ZnCl_2} < 0.30$ and $[Zn_2Cl_6]^{2-}$ (D_{2h}) between $0.30 < x_{ZnCl_2} < 0.70$ could be determined based on vibrational band assignments from literature. The formation of oligometallic $[Zn_3Cl_8]^{2-}$ and $[Zn_4Cl_{10}]^-$ anions could only be postulated due to the lack of comparative data. The identifiable changes in the cationic C-H bond frequencies were attributed to the reduced amount of H-bonding upon the formation of the larger oligomeric species.[72]

Ramen spectroscopy is limited as a speciation technique for HMILs mainly due to low resolution allowing for the identification of species only when they make up at least 5% to 10% of the total mixture. Additionally, the overlap of peaks from different species make the identification of individual species challenging. Fluorescence in ILs also hampers precise determination of species but may be overcome by using 1064 nm laser as excitation source over the conventional 785 nm lasers. The lack of comparative data for larger oligomerized species is a challenge. Computational simulation can be used to generate reference spectra and can be used in conjunction with Raman spectroscopy to determine the anionic speciation.[73]

1.3.2 NMR Spectroscopy

NMR can be used to interrogate anionic speciation and the type of NMR which can be used is determined by the composition of a HMIL, the chemical environment of nuclei of an atom and the change in chemical environment the atoms nuclei experience upon introduction of a metal halide.[1] The metal of the metal halide and halometallate anion(s) can be interrogated directly through the corresponding metal NMR such as ^{27}Al NMR for chloroaluminate systems.[74,75] HMILs can also be interrogated through ^{13}C and ^{1}H NMR. The change in the chemical shifts of the hydrogen and carbon environments in the cation give insight into

changes in anionic speciation.[1] ^{35}Cl NMR spectroscopy can potentially be used to determine the species present but ^{35}Cl NMR spectra are usually of poor quality and lack provisional reference data.[76]

Anionic speciation determined solely by the interpretation of the chemical shifts of metal centers is usually inaccurate. The NMR signals of metal centers are very sensitive to subtle changes in the chemical environment which hinder the use of reference data. Changes in anionic speciation are more accurately reflected in the shape and width of spectral peaks than the chemical shift.[1] When determining anionic speciation by evaluating peak shape, the width of the peak at half height, denoted $\Delta v_{1/2}$ is most commonly evaluated. Several factors effect $\Delta v_{1/2}$; viscosity, the spin quantum number of the nucleus (I), symmetry of the anionic species, the species participation in dynamic equilibria, temperature and the time delta between the magnetic pulse and the data acquisition known as pre-acquisition delay time, DE.[74]

For example, higher viscosity leads to longer molecular reorientation correlation times which in turn reduce the quadrupole relaxation rate, resulting in the broadening of the NMR peaks. The viscosity of HMILs decreases with an increase in x_{MX_n} due to the increased size and charge dispersion in anions. An increase in temperature also induces a decreased viscosity.

[C_4py]Cl-$AlCl_3$ was interrogated through examining the $\Delta v_{1/2}$ of ^{27}Al NMR spectra which decreased from 40 to 10 Hz between $x_{AlCl_3} = 0.44$ and 0.50 as shown in figure 1.12. Viscosity measurements correlated with the decrease from 40 to 10 Hz confirmed the effects on the reduced quadrupolar relaxation rate.[74] A similar correlation of $\Delta v_{1/2}$ with viscosity has been established for chlorostannate system.[77]

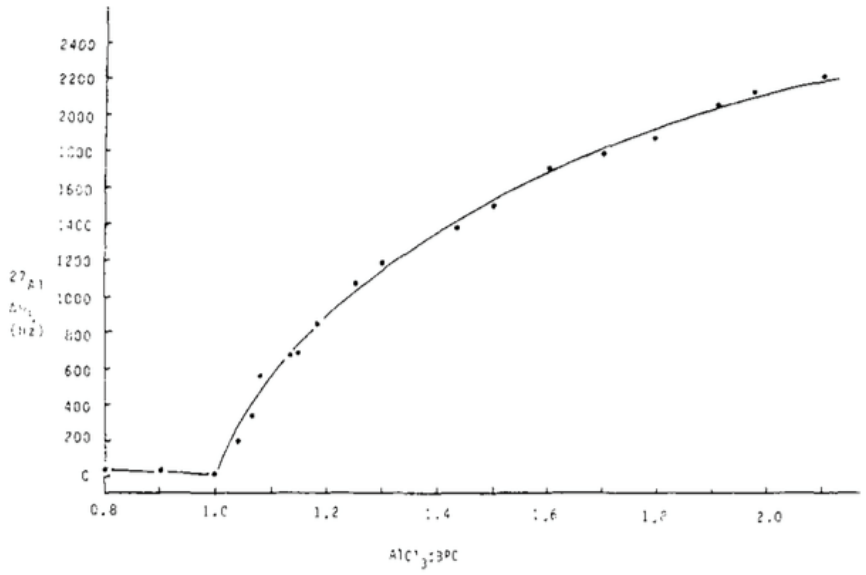


Figure 1.12: Chloroaluminate ^{27}Al $\Delta v_{1/2}$ (Hz)[y-axis] at various x_{AlCl_3} [x-axis] in the [C_4py]Cl-$AlCl_3$ system[1]

Lower symmetry in anions cause the broadening of metal NMR peaks. Metal atoms in tetrahedral (T_d) species with a high symmetry exhibit comparatively narrower peaks relative to the same atoms in a less symmetric oligomeric species. Dimers like $[Al_2Cl_7]^-$, have relatively large $\Delta\nu_{1/2}$ values as shown in figure 1.12 where the peaks broaden above $x_{AlCl_3} = 0.50$.[74]

A symmetrical peak indicates the presence of a single anionic species while species in rapid exchange, with respect to the NMR timescale, within an equilibrium process show one non-symmetrical peak. Unsymmetrical peaks have been observed for the chloroaluminate and chlorostannate systems at x_{MCl_3} where anionic equilibria have been confirmed.[74,77] The applicability of evaluating peak symmetry is limited to systems with low quadrupole moments, symmetrical anions and rapid exchange equilibria. Any spin quantum number, I, over 1/2 induces quadrupole line broadening. Table 1.3 compiles the results of $\Delta\nu_{1/2}$ with respect to changing I of 4 group 13 chlorometallate ILs at $x_{MCl_3} = 0.5$ where the only anion present is $[MCl_4]^-$ (M = Al, Ga or In). Gallium and indium NMR spectra of chlorogallates and chloroindates respectively, have exhibited no signals at any x_{MCl_3} where equilibriums were known to be present.[78,79]

Table 1.3: $\Delta\nu_{1/2}$ in selected chloroaluminate, chlorogallate and chloroindate ionic liquids at $x_{MCl_3} = 0.5$

System	Nuclei	Spin (I)	$\Delta\nu_{1/2}$ (Hz)	Referece
$[C_2C_1Im]Cl$–$AlCl_3$	^{27}Al	5/2	23	[75]
$[C_2C_1Im]Cl$–$GaCl_3$	^{71}Ga	3/2	190	[1]
$[C_8C_1Im]Cl$–$GaCl_3$	^{71}Ga	3/2	995	[1]
$[C_8C_1Im]Cl$–$InCl_3$	^{115}In	9/2	6973	[78]

Out of the different variables effecting $\Delta\nu_{1/2}$, the change in anionic symmetry is the most useful. Oligomeric anions are typically more flexible and less symmetric which gives rise to a high sensitivity to oligomeric speciation. Metal NMR as a sole technique is not informative enough as structural elucidation of anionic species is unfeasible but it is a good indicator for a change in speciation or the presence of equilibria in systems with low quadrapole moments. Hence, the optimal use of metal NMR for anionic speciation is as a complementary technique due to its extremely sensitive detection of non-symmetrical compounds. Raman spectroscopy may be used to determine the dominant anionic species in conjunction with *ab initio* calculations but metal NMR has a lower detection limit for non-symmetrical species.[77]

1.3.3 X-ray photoelectron spectroscopy (XPS)

The negligible vapor pressure of ILs allows for their interrogation through XPS. XPS is a spectroscopic technique that evaluates the kinetic energy of emitted electrons upon irradiation by incident X-Rays (photons) in vacuo. The difference in kinetic energy between the photon injected into the sample and the kinetic energy of the electron leaving the sample allows for the determination of the binding energy of electrons based on the photoelectric effect relationship represented by equation 1.3.1. [80]

$$E_{binding} = E_{photon} - (E_{kinetic} + \phi) \tag{1.3.1}$$

Where $E_{binding}$ is the binding energy, E_{photon} is the energy of the incoming photon, $E_{kinetic}$ is the kinetic energy of the ejected electron and ϕ is the work function.

XPS can be used to determine elementary compositions, oxidation states and coordination environments near the surface of the sample. XPS is useful for identifying anionic speciation but it requires more training for high quality data acquisition than vibrational spectroscopy due to the intricacies associated with the data acquisition and data processing. [1]

For example, the $[C_8C_1Im]Cl$-$InCl_3$ system was studied through XPS at compositions $x_{InCl_3} = 0.50$, where only $[C_8C_1Im][InCl_4]$ is present and $x_{InCl_3} = 0.67$, where $InCl_3$ precipitates to form a suspension. XPS evaluations at the surface of both compositions, after the suspension had settled, showed identical spectra indicating the presence of $[C_8C_1Im][InCl_4]$ exclusively. [78]

Anionic speciation in $[C_8C_1im]Cl$-$SnCl_2$ was determined using XPS. No information could be derived from the Sn $3d_{5/2}$ XPS peaks as the binding energy remained consistent when varying x_{SnCl_2}. The examination of a high resolution Cl 2p XPS allowed Cl^- and $[SnCl_3]^-$ to be distinguished at $x_{SnCl_2} = 0.33$. [77] An extension of the chlorostannate speciation study was carried out for iron, cobalt, nickel and zinc systems revealing $[MCl_4]^{2-}$ to be the dominant species at $x_{MCl_2} = 0.33$. [81]

Valence band and core level XPS outputs can be derived through computational methods. Valence shell levels can be computed through a technique described at the end of the second chapter. Core XPS levels can be calculated using the Maximum Overlap Method (MOM) in the GAMESS software package which allows for a single point energy calculation of a N-1 electron system. To generate an XPS spectrum for a particular type of excitation (correlating to a particular core energy level) 2 calculations must be undertaken and some manipulations on the orbitals of the structures of interest: initially a self-consistent field (SCF)

calculation on an unrestricted N electron system of interest is carried out. A molecular orbital coinciding with the XPS core level excitation is selected by observing orbital shapes and energies. The ordering of the orbitals is changed by placing the selected core orbital with the N electrons in the HOMO position (changing its position in the density matrix). The SCF of the N-1 electron system is calculated using MOM neglecting the HOMO (which is truly a core energy level). The difference in energy between the two SCF calculations then determines the electron binding energy directly correlating to XPS outputs.[82]

XPS is a powerful technique which can give useful insight into the anionic speciation. XPS can be supported by computational techniques and is primarily limited by availability.

1.3.4 X-ray absoroption spectroscopy (XAS)

X-Ray absorption spectroscopy (XAS) is an umbrella term referring to a group of techniques; X-ray absorption fine structure (XAFS), extended X-ray absorption fine structure (EXAFS) and X-ray absorption near-edge structure (XANES). Each technique focuses on different regions of the X-ray absorption spectrum. XAS works by irradiating samples with high energy, monochromatic X-rays which are tuned to be absorbed by the core electrons of choice in a particular element. The irradiated electrons are either promoted to higher unoccupied orbitals or ejected, effectively ionizing the atom. The promotions of the core electrons to different energy levels or the continuum corresponds to different regions of the K, L and M absorption edges which correspond to the angular momentum quantum numbers 1, 2 and 3 respectively. I.e. the excitation of a 1s electron generates a K edge, 2s a L_1 edge and 2p generates L_2 and L_3 edges. The core electrons of each element have distinct values of different absorption edges which change depending on their chemical environment and oxidation states. The spectra can be evaluated by comparison to existing data or data generated from computational calculations.[65]

XAS techniques give insight into chemical and electronic structures. The X-Ray absorption causes the excitation of a core electron which is back-scattered by the atoms within a range of 6 Angstrom from the nucleus. The back-scattering producing an oscillatory spectrum of energies beyond the absorption edge. EXAFS studies the region beyond the absorption edge. The arrangement of atoms around the specified central atom can then be determined according to the oscillatory spectrum generated. XAS requires a synchrotron to generate tuned high energy X-rays and complex data processing and interpretation.[65]

To study metal coordination environments EXAFS and XANES are the only XAS techniques that have been used to study HMILs. EXAFS has been used to study the anionic speciation of chlorogallate and chloroindate ILs where systems were evaluated as a function of x_{MCl_3} and temperature. The results clearly indicate a Ga-

Ga proximity in the chlorogallate system confirming the formation of multi-metallic complexes. In contrast, the analysis of the chloroindate system revealed no indium atoms in close proximity to one another indicating the formation of only single metal centered species.[78,79]

A study using a combined XAS (EXAFS and XANES) and DFT approach has been used to study the behavior of dissolved glucose in Cu and Cr based HMIL systems. The study found that the dissolved glucose coordinates to the chromium metal center, but undergoes a fast redox process in the Cu based system, reducing Cu(II) to Cu(I).[83]

A recent review summarized all EXAFS investigations on HMILs and found that the complexity of the equilibrium directly correlates to the applicability of EXAFS as an anionic speciation technique.[65] As an anionic equilibrium becomes more complex the EXAFS spectra become more difficult to interpret and eventually unusable. Overall, the EXAFS technique can be used to differentiate between two and sometimes three chemical environments. However, with rising complexity of a system the evaluation of the anionic speciation should be carried out with alternative techniques. Moreover the high capital cost of EXAFS limits the applicability of the technique.[1]

1.3.5 Bulk property measurements

The bulk properties of HMILs like the melting point (mp), conductivity and viscosity at various x_{MX_n} can be evaluated to indicate changes in anionic speciation. While changes in bulk properties directly correlate to changes in anionic speciation they cannot be used to directly interrogate which species form.[1]

Among other techniques, mps may be interrogated via differential scanning calorimetry (DSC), polarized optical microscopy (POM) or a visual melting point apparatus. Plotting mps versus x_{MX_n} generates a phase diagram which can be used in conjunction with computational investigations or Raman spectroscopy to determine the speciation.[1]

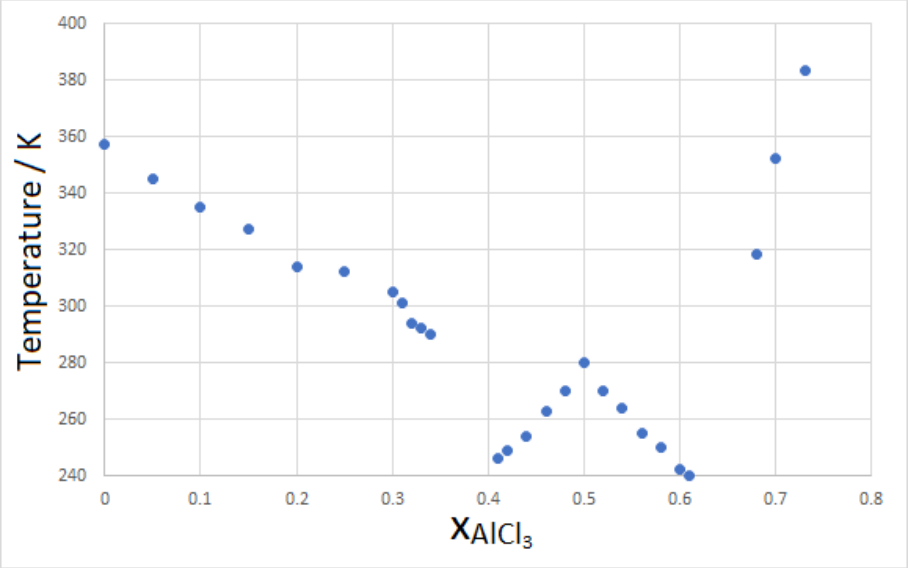


Figure 1.13: $[C_2C_1Im]Cl$-$AlCl_3$ Melting points versus x_{AlCl_3} measured by DSC

The first HMIL phase diagram for $[C_2C_1Im]Cl$–$AlCl_3$, was generated through evaluating melting points, freezing points and glass transition temperatures. The mp shown in figure 1.13, at $x_{AlCl_3} = 0.50$ reference the melting of pure $[C_2C_1Im][AlCl_4]$. The mps become lower towards $x_{AlCl_3} = 0.33$ and 0.67 from $x_{AlCl_3} = 0.5$ which highlights the eutectic behavior of both $[C_2C_1Im]Cl$ and $[C_2C_1Im][Al_2Cl_7]$ respectively. A clear change in speciation can be determined from the melting points.[84]

Specific conductivity in conjunction with viscosity measurements were used to investigate the $[C_2C_1Im][Cl$-$CuCl$ systems at different x_{CuCl}. The investigation showed that the hard Cl^- ion was replaced by $[CuCl_3]^-$ at $x_{CuCl} = 0.5$ which lead to decreased viscosity and higher conductivity thereby increasing the ion mobility.[85]

Determining the anionic speciation through the measurement of physical properties only functions as a supplemental method. Bulk property measurements can reveal changes in anionic speciation but cannot readily identify what specific species give rise to the changes. The evaluation of physical properties is most useful when used in tandem with other techniques which can be used to identify the species present.[1]

1.3.6 Theoretical methods

Theoretical methods provide an alternative route to attain data which can be used to determine anionic speciation. Computational techniques function as predictive methods or as a reference for experimental studies and must be used in tandem with experimental techniques. Theoretical methods in conjunction

with experimental techniques can provide information that is unattainable through a purely experimental approach. Computational methods can provide additional insight into nuclear and electronic structure of anions, thermodynamic and electronic behavior to predict chemical transformations and ultimately applications. Furthermore computations can be used to predict different types of spectra as shown in the prior sections.[1]

For example, The assignment of peaks in vibrational spectra and ^{27}Al quadrupole coupling constants was undertaken for different haloaluminate and alkylhaloaluminate anions using computational methods. Anionic species known to be present in an equilibrium were optimized at the RHF/6-31G* and MP2/6-31G* levels of theory in the gas phase. The vibrational spectra of the anions were calculated employing a correction factor of 0.97 and achieved a 0.999 correlation coefficient (R^2) to fit experimental spectra. The ^{27}Al quadrupole moments were calculated using HF and the B3LYP functional with basis ranging from 3-21G to cc-pVTZ. The R^2 value ranged from 0.984 for HF/3-21G to 0.9986 for B3LYP/cc-pVTZ compared to the experimental results. Based on the calculations of spectra of individual anions, complex anionic equilibria were deconvoluted into spectra for the individual species making up the anionic equilibrium, aiding in the precise assignment of spectral peaks.[86]

Short-range ordering in $[C_2C_1Im]Cl\text{-}AlCl_3$ was studied by comparing neutron scattering and crystal structures to the HF/6-31G* simulated structures. The comparison of experimental and QM structures confirmed $[Al_2Cl_7]^-$ to be two tetrahedral tetrachloroaluminates sharing a Cl, connected by a bent Al-Cl-Al bridge.[86]

Multiple studies have been carried out which compare computational to experimental Raman spectra. $[C_4C_1Im]Cl\text{-}FeCl_3$ and $[C_4C_1Im]Cl\text{-}FeCl_2$ were studied using UHF and UB3LYP with a 6-31G* basis set and Lan2DZ and CEP-31G core potentials. $[FeCl_4]^-$ and $[FeCl_4]^{2-}$ were identified as dominant structures below $x_{FeCl_3} = 0.50$ and $[Fe_2Cl_7]^-$ above $x_{FeCl_3} = 0.50$.[87] $[C_2C_1Im]Cl\text{-}InCl_3$ and $[C_4C_1Im]Cl\text{-}InCl_3$ were studied using RHF/3-21G* and confirmed $[InCl_4]^-$ to be the dominant species at $x_{InCl_3} = 0.50$.[88] $[C_2C_1Im]Cl\text{-}AuCl_3$ was studied using HF/Lan2DZ. $[AuCl_4]^-$ was found to be the most stable species and $[Au_2Cl_7]^-$ was predicted to be stable through the QM calculations but the experimental spectra did not confirm that the dimeric species was present indicating the requirement for further investigations.[89]

Molecular dynamics (MD) simulations were compared to neutron scattering, density, diffusion coefficients, vibrational frequencies and solid state crystallography to interrogate the bulk structure of $[C_4C_1Im][AlCl_4]$. The quality of the computational model was confirmed by a good fit between simulated and experimental data. The validation of the MD model for one HMIL at a particular mol fraction is not to be taken as a confirmation of the transferability of the model to model the behavior of other systems or the same system at

other mol fractions. Force fields commonly lack applicability to systems to which they were not tailored.[68]

A study used *ab initio* Car-Parrinello MD simulations to study chloroalluminate systems at high x_{AlCl_3}. A highly acidic environment was generated by simulating one $[C_2C_1Im]Cl$ ion pair dissolved in a $AlCl_3$ melt. Grothus diffusion was found to play a pivotal role in the mechanism by which oligomeric anions form. The model predicted that the tetrameric species, $[Al_4Cl_{13}]^-$, to be the predominant anionic species. Experimental studies have shown that $[Al_4Cl_{13}]^-$ can only exist in equilibrium with $AlCl_3$, above $x_{AlCl_3} = 0.67$. The discrepancy between the simulated speciation and experimentally determined speciation was a result of the unrealistically high concentration of $AlCl_3$.[90]

Theoretical studies are good at determining anionic speciation in HMIL when used in conjunction with the right experimental techniques. XPS, XAS and Raman spectroscopy are the most powerful techniques to use with a computational approach. QM and MD studies are not limited to the determination of anionic speciation. Insight into thermodynamics, kinetics and electronic structures of individual compounds can be evaluated in more detail to give insights into applications and physical data. Additionally, the interaction dynamics of different species can be evaluated to determine how intermolecular chemistry impacts the overall chemistry of the system.[91]

1.3.7 Mass spectrometry (MS)

Mass spectrometry (MS) techniques have been used extensively to characterize ionic liquids.[1] Determining HMIL anionic speciation via MS has often resulted in erroneous results. Fast atom bombardment (FAB)[92] or electrospray ionization (ESI)[93,94] MS both lead to perturbations in the anionic speciation due to a phase change and ionization.

Anionic speciation of chlorozincate by MS and alternative speciation methods highlight common discrepancies. MS reveals $[ZnCl_3]^-$ and $[Zn_2Cl_5]^-$ to be the dominant species while other speciation techniques show that $[ZnCl_4]^{2-}$ and $[Zn_2Cl_6]^{2-}$ are the prevalent species.[58] chlorohafnate and chlorozirconate anionic speciation was also studied by multiple techniques and discrepancies were found between MS and other analytical techniques. DSC investigations and the coordination chemistry of hafnium and zirconium indicated the presence of $[MCl_6]^{2-}$, $[M_2Cl_{10}]^{2-}$ and $[M_2Cl_9]^-$ at $x_{MCl_4} = 0.33$, 0.50 and 0.67 respectively. MS results indicated $[MCl_5]^-$ as the dominant species at $x_{MCl_3} = 0.50$.[95] A MS study on chloroindate HMILs indicated the presence of dimeric $[In_2Cl_7]^-$ although multiple other studies have shown that chloroindate complexes do not form dimetallic complexes in the bulk.[1]

MS results sometimes correlate with liquid phase speciation techniques. MS was used to study the anionic

speciation of chloroaluminate and chlorogallate systems in multiple studies which revealed an overlap between the speciation determined by MS and speciation determined by other LP speciation techniques at low x_MCl_3.[96–99] At $x_MCl_3 < 0.5$ the anionic speciation in chloroaluminates and chlorogallates determined by MS significantly deviates from LP speciation. The presence of $[Ga_3Cl_{10}]^-$ could not be conclusively determined at $x_GaCl_3 = 0.67$ by MS. $[Al_3Cl_{10}]^-$ was found by one MS study in minuscule quantities when evaluating the speciation of $[C_2C_1Im]Cl\text{-}AlCl_3$ but could not be found in other studies. The relative abundance of $[Al_2Cl_7]^-$ and $[Ga_2Cl_7]^-$ determined by MS studies at different $x_MCl_3 < 0.5$ is low compared to data from other speciation techniques. Additionally, the sample contamination through exposure to moisture perturbs the anionic speciation through the formation of metal oxychloride and metal hydroxychloride complexes making the results less reflective of true anionic speciation.

Metal-ligand equilibria were studied in aqueous solutions using ESI-MS to evaluate discrepancies between anionic speciation determined from MS and other techniques. The study found that the ionization process can lead to perturbations which affect the anionic speciation unpredictably for most systems. The conditions which facilitate the discrepancies in speciation are the phase transfer from liquid to gas and the ionization process. Discrepancies in speciation of the chlorozincates by ESI-MS were found to concur with those of FAB-MS indicating similar processes leading to misleading results. The sporadic overlap of MS and other analytical approaches show that MS should not be used alone as a technique to determine anionic speciation in HMILs.[100]

The speciation determined from MS results provides a unique opportunity for computational investigations. The anionic speciation in the gas phase determined by MS and the liquid phase determined by other techniques can be compared using computational investigations as all species can be modeled in both phases. Hence, the speciation determined from MS is highly relevant.

1.3.8 Alternative techniques

Three other techniques have been used sparingly to determine anionic speciation. Electron paramagnetic resonance (EPR) is an analytical technique that may interrogate magnetic nuclei such as copper and iron. EPR has been used to determine anionic speciation of copper based HMILs but bares no relevance to studies on Aluminum, Gallium and Indium.[101] UV Vis may be utilized as a fast and simple technique to speciate anions prone to absorbing light in the UV or visual light ranges. However, UV Vis is used sparingly because it is limited by the high extinction coefficient of neat systems. The high extinction coefficient leads to the requirement of ultra-thin cuvettes which in turn effect the speciation of the system rendering the results inconclusive when requiring objective in situ speciation data.[1]

Great advances in the understanding of IL liquid structures have been made thanks to Neutron scattering investigations. Only one study has used neutron scattering to evaluate $[C_2C_1Im]Cl\text{-}AlCl_3$ in conjunction with in computational techniques. The study found that the *ab initio* results matched well with the neutron scattering results. Most neutron scattering studies have focused on systems without anions in equilibrium or metal centers and hence HMILs have not been studied thoroughly with this technique. [1]

1.3.9 Speciation methods summery

A range of methods for determining anionic speciation have been outlined including vibrational spectroscopy, NMR, XPS, XAS, bulk property measurements, theoretical methods and MS. The insight from each method to determine anionic speciation varies significantly. The determination of anionic speciation must be carried out in the liquid phase to determine the speciation accurately as the discrepancies in speciation arising during a phase change can be significant. The best techniques to determine anionic speciation in the liquid phase are vibrational spectroscopy, XPS and XAS. Vibrational spectroscopy is an initial go to technique while XPS and XAS are more insightful but also more technically demanding and should be used when available. Metal NMR and bulk property measurements are ideal when speciation has already been determined as they can both be extremely sensitive in determining *changes* in speciation. Vibrational spectroscopy, XPS and XAS should ideally be backed up by alternative techniques and by adequate literature or theoretical studies to substantiate the results. It is important to remember that the speciation is determined by the x_{MCl_3} and is usually seen as independent from other factors such as the cation present in the system which may not be true in all cases. [1]

1.4 Current understanding of anionic speciation, relevant properties and potential use in applications

The anionic speciation of a HMIL determines the chemical properties and behavior of a system. The systems being investigated in this study are chloroaluminate, chlorogallate and chloroindate HMILs with four different cations. This section will focuses on the current knowledge of anionic speciation for group 13 chlorometallate systems at various x_{MCl_3}. The properties correlating to the speciation at different x_{MCl_3} of each systems will be examined.

1.4.1 Anionic speciation in chloroaluminate, chlorogallate and chloroindate Ionic Liquids in the liquid phase

The current understanding of speciation of chloroaluminate, chlorogallate and chloroindate HMILs varies in quality. The chloroaluminate system has been studied extensively compared to the chlorogallate and chloroindate systems which have been studied more sparingly. The most prevalent anions at various x_{MCl_3} for each system are summarized in table 1.4.[1]

Table 1.4: Predominant liquid phase speciation of group 13 chlorometallate Ionic liquids at selected x_{MCl_3}

x_{MCl_3}	0.25	0.33	0.50	0.60	0.67	0.75	Speciation method
Al	Cl^-; $[AlCl_4]^-$	Cl^-; $[AlCl_4]^-$	$[AlCl_4]^-$	$[AlCl_4]^-$; $[Al_2Cl_7]^-$	$[Al_2Cl_7]^-$	$[Al_xCl_y]^-$; $Al_2Cl_6\downarrow$	Raman[69,71] ^{27}Al NMR[71]
Ga	Cl^-; $[GaCl_4]^-$	Cl^-; $[GaCl_4]^-$	$[GaCl_4]^-$	$[GaCl_4]^-$; $[Ga_2Cl_7]^-$	$[Ga_2Cl_7]^-$	$[Ga_3Cl_{10}]^-$	Raman[75] ^{71}Ga NMR[70,102] EXAFS[103]
In	$[InCl_6]^{3-}$	$[InCl_5]^{2-}$	$[InCl_4]^-$	$[InCl_4]^-$; $InCl_3\downarrow$			Raman[88,104], XPS[78]

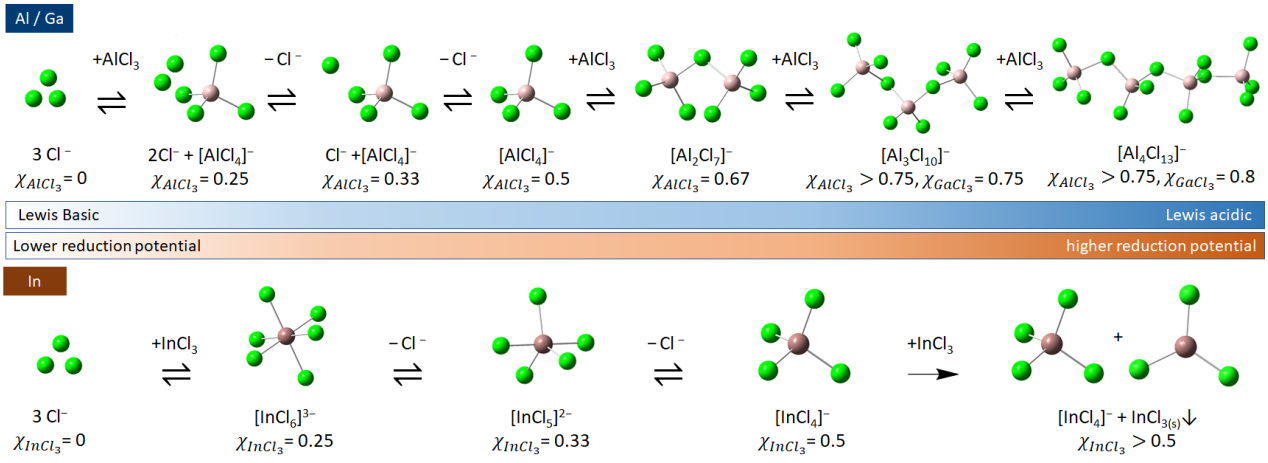


Figure 1.14: Schematic representation of the effects of speciation on Lewis acidity and electrochemical potential in the chloroalluminate, chlorogallate and chloroindate ionic liquids

Each speciation at a particular x_{MCl_3} has corresponding properties. Generally the Lewis acidity and the reduction potential increase with an increase in x_{MCl_3} as outlined in figure 1.14. The $\downarrow$ means precipitation occurs, limiting further oligomerization of the anions. The relation between speciation and selected physicochemical properties is now discussed in more detail.

1.4.2 Lewis acidity and basicity in halometallate ionic liquids

The definition of acidity is crucial in HMIL chemistry to understand the effects of anionic speciation in HMILs. The Brønsted-Lowry theory of acids and bases has a Brønsted acid which is a proton donor and a Brønsted base which is a proton acceptor. The acidity is determined by the relative affinity of different species for a proton and is commonly expressed through pK_a or pH which can be determined through the relation shown in equations 1.4.1 and 1.4.2. HMILs do however, not feature proton transfer when acid-base reactions occur, and it is necessary to define the acidity and basicity in terms of Lewis theory. [1]

$$pK_a = log_{10}\frac{[HA]}{[A]^-[H]^+} \tag{1.4.1}$$

$$pH = pK_a + log\frac{[A]^-}{[HA]} \tag{1.4.2}$$

The Lewis definition of acids and bases is conceptualized by the ability to accept or donate an electron pair to form a dative covalent bond. A Lewis acid is a species that has an empty orbital into which an electron pair can be accepted to form a Lewis adduct. A Lewis base has a filled valence orbital containing an electron pair that is donated to form a dative covalent bond with a Lewis acid, forming a Lewis adduct as shown in figure 1.15. [105]

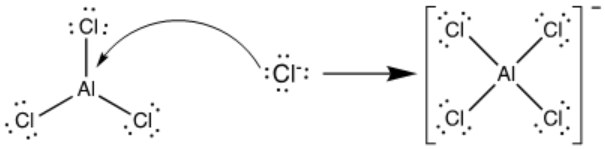


Figure 1.15: The formation of tetrachloroalluminate, $[AlCl_4]^-$, through the creation of a dative covalent bond between aluminum chloride, $AlCl_3$, and a chloride ion, Cl^-

The definition of Lewis acidity is far more difficult to apply to a species due to discrepancies which arise due to the variety of Lewis bases in a donor-acceptor interactions. Lewis acidity can be defined in three different ways; global Lewis acidity (gLA), effective Lewis acidity (eLA) and intrinsic Lewis acidity (iLA). [105]

gLA is defined by the changes in enthalpy (ΔH) and the Gibbs free energy (ΔG) upon the formation of an adduct. gLA is commonly presented in terms of a scale of affinity with either fluoride or hydride ions.[106] eLA is defined by changes to physiochemical properties of a probe base upon interaction with the Lewis acid. The most common method used to determine eLA is the Gutmann-Becket method. The Gutmann-Becket method determines the Guttmann acceptor number (AN) by evaluating the ^{31}P NMR shift of triethyl phosphine oxide (TEPO) upon Lewis acid coordination.[107,108] iLA is determined by the internal properties of a Lewis acid such as the LUMO energy and electron affinity.[109] There is no one right answer to which scale is most appropriate when selecting an appropriate Lewis acid for an application and hence one should be aware of all three ways to describe Lewis acidity to avoid confusing results.[105]

Due to the discrepancies in different scales of Lewis acidity the theory of hard and soft acids and bases (HSAB) has been introduced which tackles the concept more holistically. HSAB theory defines Lewis acidity in terms of the energy, form and diffusivity of the LUMO of the acid among other things. Table 1.5 summarizes the different properties of hard and soft acids and bases.[110] The hardness or softness of a species has measurable effects on the eLA. For example, TEPO is a hard base and when interchanged with the relatively soft trimethylphosphine sulfide a different eLA is determined.

Lewis acidity in HMILs has been determined 'conceptually' and the eLA of HMILs at a range of x_{MCl_3} has been evaluated. Each HMIL has a speciation range in which it is deemed 'basic' or 'acidic' and a point in between in which it is neutral. The basic range is that in which there are free chloride ions present as the chloride ions are inherently Lewis basic. The neutral point is reached when all chloride ions have be scavenged by MCl_3. The acidic range is that in which MCl_3 is added beyond the neutral point which generates alternative anionic speciation. The acidic range is acidic because oligomerized or over-saturated complexes function as Lewis acids.[1]

Table 1.5: Properties of hard and soft acids and bases

Property	Hard acids and bases	Soft acids and bases
atomic/ionic radius	small	large
oxidation state	high	low or zero
polarizability	low	high
electronegativity (bases)	high	low
HOMO energy of bases	low	higher (Lower than soft acid LUMO)
LUMO energy of acids	high	lower (higher than soft base HOMO)
affinity	Ionic bonding	Covalent bonding

The basic range of chloroaluminate and chlorogallate systems is below $x_{MCl_3} = 0.5$, while for the chloroindate systems it is below $x_{InCl_3} = 0.25$. The neutral point for chloroaluminates and chlorogallates is when there is an equimolar amount of MCl_3 and [Cat]Cl have been mixed. In the chloroindate system the neutral point is reached when $x_{InCl_3} = 0.25$. beyond $x_{MCl_3} = 0.5$ in the chloroaluminate and chlorogallate system and $x_{InCl_3} = 0.25$ in the chloroindate system the HMILs are considered to be conceptually acidic. [1]

The eLA has been ascertained by determining the Gutmann acceptor numbers from the ^{31}P chemical shift of TEPO at different x_{MCl_3}. The acceptor numbers have been determined for [C_4Py]Cl-$AlCl_3$ [111], [C_2C_1Im]Cl-$AlCl_3$ [111], [C_8C_1Im]Cl-$AlCl_3$ [112], [C_8C_1Im]Cl-$GaCl_3$ [112] and [C_8C_1Im]Cl-$InCl_3$. [112] In [C_4Py]Cl-$AlCl_3$ [C_4Py]Cl is 1-Butylpyridinium chloride. Figure 1.16 shows the ^{31}P Chemical shift and Gutman acceptor number of each system with respect to x_{MCl_3}. The ^{31}P NMR chemical shift is converted to the Gutmann acceptor number (AN) according to equation 1.4.3.

$$AN = 2.348\delta_{inf} \tag{1.4.3}$$

The Lewis acidity correlates strongly with the anionic speciation and the choice of cation does not significantly affect the eLA of the systems. The lack of dependence on the cation demonstrated through the ANs of [C_4Py]Cl-$AlCl_3$, [C_2C_1Im]Cl-$AlCl_3$ and [C_8C_1Im]Cl-$AlCl_3$ which are very similar at given x_{MCl_3} regardless of the cation.

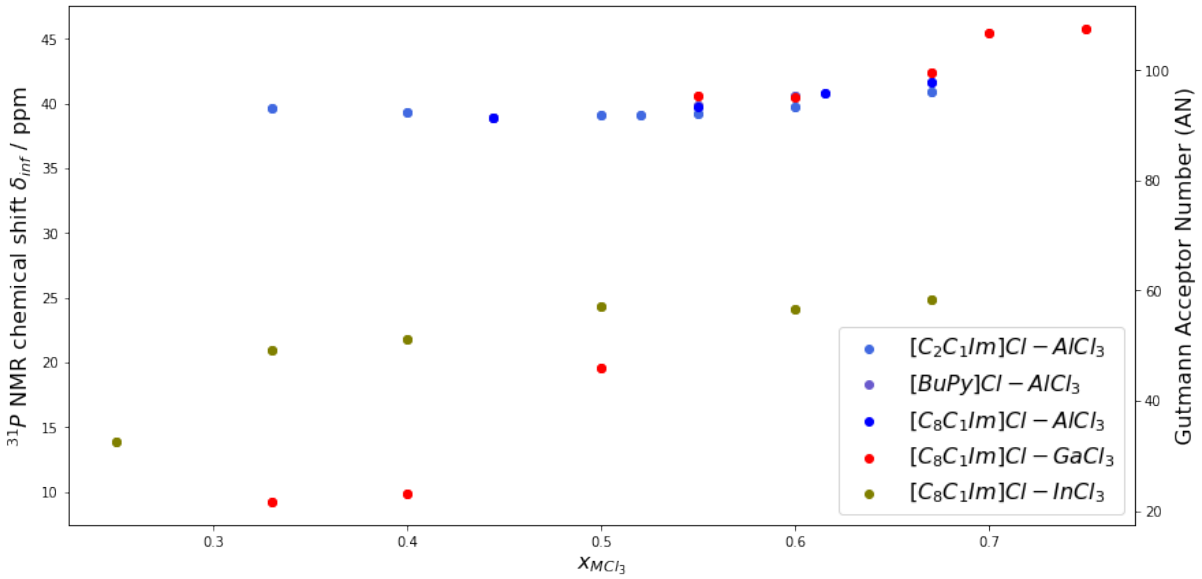


Figure 1.16: $[C_4Py]Cl\text{-}AlCl_3$, $[C_2C_1Im]Cl\text{-}AlCl_3$, $[C_8C_1Im]Cl\text{-}AlCl_3$, $[C_8C_1Im]Cl\text{-}GaCl_3$ and $[C_8C_1Im]Cl\text{-}InCl_3$ ^{31}P chemical shift (left y-axis) and the Guttman acceptor number [AN] (right y-axis) with respect to x_{MCl_3} (x-axis)

The eLA of the $[C_8C_1Im]Cl\text{-}AlCl_3$, $[C_8C_1Im]Cl\text{-}GaCl_3$ and $[C_8C_1Im]Cl\text{-}InCl_3$ systems is significantly different. The speciation of the chloroaluminate and chlorogallate system are similar but this is not reflected in the Lewis acidity. The Lewis acidity of the chloroaluminate systems is consistently between 91 and 93.2 AN below $x_{AlCl_3} = 0.5$ and rises slightly to 93.6 at $x_{AlCl_3} = 0.5$ and to 96 above $x_{AlCl_3} = 0.5$.[111,112] In contrast the AN numbers of the chlorogallate system are between 21.6 and 23.2 below $x_{GaCl_3} = 0.5$, rising to 45.9 at $x_{GaCl_3} = 0.5$ and then rising to between 95 and 107.5 above $x_{GaCl_3} = 0.5$.[112]

The difference in the chloroaluminate and chlorogallate systems can be explained by considering the acid-base equilibriums between the monometallic and dimetallic species. The equilibrium of the autosolvolysis of $[MCl_4]^-$ anions is shown in equation 1.4.4. The autosolvolysis can be broken up into the splitting of the $[MCl_4]^-$ species (eq. 1.4.5) and the reaction with $AlCl_3$ (eq.1.4.6). Upon the addition of a strong base like TEPO a competitive reaction occurs (eq. 1.4.7) and the [(tepo)MCl_3] adduct is formed.[112]

$$2[MCl_4]^- \rightleftharpoons [M_2Cl_7]^- + Cl^- \tag{1.4.4}$$

$$[MCl_4]^- \rightleftharpoons MCl_3 + Cl^- \tag{1.4.5}$$

$$[MCl_4]^- + MCl_3 \rightleftharpoons [M_2Cl_7]^- \tag{1.4.6}$$

$$tepo + MCl_3 \rightleftharpoons [(tepo)MCl_3] \tag{1.4.7}$$

Julian Estager et al. showed that the reaction in equation 1.4.6 is 24 kJ mol^{-1} more favorable in the chlorogallate system. However TEPO was found to have a 144 kJ mol^{-1} higher affinity for $AlCl_3$ than $GaCl_3$. In the chloroaluminate system the reaction with TEPO was -91 kJ mol^{-1} more favorable while in the chlorogallate system the reaction was less favorable by 78 kJ mol^{-1}. In consequence the reaction with TEPO is far more appealing in the chlorogallate system than the chloroaluminate system which induces a larger difference in AN based on speciation.[112]

The AN of the gallium system also rises from $x_{GaCl_3} = 0.5$ up to $x_{GaCl_3} = 0.67$, from 95 to 99, and beyond $x_{GaCl_3} = 0.67$ to 107. This indicates that tepo can form a stable Lewis acid with dimetallic species as shown in equation 1.4.8 to 1.4.10.[112]

$$[Ga_3Cl_{10}]^- + tepo \rightleftharpoons [(tepo)Ga_2Cl_6] + [GaCl_4]^- \tag{1.4.8}$$

$$[Ga_3Cl_{10}]^- \rightleftharpoons Ga_2Cl_6 + [GaCl_4]^- \tag{1.4.9}$$

$$Ga_2Cl_6 + tepo \rightleftharpoons [(tepo)Ga_2Cl_6] \tag{1.4.10}$$

The chloroindate system features much smaller ANs between 32 and 58, and the AN correlates with the current understanding of the systems anionic speciation. As the dominant speciation in the system goes from $[InCl_6]^{3-}$ to $[InCl_5]^{2-}$ to $[InCl_4]^-$ the AN changes according to the reactions depicted in equations 1.4.11 and 1.4.12. The equilibrium in equation 1.4.13 competes with the equilibrium of tepo and the tetrachloroindate and pentacoordinate complexes.[112]

$$[InCl_5]^{2-} + tepo \rightleftharpoons [(tepo)InCl_5]^{2-} \tag{1.4.11}$$

$$[InCl_4]^- + tepo \rightleftharpoons [(tepo)InCl_4]^- \tag{1.4.12}$$

$$2[InCl_5]^{2-} \rightleftharpoons [InCl_6]^{3-} + [InCl_4]^- \tag{1.4.13}$$

The results show that the chloroaluminate systems eLA is the least versatile with respect to changes x_{MCl_3}

while a chlorogallate system reveals a highly tunable acidity corresponding to anionic speciation. The chloroindate system has far weaker acidity than the other two systems and the anionic speciation is reflected in the acidity. In HMILs the Lewis acidity of chlorometallate species is controlled by the prevalent metal electrophilicity and speciation of the chlorometallate anions. Hence the x_{MCl_3} is the controlling variable but the speciation and the affinity of a probe molecule have to be considered. [1,105]

1.4.3 Redox potential and electrochemical window in halometallate ionic liquids

Oxidation refers to the loss of electrons and reduction to the gain of electrons. The redox potential quantifies the tendency for a species to be oxidized or reduced and is measured in volts (V). The larger the reduction potential, the greater the tendency for a species to be reduced. The electrochemical window (EW) refers to the range between the oxidation and reduction potentials of a substance, providing a range in which a substance does not undergo any redox processes induced by an external potential. [2]

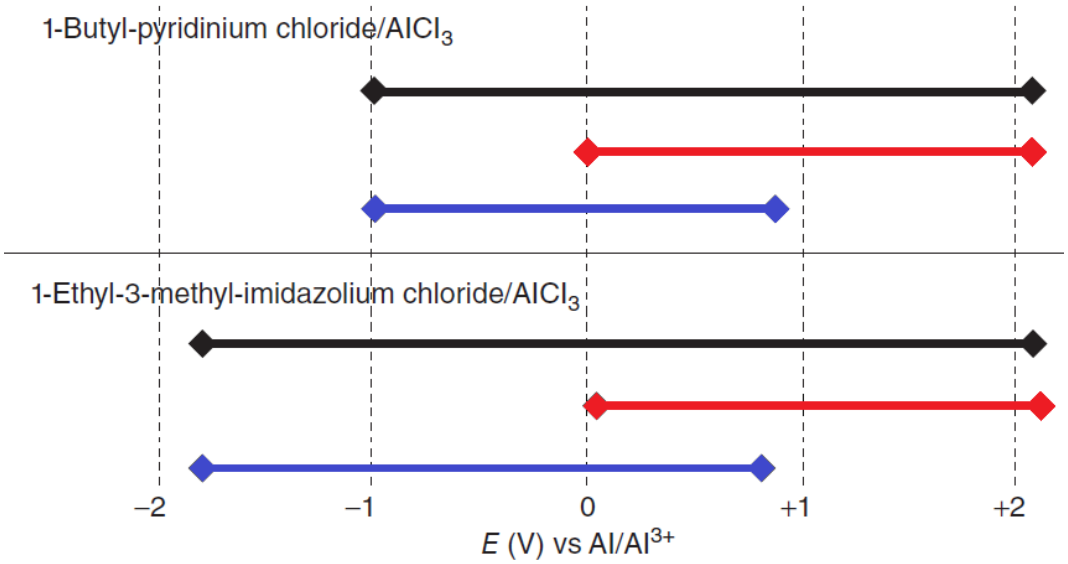


Figure 1.17: Electrochemical windows of [BuPy]Cl-$AlCl_3$ and [C_2C_1Im]Cl-$AlCl_3$ in the neutral (black), Acidic (red) and Basic (blue) regions [2]

The redox potentials of HMILs correlate with the speciation in a system and the cation present. Figure 1.17 shows the EW of [C_4Py]Cl-$AlCl_3$ and [C_2C_1Im]Cl-$AlCl_3$. Both systems show that the EW is much broader in the neutral regions than either the acidic or basic regions. The EW of the neutral region has the same minimum as the system when it is basic and the same maximum potential as the system when it is acidic. The comparison of both systems shows that the EW is broader for the [C_2C_1Im] system in the neutral

and basic range going down to -1.8 compared to -1 for the [C_4Py] system. When the systems are acidic the lower bounds of the EW are around 0 for both systems. The upper bound is lower in the basic region at around 0.8 in both systems and goes up to 2.1 and 2.2 for the [C_4Py]Cl-$AlCl_3$ and [C_2C_1Im]Cl-$AlCl_3$ systems, respectively.[2,113]

Other characteristics of HMILs such as electrical conductivity and viscosity have been shown to change with anionic speciation.[1] It is clear the speciation has an effect on acidity and electrochemical window but as seen by the measurements of eLA it is paramount to understand the correlations to anionic speciation. Once anionic speciation is precisely determined the chemistry of the anions can be determined. The development of any potential applications of HMILs requires a holistic understanding of the link between speciation and the corresponding properties.[1]

1.5 Chemistry of the halometallate ionic liquids under investigation

The twelve systems investigated are summarized in table 1.6.

Table 1.6: Investigated group 13 chlorometallate ionic liquids

	Metal Halide		
Halo Organic Salt	$AlCl_3$	$GaCl_3$	$InCl_3$
$[C_2C_1Im]Cl$	$[C_2C_1Im]Cl - AlCl_3$	$[C_2C_1Im]Cl - GaCl_3$	$[C_2C_1Im]Cl - InCl_3$
$[Choline]Cl$	$[Choline]Cl - AlCl_3$	$[Choline]Cl - GaCl_3$	$[Choline]Cl - InCl_3$
$[N_{2111}]Cl$	$[N_{2111}]Cl - AlCl_3$	$[N_{2111}]Cl - GaCl_3$	$[N_{2111}]Cl - InCl_3$
$[N_{2110}]Cl$	$[N_{2110}]Cl - AlCl_3$	$[N_{2110}]Cl - GaCl_3$	$[N_{2110}]Cl - InCl_3$

The chemistry of each system is largely dominated by the anionic speciation but as seen by the description of the redox properties the cation can have an selected properties of an HMIL. This section describes the chemical structures, functional groups and chemical behavior of the cations and anions in each of the systems studied here. Next the interactions which contribute to differing chemical properties are presented and discussed.

1.5.1 Group 13 chemistry

The group 13 post-transition metals aluminum, gallium and indium are all part of the boron group called icosagenes. The electronic configuration, accessible oxidation states and electronegativities are shown in figure 1.18 as they give insights into the chemical interactions these metals engage in.

13	$1s^2 2s^2 2p^6 3s^2 3p^1$
Al	**+3,** +2, +1, 0, -1, -2
26.982	1.61
31	$1s^2 2s^2 2p^6 3s^2 3p^6 4s^2 3d^{10} 4p^1$
Ga	**+3**, +2, +1, 0, -1, -2, -3, -4, -5
69.723	1.81
49	$1s^2 2s^2 2p^6 3s^2 3p^6 4s^2 3d^{10} 4p^6 5s^2 4d^{10} 5p^1$
In	**+3**, +2, +1, 0, -1, -2, -5
114.82	1.78

Figure 1.18: Group 13 atomic number, atomic mass, electronic configuration, accessible oxidation states and electronegativity (Pauling scale)

All three metals have a preference for the +3 oxidation state. There is no trend in electronegativity down the group but due to the difference in electronegativity, haloaluminate bonds are more ionic than the gallium and indium counter parts, which exhibit bonding with a more covalent character.

1.5.2 Cation chemistry

Out of the four different cations evaluated the most studied IL cation is $[C_2C_1Im]^+$. Imidazolium cations with a variety of primary and secondary chain lengths have been thoroughly investigated in the context of HMILs.[4] The structure of $[C_2C_1Im]^+$ is illustrated in figure 1.19.

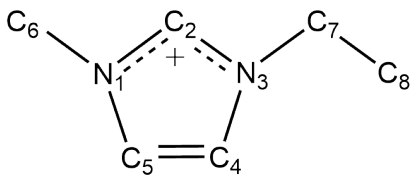


Figure 1.19: 1-ethyl-3-methylimidazolium atomic numbering

Imidazolium has a π-system composed of three carbon and two nitrogen atoms with a formal positive charge spread between the N_1 nitrogen, C_2 carbon and N_3 nitrogen. The formal charge in the structure above arises from the resonance of the electron pairs of the nitrogens between the two N-C_2 Bonds as depicted in figure 1.20.[114]

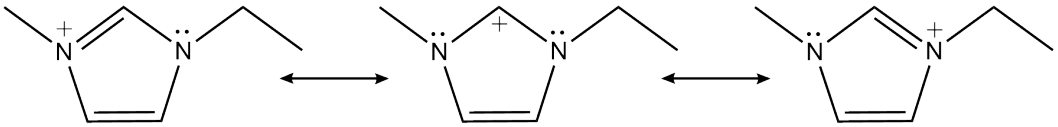


Figure 1.20: 1-ethyl-3-methylimidazolium resonance structures

The $[C_2C_1Im]^+$ cation has two stable conformers, one where the ethyl arm is in plane with the imidazolium ring and one where it is faced out of the plane which will be discussed in more detail in chapter 5.[114]

The hydrogen atoms bonded to the carbon atoms located adjacent to nitrogen atoms in imidazolium-based cations are more electropositive giving rise to a hierarchy in electropositivity of the hydrogen atoms. Disregarding the aliphatic hydrogen atoms, the hydrogen atom bonded to the C_2 carbon is the most electropositive followed by the hydrogens bonded to the C_4 and C_5 carbons. The aromatic hydrogen atoms, particularly the C_2 hydrogen, can consequentially engage in stronger hydrogen bonds than the remainder of the hydrogen atoms in imidazolium-based cations. The aromaticity of the ring allows for π-interactions to take place with the ring system. The reason the imidazolium cation was selected was to have a rigorously studied benchmark system with respect to anionic speciation. Intermolecular interactions between different anionic species and the $[C_2C_1Im]^+$ cation have not been computationally investigated holistically. The wide range of different intermolecular forces which are exhibited allow for a diverse range of interaction profiles which can affect the chemistry of the systems.[114]

The three other cations are ammonium analogs and depicted in figure 1.21. Choline and trimethyl-ethyl-ammonium are both quaternary ammonium analogs and dimethyl-ethyl-ammonium is a tertiary ammonium analog. The formal charges in each cation are located on the nitrogen but computational studies locate the actual charge on the hydrogen atoms. Trimethyl-ethyl-ammonium and dimethyl-ethyl-ammonium are exclusively composed of nitrogen, carbon and hydrogen and the difference in their chemistry is predominantly due to the hydrogen attached to the nitrogen in the dimethyl-ethyl-ammonium which allows for hydrogen bonding to occur. Choline is like the trimethyl-ethyl-ammonium in structure with an additional hydroxyl moiety at the end of the ethyl chain which also allows for hydrogen bonding.

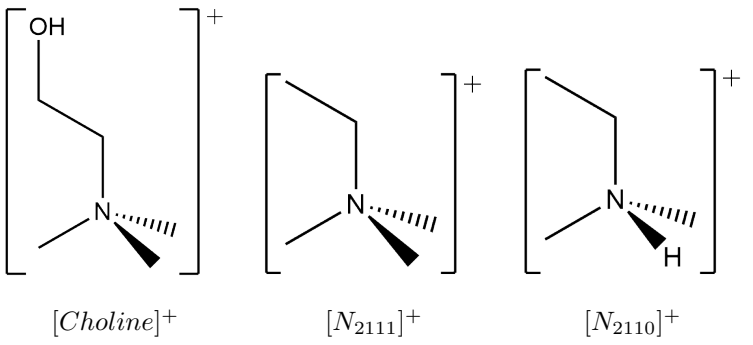


Figure 1.21: Ammonium analog cation structures: choline, trimethyl-ethyl-ammonium dimethyl-ethyl-ammonium

The three ammonium analog cations were selected as they provide a variety of different hydrogen bonding sites. The $[Choline]^+$ and $[N_{2110}]^+$ cations both feature 'classical' hydrogen bonding sites in contrast to the $[N_{2111}]^+$ cation which only has doubly ionic hydrogen bonding sites. The evaluation of the interaction profiles of the different ammonium analogs and $[C_2C_1Im]^+$ will give insight into how changing different functional groups allows for the control of the HMILs properties through the cation selection. Additionally the ammonium analogs are cheap and thus are attractive to use industrially.[115]

1.5.3 Ion - ion interactions

HMILs feature a wide variety of chemical interactions which occur between the ions. The diversity of the interactions which occur in HMILs result in complex interaction profiles which in turn have nuanced effects on the chemistry. Determining the anion-cation, anion-anion and cation-cation interactions that occur and the relative strength of each interaction is essential in understanding the chemistry that occurs and how the HMILs can be used and how the chemistry can be controlled. The analysis of specific interactions based on changing the cation and the anions allows for a more informed choice when selecting a cation and tuning properties via x_{MCl_3}.[116] A rigorous definition of all the underlying chemical interactions is required. This subsection introduces the chemical interactions which occur in the HMIL systems under investigation.

The ion-ion interactions in HMILs are dominated by the strongest interactions which are ionic interactions, also called coulombic or electrostatic interactions, expressed through the coulomb potential. The ionic interactions between ions in HMILs are analogous to those between any conventional ions. The attractive coulombic interactions between species of opposite charge (anion-cation) and the repulsive interactions between species with the same charge (anion-anion and cation-cation) are shown in figure 1.22.[117,118]

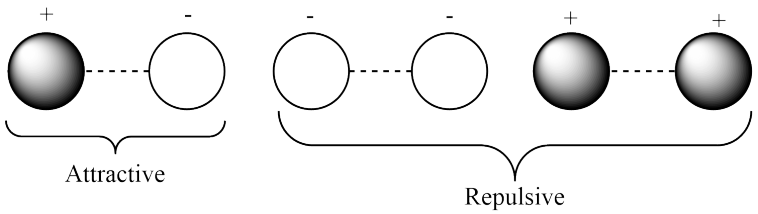


Figure 1.22: Attractive and repulsive coulombic interactions

Unlike conventional salts which are composed of atomic ions, the positive and negative charges in the constituent ions of HMILs are spread over the entire molecular ion and are not localized on a single atom. Hence the larger the ions are the more dispersed the charges and the distance between the two ions center of charge is larger. The coulomb potential is defined in equation 1.5.1 [35]

$$V(r) = \frac{Q_1 Q_2}{4\pi\varepsilon_0 r} \tag{1.5.1}$$

where V(r) is the coulomb potential between two species at distance r. Q_1 and Q_2 are the charges on species 1 and 2 and ε_0 is the vacuum permittivity. When evaluating coulombic interaction in an alternative medium the vacuum permittivity is replaced by the permittivity, ε, of the medium which is determined by equation 1.5.2. [35]

$$\varepsilon = \varepsilon_r \varepsilon_0 \tag{1.5.2}$$

Here ε_r is the relative permittivity, formally known as the dielectric constant. The relative permittivity has a strong effect on the strength of a coulombic interaction and must be considered. [35]

The coulombic interactions between the ions account for approximately 70-90% of the attraction and repulsion between ions in HMILs. The interaction strength decreases linearly at a rate of 1/r as ions move away from each other and between two species with -1 and +1 charges they contribute approximately 250-400 kJ mol^{-1} in energy to the interaction between two ions. [35]

The remainder of the interactions occurring between ions are weaker. Van der Waals forces occur between dipoles and are subdivided into permanent dipole - permanent dipole interactions (Keesom forces), permanent dipole - induced dipole interactions (Debye forces) and induced dipole - induced dipole interactions (London

dispersion forces). Apart from London dispersion forces all the other interactions require specific functional groups and geometric arrangements. The Van der Waals interactions are also coulombic in nature which is reflected in how they are formulated. [35]

An example and diagrammatic representation of Keesom interaction between two permanent dipoles is shown in figure 1.23 followed by the formalism of the interaction in equation 1.5.3 [35]

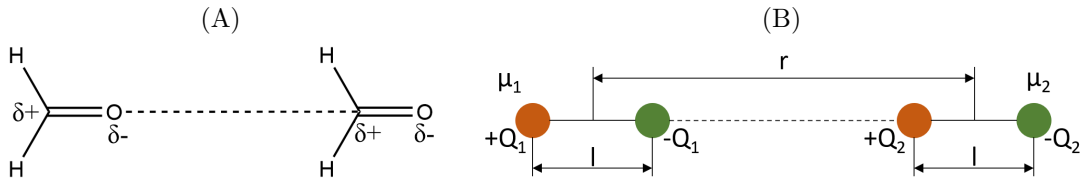


Figure 1.23: Permanent dipole - permanent dipole interactions (Keesom Forces) (A) example and (B) diagrammatic representation

$$V(r) = \frac{\mu_1 \mu_2}{2\pi\varepsilon_0 r^3} \tag{1.5.3}$$

where

$$\mu = Ql \tag{1.5.4}$$

Where l is the distance between the point charges generating a dipole. Equation 1.5.3 has a similar form to equation 1.5.1 but the formal charges (Q) are replaced by the magnitude of the dipole moment, μ given by equation 1.5.4. Additionally the denominator in equation 1.5.3 is multiplied by 2 instead of 4 and the dependence of the potential energy on the distance is now $1/r^3$. μ is defined by the charges generating a dipole as shown in the diagrammatic representation in figure 1.23 (B). The magnitude of the dipole is equal to $Q_1 l$ for μ_1. Here Q_1 is the charge of $+Q_1$ and $-Q_1$ with the distance l between them. [35]

Interacting dipole moments are typically not aligned as shown in figure 1.23 and a more complicated formulation including the orientation of the dipoles is required. Figure 1.24 shows two parallel dipole moments and equation 1.5.5 formulates how dipole changes at this orientation are computed using a cosine function. [35]

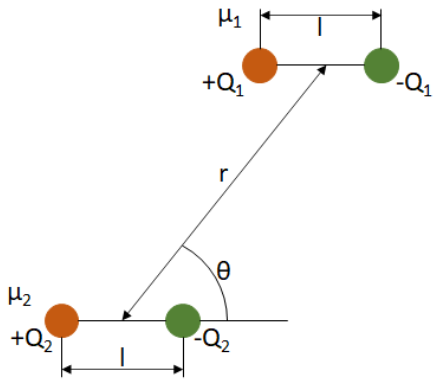


Figure 1.24: Permanent dipole - permanent dipole interactions (Keesom Forces) alternative orientation diagrammatic representation

$$V(r) = \frac{\mu_1\mu_2(1 - 3cos^2\theta)}{4\pi\varepsilon_0 r^3} \tag{1.5.5}$$

When dipole moments are parallel the expression in equation 1.5.5 is used to determine the interaction strength based on the angle θ between the dipoles, as shown in figure 1.24. Species are constantly in motion, i.e. rotating, and hence an average dipole moment is computed by considering that dipoles are in constant rotation with respect to one another. The formalism for this computation is shown in equations1.5.6 and 1.5.7.

$$V(r) = -\frac{C}{r^6} \tag{1.5.6}$$

$$where$$

$$C = \frac{2\mu_1^2\mu_1^2}{3(4\pi\varepsilon_0)^2 kT} \tag{1.5.7}$$

equations 1.5.6 and 1.5.7 encapsulate the Keesom interaction when considering rotation of the dipoles. The distance dependence of Keesom interactions between two rotating species is $1/r^6$. Note that the sign is negative meaning that the average interaction is always net attractive as even in system in motion the attractive orientation of dipoles is more commonly assumed in any medium.

An example of Debye forces (Permanent dipole - induced dipole interactions) are shown in figure 1.25 where the permanent dipole on the Formaldehyde on the right-hand side induces a dipole in the propane on the left. Debye forces are expressed via equation 1.5.8

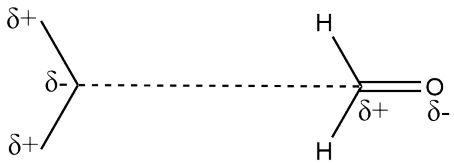


Figure 1.25: Permanent dipole - induced dipole interactions (Debye forces) example

$$V(r) = -\frac{C}{r^6}, C = \frac{\mu_1^2 a_2'}{4\pi\varepsilon_0} \tag{1.5.8}$$

Equation 1.5.8 states that the coulomb potential is dependent on the magnitude of the permanent dipole moment, μ, and the polarizability volume of the species which experiences the induced dipole, a'. The potential energy of Debye forces has a distance dependence of $1/r^6$.[35]

London dispersion forces or induced dipole - induced dipole interactions occur between all chemical species regardless of functional group. An example of induced dipoles interacting with one another is given in figure 1.26 where two butane molecules are interacting.[35]

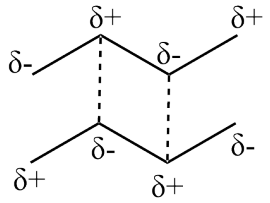


Figure 1.26: Induced dipole - induced dipole interactions (London dispersion forces) between two butane molecules

The induced dipoles are generated due to the constant fluctuation of electron positions around their nucleus. A molecule can generate an instantaneous dipole which generates an electric field which acts upon the surrounding species. The electric field in turn induces a dipole in an adjacent species. The dipoles attract and the potential energy of the adjacent species is lowered. The potential energy of a dispersion interaction is dependent on the polarizability of both species as the strength of the instantaneous dipoles depends on the looseness of the valence electrons. The formulation for the London dispersion force is given in equation 1.5.9.[35]

$$V(r) = -\frac{C}{r^6}, C = \frac{3}{2}a_1' a_2' \frac{I_1 I_2}{I_1 + I_2} \tag{1.5.9}$$

Here I_1 and I_2 are the ionization energies of the two molecules as they are a reference to how tightly bound the electrons are. London dispersion forces also have a distance dependence of $1/r^6$. All the Van der Waals interactions comparatively weak but can still dictate many of the interaction profiles between species.[35] London dispersion forces occur in every molecule while Debeye and Keesom forces require at least one or two functional groups which generate a permanent dipole, respectively.

Hydrogen bonds occur between species where there is an interaction has the structure A-H·B, where A and B are electronegative atoms or functional groups, and H is a hydrogen atom. The species with which the hydrogen bond is generated, B, has at least one lone pair of electrons which can coordinate towards the hydrogen. Hydrogen bonding has a range of contributing interactions including covalent, ionic and VdW. The ionic component of hydrogen bonding is described as an approach between partial charges of the electron deficient hydrogen atom, δ^+, and of the lone pair on the electron rich species, B, δ^-. Figure 1.27 shows a hydrogen bond formed between the oxygen of the adjacent water molecule and the hydrogen of another water molecule. Conventionally it is said that A has to be a fluorine, oxygen or nitrogen atom but a wide variety of functional groups are now known to sufficiently deplete the electron density of an adjacent hydrogen atom.[119,120]

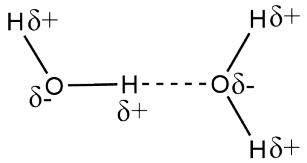


Figure 1.27: Hydrogen bonding between two water molecules

The covalent component of hydrogen bonding can be described via molecular orbital theory. A hydrogen bond can be regarded as the formation of delocalized molecular orbitals between the three participating species, A,B and H. One orbital of each of the three species; A, B and H contributes one atomic orbital which form three molecular orbitals: a bonding, a non-bonding and an anti-bonding orbital as shown in figure 1.28. Four electrons occupy the three orbitals, 2 from the A-H bond and two from the B lone pair which results in a stronger bonding interaction as the anti-bonding orbital is unoccupied.[35]

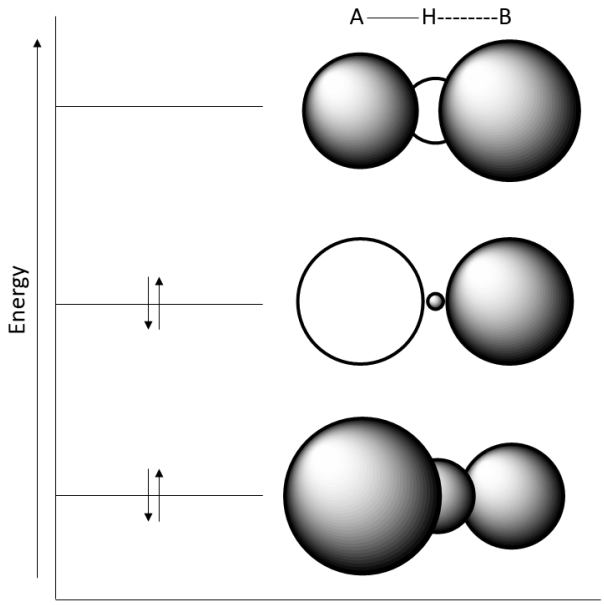


Figure 1.28: Hydrogen bonding molecular orbitals

Hydrogen bonds are typically stronger than Van der Waals interactions but have a huge range in strength; 1 - 170 kJ mol^{-1}. Hence when there is the possibility for hydrogen bonding between species it dominates the inter molecular interactions, orientations and nanostructures in systems as observed in many biological systems.[35]

σ-holes occur when the electron density of a halogen atom is polarized towards the molecular entity they are bonded to. Figure 1.29 shows σ-holes occurring in $[AlCl_4]^-$ where there is a more electron deficient region.[121] The formation of regions of higher and lower charge density can lead to interactions with electrophilic and nucleophilic sites.

Halogen bonds are defined as "a net attractive interaction between an electrophilic region associated with a halogen atom in a molecular entity and nucleophilic region in another".[121] Halogen bonds will not occur in HMILs but the cations in HMILs have highly electrophilic sites which will interact with the electron rich region, orthogonal to the σ-hole. The interaction between the cations and the σ-holes could be defining of the ion pair structures interaction profiles.[121]

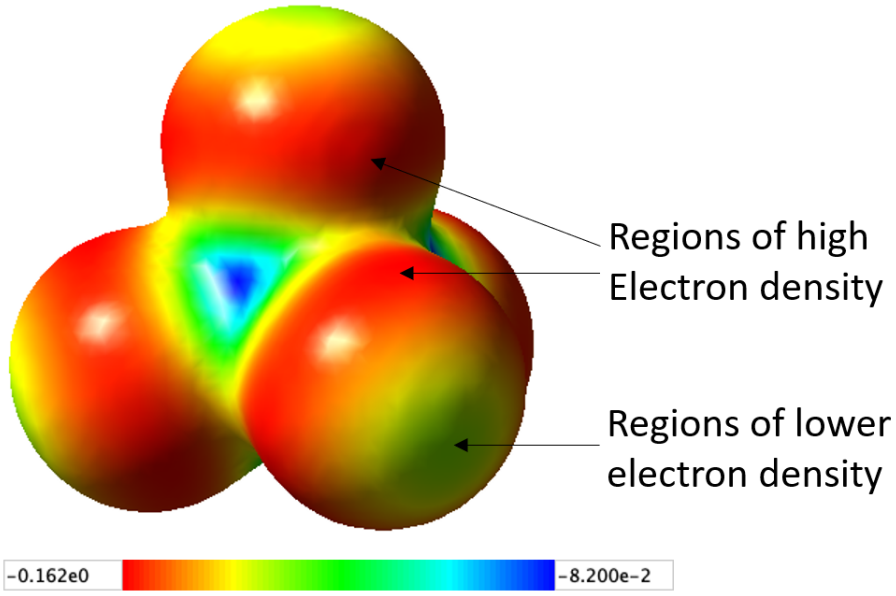


Figure 1.29: Representation of a σ-hole in $[AlCl_4]^-$ via the visualization of the molecular electrostatic potential

HMILs containing the $[C_2C_1Im]^+$ cation feature aromatic interactions. Multiple types of structural configurations of aromatic-aromatic interactions between two cations or aromatic-anion interactions between the aromatic ring and various anions can occur. Aromatic moieties feature a positive or negative quadrupole moment which depends on the substituents attached to an aromatic ring and the ring composition. For example, the aromatic benzene (C_6H_6) has a negative quadrupole moment. Figure 1.30 shows a cross section of the charge distribution in C_6H_6.[122]

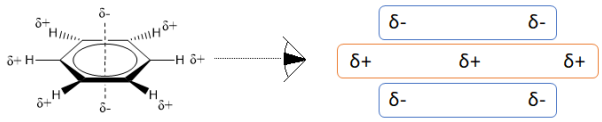


Figure 1.30: C_6H_6 2d charge distribution visualization

Aromatic-aromatic interactions are classified based on geometries of the two interacting aromatic species. The interactions can be attractive and repulsive and are depicted in figure 1.31.[122]

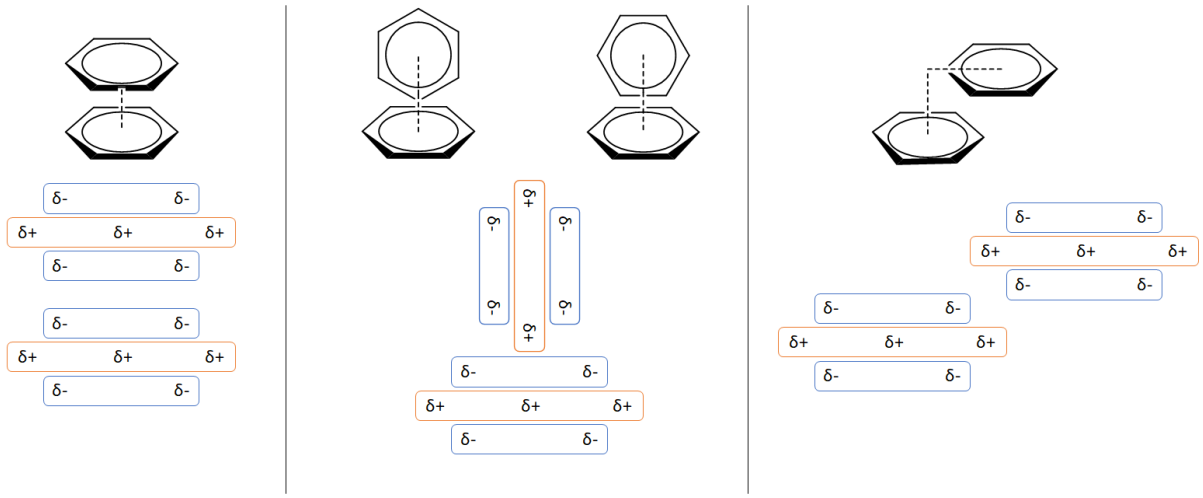


Figure 1.31: Repulsive face stacked (left), attractive Y & T shaped (center) and parallel displaced (right) aromatic interactions

Figure 1.31 shows one repulsive interaction when two electron deficient aromatic rings interact in a parallel face stacked interaction and two attractive interactions, one of which is split into two Y and T shaped interactions. Lastly the parallel displaced interaction is also favorable. The four types of aromatic interactions reveal that the driver for interactions is based on the charge distribution created by the quadrupole moment of each aromatic ring.[122]

The quadrupole moments of aromatic rings generate preferential sites of interaction, these can interact with ions and other neutral species as depicted in figure 1.32.[122]

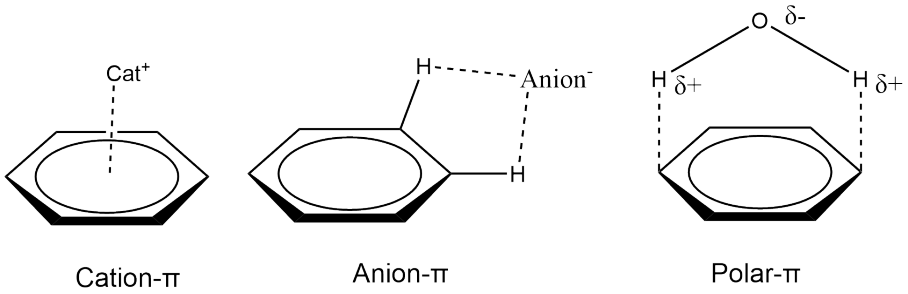


Figure 1.32: Aromatic Interactions with non-aromatic species; aromatic-cation, aromatic-anion and aromatic-permanent dipole interactions

In the systems being investigated within this thesis only aromatic-anion interactions are relevant. Upon the addition of neutral molecules or alternative cations into the system as co-catalysts, complexing agents or to

improve viscosity the cation-π, polar-π interactions become relevant.[1,2]

All the relevant intermolecular interactions which occur in HMILs have been introduced. The understanding of intermolecular interactions in combination with different interaction profiles between anions and cations will give insight into the behavior of HMILs at a molecular level. Additionally, the effects different interactions have on physiochemical properties will be explored in this thesis to guide future investigations on the choice of cation and particular speciation for specific tasks.

1.5.4 Thermodynamics of solvation

The individual interactions occurring in the HMILs provide a nuanced breakdown of how species interact with each other, but it is also critical to understand the interaction of a solute with the solvation environment in a more holistic sense. Solvation is a process in which solvent molecules surround and interact with solute molecules, resulting in the formation of a solution. Thermodynamics provides a useful framework for understanding solvation, and the Gibbs free energy (G) is a key parameter in this context. Understanding the thermodynamics of solvation is crucial as it helps predict the behaviour of solutes in different solvents and provides insights into the spontaneity and feasibility of various processes. The Gibbs free energy change of solvation (Δ G_{solv}) can be expressed as the sum of changes in enthalpy (Δ H_{solv}) and entropy (Δ S_{solv}):

$$\Delta G_{solv} = \Delta H_{solv} - T\Delta S_{solv} \tag{1.5.10}$$

Where (Δ G_{solv}) is the Gibbs free energy change of solvation, (Δ H_{solv}) is the enthalpy change of solvation, (Δ S_{solv}) is the entropy change of solvation, and T is the absolute temperature. Δ H_{solv} involves the energy changes associated with breaking and forming intermolecular forces between solute and solvent molecules. This can include processes like breaking solvent-solvent and solute-solute interactions and forming solvent-solute interactions. Δ S_{solv} accounts for the changes in the degrees of freedom and randomness in the system during solvation. In the case of solvation, if the solvent molecules become more ordered, reduced entropy, upon interaction with the solute. The entropy can offset the enthalpy term and influence the overall spontaneity of the solvation process. Δ G_{solv} contributes to the total Gibbs free energy change (Δ G_{total}) of a reaction or process. If Δ G_{total} is negative, the process is spontaneous under the given conditions. The Gibbs Free Energy of Solvation can be determined through measuring Δ H_{solv} and Δ S_{solv}, using calorimetry and spectroscopy, from which Δ G_{solv} can be calculated. Alternatively Thermodynamic models can be used to estimate Δ H_{solv} and Δ S_{solv}, and subsequently Δ G_{solv}. These models may involve empirical parameters

or be based on statistical mechanics. Lastly activity coefficients can be used to compute the Gibbs free energy change through the relation expressed through the equation:

$$\Delta G_{solv} = RTln(a_{solute}) \tag{1.5.11}$$

where R is the gas constant and a_{solute} is the activity of the solute. This approach is particularly useful for solutions that deviate from ideal behaviour. The accuracy of DFT simulations ΔS_{solv} can in turn be assessed based on the Δ G of gas phase and liquid phase structures. If kTln(P) and the ideal gas law (PV=nRT) are consistent with gas-phase calculations the behavior of the substance should resemble that of an ideal gas. If kTln(a) accurately describes the solvation behavior, it indicates how well the DFT simulations with the SMD model capture the thermodynamics of the solute in the solvent environment.

1.6 Aims of the investigation

The overarching aim of the investigation is to understand the behavior of group 13 HMILs on a molecular level to leverage their behavior for potential applications. In order to achieve this goal, the investigations aims to investigate the systems summarized in table 1.6 comprised of combinations of the $[C_2C_1Im]^+$, $[Choline]^+$, $[N_{2110}]^+$ and $[N_{2111}]^+$ cations with different group 13 chlorometallates; Cl-$AlCl_3$, Cl-$GaCl_3$ and Cl-$InCl_3$. The study aims to provide rigorous insight into the chemistry of these HMILs and provide computational methods which can be used to supplement experimental data.

The first aim of the investigation is to determine the anionic speciation respect to different metals, cations, phases and x_{MCl_3}. The anionic speciation with respect to different metals and cations will give insight into how transferable the determination of anionic speciation is between systems. The comparison of gas phase to liquid phase computations using SMD will give insight into how phase changes affect speciation. The evaluation of anionic speciation also aims to give insight into discrepancies which have been shown by different analytical techniques which may be induced by a phase change.

The second aim is to generate XPS spectral outputs from the structures generated from DFT calculation and compare them to experimental XPS data. The computationally generated XPS spectra are useful in determining anionic speciation in equilibria as they can be decomposed with respect to the prevalent species and individual environments within species. This allows for a cationic output to be subtracted from the total spectrum and the relative amounts of anions in equilibrium to be determined from the intensity of different

spectra.

The third aim is to investigate the interaction profiles with respect to metal centers, anionic speciation, and cations in the system. It is essential to understand how different ions interact with one another and what kind of interaction profiles have different effects on the relative stability of a system. To understand how these species could be modified it is essential to understand how they interact with one another and how these interactions have effects on the physiochemical properties. The interactions between all varieties of ion pairs are evaluated.

Lastly the investigation aims to determine the properties with respect to changing the anionic speciation in each system. The determination of the properties relative to changing the anionic speciation will allow for the systems to be used in novel applications or current applications may be improved.

Bibliography

[1] J Estager, JD Holbrey, and Malgorzata Swadźba-Kwaśny. Halometallate ionic liquids–revisited. *Chemical Society Reviews*, 43(3):847–886, 2014.

[2] Frank Endres, Andrew Abbott, and Douglas R MacFarlane. *Electrodeposition from ionic liquids*. John Wiley & Sons, 2017.

[3] Zhengqiang Hu, Hao Zhang, Huaizhi Wang, Fengling Zhang, Qiang Li, and Hongsen Li. Nonaqueous aluminum ion batteries: recent progress and prospects. *ACS Materials Letters*, 2(8):887–904, 2020.

[4] Tom Welton. Ionic liquids: a brief history. *Biophysical reviews*, 10(3):691–706, 2018.

[5] Emma L Smith, Andrew P Abbott, and Karl S Ryder. Deep eutectic solvents (dess) and their applications. *Chemical reviews*, 114(21):11060–11082, 2014.

[6] Benworth B Hansen, Stephanie Spittle, Brian Chen, Derrick Poe, Yong Zhang, Jeffrey M Klein, Alexandre Horton, Laxmi Adhikari, Tamar Zelovich, Brian W Doherty, et al. Deep eutectic solvents: A review of fundamentals and applications. *Chemical reviews*, 121(3):1232–1285, 2020.

[7] Justyna Płotka-Wasylka, Miguel De la Guardia, Vasil Andruch, and Mária Vilková. Deep eutectic solvents vs ionic liquids: Similarities and differences. *Microchemical Journal*, 159:105539, 2020.

[8] JOHN ANDREWS and PIERRE BONNIFAY. The ifp dimersol process for dimerization of propylene into isohexenes: An attractive alternate to propylene alkylation. ACS Publications, 1977.

[9] Paul Weaver, Leo Jansen, Geert Van Grootveld, Egbert Van Spiegel, and Philip Vergragt. *Sustainable technology development*. Routledge, 2017.

[10] C Stewart Slater and Mariano J Savelski. Towards a greener manufacturing environment. *Innov Pharm Technol*, 29:78–83, 2009.

[11] Mordechay Schlesinger and Milan Paunovic. *Modern electroplating*. John Wiley & Sons, 2011.

[12] L Martinu, O Zabeida, and JE Klemberg-Sapieha. Plasma-enhanced chemical vapor deposition of functional coatings. *Handbook of deposition technologies for films and coatings*, pages 392–465, 2010.

[13] Andresa Baptista, Francisco Silva, Jacobo Porteiro, José Míguez, and Gustavo Pinto. Sputtering physical vapour deposition (pvd) coatings: A critical review on process improvement and market trend demands. *Coatings*, 8(11):402, 2018.

[14] WA Bryant. The fundamentals of chemical vapour deposition. *Journal of Materials science*, 12: 1285–1306, 1977.

[15] Luzhao Sun, Guowen Yuan, Libo Gao, Jieun Yang, Manish Chhowalla, Meysam Heydari Gharahcheshmeh, Karen K Gleason, Yong Seok Choi, Byung Hee Hong, and Zhongfan Liu. Chemical vapour deposition. *Nature Reviews Methods Primers*, 1(1):5, 2021.

[16] E Spencer Williams, Julie Panko, and Dennis J Paustenbach. The european union's reach regulation: a review of its history and requirements. *Critical reviews in toxicology*, 39(7):553–575, 2009.

[17] Kosuke Izutsu. *Electrochemistry in nonaqueous solutions*. John Wiley & Sons, 2009.

[18] Karl Ziegler and Herbert Lehmkuhl. Die elektrolytische abscheidung von aluminium aus organischen komplexverbindungen. *Zeitschrift für anorganische und allgemeine Chemie*, 283(1-6):414–424, 1956. doi: https://doi.org/10.1002/zaac.19562830142. URL `https://onlinelibrary.wiley.com/doi/abs/10.1002/zaac.19562830142`.

[19] E Peled and E Gileadi. The electrodeposition of aluminum from aromatic hydrocarbon: I. composition of baths and the effect of additives. *Journal of the Electrochemical Society*, 123(1):15, 1976.

[20] W Kautek and S Birkle. Aluminum-electrocrystallization from metal—organic electrolytes. *Electrochimica acta*, 34(8):1213–1218, 1989.

[21] William H Kruesi and Derek J Fray. The electrowinning of lithium from chloride-carbonate melts. *Metallurgical Transactions B*, 24:605–615, 1993.

[22] DJ Fray and GZ Chen. Reduction of titanium and other metal oxides using electrodeoxidation. *Materials science and technology*, 20(3):295–300, 2004.

[23] Kai Grjotheim. *Aluminium electrolysis: fundamentals of the Hall-Héroult process*. International Publishers Service, Incorporated, 1982.

[24] Sherif Zein El Abedin and Frank Endres. Ionic liquids: the link to high-temperature molten salts? *Accounts of chemical research*, 40(11):1106–1113, 2007.

[25] N Borisenko, Sh Zein El Abedin, and F Endres. In situ stm investigation of gold reconstruction and of silicon electrodeposition on au (111) in the room temperature ionic liquid 1-butyl-1-methylpyrrolidinium bis (trifluoromethylsulfonyl) imide. *The journal of physical chemistry B*, 110 (12):6250–6256, 2006.

[26] R Al-Salman, S Zein El Abedin, and F Endres. Electrodeposition of ge, si and si x ge 1- x from an air-and water-stable ionic liquid. *Physical Chemistry Chemical Physics*, 10(31):4650–4657, 2008.

[27] LHS Gasparotto, N Borisenko, O Höfft, R Al-Salman, W Maus-Friedrichs, N Bocchi, S Zein El Abedin, and F Endres. In situ stm studies of ga electrodeposition from gacl3 in the air-and water-stable ionic liquid 1-butyl-1-methylpyrrolidinium bis (trifluoromethylsulfonyl) amide. *Electrochimica acta*, 55(1): 218–226, 2009.

[28] S Zein El Abedin, AY Saad, HK Farag, N Borisenko, QX Liu, and F Endres. Electrodeposition of selenium, indium and copper in an air-and water-stable ionic liquid at variable temperatures. *Electrochimica Acta*, 52(8):2746–2754, 2007.

[29] F Golgovici, A Cojocaru, M Nedelcu, and T Visan. Voltammetric and impedance studies of electrodeposition of te and its binary compounds with bi and sb using choline chloride-urea based electrolyte. *Chalcogenide Letters*, 6(8), 2009.

[30] Phillip J Dale, Anura P Samantilleke, Dilip D Shivagan, and Laurence M Peter. Synthesis of cadmium and zinc semiconductor compounds from an ionic liquid containing choline chloride and urea. *Thin Solid Films*, 515(15):5751–5754, 2007.

[31] Alexey Izgorodin, Orawan Winther-Jensen, Bjorn Winther-Jensen, and Douglas R MacFarlane. Cds thin-film electrodeposition from a phosphonium ionic liquid. *Physical Chemistry Chemical Physics*, 11 (38):8532–8537, 2009.

[32] QX Liu, S Zein El Abedin, and F Endres. Electrodeposition of nanocrystalline aluminum: Breakdown of imidazolium cations modifies the crystal size. *Journal of the Electrochemical Society*, 155(5):D357, 2008.

[33] S Zein El Abedin, EM Moustafa, R Hempelmann, H Natter, and F Endres. Electrodeposition of nano- and microcrystalline aluminium in three different air and water stable ionic liquids. *Chemphyschem: a European journal of chemical physics and physical chemistry*, 7(7):1535–1543, 2006.

[34] Philipp Eiden, Qunxian Liu, Sherif Zein El Abedin, Frank Endres, and Ingo Krossing. An experimental and theoretical study of the aluminium species present in mixtures of alcl3 with the ionic liquids [bmp] tf2n and [emim] tf2n. *Chemistry–A European Journal*, 15(14):3426–3434, 2009.

[35] Peter Atkins, Peter William Atkins, and Julio de Paula. *Atkins' physical chemistry*. Oxford university press, 2014.

[36] Matthew Li, Jun Lu, Zhongwei Chen, and Khalil Amine. 30 years of lithium-ion batteries. *Advanced Materials*, 30(33):1800561, 2018.

[37] Jing Xie and Yi-Chun Lu. A retrospective on lithium-ion batteries. *Nature communications*, 11(1): 2499, 2020.

[38] Giuseppe Antonio Elia, Kostiantyn V Kravchyk, Maksym V Kovalenko, Joaquín Chacón, Alex Holland, and Richard GA Wills. An overview and prospective on al and al-ion battery technologies. *Journal of Power Sources*, 481:228870, 2021.

[39] Tilmann Leisegang, Falk Meutzner, Matthias Zschornak, Wolfram Münchgesang, Robert Schmid, Tina Nestler, Roman A Eremin, Artem A Kabanov, Vladislav A Blatov, and Dirk C Meyer. The aluminum-ion battery: a sustainable and seminal concept? *Frontiers in Chemistry*, 7:268, 2019.

[40] Meng-Chang Lin, Ming Gong, Bingan Lu, Yingpeng Wu, Di-Yan Wang, Mingyun Guan, Michael Angell, Changxin Chen, Jiang Yang, Bing-Joe Hwang, et al. An ultrafast rechargeable aluminium-ion battery. *Nature*, 520(7547):324–328, 2015.

[41] Ib Chorkendorff and Johannes W Niemantsverdriet. *Concepts of modern catalysis and kinetics*. John Wiley & Sons, 2017.

[42] John N Armor. A history of industrial catalysis. *Catalysis Today*, 163(1):3–9, 2011.

[43] George A Olah, V Prakash Reddy, and GK Surya Prakash. Friedel-crafts reactions. *Kirk-Othmer Encyclopedia of Chemical Technology*, 2000.

[44] John Humphreys, Rong Lan, and Shanwen Tao. Development and recent progress on ammonia synthesis catalysts for haber–bosch process. *Advanced Energy and Sustainability Research*, 2(1): 2000043, 2021.

[45] Ralf Giernoth. Task-specific ionic liquids. *Angewandte Chemie International Edition*, 49(16):2834–2839, 2010.

[46] Devdutt Chaturvedi. Recent developments on task specific ionic liquids. *Current Organic Chemistry*, 15:1236–1248, 2011.

[47] Richard P Matthews, Claire Ashworth, Tom Welton, and Patricia A Hunt. The impact of anion electronic structure: similarities and differences in imidazolium based ionic liquids. *Journal of Physics: Condensed Matter*, 26(28):284112, 2014.

[48] Thomas Welton. Room-temperature ionic liquids. solvents for synthesis and catalysis. *Chemical reviews*, 99(8):2071–2084, 1999.

[49] Jason P Hallett and Tom Welton. Room-temperature ionic liquids: solvents for synthesis and catalysis. 2. *Chemical reviews*, 111(5):3508–3576, 2011.

[50] Robin D Rogers and Kenneth R Seddon. Ionic liquids–solvents of the future? *Science*, 302(5646): 792–793, 2003.

[51] Natalia V Plechkova and Kenneth R Seddon. Applications of ionic liquids in the chemical industry. *Chemical Society Reviews*, 37(1):123–150, 2008.

[52] Adam J Greer, Johan Jacquemin, and Christopher Hardacre. Industrial applications of ionic liquids. *Molecules*, 25(21):5207, 2020.

[53] Benworth B Hansen, Stephanie Spittle, Brian Chen, Derrick Poe, Yong Zhang, Jeffrey M Klein, Alexandre Horton, Laxmi Adhikari, Tamar Zelovich, Brian W Doherty, et al. Deep eutectic solvents: A review of fundamentals and applications. *Chemical reviews*, 121(3):1232–1285, 2020.

[54] Claire R Ashworth, Richard P Matthews, Tom Welton, and Patricia A Hunt. Doubly ionic hydrogen bond interactions within the choline chloride–urea deep eutectic solvent. *Physical Chemistry Chemical Physics*, 18(27):18145–18160, 2016.

[55] Dinis O Abranches, Mónia AR Martins, Liliana P Silva, Nicolas Schaeffer, Simão P Pinho, and João AP Coutinho. Phenolic hydrogen bond donors in the formation of non-ionic deep eutectic solvents: the quest for type v des. *Chemical Communications*, 55(69):10253–10256, 2019.

[56] HA Øye, M Jagtoyen, T Oksefjell, and JS Wilkes. Vapour pressure and thermodynamics of the system 1-methyl-3-ethyl-imidazolium chloride-aluminium chloride. In *Materials Science Forum*, volume 73, pages 183–190. Trans Tech Publ, 1991.

[57] Rolf W Berg. Raman spectroscopy and ab-initio model calculations on ionic liquids. *Monatshefte für Chemie-Chemical Monthly*, 138:1045–1075, 2007.

[58] Julien Estager, Peter Nockemann, Kenneth R Seddon, Małgorzata Swadźba-Kwaśny, and Sophie Tyrrell. Validation of speciation techniques: a study of chlorozincate (ii) ionic liquids. *Inorganic Chemistry*, 50(11):5258–5271, 2011.

[59] J Robinson, RC Bugle, HL Chum, D Koran, and RA Osteryoung. Proton and carbon-13 nuclear magnetic resonance spectroscopy studies of aluminum halide-alkylpyridinium halide molten salts and their benzene solutions. *Journal of the American Chemical Society*, 101(14):3776–3779, 1979.

[60] Vincent Lecocq, Aurélie Graille, Catherine C Santini, Anne Baudouin, Yves Chauvin, Jean Marie Basset, Laurence Arzel, Denis Bouchu, and Bernard Fenet. Synthesis and characterization of ionic liquids based upon 1-butyl-2, 3-dimethylimidazolium chloride/zncl 2. *New journal of chemistry*, 29(5): 700–706, 2005.

[61] Kerstin Thiel, Tillmann Klamroth, Peter Strauch, and Andreas Taubert. On the interaction of ascorbic acid and the tetrachlorocuprate ion [cucl 4] 2- in cucl nanoplatelet formation from an ionic liquid precursor (ilp). *Physical Chemistry Chemical Physics*, 13(30):13537–13543, 2011.

[62] Yu Su, Heather M Brown, Guosheng Li, Xiao-dong Zhou, James E Amonette, John L Fulton, Donald M Camaioni, and Z Conrad Zhang. Accelerated cellulose depolymerization catalyzed by paired metal chlorides in ionic liquid solvent. *Applied Catalysis A: General*, 391(1-2):436–442, 2011.

[63] EN Golubeva, AI Kokorin, DI Kochubei, VI Pergushov, and VV Kriventsov. Structure and composition of the anionic chloride complexes of copper (ii) as the precursors of catalysts for c–cl bond metathesis. *Kinetics and catalysis*, 43:408–411, 2002.

[64] Kevin RJ Lovelock, Ignacio J Villar-Garcia, Florian Maier, Hans-Peter Steinrück, and Peter Licence. Photoelectron spectroscopy of ionic liquid-based interfaces. *Chemical reviews*, 110(9):5158–5190, 2010.

[65] Christopher Hardacre. Application of exafs to molten salts and ionic liquid technology. *Annu. Rev. Mater. Res.*, 35:29–49, 2005.

[66] FG Edwards, JE Enderby, RA Howe, and DI Page. The structure of molten sodium chloride. *Journal of Physics C: Solid State Physics*, 8(21):3483, 1975.

[67] S Takahashi, K Suzuya, S Kohara, N Koura, LA Curtiss, and M-L Saboungi. Structure of 1-ethyl-3-methylimidazolium chloroaluminates: Neutron diffraction measurements and ab initio calculations. *Zeitschrift für Physikalische Chemie*, 209(2):209–221, 1999.

[68] Christopher J Cramer. *Essentials of computational chemistry: theories and models*. John Wiley & Sons, 2013.

[69] RJ Gale, B Gilbert, and RA Osteryoung. Raman spectra of molten aluminum chloride: 1-butylpyridinium chloride systems at ambient temperatures. *Inorganic Chemistry*, 17(10):2728–2729, 1978.

[70] SP Wicelinski, RJ Gale, Stephen D Williams, and G Mamantov. Raman spectra of molten gallium chloride: 1-methyl-3-ethylimidazolium chloride at ambient temperatures. *Spectrochimica Acta Part A: Molecular Spectroscopy*, 45(7):759–762, 1989.

[71] S Takahashi, LA Curtiss, D Gosztola, N Koura, and Marie-Louise Saboungi. Molecular orbital calculations and raman measurements for 1-ethyl-3-methylimidazolium chloroaluminates. *Inorganic Chemistry*, 34(11):2990–2993, 1995.

[72] Melquizedeque B Alves, Vianney O Santos Jr, Valerio CD Soares, Paulo AZ Suarez, and Joel C Rubim. Raman spectroscopy of ionic liquids derived from 1-n-butyl-3-methylimidazolium chloride and niobium chloride or zinc chloride mixtures. *Journal of Raman Spectroscopy: An International Journal for Original Work in all Aspects of Raman Spectroscopy, Including Higher Order Processes, and also Brillouin and Rayleigh Scattering*, 39(10):1388–1395, 2008.

[73] Paul A Madden, Mark Wilson, and Francis Hutchinson. Raman spectra of ionic liquids: Interpretation via computer simulation. *The Journal of chemical physics*, 120(14):6609–6620, 2004.

[74] Joel L Gray and Gary E Maciel. Aluminum-27 nuclear magnetic resonance study of the room-temperature melt aluminum trichloride butylpyridinium chloride. *Journal of the American Chemical Society*, 103(24):7147–7151, 1981.

[75] S Takahashi, Marie-Louise Saboungi, RJ Klingler, MJ Chen, and JW Rathke. Dynamics of room-temperature melts: nuclear magnetic resonance measurements of dialkylimidazolium haloaluminates. *Journal of the Chemical Society, Faraday Transactions*, 89(19):3591–3595, 1993.

[76] Vincent Lecocq, Aurélie Graille, Catherine C Santini, Anne Baudouin, Yves Chauvin, Jean Marie Basset, Laurence Arzel, Denis Bouchu, and Bernard Fenet. Synthesis and characterization of ionic liquids based upon 1-butyl-2, 3-dimethylimidazolium chloride/zncl 2. *New journal of chemistry*, 29(5): 700–706, 2005.

[77] Matthew Currie, Julien Estager, Peter Licence, Shuang Men, Peter Nockemann, Kenneth R Seddon, Małgorzata Swadźba-Kwaśny, and Cecile Terrade. Chlorostannate (ii) ionic liquids: speciation, lewis acidity, and oxidative stability. *Inorganic Chemistry*, 52(4):1710–1721, 2013.

[78] David C Apperley, Christopher Hardacre, Peter Licence, Richard W Murphy, Natalia V Plechkova, Kenneth R Seddon, Geetha Srinivasan, Małgorzata Swadźba-Kwaśny, and Ignacio J Villar-Garcia. Speciation of chloroindate (iii) ionic liquids. *Dalton Transactions*, 39(37):8679–8687, 2010.

[79] Christopher Hardacre, Richard W Murphy, Kenneth R Seddon, Geetha Srinivasan, and Małgorzata Swadźba-Kwaśny. Speciation of chlorometallate ionic liquids based on gallium (iii) and indium (iii). *Australian journal of chemistry*, 63(5):845–848, 2010.

[80] Joseph D Andrade. X-ray photoelectron spectroscopy (xps). *Surface and Interfacial Aspects of Biomedical Polymers: Volume 1 Surface Chemistry and Physics*, pages 105–195, 1985.

[81] Alasdair W Taylor, Shuang Men, Coby J Clarke, and Peter Licence. Acidity and basicity of halometallate-based ionic liquids from x-ray photoelectron spectroscopy. *RSC advances*, 3(24):9436–9445, 2013.

[82] Andrew TB Gilbert, Nicholas A Besley, and Peter MW Gill. Self-consistent field calculations of excited states using the maximum overlap method (mom). *The Journal of Physical Chemistry A*, 112 (50):13164–13171, 2008.

[83] Evgeny A Pidko, Volkan Degirmenci, Rutger A van Santen, and Emiel JM Hensen. Coordination properties of ionic liquid-mediated chromium (ii) and copper (ii) chlorides and their complexes with glucose. *Inorganic chemistry*, 49(21):10081–10091, 2010.

[84] Armand A Fannin Jr, Danilo A Floreani, Lowell A King, John S Landers, Bernard J Piersma, Daniel J Stech, Robert L Vaughn, John S Wilkes, and John L Williams. Properties of 1, 3-dialkylimidazolium chloride-aluminum chloride ionic liquids. 2. phase transitions, densities, electrical conductivities, and viscosities. *The Journal of Physical Chemistry*, 88(12):2614–2621, 1984.

[85] Steven A Bolkan and John T Yoke. Room temperature fused salts based on copper (i) chloride-1-methyl-3-ethylimidazolium chloride mixtures. 1. physical properties. *Journal of Chemical and Engineering Data*, 31(2):194–197, 1986.

[86] Gilbert J Mains, Evangelos A Nantsis, and W Robert Carper. Ab initio bonding, molecular structure, and quadrupole coupling constants of aluminum chlorides. *The Journal of Physical Chemistry A*, 105 (17):4371–4378, 2001.

[87] Melissa S Sitze, Eric R Schreiter, Eric V Patterson, and R Griffith Freeman. Ionic liquids based on fecl3 and fecl2. raman scattering and ab initio calculations. *Inorganic Chemistry*, 40(10):2298–2304, 2001.

[88] Jia-Zhen Yang, Peng Tian, Ling-Ling He, and Wei-Guo Xu. Studies on room temperature ionic liquid incl3–emic. *Fluid Phase Equilibria*, 204(2):295–302, 2003.

[89] Eric R Schreiter, Jonathan E Stevens, Michael F Ortwerth, and R Griffith Freeman. A room-temperature molten salt prepared from aucl3 and 1-ethyl-3-methylimidazolium chloride. *Inorganic Chemistry*, 38(17):3935–3937, 1999.

[90] Barbara Kirchner and Ari P Seitsonen. Ionic liquids from car- parrinello simulations. 2. structural diffusion leading to large anions in chloraluminate ionic liquids. *Inorganic chemistry*, 46(7):2751–2754, 2007.

[91] Ramón Alain Miranda-Quintana, Farnaz Heidar-Zadeh, Stijn Fias, Allison EA Chapman, Shubin Liu, Christophe Morell, Tatiana Gómez, Carlos Cárdenas, and Paul W Ayers. Molecular interactions from the density functional theory for chemical reactivity: The interaction energy between two-reagents. *Frontiers in Chemistry*, 10, 2022.

[92] Ala'a K Abdul-Sada, Anthony M Greenway, Kenneth R Seddon, and Thomas Welton. A fast atom bombardment mass spectrometric study of room-temperature 1-ethyl-3-methylimidazolium

chloroaluminate (iii) ionic liquids. evidence for the existence of the decachlorotrialuminate (iii) anion. *Organic mass spectrometry*, 28(7):759–765, 1993.

[93] Glen P Jackson and Douglas C Duckworth. Electrospray mass spectrometry of undiluted ionic liquids. *Chemical communications*, (5):522–523, 2004.

[94] Boris L Milman and Zeev B Alfassi. Detection and identification of cations and anions of ionic liquids by means of electrospray ionization mass spectrometry and tandem mass spectrometry. *European Journal of Mass Spectrometry*, 11(1):35–42, 2005.

[95] Paul S Campbell, Catherine C Santini, Denis Bouchu, Bernard Fenet, Leszek Rycerz, Yves Chauvin, Marcelle Gaune-Escard, Catherine Bessada, and Anne-Laure Rollet. Synthesis and characterisation of ionic liquids based on 1-butyl-3-methylimidazolium chloride and mcl4, m= hf and zr. *Dalton Transactions*, 39(5):1379–1388, 2010.

[96] Steven P Wicelinski, Robert J Gale, Krishna M Pamidimukkala, and Roger A Laine. Fast atom bombardment mass spectrometry of low temperature chloroaluminate and chlorogallate melts. *Analytical Chemistry*, 60(20):2228–2232, 1988.

[97] Ala'a K Abdul-Sada, Anthony M Greenway, Kenneth R Seddon, and Thomas Welton. A fast atom bombardment mass spectrometric study of room-temperature 1-ethyl-3-methylimidazolium chloroaluminate (iii) ionic liquids. evidence for the existence of the decachlorotrialuminate (iii) anion. *Organic mass spectrometry*, 28(7):759–765, 1993.

[98] Steven P Wicelinski, Robert J Gale, Krishna M Pamidimukkala, and Roger A Laine. Fast atom bombardment mass spectrometry of low temperature chloroaluminate and chlorogallate melts. *Analytical Chemistry*, 60(20):2228–2232, 1988.

[99] Ala'a K Abdul-Sada, Anthony M Greenway, Kenneth R Seddon, and Thomas Welton. Upon the existence of [al3cl10]- in room temperature chloroaluminate ionic liquids. *Organic mass spectrometry*, 24(10):917–918, 1989.

[100] Valerio B Di Marco, Luca Raveane, Annalisa Dean, and Pietro Traldi. Perturbations produced by electrospray ionization mass spectrometry in the speciation of aluminium (iii)/1, 6-dimethyl-4-hydroxy-3-pyridinecarboxylate aqueous solutions. *Rapid Communications in Mass Spectrometry: An International Journal Devoted to the Rapid Dissemination of Up-to-the-Minute Research in Mass Spectrometry*, 24(7):868–874, 2010.

[101] EN Golubeva, AI Kokorin, DI Kochubei, VI Pergushov, and VV Kriventsov. Structure and composition of the anionic chloride complexes of copper (ii) as the precursors of catalysts for c–cl bond metathesis. *Kinetics and catalysis*, 43:408–411, 2002.

[102] XueQi Xing, GuoYing Zhao, and JianZhong Cui. Chlorogallate (iii) ionic liquids: Synthesis, acidity determination and their catalytic performances for isobutane alkylation. *Science China Chemistry*, 55 (8):1542–1547, 2012.

[103] Christopher Hardacre, Richard W Murphy, Kenneth R Seddon, Geetha Srinivasan, and Małgorzata Swadźba-Kwaśny. Speciation of chlorometallate ionic liquids based on gallium (iii) and indium (iii). *Australian journal of chemistry*, 63(5):845–848, 2010.

[104] Jia-Zhen Yang, Peng Tian, Wei-Guo Xu, Bin Xu, and Shang-Zhang Liu. Studies on an ionic liquid prepared from incl3 and 1-methyl-3-butylimidazolium chloride. *Thermochimica acta*, 412(1-2):1–5, 2004.

[105] Philipp Erdmann and Lutz Greb. What distinguishes the strength and the effect of a lewis acid: Analysis of the gutmann–beckett method. *Angewandte Chemie*, 134(4):e202114550, 2022.

[106] Philipp Erdmann, Jonas Leitner, Julia Schwarz, and Lutz Greb. An extensive set of accurate fluoride ion affinities for p-block element lewis acids and basic design principles for strong fluoride ion acceptors. *ChemPhysChem*, 21(10):987–994, 2020.

[107] Ulrich Mayer, Viktor Gutmann, and Wolfgang Gerger. The acceptor number—a quantitative empirical parameter for the electrophilic properties of solvents. *Monatshefte für Chemie/Chemical Monthly*, 106: 1235–1257, 1975.

[108] Michael A Beckett, Gary C Strickland, John R Holland, and K Sukumar Varma. A convenient nmr method for the measurement of lewis acidity at boron centres: correlation of reaction rates of lewis acid initiated epoxide polymerizations with lewis acidity. *Polymer*, 37(20):4629–4631, 1996.

[109] Andrew R Jupp, Timothy C Johnstone, and Douglas W Stephan. The global electrophilicity index as a metric for lewis acidity. *Dalton Transactions*, 47(20):7029–7035, 2018.

[110] Ralph G. Pearson. The hsab principle — more quantitative aspects. *Inorganica Chimica Acta*, 240(1):93–98, 1995. ISSN 0020-1693. doi: https://doi.org/10.1016/0020-1693(95)04648-8. URL `https://www.sciencedirect.com/science/article/pii/0020169395046488`.

[111] Thomas A Zawodzinski Jr and Robert A Osteryoung. Donor-acceptor properties of ambient-temperature chloroaluminate melts. *Inorganic Chemistry*, 28(9):1710–1715, 1989.

[112] Julien Estager, Alexander A Oliferenko, Kenneth R Seddon, and Małgorzata Swadźba-Kwaśny. Chlorometallate (iii) ionic liquids as lewis acidic catalysts–a quantitative study of acceptor properties. *Dalton Transactions*, 39(47):11375–11382, 2010.

[113] Marek Lipsztajn and Robert A Osteryoung. Electrochemistry in neutral ambient-temperature ionic liquids. 1. studies of iron (iii), neodymium (iii), and lithium (i). *Inorganic Chemistry*, 24(5):716–719, 1985.

[114] Richard P Matthews, Tom Welton, and Patricia A Hunt. Competitive pi interactions and hydrogen bonding within imidazolium ionic liquids. *Physical Chemistry Chemical Physics*, 16(7):3238–3253, 2014.

[115] Long Chen, Mahdi Sharifzadeh, Niall Mac Dowell, Tom Welton, Nilay Shah, and Jason P Hallett. Inexpensive ionic liquids:[hso 4]–based solvent production at bulk scale. *Green Chemistry*, 16(6):3098–3106, 2014.

[116] Mónica M Lopes, Raquel V Barrulas, Tiago G Paiva, Ana SD Ferreira, Marcileia Zanatta, and Marta C Corvo. Molecular interactions in ionic liquids: the nmr contribution towards tailored solvents. *Nuclear Magnetic Resonance*, page 13, 2019.

[117] PA Hunt. The simulation of imidazolium-based ionic liquids. *Molecular simulation*, 32(01):1–10, 2006.

[118] Richard P Matthews, Tom Welton, and Patricia A Hunt. Competitive pi interactions and hydrogen bonding within imidazolium ionic liquids. *Physical Chemistry Chemical Physics*, 16(7):3238–3253, 2014.

[119] George A Jeffrey. Hydrogen-bonding: an update. *Crystallography Reviews*, 9(2-3):135–176, 2003.

[120] Patricia A Hunt, Claire R Ashworth, and Richard P Matthews. Hydrogen bonding in ionic liquids. *Chemical Society Reviews*, 44(5):1257–1288, 2015.

[121] Peter Politzer, Jane S Murray, and Timothy Clark. Halogen bonding and other σ-hole interactions: A perspective. *Physical Chemistry Chemical Physics*, 15(27):11178–11189, 2013.

[122] Marcey L Waters. Aromatic interactions in model systems. *Current opinion in chemical biology*, 6(6): 736–741, 2002.

Chapter 2

Theoretical Background

Computational chemistry is a branch of chemistry which incorporates theoretical chemistry into computer programs in which chemicals are simulated. The simulations of atoms, molecules, ions, and other species give insight into chemical structure, reaction pathways, physiochemical properties and more. The field of computational chemistry is typically divided into molecular or classical mechanics and quantum mechanics.[1] This chapter aims to describe the underlying concepts of the of density functional theory (DFT),[1] the theoretical model used to conduct the bulk of the research presented in this thesis. Essential concepts required to understand the development of DFT as well as the defining aspects of the practical application of DFT are described. Wave function theory (WFT) is described in detail, starting with the familiar Schrödinger equation, and working through to the many electron wave functions. A description of WFT is required as it heavily substantiated the development of DFT and is conceptually relevant.[2] Finally a description of DFT and its underlying components is presented. Additionally, the theory of a variety of computational techniques used for analysis is discussed; atoms in molecules (AIM)[3], reduced density gradient analysis (NCIplot)[4], interaction region indicator (IRI)[5], the assignment of net atomic charges (NACs)[6] and the gellius script generate XPS spectra[7].

The explanations of WFT and DFT are primarily based on the approaches presented in Modern Quantum mechanics by Szabo and Ostlund[2] and the Essentials of Computational Chemistry theories and models by Cramer.[1]

2.1 The Schrödinger equation

The core objective of molecular quantum mechanics is solving the time-independent, non-relativistic Schrödinger equation (eq. 2.1.1) to ascertain the electronic structure of atoms and molecules to determine their behaviour.

$$\widehat{H}\Psi = E\Psi \tag{2.1.1}$$

where

$\widehat{H} \rightarrow$ Hamiltonian Operator

$E \rightarrow$ Atomic or Molecular Total Energy

$\Psi \rightarrow$ Atomic or Molecular Wave Function

$\widehat{H}$, acts on Ψ to generate the energy of the system as an eigenvalue, E. Interpretations of the wave function are difficult but what can be stated is that the square modulus of the wave function, $|\Psi|^2$, has the units of probability density. In other words, the probability of a chemical system being located in some region of multi-dimensional space is equal to the integral of $|\Psi|^2$ over a given region of space.

Solving the Schrödinger equation requires an understanding of the motion of electrons and nuclei and how they interact. To describe these characteristics in a system of electrons and nuclei a common description for the locations of particles is established as illustrated in figure 2.1.

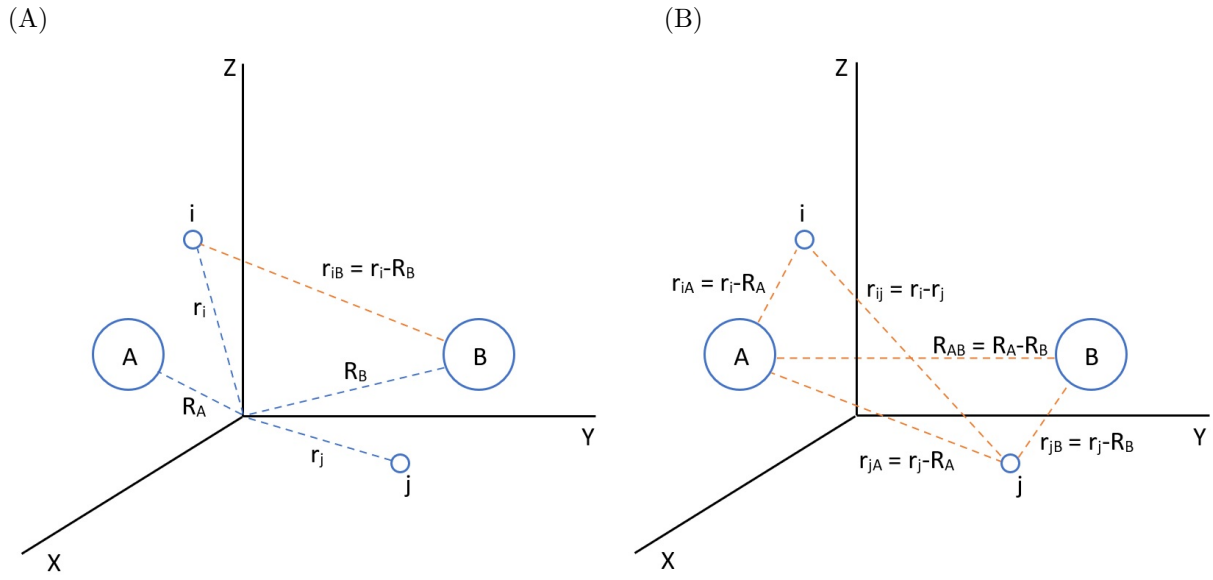


Figure 2.1: Schematic representation of a vectors present in a dihydrogen, (H_2) system; The positions of Hydrogen nuclei A and B and electrons i and j are given by r_1 represented by dashed blue lines and distances between two species, r_{12}, are shown in dashed orange lines

The location of nuclei and electrons is described by position vectors running over indices which represent each nucleus and electron in the system as follows:

amount of	Particle	indices	Position Vector
N	electrons	$i, j, k, \ldots, N$	$\vec{r}_i = (x_i, y_i, z_i)$
M	nuclei	$A, B, C, \ldots, M$	$\vec{R}_A = (x_A, y_A, z_A)$

where the distances between two particles can be expressed as follows.

$$\vec{r}_{12} = (x_2 - x_1, y_2 - y_1, z_2 - z_1) \tag{2.1.2}$$

The Hamiltonian of a system can be expressed as a sum of different operators, which depend on the position vectors $\vec{r}_i$ and $\vec{R}_A$, representing a different behavioural dynamic in a system of electrons and nuclei. The Hamiltonian is split into the sum of the kinetic energy operators of electrons, $\widehat{T}_e(\vec{r})$, and nuclei, $\widehat{T}_N(\vec{R})$, and the potential energy operators of electron – nucleus attraction, $\widehat{V}_{e-N}(\vec{r}, \vec{R})$, electron – electron repulsion, $\widehat{V}_{e-e}(\vec{r})$, and nucleus – nucleus repulsion, $\widehat{V}_{N-N}(\vec{R})$.

$$\widehat{H} = \widehat{T}_N(\vec{R}) + \widehat{T}_e(\vec{r}) + \widehat{V}_{e-N}(\vec{r}, \vec{R}) + \widehat{V}_{e-e}(\vec{r}) + \widehat{V}_{N-N}(\vec{R}) \tag{2.1.3}$$

where each term can be expanded to be expressed in the functional form.

$$\widehat{H} = -\sum_{i=1}^{N} \frac{\hbar^2}{2M_e} \nabla_i^2 - \sum_{A=1}^{M} \frac{\hbar^2}{2M_A} \nabla_A^2 - \sum_{i=1}^{N} \sum_{A=1}^{M} \frac{Z_A e^2}{4\pi\varepsilon_o r_{iA}} + \sum_{i=1}^{N} \sum_{j>i}^{N} \frac{e^2}{4\pi\varepsilon_o r_{ij}} + \sum_{A=1}^{M} \sum_{B>A}^{M} \frac{Z_A Z_B e^2}{4\pi\varepsilon_o R_{AB}} \tag{2.1.4}$$

where

$m_e \rightarrow$ mass of an electron

$M_A \rightarrow$ mass of nucleus A

$e \rightarrow$ charge of an electron

$Z_A \rightarrow$ atomic number of nucleus A

$\varepsilon_o \rightarrow$ vacuum permittivity

The Laplacian operators ∇_i^2 and ∇_A^2 are partial differentials with respect to the X,Y,Z coordinates of the ith electron and the Ath nucleus, respectively.

$$\nabla_i^2 = \frac{\partial^2}{\partial x_i^2} + \frac{\partial^2}{\partial y_i^2} + \frac{\partial^2}{\partial z_i^2} \tag{2.1.5}$$

$$\nabla_A^2 = \frac{\partial^2}{\partial x_A^2} + \frac{\partial^2}{\partial y_A^2} + \frac{\partial^2}{\partial z_A^2} \tag{2.1.6}$$

Coulombs law applies for potential energy terms between particles. Ψ is a function of 3N coordinates where N is the number of nuclei and electrons in a system. The Hamilton is sum of various expressions for the different forces occurring in a system and can thus be simplified to reduce the complexity of the problem.

There are many acceptable eigenfunctions Ψ for a system, each attached to a distinct eigenvalue E. In other words, each system has a complete set of Ψ_i coinciding eigenvalues E_i. This set of wave functions is assumed to be orthonormal, for a system which depends exclusively on three coordinates equation 2.1.7 holds true.

$$\int \Psi_i \Psi_j d\mathbf{r} = \delta_{ij} \tag{2.1.7}$$

Where dr is a 3n-dimensional volume element and δ_{ij} is the Kronecker delta. The Kronecker delta is equal to 1 if i = j and equal to 0 if it i $\neq$ j and is used to evaluate the orthonormality of the two wave functions. Orthonormality of two wave functions entails that they are orthogonal and normalized with respect to one another.

One can attempt to solve equation 2.1.1 for a specific wave function Ψ_i by multiplying both sides by Ψ_j and integrating.

$$\int \Psi_j \widehat{H} \Psi_i d\mathbf{r} = \int \Psi_j E_i \Psi_i d\mathbf{r} \tag{2.1.8}$$

Here E is a scalar value and can be moved outside of the integral. Using the equivalent established in equation 2.1.8 the Kronecker delta substitutes the two wave function terms on the right hand.

$$\int \Psi_j \widehat{H} \Psi_i d\mathbf{r} = E_i \delta_{ij} \tag{2.1.9}$$

equation 2.1.9 is useful as it provides a method by which the molecular energy can be calculated from a wave function. The equation will also prove to have significance further on in the text.

2.1.1 Atomic units

Common SI units are useful when understanding quantities of thing one works with on a human scale but in the world of molecular quantum mechanics these units become inconvenient to use. Hence, a system of atomic units is used to work at the molecular scale.

$$\begin{aligned}
\text{mass} \rightarrow m_e = 1 &\qquad = 9.109 \times 10^{-19} kg \\
\text{charge} \rightarrow e = 1 &\qquad = 1.602 \times 10^{-19} C \\
\text{angular momentum} \rightarrow \hbar = 1 &\qquad = 1.055 \times 10^{-34} Js \\
\text{relative permittivity} \rightarrow 4\pi\varepsilon_o = 1 &\qquad = 1.113 \times 10^{-16} \frac{C^2}{Jm} \\
\text{distance} \rightarrow a_0 = 1 &\qquad = 5.292 \times 10^{-11} m
\end{aligned}$$

Substituting atomic units into the expressions for the different operator components of the Hamiltonian in equation 2.1.4 allows for the constituting operators to be simplified.

$$\widehat{H} = -\sum_{i=1}^{N} \frac{1}{2}\nabla_i^2 - \sum_{A=1}^{M} \frac{1}{2M_A}\nabla_A^2 - \sum_{i=1}^{N}\sum_{A=1}^{M} \frac{Z_A}{r_{iA}} + \sum_{i=1}^{N}\sum_{j>i}^{N} \frac{1}{r_{ij}} + \sum_{A=1}^{M}\sum_{B>A}^{M} \frac{Z_A Z_B}{R_{AB}} \tag{2.1.10}$$

Henceforth all explanations will be in atomic units unless otherwise stated.

2.2 Solving the Schrödinger equation

The Schrödinger equation combines the distinct elements which are essential in describing the behaviour of subatomic particles in a given atomic or molecular composition. However, the application of the Schrödinger equation to real problems becomes impractical beyond the simplest systems. Therefor the utilization of a variety of approximations and mathematical techniques becomes a necessity to make the use of the Schrödinger equation feasible. This section describes the techniques and approximations used to facilitate solving the Schrödinger equation for more complex systems.

2.2.1 Variational principle

To solve the Schrödinger equation beyond the simplest systems a mathematical method based on the variational principle is required. The Schrödinger equation shows that prescription of an appropriate Hamiltonian to a molecular wave function can compute the energy of a system. To compute the energy via the Hamiltonian an orthonormal set of molecular wave functions is required to be operated upon, but the problem arises of how attain this set. An arbitrary trial wave function, Φ, representing a set of nuclear and electronic coordinates can be constructed. The wave function Φ is a linear combination of a complete set of Ψ_i wave functions where the set of Ψ_i is orthonormal.

$$\Phi = \sum_i c_i \Psi_i \tag{2.2.1}$$

The values of the wave function Ψ_i and the coefficients c_i are unknown. The normality of Φ constrains the coefficients which can be derived.

$$\begin{aligned}
\int \Phi^2 d\mathbf{r} &= \int \sum_i c_i \Psi_i \sum_j c_j \Psi_j d\mathbf{r} \\
&= \sum_{ij} c_i c_j \int \Psi_i \Psi_j d\mathbf{r} \\
&= \sum_{ij} c_i c_j \delta_{ij} \\
&= \sum_i c_i^2
\end{aligned} \tag{2.2.2}$$

To compute the energy of the wave function Φ the wave function is multiplied by the Hamiltonian and integrated.

$$\begin{aligned}
\int \Phi \widehat{H} \Phi d\mathbf{r} &= \int \left(\sum_i c_i \Psi_i \right) \widehat{H} \left(\sum_j c_j \Psi_j \right) d\mathbf{r} \\
&= \sum_{ij} c_i c_j \int \Psi_i \widehat{H} \Psi_j d\mathbf{r} \\
&= \sum_{ij} c_i c_j E_j \delta_{ij} \\
&= \sum_i c_i^2 E_i
\end{aligned} \tag{2.2.3}$$

Here equation 2.1.9 is substituted into equation 2.2.3. Equation 2.2.3 shows that a generic wave function Φ can be used to determine the energy, E_i of a system from the coefficients, c_i. The coefficients determine how the components of the orthonormal set of Ψ_i are portioned to form Φ. No values for any of the quantities are known so even with a methodology established to calculate a wave functions energy, input values are required. One has to make the assumption that among the set of all E_i there must be a lowest energy value which corresponds to the ground state energy, E_0. E_0 functions as a boundary condition to undertake calculations. The boundary condition allows for equations 2.2.2 and 2.2.3 can be combined.

$$\int \Phi \widehat{H} \Phi d\mathbf{r} - E_0 \int \Phi^2 d\mathbf{r} = \sum_i c_i^2 (E_i - E_0) \tag{2.2.4}$$

All coefficients c_i^2 are assumed to be real numbers and by definition the quantity of (E_i - E_0) must be greater than or equal to zero.

$$\int \Phi \widehat{H} \Phi d\mathbf{r} - E_0 \int \Phi^2 d\mathbf{r} \geq 0 \tag{2.2.5}$$

Which can be rearranged.

$$\frac{\int \Phi \widehat{H} \Phi d\mathbf{r}}{\int \Phi^2 d\mathbf{r}} \geq E_0 \tag{2.2.6}$$

Equation 2.2.6 has helpful implications for anyone attempting to solve the Schrödinger equation. In the search of an ideal wavefunction to describe a molecular system, the quality of the wave function describing the system can be quantified by the corresponding energy. The lower the energy, the better the wave function. The relationship shows that a guess wave function Φ can be constructed without the linear combination of unknown orthonormal wave functions Ψ_i but in any manner that fulfils the boundary conditions of a system. Starting from a guess wave function the tools of calculus allow for the minimization of the energy associated with the guess wave function by moving towards an energetic minimum by evaluating how changing the wave function changes the systems energy.

2.2.2 Born-Oppenheimer approximation

The Born-Oppenheimer approximation is based on the enormous difference of mass between nuclei and electrons which allows for the Hamiltonian to be simplified. Nuclei are magnitudes heavier than electrons

and consequently move much slower. Therefore, when modelling the behaviour of atoms and molecules electrons and nuclei can be treated independently. The clamped nuclei approximation states that electrons can effectively be considered to be moving in a field of stationary nuclei. The kinetic energy of nuclei, $\widehat{T}_N(R)$, can be neglected and the repulsion between nuclei, $\widehat{V}_{N-N}(R)$, can be considered constant when applying the clamped nuclei approximation. The $\widehat{V}_{N-N}(R)$ constant added to the operator has no effect on the operators eigenfunction and is explicitly added to the operators eigenvalues. The remaining components of the Hamiltonian are known as the electronic Hamiltonian ($\widehat{H}_{elec}$):

$$\widehat{H}_{elec} = -\sum_{i=1}^{N} \frac{1}{2}\nabla_i^2 - \sum_{i=1}^{N}\sum_{A=1}^{M} \frac{Z_A}{r_{iA}} + \sum_{i=1}^{N}\sum_{j>i}^{N} \frac{1}{r_{ij}} \tag{2.2.7}$$

The Schrödinger equation can be solved using the electronic Hamiltonian.

$$\widehat{H}_{elec}\phi_{elec} = E_{elec}\phi_{elec} \tag{2.2.8}$$

Where the electronic wave function is the solution.

$$\phi_{elec} = \phi_{elec}(\{r_i\}\{R_A\}) \tag{2.2.9}$$

Which describes the motion of electrons. The electronic energy depends explicitly on electronic coordinates and parametrically on nuclear coordinates.

$$E_{elec} = E_{elec}(\{R_A\}) \tag{2.2.10}$$

Parametric dependence implies that different nuclear arrangements will lead to a different function of electronic coordinates expressed by ϕ_{elec}. To calculate the total energy of a system with fixed nuclei, the nuclear repulsion constant must be included:

$$E_{tot} = E_{elec} + \sum_{A=1}^{M}\sum_{B>A}^{M} \frac{Z_A Z_B}{R_{AB}} \tag{2.2.11}$$

Once a solution to electronic problem has been found and the nuclear repulsion has been determined, the motion of nuclei can subsequently be accounted for under the same assumptions made for the electronic problem. The electronic coordinates can be substituted as values averaged over the electronic wave function into equation 2.1.10. Therefore, the nuclear Hamiltonian can be determined for nuclei moving in an averaged field of electrons.

$$\begin{aligned}\widehat{H}_{nucl} &= -\sum_{A=1}^{M}\frac{1}{2M_A}\nabla_A^2 + \left\langle -\sum_{i=1}^{N}\frac{1}{2}\nabla_i^2 - \sum_{i=1}^{N}\sum_{A=1}^{M}\frac{Z_A}{r_{iA}} + \sum_{i=1}^{N}\sum_{j>i}^{N}\frac{1}{r_{ij}}\right\rangle + \sum_{A=1}^{M}\sum_{B>A}^{M}\frac{Z_A Z_B}{R_{AB}} \\ &= -\sum_{A=1}^{M}\frac{1}{2M_A}\nabla_A^2 + E_{elec}(\{R\}) + \sum_{A=1}^{M}\sum_{B>A}^{M}\frac{Z_A Z_B}{R_{AB}} \\ &= -\sum_{A=1}^{M}\frac{1}{2M_A}\nabla_A^2 + E_{tot}(\{R\}) \end{aligned} \tag{2.2.12}$$

The potential energy of nuclear motion is determined from the total energy, E_{tot} $(\{R_A\})$. Figure 2.2 shows two potential energy surfaces (PESs) showing the dependence of E_{tot} $(\{R_A\})$ on (A) one reaction coordinate and (B) two reaction coordinates. In the Born-Oppenheimer approximation the nuclei move on a PES obtained by solving the electronic problem at different points on the PES while moving towards a minimum.

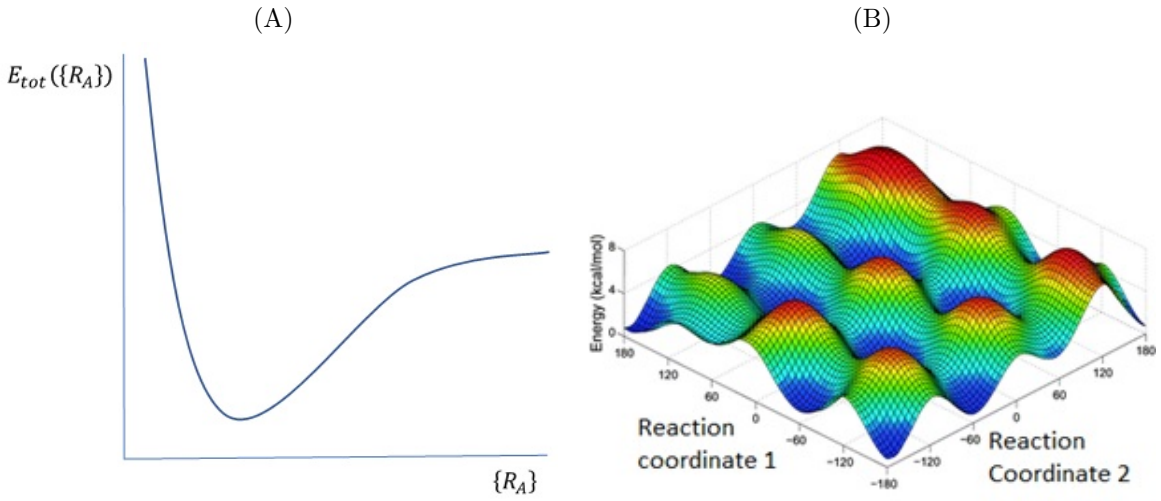


Figure 2.2: Schematic representations of a (A) one reaction coordinate dependant and (B) two reaction coordinate dependant potential energy surfaces

Figure 2.2(A) can be thought of as two atoms approaching one another where the minimum is the most energetically favourable distance between the two atoms. It is important to note that as a molecule has 3N – 6 degrees of freedom. Therefore, the full PES must have 3N – 6 dimensions. Important features such

as minima, maxima and saddle points are visualized in figure 2.2 (B). Generally, minima and saddle points correspond to stable configurations and transition states, respectively.

The solutions to the nuclear Schrödinger equation (eq.2.2.13) describe a molecular vibration, rotation, and translation.

$$H_{nucl}\phi_{nucl} = E\phi_{nucl} \tag{2.2.13}$$

The Born-Oppenheimer approximation of the total energy, E, for equation 2.1.10 include vibrational, translational, rotational, and electronic energy. The nuclear wave function depends exclusively on the nuclear positions:

$$\phi_{nucl} = \phi_{nucl}(\{R_A\}) \tag{2.2.14}$$

Combining the expressions for the nuclear and the electronic wave function, the Born-Oppenheimer approximation is summarized as follows:

$$\phi(\{r_i\};\{R_A\}) = \phi_{elec}(\{r_i\};\{R_A\})\phi_{nucl}(\{R_A\}) \tag{2.2.15}$$

2.2.3 Constructing trial wave functions - linear combination of atomic orbitals basis set approach

Equation 2.2.8 can be solved in a simpler fashion than equation 2.1.10 due to the removal of the electron nuclear correlation. Electron-electron correlation is also removed by considering a system with only one electron when constructing of a trial wave function. In the case of a molecular system, the eigenfunctions of equation 2.1.10 can henceforth be referred to as molecular orbitals albeit them only being constructed with one electron in mind. One electron wave functions, ψ are distinguished form many electron wave functions, Ψ via the symbol used.

To generate a trial wave function which can be used as an input in the attempt to find a ground state energy and wave function, a variety of different mathematical functions can be used to construct said wave function.

The set of functions which are combined to make the molecular orbitals are a set of functions called the basis set.

In a system being computed based on a QM basis with only one electron a variety of basis sets could be used with different implications. If the system were to be further simplified to one nucleus the wave function would not have to be guessed but could be determined exactly. The eigenfunctions would be composed of the hydrogenic atomic orbitals, 1s, 2s, 2p, 3s, 3p, 3d, 4s, 4p... etc. Hydrogenic orbitals can be described mathematically using spherical harmonics functions and can be useful in constructing molecular orbitals. Analogous to equation 2.2.2, a trial wave function, ϕ is constructed through the linear combination of wave functions, which in this case are atomic wave functions, φ.

$$\phi = \sum_{i=1}^{N} a_i \varphi_i \tag{2.2.16}$$

The N functions of φ_i are the basis set and the contribution of each atomic wave function is portioned by the corresponding coefficient a_i. Constructing molecular orbitals via linear combination is known as the linear combination of atomic orbitals (LCAO)

When constructing a trial wave function a variety of considerations must be made when selecting which basis set to use to ensure the accuracy of the model. Expressing MOs as a combinations of AOs distributed around a nucleus seems like the intuitive way of constructing wave functions but is not the necessarily the best solution. The limitations are apparent when considering the computations which the basis functions must undergo.

One of the electronic wave functions features is to provide information about where electrons are located in space through the measure of probability density expressed through the square modulus of the wave function, $|\Psi|^2_{el}$. As it is the goal to lower the energy associated with a particular wave function it is of practical interest to employ basis functions which provide the highest degree of flexibility while being minimalistic with respect to the complexity of the functions.

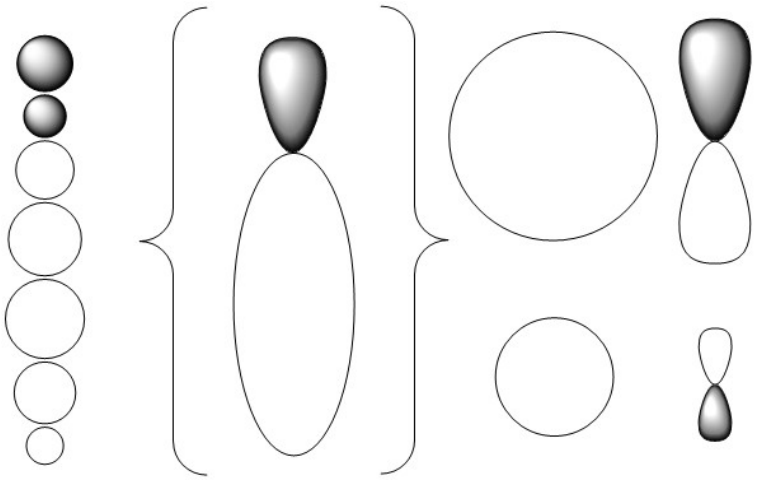


Figure 2.3: Basis function which can be used to represent a σ-bond; s functions on the left and combinations of s and p functions on the right

The schematic illustrates how a molecular orbital can be constructed out of a variety of appropriate functions in two dimensions. The use of exclusively s functions for the construction of MOs as on the left-hand side in figure 2.3 has vastly different computational implications than using s and p functions. The mathematical expression of s functions far simpler to compute than those of a p function and are consequentially used in QM computations. Since most basis sets are exclusively composed of s functions when constructing orbitals, the coefficients of 2.2.16 can lead to misleading interpretations.

2.2.4 The secular equation

The LCAO formalism for the construction of molecular orbitals allows for a trial wave function to be energetically evaluated by substituting equation 2.2.16 into equation 2.2.6.

$$\begin{aligned} E &= \frac{\int \left(\sum_i a_i \varphi_i \right) \widehat{H} \left(\sum_j a_j \varphi_j \right) d\mathbf{r}}{\int \left(\sum_i a_i \varphi_i \right) \left(\sum_j a_j \varphi_j \right) d\mathbf{r}} \\ &= \frac{\sum_{ij} a_i a_j \int \varphi_i \widehat{H} \varphi_j d\mathbf{r}}{\sum_{ij} a_i a_j \int \varphi_i \varphi_j d\mathbf{r}} \\ &= \frac{\sum_{ij} a_i a_j H_{ij}}{\sum_{ij} a_i a_j S_{ij}} \end{aligned} \tag{2.2.17}$$

Here the H_{ij} and S_{ij} integrals are known as the resonance and overlap integrals, respectively. The overlap

integral denotes the extent to which two basis functions experience an in-phase or out-of-phase overlap in space. The resonance integral is harder to interpret although for the case H_{ii} it corresponds to the energy of one electrons occupancy of basis function which is the observable equivalence of the ionization potential of the AO it represents. In a broader sense the resonance integral is associated with the delocalization of electrons.

Having selected a basis set, the best corresponding coefficients to minimize the energy of the system must be calculated for all linear combinations of the basis functions. A minimum is defined as point where the derivatives are 0 with respect to all off its free variables, formally defined as

$$\frac{\partial E}{\partial a_k} = 0 \qquad \forall k \tag{2.2.18}$$

where "$\forall$" means 'for all'. To solve this partial differentiation problem for all N coefficients a_k requires N equations to be satisfied to ensure 2.2.18 holds true.

$$\sum_{i=1}^{N} a_i(H_{kj} - ES_{ki}) = 0 \qquad \forall k \tag{2.2.19}$$

These N equations have N unknowns in the form of the individual coefficients a_i. A set of N equations with N unknowns has a non-trivial solution if the determinant of the various quantities (in this case the H_{kj} - ES_{ki} term) is equal to zero.

$$\begin{vmatrix} H_{11} - ES_{11} & H_{12} - ES_{12} & \cdots & H_{1N} - ES_{1N} \\ H_{21} - ES_{21} & H_{22} - ES_{22} & \cdots & H_{2N} - ES_{2N} \\ \vdots & \vdots & \ddots & \vdots \\ H_{N1} - ES_{N1} & H_{N2} - ES_{N2} & \cdots & H_{NN} - ES_{NN} \end{vmatrix} = 0 \tag{2.2.20}$$

Equation 2.2.20 is known as the secular equation or determinant. The secular determinant has N roots E which permit it to be true. In other words, there are N energies E_j each resulting in a different set of coefficients, a_{ij}, derived by solving the N linear equations of 2.2.19 using the energies E_j. The coefficients in turn determine the ideal wave function Φ_j in a particular basis set.

$$\Phi = \sum_{i=1}^{N} a_{ij}\varphi_i \tag{2.2.21}$$

In a system containing one electron, the lowest energy molecular orbital is defined as the ground state while the higher MOs or energy levels are defined as excited states.

To summarize, to find the ideal one-electron wave functions of a molecular system the follows steps must be undertaken.

1. Select a basis set with N basis functions
2. For the set of basis functions, determine all N^2 values of both H_{ij} and S_{ij}
3. Determine the N roots E_j from the secular determinant
4. A linear equation is solved for each of the N values of E_j as to determine the corresponding coefficients a_{aj} for a given MO.

All MOs derived through this process are mutually orthogonal.

2.3 Many-electron wave functions

The one-electron formalism described until now can be used to determine the wave functions and compute their corresponding energies. Through using an effective Hamiltonian approach, information of many electron systems, like resonance energies can also be crudely determined. However, utilizing the effective Hamiltonian method limits the accuracy of the of the results, especially with regards to the crude treatment of electron-electron repulsion. Hence, a more sophisticated approach to accurately treat many electron systems is required which accounts for the effect when increasing the number of electrons.

2.3.1 Hartree products

To construct a formalism for the treatment of a many electron system one can start by observing the Schrödinger equation in context of the established one-electron formalism. In a scenario where all the terms in the Hamiltonian are strictly reduced to being one-electron nuclear attraction and kinetic energy terms the operator can be constructed as a sum of the given terms for each electron.

$$\widehat{H} = \sum_{i=1}^{N} h_i \tag{2.3.1}$$

Here, N is the total number of electrons and h_i are one-electron Hamiltonians determined by the terms from the Schrödinger equation.

$$h(i) = \frac{1}{2}\nabla_i^2 - \sum_k^M \frac{Z_k}{r_{ik}} \tag{2.3.2}$$

Here the first term is the electrons kinetic energy, and the second term is the sum of the nuclear attractions between the ith electron over M nuclei. The Schrödinger equation applies to the eigenfunction of the one-electron Hamiltonian defined in equation 2.3.2 eigenfunction and must be satisfied.

$$h_i\psi_i = \varepsilon_i\psi i \tag{2.3.3}$$

This requirement arises from the definition established in equation 2.3.1 which regards the Hamiltonian operator as separable into many one-electron Hamiltonians. The product of one-electron eigenfunctions can be used to construct a many-electron eigenfunction.

$$\Psi_{HP} = \psi_1\psi_2\cdots\psi_N \tag{2.3.4}$$

where HP, denotes the Hartree product wave function. The validity of equation 2.3.4 can be derived as follows:

$$\begin{aligned}
\widehat{H}\Psi^{HP} &= \widehat{H}\psi_1\psi_2\cdots\psi_N \\
&= \sum_{i=1}^{N} h(i)\psi_1\psi_2\cdots\psi_N \\
&= (h_1\psi_1)\psi_2\cdots\psi_N + \psi_1(h_2\psi_2)\cdots\psi_N + \cdots + \psi_1\psi_2\cdots(h_N\psi_N) \\
&= (\varepsilon_1\psi_1)\psi_2\cdots\psi_N + \psi_1(\varepsilon_2\psi_2)\cdots\psi_N + \cdots + \psi_1\psi_2\cdots(\varepsilon_N\psi_N) \\
&= \sum_{i=1}^{N} \varepsilon_i\psi_1\psi_2\cdots\psi_N \\
&= \left(\sum_{i=1}^{N} \varepsilon_i\right)\Psi_{HP}
\end{aligned} \tag{2.3.5}$$

where the relationship described in equation 2.3.3 is repeatedly applied to show that the energy eigenvalue of a many-electron wave function is the sum of the one-electron energy eigenvalues. The many-electron wave function is normalized as long as the constituent one-electron wave functions are normalized.

2.3.2 The Hartree hamiltonian

The formalism of the Hartree product provides a relationship between one-electron wave functions and the many-electron wave function but does not take interelectronic repulsion into account. It is a gruelling to compute interelectronic repulsion due to all the simultaneous pairwise interactions occurring. The one-electron operator in 2.3.2 can be amended to include an expression to account for interelectronic repulsion.

$$h(i) = -\frac{1}{2}\nabla_i^2 - \sum_{k=1}^{M} \frac{Z_k}{r_{ik}} + V_i\{j\} \tag{2.3.6}$$

where potential term $V_i\{j\}$ describes the interaction potential of electron i with all other electron occupying a set of alternative orbitals $\{j\}$ and is given by

$$V_i\{j\} = \sum_{j \neq i} \int \frac{\rho_j}{r_{ij}} d\mathbf{r} \tag{2.3.7}$$

Here $\rho_j = |\psi_j|^2$ and expresses the charge probability density of electron j. The second and last terms of equation 2.3.6 treat electron-nuclear attraction and electron-electron repulsion, respectively. The two terms are analogous apart from their difference in how they treat nuclear and electron positions. The second term treats nuclear positions as point changes while the last term treats electronic positions as probability densities calculated via the electrons represented as wave functions. The formalism of the electron-electron repulsion term requires the idealization of a wave function of one electron with respect to an unknown wave function of another electron.

The self-consistent field (SCF) method was devised by Hartree to solve the issue of the wave functions interdependence. The SCF method is iterative, it continuously improves (lowers) the energy over multiple steps. Guess wave functions for each occupied MO, ψ, are selected and used to construct the one-electron operators h_i. The solutions to the differential resulting from equation 2.3.3 result in a new set of ψ which usually differ from the previously set. The cycle then restarts using the new set of ψ to determine the one-electron Hamiltonians to further improve ψ. The improvement upon the last set of ψ is measured through the electronic energy or the energy of individual orbitals and a computational chemist may choose a threshold of their choice to stop the iterative energy minimization process based on arbitrarily selected criteria. it is important to note that the tightness of the threshold directly correlates to the cost of the calculation as tighter convergence criteria require more iterative cycles to minimize making the computation more expensive.

The sum of the operators h, as defined in equation 2.3.6, define the Hamiltonian operator which acts upon the eigenfunction Ψ_{HP}. The resulting Hamiltonian is known as the non-interacting Hamiltonian. The nomenclature derives from the system only accounting for the electron interaction as an average and not electrons interactions in an instantaneous way. The non-interacting Hamiltonian does not approximate the true Hamiltonian well due to this disregard. Additionally, when computing the energy, it is important to notice that the aggregated one-electron Hamiltonians account for all electron-electron interactions twice as h_i accounts for the interactions with electron i with j and h_j accounts for the interaction with electron i with j. The doubly counted interactions are accounted for by multiplying the interaction term by 1/2.

$$E = \sum_i \varepsilon_i - \frac{1}{2} \sum_{i \neq j} \int \int \frac{|\psi_i|^2 |\psi_j|^2}{r_{ij}} d\mathbf{r}_i d\mathbf{r}_j \tag{2.3.8}$$

Here the energy eigenvalue is a sum of ϵ_i, which is the energy of MO i computed by equation 2.3.6, and half of the of all the integrals of interelectronic repulsion, commonly referred to as coulomb integrals, J_{ij}.

The Hartree product does not adequately describe the crucial feature of how electrons organize themselves into MOs. The formalism up until now only focuses on placing electrons into MOs based on energy but electron spin and antisymmetry as described by the Pauli exclusion principle must be considered.

2.3.3 Electron spin and antisymmetry

Each electron in a system has a distinct spin ascribed to it by a spin quantum number. This spin quantum number is functionally expressed as an eigenfunction of the spin operator S_ζ which only has two solutions $\pm \hbar/2$. The eigenfunctions are orthonormal with respect to each other and commonly denoted as α and β, resulting in up or down spin, respectively. The application of electron spin is the root of the Pauli exclusion principle which states that no two electrons can be defined through an identical set of quantum numbers. As each MO can be occupied by two electrons there has to be a distinction between the two electrons through the spin quantum number, m.

Considering the consequences implied by the Pauli exclusion principles one can construct a ground-state Hartree product wave function of a two electron system with identical spin.

$${}^3\Psi_{HP} = \psi_a(1)\alpha(1)\psi_b(2)\alpha(2) \tag{2.3.9}$$

where the left hand superscript 3 implies a triplet state and because of the Paul exclusion principle as the wave functions ψ_a and ψ_b must differ and be orthonormal. The wave function as defined in equation 2.3.9 is flawed in defining the origin of the Pauli exclusion principle as the principle derives from the requirement of a sign change of the electronic wave function upon interchanging the coordinates of two electrons. A wave function accounting for this is deemed to be antisymmetric. A permutation operator, P_{ij} which interchanges electrons i and j in a system can be applied. The Pauli exclusion principle for a system of N electron could thus be defined as follows:

$$\begin{aligned} P_{ij}\Psi[q_1(1),\ldots,q_i(i),\ldots,q_j(j),\ldots,q_N(N)] \\ = \Psi[q_1(1),\ldots,q_j(i),\ldots,q_i(j),\ldots,q_N(N)] \\ = -\Psi[q_1(1),\ldots,q_i(i),\ldots,q_j(j),\ldots,q_N(N)] \end{aligned} \tag{2.3.10}$$

where q is defined as the combination of spatial and spin coordinates.

applying the permutation operator P_{12} to a Hartree product of equation 2.3.9 shows

$$\begin{aligned} P_{12}[\psi_a(1)\alpha(1)\psi_b(2)\alpha(2)] &= \psi_b(1)\alpha(1)\psi_a(2)\alpha(2) \\ &\neq -\psi_a(1)\alpha(1)\psi_b(2)\alpha(2) \end{aligned} \tag{2.3.11}$$

which does not satisfy the Paul exclusion principle. The Hartree product wave function must be altered to fulfil the Pauli exclusion principles antisymmetry constraints.

$$^3\Psi_{SD} = 2^{-1/2}[\psi_a(1)\alpha(1)\psi_b(2)\alpha(2) - \psi_a(2)\alpha(2)\psi_b(1)\alpha(1)] \tag{2.3.12}$$

If the same permutation operator is applied the antisymmetry constrains are fulfilled.

$$\begin{aligned} P_{12}\{2^{-1/2}[\psi_a(1)\alpha(1)\psi_b(2)\alpha(2) - \psi_a(2)\alpha(2)\psi_b(1)\alpha(1)]\} &= 2^{-1/2}[\psi_b(1)\alpha(1)\psi_a(2)\alpha(2) - \psi_b(2)\alpha(2)\psi_a(1)\alpha(1)] \\ &= -2^{-1/2}[\psi_a(1)\alpha(1)\psi_b(2)\alpha(2) - \psi_a(2)\alpha(2)\psi_b(1)\alpha(1)] \end{aligned} \tag{2.3.13}$$

Integrating $|^3\Psi_{SD}|^2$ over all space results in

$$\begin{aligned}\int |^3\Psi_{SD}|^2 d\mathbf{r}_1 d\omega_1 d\mathbf{r}_2 d\omega_2 = \frac{1}{2}\Big[&\int |\psi_a(1)|^2|\alpha(1)|^2|\psi_b(2)|^2|\alpha(2)|^2 d\mathbf{r}_1 d\omega_1 d\mathbf{r}_2 d\omega_2 \\ &- 2\int \psi_a(1)\psi_b(1)|\alpha(1)|^2\psi_b(2)\psi_a(2)|\alpha(2)|^2 d\mathbf{r}_1 d\omega_1 d\mathbf{r}_2 d\omega_2 \\ &+ \int |\psi_a(2)|^2|\alpha(2)|^2|\psi_b(1)|^2|\alpha(1)|^2 d\mathbf{r}_1 d\omega_1 d\mathbf{r}_2 d\omega_2 \Big] \\ &= \frac{1}{2}(1 - 0 + 1) \\ &= 1 \end{aligned} \tag{2.3.14}$$

where ω is the integration variable of spin. The integrals can be simplified based on the orthonormality of the spin functions and MOs. the normalization factor $2^{-1/2}$ is crucial for the answer to normalized.

2.3.4 Slater determinants

equation 2.3.12 can alternatively written in a determinant form.

$$^3\Psi_{SD} = 2^{-1/2}\begin{vmatrix} \psi_a(1)\alpha(1) & \psi_b(1)\alpha(1) \\ \psi_a(2)\alpha(2) & \psi_b(2)\alpha(2) \end{vmatrix} \tag{2.3.15}$$

Conveniently, the application of the permutation operator P simply interchanges the rows of the two interchanged electrons with one another. This form also makes use of the property that determinants change sign upon to rows and columns being interchanged. Slater first used the determinant form to construct antisymmetric wave functions in 1929 and the subscript SD is a shorthand for Slater Determinant. Slater determinants for larger systems can quickly become tedious to write out however they can be abbreviated as follow:

$$\Psi_{SD} = (N!)^{-1/2}\begin{vmatrix} \chi_1(1) & \chi_2(2) & \cdots & \chi_N(1) \\ \chi_1(2) & \chi_2(2) & \cdots & \chi_N(2) \\ \vdots & \vdots & \ddots & \vdots \\ \chi_1(N) & \chi_2(N) & \cdots & \chi_N(N) \end{vmatrix} \tag{2.3.16}$$

where N is the number of electrons and χ are spin orbitals, the combination of spatial orbitals with electron spin eigenfunctions. Slater determinants may be compacted further.

$$\Psi_{SD} = |\chi_1\chi_2\chi_3 \cdot \chi_N\rangle \tag{2.3.17}$$

In equation 2.3.17 the $(N!)^{-1/2}$ is term is implicit. In this notation a doubly occupied orbital would not be written out as two distinct spin orbitals but instead as a spatial wave function with a superscript 2 indicating double occupancy.

$$\Psi_{SD} = |\psi_1^2 chi_3 \cdot \chi_N\rangle \tag{2.3.18}$$

Unlike Hartree-product wave functions, Slater determinants fulfil the indistinguishably of quantum particles which is expressed in the full expansion of a Slater determinant where every electron has a presence in every spin orbital. A more nuanced feature which is encapsulated by Slater determinants is exchange. Using equation 2.3.12 as a starting point, the interelectronic repulsion encapsulated in the wave function may be evaluated as follows:

$$\begin{aligned}
\int^3 \Psi_{SD} \frac{1}{r_{12}}\ ^3\Psi_{SD} d\mathbf{r}_1 d\omega_1 d\mathbf{r}_2 d\omega_2 & \\
=&\frac{1}{2}\Bigg[\int |\psi_a(1)|^2|\alpha(1)|^2\frac{1}{r_{12}}|\psi_b(2)|^2|\alpha(2)|^2 d\mathbf{r}_1 d\omega_1 d\mathbf{r}_2 d\omega_2 \\
&- 2\int \psi_a(1)\psi_b(1)|\alpha(1)|^2\frac{1}{r_{12}}\psi_b(2)\psi_a(2)|\alpha(2)|^2 d\mathbf{r}_1 d\omega_1 d\mathbf{r}_2 d\omega_2 \\
&+ \int |\psi_a(2)|^2|\alpha(2)|^2\frac{1}{r_{12}}|\psi_b(1)|^2|\alpha(1)|^2 d\mathbf{r}_1 d\omega_1 d\mathbf{r}_2 d\omega_2\Bigg] \\
=&\frac{1}{2}\Bigg[\int |\psi_a(1)|^2\frac{1}{r_{12}}|\psi_b(2)|^2 d\mathbf{r}_1 d\mathbf{r}_2 \\
&- 2\int \psi_a(1)\psi_b(1)\frac{1}{r_{12}}\psi_b(2)\psi_a(2) d\mathbf{r}_1 d\mathbf{r}_2 \\
&+ \int |\psi_a(2)|^2\frac{1}{r_{12}}|\psi_b(1)|^2 d\mathbf{r}_1 d\mathbf{r}_2\Bigg] \\
=&\frac{1}{2}\left(J_{ab} - 2\int \psi_a(1)\psi_b(1)\frac{1}{r_{12}}\psi_a(2)\psi_b(2) d\mathbf{r}_1 d\mathbf{r}_2 + J_{ab}\right) \\
=&J_{ab} - K_{ab}
\end{aligned} \tag{2.3.19}$$

Equation 2.3.19 adds an additional term, the correlation term K_{ab}, which is subtracted from the classically determined Coulomb repulsion between electrons. Consequentially the Pauli exclusion principle imposes a reduced probability of observing two electrons with the same spin adjacent to each other, a 'Fermi hole' is said to surround an electron in this case.

The correlation effect described in equation 2.3.19 is exclusive to electrons of the same spin. A Slater determinant constructed from electrons with opposite spin looks as follows:

$$\Psi_{SD} = 2^{-1/2}[\psi_a(1)\alpha(1)\psi_b(2)\beta(2) - \psi_a(2)\alpha(2)\psi_b(1)\beta(1)] \tag{2.3.20}$$

and can be evaluated analogously for its interelectronic repulsion.

$$\begin{aligned}
\int \Psi_{SD}\frac{1}{r_{12}}\Psi_{SD}d\mathbf{r}_1 d\omega_1 d\mathbf{r}_2 d\omega_2 & \\
&= \frac{1}{2}\Bigg[\int |\psi_a(1)|^2|\alpha(1)|^2\frac{1}{r_{12}}|\psi_b(2)|^2|\beta(2)|^2 d\mathbf{r}_1 d\omega_1 d\mathbf{r}_2 d\omega_2 \\
&\quad - 2\int \psi_a(1)\psi_b(1)\alpha(1)\beta(1)\frac{1}{r_{12}}\psi_b(2)\psi_a(2)\alpha(2)\beta(2) d\mathbf{r}_1 d\omega_1 d\mathbf{r}_2 d\omega_2 \\
&\quad + \int |\psi_a(2)|^2|\alpha(2)|^2\frac{1}{r_{12}}|\psi_b(1)|^2|\beta(1)|^2 d\mathbf{r}_1 d\omega_1 d\mathbf{r}_2 d\omega_2\Bigg] \\
&= \frac{1}{2}\Bigg[\int |\psi_a(1)|^2\frac{1}{r_{12}}|\psi_b(2)|^2 d\mathbf{r}_1 d\mathbf{r}_2 \\
&\quad - 2\cdot 0 d\mathbf{r}_1 d\mathbf{r}_2 \\
&\quad + \int |\psi_a(2)|^2\frac{1}{r_{12}}|\psi_b(1)|^2 d\mathbf{r}_1 d\mathbf{r}_2\Bigg] \\
&= \frac{1}{2}(J_{ab} + J_{ab}) \\
&= J_{ab}
\end{aligned} \tag{2.3.21}$$

The exchange correlation term disappears due to the orthogonality of α and β spin functions which results in the second integral term to be zero over either spin coordinate.

2.3.5 Hartree-Fock self-consistent field method

The Hartree SCF procedure was extended for non antisymmetrized orbitals to encompass Slater determinantal wave functions by Fock. Analogous to the Hartree-product orbitals, Hartree-Fock (HF) MOs can be individually determined as eigenfunctions of a set of one-electron operators. Unlike the Hartree-product orbitals the interaction with a static field of electrons includes exchange effects alongside the Coulomb repulsion. Later, Roothaan devised the matrix algebraic equations to make HF calculations feasible using a basis set representation of MOs. The following section presents the form of a typical closed shell system represented as Slater determinantal wave functions commonly referred to as restricted Hartree

Fock RHF.

Analogous to the Hartree-product approach each electron, i, has a defined one-electron Fock operator.

$$f_i = -\frac{1}{2}\nabla_i^2 - \sum_k^{nuclei} \frac{Z_k}{r_{ik}} + V_i^{HF}\{j\} \tag{2.3.22}$$

The last term, $V_i^{HF}\{j\}$ is known as the HF potential and is equal to $2J_i$-K_i and the J_i and K_i operators calculate the Coulomb repulsion J_{ij} and electron exchange K_{ij}. The approach Roothaan conceived starts from a set of N basis functions for which the secular equation is solved in order to find all of the roots, E_j.

$$\begin{vmatrix} F_{11} - ES_{11} & F_{12} - ES_{12} & \cdots & F_{1N} - ES_{1N} \\ F_{21} - ES_{21} & F_{22} - ES_{22} & \cdots & F_{2N} - ES_{2N} \\ \vdots & \vdots & \ddots & \vdots \\ F_{N1} - ES_{N1} & F_{N2} - ES_{N2} & \cdots & F_{NN} - ES_{NN} \end{vmatrix} = 0 \tag{2.3.23}$$

The values for all the matrix elements F and S are calculated explicitly. The S elements are the overlap matrix elements which have been previously described. The matrix element $F_{\mu v}$ is computed as follows

$$F_{\mu v} = \left\langle \mu \middle| -\frac{1}{2}\nabla^2 \middle| v \right\rangle - \sum_k^{nuclei} \left\langle \mu \middle| \frac{1}{r_k} \middle| v \right\rangle + \sum_{\lambda\sigma} P_{\lambda\sigma} \left[(\mu v|\lambda\sigma) - \frac{1}{2}(\mu\lambda|v\sigma) \right] \tag{2.3.24}$$

where the lower case greek letters indicate the indexation of basis functions instead of MOs. In the alternate notation, $\langle \mu|g|v\rangle$, g is an operator taking basis function ϕ_v as an argument and it results in a one-electron integral form.

$$\langle \mu|g|v\rangle = \int \phi_{mu}(g\phi_v) d\mathbf{r} \tag{2.3.25}$$

From equation 2.3.25 it may be deduced that the operator g functions based on the Laplacian and the distance to nuclei as shown by the first and second terms in 2.3.24, respectively. $(\mu v|\lambda\sigma)$ refers to a the integration shown below.

$$(\mu v|\lambda\sigma) = \int\int \phi_\mu(1)\phi_v(1)\frac{1}{r_{12}}\phi_\lambda(2)\phi_\sigma(2) d\mathbf{r}(1) d\mathbf{r}(2) \tag{2.3.26}$$

Here the functions ϕ_μ and ϕ_v are representative of the probability density of one electron while ϕ_λ and ϕ_σ represent another electron. In equation 2.3.24 the integral $(\mu v|\lambda\sigma)$ is factored by a half as only half of the interactions between electron, namely those interacting with the same spin quantum number are prescribed the exchange term treatment while all electrons experience Coulomb interactions.

The expression in equation 2.3.24 tackling the exchange effects weighs all the four-index integral which occur in a 'density matrix' **P**. The density matrix assists in determining magnitude of contribution from individual basis functions to a many-electron wave function by determining the significance of the Coulomb and exchange integrals in determining the energy contributed to the system. The elements of the density matrix **P** is formulated in equation 2.3.27.

$$P_{\lambda\sigma} = 2 \sum_{i}^{occupied} a_{\lambda i} a_{\sigma i} \tag{2.3.27}$$

The normalized contribution of a basis function ζ to a MO, i, is captured by the coefficients $a_{\zeta i}$. The sum is multiplied by two as RHF theory solely considers singlet state wave functions, i.e. all orbitals are doubly occupied.

The HF approach runs into a mathematical chicken and egg problem analogous to the problem described for the effective Hamiltonian method. the formation of the density matrix requires defined orbital coefficients to be used in the Fock matrix elements. simultaneously secular equation calculates the orbital coefficients and hence the employment of an iterative SCF procedure is required. Initially the orbital coefficients are guessed, and the iterative process is carried out until convergence is achieved. the flow chart below illustrates the process.

The HF SCF procedure approximates the real Hamiltonian and the associated wave function better than the Hartree product but still only treats exchange effects and ignores correlation. The method as described is sufficient to understand the underlying concepts which form the foundation for DFT which is introduced in the next section.

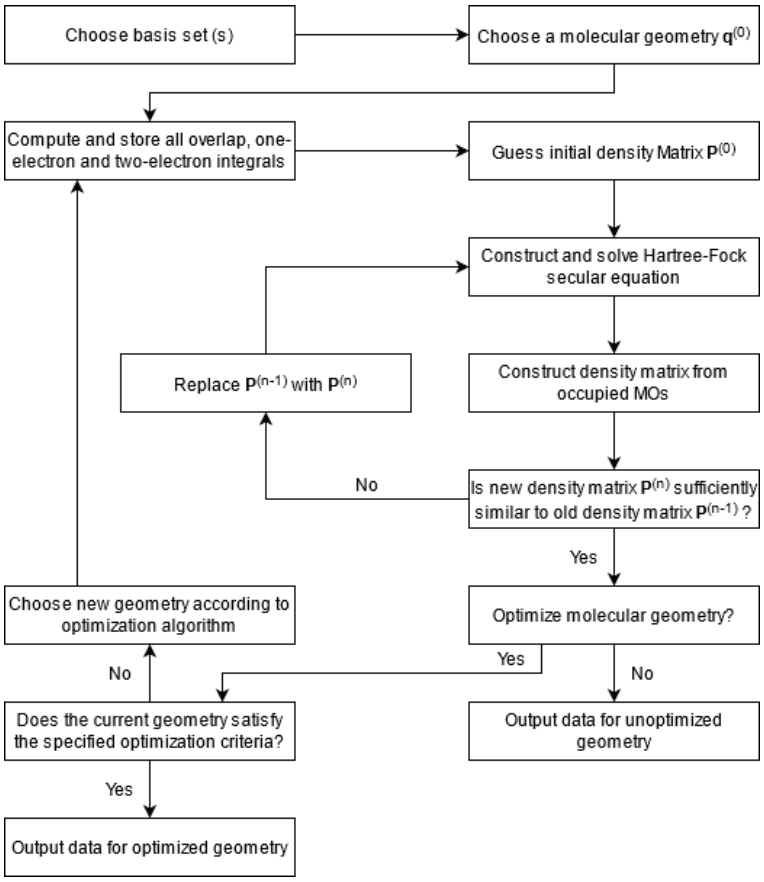


Figure 2.4: HF SCF procedure flow chart

2.4 Density functional theory

2.4.1 Theoretical motivation

The development of DFT was motivated by trying to circumvent the complexity of WFT. Even after applying the Born-Oppenheimer approximation, wave functions depend on one spin and three spatial coordinates for each electron, making it difficult to implement for larger systems. The use Slater determinants in HF theory allows for a breakdown of an electronic wave function in to contributing one-electron wave function but the computations are still demanding. The composition of the electronic wave function in which electrons preserve a degree of individuality resembles a chemical notion of electrons. However, beyond the feature of describing electrons localized into their orbitals, wave functions are not intuitive beyond the simplest systems and require thorough analysis to be understood.

The practical difficulty undertaking WFT computations is substantial enough to attempt to derive a simpler formalism to describe electronic structures. In pursuit of such a formalism the wave functions units of probability density to the power of one-half and the desire for a more intuitive approach converged to point towards electron density ρ as an alternative input variable. Initially the feasibility of ρ as a variable was elucidated by determining how well it can describe the input variables of a wave function: the positions and atomic numbers of nuclei as well as the number of electrons in the system.

The total number of electrons in a system can be determined by simply integrating ρ over all space

$$N = \int p(r)dr \tag{2.4.1}$$

The positions and atomic numbers of nuclei can be deduced from electron density as well as nuclear positions corresponding to maxima of electron density. The atomic numbers of the atoms located at the maxima of electron density can be determined by the formulation in 2.4.2.

$$\left.\frac{\partial\bar{\rho}(r_A)}{\partial r_A}\right|_{r_A=0} = -2Z_A\rho(r_A) \tag{2.4.2}$$

Here, r_A is the radial distance from atom A, Z is its atomic number and $\bar{\rho}$ is the spherically averaged density.

The relationship between ρ and the input variables of a Hamiltonian does not result in a novel formalism to describe electronic structure but does provide a relationship for a Hamiltonian operator to be composed for a known density. The Hamiltonian can in turn be used to solve the Schrödinger equation for the corresponding eigenvalues and the wave function.

Mathematical approximations were developed to compute a systems energy from ρ. To compute the energy in terms of ρ it is separated into kinetic and potential energy terms. The system is assumed to be classical which implies that the computation of potential energy is relatively straight forward. The electron density - nuclei attraction term is

$$V_{ne}[\rho(r)] = \sum_{k}^{nuclei} \int \frac{Z_k}{|r - r_k|}\rho(r)dr \tag{2.4.3}$$

while the interelectronic repulsion represented by the charge density is given by

$$V_{ee}[\rho(r)] = \frac{1}{2}\int\int \frac{\rho(r_1)\rho(r_1)}{|r_1 - r_2|} dr_1 dr_2 \tag{2.4.4}$$

where the r_1 and r_2 are dummy integration variables. The sums expressed in equations 2.4.3 and 2.4.4 provide a familiar method of calculating potential energy, however the calculations are functions of ρ.

The kinetic energy term is more difficult to compute and requires an approximation. Kinetic energy can only be calculated in a system comprised of infinite electrons moving in an endless volume with uniformly distributed positive charges known as a uniform electron gas (UEG). The system, also referred to as jellium, has a constant non-zero electron density. Through fermion statistical mechanics Thomas and Fermi determined that the kinetic energy of such a system could be computed as follows

$$T_{ueg}[\rho(r)] = \frac{3}{10}(3\pi^2)^{2/3}\int \rho^{5/3}(r) dr \tag{2.4.5}$$

Equations 2.4.3-2.4.5 are functions of the density which in turn are functionally dependent on three-dimensional spatial coordinates. A function of a function is a functional and hence the nomenclature of DFT. Potential energy, V and kinetic energy, T are computed via 'density functionals'. In tandem with the variational principle these terms can be used to calculate the energy of a system without the requirement for a guess wave function. However, the approximation is fundamentally flawed due to the inaccuracy resulting from requirement of a UEG environment. Practically applying the above functionals to a molecular system leads to the dissociation of the molecules and hence did not find any application beyond providing a theoretical basis.

One of the main faults of the Thomas-Fermi model lies in equation 2.4.4 which ignores correlation and exchange energies when treating the inter-electronic effects. One solution to this problem is to introduce A hole function to correct for the errors which arise from treating the electrons via a classical approach, specifically equation 2.4.4 can be amended as follows:

$$\left\langle \Psi \left| \sum_{i<j}^{electrons} \frac{1}{r_{ij}} \right| \Psi \right\rangle = \frac{1}{2}\int\int \frac{\rho(r_1)\rho(r_1)}{|r_1 - r_2|} dr_1 dr_2 + \frac{1}{2}\int\int \frac{\rho(r_1)h(r_1; r_2)}{|r_1 - r_2|} dr_1 dr_2 \tag{2.4.6}$$

The term on the left-hand side is the precise interelectronic repulsion as derived through an exact quantum mechanical approach. The first double integral on the right-hand side is the same term as used for the

interelectronic repulsion in the classical model. The second term is used to correct for the errors associated with it by introducing a hole function h. The hole function, associated with ρ, describes a hole cantered around electron 1 and is evaluated with respect to the spatial coordinates of electron 2 at r_2. The form of the hole function is a function of r_1 while the value associated with h is defined by r_2 relative to r_1.

HF theory inherently circumvents any self-interaction errors associated with its approach of calculating exchange energy but calculating the exact exchange via HF is computationally intensive due to the four-index integral. Slater found that exchange corrections were one to two orders of magnitude larger than correlation corrections while trying to devise methods to speed up HF calculations when correcting classical inter-electron repulsion. Following his discovery, Slater proposed to ignore electron correlation and to instead focus solely on exchange and formulated an approximation for the exchange. In the approximation placed exchange holes around a particular position which are spheres of constant potential, the magnitude of which is dependent on the local electron density. The rigorous mathematical approach to determine the exchange energy E_x deriving from his approximation is shown in equation 2.4.7.

$$E_x[\rho(r)] = -\frac{9\alpha}{8}\left(\frac{3}{\pi}\right)^{1/3}\int \rho^{4/3}(r)dr \tag{2.4.7}$$

where the constant α is equal to one in Slater's derivation of what is known as 'Slater exchange'. A similar expression had been derived previously by Bloch and Dirac when working with the concept of UEG although the coefficient α was equal to 2/3. Equation 2.4.3-2.4.5 combined with the approximation of 2.4.7 form the Thomas-Fermi-Dirac model. Although it is a better approximation than equation 2.4.3-3.4.5, it is still insufficient in describing molecules accurately.

2.4.2 Hohenberg - Kohn theorems

The Thomas-Fermi-Dirac model may not describe electronic structure sufficiently to study molecular compounds but was used avidly by the solid state physics community which cherished the low computational intensity as well as the relative applicability of the approximations to the systems they investigated. Although a rigorous foundation for the use of DFT and an appropriate variational theorem had to be devised the simplicity of the early DFT formulations remained seductive compared to WFT. A solution for both the afore mentioned problems were later meticulously derived by Hohenberg and Kohn in 1964. Two theorems critical to establishing DFT, known as the existence and varational theorems, were devised to elevate DFT into the realm of legitimate quantum chemical methods.

Existence theorem

In a DFT formalism, electrons interact with both each other and an 'external potential'. In the UEG approximation, the external potential is a positive charge equally distributed through space while in a molecule the external potential is the attraction from the nuclei. To determine a practical method through which energy can be computed from density in a molecular system, Hohenberg and Kohn showed that it is solely the ground state density that is required to determine the Hamiltonian operator. Equation 2.4.1 states the relationship between ρ and the number of electrons and hence the remaining component required to adequately describe a system is an operator to determine external potential and in turn the nuclear positions and their charges. It can be proved that the external potential can be calculated exclusively from the ground-state density by showing that the assumption of the antithetical provides an impossible result.

As a starting point it is assumed that a non-degenerate ground-state density ρ_0 is consistent with two different external potentials, v_a and v_b. The Hamiltonian operators corresponding to the two potentials are called $\widehat{H}_a$ and $\widehat{H}_b$. Each Hamiltonian is attached to the ground-state wave function Ψ_0 and a corresponding eigenvalue E_0. Applying the principles from variational theorem of MO theory which determines that the expectation value of $\widehat{H}_a$ over the wave function b must be greater than the ground-state energy.

$$E_{0,a} < \langle \Psi_{0,b} | \widehat{H}_a | \Psi_{0,b} \rangle \tag{2.4.8}$$

The expression can be rewritten.

$$\begin{aligned} E_{0,a} &< \langle \Psi_{0,b} | \widehat{H}_a - \widehat{H}_b + \widehat{H}_b | \Psi_{0,b} \rangle \\ &< \langle \Psi_{0,b} | \widehat{H}_a - \widehat{H}_b | \Psi_{0,b} \rangle + \langle \Psi_{0,b} | \widehat{H}_b | \Psi_{0,b} \rangle \\ &< \langle \Psi_{0,b} | v_a - v_b | \Psi_{0,b} \rangle + E_{0,b} \end{aligned} \tag{2.4.9}$$

The integral in the last line of equation 2.4.9 can be modified in terms the ground-state density as v_a and v_b are one-electron operators.

$$E_{0,a} < \int [v_a(r) - v_b(r)] \rho_0(r) dr + E_{0,b} \tag{2.4.10}$$

As a and b have not been differentiated in any significant way the terms may be interchanged.

$$E_{0,b} < \int [v_b(r) - v_a(r)]\rho_0(r)dr + E_{0,a} \tag{2.4.11}$$

if equations 2.4.10 and 2.4.11 are summed an impossible answer is derived.

$$\begin{aligned} E_{0,a} + E_{0,b} &< \int [v_b(r) - v_a(r)]\rho_0(r)dr + \int [v_a(r) - v_b(r)]\rho_0(r)dr + E_{0,b} + E_{0,a} \\ &< \int [v_b(r) - v_a(r) + v_a(r) - v_b(r)]\rho_0(r)dr + E_{0,b} + E_{0,a} \\ &< E_{0,b} + E_{0,a} \end{aligned} \tag{2.4.12}$$

The initial assumption that the ground-state densities defined by wave functions a and b are equal allows for the elimination of the integrals as they must sum up to zero. The result that the two energies are not equal to themselves shows that the assumption that two divergent external potentials can be consistent with a ground-state density, ρ_0, must be wrong and hence the non-degenerate ground-state density has to determine the external potential and in turn the Hamiltonian and the associated wave function. The ground state density can reveal excited state wave functions as the Hamiltonian derived from the ground-state density describes the ground state and all excited states.

Variational theorem

The existence theorem provides a rigorous conceptual backbone to DFT but no practical application can derived from it as it does not provide means by which to determine the density of a system. The statements made by the existence theorem became useful for practical application after showing that the variational principle is applicable to the optimization of density.

A guess density which can be integrated to the correct number of electrons, N can be used as a starting point. The guess wave function and Hamiltonian are determined by the candidate density according to the existence theorem. The expectation value of the energy can be deduced according to the relationship stated in equation 2.4.13.

$$\langle \Psi_{guess} | \widehat{H}_{guess} | \Psi_{guess} \rangle = E_{guess} \geq E_0 \tag{2.4.13}$$

The energy resulting from the calculation on the left-hand side must be equal to or greater than the ground state energy to agree with the variational principle stated for WFT theory.

By optimizing the densities with the criteria for obtaining ever lower energies as calculated in 2.4.13 the system will slowly move closer to an idealized ground state energy. The variational and existence theorems had unresolved issues with respect to their practical application in that there were no provisions in how to determine good guess densities. Furthermore, it requires the user to revert back to the Schrödinger equations Hamiltonian instead of trying to circumvent the computation of energy via a pure DFT formalism.

The challenge of solving an electronic structure problem via DFT lies within the functional itself. The Hohenberg-Kohn theorems show that the density can be mapped onto the Hamiltonian and the wave function and in turn the energy of the system can be computed but no method is described in which density can be employed as a variable to determine the energy of a system. The method to undertake such a computation was devised in 1965.

2.4.3 Kohn - Sham self-consistent field method

The application of the Hohenberg-Kohn Theorems requires the Schrödinger equation to be solved albeit through using electron density as the input variable. There is no advantage in computational efficiency over using WTF theory-based approaches when using density as an input variable. Kohn and Sham realized that the difficulty in solving the Schrödinger equation based on density lays in computing the electron-electron interaction term in most correct Hamiltonian operators. Kohn and Sham had a breakthrough when they circumvented a large portion of this problem by devising a Hamiltonian for a system of non-interacting electrons. The non-interacting Hamiltonian can be expressed as a sum of one-electron operators where the eigenfunctions have Slater determinantal form composed of individual one-electron eigenfunctions.

In the practical applications of this method, a system of non-interacting electrons that have the same ground-state density as a real system with interacting electrons is used as a starting point. Next the energy functional is divided into its contributing components.

$$E[\rho(r)] = T_{ni}[\rho(r)] + V_{ne}[\rho(r)] + V_{ee}[\rho(r)] + \Delta T[\rho(r)] + \Delta V_{ee}[\rho(r)] \tag{2.4.14}$$

The terms on the right-hand refer to the kinetic energy of the non-interacting electrons (T_{ni}), the nuclear electron attraction as given by equation 2.4.3 (V_{ne}), the classical electron-electron repulsion as given by

equation 2.4.4 (V_{ee}), the kinetic energy correction derived from the nature of electrons (ΔT) and the non-classical corrections to the electron-electron repulsion (ΔV_{ee}), respectively.

The Kinetic energy of the non-interacting system of the electrons is expressed as a sum of the kinetic energies of the individual electrons. Equation 2.4.14 can be rephrased in terms of the orbital expressions of ρ.

$$E[\rho(r)] = \sum_{i}^{N} \left(\left\langle \chi_i - \frac{1}{2}\nabla_i^2 | \chi_i \right\rangle - \left\langle \chi_i | \sum_{k}^{nuclei} \frac{Z_k}{|r_i - r_k|} | \chi i \right\rangle \right) + \sum_{i}^{N} \left\langle \chi_i | \frac{1}{2} \int \frac{\rho(r')}{|r_i - r'} | dr' | \chi_i \right\rangle + E_{xc}[\rho(r)] \tag{2.4.15}$$

N is the number of electrons, and the density has been formulated as Slater determinantal wave functions and is given by 2.4.16.

$$\rho = \sum_{i=1}^{N} \langle \chi_i | \chi_i \rangle \tag{2.4.16}$$

In equation 2.4.15 the term E_{xc} compounds the terms δT and δV_{ee} together and is defined as the exchange-correlation (xc) term. The nomenclature is misleading as the E_{xc} describes more than just exchange and correlation. E_{xc} additionally corrects for the classical treatment of electron self-interaction and the difference of kinetic energy between the real and the postulated non-interacting system.

The pseudoeigenvalue equation is satisfied if the orbitals χ which minimize the energy, E, in equation 2.4.15 are plugged in.

$$h_i^{KS} \chi_i = \varepsilon_i \chi_i \tag{2.4.17}$$

Here the Kohn-Sham (KS) one-electron operator (h_i^{KS}) is formulated as follows:

$$h_i^{KS} = -\frac{1}{2}\nabla_i^2 - \sum_{k}^{nuclei} \frac{Z_k}{|r_i - r_k|} + \int \frac{\rho(r')}{|r_i - r'} | dr' + V_{xc} \tag{2.4.18}$$

and the potential V_{xc} is a functional derivative of energy defined as

$$V_{xc} = \frac{\delta E_{xc}}{\delta \rho} \tag{2.4.19}$$

The V_{xc} functional derivative is interpreted as a one-electron operator in the KS Slater determinant with a corresponding expectation value of E_{xc}.

The energy minimization in equation 2.4.14 is exact and hence the orbitals, χ, which correspond to it provide an exact density. The Slater-determinantal eigenfunctions are composed of the orbitals for the separable non-interacting Hamiltonian which are defined as the sum of the Kohn-Sham operators in equation 2.4.18, acting upon the orbitals.

$$\sum_{i=1}^{N} h_i^{KS} |\chi_1 \chi_2 \cdots \chi_N\rangle = \sum_{i=1}^{N} \varepsilon_i |\chi_1 \chi_2 \cdots \chi_N\rangle \tag{2.4.20}$$

The internal consistency of the Kohn-Sham method between the non-interacting system and the density resembling that of the real system is maintained by applying the KS operator in this manner. The first term of equation 2.4.15 is used to compute the kinetic energy for the non-interacting electrons which provide a large proportion of the kinetic energy of the real system. The computation of the kinetic energy in equation 2.4.15 is justified due to the internal consistency between the non-interacting and the real system.

The KS orbitals are conceptually constructed analogously to the orbitals used in MO theory. A set of basis functions $\{\phi\}$, is used to express the orbitals and the secular equation as described for HF theory is used to optimize the coinciding orbital coefficients for a given basis. The elements $F_{\mu v}$ are replaced by elements $K_{\mu v}$ in the DFT approach

$$K_{\mu v} = \left\langle \phi_\mu \right| - \frac{1}{2}\nabla^2 - \sum_{k}^{nuclei} \frac{Z_k}{|r_i - r_k|} + \int \frac{\rho(r')}{|r_i - r'} |dr' + V_{xc} |\phi_v \right\rangle \tag{2.4.21}$$

The DFT and HF approach have a lot in common beyond using the variational principle. Nuclear attraction and kinetic energy are expressed identically in the matrix elements K and F. Assuming the same basis function is used to express the density in classical interelectronic repulsion operator as for the Kohn-Sham orbitals, the four index electron repulsion integrals are synonymous in K and F. The Kohn-Sham method must also be carried out as an iterative process which is outlined in the following subsection. A known density is required to compute the secular equation matrix elements and the density is also a result of computing the idealized combination of orbitals calculated via the secular equation. Hence an analogous SCF procedure is required as for the HF process.

Kohn-Sham SCF procedure

The Kohn-Sham SCF procedure as presented in figure 2.5 is analogous to the HF SCF procedure apart from some key differences. The selection of a basis set for HF methods is straight forward as only one basis is used while DFT methods can incorporate two basis sets. One basis forms the Kohn-Sham orbitals and the second basis describes the density and is known as an 'auxiliary' basis set as in DFT there are no exchange integrals and hence it is convenient to represent ρ as follows:

$$\rho(r) = \sum_{i=1}^{M} c_i \Omega_i(r) \tag{2.4.22}$$

Here Ω_i has units of probability density, M represents the number of basis functions and c_i are coefficients. The c_i coefficients are fitted according to a least-square method to the density determined by the KS orbitals as described in equation 2.4.18. The number of Coulomb integrals which require evaluation are N^2M, where N is the number of KS AO basis functions. The bottleneck of KS SCF is the matrix diagonalization which scales as N^3 instead of the integrals of HF which scale at N^4, hence DFT scales better than HF and is consequentially preferable for larger systems. Many programs which calculate electronic structure methods do not employ auxiliary basis sets and choose a pathway which is HF-like to compute the product of KS-orbital basis functions. The convenience of transposing code written for HF methods onto that of DFT methods is the motivation for omitting auxiliary basis sets.

Following the selection of the basis set a molecular geometry is selected and the overlap, kinetic energy and nuclear attraction integrals are computed. The density matrix is initially guessed analogously to the construction of a density matrix in HF theory to calculate the integrals. The guess density is used to determine the KS matrix elements and derive V_{xc}. After the KS matrix elements are evaluated, the iterative procedure is analogous the HF SCF procedure. The generated orbitals determined by the secular equation determine a new density which is evaluated against the prior density. After a number of iterations, the difference between the densities fits within the convergence criteria which concludes the optimization and the program evaluates whether a stationary point, ideally a minimum, is reached.

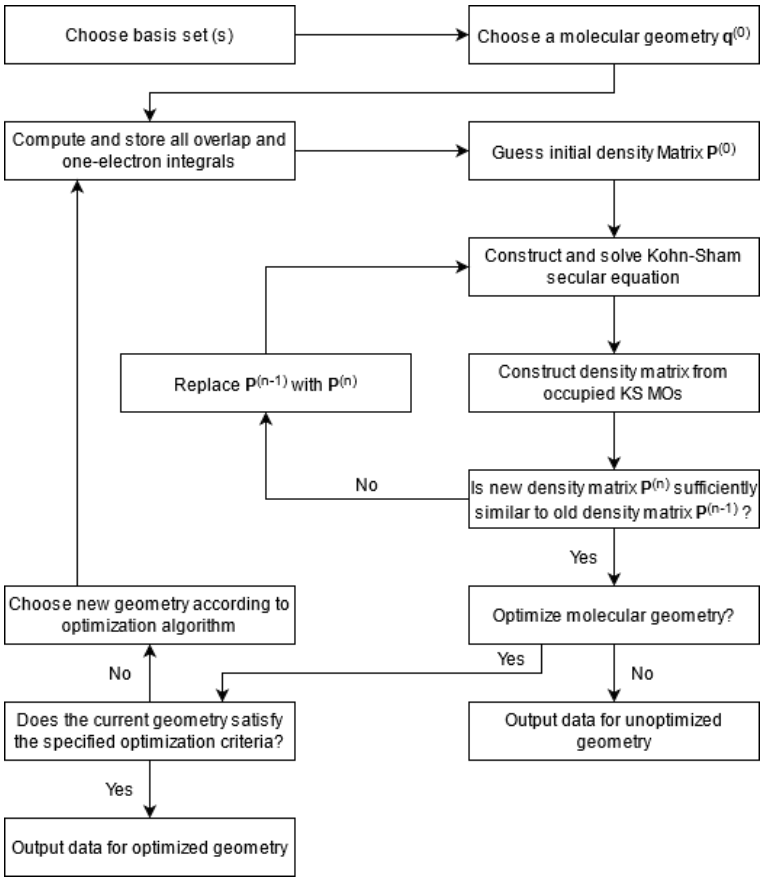


Figure 2.5: KS SCF procedure flow chart

Fundamentally DFT and HF differ in that HF is a deliberately approximate theory whose equations can be solved exactly while DFT is an exact theory with approximate solutions due to the lack of ideal operators. The challenge of KS-DFT lies with the precise construction of the E_{xc} operator as a function of ρ. Hohenberg and Kohn showed that there is a precise functional of density, however, how to acquire this functional is still being speculated upon today, 55 years after the theorem's inception. The next section will discuss different nuances of designing E_{xc} functionals and introduce a hierarchy by which E_{xc} functionals are broadly classified.

2.4.4 Exchange-correlation functionals

The correct formulation of E_{xc} functionals requires recapitulating the purpose of E_{xc} functionals, they account for

1. The difference between classical and quantum interelectronic repulsion
2. The difference between the kinetic energy of the non-interacting and the real system

The difference in kinetic energy is usually not calculated explicitly but instead a hole function analogous to that presented in equation 2.4.6 providing an embedded kinetic energy correction is used. Alternatively, some functionals correct the kinetic energy terms with empirical parameters based on experimental data.

It is helpful to understand the common notation employed for exchange-correlation functionals to better understand how various functionals work. E_{xc} is functionally dependent on electron density via energy density ε_{xc}.

$$E_{xc}[\rho(r)] = \int \rho\varepsilon_{xc}[\rho(r)]dr \tag{2.4.23}$$

Energy density is expressed as a sum of all the compounding exchange and correlation contributions. Due to the use of two different densities confusion can arise but while electron density is measured per unit volume, energy density is measured per particle density. Combining the formalism of energy and electron density with equation 2.4.7 the Slater exchange energy density can be expressed (eq. 2.4.24).

$$E_x[\rho(r)] = -\frac{9\alpha}{8}\left(\frac{3}{\pi}\right)^{1/3}\rho^{1/3}(r) \tag{2.4.24}$$

Electron density is expressed through an effective radius. An electron is restricted to be located within a sphere defined by a given radius which has a continuous density throughout.

$$r_S(r) = \left(\frac{3}{4\pi\rho(r)}\right)^{1/3} \tag{2.4.25}$$

Spin can also be described in DFT through individual density functionals incorporating α and β densities. Commonly the spin density at any position is expressed in terms of a normalized spin polarization, ζ.

$$\zeta(r) = \frac{\rho^{\alpha}(r) - \rho^{\beta}(r)}{\rho(r)} \tag{2.4.26}$$

Here half of the product of the total density, ρ, and $(\zeta + 1)$ is the α in density, while the β spin density is computed as the difference between the α and total density ρ.

Two different philosophical approaches are taken to developing E_{xc} functionals. The first is the non-empirical approach in which a functional is designed to exact constraints, i.e. constraints which are ideally universally

true for all electron densities. The second approach to functional design is the semi-empirical route with a more flexible functional form which is fit in a polynomial fashion to satisfy selected constraints such as ρ, $\nabla\rho$ and others to reference values computed through calculation at the highest level of WFT theory available, coupe cluster with singles, doubles and probative triples using a complete basis set (CCSD(T)/CBS).

A crucial challenge in the development of E_{xc} functionals is that they cannot be improved with a particular methodical procedure in mind. Successively developed functions can commonly not be appended by some additional constraint or fitting to be successively improved performance for all chemical nuances. Consequentially DFT does not follow a strict hierarchy as WFT does. The 'Jacobs Ladder' suggested by John Perdew is the closest thing to an established hierarchy in E_{xc} functionals.[8] The ladder starts on the Hartree rung where exchange-correlation is 0 and electron-electron interaction is computed classically. The subsequent rungs of the ladder follow the order; local density approximation (LDA)/ local spin density approximation (LSDA), generalized gradient approximation (GGA), meta-generalized gradient approximation (mGGA), hybrid-functional and double hybrid functionals. Each rung includes an improvement in the form of introducing a new variable to describe the system or mixing different concepts in a variety of ways. The next section will introduce the concepts surrounding different rungs of the density functionals, commonly used functionals at each rung and a broad overview of their performance.

Local density approximation and local spin density approximation

the terms LDA and LSDA describe the simplest class of E_{xc} functionals which depend singularly on electron density as a variable. LDA and LSDA functionals are exact for UEG but cannot describe molecular systems accurately due to the inconsistency in electron density which cannot be described by this class of functional. The exact analytical exchange functional form dates to the Slater-Dirac model and is shown in equations 2.4.27 and 2.4.28 in the spin unpolarized and spin polarized forms, respectively. There are no exact analytical forms of correlation functionals but various popular parameterizations exist, the most popular correlation functionals being PW92[9], PZ81[10] and VWN5.[11] The correlation functionals were all fitted using quantum monte-carlo reference data. The combination of Slater-dirac exchange (S) and PW92 correlation form the E_{xc} called SPW92.[8]

$$E_x^{LDA} = \sum_{\sigma}^{\alpha,\beta} \int e_{x,\sigma}^{UEG} dr = -\frac{3}{2}\left(\frac{3}{8\pi}\right)^{1/3} \int \rho_\sigma^{4/3} dr \tag{2.4.27}$$

$$E_x^{LSDA} = \sum_{\sigma}^{\alpha,\beta} \int e_{x,\sigma}^{UEG} dr = -\frac{3}{2}\left(\frac{3}{4\pi}\right)^{1/3} \sum_{\sigma}^{\alpha,\beta} \int \rho_{\sigma}^{4/3} dr \tag{2.4.28}$$

The correlation functional selected has a marginal effect on the results of the DFT computation. Head-Gordon et al. found that over 4986 data points of the mean absolute deviation between SPW92 and SVWN5 interaction energies was only 0.17 kJ mol^{-1}. Generally, SPW92 tends to overbind atoms and results excessively contracted bonds and large binding energies of any interaction ranging from IMF to covalent bonds. [8]

Most exchange functionals are spin polarized. Spin is introduced through a spin polarization attenuation to convert equation 2.4.27 to equation 2.4.28 through the exact spin-scaling of the exchange energy (eq. 2.4.29).

$$E_x[\rho_\alpha, \rho_\beta] = \frac{1}{2}E_x[2\rho_\alpha] + \frac{1}{2}E_x[2\rho_\beta] \tag{2.4.29}$$

Generalized gradient approximation

The next rung of on Jacob's ladder is occupied by GGA functionals which introduce the density gradient $\nabla\rho$ as a variable to account for the inconsistency in the density throughout a system. GGA functionals are formulated as in equation 2.4.30.

$$E_x^{GGA} = \sum_{\sigma}^{\alpha,\beta} \int e_{x,\sigma}^{UEG} g_{x,\sigma}^{GGA} dr \tag{2.4.30}$$

Here the function $g_{x,\sigma}^{GGA}$ is an inhomogeneity correction factor (ICF) acting upon $e_{x,\sigma}^{UEG}$, effectively supplementing the UEG exchange energy density per unit volume. $g_{x,\sigma}^{GGA}$ can take various forms but the first one was proposed in the X$\alpha\beta$ exchange functional developed by Herman which has the form of

$$g_{x,\sigma}^{GGA} = 1 + c_{x,1}x_{\sigma}^2 \tag{2.4.31}$$

where

$$x_\sigma = \frac{|\nabla\rho_\sigma|}{\rho_\sigma^{4/3}} \tag{2.4.32}$$

is a dimensionless variable depending on a dimensional analysis of the density gradient $\nabla\rho$ in a semi-infinite domain. The X$\alpha\beta$ functional outperformed LSDA functionals in computing atomic energies but due to the asymptotical divergence of the exchange functional it had to be truncated at large density gradient values. Consequentially Becke developed an alternative to x_σ within a finite domain.

$$u_\sigma = \frac{\gamma x_\sigma^2}{1+\gamma x_\sigma^2} \tag{2.4.33}$$

where γ is a nonlinear parameter used in P86[12] and PBE[13] exchange functionals where

$$g_{x,\sigma}^{GGA} = 1 + c_{x,1} u_\sigma \tag{2.4.34}$$

Finally, Becke used a power series in the B97[14] functional which expresses the exchange ICF exactly.

$$g_{x,\sigma}^{GGA}(u_\sigma) = \sum_{j=0}^{N} c_{x,j} u_\sigma^j \tag{2.4.35}$$

Amongst GGA functionals the most popular exchange functionals are the B88[15], PW91[16], PBE[13], revPBE[17], RPBE[18] and PBEsol[19] and the most commonly used correlation functionals are P86[12], LYP[20], PW91[16], PBE[13] and PBEsol[19]. The exchange and correlation functionals can be freely combined to provide a complete E_{xc} functional. the most popular combinations is the PBE E_{xc} functional (PBE exchange with PBE correlation) but other commonly employed E_{xc} functionals include BP86 (B88 with P86)[12,15], BLYP (B88 with LYP)[15,20], PW91 (PW91 with PW91)[16], revPBE (revPBE with PBE)[13,17], RPBE (RPBE with PBE)[13,18] and PBEsol (PBEsol with PBEsol).[19]

Meta-generalized gradient approximation

meta-Generalized Gradient Approximation (mGGA), which occupies the third rung of the Jacobs ladder, utilizes two further variables to enhance the accuracy of the E_{xc} functionals, the Laplacian of the density, $\nabla^2\rho_\sigma$ or the kinetic energy density.

$$\tau_\sigma = \sum_{i}^{n_\sigma} |\nabla\phi_{i,\sigma}|^2 \tag{2.4.36}$$

Both variables depend on the second derivative information and are related through equation 2.4.37 and are usually utilized exclusive from one another. The kinetic energy density is the more commonly used variable amongst the two variables used to alter the E_{xc} functional forms. Additionally, the kinetic energy density is instructive as it allows for the detection of electron delocalization in molecules. Other dimensionless variables to the reduced density gradient are used as alternatives but this form is exceedingly the most popular.

$$\tau_\sigma = \frac{\nabla^2 \rho_\sigma}{2} - \sum_{i=1}^{n_\sigma} \left|\nabla \phi_{i,\sigma}^*(r)\right|^2 (r) \tag{2.4.37}$$

The standard formalism of mGGA functionals is as follows:

$$E_x^{mGGA} = \sum_{\sigma}^{\alpha,\beta} \int e_{x,\sigma}^{UEG} g_{x,\sigma}^{mGGA} dr \tag{2.4.38}$$

where

$$g_{x,\sigma}^{mGGA}(u_\sigma) = \sum_{i=0}^{N'} \sum_{j=0}^{N} c_{x,ij} \omega_\sigma^i u_\sigma^j \tag{2.4.39}$$

The most popular non-empirical mGGA E_{xc} functionals are primarily from Perdew; TPSS[21], revTPSS[22], PKZB[23], MS0[24], MS1[25],MS2[25], MVS[26] and SCAN[27] functionals. alternative non-empirical functions are BLOC[28] and TM.[29] Semi-empirical mGGA functionals were primarily parameterized by the Truhlar group and include the popular M06-L[30], M11-L[31], MN12-L[32] and MN15-L[33]. Other groups have developed the semi-empirical mGGA functionals VSXC[34], τ-HCTH[35] oTPSS[36] and mBEEF.[37]

mGGA functionals provide more accurate results for atomisation energies and barrier heights. mGGA functionals can be embedded with 'medium-range' dispersion and functions like SCAN and M06-L have been able to show parallel displacement of benzene dimers. mGGA functionals have a higher responsiveness to changes in the integration grid compared to GGA functionals and more care must be taken when selecting an adequate grid, particularly with respect to weakly interacting systems.

Although going from LDA/LSDA to GGA to mGGA yields significantly better results there are a few insurmountable issues when relying on ρ, $\nabla\rho$ and τ;

1. Self interaction error (SIE), the error occurring when electron interact with themselves
2. Correct description of dispersion interaction or long-range dynamic correlation
3. strong correlation

Hybrid functionals

The SIE inherent in DFT functionals up to the mGGA rung of the Jacobs ladder can be tackled by substituting the DFT exchange functional with an exact one computed through the HF method. Simultaneously a local correlation functional which results in zero correlation energy for a one electron system, such a LYP, must be utilized. Initially ideas of combining exact exchange with local correlation (HFLYP) resulted in improvements which were too marginal to pursue. Later Becke came up with the idea to combine a global fraction of exact exchange with an E_{xc} functional. Global hybrid (GH) functionals, which define the fourth rung of the Jacobs ladder, are generally formulated as in 2.4.40.

$$E_x^{GH} = c_x E_x^{HF} + (1 - c_x) E_x^{DFT} + E_c^{DFT} \tag{2.4.40}$$

GH functionals are rationalized through the adiabatic connection formula. A more empirical approach to understanding how GH functionals work can be achieved by considering the way atomisation energies are computed by HF and SPW92. HF vastly underestimates the energies of 124 atoms tested by a mean square error (MSE) of 471.91 kJ mol^{-1} and SPW92 overestimates them by a MSE of 243.13 kJ mol^{-1}. At a value of c_x=0.34 being plugged into equation 2.8.40 non-self-consistently leads to MSEs summing to zero.

Becke first developed GH functionals in 1993 by fitting three linear parameters to 56 atomisation energies. The B3PW91[38] GH GGA functional is composed as follows:

$$E_x^{B3PW91} = c_x E_x^{HF} + (1 - c_x - a_x) E_x^{S} + a_x E_x^{B88} + (1 - a_c) E_x^{PW92} + a_c E_c^{PW91} \tag{2.4.41}$$

where c_x=0.20, a_x=0.72 and a_c=0.81. The most popular GH GGA functionals exact exchange is parameterized to contribute 20% to 25% where the most used GH GGA functional, B3LYP[38] also uses an exact exchange contribution of 20%. In the B3LYP functional the PW92[9] and PW91[16] are replaced with the VWN1RPA[39] and LYP[20] correlation functionals, respectively.

Among non-empirical GH GGA functionals PBE0 with 25% exact exchange is the most popular which has also been analogously developed with revPBE0 exchange functional. Next to B3LYP, the most commonly used semi-empirical functional is B97[14] which has also been thoroughly developed through alternative parameterization in the forms B97-1[40] B97-2[41] and B97-3.[42] The portion of exact exchange can also vary a lot depending on the choice of data set used for the parameterization exemplified by the B97-K[43] and

SOGGA11-X[44] functionals which have 42% and 40.15% exact exchange, respectively. The general trend of GH functionals is that they remediate overbinding associated with GGA functionals. The change from PBE to PBE0 improves the binding mean square error over bond energies from -50.91 kJ mol^{-1} to 4.68 kJ mol^{-1}.

Next to the improvement of GGA functionals through inclusion of exact exchange, mGGA functionals have also benefited from mixing with exact exchange. On the non-empirical side TPSSh[45], revTPSSh[46] and MS2h[47] have approximately 10% exact exchange while MVSh[48] and SCAN0[49] have 25% exchange. The Truhlar group has been most prolific in the publication of GH mGGA functionals having published 12 such functionals since 2004; MPW1B95[49], MPWB1K[50], PW6B95[51], PWB6k[51], M05[52], M05-2X[53], M06[54], M06-2X[54], M06-HF[55], M08-HX[56], M08-SO[56], and MN15.[57] The amount of exact exchange varies from 27% to 54% an goes up 100% in the M06-HF functional.

Range seperated functionals

The improvement of GH functionals over their local counterparts is significant with respect to treating interactions and kinetics but the commonly encountered SIE is only partially remediated. An ongoing attempt to account for SIE is through implementing range separated treatment of exact exchange. In the case of range separated functionals, exact exchange contribution is separated into short $E_{x,sr}^{HF}$ and long $E_{x,lr}^{HF}$ range components where the coulomb operators are treated by different error functions. The functionals are parameterized so the short range interaction accounts for a non-zero exact exchange interaction while the long range functional is set to ensure that the long range interactions remain SIE free.

$$E_{xc}^{RSH} = c_{x,sr}E_{x,sr}^{HF} + c_{x,lr}E_{x,lr}^{HF} + (1 - c_{x,sr})E_{x,sr}^{DFT} + (1 - c_{x,lr})E_{x,lr}^{DFT} +)E_{c}^{DFT} \tag{2.4.42}$$

here the short and long range scaler values will always sum to 1.

The two most popular range separated functionals are ωB97[58] and ωB97X[58] which include 0 and 15.77% exact short-range exchange and 100% exact long range exchange. The error function ω are empirically parameterized into the ωB97 functionals. Non-empirical range separated hybrid (RSH) functionals include LC$-\omega$PBE08[59], LRC$-\omega$PBE[60], LRC$-\omega$PBEh[60] and CAM-B3LYP[61] by Handy. The concept of subdividing the application of exact exchange based on distance also allows for long range exact exchange to be removed and in subsequently create screened exchange functionals such as HSE-HJS[62] and N12-SX.[63] Two RSH-mGGA functionals have also been parameterized by the Truhlar group; M11[64] and MN12-SX.[63]

Treating dispersion

The second main issues of GGA functionals which is not tackled by GH and RSH functionals is the treatment of long-range dynamic correlation, dispersion. If one were to scan the dispersion of two helium atoms using LSDA, GGA, mGAA, GH or RSH functionals the energetic decay would be exponential instead of the proper R^{-6} decay. Two popular approximations are employed to account for this; dispersion tails developed by Grimme and co-workers and non-local correlation functionals developed by various groups.

DFT - D dispersion tails

The dispersion tails developed by Grimme are a damped atom-atom empirical potential which is trained for a given functional and is then appended onto the functional to account for long range correlation. [8]

$$E_{disp}^{DFT-D} = -\sum_{A<B}\sum_{n=6,8,....} s_n \frac{C_n^{AB}}{R_{AB}^n} f_{damp,n}(R_{AB}) \tag{2.4.43}$$

Three versions of dispersion correction were developed by Grimme; D1 [65], D2 [66] and D3 [67] out of which the D3 is commonly used in conjunction with a damping function developed by Becke and Johnson (BJ) (D3-BJ). [68] The training of the dispersion is commonly carried out in isolation of the E_{xc} functional but recently semi-empirical functionals where trained alongside dispersion corrections. The resulting functionals were B97-D [66] functionals, a local GGA functional with a D2 tail. further bilateral optimizations have been carried out with mGGA, GH and RSH functionals.

DFT-D corrections work most effectively when combined with E_{xc} functionals which tend to underbind non-covalent interactions. This is particularly emphasized when fitting dispersion tails to functionals which overbind non-covalent interactions such as PBE where the resulting 'correction' results in bigger margins of error. Hence it is key to know the functional which is being used and what type of chemistry is being investigated.

nonlocal correlation functionals

Alternatively to dispersion tails, non-local correlation functionals (NLCs) have been developed as an alternative solution to account for dispersion. NLC functionals like VV10 [69] take the following functional form

$$E_{disp}^{VV10} = \int dr\rho(r) \left[\frac{1}{32} \left(\frac{3}{b^2} \right)^{\frac{3}{4}} + \frac{1}{2} \int dr' \rho(r') \Omega(r, r') \right] \tag{2.4.44}$$

and are less empirical than the DFT-D approach, containing only two fitted parameters. Head-Gordon and Mardirossian utilized the VV10 functional to parameterized three semi-empirical functionals; an RSH GGA functional ωB97X-V[70], a local mGGA functional B97M-V[71] and an RSH mGGA functionanl ωB97M-V.[72] The functional parameterized with NLC functionals outperform other functionals at the same rung but compared with the DFT-D approach the energy evaluation is computationally more expensive.

2.5 Basis sets variants

Basis sets are introduced in the LCAO section as a group of 'base' functions which are used to construct electronic wave functions. When undertaking an electronic structure computation, a basis set is a set of atomic orbital basis functions which are pre-determined for all or a selected group of atoms, depending on the particular basis set. A variety of different basis sets with different computational cost are commonly employed. Additional functions can be introduced into basis sets to better represent chemical behaviour. This section gives insight into some of the essential concepts of basis sets and dissects the nomenclature of the most popular basis sets commonly used.[73]

The first major concept which subdivides basis sets are the different approaches championed by the physics and chemical communities. Chemists undertake electronic structure calculations of molecular species while physicists usually work with solid state materials. This differentiation results in chemists using Gaussian-type orbitals (GTOs) and Slater-type orbitals (STOs) as their basis sets and physicists use plane-wave basis sets. The difference arises from the reference material where chemists use localized atomic orbitals as the reference to generate their basis sets and physicists use free-electrons and introduce potentials which function as perturbations on the plane waves. All computations undertaken were of molecular nature and hence the Basis sets discussed are GTOs but the concept of STOs is also introduced.[1]

Chemical intuition suggests that STOs can be used as a good basis set for molecular calculation. STOs describe an s orbital as follows:

$$\phi_{abc}^{STO}(x, y, z) = N x^a y^b z^c e^{\zeta r} \tag{2.5.1}$$

where N is a normalization factor. a, b, and c sum to the angular momentum and ζ controls the orbitals width, small ζ generates diffuse functions while a large ζ generates tight functions. STOs describe hydrogen-like orbitals, particularly 1s but can be fine-tuned to describe higher angular momenta through correcting short and long range behaviour.

GTOs take the functional form of

$$\phi_{abc}^{GTO}(x,y,z) = Nx^a y^b z^c e^{\zeta r^2} \tag{2.5.2}$$

which is analogous to STOs apart from the r^2. This results in a cruder representation of a hydrogen 1 s orbital as illustrated in figure 2.6.

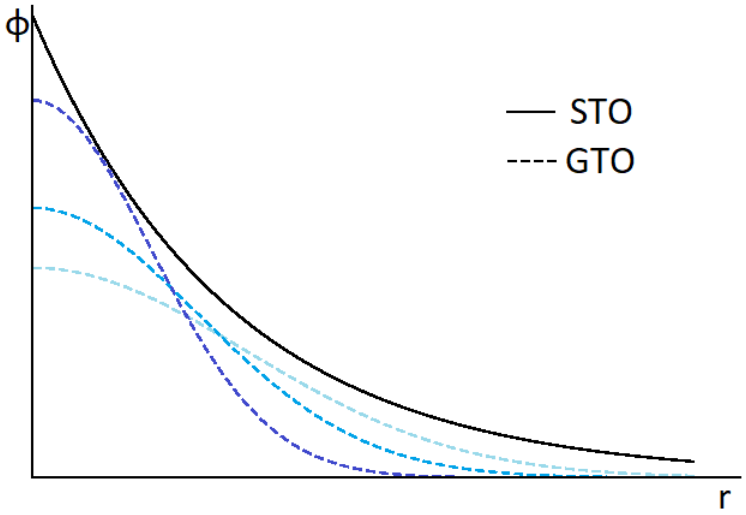


Figure 2.6: 2D representation of 1s STOs and 3 GTOs

The dilemma is that STOs are more accurate, but they make the computation of integrals significantly more computationally intensive. The solution is to use a linear combination of GTOs fitted to an STO to undertake the computation.

$$\phi_{abc}^{cGTO}(x,y,z) = N\sum_{i=1}^{n} c_i x^a y^b z^c e^{\zeta_i r^2} \tag{2.5.3}$$

which is illustrated in figure 2.7.

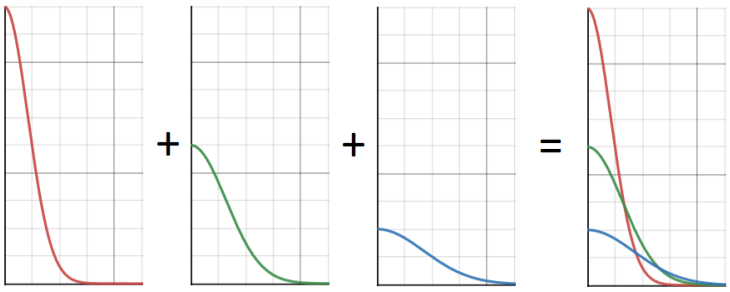


Figure 2.7: Schematic representation of LCGTO

The form of the individual GTOs and their coefficients forming the cGTOs are predetermined for each atom various basis sets are designed to function for. Higher quality basis sets will usually describe core orbitals by combining larger amounts of GTOs to be more precise. A cGTOs constituent GTOs are referred to as primitive Gaussian orbitals.

Different atoms require different types of functions to describe their chemistry adequately. The electrons with the highest angular momenta present in the atoms which are treated must be described correctly. Consequentially hydrogen and helium only require 1s function, lithium through neon require 3 functions, two s and one p, and sodium through argon require 5 functions, three s and two p. When treating a molecular system with a basis set as described it is coined a minimal basis as the number of functions used to describe the system are the bare minimum of functions required. Alternatively, it is known and a single-zeta basis set where zeta refers to the number of functions used to describe the valence electrons.

Type	H,He	Li-Ne	Na-Ar	examples
Minimal or single zeta	1s	2s, 1p (p_x, p_y, p_z)	3s, 2p (p_x, p_y, p_z)	STO-3G

Note that in the single-zeta basis set STO-3G the notation 3G denotes that each orbital is a linear combination of 3 primitive Gaussian functions. Precisely the STO 3 can be summed up as follows:

$$\phi^{(s)}_{STO-3G} = c_1\psi_1 + c_2\psi_2 + c_3\psi_3 \tag{2.5.4}$$

where

$$\psi_1 = \frac{2\alpha_1}{\pi}^{3/4} e^{-\alpha_1 r^2}$$
$$\psi_2 = \frac{2\alpha_2}{\pi}^{3/4} e^{-\alpha_2 r^2}$$
$$\psi_3 = \frac{2\alpha_3}{\pi}^{3/4} e^{-\alpha_3 r^2} \tag{2.5.5}$$

Double- and triple-zeta functions are describe valence electrons with two or three functions per valence electron, respectively.

Type	H,He	Li-Ne	Na-Ar	examples
Double-zeta	2s	3s, 2p	4s, 3p	3-21G, 6-31G, DZ
tripple-zeta	3s	4s, 3p	5s, 4p	6-311G, TVZ

The notation for the Pople double-zeta basis sets[74–76], 3-21g and 6-31g, refer to the amount of primitive Gaussian functions combined to form various orbitals. The first number denotes the number of primitives in the core orbitals. The second number refers to the number of Gaussian functions combined to form the first cGTO describing valence shell and the last number is the number of Gaussian functions combined to form the second cGTO describing valence shell. This notation gives insight into the functional composition of the triple-zeta basis set 6-311G where everything is analogous to the 6-31g apart from the additional single cGTO of the valence shell.

Increasing the zeta for larger atoms such as transition metals is less clear cut as there is a different significance is assigned to different angular momenta. It is debated which occupied shells make up the valence shell and hence different basis sets are designed with different chemical processes in mind. There can hence be alternations in how different basis sets describe the valence electrons of a transition metal.

The basis sets up until now do not include functions with higher angular momenta than the occupied orbitals. Basis sets can be used in conjunction with a polarization function, denoted with a "p". Polarization functions introduce additional basis functions with an angular momentum higher than the occupied orbitals. The introduction of polarization is essential to describe polarizability and hyper valency in molecular systems. Basis sets can be used with multiple polarizability functions, hence introducing multiple functions with an angular momentum one larger than the occupied maximum.

Type	H,He	Li-Ne	Na-Ar	examples
Double-zeta polarized	2s, 1p	3s, 2p, 1d	4s, 3p, 1d	6-31G*, DZP
tripple-zeta polarized	3s, 1p	4s, 3p, 1d	5s, 4p, 1d	6-311G(d,p), TVZP
Double-zeta double polarized	2s, 2p	3s, 2p, 2d	4s, 3p, 2d	6-31G-2P, DZ2P
tripple-zeta double polarized	3s, 2p	4s, 3p, 2d	5s, 4p, 2d	6-311G(d,2p), TVZ2P

Diffuse functions can modify basis sets by introducing GTOs a minimum alpha, denoted with the prefix 'aug-' or the suffix '+' for Dunning[77–79] and Pople basis sets, respectively. Diffuse functions allow electrons to be located further from the nucleus and are essential for the computation of anions, Rydberg state and species with high electronegativity and electron density.

There is a wide variety of basis sets parameterized for specific tasks. The most universally employed basis sets are the Pople-syle basis sets (3-21G, 6-31G etc.) and the correlation consistent basis sets developed by Dunning and co. wokers (DZ, TZ, TVZP etc.). Discussion of additional basis sets has been omitted as they have not been used in the investigation, but a comprehensive review of basis sets has been published.[80]

2.5.1 Basis set superposition error

Basis set superposition errors (BSSEs)[81] arise when computing the interaction two different species. The interaction energy is normally calculated as follows:

$$E_{int} = E(AB, r_c) - E(A, r_e) - E(B, r_e) \tag{2.5.6}$$

where r_c denotes the geometry of two interacting species, A and B while r_e refers to the independent geometries of the isolated species. In a system which includes dispersion interactions and/or hydrogen bonding the interaction energies computed are commonly erroneous. The erroneous results are the associated with the BSSE.

The BSSE arises due to the discrepancy between the basis functions available to describe A and B in isolation versus AB when they are interacting. Species A in isolation only has the basis associated with species A to describe its electronic structure and the same thing is true for species B. In the interacting structure the incompleteness of the basis of A is compensated for by the basis functions of species B and vice versa. Hence species A in the complex is described better than species A in isolation and the same is true for species B.

There are two possible solutions to tackle the issue. The first solution is to use a more complete basis set as

the more complete the basis on the individual species the less compensation must be accounted for. High level basis sets can work for small systems but are practically unfeasible for larger systems as the computational cost for utilizing complete bases is too high. The alternative solution is called the counterpoise method (CP). The CP method is an approximate approach to calculating the BSSE. The error is accounted for by computing the energy of the isolated species A and B while providing them with the basis analogous to the one present in the complex AB. Hence the interaction energy can be computed as follows:

$$E_{int} = E(AB, r_c)^{AB} - E(A, r_e)^{AB} - E(B, r_e)^{AB} \tag{2.5.7}$$

Here the superscripts AB denote that each species is described with the basis which is prevalent in the arrangement when A and B are interacting.

2.6 Additional approximations

In the conducted investigations the species studied require additional approximations due to the incorporation of larger atoms in which core electrons are replaced. The species are also simulated in a liquid environment which must be accounted for. The models used to make the appropriate approximations and simulate alternative phase environments are discussed in this section.

2.6.1 Effective core potentials

Core and valence electrons are treated differently in the scope of chemical transformations. Core electrons are assumed to be inert apart from the modification of the nuclei's effective potential on the valence electrons through shielding. In contrast, valence electrons actively participate in chemical transformations like the formation of a chemical bond. The computational expense of calculating electronic structures of molecules rises exponentially with the number of electrons in a system. Exponentially rising calculation cost and the relative redundancy of core electrons, especially for larger atoms, lead to the development of effective core potentials (ECP) to replace core electrons with an ECP. ECPs are commonly used to reduce the calculative costs while preserving accuracy and precision of the results. The second reason for the popularity of ECPs is the implicit treatment of relativistic effects which become more relevant when studying bigger atoms.[82]

In various ECP methods the idea is to create a valence only (VO) Hamiltonian for n_v valence electrons, where the subscripts v and c refers to valence to core electrons respectively, that are treated independently

in the calculation with N cores as follows:

$$\widehat{H}_v = \sum_{i}^{n_v} \widehat{h}_v(i) + \sum_{i<j}^{n_v} \widehat{g}_v(i,j) + \widehat{V}_{ccp} + V_{cc} \tag{2.6.1}$$

In this equation $\widehat{h}_v$ and $\widehat{g}_v$ are the one (kinetic) and two electron (coulomb) operators treating the behaviour of valence electrons explicitly, $\widehat{V}_{ccp}$ is a core-polarization potential (CPP) accounting for static core-polarization (the degree to which a dipole may be induced through polarization at the HF level) and dynamic core polarization (core–valence correlation) and V_{cc} is representative of the repulsion between all cores and nuclei. The amount of valence electrons is obtained by subtracting the number of core electrons from the total number of electrons which equates to the difference between the nuclear charge Z_λ and the core charge Q_λ.

$$n_v = n - n_c = n - \sum_{\lambda}^{N} (Q_\lambda - Z_\lambda) \tag{2.6.2}$$

Non-relativistic, scalar-relativistic, and quasi-relativistic ECPs make use of a valence-model Hamiltonian which is formally non-relativistic in that the operators are denoted as follows:

$$\widehat{h}_v(i) = -\frac{1}{2}\widehat{\nabla}_i^2 + \widehat{V}_{cv}(i) \tag{2.6.3}$$

$$\widehat{g}_v(i,j) = \frac{1}{r_{ij}} \tag{2.6.4}$$

The two operators above are only distinguished from standard Hamiltonian operators by the core-valence operator term, $\widehat{V}_{cv}$. If $\widehat{V}_{ccp}$ and V_{cc} from equation 2.6.1 are neglected temporarily it may be assumed that all relativistic effects may be modelled through the parameterization of $\widehat{V}_{cv}$. The use of a ECP assumes that the non-relativistic kinetic and coulomb operators suffice in describing the electrons well enough in the positions around the atom unaffected by relativistic effects.

While accounting for relativistic effects $\widehat{V}_{cv}$ must describe all interactions of valence electrons with the nucleus and the replaced core electrons while taking various core-valence orthogonality constraints into account. The common way to formalize $\widehat{V}_{cv}$ is:

$$\widehat{V}_{cv}(i) = \frac{Q}{r_{ij}} + \Delta\widehat{V}_{cv}(i) \tag{2.6.5}$$

The $\widehat{V}_{cv}$ operator essentially describes an adjustment to the potential the ith electron experiences from the core (Q/r_i) through an adjusted valence core potential ($\Delta\widehat{V}_{cv}(i)$) with respect to the ith electrons position. While simulating a molecule it is assumed $\widehat{V}_{cv}$ is a superposition of N atomic contributions:

$$\widehat{V}_{cv}(i) = \sum_{\lambda}^{N} \left[\frac{Q_\lambda}{r_{\lambda i}} + \Delta\widehat{V}_{cc}^{\lambda\mu}(i) \right] \tag{2.6.6}$$

The correlations used ($\Delta\widehat{V}_{cc}^{\lambda\mu}$) represents the repulsion between mutually penetrating cores which depend on electrostatic contributions, orthogonality constraints and the pauli-repulsion between electron shells localized on different cores. The correlations ($\Delta\widehat{V}_{cc}^{\lambda\mu}$) for these effects only come into effect for large cores, and the correlations have only been derived for a number of ECPs.

The CPP operator ($\widehat{V}_{ccp}$) depends on the electric field experienced ($\overrightarrow{f}_\lambda$) at the core λ by all valence electrons ,i, and all other nuclei/cores, μ, and may be expressed as follows:

$$\overrightarrow{f}_\lambda = -\sum_{i} \frac{\overrightarrow{r}_{i\lambda}}{r_{i\lambda}^3} + \sum_{\mu\neq\lambda} \frac{\overrightarrow{r}_{\mu\lambda}}{r_{\mu\lambda}^3} \tag{2.6.7}$$

The dipole moment, $\overrightarrow{u}_\lambda$ of a polarizable core λ under the influence of an electric field experienced ($\overrightarrow{f}_\lambda$) is given as follows

$$\overrightarrow{u}_\lambda = a_\lambda \overrightarrow{f}_\lambda \tag{2.6.8}$$

where a_λ states the dipole polarizability of the core λ. The interaction of an external field with the induced dipoles results in this expression for the CCP:

$$\widehat{V}_{ccp} = -\frac{1}{2}\sum_{\lambda} \overrightarrow{u} \cdot \overrightarrow{f}_\lambda = -\frac{1}{2}\sum_{\lambda} a_\lambda \overrightarrow{f}_\lambda^2 \tag{2.6.9}$$

The degree to which various bodies have an impact on the electric field has been parameterized through employing cutoff points for interactions and various other approximations summarized in a comprehensive review.[82]

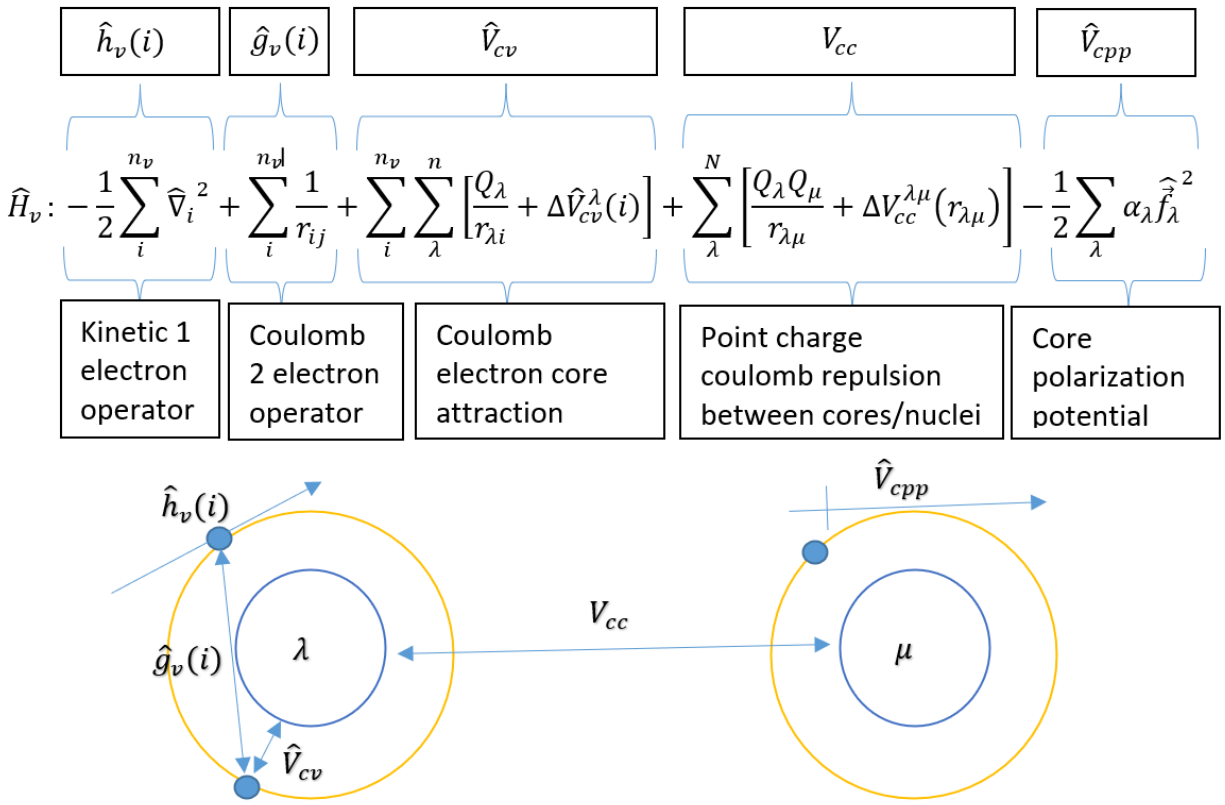


Figure 2.8: Diagrammatic representation of effective core potential components alongside the ECP equation

The above equation highlights different effects that are accounted for in a pseudopotential model. $\Delta\widehat{V}_{cv}^{\lambda}$ is the potential that is modelled for conventional ECP calculation where various potentials have various analytical forms depending on what considerations are made. The analytical form of pseudopotentials will be elaborated on further. $\Delta\widehat{V}_{cc}^{\lambda\mu}$ is only be parameterized for larger atoms which experience the mutual penetration of cores. $\widehat{V}_{cpp}$ is the polarization potential which accounts for the polarizability.

The development of ECPs depends on finding ever better analytical forms for $\Delta\widehat{V}_{cv}$, C_{cc} and $\widehat{V}_{cpp}$ which are accurate and computationally inexpensive. Under the umbrella of ECPs there are two main branches: model potentials (MPs) and pseudopotentials (PPs). MPs attempt to accurately model All electron Hartree-Fock (HF) potentials for valence electrons hence producing an accurate nodal structure for the valence orbitals. PPs formally transform valence orbitals to pseudovalence orbitals, simplifying the nodal structure. The simplified nodal structure leads to further computational savings in one-electrons basis sets.[82]

The assumption of the superposition of PPs as indicated by the expanded eq. 2.6.1 (shown in figure 2.8) lets one write the semi-local PP ansatz for a core λ as

$$\Delta\widehat{V}_{cv}^{\lambda}(i) \cong \Delta\widehat{V}_{PP}^{\lambda}(i) = \sum_{l=0}^{l=\infty} V_l^{\lambda}(r_{i\lambda})\widehat{P}_l^{\lambda}(i) \tag{2.6.10}$$

Where the angular momentum projection operator ($\widehat{P}_l^{\lambda}(i)$) is based on spherical harmonics with respect to the core λ

$$\widehat{P}_l^{\lambda}(i) = \sum_{m=-1}^{m=l} |lm,\lambda\rangle\langle lm,\lambda| \tag{2.6.11}$$

When $l \geq L$, where usually (L-1) is the largest angular momentum employed by the core orbitals on a core λ, the PPs $V_l^{\lambda}(r_{i\lambda})$ are only minutely different:

$$V_l^{\lambda}(r_{i\lambda}) \cong V_L^{\lambda}(r_{i\lambda}) for l \geq L \tag{2.6.12}$$

It may be assumed that $\mathrm{V}_l^{\lambda}(r_{i\lambda}) = \mathrm{V}_L^{\lambda}(r_{i\lambda})$ for $l \geq L$ and the closure property of the projection operator lets one derive:

$$\Delta\widehat{V}_{PP}^{\lambda}(i) = V_L^{\lambda}(r_{i\lambda}) + \sum_{l=0}^{L-1}[V_l^{\lambda}(r_i\lambda) - V_L^{\lambda}(r_{i\lambda})]\widehat{P}_l^{\lambda}(i) \tag{2.6.13}$$

The $\Delta\widehat{V}_{PP}^{\lambda}(i)$ operator in equation 2.6.13 is referred to as a semi-local PP. $\Delta\widehat{V}_{PP}^{\lambda}(i)$ constitutes of a sum of local potentials acting on angular momentum symmetry $0 \leq l \leq L-1$ of each l up to an angular momentum of L–1 in core λ and angular momentum symmetries $l \geq L$ are acted upon by a local potential $V_L^{\lambda}(r_{i\lambda})$. Essentially different orbitals will be acted upon by different potentials depending on their angular momenta.

The analytical forms derived for PPs up until now have not incorporated relativistic effects. Unlike MPs, PPs do not have the possibility to accurately evaluate relativistic effects via an all electron model reference. The ansatz described up to here suffices for the use of scalar-relativistic PPs fitted to activation energy data. To describe relativistic effects adequately, next to the principle (n) and Azimuthal (l) quantum numbers the total angular momentum of orbitals (j) must be considered. A relativistic semi-local PP with lj dependence is generated.

$$\Delta\widehat{V}_{cv}^{\lambda}(i) \cong \Delta\widehat{V}_{PP}^{\lambda}(i) \sum_{l=0}^{l=\infty} \sum_{j=|l-1/2|}^{j=l+1/2} V_{lj}^{\lambda}(r_{i\lambda}) \widehat{P}_{ij}^{\lambda}(i) \tag{2.6.14}$$

The projection operator $\widehat{P}_{ij}^{\lambda}$ now incorporates an additional total angular momentum, j, dependency with respect to core λ:

$$\widehat{P}_{ij}^{\lambda}(i) = \sum_{m=-j}^{m=j} |ljm,\lambda\rangle\langle ljm,\lambda| \tag{2.6.15}$$

Analogous to the non-relativistic case $\Delta\widehat{V}_{PP}^{\lambda}(i)$ may be approximated as:

$$\Delta\widehat{V}_{PP}^{\lambda}(i) = V_{LJ}^{\lambda} + \sum_{l=0}^{l=L-1} \sum_{j=|l-1/2|}^{j=l+1/2} V_{lj}^{\lambda}(r_{i\lambda}) - V_{LJ}^{\lambda}(r_{i\lambda}) \widehat{P}_{ij}^{\lambda}(i) \tag{2.6.16}$$

Where the Projection operator and the local potentials are given by:

$$\widehat{P}_{l}^{\lambda}(i) = \sum_{j} \widehat{P}_{ij}^{\lambda}(i) = \widehat{P}_{l,|l-1/2|}^{\lambda}(r_{i\lambda}) + \widehat{P}_{l,l+1/2}^{\lambda}(i) \tag{2.6.17}$$

$$V_{l}^{\lambda}(r_{i\lambda}) = \frac{1}{2l+1}[lV_{l,|l-1/2|}^{\lambda}(r_{i\lambda}) + (l+1)V_{l,l+1/2}^{\lambda}(r_{i\lambda})] \tag{2.6.18}$$

In equation 2.6.16 $\Delta\widehat{V}_{PP}^{\lambda}$ may be rewritten as the sum of the spin-free averaged (av) and spin-dependent (so) terms.

$$\Delta\widehat{V}_{PP}^{\lambda}(i) = \Delta\widehat{V}_{PP,av}^{\lambda}(i) + \Delta\widehat{V}_{PP,so}^{\lambda}(i) \tag{2.6.19}$$

Where the so term is given by

$$\Delta\widehat{V}_{PP,so}^{\lambda}(i) = \sum_{l=0}^{L-1} \frac{\Delta V_{l}^{\lambda}(r_{i\lambda})}{2l+1}[l\widehat{P}_{l,l+1/2}^{\lambda}(i) + (l+1)\widehat{P}_{l,l-1/2}^{\lambda}(i)] \tag{2.6.20}$$

In this formulation $\Delta V_{l}^{\lambda}(r_{i\lambda})$ gives the difference between corresponding relativistic PPs.

$$\Delta V_l^{\lambda}(r_{i\lambda}) = V_{l,l+1/2}^{\lambda}(r_{i\lambda}) - V_{l,|l-1/2|}^{\lambda}(r_{i\lambda}) \tag{2.6.21}$$

Without inclusion of SO coupling The $\Delta\widehat{V}_{PP,av}^{\lambda}$ operator is still a scalar-relativistic PP and corresponds to the PP defined by eq. 2.6.13 if the $V_L^{\lambda}(r_{i\lambda})$ and $V_{LJ}^{\lambda}(r_{i\lambda})$ terms are neglected. A simpler and much more commonly used approach to incorporate relativistic effects is to employ a scalar in the $\Delta\widehat{V}_{PP,so}^{\lambda}$ term to generate a scalar relativistic PP based on solutions to HF.

$$\Delta\widehat{V}_{PP,so}^{\lambda}(i) = \sum_{l=0}^{L-1} \frac{2\Delta V_l^{\lambda}(r_{i\lambda})}{2l+1} \widehat{P}_l^{\lambda}(i) \widehat{\overrightarrow{l}}_{\lambda l} \cdot \widehat{\overrightarrow{s}}_l \widehat{P}_l^{\lambda}(i) \tag{2.6.22}$$

The above-mentioned theoretical background should give a good insight into the philosophies flowing into the construction of ECPs. However, the Pseudopotentials as displayed above are not utilized in the Gaussian software suite as they do not facilitate the use of Gaussian basis sets. To be utilized ECPs are expressed as sums of products of polynomial radial functions, Gaussian radial functions, and angular momentum projection operators. In a practical sense each variant of atom will be assigned a ECP input which constitutes of a coefficient, power of R and exponent of every potential acting on different angular momenta expressed as follows:

$$V_m^{\lambda}(r_{i\lambda}) = \sum_k A_{km}^{\lambda} r_{i\lambda}^{n_{km}} e^{-a_{km}^{\lambda} r_{i\lambda}^{r^2}} \tag{2.6.23}$$

$$where$$

$$m = l, L, lj, LJ$$

The potentials are generally expressed in d, f or higher projects as and separate angular momentum operators are used for smaller values of l. For example, in the LP-31-G potentials there are s and p projections expressed in terms of $l \geq 2$ projection. there is a general term for $l \geq 2$, a s-d term for $l = 0$ and a p-d term for $l = 1$.[82]

2.6.2 SMD continuum solvation model

When simulating solvation one can take the approach to explicitly model solvation by introducing explicit solvent molecules around the solute. Alternatively, an implicit solvation model in which an equilibrium average of the dielectric the solute experiences is applied to it. Explicit models are usually more expensive as

the distinct solvent molecules have to be treated at the same level of theory as the solute while the implicit model is more computationally effective but implicit solvation gives less insight into the nuanced chemical interaction between solute and solvent.[83]

Computing the solvation energy using the implicit solvation model SMD[83] requires the description of the related forces which play a role in solvation. The compounding factors to the solvation energy can be summed up as follows:

$$\Delta G_S^o = \Delta G_{ENP} + \Delta G_{CDS} \tag{2.6.24}$$

Here ENP term represents electronic, nuclear and polarization components of the free energy. the nuclear term accounts for differences in the structure between the gas and liquid phase minimum energy structures. In the case that the structures are analogous the term is shortened to EP. CDS stands for cavitation, changes in dispersion and changes to the local solvent structure.

The solutions to ΔG_{EP} are derived by solving a self-consistent reaction field (SCRF) calculation. To solve the SCRF one must solve or approximate the Poisson equation, which is a generalization of the Laplace equation. The Poisson equation is solved as an elliptical partial differential equation. The equation can be solved to attain the potential field caused by a given electrical charge. The Poisson equation establishes a relationship between the relative permittivity, ε of a solvent and the solutes free charge density ρ_f as follows:

$$\varepsilon \nabla^2 \Phi = -4\pi\rho_f \tag{2.6.25}$$

which can be reformulated to the nonhomogeneous Poisson equation (NPE):

$$\nabla \cdot (\varepsilon \nabla \Phi) = -4\pi\rho_f \tag{2.6.26}$$

The quantum mechanical description of the solute coupled with the NPE can be solved to obtain the electric potential which arises due to the polarization of the solute and the dielectric continuum. The computed potential known as the reaction field, ϕ, is equal to the difference between the total potential, Φ, and the electrostatic potential $\Phi^{(0)}$ of the solute in the gas phase. If the solute is assumed to be rigid with respect to the phase change the Gibbs free energy of solvation is computed.

$$\Delta G_{EP} = \left\langle \Psi \left| H^{(0)} - \frac{e}{2}\psi \right| (\Psi \right\rangle + \frac{e}{2}\sum_{k} Z_k \psi_k - \left\langle \Psi^{(0)} \left| H^{(0)} \right| \Psi^{(0)} \right\rangle \tag{2.6.27}$$

Here e is the atomic unit of charge, ψ_k and Z_k are the reaction field and atomic number of atom k, $H^{(0)}$ and $\Psi^{(0)}$ are the solute electronic Hamiltonian and wave function in the gas phase. Ψ is the polarized solute electronic wave function in solution.

The main challenge when undertaking computations including implicit solvation is defining the boundary between solute and solvent continuum. When treating individual atoms, the math is simpler as spherical cavity is generated but for molecules the boundary of the solute cavity is defined through encapsulating the superposition of nuclear cantered spheres each defined with a radius ρ_k. These radii are known as intrinsic coulomb radii and are determined by the atomic numbers of each species in a system. The boundary which is defined through these radii is known as the solvent accessible surface (SAS). The so-called boundary element method is utilized for the solution of equation 2.6.26. The discrete expression of the cavity allows for the reaction field to be approximated at an arbitrary position r in the cavity by the following formulation:

$$\phi(r) = \sum_{m} \frac{q_m}{|r - r_m|} \tag{2.6.28}$$

Here r_m is the localization of a tesserae, m, on the surface area on the SAS. q_m is the surface charge localised at tesserae, m. These tesserae are products of tessellating the SAS via algorithms like GEPOL and their evolutions which have been implemented in common Quantum software suites.

The cavity-dispersion-solvent-structure free energy contribution to solvation, G_{CDS}, is given by the following equation:

$$G_{CDS} = \sum_{k}^{atoms} \sigma_k A_k(R, \{R_{Z_k} + r_s\}) + \sigma^{[}M] \sum_{k}^{atoms} A_k(R, \{R_{Z_k} + r_s\}) \tag{2.6.29}$$

Here σ_k and $\sigma^{[}M]$ represent surface tension of the atom k and the molecular surface tension, respectively. The solvent-accessible surface area (SASA) of atom k is represented by A_k. SASA depends on the geometry R were $\{R_{Z_k}\}$ is a set of all atomic VdW radii as well as the solvent radius, r_s. Bondi radii are used as values for the VdW radii and the solvent radius is defined as r_s=0.4 $\AA$ in the SMD model.

Atomic surface tensions are represented by:

$$\sigma_k = \tilde{\sigma}_{Z_k} + \sum_{k'}^{atoms} \tilde{\sigma}_{Z_k Z_{k'}} T_k(\{Z_{k'}, R_{kk'}\}) \tag{2.6.30}$$

here $\tilde{\sigma}_Z$ is a parameter specific to atomic numbers and $\tilde{\sigma}_{ZZ'}$ depends on both the atomic numbers of k and k'. $T_k(\{Z_{k'}, R_{kk'}\})$ is a geometry dependent function known at cutoff tanh.

The atomic surface tensions in the SMD model depend on the solvent through the parameters $\tilde{\sigma}_Z$ and $\tilde{\sigma}_{ZZ'}$. These parameters are functions of a set of solvent descriptors which are given by:

$$\tilde{\sigma}_i = \tilde{\sigma}_i^{[n]} n + \tilde{\sigma}_i^{[\alpha]} \alpha + \tilde{\sigma}_i^{[\beta]} \beta \tag{2.6.31}$$

Here $\tilde{\sigma}_i$ is either $\tilde{\sigma}_Z$ or $\tilde{\sigma}_{ZZ'}$, n is the room temperature refractive index, α is the Abraham's hydrogen bond acidity parameter and β is the Abraham's hydrogen bond basicity parameter. The empirical parameters $\tilde{\sigma}_i^{[n]}$, $\tilde{\sigma}_i^{[\alpha]}$ and $\tilde{\sigma}_i^{[\beta]}$ depend on i. Furthermore, the product of the molecular surface tension and the total SASA is computed in SMD. the molecular surface tension used is given by a series of solvent descriptors as follows:

$$\sigma^{[M]} = \tilde{\sigma}^{[\gamma]}(\gamma/\gamma_0) + \tilde{\sigma}^{[\phi^2]}\phi^2 + \tilde{\sigma}^{[\psi^2]}\psi^2 + \tilde{\sigma}^{[\beta^2]}\beta^2 \tag{2.6.32}$$

Here γ is the solvents macroscopic surface tension at the solvent/air interface at STP expressed in units cal mol^{-1} $\mathring{A}^{-2}$. ψ^2 represents the square fraction of solvent atoms which are either Fluorine, Chlorine or Bromine (electronegative halogens). β^2 is the square of the Abraham's hydrogen bond basicity parameter of the solvent. $\tilde{\sigma}^{[\gamma]}$, $\tilde{\sigma}^{[\phi^2]}$, $\tilde{\sigma}^{[\psi^2]}$ and $\tilde{\sigma}^{[\beta^2]}$ are parameters empirically derived independently for each solvent.

So long someone has the macroscopic descriptors of the solvent including the dielectric constant, ε, the refraction index at 298k, n^2, the Abraham's hydrogen bond acidity parameter, α, the Abraham's hydrogen bond basicity parameter, β, the macroscopic surface tension, λ, the fraction of non-hydrogenic solvent atoms, Φ and the fraction of non-hydrogenic solvent atoms which are halogens F, Cl or Br, Ψ one can employ the SMD continuum model readily.[83]

2.7 Theory of analytical tools

The next section focuses on the theory used to conduct various analyses on the optimized structures.

2.7.1 Net atomic charge determination methods

There are a variety of ways in which net atomic charges (NAC), also commonly known as partial charges, can be assigned to atoms in a molecule. The challenge in assigning the correct NAC to each atom is a highly contentious topic in chemistry as there is not a single rigorous way in which it can be executed. The contention arises due to the arbitrary cutoff points between species. The Mulliken Population analysis was the first widely used partial charge assignment model but has become outdated, but it is instructive to look at the underlying theory. Natural population analysis (NPA), CHarges from Electrostatic Potentials using a Grid based method (CHELPG) and Atomic dipole corrected Hirshfield charges (ADCH) are all subsequently developed schemes which rely on different approaches to determine the NACs in a system.[6]

Mulliken population analysis

The Mulliken population analysis[84] provides a method by which approximate NACs in molecular structures can be calculated. The density matrix terms can be expressed as

$$D_{\mu v} = 2 \sum_{i} C_{\mu i} C_{vi}^{*} \tag{2.7.1}$$

where of $C_{\mu i}$ is the coefficient of the μth basis function in the ith molecular orbital. The Population matrix in a closed shell system which is in turn defined by the density matrix as follows:

$$P_{\mu v} = D_{\mu v} S_{\mu v} \tag{2.7.2}$$

Where S is the overlap matrix of the basis functions. The gross orbital product of orbital v, GOP_v is given by the sum of all $P_{v\mu}$ terms over μ. N gives the sum of all GOPs and is the number of electrons in the system. An electric charge is assigned to each atom called the gross atom population, GAP_A for atom A, as a sum of GOP_v over all the orbitals v associated with atom A. The difference between the GAP and the atomic number of an atom results in the NAC, Q_A.

$$Q_A = Z_A - GAP_A \tag{2.7.3}$$

Natural population analysis

Natural Population analysis (NPA)[85] refers to a group of algorithms which helps analyse electronic wave functions. In simplistic terms the algorithm gives insight into electronic structures by transforming them into groups of localized Lewis-like chemical bonds. These groups can be interpreted as basis set which favours chemical intuition by differentiating between Lewis-type and non-Lewis-type natural bonding orbital (NBO) representations. Mathematically NBO theory leads back to the theory of natural orbitals developed by Loewdin.[86]

To construct natural atomic orbitals (NAOs) and subsequently NBOs a number of steps have to be taken. Initially the set of orbitals $\{\phi_i\}$ originating at each atomic centre is subdivided into minimal $\{\phi_{im}\}$ and Rydberg $\{\phi_{ir}\}$ orbital sets. Here the minimal set of orbitals refers to all atomic orbitals of non-zero occupancy while the Rydberg set encompasses all formally unoccupied orbitals. A occupancy weighted symmetric orthogonalization $(\widehat{W})$ is carried out on all the minimal functions $\{\phi_{im}\}$ while the set of Rydberg orbitals $\{\phi_{ir}\}$ are Schmidt orthogonalized $(\widehat{S})$ to the same manifold as the minimal functions. lastly another occupancy weighted symmetric orthogonalization $(\widehat{W})$ is carried out on the Rydberg set. This produces the NAOs after finally computing the eigenfunctions using the transformed bases obtained by the WSW transformation. The occupancy of the Rydberg orbitals associated with a particular atom is that atoms NACs. More details of the occupancy weighted transformations can be found in the original paper.[85] One of the main issues with employing NPAs to assign NACs is that some of the orbitals can overlap which results in skewed charge distributions.

Atomic dipole corrected Hirshfield charges

The ADCH[87] charge distribution method is based on the Hirschfeld method[88] which partitions the electron density in a system based on atomic densities through a weighting function. The weighting function, $\mathrm{w}_A(\vec{r})$, is a scalar weighted function based on the ratio of atomic density of the isolated atom in a ground state, (ρ_A^0), to the sum of all atomic densities in a system in their ground states, $\sum_A \rho_A^0(\vec{r}_A$ as given in eq. 2.7.4.

$$w_A(\vec{r}) = \frac{\rho_A^0(\vec{r}_A)}{\sum_A \rho_A^0(\vec{r}_A)} \tag{2.7.4}$$

The weighting function acts upon the deformation density which is the difference between the electron density in the system around a given atom and the electron density of the isolated atom in its ground state as given in equation 2.7.5.

$$\Delta\rho(\vec{r}) = \rho(\vec{r}) - \sum_{A} \rho_A^0(\vec{r}_A) \tag{2.7.5}$$

The deformation density of the system is then partitioned according to the weighting function and integrated over all space which determines the number of electrons situated on each atom.

$$q_A = -\int w_A(\vec{r})\Delta\rho(\vec{r})d\vec{r} \tag{2.7.6}$$

The charge q_A can then be subtracted from the atomic number, Z_A to determine the partial charge. Hirschfeld charges are efficient to use and unlike Mulliken and Loewdin charges they are independent of the basis set. The input of the deformation density can be acquired outside of QM calculations through x-ray crystallography. However, Hirschfeld charges are commonly too low in magnitude and describe observable properties like electrostatic potential (ESP) poorly.

The ADCH charge scheme rectifies the issue of low charge magnitude by generating atomic dipole moments from a weighted function w_A. The atomic dipole moments can be defined on the deformation density as follows:

$$\vec{\mu}_A = -\int w_A\Delta\rho(\vec{r}) \cdot (\vec{r} - \vec{r}_A)d\vec{r} \tag{2.7.7}$$

Through which the overall dipole can be defined as:

$$\vec{\mu}^{Hirshfield} = \sum_{A} \vec{\mu}_A + \sum_{A} q_A\vec{r}_A \tag{2.7.8}$$

where q_A is the Hirshfield charge. The dipole moment is hence defined by contributions from the atomic dipole and the Hirshfeld charges. The problem arises when the sum of the dipole moments of the individual atoms is 0, implying the molecular dipole moment is not described correctly. In consequence Lu and Chen altered the description of the dipole moment to account for the polarization which occurs between two point charge, A and B.[87]

$$\vec{\mu}^{ADCH} = \sum_{A}(q_A^{Hirshfield} + \sum_{A\neq B} \Delta q_{AB})\vec{r}_A \tag{2.7.9}$$

The ADCH scheme introduces charges, Δq_{AB}, to correct the molecular dipole moment. The correction charges must fulfil two conditions; the total charge surrounding j is consistent and the atomic dipole moment of A is a linearly expanded combination of all contributing atoms.

Net atomic charges via ChelpG

Charges from electrostatic potentials using a grid based method (ChelpG)[89] is a scheme used to calculate the MEP through fitting atomic charges at a number of points around a species on a grid. Initially the points on the grid are selected with a spacing of 3.0 pm apart and distributed regularly in a cube. The species is located at the centre of said cube with 28.0 pm head space in all directions. The grid points of the species within the VdW radii of the constituent atoms are discarded as fitting points. The MEP is evaluated at all the remaining grid points and this MEP is used to derive the atomic charges to generate this MEP.

ChelpG is computed by minimizing a deviation function (eq. 2.7.10) to calculate the atomic charges, V_q.

$$F(q_1, q_2 \dots q_N) = \sum_i [V_q(r_i) - V(r_i)]^2 \tag{2.7.10}$$

r_i are the coordinates of the fitting points i, $\{q\}$ is a set of fitted point charges called fitting centres. The fitting is executed by formulating a matrix as shown in 2.7.11.

$$\begin{bmatrix} A_{11} & A_{12} & \cdots & A_{1N} & 1 \\ A_{21} & A_{22} & \cdots & A_{2N} & 1 \\ \vdots & \vdots & \ddots & \vdots & 1 \\ A_{N1} & A_{N2} & \cdots & A_{NN} & 1 \\ 1 & 1 & 1 & 1 & 0 \end{bmatrix} \begin{bmatrix} q_1 \\ q_2 \\ \vdots \\ q_N \\ \lambda \end{bmatrix} = \begin{bmatrix} B_1 \\ B_2 \\ \vdots \\ B_N \\ q_{tot} \end{bmatrix} \tag{2.7.11}$$

where

$$A_{A,B} = \sum_i \frac{1}{r_{iA} r_{iB}} \tag{2.7.12}$$

$$B_A = \sum_i \frac{V(r_i)}{r_{iA}} \tag{2.7.13}$$

$$q_{tot} = \sum_A q_A \tag{2.7.14}$$

N is the total number of fitting centres and A, and B are the indices over which they run. The N values of q must be determined which correspond to the charges of the fitting centres. q is computed as $q=A^{-1}B$.

2.7.2 Molecular electrostatic potential

At a particular point $p(r)$ the molecular electrostatic potential (MEP) in the surrounding of a molecule is expressed as the force acting upon a positive dummy charge located at the point of interest. The charge experienced at this point is a consequence of the constituent atoms and the geometric arrangement of a molecule. The MEP gives insight into geometric regions of a molecule which are more prone to reacting or interacting with different species i.e. a more positive region which may be adjacent to a hydrogen is more prone to interact with a negative species while a more negative region which may be adjacent to a halide would prefer to interact with a positive species. An MEP will give quantitative insight into the favourability of a point on a molecule for a chemical reaction or attraction to another point on another molecules structure. MEPs are typically colour mapped atop a chemical structure at arbitrary distances but a commonly utilized one is the VdW radii. The computation of the MEP at different points is analogous to that described for the ChelpG scheme but does not associate the charges with particular atoms but instead visualizes the electrostatic potential determined at each fitting centre.[89]

2.7.3 Fukui functions

The Fukui function[90], also named the frontier function, represents the electron density of a frontier orbital. A frontier orbital is either the highest occupied or the lowest unoccupied molecular orbital, i.e. the HOMO and the LUMO. Condensed Fukui functions reveal the electron density of frontier orbitals but apply the difference in electron density to individual atoms in a structure. Fukui functions reveals the most electrophilic and nucleophilic sites on a species structure.

The formalism of the Fukui function evaluates a difference in electron density with respect to changing N electrons as stated in 2.7.15.

$$f(r) = \frac{\delta\rho(r)}{\delta N_{electron}} \tag{2.7.15}$$

The Fukui function is commonly only applied to the loss or gain of a single electron. The positive Fukui function (f_+) represents the difference in electron density when an electron is gained (equation 2.7.16) and

the negative Fukui function (f_) represents the difference in electron density when a electron is lost (equation 2.7.17).

$$f_+(r) = \rho_{N+1}(r) - \rho_N(r) \tag{2.7.16}$$

$$f_-(r) = \rho_N(r) - \rho_{N-1}(r) \tag{2.7.17}$$

2.7.4 Atoms in molecules

The quantum theory of atoms in molecules (QTAIM)[3], commonly referred to as atoms in molecules (AIM) is a technique based on evaluating the topology of the electron density, $\rho(r)$, of a system. In the topological model nuclei function as point attractors which are engulfed in a cloud of electron density, $\rho(r)$. The electron density is a measurable property which describes how charge is spread out through three-dimensional space. When modelling molecules based on electron density, atoms are described as maxima of electron density at the locations of the nuclei which decays away exponentially.

The electron density can be analysed by tracing trajectories of gradient vectors of the density. Starting from a random point, the gradient of $\rho(r)$ can be determined and the input vector is used to point towards the maximum increase in $\rho(r)$. A minuscule step is taken in the direction the vector points in, and the gradient is subsequently calculated again and the processes is repeated. The repletion of this process allows for the trajectory of $\nabla\rho(r)$. A compilation of trajectories starting at different points allows for the generation of an electron density gradient vector map. All the trajectories terminate at nuclear centres as they are attractors to the electron density represented by the gradient vector field. The vectors derived from $\rho(r)$ partition the space around and within the molecule into basins. In the context of AIM basins are defined as a locality in space passed through by the vectors ending at a given nucleus. QTAIM can be applied to molecular systems to generate a space of point attractors and basins and an atom can be defined as the concerto of a localized attractor and their basins within that system.

A set of unique trajectories exists which include a point where $\nabla\rho(r) = 0$. The point where $\nabla\rho(r) = 0$ is called a critical point in QTAIM and these points characterize four different features of molecular system; nuclear positions, covalent bonds, ring centres, as found in a benzene ring, and cage centres, as found in fullerenes. The type of critical point encountered is mathematically defined by the Hessian of $\rho(r)$ a function of the position, r = (x,y,z), of the critical point. The Hessian $H(\rho, r)$ can be diagonalized which leads to three possible eigenvalues; λ_1, λ_2 and λ_3. The sum of the eigenvalues is the Laplacian of the electron density, $\nabla^2\rho(r)$. The classification of the critical points depends on

$$S = \sum_{i}^{3} \lambda_i / |\lambda_i| \tag{2.7.18}$$

which is a measurement of definiteness of the Hessian, $H(\rho, r)$, and gives these four possible results:

$S = -3$ indicates a local maximum at a nuclear position

$S = -1$ indicates a saddle point representative of a bond

$S = 1$ indicates a saddle point representative of a ring centre

$S = 3$ indicates a local minimum representative located at the centre of a cage

The definiteness expresses in how many spatial directions the gradients sign is consistent or inconsistent. At S(r) = -3 the change in electron density in all directions is negative while at S(r) = -1 there is a decay in two spatial directions and an increase in density in one etc. Furthermore the critical points at S = -1 can be further classified with respect to the Laplacian in covalent interactions if $\nabla^2\rho(r)) < 0$ and ionic and weak (closed-shell) interactions when $\nabla^2\rho(r) > 0$. The QTAIM can hence give insights into the chemical interactions in molecules and between them. These insights can be used to understand how individual functional groups behave in different chemical environments and what kind of interaction profiles chemicals have and why they are energetically preferable.

2.7.5 Non-covalent interaction plot

The Non-covalent interaction plot (NCIplot)[91] is a tool to visualize inter and intra molecular interactions through processing the reduced-density gradient (RDG) of a system. The RDG represents the gradient of electron density in a dimensionless form.

$$RDG(r) = \frac{1}{1(3\pi^2)^{1/3}} \frac{|\nabla\rho(r)|}{[\rho(r)]^{4/3}} \tag{2.7.19}$$

The NCIplot is evaluates points where the RDG(r)=0, but not due to $\nabla\rho(r) = 0$, which would be an AIM critical point. RDG(r)=0 occurs when

$$\frac{\nabla^2\rho(r)}{\rho(r)} = \frac{4}{3} \frac{(\nabla\rho(r))^2}{\rho^2(r)} \tag{2.7.20}$$

equation 2.7.20 requires the Laplacian to be positive and hence all the described interactions to be closed-shell. The points in space for which equation 2.7.20 displays minute variations in electron density while the density itself is very low are important. Local non-covalent interactions (NCIs) are attributed with the characteristics of low electron density and low variability in electron density. Additionally, the annihilation of opposite phase exponentials (weak repulsive forces) can be described through this.

When undertaking the computation of RDG(r) the vast number of points are omitted when generating iso-surfaces. Instead, the computations of iso-surfaces occur around RDG(r)=0 and are expanded spatially to go beyond the critical points themselves. This provides interaction surfaces which reflect the delocalization of NCIs better.

To visualize NCI properly one must consider both the RDG(r) and the $\rho(r)$. Typically, the values of RDG(r)=0.3-0.5 represent NCIs of interest but these can also show some weak covalent bonds or AIM critical points. To show NCIs exclusively a cutoff of the $\rho(r)$ is used as bonds and other non-NCI regions are ignored. A 2D representation with RDG(r) on the Y-axis and $\rho(r)$ on the X-axis is used to define ideal cutoff points of $\rho(r)$ in different systems.

NCIs can be qualitatively evaluated using NCIplot. The product density and the sign of the second eigenvalue of the Hessian can be plotted against RDG(r). The value plotted against RDG(r) is conventionally coined $sign(\lambda_2)\rho(r)$. $sign(\lambda_2)\rho(r)$ function can designate different NCIs into strong NCIs (H-bonds)$[sign(\lambda_2)\rho(r) > 0]$, weak NCIs (VdW forces)$[sign(\lambda_2)\rho(r) \cong 0]$ and steric repulsion$[sign(\lambda_2)\rho(r) < 0]$.

According to these classifications 2D and 3D representations are colour coded as follows:

Blue : strong NCIs (H-bonds)$[sign(\lambda_2)\rho(r) > 0]$
Green : weak NCIs (VdW forces)$[sign(\lambda_2)\rho(r) \cong 0]$
Red : steric repulsion$[sign(\lambda_2)\rho(r) < 0]$

which is illustrated in an example showing interactions between RNA base pairs:

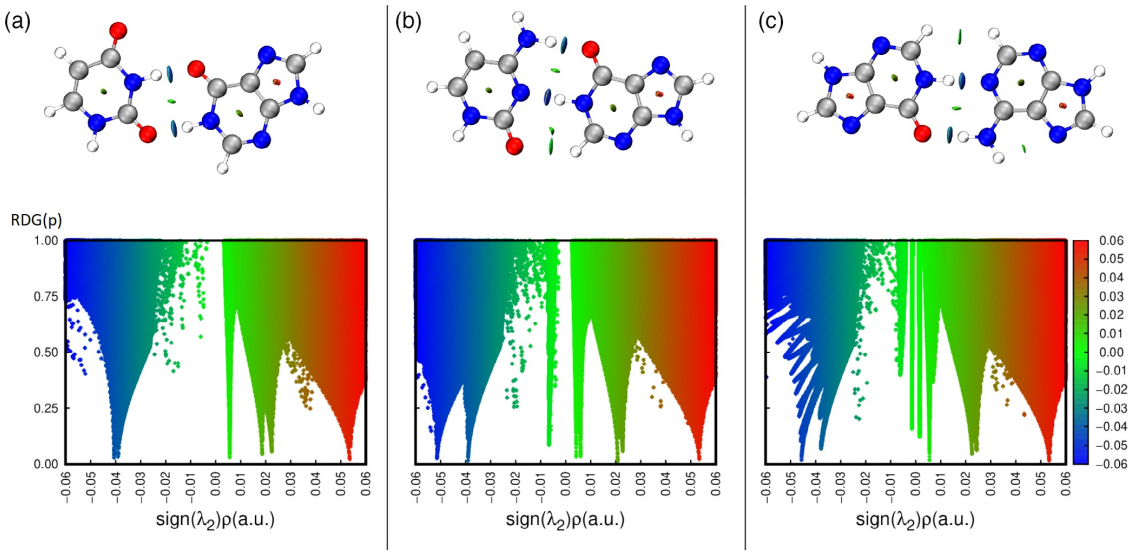


Figure 2.9: 3 RNA Base Pairs showing various NCIs represented in 3D and 2D

The visual aid in understanding what is occurring in a system clarifies nuanced NCIs which cannot be determined by just looking at ion pair structures. Additionally, NCI plot has been developed based on DFT and has been proved to provide reliable information as long as a basis set of good quality is used; double zeta with diffuse functions or a triple zeta basis sets are recommended.

2.7.6 Interaction region indicator

The interaction region indicator (IRI)[5] is a real space function which was developed trying to circumvent the shortcoming of RDG analyses, namely being focused on weak interactions without being able to visualize chemical bonding. IRI has a simpler mathematical definition than RDG and in consequence has a low computational cost than density overlap region indicator (DORI), which was developed with the same application in mind. A specialized version of IRI called $IRI - \pi$ has also been developed to study π-interactions.

IRI is defined as follows:

$$\frac{|\nabla\rho(r)|}{[\rho(r)]^{1.1}} \tag{2.7.21}$$

IRI represents a scaled electron density weighted gradient norm of the electron density. IRI only differentiates itself from RDG through the pre-factor and the power to 1.1. It is projected analogously to the RDG(r)

in NCIPlot using the $sign(\lambda_2)\rho(r)$ function to map an isosurface and show different types of interactions elucidated by IRI via 3D projections.

2.7.7 Computing XPS spectra from optimized structures

A Mulliken population analysis can be used to determine the contribution of each atomic orbital or basis function of constituent MOs of a species. The coefficients of the atomic orbital contributions to the density matrix, $C_{\mu i}$ (eq. 2.7.1) are multiplied by AO cross-sections. The values of the AO photoionization cross-section ($\sigma_{n,l}(E)$) are given by equation 2.7.22.

$$\sigma_{n,l}(E) = \frac{4}{3}\pi^2 a_0^2 \alpha [N_{n,l}[E - E_{n,l}]\frac{1}{2l+1}][lR^2_{E,l-1} + (l+1)R^2_{E,l+1}] \tag{2.7.22}$$

where n,l are the particle and angular momentum quantum numbers, a_0 is the Bohr radius, α is the fine structure constant, $N_{n,l}$ represents the number of electrons in a particular subshell, $E_{n,l}$ is the energy of the nl electrons, E is the kinetic energy of the electron which is ejected, and $R_{E,l\pm1}$ is the radial dipole matrix. A database of AO cross-sections is accessed for the multiplication procedure.

A Gaussian-Lorentzian function is centred at a MO energy. The area of the function is equal to the intensity derived by multiplying the coefficients of each AOs contribution to the MO via the cross-section computation with respect to the contributing AOs and a photon energy.

The technique can be used to separate different contributions from different chemical environments. The contributions from different chemical environments can be summed to give a complete XPS output for a chemical species or a composition of different species.[7]

Bibliography

[1] Christopher J Cramer. *Essentials of computational chemistry: theories and models*. John Wiley & Sons, 2013.

[2] A Szabo and NS Ostland. Modern quantum mechanics: Introduction to advanced electronic structure theory. *McGrew-Hill Publication Company*, 1982.

[3] Richard FW Bader. Atoms in molecules. *Accounts of Chemical Research*, 18(1):9–15, 1985.

[4] Julia Contreras-García, Erin R Johnson, Shahar Keinan, Robin Chaudret, Jean-Philip Piquemal, David N Beratan, and Weitao Yang. Nciplot: a program for plotting noncovalent interaction regions. *Journal of chemical theory and computation*, 7(3):625–632, 2011.

[5] Tian Lu and Qinxue Chen. Interaction region indicator: A simple real space function clearly revealing both chemical bonds and weak interactions. *Chemistry-Methods*, 1(5):231–239, 2021.

[6] Tian LU and Fei-Wu CHEN. Comparison of computational methods for atomic charges. *Acta Physico-Chimica Sinica*, 28(1):1–18, 2012.

[7] Jake M Seymour, Ekaterina Gousseva, Alexander I Large, Coby J Clarke, Peter Licence, Richard M Fogarty, David A Duncan, Pilar Ferrer, Federica Venturini, Roger A Bennett, et al. Experimental measurement and prediction of ionic liquid ionisation energies. *Physical Chemistry Chemical Physics*, 23(37):20957–20973, 2021.

[8] Narbe Mardirossian and Martin Head-Gordon. Thirty years of density functional theory in computational chemistry: an overview and extensive assessment of 200 density functionals. *Molecular Physics*, 115(19):2315–2372, 2017.

[9] John P. Perdew and Yue Wang. Accurate and simple analytic representation of the electron-gas correlation energy. *Phys. Rev. B*, 45:13244–13249, Jun 1992. doi: 10.1103/PhysRevB.45.13244. URL `https://link.aps.org/doi/10.1103/PhysRevB.45.13244`.

[10] John P Perdew and Alex Zunger. Self-interaction correction to density-functional approximations for many-electron systems. *Physical Review B*, 23(10):5048, 1981.

[11] Seymour H Vosko, Leslie Wilk, and Marwan Nusair. Accurate spin-dependent electron liquid correlation energies for local spin density calculations: a critical analysis. *Canadian Journal of physics*, 58(8):1200–1211, 1980.

[12] John P. Perdew. Density-functional approximation for the correlation energy of the inhomogeneous electron gas. *Phys. Rev. B*, 33:8822–8824, Jun 1986. doi: 10.1103/PhysRevB.33.8822. URL https://link.aps.org/doi/10.1103/PhysRevB.33.8822.

[13] John P Perdew, Kieron Burke, and Matthias Ernzerhof. Generalized gradient approximation made simple. *Physical review letters*, 77(18):3865, 1996.

[14] Axel D Becke. Density-functional thermochemistry. v. systematic optimization of exchange-correlation functionals. *The Journal of chemical physics*, 107(20):8554–8560, 1997.

[15] A. D. Becke. Density-functional exchange-energy approximation with correct asymptotic behavior. *Phys. Rev. A*, 38:3098–3100, Sep 1988. doi: 10.1103/PhysRevA.38.3098. URL https://link.aps.org/doi/10.1103/PhysRevA.38.3098.

[16] John P. Perdew, J. A. Chevary, S. H. Vosko, Koblar A. Jackson, Mark R. Pederson, D. J. Singh, and Carlos Fiolhais. Atoms, molecules, solids, and surfaces: Applications of the generalized gradient approximation for exchange and correlation. *Phys. Rev. B*, 46:6671–6687, Sep 1992. doi: 10.1103/PhysRevB.46.6671. URL https://link.aps.org/doi/10.1103/PhysRevB.46.6671.

[17] Yingkai Zhang and Weitao Yang. Comment on "generalized gradient approximation made simple". *Phys. Rev. Lett.*, 80:890–890, Jan 1998. doi: 10.1103/PhysRevLett.80.890. URL https://link.aps.org/doi/10.1103/PhysRevLett.80.890.

[18] B. Hammer, L. B. Hansen, and J. K. Nørskov. Improved adsorption energetics within density-functional theory using revised perdew-burke-ernzerhof functionals. *Phys. Rev. B*, 59:7413–7421, Mar 1999. doi: 10.1103/PhysRevB.59.7413. URL https://link.aps.org/doi/10.1103/PhysRevB.59.7413.

[19] John P. Perdew, Adrienn Ruzsinszky, Gábor I. Csonka, Oleg A. Vydrov, Gustavo E. Scuseria, Lucian A. Constantin, Xiaolan Zhou, and Kieron Burke. Restoring the density-gradient expansion for exchange in solids and surfaces. *Phys. Rev. Lett.*, 100:136406, Apr 2008. doi: 10.1103/PhysRevLett.100.136406. URL https://link.aps.org/doi/10.1103/PhysRevLett.100.136406.

[20] Chengteh Lee, Weitao Yang, and Robert G. Parr. Development of the colle-salvetti correlation-energy formula into a functional of the electron density. *Phys. Rev. B*, 37:785–789, Jan 1988. doi: 10.1103/PhysRevB.37.785. URL https://link.aps.org/doi/10.1103/PhysRevB.37.785.

[21] Jianmin Tao, John P. Perdew, Viktor N. Staroverov, and Gustavo E. Scuseria. Climbing the density functional ladder: Nonempirical meta–generalized gradient approximation designed for molecules and solids. *Phys. Rev. Lett.*, 91:146401, Sep 2003. doi: 10.1103/PhysRevLett.91.146401. URL https://link.aps.org/doi/10.1103/PhysRevLett.91.146401.

[22] John P. Perdew, Adrienn Ruzsinszky, Gábor I. Csonka, Lucian A. Constantin, and Jianwei Sun. Workhorse semilocal density functional for condensed matter physics and quantum chemistry. *Phys. Rev. Lett.*, 103:026403, Jul 2009. doi: 10.1103/PhysRevLett.103.026403. URL https://link.aps.org/doi/10.1103/PhysRevLett.103.026403.

[23] John P. Perdew, Stefan Kurth, Ale š Zupan, and Peter Blaha. Accurate density functional with correct formal properties: A step beyond the generalized gradient approximation. *Phys. Rev. Lett.*, 82:2544–2547, Mar 1999. doi: 10.1103/PhysRevLett.82.2544. URL https://link.aps.org/doi/10.1103/PhysRevLett.82.2544.

[24] Jianwei Sun, Bing Xiao, and Adrienn Ruzsinszky. Communication: Effect of the orbital-overlap dependence in the meta generalized gradient approximation. *The Journal of Chemical Physics*, 137 (5), 08 2012. ISSN 0021-9606. doi: 10.1063/1.4742312. URL https://doi.org/10.1063/1.4742312. 051101.

[25] Jianwei Sun, Robin Haunschild, Bing Xiao, Ireneusz W. Bulik, Gustavo E. Scuseria, and John P. Perdew. Semilocal and hybrid meta-generalized gradient approximations based on the understanding of the kinetic-energy-density dependence. *The Journal of Chemical Physics*, 138(4), 01 2013. ISSN 0021-9606. doi: 10.1063/1.4789414. URL https://doi.org/10.1063/1.4789414. 044113.

[26] Jianwei Sun, John P. Perdew, and Adrienn Ruzsinszky. Semilocal density functional obeying a strongly tightened bound for exchange. *Proceedings of the National Academy of Sciences*, 112(3):685–689, 2015. doi: 10.1073/pnas.1423145112. URL https://www.pnas.org/doi/abs/10.1073/pnas.1423145112.

[27] Jianwei Sun, Adrienn Ruzsinszky, and John P. Perdew. Strongly constrained and appropriately normed semilocal density functional. *Phys. Rev. Lett.*, 115:036402, Jul 2015. doi: 10.1103/PhysRevLett.115.036402. URL https://link.aps.org/doi/10.1103/PhysRevLett.115.036402.

[28] Lucian A. Constantin, E. Fabiano, and F. Della Sala. Meta-gga exchange-correlation functional with a balanced treatment of nonlocality. *Journal of Chemical Theory and Computation*, 9(5):2256–2263, 2013. doi: 10.1021/ct400148r. URL https://doi.org/10.1021/ct400148r. PMID: 26583719.

[29] Jianmin Tao and Yuxiang Mo. Accurate semilocal density functional for condensed-matter physics and quantum chemistry. *Phys. Rev. Lett.*, 117:073001, Aug 2016. doi: 10.1103/PhysRevLett.117.073001. URL https://link.aps.org/doi/10.1103/PhysRevLett.117.073001.

[30] Yan Zhao and Donald G. Truhlar. A new local density functional for main-group thermochemistry, transition metal bonding, thermochemical kinetics, and noncovalent interactions. *The Journal*

of Chemical Physics, 125(19), 11 2006. ISSN 0021-9606. doi: 10.1063/1.2370993. URL https://doi.org/10.1063/1.2370993. 194101.

[31] Roberto Peverati and Donald G. Truhlar. M11-l: A local density functional that provides improved accuracy for electronic structure calculations in chemistry and physics. *The Journal of Physical Chemistry Letters*, 3(1):117–124, 2012. doi: 10.1021/jz201525m. URL https://doi.org/10.1021/jz201525m.

[32] Roberto Peverati and Donald G. Truhlar. An improved and broadly accurate local approximation to the exchange–correlation density functional: The mn12-l functional for electronic structure calculations in chemistry and physics. *Phys. Chem. Chem. Phys.*, 14:13171–13174, 2012. doi: 10.1039/C2CP42025B. URL http://dx.doi.org/10.1039/C2CP42025B.

[33] Haoyu S. Yu, Xiao He, and Donald G. Truhlar. Mn15-l: A new local exchange-correlation functional for kohn–sham density functional theory with broad accuracy for atoms, molecules, and solids. *Journal of Chemical Theory and Computation*, 12(3):1280–1293, 2016. doi: 10.1021/acs.jctc.5b01082. URL https://doi.org/10.1021/acs.jctc.5b01082. PMID: 26722866.

[34] Troy Van Voorhis and Gustavo E. Scuseria. A novel form for the exchange-correlation energy functional. *The Journal of Chemical Physics*, 109(2):400–410, 07 1998. ISSN 0021-9606. doi: 10.1063/1.476577. URL https://doi.org/10.1063/1.476577.

[35] A. Daniel Boese and Nicholas C. Handy. New exchange-correlation density functionals: The role of the kinetic-energy density. *The Journal of Chemical Physics*, 116(22):9559–9569, 05 2002. ISSN 0021-9606. doi: 10.1063/1.1476309. URL https://doi.org/10.1063/1.1476309.

[36] Lars Goerigk and Stefan Grimme. A general database for main group thermochemistry, kinetics, and noncovalent interactions- assessment of common and reparameterized (meta-) gga density functionals. *Journal of Chemical Theory and Computation*, 6(1):107–126, 2010.

[37] Jess Wellendorff, Keld T. Lundgaard, Karsten W. Jacobsen, and Thomas Bligaard. mBEEF: An accurate semi-local Bayesian error estimation density functional. *The Journal of Chemical Physics*, 140 (14), 04 2014. ISSN 0021-9606. doi: 10.1063/1.4870397. URL https://doi.org/10.1063/1.4870397. 144107.

[38] Axel D. Becke. Density-functional thermochemistry. III. The role of exact exchange. *The Journal of Chemical Physics*, 98(7):5648–5652, 04 1993. ISSN 0021-9606. doi: 10.1063/1.464913. URL https://doi.org/10.1063/1.464913.

[39] Seymour H Vosko, Leslie Wilk, and Marwan Nusair. Accurate spin-dependent electron liquid correlation energies for local spin density calculations: a critical analysis. *Canadian Journal of physics*, 58(8):1200–1211, 1980.

[40] Fred A. Hamprecht, Aron J. Cohen, David J. Tozer, and Nicholas C. Handy. Development and assessment of new exchange-correlation functionals. *The Journal of Chemical Physics*, 109(15):6264–6271, 10 1998. ISSN 0021-9606. doi: 10.1063/1.477267. URL https://doi.org/10.1063/1.477267.

[41] Philip J. Wilson, Thomas J. Bradley, and David J. Tozer. Hybrid exchange-correlation functional determined from thermochemical data and ab initio potentials. *The Journal of Chemical Physics*, 115(20):9233–9242, 11 2001. ISSN 0021-9606. doi: 10.1063/1.1412605. URL https://doi.org/10.1063/1.1412605.

[42] Thomas W. Keal and David J. Tozer. Semiempirical hybrid functional with improved performance in an extensive chemical assessment. *The Journal of Chemical Physics*, 123(12), 09 2005. ISSN 0021-9606. doi: 10.1063/1.2061227. URL https://doi.org/10.1063/1.2061227. 121103.

[43] Roberto Peverati and Donald G. Truhlar. Communication: A global hybrid generalized gradient approximation to the exchange-correlation functional that satisfies the second-order density-gradient constraint and has broad applicability in chemistry. *The Journal of Chemical Physics*, 135(19), 11 2011. ISSN 0021-9606. doi: 10.1063/1.3663871. URL https://doi.org/10.1063/1.3663871. 191102.

[44] Roberto Peverati and Donald G. Truhlar. Communication: A global hybrid generalized gradient approximation to the exchange-correlation functional that satisfies the second-order density-gradient constraint and has broad applicability in chemistry. *The Journal of Chemical Physics*, 135(19), 11 2011. ISSN 0021-9606. doi: 10.1063/1.3663871. URL https://doi.org/10.1063/1.3663871. 191102.

[45] Viktor N. Staroverov, Gustavo E. Scuseria, Jianmin Tao, and John P. Perdew. Comparative assessment of a new nonempirical density functional: Molecules and hydrogen-bonded complexes. *The Journal of Chemical Physics*, 119(23):12129–12137, 12 2003. ISSN 0021-9606. doi: 10.1063/1.1626543. URL https://doi.org/10.1063/1.1626543.

[46] Gábor I. Csonka, John P. Perdew, and Adrienn Ruzsinszky. Global hybrid functionals: A look at the engine under the hood. *Journal of Chemical Theory and Computation*, 6(12):3688–3703, 2010. doi: 10.1021/ct100488v. URL https://doi.org/10.1021/ct100488v.

[47] Jianwei Sun, Robin Haunschild, Bing Xiao, Ireneusz W. Bulik, Gustavo E. Scuseria, and John P. Perdew. Semilocal and hybrid meta-generalized gradient approximations based on the understanding

of the kinetic-energy-density dependence. *The Journal of Chemical Physics*, 138(4), 01 2013. ISSN 0021-9606. doi: 10.1063/1.4789414. URL https://doi.org/10.1063/1.4789414. 044113.

[48] Jianwei Sun, John P. Perdew, and Adrienn Ruzsinszky. Semilocal density functional obeying a strongly tightened bound for exchange. *Proceedings of the National Academy of Sciences*, 112(3):685–689, 2015. doi: 10.1073/pnas.1423145112. URL https://www.pnas.org/doi/abs/10.1073/pnas.1423145112.

[49] Kerwin Hui and Jeng-Da Chai. SCAN-based hybrid and double-hybrid density functionals from models without fitted parameters. *The Journal of Chemical Physics*, 144(4), 01 2016. ISSN 0021-9606. doi: 10.1063/1.4940734. URL https://doi.org/10.1063/1.4940734. 044114.

[50] Yan Zhao and Donald G Truhlar. Hybrid meta density functional theory methods for thermochemistry, thermochemical kinetics, and noncovalent interactions: the mpw1b95 and mpwb1k models and comparative assessments for hydrogen bonding and van der waals interactions. *The Journal of Physical Chemistry A*, 108(33):6908–6918, 2004.

[51] Yan Zhao and Donald G. Truhlar. Design of density functionals that are broadly accurate for thermochemistry, thermochemical kinetics, and nonbonded interactions. *The Journal of Physical Chemistry A*, 109(25):5656–5667, 2005. doi: 10.1021/jp050536c. URL https://doi.org/10.1021/jp050536c. PMID: 16833898.

[52] Yan Zhao, Nathan E. Schultz, and D. G. Truhlar. Exchange-correlation functional with broad accuracy for metallic and nonmetallic compounds, kinetics, and noncovalent interactions. *The Journal of Chemical Physics*, 123(16), 10 2005. ISSN 0021-9606. doi: 10.1063/1.2126975. URL https://doi.org/10.1063/1.2126975. 161103.

[53] Yan Zhao, Nathan E. Schultz, and Donald G. Truhlar. Design of density functionals by combining the method of constraint satisfaction with parametrization for thermochemistry, thermochemical kinetics, and noncovalent interactions. *Journal of Chemical Theory and Computation*, 2(2):364–382, 2006. doi: 10.1021/ct0502763. URL https://doi.org/10.1021/ct0502763. PMID: 26626525.

[54] Yan Zhao and Donald G Truhlar. The m06 suite of density functionals for main group thermochemistry, thermochemical kinetics, noncovalent interactions, excited states, and transition elements: two new functionals and systematic testing of four m06-class functionals and 12 other functionals. *Theoretical chemistry accounts*, 120:215–241, 2008.

[55] Yan Zhao and Donald G Truhlar. Density functional for spectroscopy: no long-range self-interaction error, good performance for rydberg and charge-transfer states, and better performance on average than b3lyp for ground states. *The Journal of Physical Chemistry A*, 110(49):13126–13130, 2006.

[56] Yan Zhao and Donald G. Truhlar. Exploring the limit of accuracy of the global hybrid meta density functional for main-group thermochemistry, kinetics, and noncovalent interactions. *Journal of Chemical Theory and Computation*, 4(11):1849–1868, 2008. doi: 10.1021/ct800246v. URL https://doi.org/10.1021/ct800246v. PMID: 26620329.

[57] S Yu Haoyu, Xiao He, Shaohong L Li, and Donald G Truhlar. Mn15: A kohn–sham global-hybrid exchange–correlation density functional with broad accuracy for multi-reference and single-reference systems and noncovalent interactions. *Chemical science*, 7(8):5032–5051, 2016.

[58] Jeng-Da Chai and Martin Head-Gordon. Systematic optimization of long-range corrected hybrid density functionals. *The Journal of Chemical Physics*, 128(8), 02 2008. ISSN 0021-9606. doi: 10.1063/1.2834918. URL https://doi.org/10.1063/1.2834918. 084106.

[59] Elon Weintraub, Thomas M. Henderson, and Gustavo E. Scuseria. Long-range-corrected hybrids based on a new model exchange hole. *Journal of Chemical Theory and Computation*, 5(4):754–762, 2009. doi: 10.1021/ct800530u. URL https://doi.org/10.1021/ct800530u. PMID: 26609580.

[60] Mary A. Rohrdanz, Katie M. Martins, and John M. Herbert. A long-range-corrected density functional that performs well for both ground-state properties and time-dependent density functional theory excitation energies, including charge-transfer excited states. *The Journal of Chemical Physics*, 130 (5), 02 2009. ISSN 0021-9606. doi: 10.1063/1.3073302. URL https://doi.org/10.1063/1.3073302. 054112.

[61] Takeshi Yanai, David P Tew, and Nicholas C Handy. A new hybrid exchange–correlation functional using the coulomb-attenuating method (cam-b3lyp). *Chemical Physics Letters*, 393 (1):51–57, 2004. ISSN 0009-2614. doi: https://doi.org/10.1016/j.cplett.2004.06.011. URL https://www.sciencedirect.com/science/article/pii/S0009261404008620.

[62] Aliaksandr V. Krukau, Oleg A. Vydrov, Artur F. Izmaylov, and Gustavo E. Scuseria. Influence of the exchange screening parameter on the performance of screened hybrid functionals. *The Journal of Chemical Physics*, 125(22), 12 2006. ISSN 0021-9606. doi: 10.1063/1.2404663. URL https://doi.org/10.1063/1.2404663. 224106.

[63] Roberto Peverati and Donald G Truhlar. Screened-exchange density functionals with broad accuracy for chemistry and solid-state physics. *Physical Chemistry Chemical Physics*, 14(47):16187–16191, 2012.

[64] Roberto Peverati and Donald G Truhlar. Improving the accuracy of hybrid meta-gga density functionals by range separation. *The Journal of Physical Chemistry Letters*, 2(21):2810–2817, 2011.

[65] Stefan Grimme. Accurate description of van der waals complexes by density functional theory including empirical corrections. *Journal of computational chemistry*, 25(12):1463–1473, 2004.

[66] Stefan Grimme. Semiempirical gga-type density functional constructed with a long-range dispersion correction. *Journal of computational chemistry*, 27(15):1787–1799, 2006.

[67] Stefan Grimme, Jens Antony, Stephan Ehrlich, and Helge Krieg. A consistent and accurate ab initio parametrization of density functional dispersion correction (dft-d) for the 94 elements h-pu. *The Journal of chemical physics*, 132(15):154104, 2010.

[68] Stefan Grimme, Stephan Ehrlich, and Lars Goerigk. Effect of the damping function in dispersion corrected density functional theory. *Journal of computational chemistry*, 32(7):1456–1465, 2011.

[69] Oleg A Vydrov and Troy Van Voorhis. Nonlocal van der waals density functional: The simpler the better. *The Journal of chemical physics*, 133(24):244103, 2010.

[70] Narbe Mardirossian and Martin Head-Gordon. ωb97x-v: A 10-parameter, range-separated hybrid, generalized gradient approximation density functional with nonlocal correlation, designed by a survival-of-the-fittest strategy. *Physical Chemistry Chemical Physics*, 16(21):9904–9924, 2014.

[71] Narbe Mardirossian and Martin Head-Gordon. Mapping the genome of meta-generalized gradient approximation density functionals: The search for b97m-v. *The Journal of chemical physics*, 142(7): 074111, 2015.

[72] Narbe Mardirossian and Martin Head-Gordon. ω b97m-v: A combinatorially optimized, range-separated hybrid, meta-gga density functional with vv10 nonlocal correlation. *The Journal of chemical physics*, 144(21):214110, 2016.

[73] David Feller. The role of databases in support of computational chemistry calculations. *Journal of computational chemistry*, 17(13):1571–1586, 1996.

[74] RBJS Krishnan, J Stephen Binkley, Rolf Seeger, and John A Pople. Self-consistent molecular orbital methods. xx. a basis set for correlated wave functions. *The Journal of chemical physics*, 72(1):650–654, 1980.

[75] Michelle M Francl, William J Pietro, Warren J Hehre, J Stephen Binkley, Mark S Gordon, Douglas J DeFrees, and John A Pople. Self-consistent molecular orbital methods. xxiii. a polarization-type basis set for second-row elements. *The Journal of Chemical Physics*, 77(7):3654–3665, 1982.

[76] AD McLean and GS Chandler. Contracted gaussian basis sets for molecular calculations. i. second row atoms, z= 11–18. *The Journal of chemical physics*, 72(10):5639–5648, 1980.

[77] Thom H Dunning Jr. Gaussian basis sets for use in correlated molecular calculations. i. the atoms boron through neon and hydrogen. *The Journal of chemical physics*, 90(2):1007–1023, 1989.

[78] Rick A Kendall, Thom H Dunning Jr, and Robert J Harrison. Electron affinities of the first-row atoms revisited. systematic basis sets and wave functions. *The Journal of chemical physics*, 96(9):6796–6806, 1992.

[79] David E Woon and Thom H Dunning Jr. Gaussian basis sets for use in correlated molecular calculations. iii. the atoms aluminum through argon. *The Journal of chemical physics*, 98(2):1358–1371, 1993.

[80] Frank Jensen. Atomic orbital basis sets. *Wiley Interdisciplinary Reviews: Computational Molecular Science*, 3(3):273–295, 2013.

[81] M Gutowski, JH Van Lenthe, J Verbeek, FB Van Duijneveldt, and G Chałasinski. The basis set superposition error in correlated electronic structure calculations. *Chemical Physics Letters*, 124(4): 370–375, 1986.

[82] Michael Dolg and Xiaoyan Cao. Relativistic pseudopotentials: their development and scope of applications. *Chemical reviews*, 112(1):403–480, 2012.

[83] Aleksandr V Marenich, Christopher J Cramer, and Donald G Truhlar. Universal solvation model based on solute electron density and on a continuum model of the solvent defined by the bulk dielectric constant and atomic surface tensions. *The Journal of Physical Chemistry B*, 113(18):6378–6396, 2009.

[84] Robert S Mulliken. Electronic population analysis on lcao–mo molecular wave functions. i. *The Journal of Chemical Physics*, 23(10):1833–1840, 1955.

[85] Per-Olov Löwdin and Harrison Shull. Natural orbitals in the quantum theory of two-electron systems. *Physical Review*, 101(6):1730, 1956.

[86] Per-Olov Löwdin. Quantum theory of many-particle systems. i. physical interpretations by means of density matrices, natural spin-orbitals, and convergence problems in the method of configurational interaction. *Physical Review*, 97(6):1474, 1955.

[87] Tian Lu and Feiwu Chen. Atomic dipole moment corrected hirshfeld population method. *Journal of Theoretical and Computational Chemistry*, 11(01):163–183, 2012.

[88] Fred L Hirshfeld. Bonded-atom fragments for describing molecular charge densities. *Theoretica chimica acta*, 44:129–138, 1977.

[89] Curt M Breneman and Kenneth B Wiberg. Determining atom-centered monopoles from molecular electrostatic potentials. the need for high sampling density in formamide conformational analysis. *Journal of Computational Chemistry*, 11(3):361–373, 1990.

[90] Yan Li and Jeremy NS Evans. The fukui function: a key concept linking frontier molecular orbital theory and the hard-soft-acid-base principle. *Journal of the American Chemical Society*, 117(29):7756–7759, 1995.

[91] Rubén Laplaza, Francesca Peccati, Roberto A. Boto, Chaoyu Quan, Alessandra Carbone, Jean-Philip Piquemal, Yvon Maday, and Julia Contreras-García. Nciplot and the analysis of noncovalent interactions using the reduced density gradient. *Wiley Interdisciplinary Reviews: Computational Molecular Science*, 11(2):e1497, 2021.

Chapter 3

Methodology

The methodology chapter outlines the computational methods and techniques used to in the DFT calculations. The investigation strategy of the structure search of isolated anions and cations as well as the IP structures is detailed. The workflows of generating MEPs, Fukui functions and XPS spectra from the stable conformers of each anion, cation and IP are also discussed.

3.1 Computational methods

DFT optimizations and frequency calculations were carried out in the Gaussian 16 software suite.[1] Visualizations of structures and manipulations of input structures were carried out in the Gaussview GUI interface.[1] Unless otherwise stated all DFT calculations were carried out using the B3LYP functional[2] in conjunction with the D3 dispersion correction by Grimme[3] with Becke-Johnson damping D3(BJ).[4] The B3LYP-D3(BJ) functional was used because it has been shown to perform well while being relatively computationally inexpensive.[5] Additionally, the Hunt group has used the B3LYP-D3(BJ) functional to study various ILs[6–8] and bismuth HMILs[9] so reference calculations with the same functional were readily accessible. Selected structures were benchmarked using MP2[10] and CCSD.[11,12] Solvation effects were studied using the solvation model based on density (SMD)-continuum solvation model.[13]

Small nuclei (H, C, N, O, Al and Cl) were treated with the 6-311+G(d,p) basis set.[14–16] The Lan2dz pseudopotential and associated basis sets were used for larger nuclei (Ga and In).[17] The aug-cc-pVTZ[18–20] and Stuttgart pseudopotentials[21] were used to benchmark selected structures. The strategy of the project is to use computationally inexpensive methods and basis sets for the initial calculations and higher-level methods and basis sets to benchmark some key structures and clusters.

The input parameters used for the SMD solvation model are modified SMD-GIL(generic ionic liquid) parameters. Each of the SMD-GIL parameters are average values of 8 or 11 different ILs. Eight of the ILs used to parameterize the SMD-GIL parameters have imidazolium cation with a variety of anions which are common in ILs.[22] The fractions of non-hydrogen aromatic carbons, ψ, and non-hydrogen electronegative halogens, ψ, which were specified for each computation with respect to the atomic composition, given by x_{MCl_3}. The dielectric constant, ε is 11.5, the squared index of refraction, n^2, is 2.0449, the macroscopic surface tension in cal $mol^{-1}A^{-2}$, γ, is 61.24 Abraham hydrogen bond acidity parameter,$\sum \alpha_2^H$, is 0.383 and Abraham hydrogen bond basicity parameter,$\sum \beta_2^H$, is 0.089.

Optimizations were carried out with no symmetry constraints. SCF=tight was used which sets the SCF convergence criteria to 10^{-8} which means the SCF convergence demands $< 10^{-8}$ RMS change in the density

matrix as well as $< 10^{-6}$ change in the density matrix to converge. Int=ultrafine is specified requesting a pruned integration grid with 99 radial shells and 590 angular points per shell. Stationary points on the potential energy surface (PES), minima and transition states, were evaluated through frequency analyses. Frequency analysis provided thermochemical data including zero-point energy correction, Gibbs free energy (G), enthalpy (H), and Entropy (S). The BSSE was analysed on selected structures via the counterpoise method.[23]

Advanced analyses of the optimized structures of isolated species and IP structures were carried out in the Gaussview GUI, multiwfn and VMD. The Assignment of NACs[24–30], as well as electronic structure analysis through AIM[31], NCIplot[32] and IRI[33] were carried out in the multiwfn software suite.[34] Visualizations of NCIplot and IRI were done using the visual molecular dynamics (VMD) software suite.[35] Molecular orbitals (MOs), electrostatic potentials via ChelpG and Fukui functions were visualized in the Gaussview GUI. XPS spectra were generated with multiwfn and the Gellius script developed by Richard Fogarty.[36] The NAC schemes used were Mulliken, ChelpG, NPA and ADCH charges.

3.2 Investigation strategy

Anionic speciation in the gas phase (GP) and liquid phase (LP) at different x_{MCl_3} was determined by evaluating the relative stability of different species in each phase using the Gibbs free energy of structures. Initially the most stable constitutional isomers and most stable conformers of each isomer were determined in a structure search from a variety of starting structures described in the next section. Each isomer within 50 kJ mol^{-1} of the lowest energy isomer was considered for the various evaluated molecular formulas. The most stable conformers of the most stable constitutional isomers were used to compute which structures resemble the anionic speciation by calculating bond dissociation energies (BDEs). The 50 kJ mol^{-1} was chosen as an arbitrary cutoff point as structures which are 50 kJ mol^{-1} less stable than the lowest energy structure are typically not stable under most operating conditions. However, less stable structures can give insight into the chemical behaviour of substances in higher energy states induced by higher temperature so they are included in selected evaluations.

The strategy was to successively increase the number of species present in the computations. Initially different chlorometallate species and the cations were optimized in isolation. The isolated chlorometallate species and cations were optimized and evaluated to determine which species and conformations are thermodynamically the most stable. All of the chlorometallate structures were optimized with Al, Ga and In in a +3 oxidation state while Cl was in a -1 oxidation state. Following the evaluations of isolated

species, the most stable structures were used to construct the IP structures. Stable IP structures were used to evaluate the intermolecular forces and the change in electronic structure of the individual species upon interacting with each other. IPs were constructed based on known IP structures from literature, NACs, molecular electrostatic potential, and Fukui functions of the constituent species. The anionic speciation was evaluated based on the isolated chlorometallate species and the IP structures.

3.2.1 Isolated chlorometallate anion and cation structure searches

The starting structures used for the chlorometallate structure search were selected to achieve a comprehensive investigation of anionic speciation and possible reaction products while accounting for computational cost. All known anionic structures were considered while evaluating as many alternative structural configurations as possible. Chlorometallate anions, neutral and cationic complexes were used as starting structures. In the bulk solution only organic cations and chlorometallate anions are present but during reduction processes and reactions neutral and cationic chlorometallate complexes could be generated. Chlorometallate cations and neutral complexes were considered as the structures could give insight into the chemical transformations occurring during catalysis, electrodeposition, and energy storage.

Two approaches were used to select the starting structures, depending on the number of metals present. All possible chlorometallate isomers were evaluated for molecular formulas with one or two metals centres, limited only by the maximum coordination number of the metal centres; 6. In consequence the complete homologous series of $[MCl]^{2+}$, $[MCl_2]^{+}$, MCl_3, $[MCl_4]^{-}$, $[MCl_5]^{2-}$ and $[MCl_6]^{3-}$ was evaluated to cover all possible atomic monometallic complexes. Additionally, different molecular geometries were evaluated for each atomic composition when necessary. $[MCl_2]^{+}$ was optimized from a linear and a bent starting structure, MCl_3 from a trigonal planer and trigonal pyramidal structure, $[MCl_4]^{-}$ from a tetrahedral and a square planer structure and $[MCl_5]^{2-}$ from a trigonal bipyramidal and a square planer structure. All monometallic starting structures are depicted in figure 3.1 with their corresponding numeric markers (01-10).

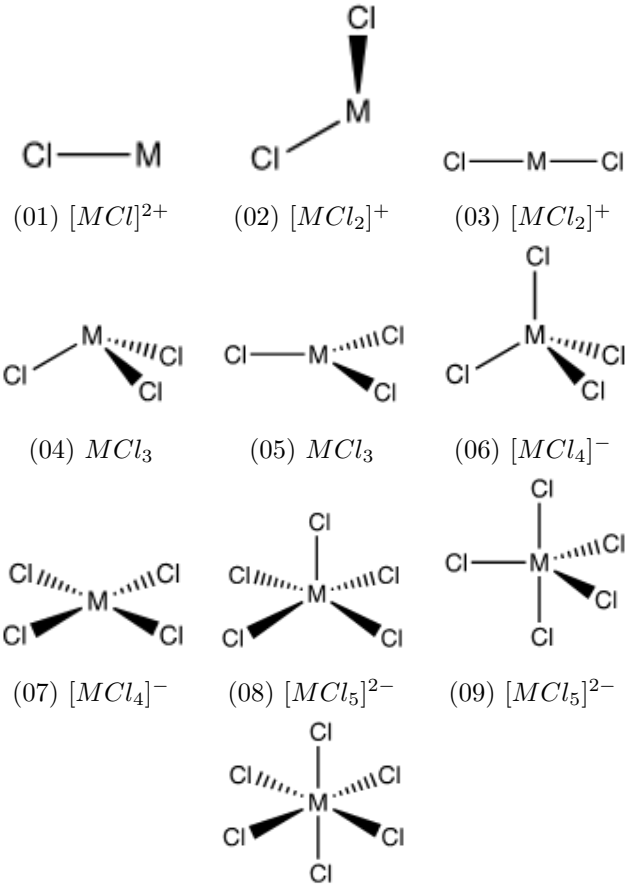
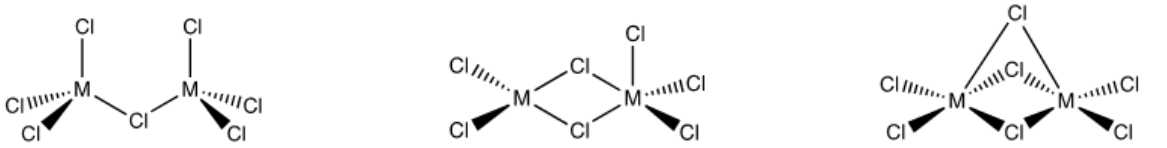


Figure 3.1: Monometallic guess structures where M=Al, Ga or In

The bimetallic starting structures were generated based on the same principles as the monometallic structures, i.e. varying to amount of halide saturation on each metal centre and the geometric positions the halides assume around the metal centres. Two additional considerations had to be made when setting up the bimetallic structures: the amount of bridging versus terminal chlorides and the orientation of each metal centres geometry towards each another.

The amount of bridging (ligands bonded to two or more metal centres) versus terminal (ligands which are bonded to a single metal) chlorides is illustrated in the series of structural isomers in figure 3.2. In figure 3.2, starting structures (11), (54) and (16) represent three starting structures with the molecular formula M_2Cl_7 but they feature different amounts chloride bridging and terminal chlorides.



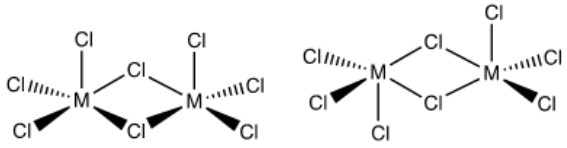
(11) 1 bridging, 6 terminal
two 4 coordinate tetrahedral

(54) 2 bridging, 5 terminal
one 4 cooridnate square planar
one 5 coordinate squared based pyramidal

(16) 3 bridging, 4 terminal
two 5 coordinate
distorted geometries

Figure 3.2: Three $[M_2Cl_7]^-$ starting structures with different numbers of bridging halides

The orientation with which two metal centres are bound has to be considered because depending on the orientation toward each other different stereoisomers can form. The two $[M_2Cl_8]^{2-}$ structures depicted in figure 3.3 are two stereoisomers of conjoint square based pyramidal MCl_5 structures. The terminal chlorides of the resulting structures are either cis or trans. The complete set of bimetallic starting structures which have been evaluated and the corresponding optimized geometries for each metal can be found in the appendix in tables 4-9 and 36-42.



(15) $[M_2Cl_8]^{2-}$ (64) $[M_2Cl_8]^{2-}$

Figure 3.3: $[M_2Cl_8]^{2-}$ stereo isomeric starting structures example

Starting structures with three or more metal centres were selected with more scrutiny to avoid excessive computational cost. Trimetallic and tetrametallic structures were selected exclusively based on known group 13 chlorometallate speciation in the GP and LP[37] and crystallographic data from the Cambridge crystallographic structure database (CCSD)[38]. All trimetallic and tetrametallic starting structures can be found in tables 10 and 11 or tables 43 and 44 of the appendix.

3.2.2 Optimization

The optimization of each starting structure can converge to a potentially optimized structure or fail due to a variety of reasons. Figure 3.4 shows the flow of the error messages encountered of an optimization from a

starting structure.

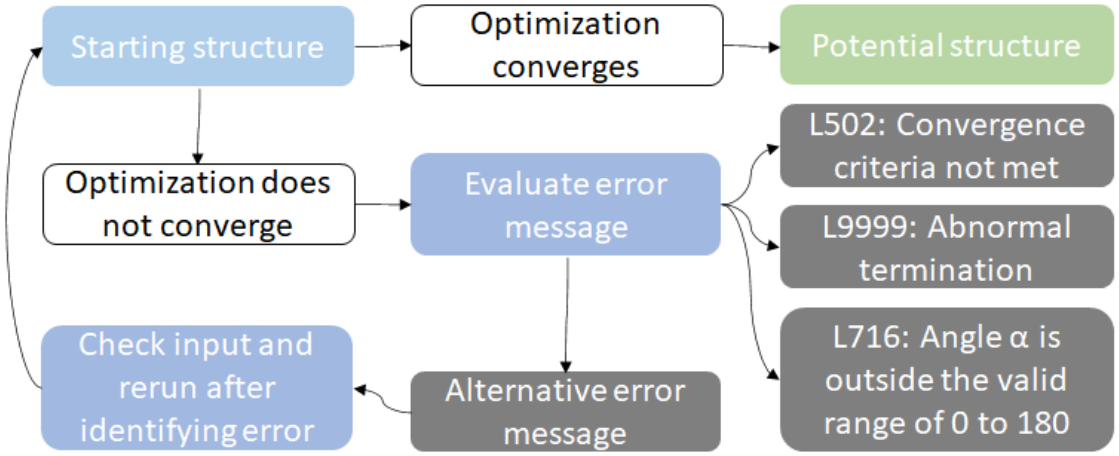


Figure 3.4: Optimization flowchart with possibilities in white, actions in light blue, error messages in grey and results in green

As seen in figure 3.4, the error messages encountered can largely be grouped into four categories. The alternative error messages are usually the result of something trivial such as an erroneous input of some input parameters which must be remedied. Alternatively, there may be an issue with the assigned number of processors and memory which must be adjusted. The other three error messages; L716, L9999 and L502 were commonly encountered and required the erroneous optimization to be evaluated in more detail to determine which actions would be most likely to solve the problem.

Figure 3.5 shows what is done in the case of the error L716: when an angle α is outside of the acceptable 0 - 180 range. The first option is to distort the atoms in the final structure of the optimization leading to the invalid bond angle and subsequently restart the optimization with the distorted structure. Alternatively, the optimization can be restarted from the final structure with the opt=Cartesian keywords. The opt=cartesian keyword changes the coordinate system from internal to cartesian coordinates and can be used to avoid L716 but requires more memory.

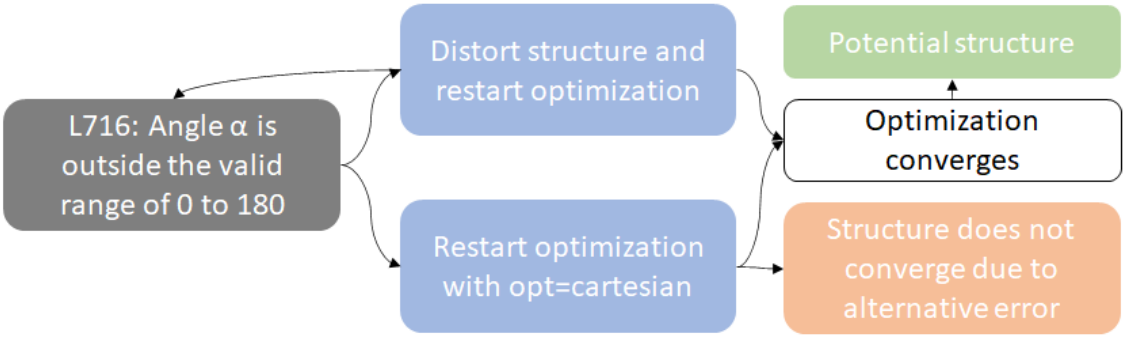


Figure 3.5: Error L716 flowchart with possibilities in white, actions in light blue, error messages in grey and results in green or orange

Figure 3.6 shows the possible solutions to the L9999 and L502 error messages. Although the error messages are different the solutions are the same. The changes in structure, the change in SCF energy and the force constants should be evaluated at each step of the optimization to determine which solution best suits the issue at hand.

When a starting structure is not very good is commonly results in a large structural change in the first step of the optimization which is also reflected in large displacement force constants in the first step of the optimization. In this case it is useful to pre-optimize the starting structure at a lower level of theory and using the resulting structure to restart the optimization. Lower level of theory refers to HF or using less complete basis set.

When an optimization reaches a point where there are high displacement force constants and the calculation terminates erroneously the calculation can restart with the keyword Opt=calcfc or in very severe cases opt=calcall which specify that the force constants be computed at the first point or all points, respectively. The computation of the force constants at each point allows for a more precise execution of the optimization. Commonly the force constants need to only be explicitly computed once at the first step but in rare cases the explicit computation of the force constants at each step is imperative.

If an optimization reaches a point at which it is oscillating between two geometries the last reasonable structure should be found and the optimization should be restarted with the keywords SCF=QC or SCF=XQC. SCF=QC means the SCF procedure is quadratically convergent and XQC adds a quadratically convergent SCF step if the conventional step did not converge.

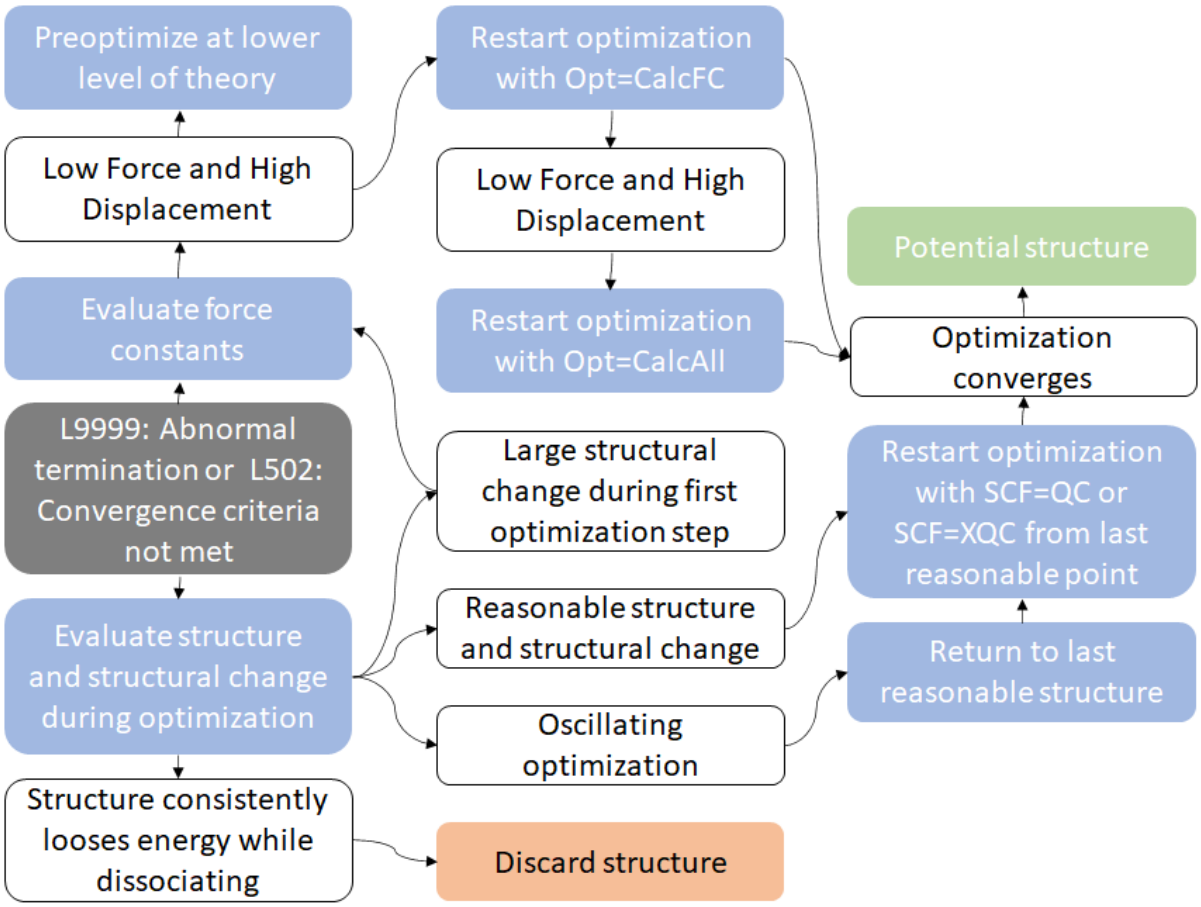


Figure 3.6: L9999 and L502 flowchart with possibilities in white, actions in light blue, error messages in grey and results in green or orange

Once all optimizations have terminated the successfully optimized structures are compared. If a structure is unique a frequency calculation will be conducted on it. If there are two or more structures with minor differences in geometry the lowest energy structure will be used in a frequency calculation and the other structures will be discarded.

3.2.3 Frequency analysis

The position of the potential structures on the PES is evaluated by conducting a frequency analysis. A structure is only considered stable if it converges during a frequency analysis and has no imaginary frequencies. Figure 3.7 shows a flow chart of how frequency calculations which did not converge and feature imaginary frequencies are dealt with.

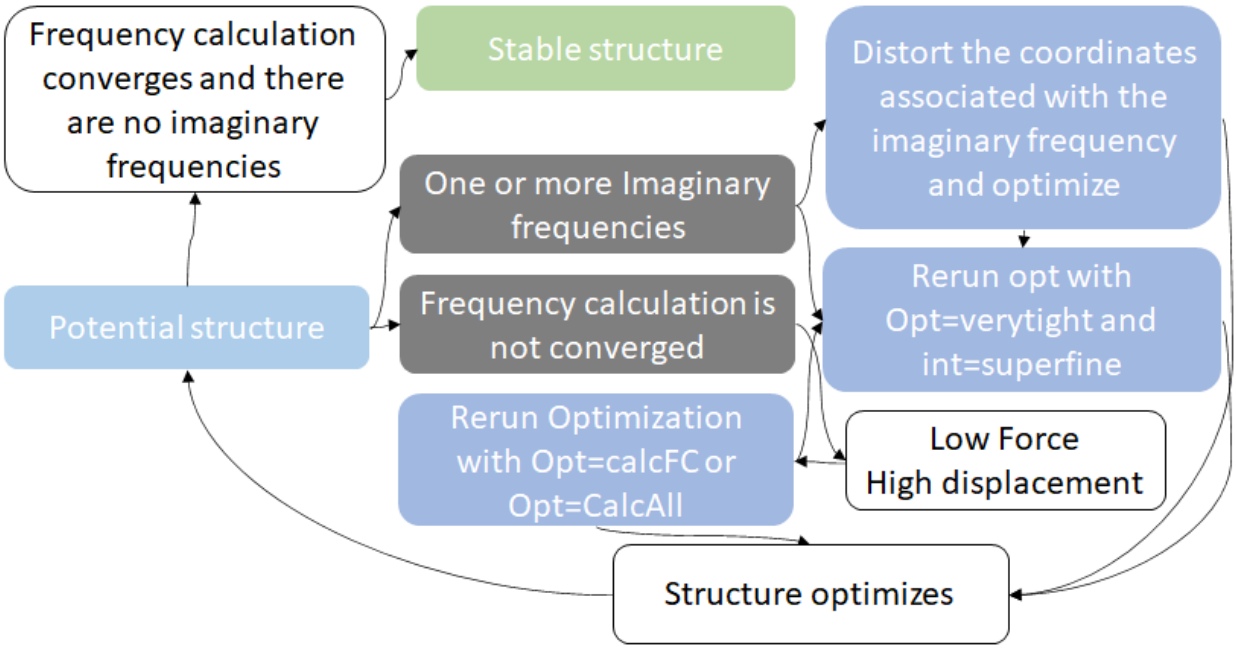


Figure 3.7: Frequency flowchart with possibilities in white, actions in light blue, possible errors in grey and results in green

When a calculation has imaginary frequencies, it is distorted along the coordinates of the imaginary frequency and reoptimized and another frequency calculation is carried out. Alternatively, a calculation is optimized with tighter convergence criteria i.e. opt=verytight and int=superfine keywords are used to find a minimum. the two techniques can be used in conjunction with one another to initially distort the structure along the imaginary frequency coordinates and then optimize the structure with tighter convergence criteria.

Some calculations converge during the optimization but do not converge during the frequency calculation. In all cases when the frequency calculation did not converge it was due to the displacement convergence criteria not being met. When the displacement criteria were not met the structures were optimized with opt=calcFC and opt=calcall if they still did not converge. If the frequency calculations still did not converge, the structures were reoptimized with calc=all and opt=verytight and grid=superfine.

3.2.4 Isolated chlorometallate species

Each stable structure is presented with descriptors in the following configuration; $[M_xCl_y]^{3x-y}$ $\{Q\}$ $[P]$ (R). The format can be interpreted as follows: $[M_xCl_y]^{3x-y}$ is the molecular formula of the species, $\{Q\}$ refers

to the starting structure from which the structure optimized (as seen in the appendix), $[P]$ or sometimes $[LowP]$ describes the amount of imaginary frequencies in the system and (R) is a structures Gibbs free energy relative to the lowest energy isomer (ΔG) in kJ mol^{-1}. Note the $\{Q\}$ is only referenced when the initial structure does not correspond to the output structure. (R) is only mentioned when there is a comparable structure with the same atomic configuration.

In the case when a structure optimized for one metal but not another it is omitted and the reason for it not optimizing is presented. SD means the structure dissociated, TS structure means the optimized structure has one high imaginary frequency and it is a transition state and MHF means that there were multiple high imaginary frequencies. Converges to XX means the structure converges to another configuration which also optimized. Converged to XX means the structure converged to another configuration which also optimized.

3.2.5 Thermodynamic comparison

The stability of optimized structures was compared using the structures Gibbs free energy (G). When a molecular formula featured multiple stable constitutional isomers and stereoisomers, initially the relative stability of the isomers was determined by comparing G of each isomer. The lowest energy isomers (>50 kJ mol^{-1}) were used to determine the anionic speciation at different x_{MCl_3}.

Once the lowest energy isomers were determined for each species the objective of determining anionic speciation at different x_{MCl_3} was tackled by comparing the relative stability of species to one another. Since the x_{MCl_3} is known, the atomic composition is known and hence the Gibbs free energy (G) of species with a given atomic composition were compared. Table 3.1 shows selected anionic speciations at different x_{MCl_3}. For example, at $x_{MCl_3} = 0.67$ the anionic speciation was determined by calculating the difference in energy between $[MCl_4]^-$ + MCl_3 to M_2Cl_7, i.e. G(M_2Cl_7) – (G(MCl_4) + G(MCl_3)). The most stable species or combination thereof which are within 50 kJ mol^{-1} of the lowest energy species or combination of species at different x_{MCl_3} were scanned and used in ion pair calculations.

Table 3.1: Mol fraction of metal halide introduced, x_{MCl_3}, the corresponding empirical formula of the anions and selected speciations of the anions

x_{MCl_3}	Empirical formula	Selected possible speciation
0.25	MCl_6	$[MCl_6]^{3-} \rightleftharpoons [MCl_5]^{2-} + Cl^- \rightleftharpoons [MCl_4]^- + 2Cl^-$
0.33	MCl_5	$2[MCl_5]^{2-} \rightleftharpoons 2[MCl_4]^- + 2Cl^- \rightleftharpoons [M_2Cl_{10}]^{4-}$
0.5	MCl_4	$2[MCl_4]^- \rightleftharpoons MCl_3 + [MCl_5]^{2-} \rightleftharpoons [M_2Cl_8]^{2-}$
0.67	M_2Cl_7	$2[M_2Cl_7]^- \rightleftharpoons 2MCl_3 + 2[MCl_4]^- \rightleftharpoons [M_4Cl_{14}]^{2-}$
0.75	M_3Cl_{10}	$[M_3Cl_{10}]^- \rightleftharpoons MCl_3 + 2[MCl_4]^- \rightleftharpoons [M_2Cl_7]^- + MCl_3$
0.8	M_4Cl_{13}	$[M_4Cl_{13}]^- \rightleftharpoons MCl_3 + 3[MCl_4]^- \rightleftharpoons [M_2Cl_7]^- + M_2Cl_6$

It is important to note that it is impossible to be certain that all possible stable conformations were deduced through this approach. The knowledge of the steric and electrostatic characteristics of the individual ions allows for very good guesses but some structures are difficult to find, either due to an error in judgment or an algorithmic fault.

3.2.6 Conformer search and bond dissociation energy via scans

Scans were conducted to determine all the accessible stable conformers of each structure and evaluate the dissociation of each structure. Scans were only carried out on structures which had been shown to be thermodynamically stable according to their relative Gibbs free energy. The scans were carried out with one internal coordinate being scanned while the remainder of a structure optimized with respect to the change in the internal coordinate at each step using the opt=modredundant keyword in Gaussian. The stable conformations, located at minimums of the PES, which were revealed by a scan were subsequently optimized and frequency analysed.

Three different types of internal coordinates were scanned: distances between two atoms, angles between three atoms and dihedral angles between four atoms. An internal coordinate was selected based on the plausible changes in a species structure. For example, the $[Al_4Cl_{13}]^-$ anions is a linear structure which can fold in on itself as shown in figure 3.8. The reaction coordinate to evaluate what stable conformers can result from the $[Al_4Cl_{13}]^-$ anion folding is the distance between the two terminal Al atoms. The distance between the two Al atoms was successively decreased or increased by 0.2 Angstrom steps over 15 steps. Scans were always conducted with a maximum of 20 steps as the accuracy of the computation declines with every successive step. If a scan finished but the full range of structures which could be elucidated from scanning

the internal coordinate had not been found, a scan was re-initiated from the final structure of the previous scan.

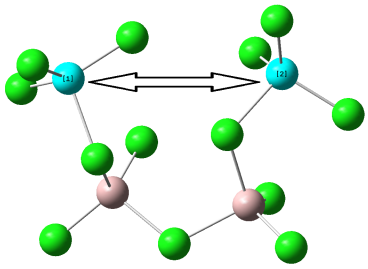


Figure 3.8: Depiction of the terminal Al - terminal Al distance scan coordinate (turquoise) of the $[Al_4Cl_{13}]^-$ anion

As shown in figure 3.8 the distance between the outer most aluminium atoms, depicted as turquoise [1] and [2], was scanned. The SCF energy corresponding to the change in Al-Al distance can be seen in figure 3.9.

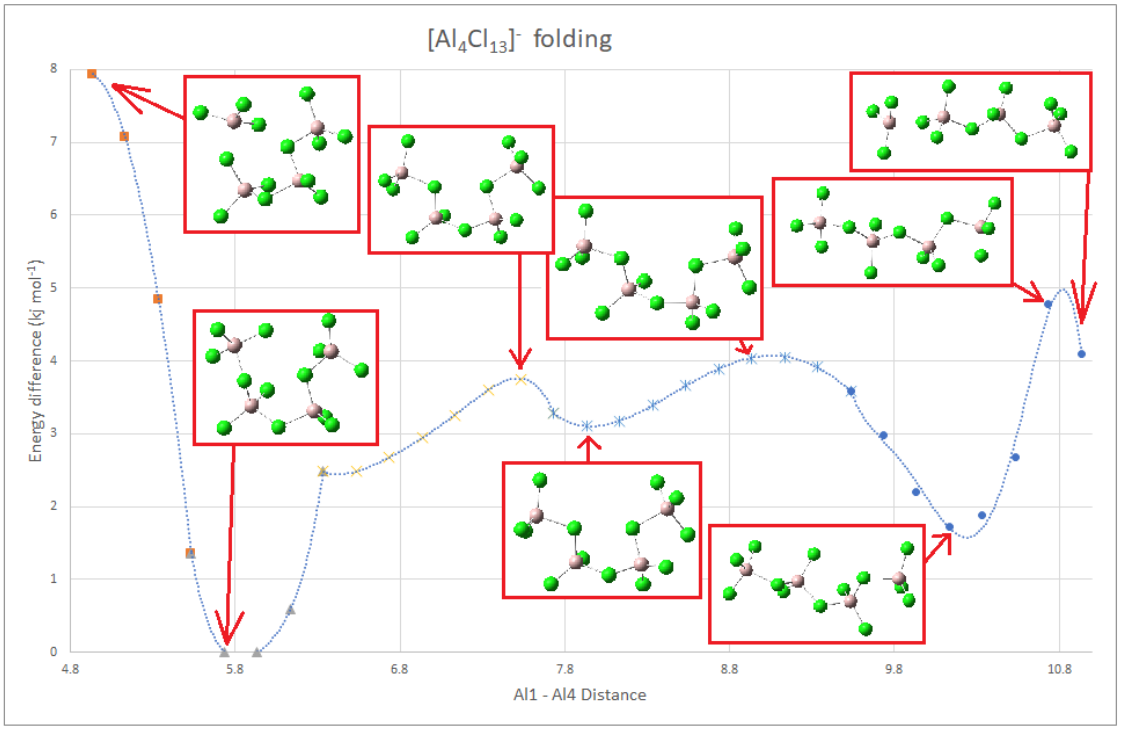


Figure 3.9: SCF energy change versus the terminal Al- terminal Al distance of the $[Al_4Cl_{13}]^-$ anion

The dihedral angle of different complexes were scanned to determine different stable conformational isomers which may arise due to the rotation along different bonds. The scan coordinates of the rotation of the

$C_2C_1Im]^+$ ethyl arm is depicted in figure 3.10. Rotational scans based on dihedral angles were also carried out for the chlorometallate anions to determine additional anion conformers.

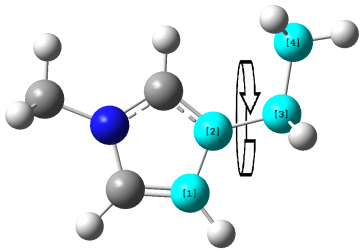


Figure 3.10: Depiction of the $[C_2C_1Im]^+$ ethyl arm rotation via the dihedral angle scan coordinate (turquoise)

Analogously to the scans of internal coordinates used to reveal different conformations of structures, scans were also used to scan the dissociation of different complexes. The dissociation was scanned to determine where a structure fragments and reveal the thermodynamics of the dissociation process.

3.2.7 Anionic speciation from isolated chlorometallate species

To ascertain the anionic speciation from the isolated chlorometallate species the species were compared analogously to the method described in the thermodynamic comparison section. The Gibbs free energy of different species and combinations thereof resulting in the atomic compositions at specific x_{MCl_3} were used to determine the speciation.

The anionic speciation was determined from the isolated anions through two methods. One method only used the lowest energy isomer of each possible speciation in the comparison. The other method computed the energy of a particular speciation via the Boltzmann distribution of all the accessible isomers of a particular speciation. For example if speciation A has three isomers with a ΔG of 0, 5 and 10 kJ mol^{-1} and speciation B has one conformer of 3 kJ mol^{-1} then the first method will favour speciation A by 3 kJ mol^{-1}. According to the method using the Boltzmann distribution the energy of speciation A is 5 kJ mol^{-1} so speciation B would be more stable by 2 kJ mol^{-1}. Method A is a faster method while method B is more accurate. Both approaches are used to compare speciation to other computational speciation studies.

3.2.8 Electronic structure evaluation - net atomic charges, molecular electrostatic potential and Fukui functions

After determining which species conformers are stable at different x_{MCl_3}, the electronic structure of each species was evaluated. NACs, MEPs and Fukui function were determined for all structures. The assignment of NACs is a straightforward process in which the formatted checkpoint files (.fchk) of stable structures are evaluated in Multiwfn. The four different charge distribution schemes; Mulliken, ChelpG, NAP and ADCH assigned the charges according to the respective formulations.

NACs are helpful to determine how charge is distributed around molecules but can omit crucial information about the nuance of how the charge is projected into the space around the molecule. Hence the molecular electrostatic potentials (MEPs) were mapped onto the total electron density to determine which ion-ion interactions are likely to be most stabilizing.

to generate the MEP surfaces, the electrostatic potential (ESP) was mapped onto the electron density. An isovalue of the total density was selected for the ESP to be mapped on. The density isovalues represent the probability density at different regions in space and are measured in electrons per cubic boar distance, e a_0^{-3}. At a selected isovalue of the total density the ESP, measured in E_h e^{-1}, is mapped. The electrostatic potential is then mapped onto the isovalue of choice as shown in figure 3.11.

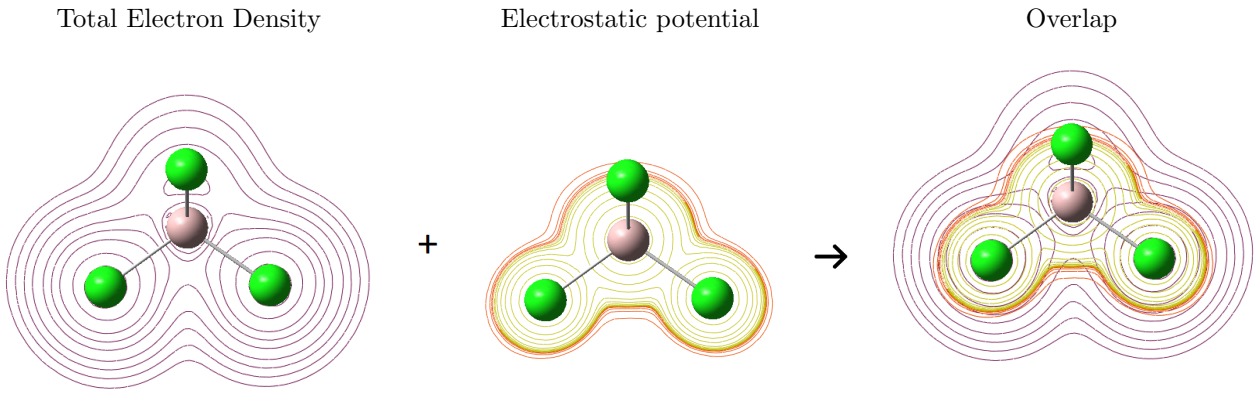


Figure 3.11: $[AlCl_4]^-$ Total electron density, electrostatic potential and overlap contours

The image on the left of figure 3.11 shows contours of the total electron density in the plane of the central aluminium and two chlorides. Each of the purple lines represents a different isovalue. The central image shows the contours of different isovalues of the ESP where the orange lines representing negative values and

the yellow lines representing positive values. The right-hand image shows the overlap of how the contours would be mapped onto one another in the plane of the aluminium and two chlorides. When selecting a particular isovalue of total density the ESP is mapped onto the selected isovalue in three dimensions. The ESP mapped onto a selected total density isovalue will show regions of higher and lower ESP around the species.

The visualizations of Fukui functions were made by taking stable structures and running a single point energy calculation with one more or less electron for the cations and anions, respectively. The total density of the anions and cations in their natural state were generated as cube files. Subsequently the cube files of the total density of the anions and cations from the single point calculations with one less or more electron were generated. The cube files are subtracted from one another using the cubman program in the Gaussian program suite according to eq. 3.2.1 and 3.2.2.

$$Anions : f_+(r) = \rho_{N+1}(r) - \rho_N(r) \tag{3.2.1}$$

$$Cations : f_-(r) = \rho_N(r) - \rho_{N-1}(r) \tag{3.2.2}$$

The difference in total density was mapped onto the total density of the cations with their original charge, analogously to the mapping of the MEP. An isovalue of total density of the natural ions state was selected and the difference in total density upon a change in the number of electrons is projected onto the total density isovalue contour in three dimensions.

3.2.9 Ion pair input structure construction

The anion structures which reflect the speciation were placed around all stable cation conformations. The positions of anions around the imidazolium cation are based on the known stable positions for chloride ions around $[C_2C_1Im]^+$ elucidated by Hunt and coworkers. Key sites where chloride ions are located around the $[C_2C_1Im]^+$ cation are shown in figure 3.12.[6]

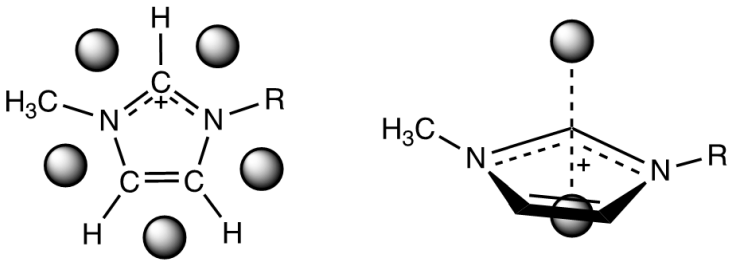


Figure 3.12: Stable positions of Cl^- around the $[C_nC_1Im]^+$ cation

The different orientations of anions towards the cations at each position around the cation were determined by the geometry of the anion. For example, The tetrahedral MCl_4 features corners, edges and faces on the tetrahedral structure as depicted in figure 3.13. Each of the three features were oriented towards the cation at each anionic position. Stable ion pair conformers within $50 kJ mol^{-1}$ of the lowest energy structure were used to evaluate intermolecular interactions and the anionic speciation. Structures above 50 kJ mol^{-1} of the lowest energy structure were discarded unless they gave valuable insight into probable interactions in the bulk solution.

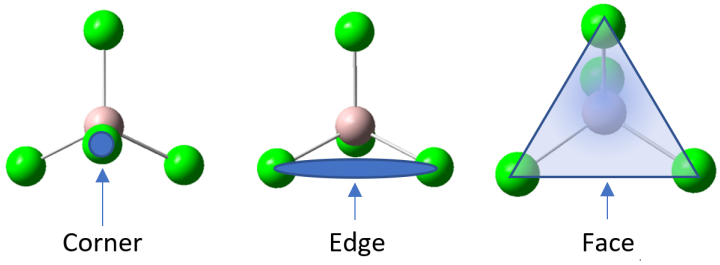


Figure 3.13: Geometric elements of the MCl_4 tetrahedron which can face the cations

3.2.10 Ion pair nomenclature

A nomenclature standard was established to distinguish optimized IP structures from one another effectively. Stable IP structures have been named according to a variety of structural features including Bond distances, bond angles and dihedral angles. A streamlined naming scheme for a better understanding of the individual structures was generated based on features describing the internal structure of the cation and the positions of the anion relative to the cation.

In the $[C_2C_1Im]Cl$ - MCl_3 systems, four structural features were used to differentiate between the IP structures. The first structural feature used to distinguish IP structures featuring the $[C_2C_1Im]^+$ cation was the ethyl arms dihedral angle, as depicted in figure 3.14. The dihedral angle is not consistent in all IP

structures so it is structural feature which can be used effectively to differentiate between IPs.

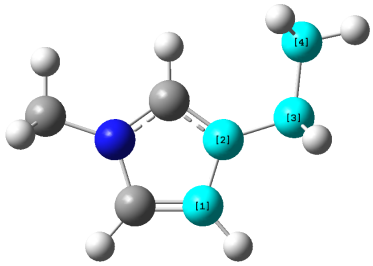


Figure 3.14: $[C_2C_1Im]^+$ dihedreal angle

The second structural feature used was the distance between the C_2 carbon and the central atom of the corresponding anion. The distance between these two points is a key feature in describing the position of the anion relative to the cation as it determines the cation-anion proximity as shown for the $[C_2C_1Im][AlCl_4]$ ion pair in figure 3.15.

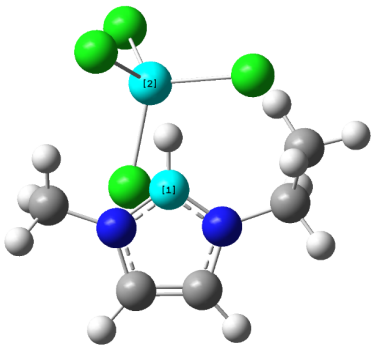


Figure 3.15: $[C_2C_1Im][AlCl_4]$ C_2 - Al distance

In the case of monometallic complexes, the central point of the anion is always the metal. In the case of multimetallic anions alternative molecular centres were used and the central atoms were selected according to the depiction in figure 3.16.

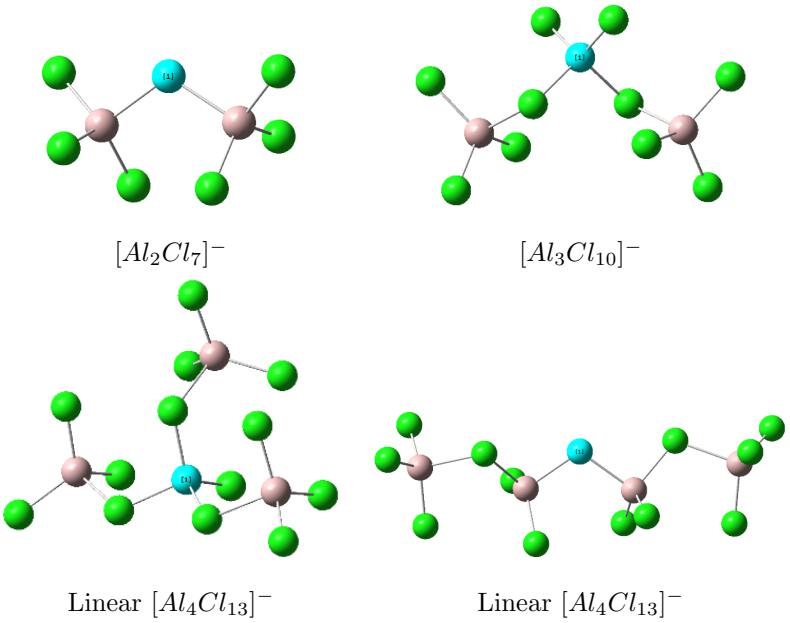


Figure 3.16: $[Al_2Cl_7]^-$, $[Al_3Cl_{10}]^-$, linear $[Al_4Cl_{13}]^-$ and branched $[Al_4Cl_{13}]^-$ anions central atoms

The third feature used to describe the IP structures is the angle relative to the symmetry of the imidazolium ring plane, defined by three coordinates. To ensure that the symmetry of the imidazolium ring was reflected, a dummy atom was placed between the C_4 and C_5 carbon atoms which functions as the first of the three points. the C_2 carbon is the second point at which the angle is measured and the last point was the central atom of the anion, analogous to the positions described for the distance between the C_2 carbon. The angles are illustrated for the $[C_2C_1Im][AlCl_4]$ and $[C_2C_1Im][Al_2Cl_7]$ IPs in figure 3.17.

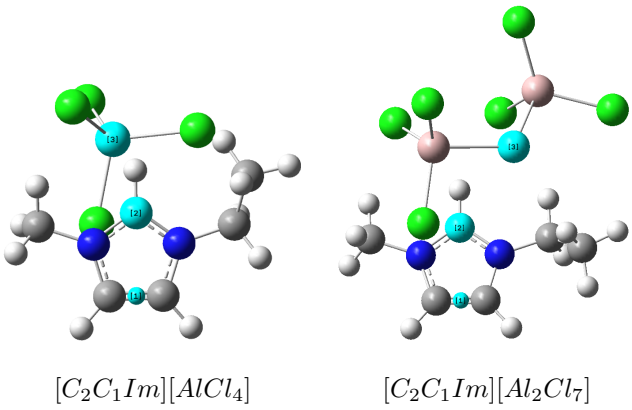
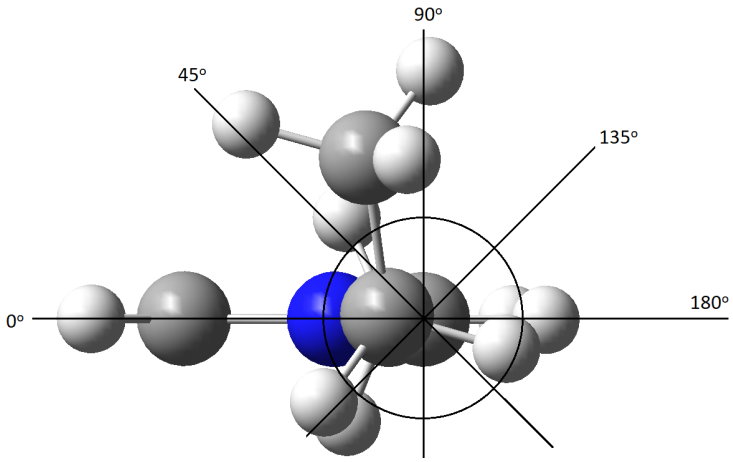


Figure 3.17: $[C_2C_1Im][AlCl_4]$ and $[C_2C_1Im][Al_2Cl_7]$ ion pairs 'plane - angle'

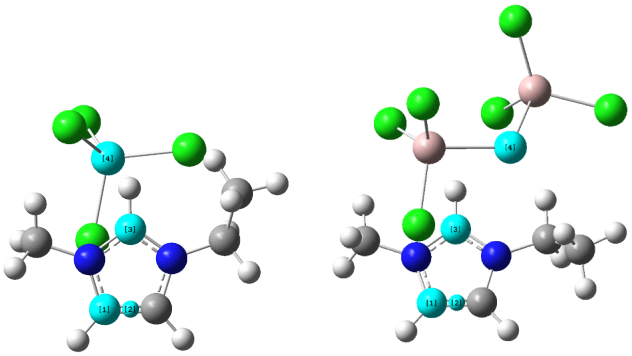
The angles, as shown in figure 3.17, give insight into where the anion is relative to the imidazolium rings line of symmetry and in turn which sites on the ring it is predominantly interacting with. The angles are used a guide as the larger anions interact with multiple points on the cation, but it gives insight into where the centre of the anion is located with respect to the cation and allows for distinction between different IP structures. The interactions the angles imply are visualized and listed below in figure 3.18.



Angle	Anion position and predicted interactions
0° - 30°	Back of the ring interacting with the C_4 and C_5 hydrogen atoms
30° - 70°	above or below the back of the ring, interacting with the imidazolium π-system and the hydrogen atoms on the C_4 and C_5 carbons
70° - 110°	Above or below the ring, anion – π interactions are predominant
110° - 150°	In the front above or below the ring interacting with the C_2 hydrogen and another part interacting with the imidazolium π-system
150° - 180°	In front of the ring interacting with the adjacent C_2 carbon and the methyl arm and ethyl arm hydrogen atoms

Figure 3.18: $[C_2C_1Im]^+$ angle information

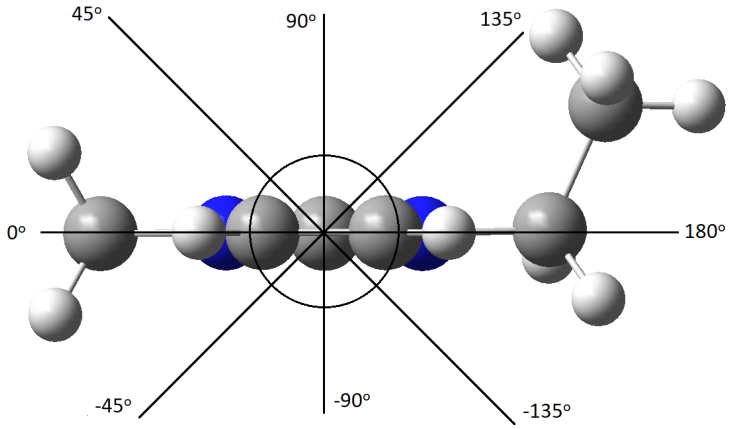
There is a problem with using the angle described above in isolation as it does not specify the plane of the angle. The angle relative to the line of symmetry of the imidazolium structure between the centralized dummy atom and the C_2 carbon is insufficient as the anion could be on the right, next to the ethyl arm and the angle would be 90°. Hence another parameter must be defined to determine the exact position of the anion relative to the cation. The fourth parameter used to differentiate between the IP structures is hence the dihedral angle between C_4 carbon [1] – the dummy atom (C_4-C_5) [2] – the C_2 carbon [3] – anion center [4] as shown below for $[C_2C_1Im][AlCl_4]$ and $[C_2C_1Im][Al_2Cl_7]$ in figure 3.19.



$[C_2C_1Im][AlCl_4]$ $[C_2C_1Im][Al_2Cl_7]$

Figure 3.19: $[C_2C_1Im][AlCl_4]$ and $[C_2C_1Im][Al_2Cl_7]$ ion pairs 'plane - dihedral angle'

In conjunction with the angle and the distance the position of an anions central atom relative to the cation can be determined. The information from the dihedral angle is summarized in figure 3.20.



Angle	Anion position and predicted interactions
+	on top the ring
-	on the bottom of the ring
± 0° - 60°	on the left, Interacting predominantly with the methyl arm
± 60° - 120°	on top, interacting primarily with the π-system of the imidazolium ring, the C_2 hydrogen atom or the back C_4 and C_5 hydrogen atoms
± 120° - 180°	On the right, interacting predominantly with the ethyl arm

Figure 3.20: $[C_2C_1Im]^+$ Dihedral angle information

The naming scheme is not exhaustive in describing the structural variables occurring in the IPs. The C_2 carbon and the imidazolium ring were selected as a reference points due to the rigidity of this structural feature of in cation in the IPs. The anions are more flexible outside of the ethyl and methyl arms rotations and hence defining all structural features of the anions exhaustively is not valuable to differentiate between the individual IPs. An example of how the naming would work is as follows: cation_anion_ethyl-arm-dihedral_C_2-anion-center-distance_cation-anion-angle_cation-anion-dihedral-angle. Figure 3.21 shows an example of the nomenclature applied to an IP structure.

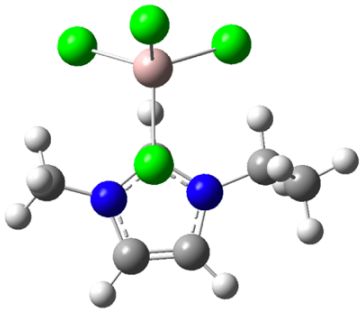
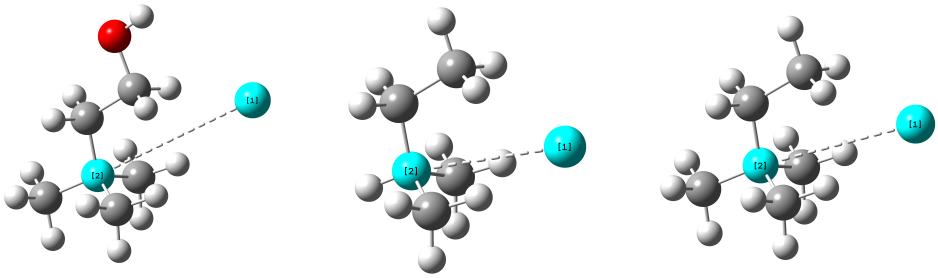


Figure 3.21: $[C_2C_1Im][AlCl_4]$_-58_3.7_122_87

The naming indicates the ethyl arms dihedral angle is -58°, the aluminium atom is 3.7 angstrom from the C_2 carbon while the angle is 122° which indicates the anion is on top in the front. the dihedral angle is 87° and hence the anion is relatively cantered on top of the ring. All the structural features cannot be seen but can be extracted from the defined structural information. The limitations are clear in that the anion could rotate across any axis and it would not change the values but among all the evaluated structures the defined features are enough to differentiate between the IP structures as at each position of the anions central atom there is usually one stable conformation.

The IPs featuring the three ammonium based cations were named according to similar principles described for the $[C_2C_1Im]^+$. The distance, angle, and dihedral of the anion relative to one, two and three distinct points on the cation determine the name of the IP structures. $[Choline]^+$ has one additional coordinate due to the rotation of the ethyl hydroxyl arm. The central atoms of the anions are analogous to those described for the imidazolium IPs.

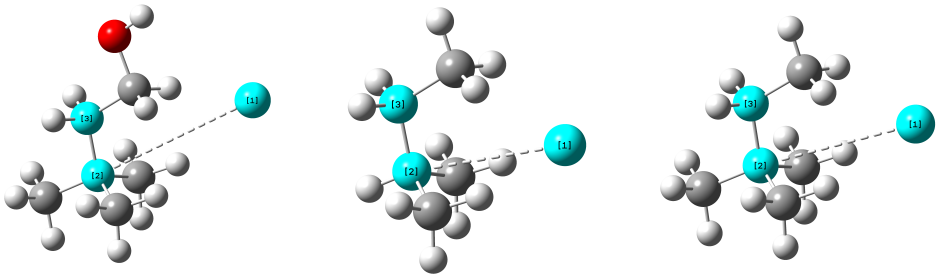
The first coordinate is the distance between the nitrogen and the centre of the anions illustrated in figure 3.22 for all three cations.



$[Choline]^+$ $[N_{2110}]^+$ $[N_{2111}]^+$

Figure 3.22: Ammonium based cation - anion distance

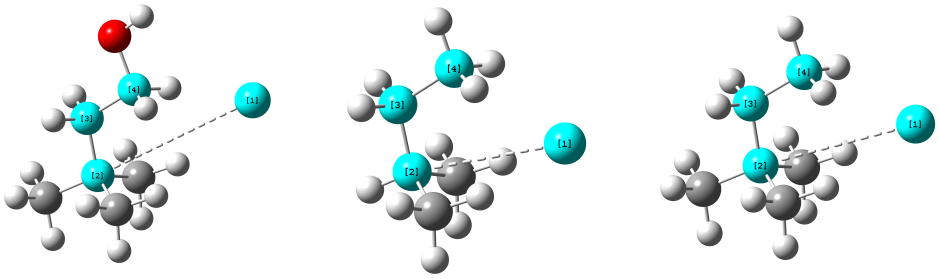
The second coordinate, shown in figure 3.23, is the angle between the anion centre, the nitrogen and the first carbon in ethyl moiety in $[N_{2110}]^+$ and $[N_{2111}]^+$ or ethyl hydroxyl moiety of $[Choline]^+$.



$[Choline]^+$ $[N_{2110}]^+$ $[N_{2111}]^+$

Figure 3.23: Amonium based cation - anion angle

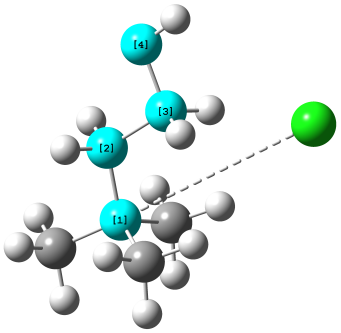
The third coordinate is the dihedral angle between the anion centre, the nitrogen and the first and second carbons on the ethyl or ethyl hydroxyl arm as shown in figure 3.24.



$[Choline]^+$ $[N_{2110}]^+$ $[N_{2111}]^+$

Figure 3.24: Ammonium based cation - anion dihedral angle

The OH moiety of the choline $[Choline]^+$ can rotate as shown via the trans and gauche conformers and hence the $[Choline]^+$ cation features one additional internal coordinate which can be described through the dihedral angle illustrated in figure 3.25.



Trans $[Choline]^+$

Figure 3.25: $[Choline]^+$ internal dihedral angle

For the $[N_{2110}]^+$ and $[N_{2111}]^+$ cations the naming is as follows: $[N_{211X}]$[Anion]_Distance_Angle_dihedral. The $[Choline]^+$ naming is the same but the three anion position values are preceded by the internal dihedral angle as follow [Choline][Anion]_internal dihedral_Distance_Angle_dihedral.

3.2.11 Ion pair convergence evaluation

The same starting structures of each IP combination were optimized in the GP and LP. If a structure was found to be stable in either the GP or LP, the stable structure was used as an additional initial structure in

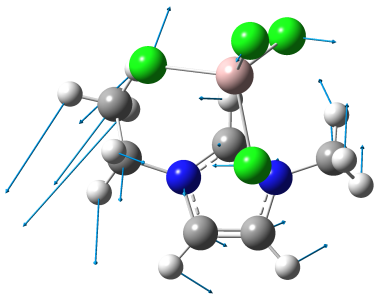
the other phase.

Some structures converged during optimization but in the frequency analysis they were found to be non-converged despite the application of all possible steps described in section 3.2.3. In the case of a non-converged frequency calculation the displacement and force values were assessed to determine whether the structure can be considered stable. High displacement values in conjunction with negligible force values are indicative of a flat PES which in turn means that the structures can still be considered a viable structure regardless of the fulfilment of the Gaussian convergence criteria in a frequency calculation. An example of such force constants can be found in the table 3.2. The non-converged structures were only considered stable if the maximum displacement and RMS displacement did not exceed the convergence criteria by a factor of 5.

Item	Value	Threshold	Converged?
Maximum Force	0.000006	0.000450	YES
RMS Force	0.000002	0.000300	YES
Maximum Displacement	0.03541	0.001800	NO
RMS Displacement	0.004338	0.001200	NO

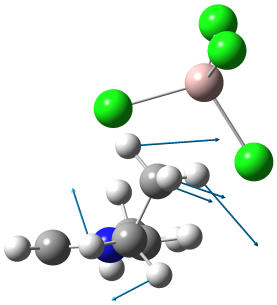
Table 3.2: Frequency calculation convergence criteria example

Some of the optimized structures were found to have one or more imaginary frequencies despite the methods used in section 3.2.3. The structures were only considered as stable if the imaginary frequencies are low frequency vibrations of a soft intermolecular translational motions exhibited by one or both species in the IP as shown in figure 3.26. A low imaginary frequency vibration is defined as a vibration which has a frequency smaller than 50 cm^{-1}. Structures with large imaginary frequencies were discarded.



-112_4_113_82

-8.49 cm^{-1} Soft Motion by both species



-148_3.7_115_-87

-4.11 cm^{-1} Soft Motion by one species

Figure 3.26: $[C_2C_1Im][AlCl_4]$ low frequency rotational and translational motion vibration examples

3.2.12 Ion pair structural evaluation

IPs were computed in the GP (without SMD, with D3BJ dispersion correction) and in the LP (with SMD and D3BJ dispersion correction) to evaluate how the solvation environment effects the formation of different IP structures. The interactions between ions were evaluated to determine which of the electronic structure methods; Fukui functions, ESPs, and NAC assignment schemes, most accurately describe the interactions featured in IP structures, in both phases. The methods which most precisely describes the interactions can be used ideally to predict the interactions between the IPs and potentially alternative chlorometallates.

The interaction profiles of all IPs have a lot of common features so only a selection of structures is presented. The structures shown have been chosen based on their relative Gibbs free energies, their interaction profiles, and structural features. Interaction profiles were selected based on the unique insight they provide into the behaviour of the HMILs in the GP and LP. The position of the ions relative to each other alongside the relative Gibbs free energies show which sites of the counter ion are most attractive. The deformation of anions and cations upon interacting, such as changes in bond angles between the ligands of the anions, contortion of an anions and bond length changes were evaluated. The rotation of the ethyl arm of the $[C_2C_1Im]^+$ cation and the ethyl hydroxyl arm of the $[Choline]^+$ cation and their position relative to the anion impact the stability of the IP structures formed and hence structural features of the cations were evaluated as well.

A comprehensive tabulation of all stable IP structures can be found in tables 9.93-9.118 in section 9.2.1 and tables 9.124-9.136, 9.138-9.150, 9.152-9.164 in section 9.2.5-7 in the appendix for each of the phases in which

they were studied, GP and LP. The structures in the results chapters and appendix are listed by name, relative Gibbs free energy in curved brackets and if there is a low imaginary frequency or the structure did not converge in the frequency analysis this is shown in square brackets with the number of low imaginary frequencies or fnc (frequency not converged), respectively. All structures featuring the imidazolium cation are shown from a top-down view of the imidazolium ring with the methyl arm on the left and the ethyl arm on the right. The view of all the remaining cations was also consistent with each other. Selected IPs are shown from alternative perspectives to give a better insight into intermolecular interactions.

The IP structures interaction profiles were evaluated from a structural perspective. The electronic structure was subsequently evaluated using AIM analysis, NCIplot and IRI analysis to confirm that the evaluation of the IP structures coincides with the electronic structure of the IPs.

Bibliography

[1] M. J. Frisch, G. W. Trucks, H. B. Schlegel, G. E. Scuseria, M. A. Robb, J. R. Cheeseman, G. Scalmani, V. Barone, G. A. Petersson, H. Nakatsuji, X. Li, M. Caricato, A. V. Marenich, J. Bloino, B. G. Janesko, R. Gomperts, B. Mennucci, H. P. Hratchian, J. V. Ortiz, A. F. Izmaylov, J. L. Sonnenberg, D. Williams-Young, F. Ding, F. Lipparini, F. Egidi, J. Goings, B. Peng, A. Petrone, T. Henderson, D. Ranasinghe, V. G. Zakrzewski, J. Gao, N. Rega, G. Zheng, W. Liang, M. Hada, M. Ehara, K. Toyota, R. Fukuda, J. Hasegawa, M. Ishida, T. Nakajima, Y. Honda, O. Kitao, H. Nakai, T. Vreven, K. Throssell, J. A. Montgomery, Jr., J. E. Peralta, F. Ogliaro, M. J. Bearpark, J. J. Heyd, E. N. Brothers, K. N. Kudin, V. N. Staroverov, T. A. Keith, R. Kobayashi, J. Normand, K. Raghavachari, A. P. Rendell, J. C. Burant, S. S. Iyengar, J. Tomasi, M. Cossi, J. M. Millam, M. Klene, C. Adamo, R. Cammi, J. W. Ochterski, R. L. Martin, K. Morokuma, O. Farkas, J. B. Foresman, and D. J. Fox. Gaussian˜16 Revision C.01, 2016. Gaussian Inc. Wallingford CT.

[2] Axel D. Becke. Density-functional thermochemistry. III. The role of exact exchange. *The Journal of Chemical Physics*, 98(7):5648–5652, 04 1993. ISSN 0021-9606. doi: 10.1063/1.464913. URL `https://doi.org/10.1063/1.464913`.

[3] Stefan Grimme, Jens Antony, Stephan Ehrlich, and Helge Krieg. A consistent and accurate ab initio parametrization of density functional dispersion correction (dft-d) for the 94 elements h-pu. *The Journal of chemical physics*, 132(15):154104, 2010.

[4] Stefan Grimme, Stephan Ehrlich, and Lars Goerigk. Effect of the damping function in dispersion corrected density functional theory. *Journal of computational chemistry*, 32(7):1456–1465, 2011.

[5] Narbe Mardirossian and Martin Head-Gordon. Thirty years of density functional theory in computational chemistry: an overview and extensive assessment of 200 density functionals. *Molecular Physics*, 115(19):2315–2372, 2017.

[6] Patricia A Hunt, Barbara Kirchner, and Tom Welton. Characterising the electronic structure of ionic liquids: an examination of the 1-butyl-3-methylimidazolium chloride ion pair. *Chemistry–A European Journal*, 12(26):6762–6775, 2006.

[7] Heiko Niedermeyer, Jason P Hallett, Ignacio J Villar-Garcia, Patricia A Hunt, and Tom Welton. Mixtures of ionic liquids. *Chemical Society Reviews*, 41(23):7780–7802, 2012.

[8] Richard P Matthews, Tom Welton, and Patricia A Hunt. Competitive pi interactions and hydrogen bonding within imidazolium ionic liquids. *Physical Chemistry Chemical Physics*, 16(7):3238–3253, 2014.

[9] Rebecca Rowe, Kevin RJ Lovelock, and Patricia A Hunt. Bi (iii) halometallate ionic liquids: Interactions and speciation. *The Journal of Chemical Physics*, 155(1):014501, 2021.

[10] Martin Head-Gordon, John A Pople, and Michael J Frisch. Mp2 energy evaluation by direct methods. *Chemical physics letters*, 153(6):503–506, 1988.

[11] John D Watts and Rodney J Bartlett. The coupled-cluster single, double, and triple excitation model for open-shell single reference functions. *The Journal of chemical physics*, 93(8):6104–6105, 1990.

[12] Stanislaw A Kucharski and Rodney J Bartlett. The coupled-cluster single, double, triple, and quadruple excitation method. *The Journal of chemical physics*, 97(6):4282–4288, 1992.

[13] Aleksandr V Marenich, Christopher J Cramer, and Donald G Truhlar. Universal solvation model based on solute electron density and on a continuum model of the solvent defined by the bulk dielectric constant and atomic surface tensions. *The Journal of Physical Chemistry B*, 113(18):6378–6396, 2009.

[14] RBJS Krishnan, J Stephen Binkley, Rolf Seeger, and John A Pople. Self-consistent molecular orbital methods. xx. a basis set for correlated wave functions. *The Journal of chemical physics*, 72(1):650–654, 1980.

[15] Michelle M Francl, William J Pietro, Warren J Hehre, J Stephen Binkley, Mark S Gordon, Douglas J DeFrees, and John A Pople. Self-consistent molecular orbital methods. xxiii. a polarization-type basis set for second-row elements. *The Journal of Chemical Physics*, 77(7):3654–3665, 1982.

[16] AD McLean and GS Chandler. Contracted gaussian basis sets for molecular calculations. i. second row atoms, z= 11–18. *The Journal of chemical physics*, 72(10):5639–5648, 1980.

[17] P Jeffrey Hay and Willard R Wadt. Ab initio effective core potentials for molecular calculations. potentials for k to au including the outermost core orbitals. *The Journal of chemical physics*, 82(1): 299–310, 1985.

[18] Thom H Dunning Jr. Gaussian basis sets for use in correlated molecular calculations. i. the atoms boron through neon and hydrogen. *The Journal of chemical physics*, 90(2):1007–1023, 1989.

[19] Rick A Kendall, Thom H Dunning Jr, and Robert J Harrison. Electron affinities of the first-row atoms revisited. systematic basis sets and wave functions. *The Journal of chemical physics*, 96(9):6796–6806, 1992.

[20] David E Woon and Thom H Dunning Jr. Gaussian basis sets for use in correlated molecular calculations. iii. the atoms aluminum through argon. *The Journal of chemical physics*, 98(2):1358–1371, 1993.

[21] Andreas Bergner, Michael Dolg, Wolfgang Küchle, Hermann Stoll, and Heinzwerner Preuß. Ab initio energy-adjusted pseudopotentials for elements of groups 13–17. *Molecular Physics*, 80(6):1431–1441, 1993.

[22] Varinia S Bernales, Aleksandr V Marenich, Renato Contreras, Christopher J Cramer, and Donald G Truhlar. Quantum mechanical continuum solvation models for ionic liquids. *The Journal of Physical Chemistry B*, 116(30):9122–9129, 2012.

[23] M Gutowski, JH Van Lenthe, J Verbeek, FB Van Duijneveldt, and G Chałasinski. The basis set superposition error in correlated electronic structure calculations. *Chemical Physics Letters*, 124(4): 370–375, 1986.

[24] Tian LU and Fei-Wu CHEN. Comparison of computational methods for atomic charges. *Acta Physico-Chimica Sinica*, 28(1):1–18, 2012.

[25] Alan E Reed, Robert B Weinstock, and Frank Weinhold. Natural population analysis. *The Journal of Chemical Physics*, 83(2):735–746, 1985.

[26] Robert S Mulliken. Electronic population analysis on lcao–mo molecular wave functions. i. *The Journal of Chemical Physics*, 23(10):1833–1840, 1955.

[27] Per-Olov Löwdin and Harrison Shull. Natural orbitals in the quantum theory of two-electron systems. *Physical Review*, 101(6):1730, 1956.

[28] Per-Olov Löwdin. Quantum theory of many-particle systems. i. physical interpretations by means of density matrices, natural spin-orbitals, and convergence problems in the method of configurational interaction. *Physical Review*, 97(6):1474, 1955.

[29] Tian Lu and Feiwu Chen. Atomic dipole moment corrected hirshfeld population method. *Journal of Theoretical and Computational Chemistry*, 11(01):163–183, 2012.

[30] Curt M Breneman and Kenneth B Wiberg. Determining atom-centered monopoles from molecular electrostatic potentials. the need for high sampling density in formamide conformational analysis. *Journal of Computational Chemistry*, 11(3):361–373, 1990.

[31] Richard FW Bader. Atoms in molecules. *Accounts of Chemical Research*, 18(1):9–15, 1985.

[32] Julia Contreras-García, Erin R Johnson, Shahar Keinan, Robin Chaudret, Jean-Philip Piquemal, David N Beratan, and Weitao Yang. Nciplot: a program for plotting noncovalent interaction regions. *Journal of chemical theory and computation*, 7(3):625–632, 2011.

[33] Tian Lu and Qinxue Chen. Interaction region indicator: A simple real space function clearly revealing both chemical bonds and weak interactions. *Chemistry-Methods*, 1(5):231–239, 2021.

[34] Tian Lu and Feiwu Chen. Multiwfn: A multifunctional wavefunction analyzer. *Journal of computational chemistry*, 33(5):580–592, 2012.

[35] William Humphrey, Andrew Dalke, and Klaus Schulten. Vmd: visual molecular dynamics. *Journal of molecular graphics*, 14(1):33–38, 1996.

[36] Jake M Seymour, Ekaterina Gousseva, Alexander I Large, Coby J Clarke, Peter Licence, Richard M Fogarty, David A Duncan, Pilar Ferrer, Federica Venturini, Roger A Bennett, et al. Experimental measurement and prediction of ionic liquid ionisation energies. *Physical Chemistry Chemical Physics*, 23(37):20957–20973, 2021.

[37] J Estager, JD Holbrey, and Malgorzata Swadźba-Kwaśny. Halometallate ionic liquids–revisited. *Chemical Society Reviews*, 43(3):847–886, 2014.

[38] Colin R Groom, Ian J Bruno, Matthew P Lightfoot, and Suzanna C Ward. The cambridge structural database. *Acta Crystallographica Section B: Structural Science, Crystal Engineering and Materials*, 72 (2):171–179, 2016.

Chapter 4

Isolated Ions

This chapter discusses the group 13 Chlorometallate structures which were found to be stable in the gas phase (GP) and/or liquid phase (LP). All starting structures which were described in section 3.2.1 were computed and the resulting stable structures in both phases are presented in this section. The Gibbs free energies of constitutional and conformational isomers are compared to determined which isomers are representative of the lowest energy state of a molecular configuration. The most stable states are used to determine the speciation in the GP and LP by comparing the Gibbs free energy of different possible speciations as described in section 3.2.4. The anionic speciation is discussed in depth in chapter 7.

4.1 Isolated group 13 chlorometallate structures in the gas phase and liquid phase

Within this section the figures depict stick-and-ball representations of structures, where the group 13 metals; aluminium, gallium and indium are represented by pink and purple coloured spheres and the chlorine atoms are depicted as lime green spheres as shown in figure 4.1.

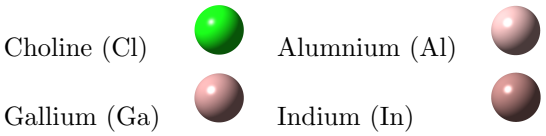


Figure 4.1: The colour scheme of chlorine, aluminium, gallium and indium atoms in this chapter

If the optimization of a structure has not completed successfully, the reason is noted by an acronym in the figures. If a structure dissociated during the optimization process it is denoted SD (structure dissociated). When a structure optimized but during the frequency analysis it was determined to be a transition state structure featuring one high imaginary frequency it is denoted a TS (transition state) structure. When a structure converged but featured multiple high imaginary frequencies, it is denoted MHF (Multiple high frequencies). When structures converged to TS structures or feature MHF they are not considered stable structures. A starting structure which converged to a structure already known to be stable is denoted as converges to XX, where XX is a number representing the starting structure which the computation converged to. A full list of numbers corresponding to different structures can be found in the appendix section 9.1.1.

4.1.1 Gas phase group 13 chlorometallate structures

This subsection presents and discusses the stable chlorometallate GP structures. In the GP, 67 distinct chlorometallate structures were found within the threshold of the optimization and frequency analysis convergence criteria; 23 chloroalluminate, 23 chlorogallate and 22 chloroindate structures. All stable structures are shown this subsection. The discussion of structures in this section is subdivided by the number of metal centres in the species. An extensive list of all starting structures and corresponding stable GP structures can be found in the appendix section 9.1.1.

Stable monometallic structures in the gas phase

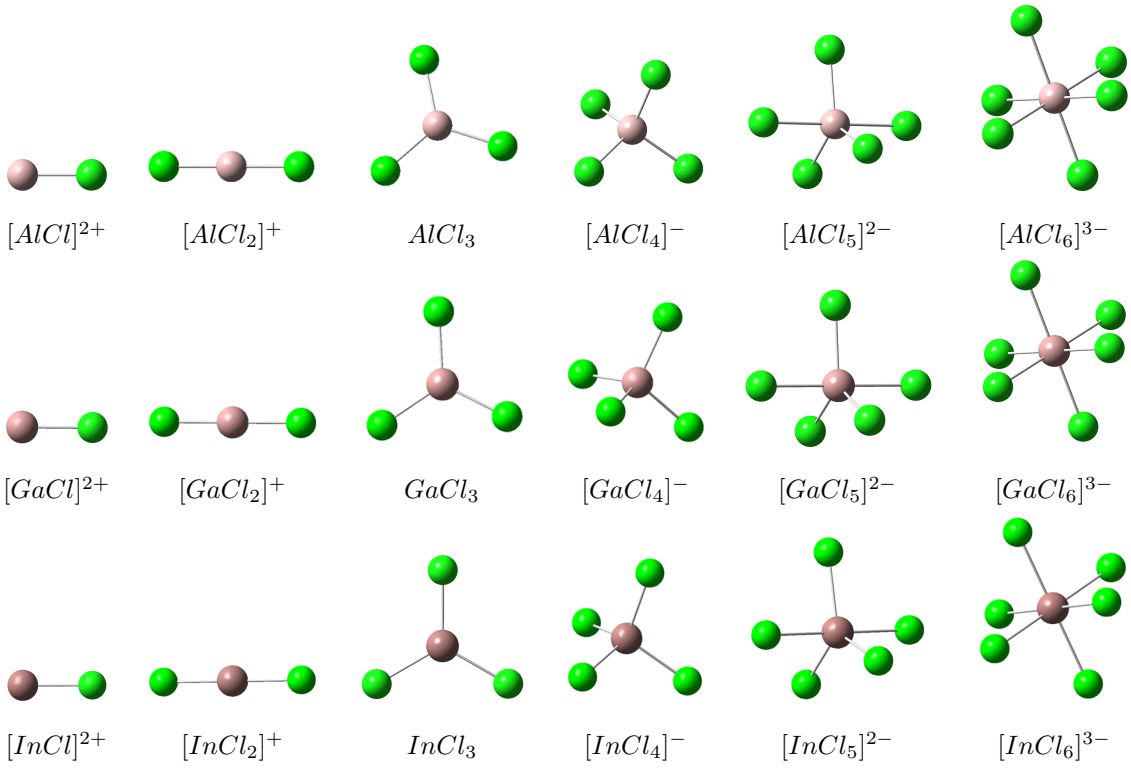


Figure 4.2: Optimized monometallic chlorometallate species in the gas phase

In the GP the complete series of monometallic homologs; $[MCl]^{2+}$, $[MCl_2]^{+}$, MCl_3, $[MCl_4]^{-}$, $[MCl_5]^{2-}$ and $[MCl_6]^{3-}$ were found to have stable structures. Each species has a distinct molecular geometry which is consistent across chloroaluminates, chlorogallates and chloroindates, as depicted in figure 4.2. The $[MCl]^{+2}$ and $[MCl_2]^{+}$ cations have a linear geometry. The MCl_3 species have a trigonal planer geometry while the

$[MCl_4]^-$ anions has tetrahedral geometry. The $[MCl_5]^{-2}$ anion arranges in a trigonal bipyramidal geometry and the $[MCl_6]^{-3}$ anion is configured in an octahedral geometry. The chemical structures of the monometallic complexes are analogous across the three metals. The bond angles of the stable structures are consistent across all metals while the M-Cl bond distances get longer when going down the group.

Stable bimetallic structures in the gas phase

Among the bimetallic structures, stable structures were found for all species containing between 3 and 7 chlorides for all metals in the GP. Stable GP structures with 9 and 10 chlorides were found exclusively in chloroaluminate and chloroindate systems as the chlorogallate structures dissociated during the optimization. The $[M_2Cl_4]^{2+}$, M_2Cl_6, $[M_2Cl_7]^-$, $[M_2Cl_9]^{3-}$ and $[M_2Cl_{10}]^{4-}$ structures found, depicted in figure 4.3, are structurally analogous across the group.

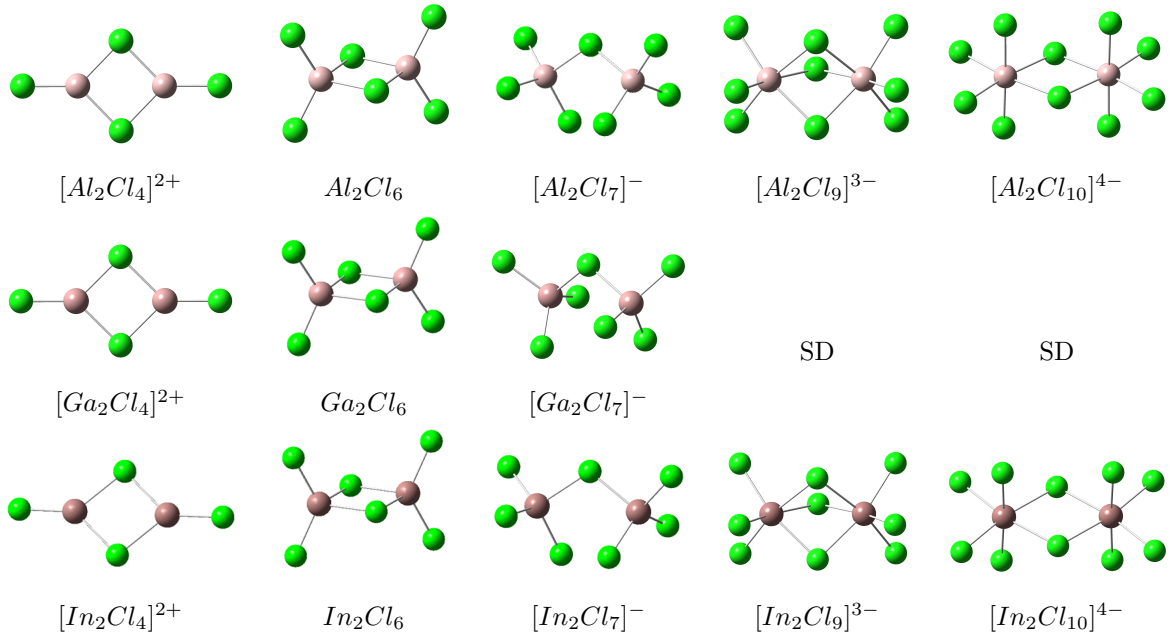


Figure 4.3: Stable $[M_2Cl_4]^{2+}$, M_2Cl_6, $[M_2Cl_7]^-$, $[M_2Cl_9]^{3-}$, and $[M_2Cl_{10}]^{4-}$ species in the gas phase, SD = structure dissociates

$[M_2Cl_4]^{2+}$, depicted in the first column of figure 4.3 are two joint trigonal planer geometries sharing two chlorides. M_2Cl_6 and $[M_2Cl_7]^-$, in the next two columns over are arranged as two tetrahedral structures sharing two chlorides and one chloride, respectively. In the last two columns $[M_2Cl_9]^{3-}$ and $[M_2Cl_{10}]^{4-}$ are two octahedral structures sharing three and two chlorides, respectively.

Multiple stable constitutional isomers of $[M_2Cl_3]^{3+}$ and $[M_2Cl_5]^{+}$ were found in the GP for each metal. The dimetallic isomers with three and five chlorides can be differentiated by the number of bridging and terminal chlorides. The stable GP structures of $[M_2Cl_3]^{3+}$ and $[M_2Cl_5]^{+}$ are depicted in figures 4.4 and 4.5, respectively.

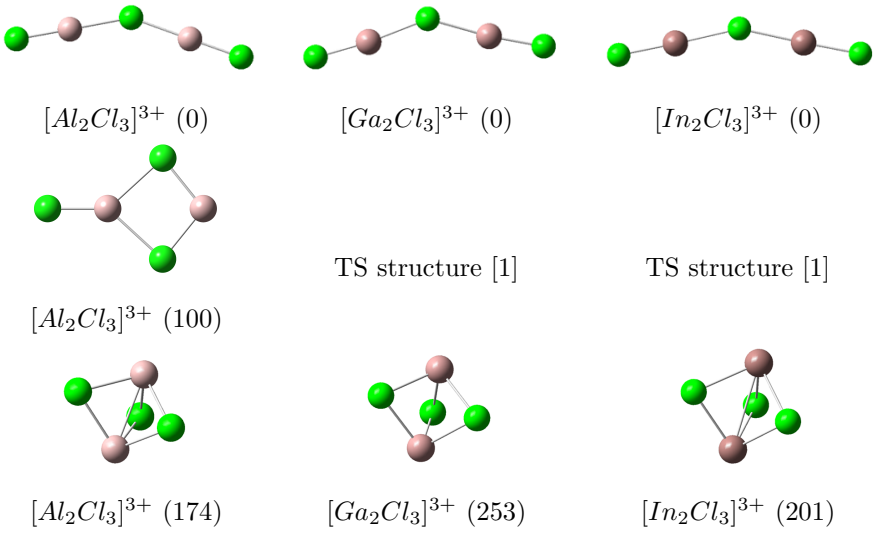


Figure 4.4: Stable $[M_2Cl_3]^{3+}$ species in the gas phase, relative Gibbs free energy in kJ mol^{-1}, TS structure = transition state structure

In the GP there is a preference for singly Cl-bridged $[M_2Cl_3]^{3+}$ structures. Among the chloroaluminate structures the doubly Cl-bridged structure is 100 kJ mol^{-1} and the triply Cl-bridged structure is 174 kJ mol^{-1} higher in energy than the singly Cl-bridged structure. The trend in Gibbs free energy with respect to the number of bridging chlorides indicates that the formation of doubly and triply bridged complexes is highly unfavourable in the GP. The preference for the singly Cl-bridged structures is likely due to a combination of maximizing the distance between the highly charged M centres, and minimizing the steric strain generated by small M-Cl-M angles. For example, for the conformers of increasing energy the r(Al-Al) is 4.40Å, 3.16Å and 2.54Å respectively. The close proximity of the metals in the triply bridged structure causes the Van der Waals radii of the Al and In metal centres to overlap, indicated by the bond between the triply bridged structure.

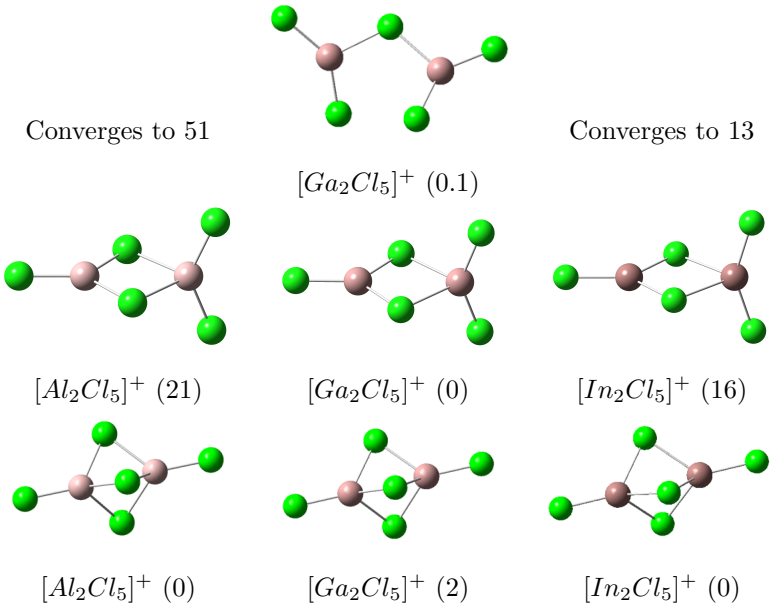


Figure 4.5: Stable dimetallic $[M_2Cl_5]^+$ species in the gas phase, relative Gibbs free energy in kJ mol^{-1}, converges to XX = converges to an alternative conformational isomer which can be found in the appendix

The $[M_2Cl_5]^+$ structures also have varying numbers of bridging and terminal chlorides. For $[M_2Cl_5]^+$ the correlation between stability and the number of bridging chlorides is miniscule. The largest ΔG is 21 kJ mol^{-1} between the doubly and triply bridged isomers of the chloroaluminate system, depicted in the second and third row in the first column of figure 4.5 respectively. The low relative ΔG of the doubly and triply bridged $[Al_2Cl_5]^+$ isomers indicates they are easily accessible in the GP. The doubly and triply bridged $[In_2Cl_5]^+$ isomers have a ΔG of 16 kJ mol^{-1} so both structures are accessible in the GP. The singly and triply bridged $[Ga_2Cl_5]^+$ isomers are 0.1 and 2 kJ mol^{-1} less stable than the doubly bridged isomer. The ΔG of the $[Ga_2Cl_5]^+$ isomers is so marginal that it falls within the error margin of the method. Consequentially one $[Ga_2Cl_5]^+$ isomer is not conclusively more stable than another and can be regarded as energetically degenerate in the GP.

The low differences in energy are unexpected considering the results from the $[M_2Cl_3]^{3+}$. In $[M_2Cl_5]^+$ species there is a lower overall charge on the species resulting in lower Coulomb repulsion between the metal centres. Moreover, there are more Cl anions which are better able to screen the positive charge. For example, r(Al-Al) for the triply and doubly Cl bridged conformers is 2.69Å and 3.20Å respectively.

Stable trimetallic structures in the gas phase

The starting structures of the trimetallic and tetrametallic complexes were more selectively chosen, see section 3.2.1. The starting structures were selected based on known speciation of group 13 HMILs.[1] Therefor the results for the structures featuring three and four metal centres are indicative but not conclusive of which structures are a part of the chlorometallate speciation. The computations of trimetallic structures indicate that there is one stable $[M_3Cl_{10}]^-$ structure, in two different conformations, depicted on the two top rows of figure 4.6. Two distinct M_3Cl_9 structures, shown on the two bottom rows of figure 4.6, were found to be stable. The trimetallic chlorometallate structures are analogous across all three metals.

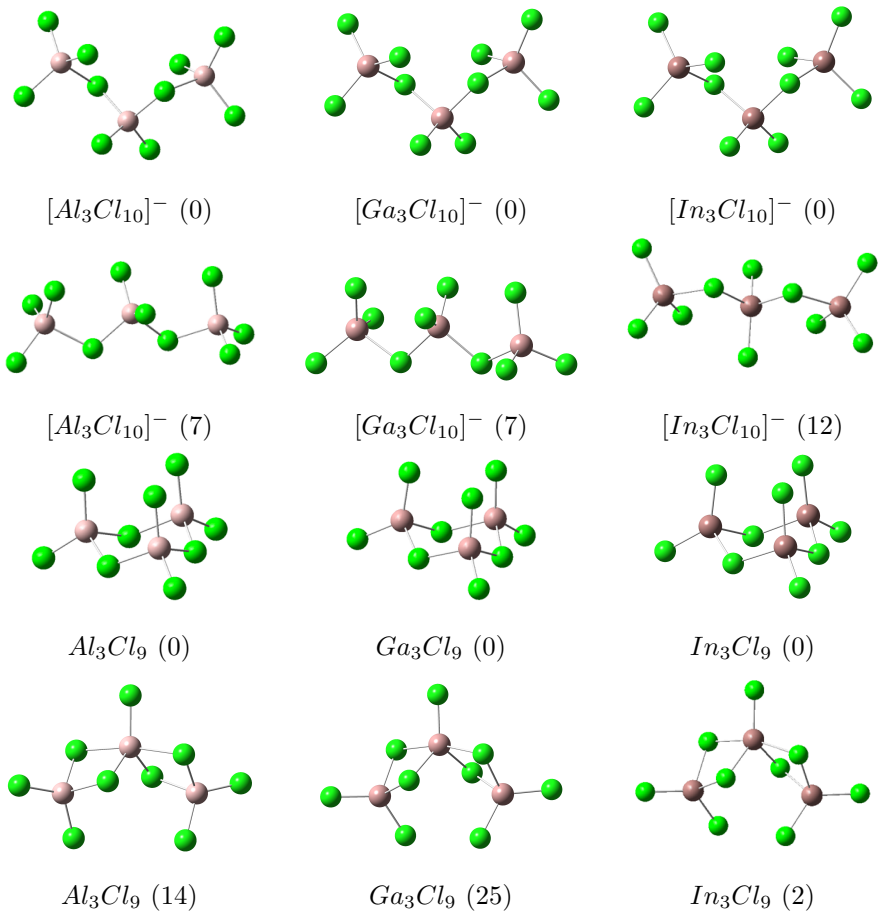


Figure 4.6: Stable trimetallic species in the gas phase, relative Gibbs free energy in kJ mol^{-1}

The $[M_3Cl_{10}]^-$ structures in the two top rows of figure 4.6 are conformational isomers. The conformers on the top row of figure 4.6 are more contracted than the conformers on the second row which are more elongated. The two conformers indicate that the linear $[M_3Cl_{10}]^-$ structure has the ability to fold. The

elongated structures are 7, 7 and 12 kJ mol^{-1} higher in energy than the contracted ones in the Al, Ga and In systems, respectively. The flexibility observed for $[M_3Cl_{10}]^-$ warrants further investigation as the reason why the contracted structures are more stable is not clear.

Chlorogallate[2] and chloroindate[1] $[M_3Cl_{10}]^-$ structures have not been identified in the GP by MS speciation studies and $[Al_3Cl_{10}]^-$ has only been found in small amounts by one study.[3] Three other MS studies of chloroaluminate species did not identify $[Al_3Cl_{10}]^-$ at $x_{MCl_3} = 0.67$. In MS studies of the GP speciation of the group 13 chlorometallate systems the $[M_2Cl_7]^-$ complexes were identified at $x_MCl_3 > 0.5$ and above but the $[M_3Cl_{10}]^-$ structures could not be found.[2,4,5] The structures found here indicate that trimetallic complexes are stable in the GP.

The MS procedure likely leads to the fragmentation of $[M_3Cl_{10}]^-$ complexes. The MS studies of group 13 chlorometallate systems have not been carried out at $x_{MCl_3} > 0.67$ so $[M_3Cl_{10}]^-$ could possibly be identified at higher x_{MCl_3}. However, due to the relatively low abundance of $[M_2Cl_7]^-$ identified in the chloroaluminate and chlorogallate systems by MS the multimetallic complexes may be too prone to fragmentation, even at high x_{MCl_3}, to be stabilized.

In the LP the precipitation of $InCl_3$ beyond $x_{InCl_3} = 0.5$ prevents the formation of multimetallic complexes but through perturbations associated with MS the formation of $[In_2Cl_7]^-$ is possible.[1] At a molecular level, the precipitation and thus removal of $InCl_3$ prevents the local accumulation of indium chloride required to form species with more than two metal centres. Moreover, The formation of trimetallic chloroindate complexes has not been achieved at any level of x_{InCl_3}.

The M_3Cl_9 ring structure, shown in the third row of figure 4.6 is most stable isomer for each chlorometallate system in the GP. The other M_3Cl_9 structure, depicted in the bottom row of figure 4.6, has a linear geometry featuring the metal centres doubly bridged by chloride ligands. The linear M_3Cl_9 structures are 14, 25 and 2 kJ mol^{-1} less stable than the ring structures for Al, Ga and In respectively. The ring structures are likely more stable because there is less torsional strain on the bonds. $[Al_3Cl_9]^-$ has been identified in a MS study but the molecular structure was not determined.[2] The relative stability of the ring and linear structures determined here indicate that the ring structure will dominate but the linear isomer may occur in small quantities. A ring structure will better stabilize the -1 charge in the GP, however external influences such as local solvation and/or coulomb shielding in the LP may allow the linear structure to be further stabilized.

Stable tetrametallic structures in the gas phase

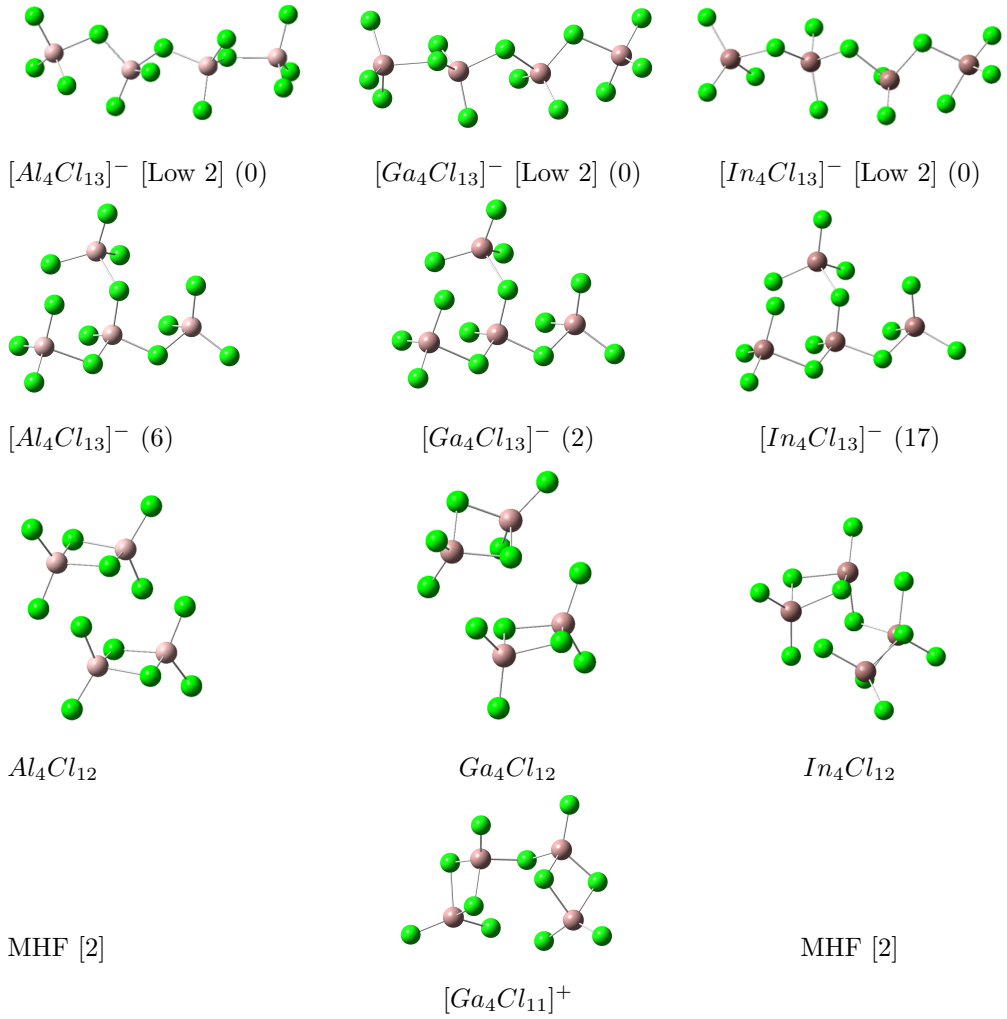


Figure 4.7: Stable tetrametallic species in the gas phase, relative Gibbs free energy in kJ mol^{-1} where [Low X] indicates X imaginary frequencies smaller than 50 cm^{-1} and MHF indicates the structures did not converge due to the structures featuring multiple high frequencies

The calculations of tetrametallic complexes are indicative of two constitutional $[M_4Cl_{13}]^-$ isomers which are stable for each metal. There is a linear $[M_4Cl_{13}]^-$ isomer, shown in the top row of figure 4.7, and a branched $[M_4Cl_{13}]^-$ isomer, shown in the second row of the same figure. The linear isomer has previously been identified in the LP by other speciation studies while the branched isomer is novel.[1] The branched structure is only 6, 2 and 17 kJ mol^{-1} higher in energy for the Al, Ga and In systems, respectively. The low energy difference between the constitutional isomers indicates that the branched structure could feasibly be

part of the GP speciation of each chlorometallate system.

$[M_4Cl_{13}]^-$ isomers have not previously been identified by MS in the GP in the chloroaluminate, chlorogallate or chloroindate systems.[1–5] The possible reasons for $[M_4Cl_{13}]^-$ species not being found are analogous to those described for the $[M_3Cl_{10}]^-$ structures, the fragmentation occurring during MS in combination with the sample contamination by water has prevented $[M_4Cl_{13}]^-$ from forming. MS studies have not yet been carried out at x_{MCl_3} in which $[M_4Cl_{13}]^-$ structures could be expected to form. Due to precipitation of $InCl_3$, Al_2Cl_6 and Ga_2Cl_6 in the LP it may not be possible to achieve the required mol fractions in the GP.

Additionally, one M_4Cl_{12} structure was found for each of Al, Ga and In and a $[Ga_4Cl_{11}]^+$ structure was found exclusively in the chlorogallate system. Stable M_4Cl_{12} structures were found for each chlorometallate system and are depicted in the third row of figure 4.7. The M_4Cl_{12} or the $[Ga_4Cl_{11}]^+$ structures have not previously been identified by MS.

The M_4Cl_{12} structures of the chloroaluminate and chlorogallate systems optimized to two adjacent M_2Cl_6 molecules while the In_4Cl_{12} is a single continuous species. The chloroaluminate and chlorogallate systems are known to precipitate M_2Cl_6 at high x_{MCl_3} in the LP so the optimization to two separate M_2Cl_6 molecules may be indicative of the mechanism of precipitation. The calculations here were undertaken in the GP and $M_2Cl_6^-$ structures have not yet been identified in any MS investigation. The distance between the M_2Cl_6 dimers in M_4Cl_{12} is 4.90Å, 4.64Å and 3.70Å respectively for Al, Ga and In. The differences in structures are due to rotation around the M-M dimer bond shifting the relative position of bridging and terminal Cl between dimers. The preliminary survey carried out here was to confirm the stability of M_4Cl_{12} clusters, a much larger study would be needed to fully explore the conformational space.

4.1.2 Liquid phase group 13 chlorometallate structures

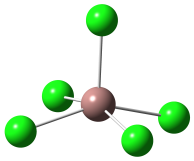
This section introduces and discusses the chlorometallate structures which were found to be stable in the LP. The structures are introduced by the number of metal centres present in each species, analogously to the GP structures. Appendix, section 9.1.4 contains an extensive list of all starting structures and the resulting stable LP structures.

Stable monometallic structures in the liquid phase

The stable monometallic structures found in the LP are analogous to those found in the GP. There are minor differences in geometric parameters like bond lengths and angles which fall within the error margin of the

method used. The molecular structures remain unchanged for all six species found to be stable in every chlorometallate system. The structures are depicted in the appendix, section 9.1.4 detailing the stable LP structures. Some structures presented here are not found in the appendix as they were not found in the structure search but through additional scans.

In the LP one additional square pyramidal $[InCl_5]^{2-}$ structure was found to be stable. Figure 4.8 shows the square pyramidal chloroindate structure.



$[InCl_5]^{2-}$ (3)

Figure 4.8: Stable square pyramidal $[InCl_5]^{2-}$ species in the liquid phase and the relative Gibbs free energy in kJ mol^{-1}

The structure is 3 kJ mol^{-1} less stable than the trigonal bipyramidal structure. The low difference in stability between the two stereoisomers indicates that both should be accessible. A scan of the berry pseudo-rotation showed that the isomerization has an energy barrier of 5 kJ mol^{-1} which indicates that both stereoisomers should be able to freely interconvert between one another at standard temperature and pressure.

Stable dimetallic structures in the liquid phase

Figure 4.9 shows the stable dimetallic structures found in the LP of atomic compositions with a single constitutional isomer. The rows in figure 4.9 represent one chlorometallate system with chloroaluminate structures in the top row followed by chlorogallate structures in the second row and chloroindate structures in the third row. Different molecular compositions are shown in each column.

The optimizations of $[Al_2Cl_{11}]^{5-}$, $[Ga_2Cl_9]^{3-}$, $[Ga_2Cl_{10}]^{4-}$ and $[Ga_2Cl_{11}]^{5-}$ ended in the l502 error message. The change to the chemical structures over the course of the optimizations were subsequently evaluated which showed the structures dissociate over the course of the optimization. The $[In_2Cl_4]^{2+}$ structure converged to zero force and displacement during the optimization but was found to have two high imaginary frequencies.

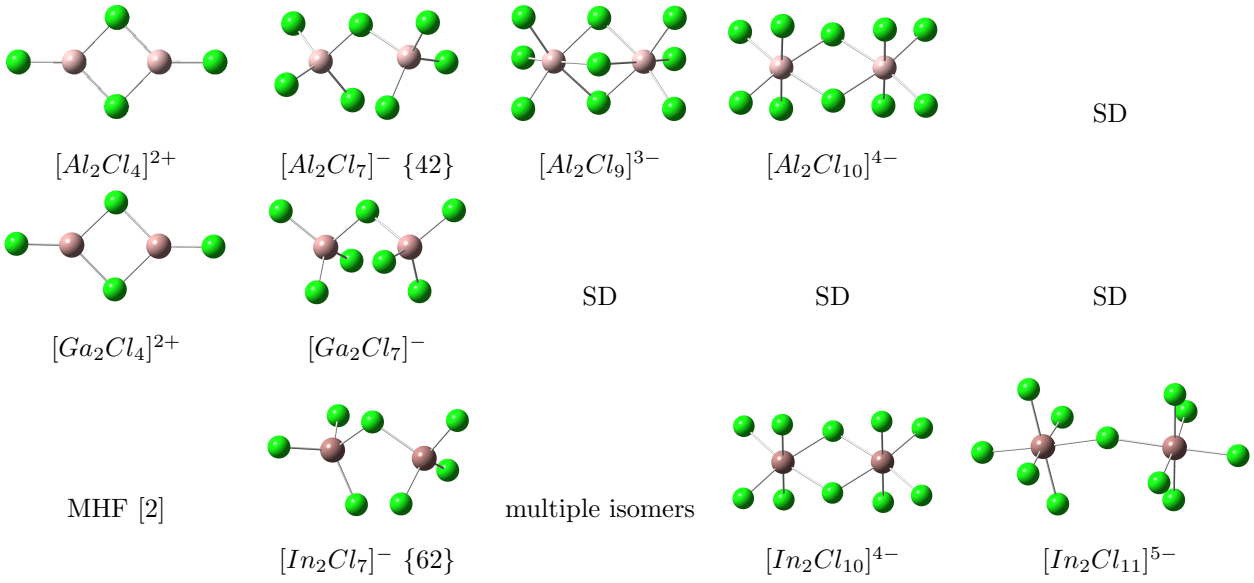


Figure 4.9: Stable $[M_2Cl_4]^{2+}$, $[M_2Cl_7]^-$, $[M_2Cl_9]^{3-}$, $[M_2Cl_{10}]^{4-}$, $[M_2Cl_{11}]^{5-}$ species in the liquid phase

Some of the geometries of the stable dimetallic structures found in the LP are analogous to those found in the GP. The $[M_2Cl_4]^{2+}$ structures of the chloroaluminate and chlorogallate systems found in the LP are the same as in the GP. The $[In_2Cl_4]^{2+}$ structure which was found to be stable in the GP did not converge to a minimum in the LP. The $[M_2Cl_7]^-$, $[Al_2Cl_9]^{3-}$ and $[M_2Cl_{10}]^{4-}$ structures are analogous in the GP and LP for all systems. The M_2Cl_6 structures and the $[In_2Cl_9]^{3-}$ structure feature two structural isomers which are shown in figure 4.12 and 4.13, respectively. The $[In_2Cl_{11}]^{5-}$ structure is exclusive to the LP and constitutes of two octahedral $InCl_6$ bridged by a single shared chloride.

the $[M_2Cl_4]^{2+}$, $[M_2Cl_9]^{3-}$, $[M_2Cl_{10}]^{4-}$ and $[M_2Cl_{11}]^{5-}$ structures have not be found previously been identified by other speciation studies in the HMIL LP. Due to the highly charged nature of these species, they are most likely unstable when compared to alternative structures and are not representative of LP speciation as they are likely to disproportionate to less charged species.

Figure 4.10 shows the constitutional isomers of structures with the $[M_2Cl_3]^{3+}$ molecular formula. In contrast to the GP, the linear singly bridged $[In_2Cl_3]^{3+}$ structure dissociated during the optimization. The doubly bridged $[M_2Cl_3]^{3+}$ structures optimized for all systems, including the chloroindate system in which it did not optimize in the GP.

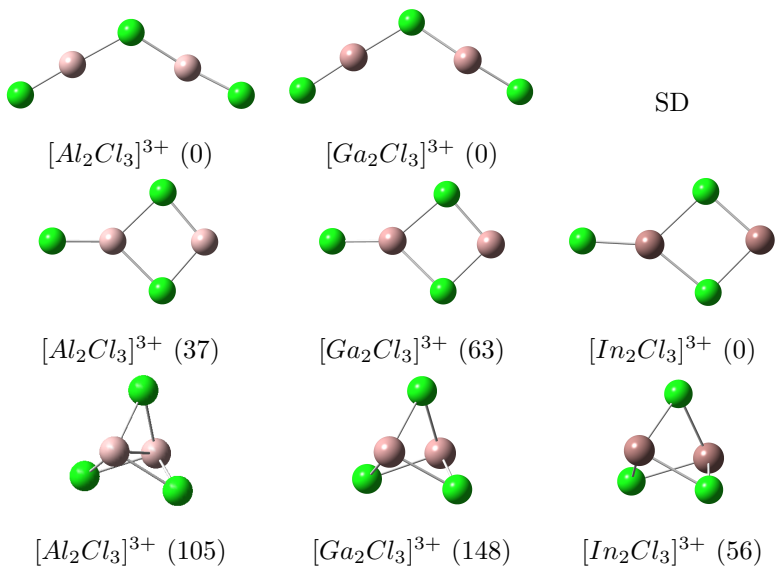


Figure 4.10: Stable $[M_2Cl_3]^{3+}$ species in the liquid phase and their relative Gibbs energy in kJ mol^{-1}

The trend of stability among the $[M_2Cl_3]^{3+}$ structures with respect to the number of bridging chlorides is the same in the LP. The fewer bridging chlorides the structure features the more stable the structures are. The singly bridged structures were found to be the most stable structure in the GP and are also in the LP for the chloroaluminate and chlorogallate systems. The doubly bridged structure is most stable for the chloroindate system over the triply bridged $[In_2Cl_3]^{3+}$. The trend in stability with respect to the number of bridging chlorides indicates that the closer proximity of the metal centres described for the GP structures translates to the LP. The magnitude of the relative stability is smaller in the LP which indicates that the less stable structures are far more stabilized. The differences in energy between the different isomers are too large to for any structure apart from the single bridged $[Al_2Cl_3]^{3+}$ and $[Ga_2Cl_3]^{3+}$ and the doubly bridged $[In_2Cl_3]^{3+}$ structures to be accessible.

Different types of reduction pathways of the species in the bulk LP are possible when reducing chlorometallate species in electrochemical procedures. The relative stability of the structures computed here could be indicative of specific pathways being more favourable when a specific chlorometallate is being reduced in the LP.

Figure 4.11 shows the constitutional isomers of the structures with the molecular formula $[M_2Cl_5]^+$. The singly bridged $[Al_2Cl_5]^+$ structure in the second row of the first column did not optimize in the GP and is exclusive to the LP. The structure in the second row of figure 4.11 has a geometry in which a trigonal planer structure and a linear MCl_2 structure sharing one of the MCl_2 chlorides. The corresponding chloroindate

and chlorogallate structures dissociated during the optimization. The other singly bridged chloroaluminate and chlorogallate structures corresponding to the $[In_2Cl_5]^+$ structure in the third column and row featured multiple high frequencies.

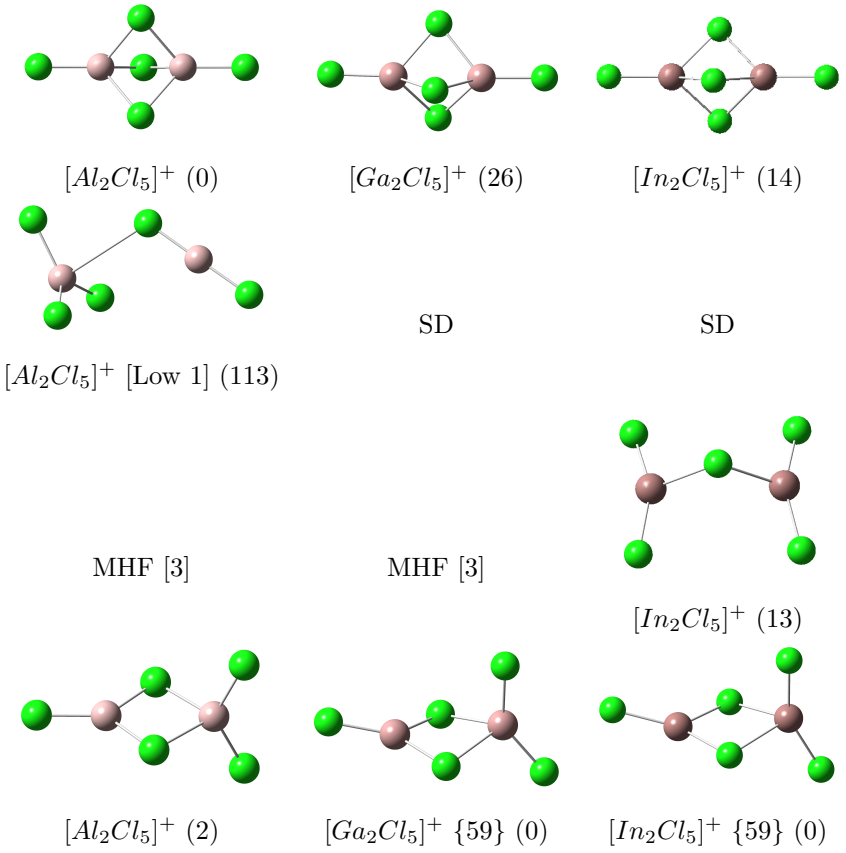


Figure 4.11: Stable $[M_2Cl_5]^+$ species in the liquid phase and their relative Gibbs energy in kJ mol^{-1}

In contrast to the GP, the doubly bridged $[M_2Cl_5]^+$ isomers, shown in the bottom row of figure 4.11, are most stable for the chlorogallate and chloroindate systems in the LP. In the chloroaluminate system, the triply bridged structure is slightly more stable than the doubly bridged isomer which are both significantly more stable than the singly bridged isomer by more than 100 kJ mol^{-1}. The doubly and triply bridged structures of the chloroaluminate systems are hence both accessible. The doubly bridged isomer in the chlorogallate system is only 26 kJ mol^{-1} more stable than the triply bridged structure. Both the doubly and triply bridged structures are accessible under normal conditions with a clear preference for the doubly bridged structure. In the chloroindate system the singly and triply bridged isomers of the system are 13 and 14 kJ mol^{-1} less stable than the doubly bridged structure, respectively. Consequentially all three of the chloroindate isomers are accessible in the LP with a preference for the doubly bridged structure.

Figure 4.12 shows the constitutional isomers of the structures with the molecular formula M_2Cl_6 found in the LP. The isomers in the top row are analogous to those which were found in the GP while the singly bridged structures in the bottom row are exclusive to the LP. The novel M_2Cl_6 isomers in the second row are a tetrahedral and a trigonal planer connected by a single bridging chloride.

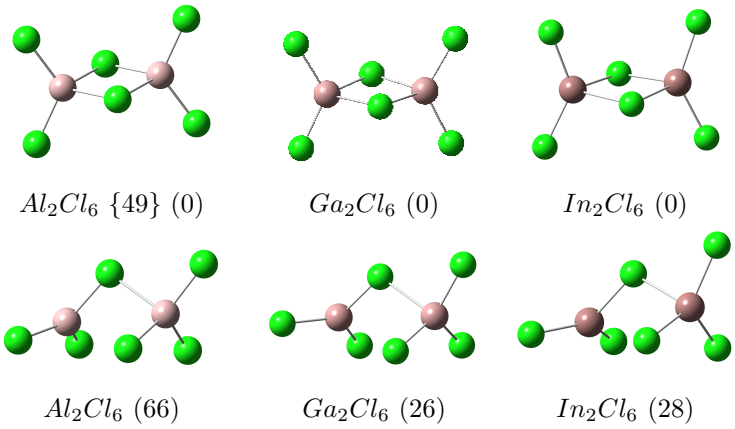


Figure 4.12: Stable M_2Cl_6 species in the liquid phase and their relative Gibbs energy in kJ mol^{-1}

The doubly bridged M_2Cl_6 isomers are more stable than the singly bridged isomers in all chlorometallate systems. The difference in stability is the most significant the chloroaluminate system at 66 kJ mol^{-1} which means the singly bridged structure is not accessible under standard conditions. In the chlorogallate and chloroindate systems the singly bridged isomers are 26 and 28 kJ mol^{-1} less stable than the doubly bridged isomers, respectively.

Figure 4.13 shows the two constitutional isomers of the $[In_2Cl_9]^{3-}$ species in the LP. The isomers depicted on the left of figure 4.13 is triply bridged and is analogous to the structure found in the GP. The isomer depicted on the right-hand side of figure 4.13 is doubly bridged and exclusive to the LP.

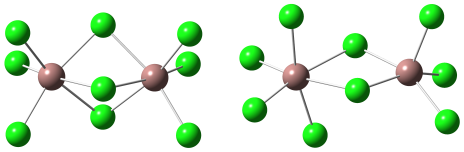


Figure 4.13: Additional Stable $[In_2Cl_9]^{3-}$ species in the liquid phase and their relative Gibbs energy in kJ mol^{-1}

The triply bridged structure is 11 kJ mol^{-1} more stable than the doubly bridged structure. Both structures are accessible under standard conditions but are likely to disproportionate relative to species with a less highly charged nature.

Scans of the $[M_2Cl_7]^-$ species

The flexibility of the $[M_2Cl_7]^-$ complexes was evaluated by scanning atomic distances and dihedral angles to determine additional stable conformations and evaluate energy barriers associated with rotation and folding. Scan coordinates were strategically selected to determine how the anions can contort to interact with their surroundings.

The distance between the terminal metals of the anions was used as a scan coordinate to scan the contortion of the multimetalic complexes. The twisting of the complexes was scanned via dihedral angles of eclipsed chlorides attached to the terminal metals and the terminal metals in each of the complexes. The scan coordinates of the twisting scan are in the order Cl-M-M-Cl.

The contortion scans of the $[M_2Cl_7]^-$ depicting the SCF energy relative to the scan coordinate is depicted on the left of figure 4.14. The $[M_2Cl_7]^-$ scan coordinate is depicted on the right hand side of figure 4.14 in turquoise.

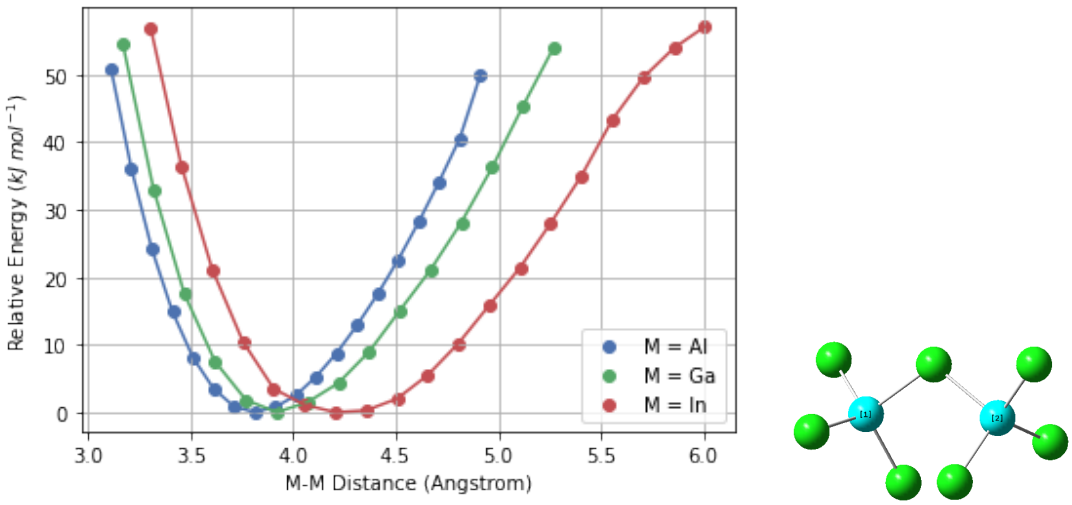


Figure 4.14: liquid phase $[M_2Cl_7]^-$ contortion scans and scan coordinate (M(1)-M(2) distance) with respect to SCF energy where M=Al, Ga or In

The $[M_2Cl_7]^-$ anions flexibility can be viewed through the chloride bridges as springs. The stability of the

$[M_2Cl_7]^-$ anion changes with respect to the M-M bond distance according to Hooke's law. The energy profile with respect to the scan coordinate is a parabola for the chloroaluminate, chlorogallate and chloroindate species. The structure can fold by changing the M-M bond distance within a range confined by the total energy of the system. The relative energy of this spring motion can be used to parameterize components of force fields that can be used in molecular dynamics computation to evaluate the systems at larger scales. The M-M distance which corresponds to the lowest energy $[M_2Cl_7]^-$ structure becomes larger going down group 13 from Al to In. The location of the minima show that the M-M distance at the minima of the chloroaluminate and chlorogallate systems are closer together than the M-M distance of the chloroindate system.

The $[M_2Cl_7]^-$ anions can also contort by rotating across the M-Cl-M bridge. The rotation can be evaluated by scanning the dihedral angle of the M-Cl planes of the terminal metals and chlorides. The scan coordinate of $[M_2Cl_7]^-$ dihedral angles scanned is depicted on the right hand side of figure 4.15. The rotation across the M-Cl-M bridge gives insight into the energy barriers associated with the rotation.

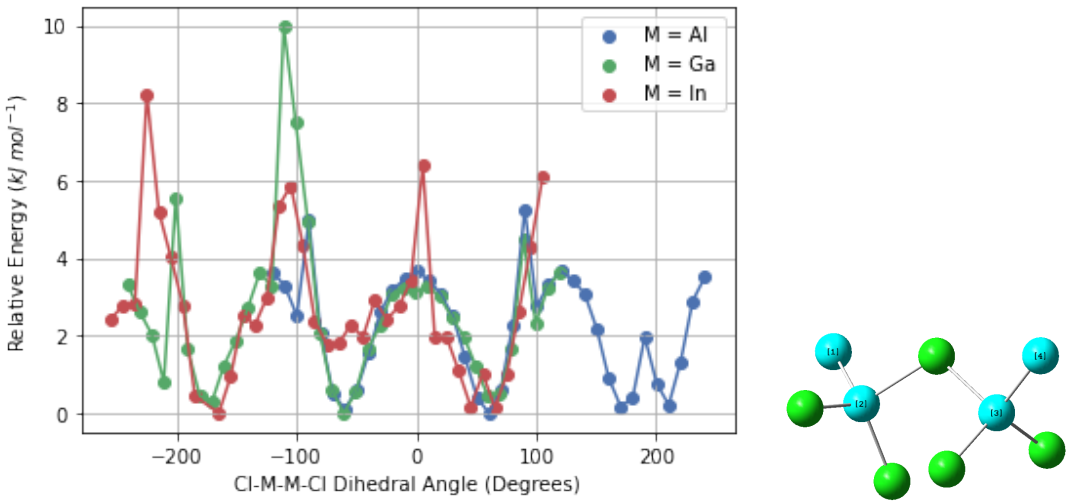


Figure 4.15: $[M_2Cl_7]^-$ rotational scans and scan coordinates (Cl(1)-M(2)-M(3)-Cl(4) dihedral angle) with respect to SCF energy where M = Al, Ga or In

The energy energy profile of the twisting scans of the $[M_2Cl_7]^-$ species are similar in all chlorometallate species. The magnitude in energy profiles varies, particularly at a scan coordinate of approximately -110^o. The large relative SCF energy of the chlorogallate complex is due to two terminal chlorides eclipsing each other. The relative energy of the all different contortions do not exceed 10 kJ mol^{-1} which means all structures are accessible and the terminal units can rotate fully in both directions. No novel confirmations

were found through the twisting scans.

The twisting of the dimetallic species show that there are two main factors to the stabilization of the different conformers. The factors effecting the energy are related to the proximity of chlorides and can be split into the proximity of terminal chlorides to one another and the proximity of terminal chlorides to bridging chlorides. The proximity of two terminal chlorides is the larger contributing factor to the structures energy. In the highest energy structures of $[M_2Cl_7]^-$ feature two terminal chlorides, attached to different metal centers, in a proximity of approximately 3.6 Angstroms in the chloroaluminate and chlorogallate systems and 3.8 Angstroms in the chloroindate system which contributes to the rise in energy that both the chloroaluminate, chlorogallate and chloroindate structures structures experience as depicted on the left side of figure 4.16.

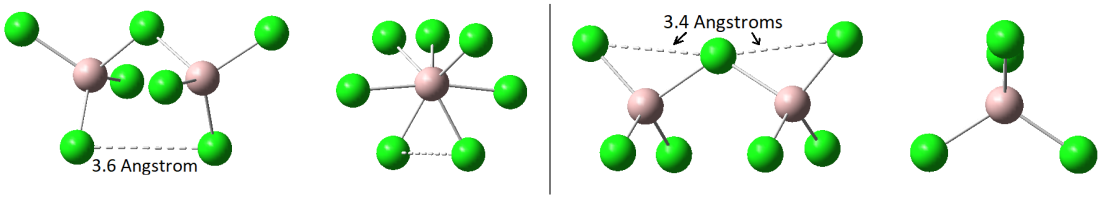


Figure 4.16: Structural features contributing to high energy in the $[Al_2Cl_7]^-$ structure at scan coordinate -90 (right) and 0 (left) from a side and front view

The eclipsing of two terminal chlorides with the bridging chloride is the second largest factor in inducing a rise in energy. Two of the terminal chlorides within 3.4 (Al), 3.5 (Ga), 3.7 (In) Angstroms of the bridging chloride cause the energy to rise but less so than the two terminal chlorides in close proximity. The minima of $[M_2Cl_7]^-$ effectively minimize the proximity of both sets of chlorides by staggering and maximizing terminal - terminal chloride and terminal - bridging chloride distance. The proximity of the chlorides being a contributing factor also coincides with the data of the contortion scans of the $[M_3Cl_{10}]^-$ and $[M_4Cl_{13}]^-$ species which showed that the structures with eclipsed chlorides were less stable. The terminal chlorides likely have a higher charge density than the bridging chlorides and hence the repulsion between the terminal chlorides is stronger leading to a larger magnitude of energy increase upon eclipsing. The charge distribution analyses should confirm this.

Stable trimetallic structures in the liquid phase

As in the GP, a limited selection of starting structures was used to evaluate trimetallic and tetrametallic complexes in the LP. The results for the trimetallic and tetrametallic species are indicative and not conclusive of possible structures which make up the anionic speciation of the investigated chlorometallate systems.

Figure 4.17 show the different conformers of the linear $[M_3Cl_{10}]^-$ isomers. The linear $[M_3Cl_{10}]^-$ isomers were all found through optimizations of starting guess structures and optimizing and frequency analysing minimums which were found when scanning the flexibility of the structure by changing the distance between the terminal metals. Each linear $[M_3Cl_{10}]^-$ conformer is described with its relative energy and the distance between the terminal metals.

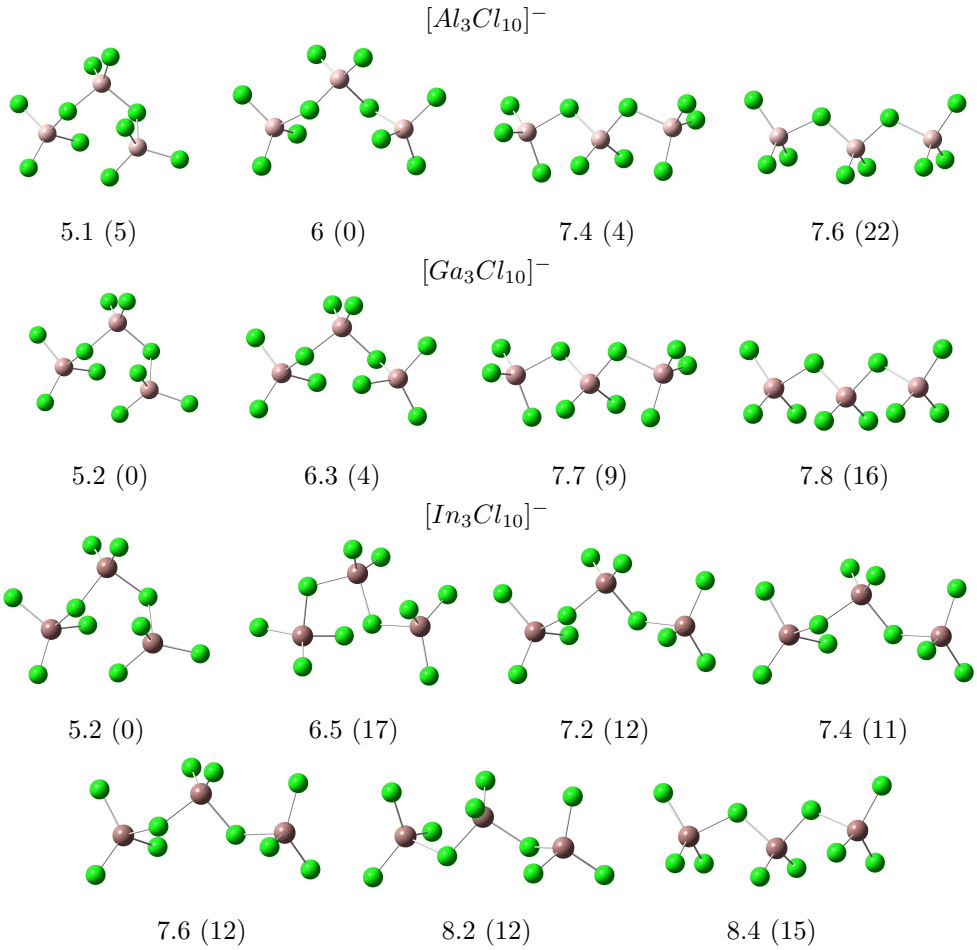


Figure 4.17: Stable linear $[M_3Cl_{10}]^-$ conformers in the liquid phase, terminal indium - terminal indium distance in Angstrom and relative Gibbs free energies (kJ mol^{-1})

The linear $[M_3Cl_{10}]^-$ conformers are distinguished by the degree of each conformers contortion which is measured by the metal - metal distance between the terminal metals. The distance between the terminal metals of the conformers depicted in figure 4.17 increases when moving from left to right across the rows which corresponds to a change in relative stability.

The stable conformers of the linear $[M_3Cl_{10}]^-$ isomers found in the LP and their relative stability are

indicative of the isomers flexibility. The linear $[Al_3Cl_{10}]^-$ and $[Ga_3Cl_{10}]^-$ isomers both have four stable conformers while the $[In_3Cl_{10}]^-$ has seven stable conformers. The relative Gibbs free energy of all the conformers of the linear isomers are within 22 kJ mol^{-1} of the lowest energy structures meaning they are all accessible states. The chloroaluminate and chlorogallate systems both feature three conformers within 10 kJ mol^{-1} while the linear $[In_3Cl_{10}]^-$ structure features one distinctly more stable conformer with a metal - metal distance of 5.2 Å.

For the linear $[Ga_3Cl_{10}]^-$ and $[In_3Cl_{10}]^-$ isomers the conformers with the shortest metal - metal distance are the most stable conformers. The $[Al_3Cl_{10}]^-$ conformer with the second shortest metal - metal distance is the most stable conformer in the chloroaluminate system. The larger M-Cl bond distances in the chlorogallate and chloroindate structures likely allow for more contortion in contrast to the chloroaluminate structure.

The energy difference between the conformers of all linear $[M_3Cl_{10}]^-$ conformers are low enough that interactions with the anions could make each conformation feasible. I.e. if a the $[Al_3Cl_{10}]^-$ conformer with the longest metal - metal distance at 22 kJ mol^{-1} results in better inter molecular interactions with the surrounding environment it may be more stable in the bulk solution. The IP calculations will give additional insight into the change in relative stability with respect to changes in the conformation.

Figure 4.18 shows the stable non-linear $[M_3Cl_{10}]^-$ isomers. Each chlorometallate system features a ring structure with a chloride localized in the centre, depicted in the top row of figure 4.18. One additional structure was found in the chloroindate system which resembles a MCl_2 surrounded by two MCl_4 tetrahedrons where the central metal of the MCl_2 unit binds with two of the chlorides from each MCl_4 unit in an octahedral configuration.

The relative stability of each ring isomer indicates that the linear isomers are more favourable than the ring isomer. The $[M_3Cl_{10}]^-$ ring isomers with a central chloride are all at least 43 kJ mol^{-1} higher in energy than the lowest energy linear $[M_3Cl_{10}]^-$ conformers. In the chloroaluminate system the ring structure is 111 kJ mol^{-1} less stable. In the chlorogallate and chloroindate systems the ring structures are 47 and 43 kJ mol^{-1} less stable, respectively.

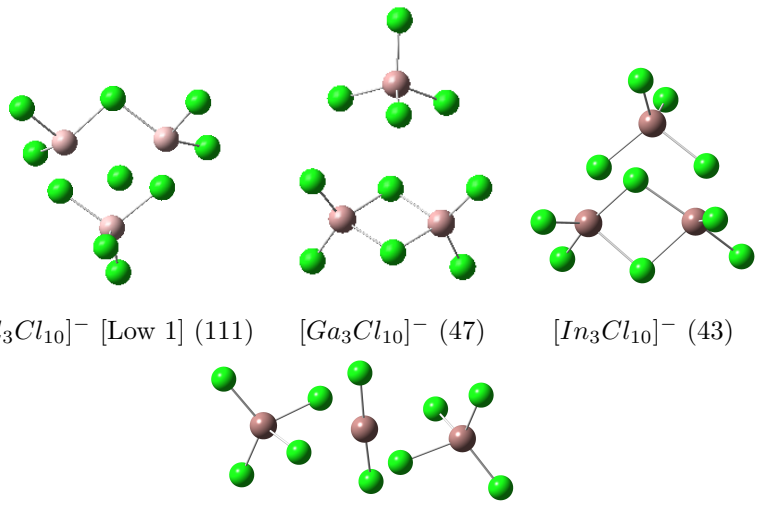


Figure 4.18: Stable non-linear $[M_3Cl_{10}]^-$ species in the liquid phase and their relative Gibbs energy in kJ mol^{-1}

The $[M_3Cl_{10}]^-$ ring isomers of the chloroaluminate system is visually different from the ring isomers of the chlorogallate and chloroindate system. The chloroaluminate structure looks like a singly bridged $[Al_2Cl_5]^+$ and a tetrahedral $[AlCl_4]^-$ arranged around a loose chloride ion. The chlorogallate and chloroindate isomers look like the $[M_3Cl_{10}]^-$ structure dissociates into M_2Cl_6 and $[MCl_4]^-$.

The $[M_3Cl_{10}]^-$ ring structures may not be the most stable isomers but may reveal possible pathways for the precipitation of M_2Cl_6 at higher x_{MCl_3} in the chloroaluminate and chlorogallate systems. The $[Al_3Cl_{10}]^-$ ring structures has a very low imaginary frequency meaning it is a TS structure on a flat PES. The $[Ga_3Cl_{10}]^-$ and $[In_3Cl_{10}]^-$ ring isomers do not have low imaginary frequencies. The lack of low imaginary frequencies in conjunction with the more progressed dissociation into M_2Cl_6 and $[MCl_4]^-$ is indicative that if structures like the ring structure would be formed that the structures would eventually dissociate and partially precipitate.

The $[In_3Cl_{10}]^-$ isomer in the bottom row of figure 4.18 is only 14 kJ mol^{-1} less stable than the most stable linear $[In_3Cl_{10}]^-$ conformer. The structure is feasibly accessible and looks as through the structure is dissociating into $2[InCl_4]^{-1} + [InCl_2]^{+1}$. The relative stability of the $[In_3Cl_{10}]^-$ indicates that the structures of the chloroindate system could disproportionate into smaller species.

The linear $[M_3Cl_{10}]^-$ isomers have previously been identified in the LP by Raman spectroscopy, metal NMR and EXAFS in the chloroaluminate[6–8] and chlorogallate[9–11] systems. The $[In_3Cl_{10}]^-$ structure has never been identified as part of the LP speciation of the chloroindate system.[1] The possible species which are part

of the chloroaluminate and chlorogallate anionic speciation profiles found here concur with those found in other studies while the stability of the chloroindate system indicates that oligomerized chloroindate structures should be stable.

Figure 4.19 shows two stable M_3Cl_9 isomers. One In_3Cl_9 ring structure was found in each chlorometallate system the LP. The structures at the bottom of figure 4.19 which looks like a tetrahedral MCl_4 sharing a chloride with a doubly bridged M_2Cl_6 were found exclusively in the chloroaluminate and chloroindate systems. The geometries are analogous to the corresponding structures found in the GP. The corresponding structure from the chlorogallate system dissociated.

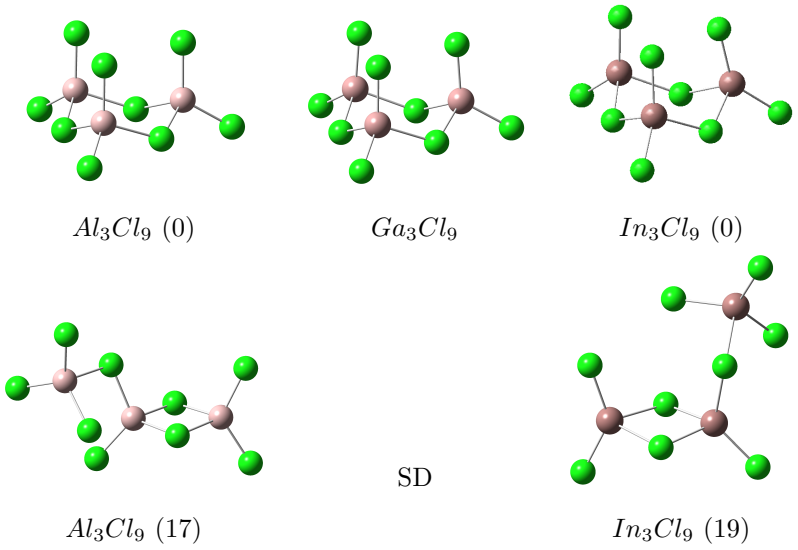


Figure 4.19: Stable M_3Cl_9 species in the liquid phase

The M_3Cl_9 structures have not been identified previously by other speciation studies in the LP in the chloroaluminate or the chloroindate systems.[1] Prior investigations have shown that Al_2Cl_6 precipitates in the in the chloroaluminate system and $InCl_3$ precipitates in the chloroindate system. It is consequentially unlikely that oligomerized structures depicted here would feasibly form in the chlorometallate systems investigated and the thermodynamic comparison in chapter 7 will give more insight into the likelihood of these species being part of the chlorometallate speciation profiles.

Scans of the linear $[M_3Cl_{10}]^-$ species

The flexibility of the linear $[M_3Cl_{10}]^-$ isomers is evident from the multiple stable conformers found in each system in the LP. The various conformers are only accessible if the energy barriers between the structures

are low enough. Hence the true flexibility of the linear $[M_3Cl_{10}]^-$ isomers was evaluated by evaluating the folding of via the distance between the terminal metals. Figure 4.20 shows the relative SCF energy versus the metal-metal distance of all three linear $[M_3Cl_{10}]^-$ isomers alongside the visualization of the scan coordinate.

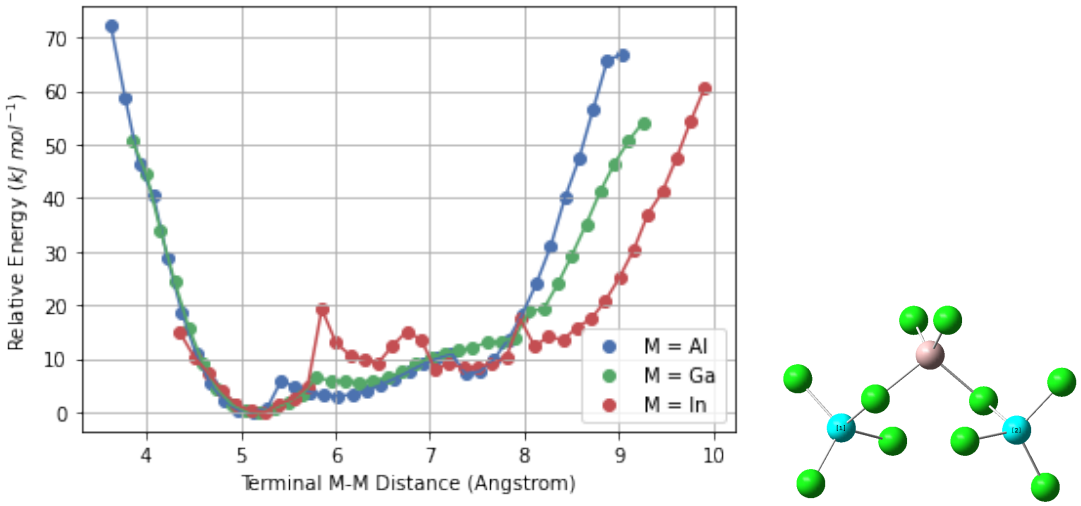


Figure 4.20: Liquid phase $[M_3Cl_{10}]^-$ contortion scans and scan coordinate (M(1)-M(2) distance) with respect to SCF energy where M=Al, Ga or In

The linear $[M_3Cl_{10}]^-$ isomers has a M-Cl-M-Cl-M backbone so the contortion of the structure cannot be described by Hooke's law because the species has more bond angles which can change. The relatively flat PES between 4.5 and 7.8 Å metal - metal distance indicate that the chloroaluminate and chlorogallate anions can readily contort. The PES of the chloroindate species is flat between 4.2 and 8.4 Å indium - indium distance but has barrier heights of up to 20 kJ mol^{-1} which can be overcome. The linear $[M_3Cl_{10}]^-$ isomers of all chlorometallate systems can freely contort.

Three minimums were identified in the scan of the $[Al_3Cl_{10}]^-$ anion and two minimums were found in the scan of $[Ga_3Cl_{10}]^-$. Five minimums of the $[In_3Cl_{10}]^-$ isomers were found. The scans revealed additional stable conformers of all three linear $[M_3Cl_{10}]^-$ isomers.

Additionally to evaluating the energy barriers associated with the linear $[M_3Cl_{10}]^-$ isomers folding, the energy barriers of the rotation across the M-Cl-M-Cl-M backbone was evaluated. Figure 4.21 depicts the relative SCF energy with respect to the dihedral angle of two M-Cl planes of the linear $[M_3Cl_{10}]^-$ isomers as depicted on the right hand of the same figure.

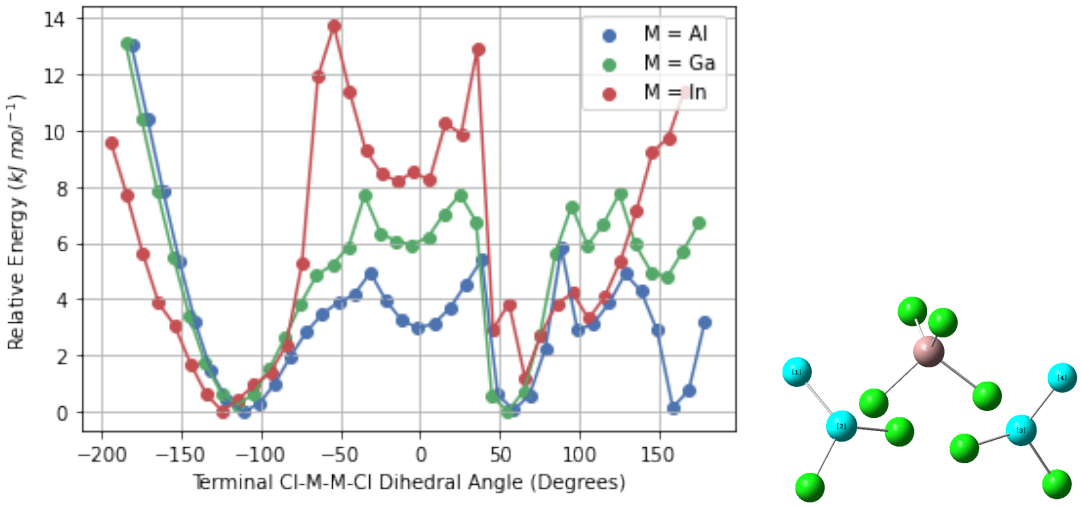


Figure 4.21: $[M_3Cl_{10}]^-$ rotation scans and scan coordinates (Cl(1)-M(2)-M(3)-Cl(4) dihedral angle) with respect to SCF energy where M=Al, Ga or In

The energy profile with respect to the change in dihedral angle is analogous across all three systems. The barrier heights associated with rotation become larger when going down the group from the chloroaluminate to the chloroindate system. The energy barriers to rotation never exceed 14 kJ mol^{-1} in the chloroindate system meaning that all conformations are also accessible with respect to the rotation along the M-Cl-M-Cl-M backbone.

Stable tetrametallic structures in the liquid phase

Figures 4.22, 4.23 and 4.24 shows the stable conformers of the linear $[M_4Cl_{13}]^-$ isomers in the LP for the chloroaluminate, chlorogallate and chloroindate systems, respectively. The linear $[M_4Cl_{13}]^-$ isomers are presented alongside the distance between the terminal metals in Angstroms and the relative Gibbs free energy in kJ mol^{-1}. The different conformers of the linear $[M_4Cl_{13}]^-$ isomers were found by optimizing initial starting structures and minima found along the PES of the folding scan.

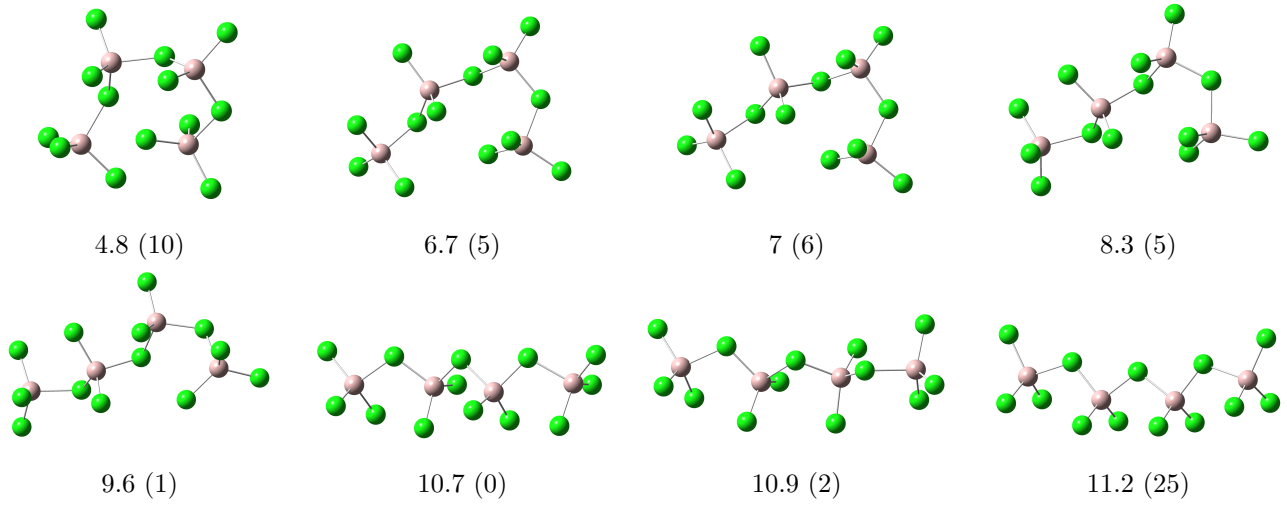


Figure 4.22: Stable linear $[Al_4Cl_{13}]^-$ conformers, terminal aluminum - terminal aluminum distance in Angstrom and relative Gibbs free energies in kJ mol^{-1}

The linear $[Al_4Cl_{13}]^-$ conformers feature one structure which is 25 kJ mol^{1-} less stable than the lowest energy conformer at a Al - Al distance of 11.2 Angstroms. All structures between Al-Al distance of 4.8 and 10.9 are within $\leq$ 10 kJ mol^{-1} of the lowest energy conformer. The number of stable $[Al_4Cl_{13}]^-$ conformers and the low difference in energy indicate a high degree of flexibility of the linear $[Al_4Cl_{13}]^-$ isomer.

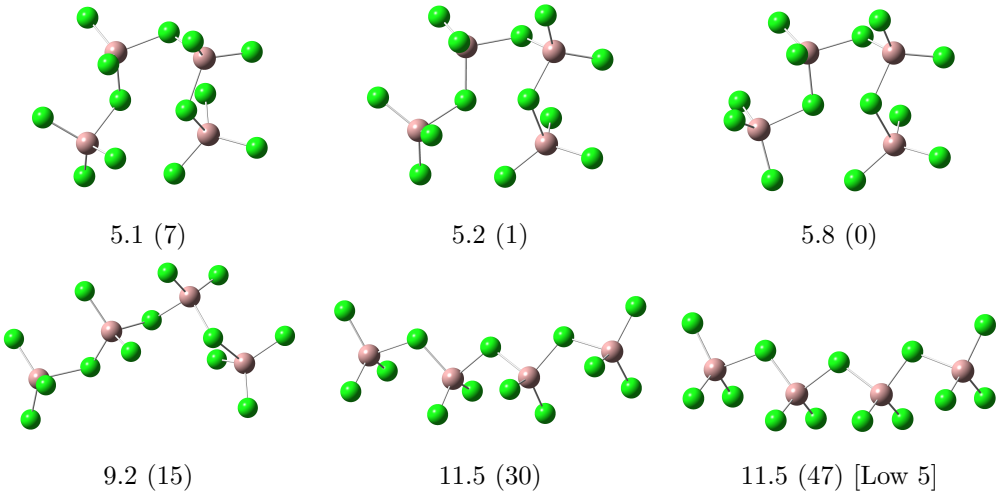


Figure 4.23: Stable linear $[Ga_4Cl_{13}]^-$ conformers, terminal gallium - terminal gallium distance in Angstrom and relative Gibbs free energies in kJ mol^{-1}

In the chlorogallate system there is a distinct preference for the more contorted conformers of the linear

$[Ga_4Cl_{13}]^-$ isomer. The three structures at 9.2, 11.5 and 11.5 Angstroms Ga - Ga distance are $\geq$ 15 kJ mol^{-1} less stable than the lowest energy conformer. The structures at 5.1, 5.2 and 5.8 Angstroms Ga - Ga distance are within $\leq$ 7 kJ mol^{-1} of the lowest energy conformer.

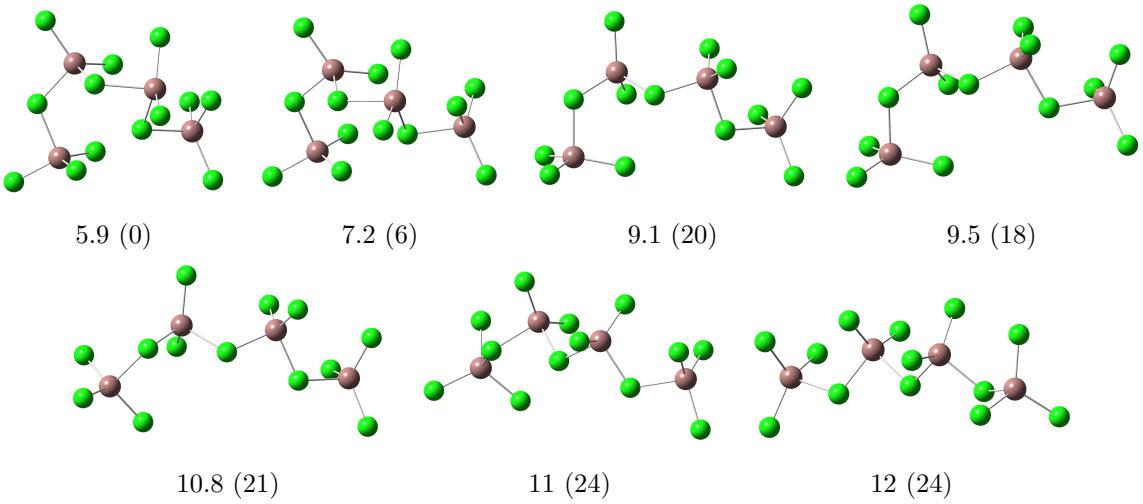


Figure 4.24: Stable linear $[In_4Cl_{13}]^-$ conformers, terminal indium - terminal indium distance in Angstrom and relative Gibbs free energies in kJ mol^{-1}

The linear $[In_4Cl_{13}]^-$ isomer has a preference for more contorted conformations over the straight ones. The five species with an In-In metal distance between 9.1 and 12 Angstroms are at least 18 kJ mol^{-1} less stable than the lowest energy conformer. The two conformers which feature the two terminal indium metals at 5.9 and 7.2 Angstroms distance are both within $\leq$ 6 kJ mol^{-1} of one another.

The flexibility of the linear $[M_4Cl_{13}]^-$ isomers is evident from the variety of different conformers in each chlorometallate system. Based on the relative Gibbs free energy of the conformers of each linear $[M_4Cl_{13}]^-$ isomer, the flexibility of the linear $[Al_4Cl_{13}]^-$ is the greatest. In contrast, the linear chlorogallate and chloroindate $[M_4Cl_{13}]^-$ isomers have a clear preference for the contorted conformers. The barrier heights between the different conformers will be shown in the folding scan will give additional insight into the flexibility of the linear $[M_4Cl_{13}]^-$ conformers.

Figure 4.25 shows the conformers of the branched $[M_4Cl_{13}]^-$ isomers in the LP. The branched $[M_4Cl_{13}]^-$ isomers of the chloroaluminate and chlorogallate systems have two additional stable conformers in the LP which were not found to be stable in the GP.

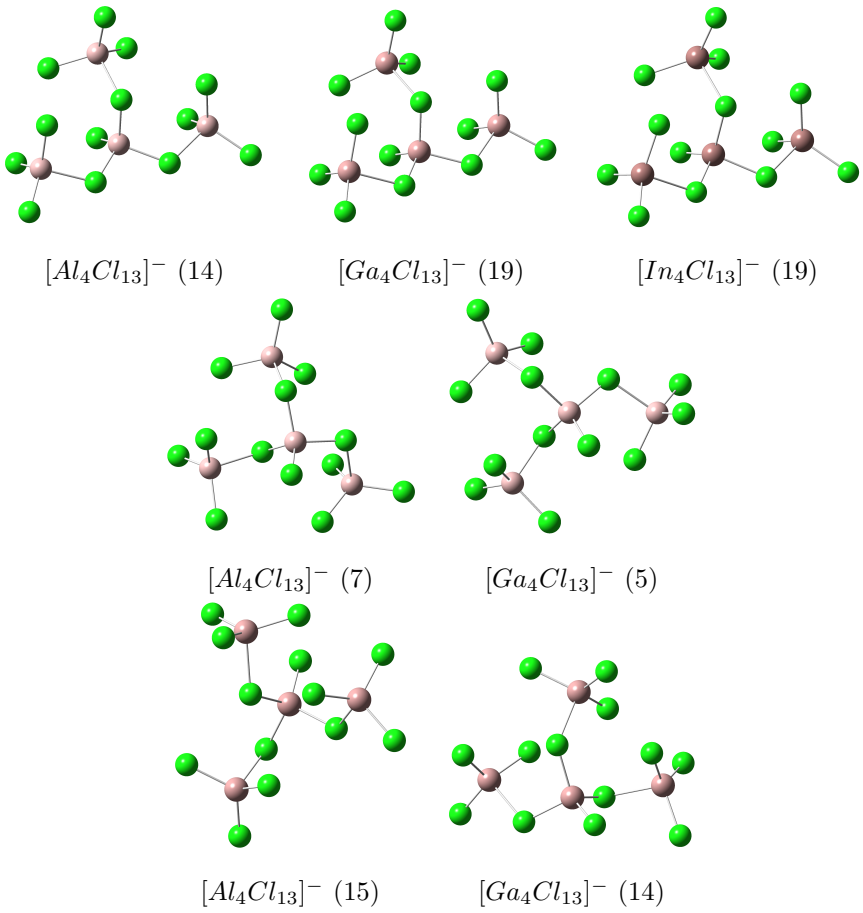


Figure 4.25: Branched $[M_4Cl_{13}]^-$ chlorometallate structures in the liquid phase and their relative Gibbs energy in kJ mol^{-1}

As in the GP The branched $[M_4Cl_{13}]^-$ isomers are slightly less stable compared to the linear $[M_4Cl_{13}]^-$ isomers. In the LP the most stable conformers of the branched $[M_4Cl_{13}]^-$ isomers are 7 and 5 kJ mol^{-1} less stable than the most stable conformers of the linear $[M_4Cl_{13}]^-$ isomers in the chloroaluminate and chlorogallate systems, respectively.

The linear $[M_4Cl_{13}]^-$ isomer has previously been identified in the chloroaluminate and the chlorogallate system in the LP.[1] The branched $[M_4Cl_{13}]^-$ isomers and the linear $[In_4Cl_{13}]^-$ isomers have not been identified as part of the LP speciation in each system at higher x_{MCl_3}. The multitude of species in equilibrium at high x_{MCl_3} may have hampered the identification of the alternative stable species found here due to the challenging interpretations of spectra when a multitude of similar species are present.

Figure 4.26 shows the alternative tetrametallic species which were found in the LP; $[M_4Cl_{11}]^+$, M_4Cl_{12} and

$[M_4Cl_{18}]^{6-}$. Each species is shown in different row of figure 4.26; $[M_4Cl_{11}]^+$ in the first row, M_4Cl_{12} in the second row and $[M_4Cl_{18}]^{6-}$ in the third row.

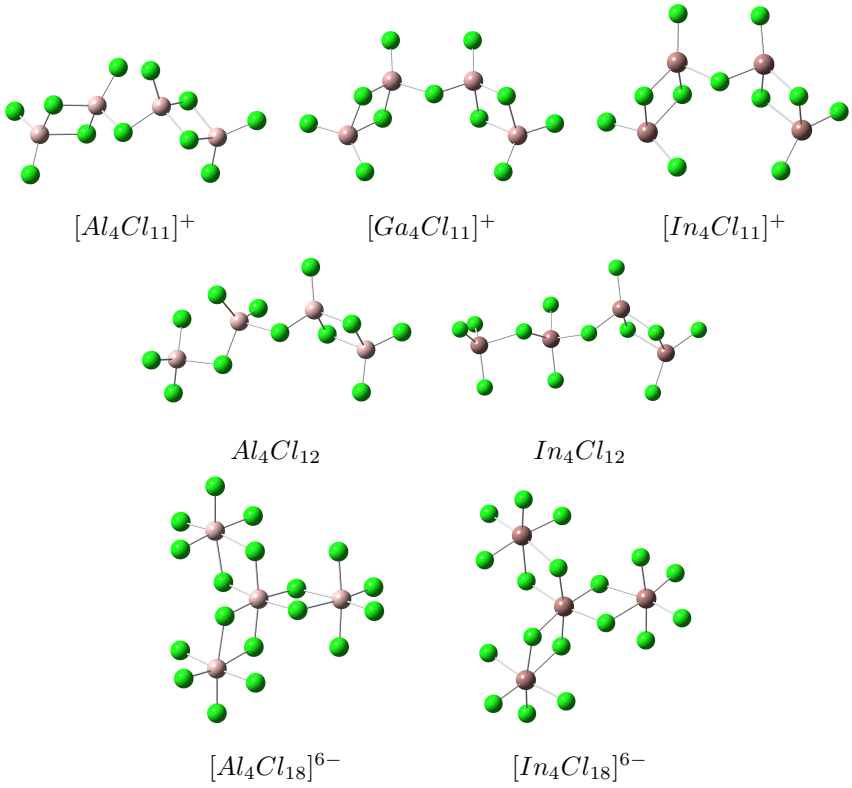


Figure 4.26: Branched $[M_4Cl_{13}]^-$ chlorometallate structures in the liquid phase and their relative Gibbs energy in kJ mol^{-1}

The $[M_4Cl_{11}]^+$ structure in each system is analogous; two doubly bridged M_2Cl_6 species sharing one terminal chloride. The M_4Cl_{12} structures of the chloroaluminate and chloroindate systems are a singly bridged M_2Cl_7 structures sharing one chloride with a doubly bridged M_2Cl_6 structure. The $[M_4Cl_{18}]^{6-}$ structures of the chloroaluminate and chloroindate system are 4 MCl_6 octahedral species of which one is surrounded by three others, sharing 2 chloride ligands with each of the three surrounding species.

Neither of the $[M_4Cl_{11}]^+$, M_4Cl_{12} and $[M_4Cl_{18}]^{6-}$ species have been identified by other studies as part of the LP speciation. The $[M_4Cl_{11}]^+$ and M_4Cl_{12} species may be part of the speciation but the relative stability of the structure has to be evaluated. The dissociating M_4Cl_{12} structures which were found to be stable in the GP speciation here were not found to be stable in the LP but the structures are instead conjoint and do not look like they could lead to the formation of M_2Cl_6. Since the dissociating M_4Cl_{12} species were not found to be stable in the LP there is likely another mechanism for the precipitation of M_2Cl_6 in the chloroaluminate

and chlorogallate systems than the one postulated in the GP section.

Scans of the linear $[M_4Cl_{13}]^-$ species

The flexibility of the linear $[M_4Cl_{13}]^-$ isomers has to be evaluated as multiple stable conformers of the isomers have been found in each system in the LP. The energy barriers of the contortion were evaluated by scanning the folding and rotation of the structural features, analogously to the $[M_3Cl_{10}]^-$ isomers. Figure 4.27 shows the relative SCF energy versus the metal - metal distance of the terminal metal centres of all three linear $[M_4Cl_{13}]^-$ isomers alongside the visualization of the scan coordinate on the right hand side.

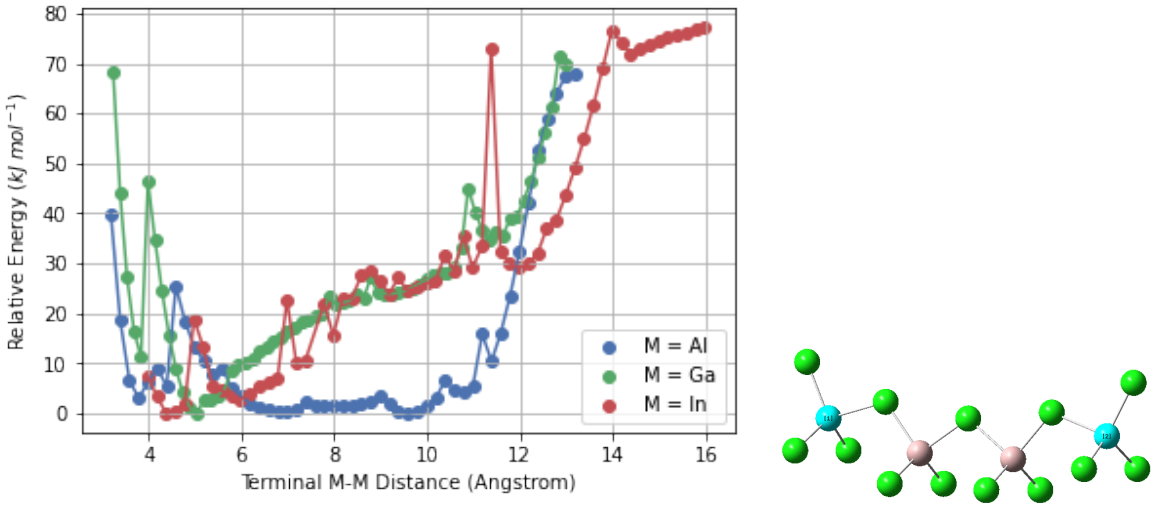
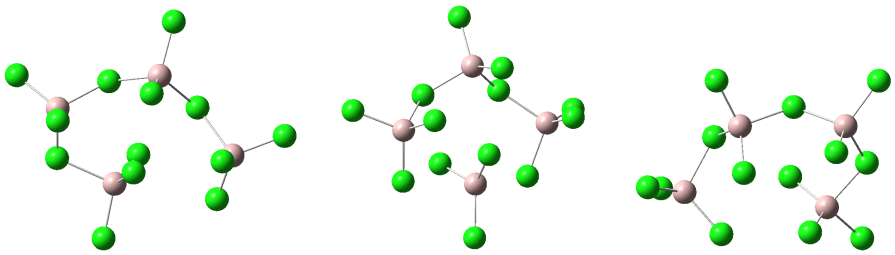


Figure 4.27: Liquid phase linear $[M_4Cl_{13}]^-$ contortion scans and scan coordinate (M(1)-M(2) distance) with respect to SCF energy where M=Al, Ga or In

The contortion scans of the linear $[M_4Cl_{13}]^-$ species have different indications for the chloroaluminate system than for the chlorogallate and chloroindate systems. The $[Al_4Cl_{13}]^-$ has a very flat PES between 4.8 and 11.6 Angstroms of the scanned Al-Al distance with energy barriers up to 27 kJ mol^{-1}. The flexibility of the linear $[Al_4Cl_{13}]^-$ isomer hence increases with respect to the number of metal centres present. In contrast, the scan of the linear $[Ga_4Cl_{13}]^-$ and $[In_4Cl_{13}]^-$ isomers indicate a strong preference for the contorted conformers as the energy is lower when the metal - metal distance is lower. The difference between the highest energy local minimum and the global minimum found are 35 and 30 kJ mol^{-1} in the chlorogallate and chloroindate scans, respectively. Additionally, the barriers are up to 47 and 73 kJ mol^{-1} in the chlorogallate and chloroindate scans, respectively. The scans show that the flexibility of the linear $[M_4Cl_{13}]^-$ isomers is limited in the chlorogallate and chloroindate systems as a result of the strong preference for the contorted conformations.

The linear $[Ga_4Cl_{13}]^-$ and $[In_4Cl_{13}]^-$ isomers can elongate but strongly favour a highly contorted conformation. The linear chlorogallate and chloroindate isomers could favour a higher number of self-interactions or the SMD model may be inadequately parameterized leading to a smaller solvent accessible surface area of the contorted structures being more stabilizing.

The scan of the linear $[Al_4Cl_{13}]^-$ revealed that the structure can lose a terminal $AlCl_3$ unit which requires 25 kJ mol^{-1} before reattaching to the other end of the chain. The rise in SCF energy from 5.4 to 4.6 Al-Al distance is with respect to the dissociation of a MCl_3 unit from the remainder of the structure. The stabilization from 4.6 to 4.4 Al-Al distance is due to the remainder of the $[Al_3Cl_{10}]^-$ structure stabilizing around the dissociated MCl_3 unit. The slight rise from 4.4 to 4.2 Al-Al distance is with respect to the MCl_3 unit creating further distance and the drop in energy from 4.2 to 3.8 Al-Al distance is due to the reattachment of the MCl_3 unit at the other end of the $[Al_3Cl_{10}]^-$ structure. The three minimums along the scan coordinate are shown in figure 4.28.



3.8 (3) 4.4 (5) 5.4 (8)

Figure 4.28: Linear $[Al_4Cl_{13}]^-$ scan $AlCl_3$ rearrangement conformers, aluminium - aluminium distance scan coordinate (Angstrom) and relative SCF energies (kJ mol^{-1})

The contortion the $[Al_4Cl_{13}]^-$ structure undergoes is initially only has a small effect on the Al-Al distance (10.7-11.2). Here the structure mainly staggers the bridged and terminal chlorides to idealize the repulsion between the regions of high charge density. subsequently one of the $AlCl_3$ units folds in on the remaining Al_3Cl_{10} structure which remains linear. The Al_3Cl_{10} segment remains linear between the 7 to 9.6 Angstroms of the Al-Al distance. The Al_3Cl_{10} segment which remained linear starts contorting below 7 angstroms of the scan coordinate.

The $[Ga_4Cl_{13}]^-$ structure also has an energy barrier to the rearrangement of the structure which is 46 kJ mol^{-1} at around 4 Angstroms of the scan coordinate. Compared to the 25 kJ mol^{-1} barrier of the chloroaluminate system the barrier is relatively high and no intermediate structure was found. Instead the $GaCl_3$ unit is directly detached on one end of the remaining Ga_3Cl_{10} segment and reattached attached on

the other end. The lack of an intermediate step and the higher energy barrier indicate that the gallium structure is less likely to rearrange and resulting in a less dynamic system. The intermediate structure was not found for the linear $[In_4Cl_{13}]^-$ isomer.

The energy barriers of the rotation across the M-Cl-M-Cl-M-Cl-M backbone of the linear $[M_4Cl_{13}]^-$ isomers was evaluated. Figure 4.29 depicts the relative SCF energy with respect to the dihedral angle of two M-Cl planes of the linear $[M_4Cl_{13}]^-$ isomers as depicted on the right hand of the same figure.

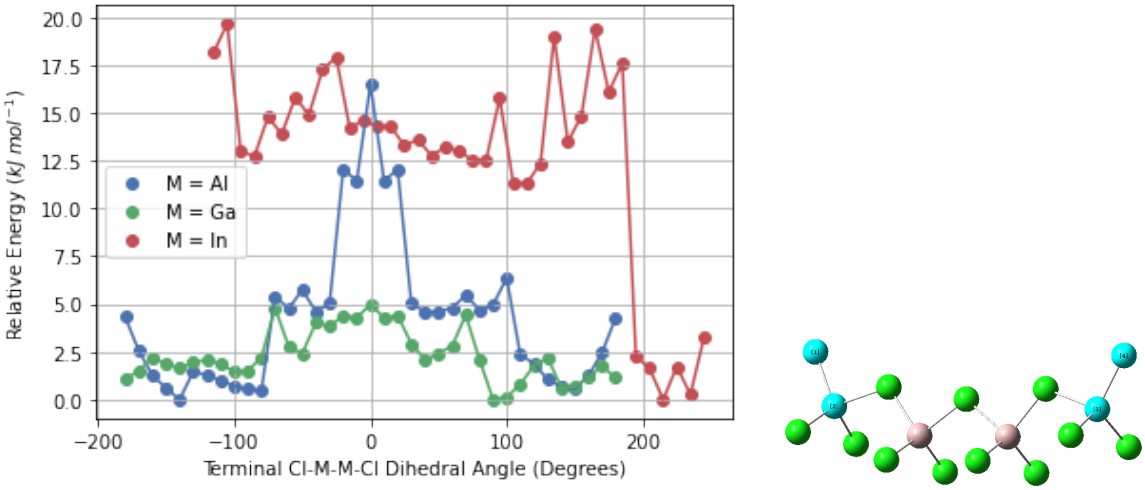


Figure 4.29: Linear $[M_4Cl_{13}]^-$ twisting Scans and scan coordinates (Cl(1)-M(2)-M(3)-Cl(4) dihedral angle) with respect to SCF energy where M = Al, Ga or In

The energy profile with respect to the change in dihedral of the angle of the $[M_4Cl_{13}]^-$ M-Cl planes is very similar for the chloroaluminate and chlorogallate species and different for the chloroindate species. The barrier heights associated with rotation become larger when going down the group, increasing from the chloroaluminate system which has no barriers above 5 kJ mol^{-1} to the chloroindate which has a few barriers just under 20 kJ mol^{-1}. As the energy barriers to rotation never exceed 20 kJ mol^{-1} in all systems, all conformations are also accessible with respect to the rotation along the M-Cl-M-Cl-M-Cl-M backbone.

4.2 Stable cation conformers

Prior to setting up the Ion pair (IP) calculations composed of the anions determined to be part of the anionic speciation at different x_{MCl_3} in the seventh chapter and the cations the stable conformers of the isolated cations have to be determined. The structural features of $[C_2C_1Im]^+$, [Choline]$^+$, $[N_{2110}]^+$ and $[N_{2111}]^+$

cations stable conformers were scanned to ensure all accessible conformers were found and to evaluate the flexibility of the cation.

4.2.1 1-ethyl-3-methyl-imidazolium structural analysis

Two conformers of $[C_2C_1Im]^+$ were found and confirmed to be stable in both the GP and the LP. The two conformers found are different with respect to changes in the ethyl arms rotation, as depicted in figure 4.30. One conformer features the ethyl arm in the plane of the imidazolium ring, shown on the left side of figure 4.30, and the other features the ethyl arm out of plane of the imidazolium ring, as depicted on the right side of figure 4.30.

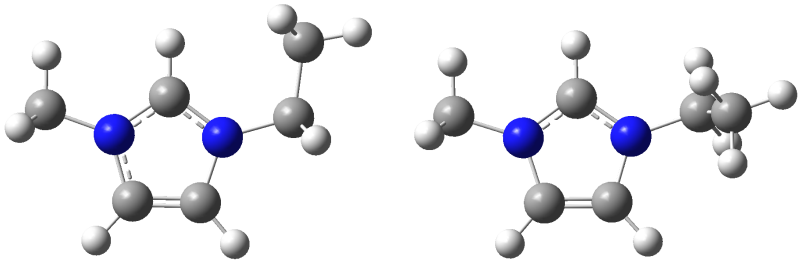
	In-plane ethyl arm $[C_2C_1Im]^+$	out of plane ethyl arm $[C_2C_1Im]^+$
structure		
	Relative Gibbs free energy (ΔG) in kJ mol^{-1}	
Gas phase	1	0
Liquid phase	1	0
	Ethyl arm dihedral Angle (degrees)	
Gas phase	180°	−72°
Liquid phase	180°	−75°

Figure 4.30: Stable conformers of the $[C_2C_1Im]^+$ cation, the relative Gibbs free energy and dihedral angle of the ethyl arm in the gas phase and liquid

The two conformers of $[C_2C_1Im]^+$ have been found previously and their relative stability in the GP and LP align with results from literature.[12] The out of plane structure is marginally more stable in the GP and LP but the difference in stability is so small that it can effectively be considered degenerate. The minima were evaluated by scanning the 360° rotation of the ethyl arm which can be found in the appendix.

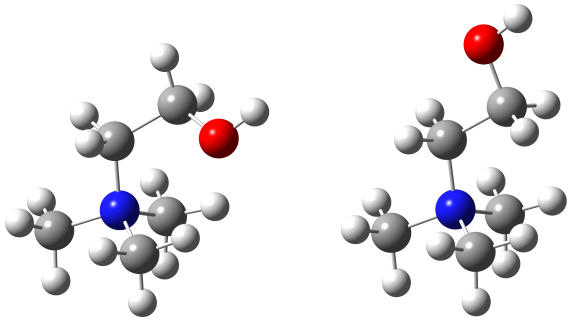
The dihedral angles, listed at the bottom of figure 4.30, are between the carbons of the ethyl arm, the nitrogen adjacent to the first carbon of the ethyl arm and the carbon in the imidazolium ring adjacent to that nitrogen which is not wedged between the two nitrogen atoms. The dihedral angles vary slightly for the

out of plane structure between the GP and LP. The difference in the dihedral angle between the phases is also so small that it falls within the error margin of the method. The dihedral Angles of the in-plane ethyl arm are consistent in the GP and LP.

4.2.2 Isolated gas phase [Choline]$^+$, [N_{2110}]$^+$ and [N_{2111}]$^+$ cation structures

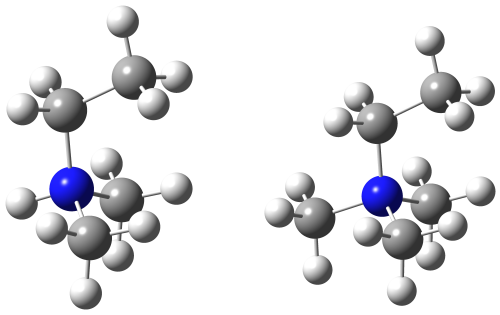
Analogously to the evaluation of the $[C_2C_1Im]^+$ cation, initially the different stable conformers of the isolated $[Choline]^+$, $[N_{2110}]^+$ and $[N_{2111}]^+$ were determined and the electronic structure was evaluated. The electronic structure of the cations is evaluated via the MEPs and Fukui functions.

Figures 4.31 and 4.32 show the stable conformers of the $[Choline]^+$, $[N_{2110}]^+$ and $[N_{2111}]^+$ cations, respectively.



Gauche (0) Trans (14)

Figure 4.31: Stable conformers of the $[Choline]^+$ and their relative Gibbs free energies in the gas phase



$[N_{2110}]^+$ $[N_{2111}]^+$

Figure 4.32: Stable conformers of the $[N_{2110}]^+$ and $[N_{2111}]^+$ cations in the gas phase

The $[Choline]^+$ cation is the only cation which has two stable conformers while the other two cations only have one. One additional stable conformer of $[Choline]^+$ has been found in a previously but could not be determined here through scanning.[13] The missing conformer is analogous to the trans conformation with the hydrogen atom of the O-H group rotated but the minimum was not found for the isolated $[Choline]^+$ cation. Many of the IPs constituting of $[Choline]^+$ and the halometallate anions feature $[Choline]^+$ in this conformation.

Bibliography

[1] J Estager, JD Holbrey, and Malgorzata Swadźba-Kwaśny. Halometallate ionic liquids–revisited. *Chemical Society Reviews*, 43(3):847–886, 2014.

[2] Steven P Wicelinski, Robert J Gale, Krishna M Pamidimukkala, and Roger A Laine. Fast atom bombardment mass spectrometry of low temperature chloroaluminate and chlorogallate melts. *Analytical Chemistry*, 60(20):2228–2232, 1988.

[3] Ala'a K Abdul-Sada, Anthony M Greenway, Kenneth R Seddon, and Thomas Welton. Upon the existence of [al3cl10]- in room temperature chloroaluminate ionic liquids. *Organic mass spectrometry*, 24(10):917–918, 1989.

[4] Bradley L Ackermann, Anthony Tsarbopoulos, and John Allison. Fast atom bombardment mass spectrometric studies of the aluminum chloride/n-butylpyridinium chloride molten salt. *Analytical chemistry*, 57(8):1766–1768, 1985.

[5] Ala'a K Abdul-Sada, Anthony M Greenway, Kenneth R Seddon, and Thomas Welton. A fast atom bombardment mass spectrometric study of room-temperature 1-ethyl-3-methylimidazolium chloroaluminate (iii) ionic liquids. evidence for the existence of the decachlorotrialuminate (iii) anion. *Organic mass spectrometry*, 28(7):759–765, 1993.

[6] RJ Gale, B Gilbert, and RA Osteryoung. Raman spectra of molten aluminum chloride: 1-butylpyridinium chloride systems at ambient temperatures. *Inorganic Chemistry*, 17(10):2728–2729, 1978.

[7] S Takahashi, LA Curtiss, D Gosztola, N Koura, and Marie-Louise Saboungi. Molecular orbital calculations and raman measurements for 1-ethyl-3-methylimidazolium chloroaluminates. *Inorganic Chemistry*, 34(11):2990–2993, 1995.

[8] S Takahashi, Marie-Louise Saboungi, RJ Klingler, MJ Chen, and JW Rathke. Dynamics of room-temperature melts: nuclear magnetic resonance measurements of dialkylimidazolium haloaluminates. *Journal of the Chemical Society, Faraday Transactions*, 89(19):3591–3595, 1993.

[9] SP Wicelinski, RJ Gale, Stephen D Williams, and G Mamantov. Raman spectra of molten gallium chloride: 1-methyl-3-ethylimidazolium chloride at ambient temperatures. *Spectrochimica Acta Part A: Molecular Spectroscopy*, 45(7):759–762, 1989.

[10] XueQi Xing, GuoYing Zhao, and JianZhong Cui. Chlorogallate (iii) ionic liquids: Synthesis, acidity determination and their catalytic performances for isobutane alkylation. *Science China Chemistry*, 55 (8):1542–1547, 2012.

[11] Christopher Hardacre, Richard W Murphy, Kenneth R Seddon, Geetha Srinivasan, and Małgorzata Swadźba-Kwaśny. Speciation of chlorometallate ionic liquids based on gallium (iii) and indium (iii). *Australian journal of chemistry*, 63(5):845–848, 2010.

[12] PA Hunt. The simulation of imidazolium-based ionic liquids. *Molecular simulation*, 32(01):1–10, 2006.

[13] Claire R Ashworth, Richard P Matthews, Tom Welton, and Patricia A Hunt. Doubly ionic hydrogen bond interactions within the choline chloride–urea deep eutectic solvent. *Physical Chemistry Chemical Physics*, 18(27):18145–18160, 2016.

Chapter 5

Isolated Ions Electronic Structure

This chapter discusses the electronic structure of stable conformers of all species which are known to be part of the speciation according to experimental speciation. The branched $[M_4Cl_{13}]^-$ isomers electronic structure has also been evaluated due to the small difference in stability between the branched and linear $[M_4Cl_{13}]^-$ isomers found. The electronic structure of different anionic chlorometallate species and the cations was evaluated to determine which sites on the anions and cations are most attractive for a counter ion to interact with. The attractiveness of sites reveals which interactions result in the most stable IPs. Additionally, the electronic structures give insight into how the species may behave when they are exposed to a potential. All the electronic structure evaluations were carried out on stable LP structures. Initially the NACs, determined by three different charge assignment schemes of each species are discussed. Next the MEPs of all the species and Fukui functions are discussed. Both MEPs and Fukui functions were used as they describe hard and soft nucleophilicity of different sites around the anions, respectively.

5.1 Liquid phase chlorometallate anion electronic structure evaluation via net atomic charge assignments, molecular electrostatic potentials and Fukui functions

5.1.1 Net atomic charges of anionic species species

Three schemes were used to assign NACs[1] of the stable anions; ChelpG[2], NPA[3] and ADCH.[4]

Net atomic charges of $[MCl_4]^-$ species

Table 5.1 displays the NACs assigned to each chemical environment in the $[MCl_4]^-$ species of the chloroaluminate, chlorogallate and chloroindate systems. The chemical environments of the chlorides in the $[MCl_4]^-$ species are the same, meaning the NACs assigned are degenerate according to all NAC assignment methods. Atoms of each species were grouped together when expressing NACs based on whether the chemical environments are degenerate in nature. The ratio of the magnitude of the chloride charge to the magnitude of the metal charges are also shown in table 5.1 for each NAC assignment scheme for the $[MCl_4]^-$ species of each chlorometallate system.

Table 5.1: $[MCl_4]^-$ net atomic charges and ratios with respect to absolute values of NACs according to the NPA, ChelpG and ADCH NAC assignment methods

Species	$[AlCl_4]^-$			$[GaCl_4]^-$			$[InCl_4]^-$		
NACs Scheme	NPA	ChelpG	ADCH	NPA	ChelpG	ADCH	NPA	ChelpG	ADCH
M	1.230	0.873	0.373	1.381	0.950	0.523	1.635	1.170	0.629
Cl	-0.567	-0.468	-0.343	-0.595	-0.488	-0.381	-0.659	- 0.543	-0.408
Ratio	2.207	1.866	1.088	2.321	1.949	1.375	2.479	2.152	1.535

The magnitude of the assigned NACs is always largest in the NPA scheme, followed by the ChelpG scheme. The ADCH scheme assigns the charges with the lowest magnitude. The ratios of charge magnitudes between the chlorides and metals increases when going from $[AlCl_4]^-$ to $[InCl_4]^-$ in all of the NAC schemes as the polarization of the M-Cl bond increases.

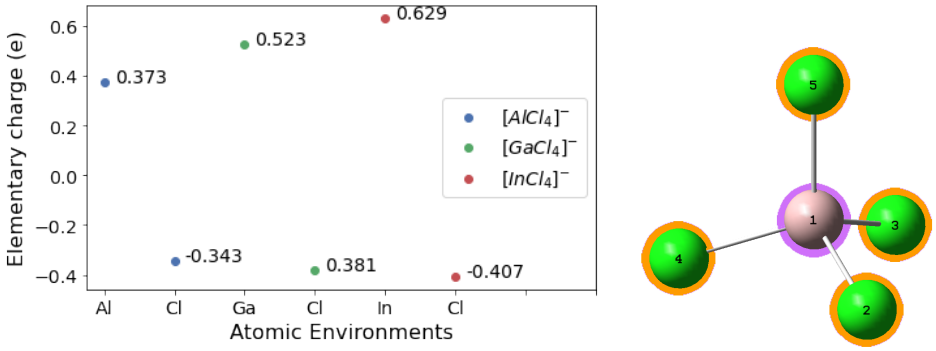


Figure 5.1: $[MCl_4]^-$ net atomic ADCH charges and chemical environments; ● chlorides (Cl) and ● metals; Al, Ga and In

The ratios at the bottom of table 5.1 are based on the absolute values of the NACs. The ratio of the absolute magnitude of the charges assigned to the chlorides versus the absolute magnitude of the charges assigned to the metals is larger according to the NPA and ESP schemes than for the ADCH scheme. A key difference between the NAC assignment schemes is the trend in absolute ratio between the different chlorometallate systems. The NPA and ChelpG NAC assignment schemes indicate a slight increase in the polarization of the M-Cl bonds when going from $[AlCl_4]^-$ to $[InCl_4]^-$. Additionally, the NPA and ChelpG schemes indicate that the M-Cl bonds of all species are highly polarized. The ADCH scheme best represents the change in bonding character going across the chlorometallate systems for two reasons. All M-Cl bonds are highly ionic

according to the NPA and ChelpG schemes which is known to be false. Consequentially the NPA and ChelpG schemes indicate a smaller change in bonding character from covalent to ionic when going down the group. The ADCH scheme best represents the known understanding in the M-Cl bonding and will henceforth be used exclusively to evaluate the assignment of NACs and the information presented is condensed as shown in figure 5.1. The full range of NACs assigned by all schemes for all evaluated species can be found in the appendix, section 9.1.8.

Net atomic charges of $[InCl_5]^{2-}$ and $[InCl_6]^{3-}$ species

Figure 5.2 shows the ADCH charges of $[InCl_5]^{2-}$ and $[InCl_6]^{3-}$. The $[InCl_5]^{2-}$ structure has five chloride ligands in two different environments. Two chlorides are in the axial position and three in the equatorial position. The chlorides in the octahedral $[InCl_6]^{3-}$ species are all degenerate.

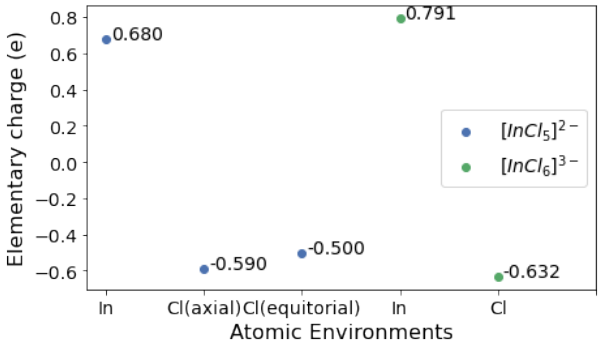


Figure 5.2: $[InCl_5]^{2-}$ and $[InCl_6]^{3-}$ net atomic ADCH charges

The axial chlorides of $[InCl_5]^{2-}$ carry more negative charge than the equatorial chlorides. The axial chlorides are in closer proximity to the indium and can in turn polarize more charge from the central metal. The axial chlorides are closer to the central indium because they experience less steric hindrance from the adjacent chlorides. This implies that an interaction of a cation with axial chlorides of $[InCl_5]^{2-}$ will be more stabilizing than one with the equatorial chlorides.

In the $[InCl_4]^{-}$, $[InCl_5]^{2-}$ and $[InCl_6]^{3-}$ complexes the magnitude of the positive charge of the metals and the negative charge of the chloride ligands becomes larger with the addition of each chloride. The large difference in charge between the chloride ligands and the indium metals as the coordination sphere becomes more saturated shows that the indium complexes In-Cl bonds become more ionic in character the lower the x_{InCl_3} in the system.

Net atomic charges of $[M_2Cl_7]^-$ chloroaluminate and chlorogallate species

Figure 5.3 displays the NACs of the chloroaluminate and chlorogallate $[M_2Cl_7]^-$ complexes. The $[M_2Cl_7]^-$ species have three distinct environments. The two metals are degenerate, and all six terminal chlorides are degenerate. The bridging chloride has a unique chemical environment. The three chemical environments are depicted on the right-hand side of figure 5.3.

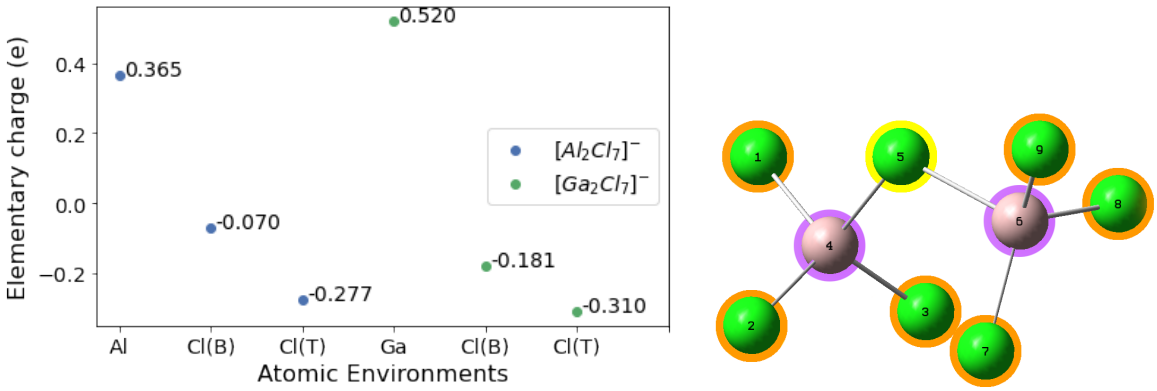


Figure 5.3: $[M_2Cl_7]^-$ net atomic ADCH charges and chemical environments; terminal chlorides (Cl(T)), bridging chlorides (Cl(B)) and metals; Al and Ga

The single negative charge of the $[M_2Cl_7]^-$ species is more dispersed than in the $[MCl_4]^-$ species as the total charge is the same but there are more atoms which the charge is spread across. In consequence the difference in charge between the metals and chlorides is smaller in the $[M_2Cl_7]^-$ species compared to the $[MCl_4]^-$ complexes. The positive NACs on the metals of the dimetallic species are almost the same as those in the $[MCl_4]^-$ species in both the chloroaluminate and chlorogallate complexes.

The negative NACs of the chlorides are much lower in magnitude in the dimetallic species than the monometallic species. The terminal chlorides of $[M_2Cl_7]^-$ are approximately 80% as negative as the chlorides in the $[MCl_4]^-$ complexes. The bridging chloride of the $[M_2Cl_7]^-$ species are 20% and 50% as negative as the chlorides in the $[MCl_4]^-$ complexes in the chloroaluminate and chlorogallate systems, respectively. An interaction with the side of the anion where the bridging chloride is located will be less stabilizing for a cation-anion interaction as there is proportionally less charge localized there.

Net atomic charges of $[M_3Cl_{10}]^-$ chloroaluminate and chlorogallate species

Figure 5.4 shows the NACs of each chemical environment of the $[M_3Cl_{10}]^-$ species of the chloroaluminate and chlorogallate systems. The $[M_3Cl_{10}]^-$ species have five distinct chemical environments. There are two different metal and three different chloride environments; the terminal [M (T)] metals, the bridging metal [M (B)], terminal chlorides attached to terminal metals [Cl (T)], terminal chlorides attached to the bridging metal [Cl (T-BM)] and the bridging chlorides [Cl (B)]. The different chemical environments are shown at the top of figure 5.4.

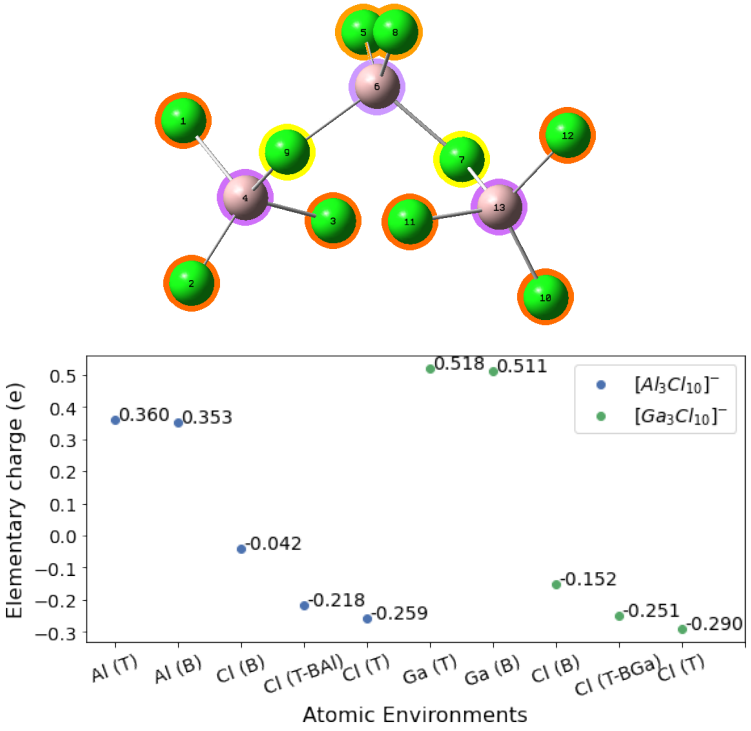


Figure 5.4: $[M_3Cl_{10}]^-$ net atomic ADCH charges and chemical environments; terminal metal (M(T)), bridging metals (M(B)), bridging chlorides, terminal chlorides attached to bridging metals (Cl(T-BM)) and terminal chlorides attached to terminal metals (Cl(T)) where M = Al or Ga

The negative charge of the $[M_3Cl_{10}]^-$ species is more dispersed over the larger structure compared to the $[M_2Cl_7]^-$ species. The difference in charge between the metals and chlorides is even smaller than in the dimetallic and monometallic species in the respective systems. The lower magnitude of charges is consistent with the trend observed going from the $[MCl_4]^-$ to the $[M_2Cl_7]^-$ species. The largest changes in NAC occur on the bridging chlorides and the terminal chlorides attached to the bridging metals while the changes in

the magnitude of the positive charge of the terminal metals is the smallest.

The bridging chlorides of $[M_3Cl_{10}]^-$ have the smallest negative NAC followed by the terminal chlorides attached to bridging metals followed by terminal chlorides attached to terminal metals. The difference in NAC between the bridging and terminal chlorides and the geometry of the $[M_3Cl_{10}]^-$ anions makes it most likely that the lowest energy IP structures will feature an interactions between the terminal chlorides attached to the terminal metals. Since the structure can contort an interaction with all terminal chlorides may lead to the most stabilizing interaction between the $[M_3Cl_{10}]^-$ species and the cations.

Net atomic charges of linear $[M_4Cl_{13}]^-$ chloroaluminate and chlorogallate species

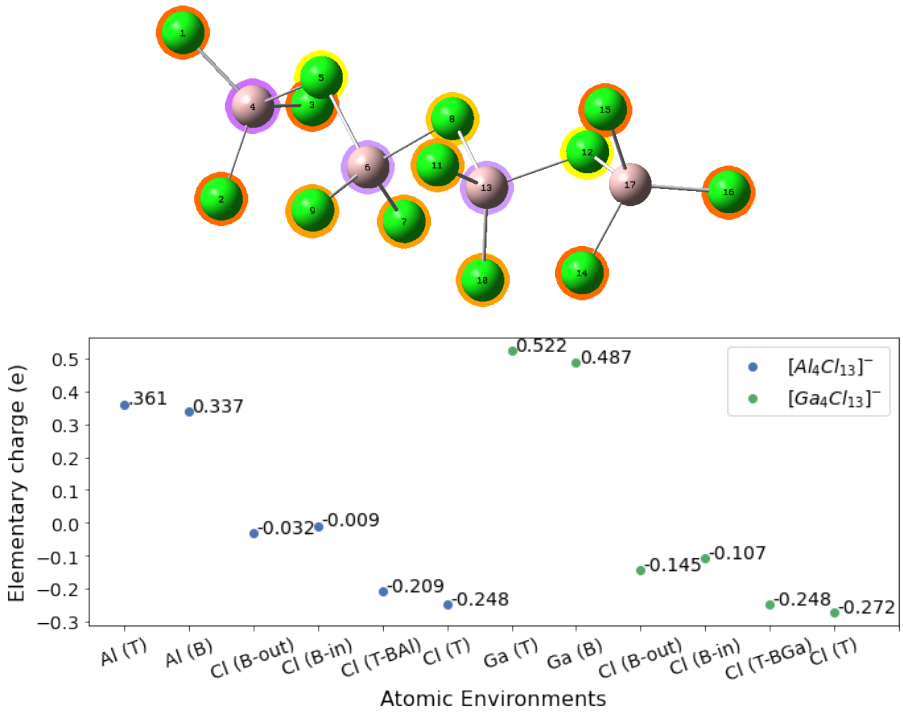


Figure 5.5: Linear $[M_4Cl_{13}]^-$ net atomic ADCH charges and chemical environments; terminal metals (M(T)), bridging metals (M(B)), outter bridging chlorides (Cl(B-out)), inner bridging chloride (Cl(B-in)), terminal chlorides attached to bridging metals (Cl(T-BM)) and terminal chlorides attached to terminal metals (Cl(T)) where M = Al or Ga

Figure 5.5 depicts the different chemical environments and the NACs of the different chemical environments of the linear $[M_4Cl_{13}]^-$ species of the chloroaluminate and chlorogallate systems. The linear $[M_4Cl_{13}]^-$

species features six distinct chemical environments. There are two aluminium environments, terminal, and bridging. There are four distinguishable chloride environments: outer bridging (B-out), inner bridging (B-in), terminal chlorides adjacent to terminal metals (T) and terminal chlorides adjacent to the bridging metals (T-BAl and T-BGa).

The difference in charge between the positively charged metals and the negatively charged chlorides is smaller in the $[M_4Cl_{13}]^-$ species compared to the $[M_3Cl_{10}]^-$ anion. The terminal metals of the linear $[M_4Cl_{13}]^-$ species have a marginally higher magnitude of positive charge in both the chloroaluminate and chlorogallate species compared to the terminal metals of the $[M_3Cl_{10}]^-$ species of the same system. The magnitude of the negative charge of the chlorides of $[M_4Cl_{13}]^-$ is smaller which contributes to the gap between the metal and chloride charges being narrowed. The increase in the magnitude of positive charge of the terminal metals indicates that the charge is more polarized in the $[M_4Cl_{13}]^-$ species.

The negative charge of the bridging chloride ligands has the smallest magnitude in both systems. The inner bridging chloride features the smallest magnitude of charge followed by the outer bridging chloride ligand. The inner bridging chloride of the linear $[Al_4Cl_{13}]^-$ species are close to neutral. The magnitude of the negative charge of the bridging chloride ligands of the linear $[Ga_4Cl_{13}]^-$ have a larger magnitude. The higher charge magnitudes of the chloride ligands in the chlorogallate species versus the chloroaluminate species is in line with the NACs from the monometallic, dimetallic and trimetallic structures where more charge is polarized away from the gallium atoms than the aluminium atoms.

The negative charge is concentrated in the terminal chlorides of the linear $[M_4Cl_{13}]^-$ structure in both systems. The terminal chlorides adjacent to the terminal metals have a higher charge concentration than the terminal chloride ligands attached to the bridging metals. The dispersed charge in combination with the high degree of flexibility of the linear $[M_4Cl_{13}]^-$ structures makes interaction profiles where the side of the anions with all the terminal chlorides interacts with the cation the most favourable. The linear structure will likely contort to accommodate interactions between all the electron rich terminal chlorides with the cations most electron deficient sites.

Net atomic charges of branched $[M_4Cl_{13}]^-$ chloroaluminate and chlorogallate species

Figure 5.6 shows the chemical environments and the ADCH NAC charges of the chemical environments of the branched $[M_4Cl_{13}]^-$ species of the chloroaluminate and chlorogallate systems. The branched $[M_4Cl_{13}]^-$ species features 8 distinct chemical environments. There are three distinct metal environments: the terminal metal atoms in the linear portion of the structure (T-lin), the terminal metals in non-linear portion (T-Bra)

and the central bridging aluminum (B). There are five distinct chloride environments; the bridging chlorides in the linear structure (B-Lin), the bridging chloride connecting the branch (B-Bra), the terminal chloride of the central bridging metal (T-B), the terminal chlorides of the terminal metals of the linear segment of the structure (T-Lin) and terminal chlorides attached to the metal outside of the linear portion of the species (T-Bra).

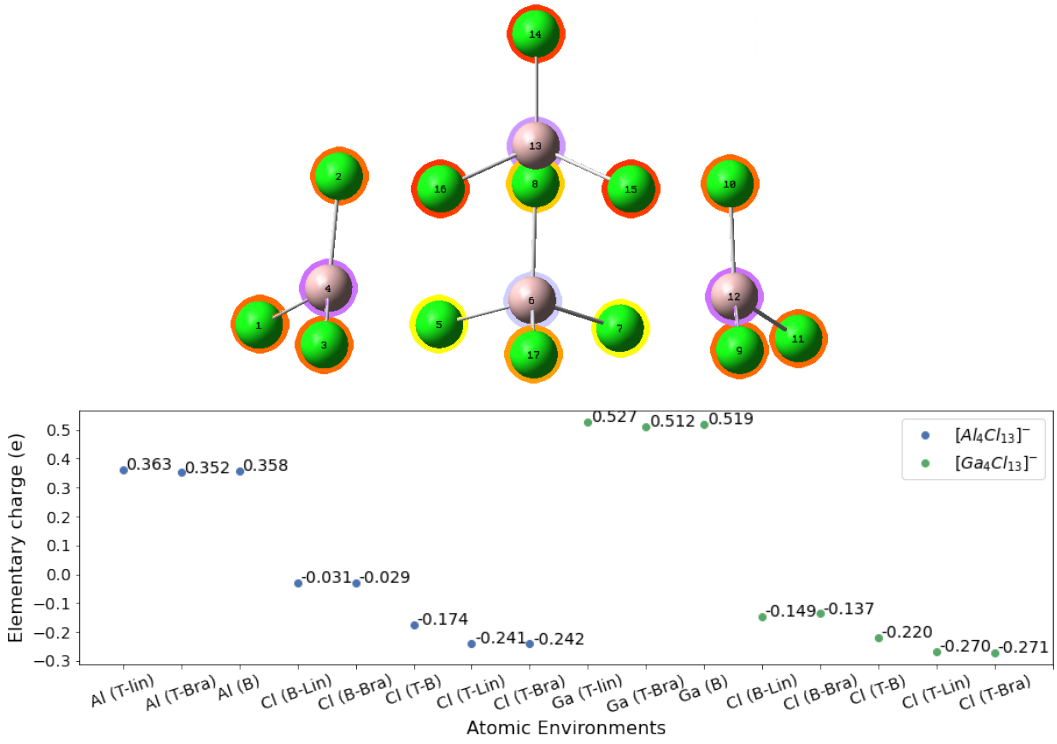


Figure 5.6: Branched $[M_4Cl_{13}]^-$ net atomic ADCH charges and charge environments; terminal metal of the linear segment (M(T-Lin)), terminal metal of the branched segment (M(T-Bra)), bridging metal (M(B)), bridging chloride of the linear segment (Cl(B-Lin)), bridging chloride of the branched segment (Cl(B-Bra)), terminal chloride attached to the bridging metal (Cl(T-BM), terminal chloride attached to the terminal metal of the linear segment (Cl(T-Lin)), terminal chloride attached to the terminal metal of the branched segment (Cl(T-Lin)) where M = Al or Ga

The charge of the branched $[M_4Cl_{13}]^-$ species is more homogeneously distributed than in the linear $[M_4Cl_{13}]^-$ species. In the branched $[M_4Cl_{13}]^-$ species the charge is less polarized between the metals and chlorides. The homogeneity of the charge distribution is exhibited by the smaller difference between the charges of the most positively charged aluminium atoms and the most negatively charged chloride ligands in the branched structure. The homogeneous distribution of charge can be attributed to the higher number of terminal

chlorides attached to terminal aluminium atoms and the higher amount of molecular symmetry. The terminal chlorides, regardless of whether on the branched or linear portion of the anion are always feature the most negative NACs.

The charge distribution of the branched $[M_4Cl_{13}]^-$ and the higher degree of rigidity, when compared to the linear structure, will likely lead to less stabilizing interactions in the IP evaluations. The ridged structure of the branched $[M_4Cl_{13}]^-$ structure in conjunction the most negatively charged regions pointing in three different directions will likely prevent all of the anion from interacting with a single cation to lower the IP energy effectively. In the bulk solution the structure could however lower the systems energy better than the linear structure. The sites of stronger negative NAC can interact with multiple cations surrounding the species to lower system energy more effectively.

5.1.2 Molecular electrostatic potentials of the chlorometallate anions in the liquid phase

The MEPs[2] were mapped to reveal the most nucleophilic sites on the anions and in turn show where cations are most likely to interact with the anions. The MEPs shown in the figures in this section show the MEP maps and a range of the potentials below. Some MEPs are shown with an opaque surface and other with a slightly transparent surface where the structures of the species are less obvious. Note that the MEPs shown in the section show exclusively negative potentials and hence the ranges shown are from the strongest negative potential to the weakest negative potential. The strongest negative potential is red going via yellow, green, and turquoise to the weakest negative potential in blue.

Molecular electrostatic potentials of the $[MCl_4]^-$ species

The MEPs of the anionic species were mapped onto the electron density at an isovalue of 0.0008 to evaluate which sites of the anions have the strongest negative potential. Figure 5.7 shows a visualization of the MEP of the $[MCl_4]^-$ species of each chlorometallate system at a 0.0008 isovalue.

The visualized MEPs of the $[MCl_4]^-$ species, depicted in figure 5.7, show that each chloride has a sigma hole. The sigma holes arise due to the anisotropic charge distribution in the complexes as described in section 1.6.3. Sigma holes are well known in many types of molecules but have not been identified in HMILs. The sigma holes are more pronounced in the $[AlCl_4]^-$ and $[GaCl_4]^-$ species because the regions with the weakest negative potential in the $[InCl_4]^-$ species occurs where some of the indium metal is exposed shown by the

blue wedged between the three chloride ligands.

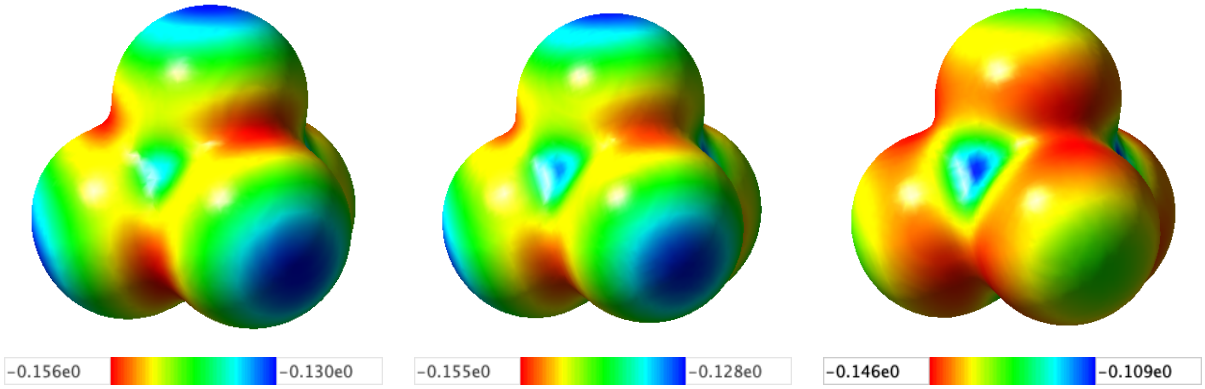


Figure 5.7: $[MCl_4]^-$ molecular electrostatic potentials projected onto the $[MCl_4]^-$ total density at an isovalue of 0.0008

The regions of the strongest negative electrostatic potential are situated between the chloride ligands. A cations most electrophilic regions will likely interact with the region between two chlorides while minimizing steric hindrance. Flexible cations would ideally contort to interact with as many of the six regions located between the chloride ligands, where the regions of most negative electrostatic potential are located.

Molecular electrostatic potentials of the $[InCl_5]^{2-}$ and $[InCl_6]^{3-}$ species

The MEPs of $[InCl_5]^{2-}$ and $[InCl_6]^{3-}$ are shown on the left and right of figure 5.8, respectively. The range of negative potential exhibited by the two species is stronger or more negative, than that of the $[MCl_4]^-$ species. The charge of the species contributes to the larger magnitude in negative potential as the anions have a -2 and -3 charge.

The MEPs of $[InCl_5]^{2-}$ and $[InCl_6]^{3-}$ reveal sigma holes which are more pronounced than in the tetrahedral chloroindate complex as none of the metal is exposed. The sigma holes on the $[InCl_5]^{2-}$ complex are more pronounced on the equatorial than the axial chlorides. The sigma holes of the equatorial chlorides have an oval shape while the sigma holes on the other species and on the axial positions are round.

In the MEP of the $[InCl_5]^{2-}$ anion the regions of the strongest negative potential are located between the axial and equatorial chlorides. There are two continuous rings, wedged between the axial and all three equatorial chloride ligands where the negative potential is the strongest. Previous studies have found that

$[InCl_5]^{2-}$ is the predominant anionic speciation at $x_{MCl_3} = 0.33$ which means the ratio of cations to anions is 2:1. It is likely that each cation will interact with one of the regions around the axial ligands to generate the most stable 2 cation : 1 anion configurations. The regions between the equatorial chlorides also feature a potential which is more negative than the sigma holes. If a cation is large enough it could potentially interact with both the regions of the strongest negative potential adjacent to either axial chloride ligands. The remainder of the cations structure could wedge the remainder of their structures between the equatorial chlorides.

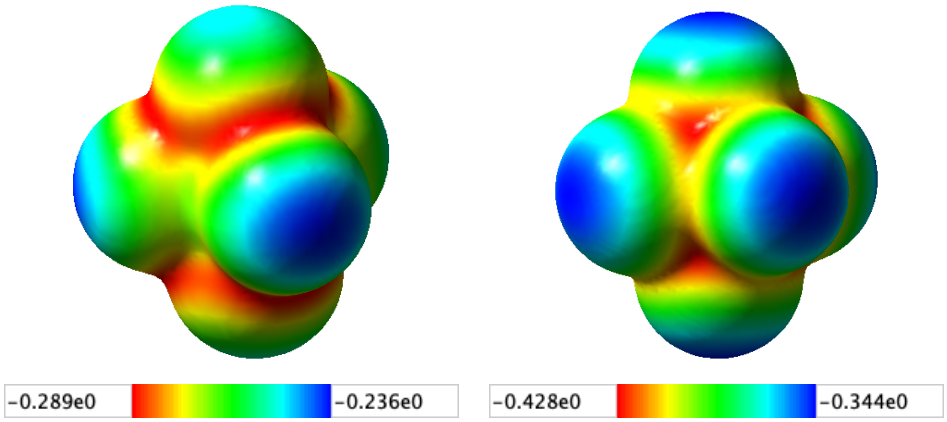


Figure 5.8: $[InCl_5]^{2-}$ and $[InCl_6]^{3-}$ molecular electrostatic potentials projected onto the $[InCl_5]^{2-}$ and $[InCl_6]^{3-}$ total densities at an isovalue of 0.0008

The MEP of the $[InCl_6]^{3-}$ anion shows that there are eight regions where the strongest negative potential is localized. The regions of the strongest negative potential are located between three chloride ligands, corresponding to the centre of the faces of the octahedral structure. The regions of strong negative potential are relatively small so interactions with cations may be limited by the size of the interacting moieties as steric hindrance may affect the interactions. Consequentially small positive moieties like hydrogen atoms may be best suited to interact with as the eight sites around the $[InCl_6]^{3-}$ anion.

Molecular electrostatic potentials of the $[M_2Cl_7]^-$ species

The MEPs of the $[Al_2Cl_7]^-$ and $[Ga_2Cl_7]^-$ anions are analogous with regard to where the weaker and stronger negative potentials are localized. The MEPs are similar with respect to the magnitude of negative potential exhibited by each region. Unlike in the monometallic species, the $[M_2Cl_7]^-$ species do not feature sigma holes. The region of the lowest negative potential is located between the three terminal chlorides at either

end of the structures in both $[M_2Cl_7]^-$ anions. Most likely the aluminium and gallium metals are slightly exposed due to the distortion of the two tetrahedral configurations at either end.

Figure 5.9 shows the MEPs of the $[Al_2Cl_7]^-$ and $[Ga_2Cl_7]^-$ anions on the left and right, respectively. The range in negative potential is lower in magnitude compared to the $[MCl_4]^-$ species of the same systems. The lower magnitude of negative potential, relative to the $[MCl_4]^-$ anions, is a result of the more dispersed charge observed for the oligomerized structures in the NACs.

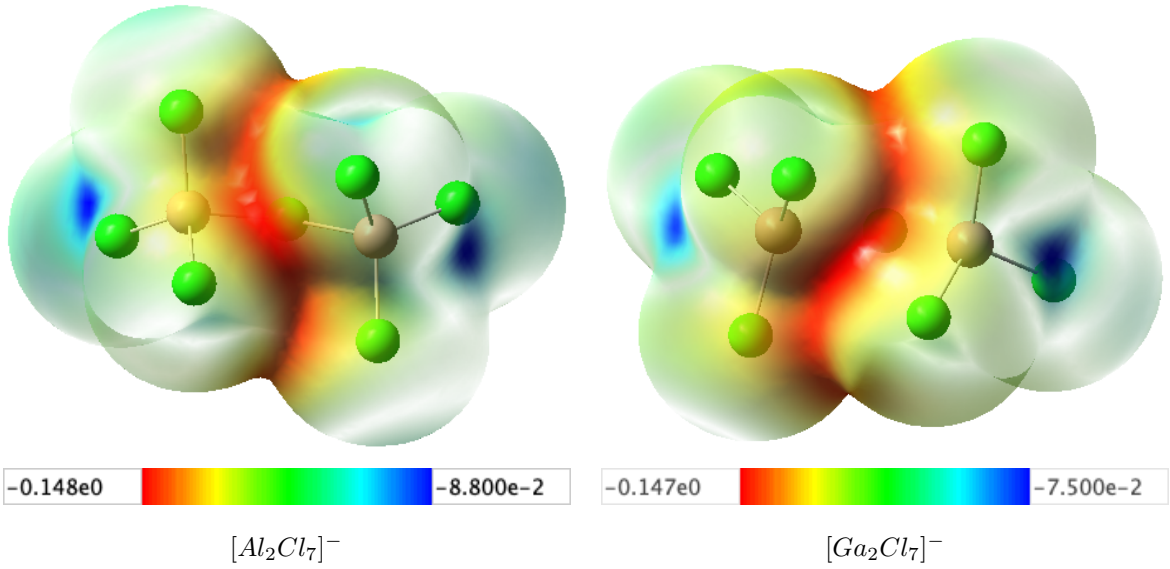


Figure 5.9: $[M_2Cl_7]^-$ molecular electrostatic potentials projected onto the $[M_2Cl_7]^-$ total densities at an isovalue of 0.0008

The region of the strongest negative potential is wedged between the terminal chlorides on the opposite side of the bridging chloride visualized as S and Z shaped twists on the $[Al_2Cl_7]^-$ and $[Ga_2Cl_7]^-$ anions, respectively. The MEPs coincides with the results from the NAC assignments in that the side where the most terminal chlorides are concentrated is the region where a cation is most likely to interact with the anion. The most stable IP structures will likely feature and an interaction of the cation with the side of the $[M_2Cl_7]^-$ anions where the four terminal chloride ligands are located, opposite to the bridging chloride ligand.

Molecular electrostatic potentials of the $[M_3Cl_{10}]^-$ species

Figure 5.10 depicts the MEPs of $[Al_3Cl_{10}]^-$ and $[Ga_3Cl_{10}]^-$ on the left and right, respectively. The magnitude of the strongest negative potential and weakest negative potential is similar in both species and is lower compared to the $[M_2Cl_7]^-$ species of the same system.

The MEPs of the $[M_3Cl_{10}]^-$ structures of both systems feature four regions of relatively weak negative potential. There are two regions of low potential sandwiched between the three terminal chlorides of each terminal metal, analogous to the regions of weak negative potential observed in the $[M_2Cl_7]^-$ species. The other two regions of weak negative potential are located at the extensions of the bonds between the bridging aluminium and bridging chloride ligands. the weak potential is likely generated by the charge being polarized away from the metal towards the bridging chloride ligand generating a weak negative potential on the opposite side of the metal.

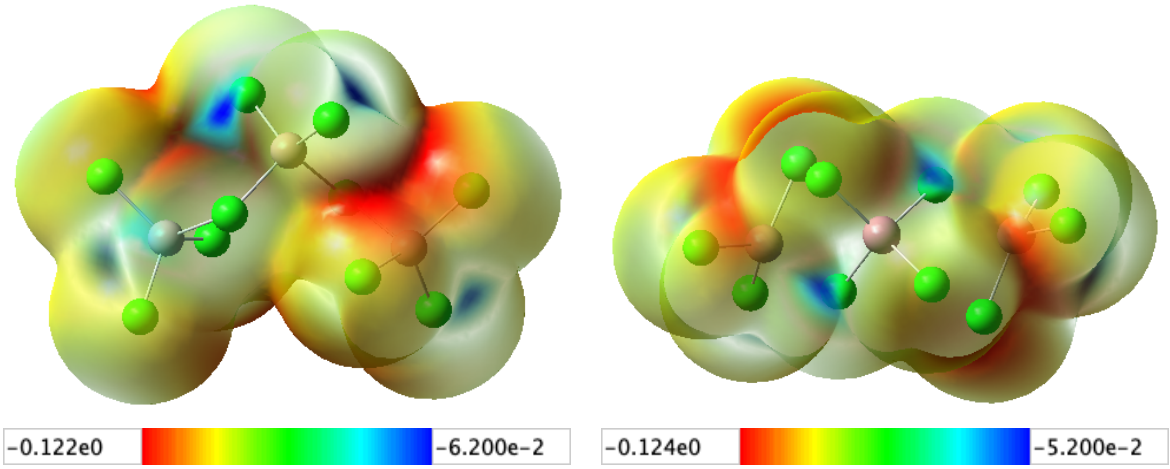


Figure 5.10: $[M_3Cl_{10}]^-$ molecular electrostatic potentials projected onto the $[M_3Cl_{10}]^-$ total densities at an isovalue of 0.0008

In the $[Al_3Cl_{10}]^-$ species the extension of the bridging M-Cl bonds features the weakest negative potential on the MEP. The weakest negative potential on the $[Ga_3Cl_{10}]^-$ species is located between the terminal chlorides attached to the terminal metals. The difference in the location of the regions of weakest negative potential between the $[Al_3Cl_{10}]^-$ and $[Ga_3Cl_{10}]^-$ is likely due to slightly different geometries the structures have and the size of the gallium versus the aluminium atoms. As the NACs show that the charge distribution is similar and the $[InCl_4]^-$ species showed the weakest negative potential to be on some of the exposed indium it is

likely that the terminal chloride ligands are contorted so the MEP shows the potential of the gallium atom.

The strongest negative potential is localized on two sites on both $[M_3Cl_{10}]^-$ anions. The regions of the strongest negative potential is localized between the two of the terminal chlorides of the terminal metal and a terminal chloride on the bridging metal on both sides of the species. Another region of relatively strong negative potential is on the opposite site of the anion between four terminal chlorides of the two terminal metals, similar to the region of the strongest negative potential of the $[M_2Cl_7]^-$ species. Due to the $[M_3Cl_{10}]^-$ anions high degree of flexibility and variety of sites with a relatively strong negative potential there will likely be a high number of stable IP structures. The $[M_3Cl_{10}]^-$ species will likely contort and there will be stabilizing interactions with the three regions where the negative potential is the strongest. The region of negative potential between the four terminal chlorides is continuous and larger than the two site of the most negative potential which may make it more attractive for cations to intact with.

Molecular electrostatic potentials of the linear $[M_4Cl_{13}]^-$ species

Figure 5.11 shows the MEPs of the linear $[M_4Cl_{13}]^-$ species of the chloroaluminate and chlorogallate systems on the left and right, respectively. The range of magnitude of the negative potential is lowered when compared to the trimetallic species of the same system. The magnitude of the range of negative potentials lowers upon every subsequent oligomerization. The magnitude of negative potentials becoming lower upon oligomerization aligns with the trend of the charge being more dispersed upon further oligomerization as described by the NACs.

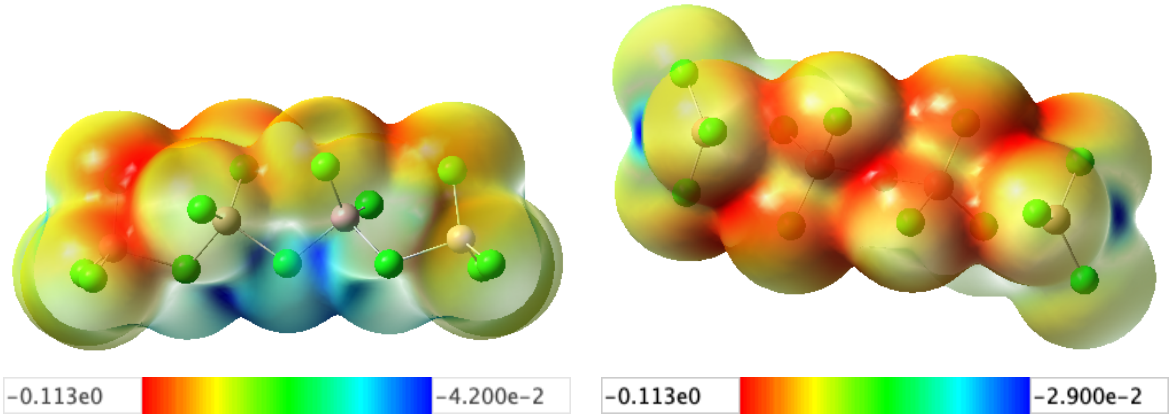
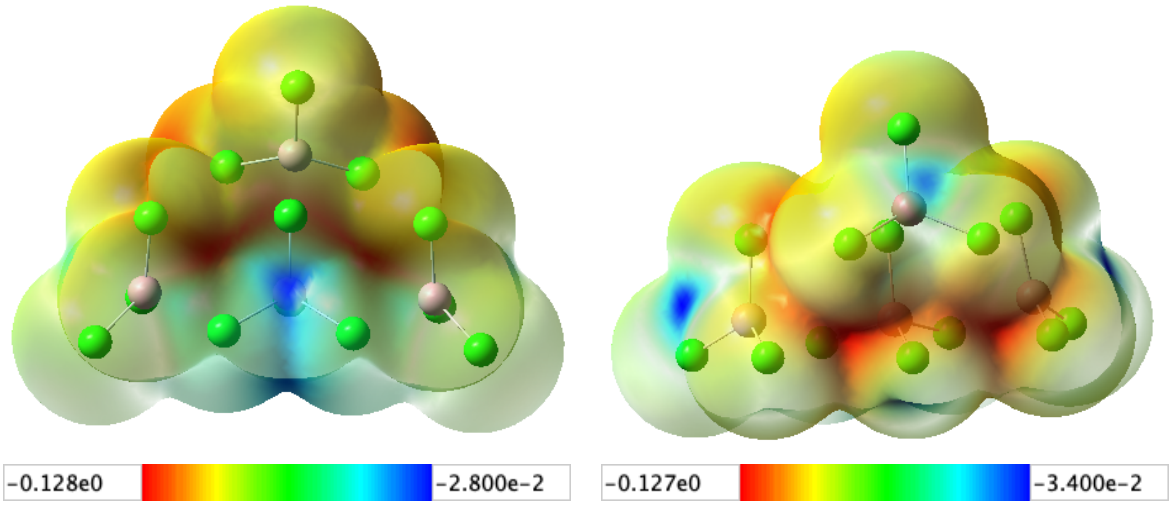


Figure 5.11: Linear $[M_4Cl_{13}]^-$ molecular electrostatic potentials projected onto the linear $[M_4Cl_{13}]^-$ total densities at an isovalue of 0.0008

The linear $[M_4Cl_{13}]^-$ species have three regions of relatively weak negative potential; two at each terminal metal, between the three terminal chloride ligands and one adjacent to the bridging chloride ligands. In the $[Al_4Cl_{13}]^-$ species the region of the weakest negative potential is adjacent to all the bridging chloride ligands. In the $[Ga_4Cl_{13}]^-$ species the weakest negative potential is located between the three terminal chlorides of the terminal gallium atoms as shown in figure 5.11. The difference in the location of the weakest negative potential of the linear $[M_4Cl_{13}]^-$ species is analogous to the difference in locations of weakest negative potential observed in the $[M_3Cl_{10}]^-$ species. The reasons why the weakest negative potentials are in different locations in the chloroaluminate and chlorogallate structures are the same as those described for the trimetallic species.

The linear $[M_4Cl_{13}]^-$ in both systems have analogous regions of the strongest negative potential. The regions of the strongest negative potential are located on the side of the anions where the terminal chlorides attached to bridging metals are situated. The strongest negative potentials are localized between the terminal chlorides. Both structures are most likely to interact with cations via the side where the terminal chlorides are located. The flexibility of the tetrametallic species allows the structure to readily contort to conformations which idealize the cation-anion interactions by maximizing the number and quality of intermolecular interactions between the terminal chlorides and the most electrophilic sites on the cation. It is likely that there will be a wide variety of different stable IP structure featuring the linear $[M_4Cl_{13}]^-$ species in different conformations which maximize the interactions with the cation.

Molecular electrostatic potentials of the branched $[M_4Cl_{13}]^-$ species



$[Al_4Cl_{13}]^-$ $[Ga_4Cl_{13}]^-$

Figure 5.12: Branched $[M_4Cl_{13}]^-$ molecular electrostatic potentials projected onto the branched $[M_4Cl_{13}]^-$ total densities at an isovalue of 0.0008

On the left and right side of figure 5.12 the MEPs of the branched $[Al_4Cl_{13}]^-$ and $[Ga_4Cl_{13}]^-$ species are shown, respectively. The magnitude of the strongest negative potential is larger than that of the $[M_3Cl_{10}]^-$ species of the same systems, going against the previously observed trend that the magnitude of potential drops upon subsequent oligomerization.

The weakest negative potential of the branched $[Al_4Cl_{13}]^-$ species is located in the wedge between the two bridging chlorides of the linear segment of the structure, shown on the chloroaluminate structure on the left of figure 5.12. The region of the weakest negative potential of the $[Ga_4Cl_{13}]^-$ species is located at the end of the linear segment of the structure. The difference in the location of the least negative sites between the branched chloroaluminate and chlorogallate structures is consistent with the differences observed for the $[M_3Cl_{10}]^-$ and linear $[M_4Cl_{13}]^-$ species.

The regions with the strongest negative potential on the branched tetrametallic structures are in the same place on both species. The sites of the most negative potential are situated on the side of the anions where the most terminal chlorides are situated, which can be seen in the $[Ga_4Cl_{13}]^-$ MEP, on the right hand side of in figure 5.12. Interactions between the cations and the side of the branched anions with most of the terminal chlorides in chloroaluminate and the chlorogallate systems will lead to the lowest energy IP structures. As

one side of the anion features a much higher negative potential it should be useful to evaluate IP dimer structures as competing cations will be located on both sides of the anions in the bulk liquid.

5.1.3 Fukui Functions of the liquid phase anion structures

Condensed Fukui functions and Fukui functions[5] were computed to show the nucleophilic sites as well. This section discusses the Fukui functions of the anions which are presented as projections onto the total density at an isovalue of 0.008. The Fukui functions of the anions depicted in this section are the Fukui functions for the removal of an electron. The projected function shows where electron density is lost between the electronic structure of $[M_xCl_{3x+1}]^-$ and the electronic structure of M_xCl_{3x+1} upon the removal of an electron density. In the figures the most negative regions, in red, represent the greatest loss of electron density occurring while the blue regions indicate no difference in electron density upon the loss of an electron. In all evaluated species there was no increase in electron density in any region due to polarization.

Fukui function of the $[MCl_4]^-$ species

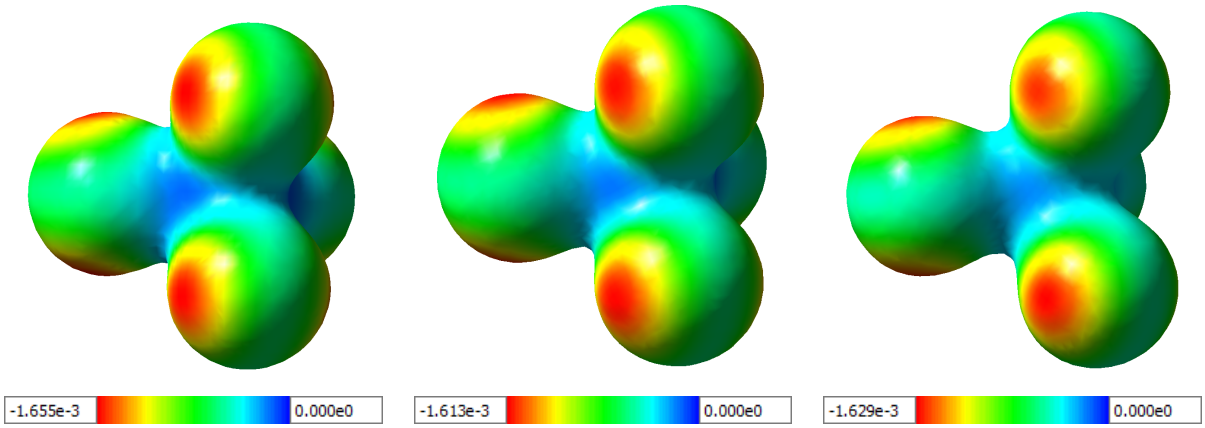


Figure 5.13: $[MCl_4]^- \rightarrow MCl_4$ Fukui functions projected onto the $[MCl_4]^-$ total density at an isovalue of 0.008

Figure 5.13 shows the projected Fukui functions of the $[MCl_4]^-$ species. The magnitude of the electron density lost at the sites where the greatest loss of electron density occurs is the largest in the $[AlCl_4]^-$, followed by $[InCl_4]^-$ and $[GaCl_4]^-$, respectively. The Fukui functions show that the electron density is lost from the chlorides ligands in every $[MCl_4]^-$ species. The loss of electron density occurs in what looks to be

two sets of 3p orbitals which are parallel to each other and perpendicular to the other set of 3p orbitals as seen in figure 5.13. To confirm whether the loss of electron density occurs from the p orbitals the HOMOs of $[AlCl_4]^-$, $[GaCl_4]^-$ and $[InCl_4]^-$ were evaluated. The HOMOs of each $[MCl_4]^-$ species are depicted in figure 5.14.

As shown in figure 5.14, each species has three degenerate HOMOs. The loss of electron density depicted in the Fukui function aligns with a partial loss of each of the three degenerate HOMOs. The MOs are composed predominantly from mixtures of the chloride ligands 3p orbitals. The Fukui functions indicate that regions of strong nucleophilicity are even more localized based on the electrons being lost primarily from chloride p orbitals. The Fukui function implies that a cation would best interact with the $[MCl_4]^-$ species if the cation has the ability to interact with the chlorides from two sides by clamping around the chlorides to interact with both sides of the p orbitals.

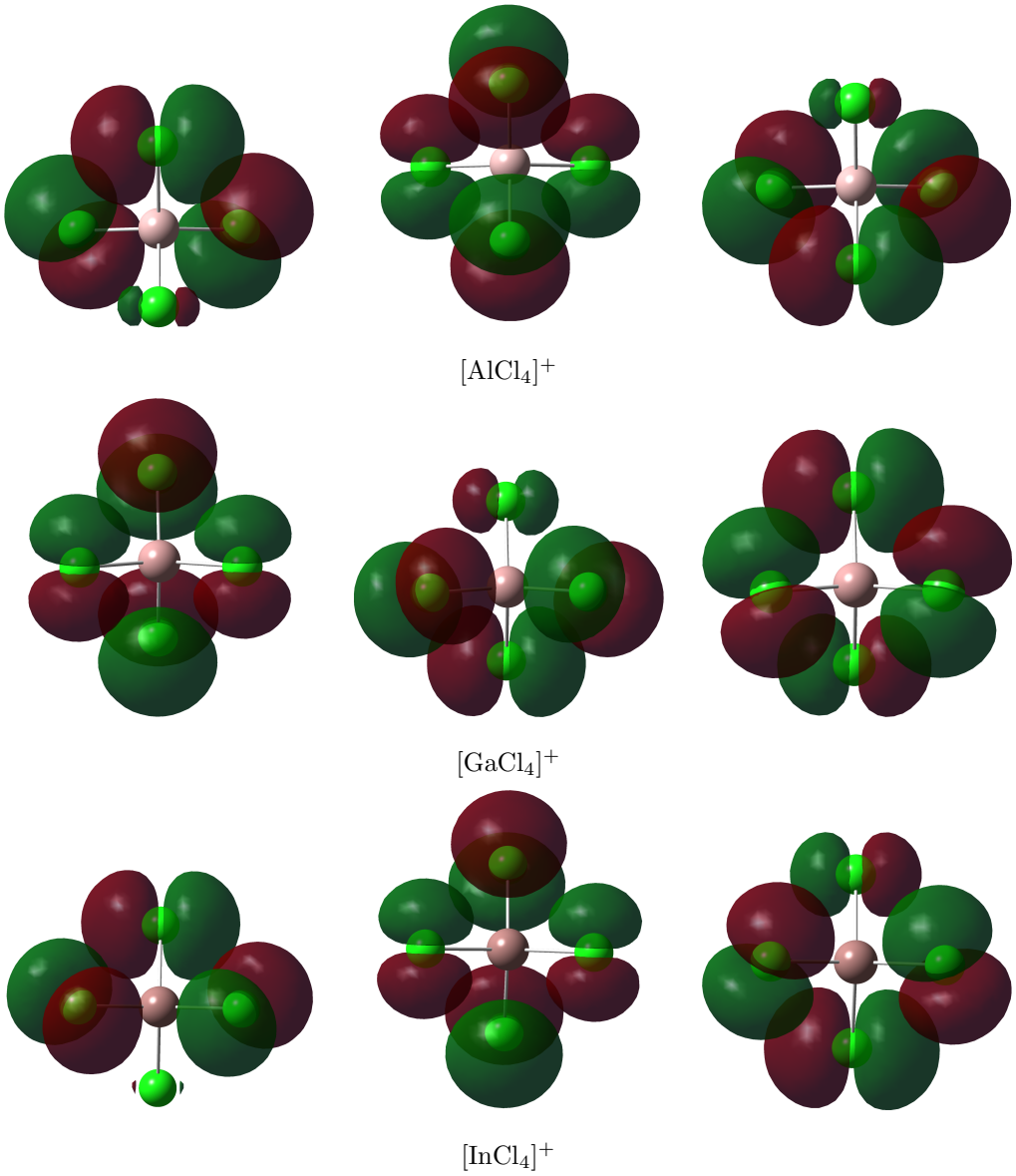


Figure 5.14: The three degenerate HOMOs of each $[MCl_4]^-$ species at an isovalue of 0.02

Fukui functions of the $[InCl_5]^{2-}$ and $[InCl_6]^{3-}$ species

Figure 5.14 shows the projected Fukui functions of the $[InCl_5]^{2-}$ and $[InCl_6]^{3-}$ species. The Fukui functions of the $[InCl_5]^{2-}$ and $[InCl_6]^{3-}$ reflect the loss of one electron and not the total 3- and 2- charges. The magnitude of the loss in charge density of the $[InCl_5]^{2-}$ species is greater than that in the $[InCl_4]^-$ but lower in the $[InCl_6]^{3-}$ species. A larger magnitude in the loss of electron density indicates that the loss of one electron is more localized, Hence the $[InCl_5]^{2-}$ species loss of electron density is more localized than in the

$[InCl_4]^-$ species and the loss of electron density is more delocalized in the $[InCl_6]^{3-}$ species.

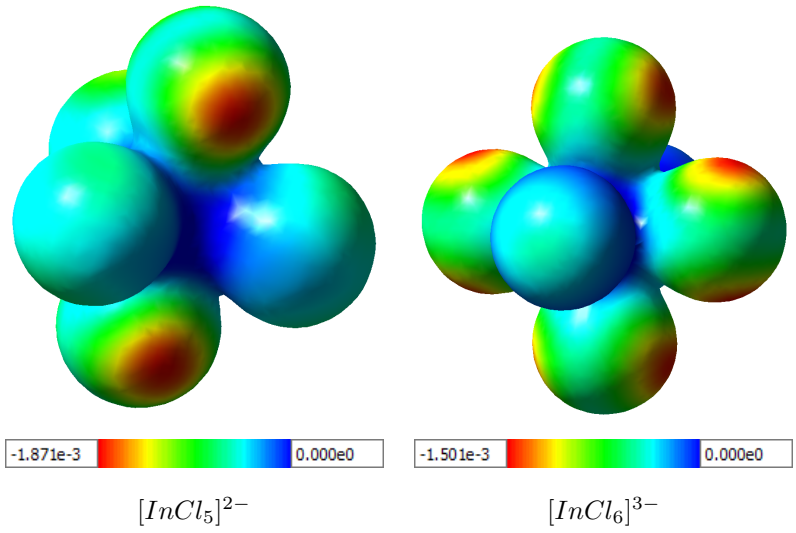


Figure 5.15: $[InCl_5]^{2-} \rightarrow [InCl_5]^-$ Fukui Function projected onto the $[InCl_5]^{2-}$ total density at an isovalue of 0.008 and $[InCl_6]^{3-} \rightarrow [InCl_6]^{2-}$ Fukui functions projected onto the $[InCl_6]^{3-}$ total density at an isovalue of 0.008

The electron density of $[InCl_5]^{2-}$ is mostly lost in two parallel 3p orbitals of the axial chlorides. There is also a small loss in electron density in the 3p orbitals of the equatorial chloride ligands, but it is marginal compared to the loss of electron density in the axial ligands. The ideal interaction with a cation should hence occur with the axial ligands but loss of the electron density from the p orbitals in conjunction with the anions structures indicates that there is a preferential side to interact with where the nucleophilic sites are wedged between equatorial ligands. As there will be two cations for each anions when $[InCl_5]^{2-}$ is the predominant speciation, each cation may interact with one axial chloride ligand on either side of the anion.

The Fukui function of the $[InCl_6]^{3-}$ anion shows the largest loss of electron density is in 4 3p orbitals of the chloride ligands. Analogously to the $[MCl_4]^-$, the four 3p orbitals are in two sets of parallel p orbitals which are perpendicular to one another. However, all p orbitals are on the same plane of symmetry. The loss from four rather than 6 3p orbitals is likely due to one electron being lost from the e_g level, as described in crystal field theory. The localization onto four instead of all six ligands could indicate that there is a preference for an interaction with two rather than three of the chloride ligands when the geometry of the cation only permits the approach from one side. The magnitude of electron density lost in the regions of the largest loss of electron density is lower than in the $[InCl_4]^-$ species because a small amount of electron density is also lost in the two other chloride ligands.

Fukui function of the $[M_2Cl_7]^-$ species

Figure 5.16 shows the projected Fukui functions of the $[Al_2Cl_7]^-$ and $[Ga_2Cl_7]^-$ species. The magnitude of electron density lost in the regions with the largest loss of electron density is lower than in $[AlCl_4]^-$ and $[GaCl_4]^-$ species.

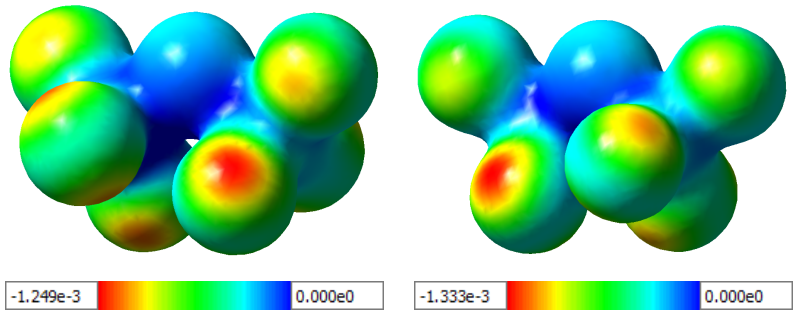


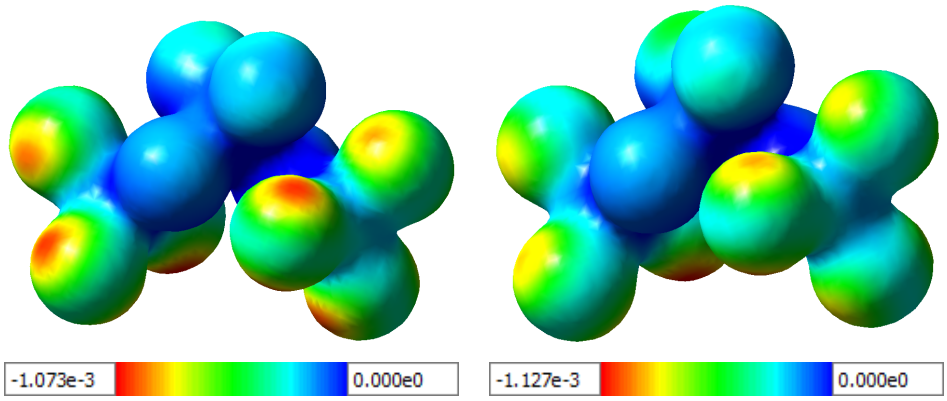
Figure 5.16: $[M_2Cl_7]^- \rightarrow M_2Cl_7$ Fukui functions projected onto the $[M_2Cl_7]^-$ total density at an isovalue of 0.008

The Fukui functions of the $[M_2Cl_7]^-$ species show that the loss of electron density is localized in the same way in the chloroaluminate and chlorogallate systems. The loss of the most electron density occurs in the terminal chloride ligands which are furthest from the bridging chloride ligand. analogously to the monometallic anions the loss of electrons is predominantly from the 3p orbitals of the chloride ligands. The bridging chloride only experiences a marginal loss of electrons compared to the terminal chlorides.

The most favourable interactions between $[M_2Cl_7]^-$ species and cations predicted by the Fukui function is similar to that predicted by the MEPs. The ideal location based on both analyses is a cation placed on the side of the anion opposite of the bridging chloride ligand. Assuming the cation is rigid it should ideally interact with the maximum number of nucleophilic points and hence it will be wedged in between the terminal chlorides on the opposite side of the bridging chloride.

Fukui function of the $[M_3Cl_{10}]^-$ species

Figure 5.17 shows the projected Fukui functions of the $[Al_3Cl_{10}]^-$ and $[Ga_3Cl_{10}]^-$ species. The magnitude of the loss of electron density lost in the regions with the biggest loss in electron density is lower when compared to $[Al_2Cl_7]^-$ and $[Ga_2Cl_7]^-$.



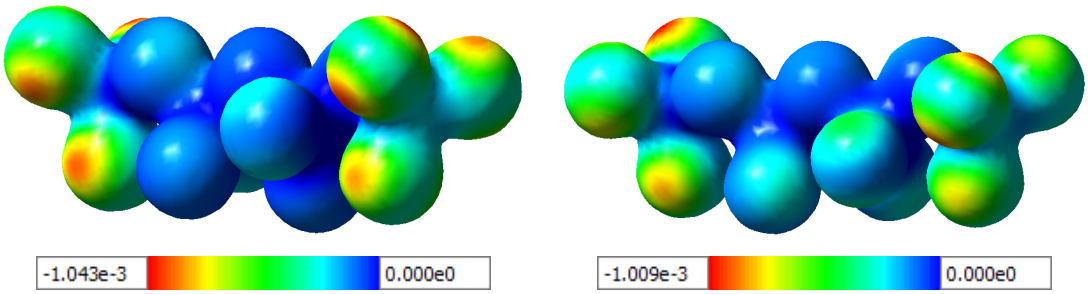
$[Al_3Cl_{10}]^-$ $[Ga_3Cl_{10}]^-$

Figure 5.17: $[M_3Cl_{10}]^- \rightarrow M_3Cl_{10}$ Fukui functions projected onto the $[M_3Cl_{10}]^-$ total density at an isovalue of 0.008

The projections of the Fukui functions of the $[M_3Cl_{10}]^-$ anions show that the loss of electron density occurs primarily on the terminal chlorides 3p orbitals attached to terminal metals. The strongest loss of electron density occurs primarily on the 3p orbitals of the chloride ligands which are furthest from the bridging chloride ligands. The Fukui function indicates that an interaction of a cation with the terminal chlorides of the terminal metals of the $[M_3Cl_{10}]^-$ species will result in the most stable ion pair structures.

Fukui function of the linear $[M_4Cl_{13}]^-$ species

Figure 5.18 shows the projected Fukui functions of the linear $[Al_4Cl_{13}]^-$ and $[Ga_4Cl_{13}]^-$ species. The magnitude of the greatest loss of electron density is lower than in the $[M_3Cl_{10}]^-$ anions of the same system meaning that the loss in charge is more delocalized.



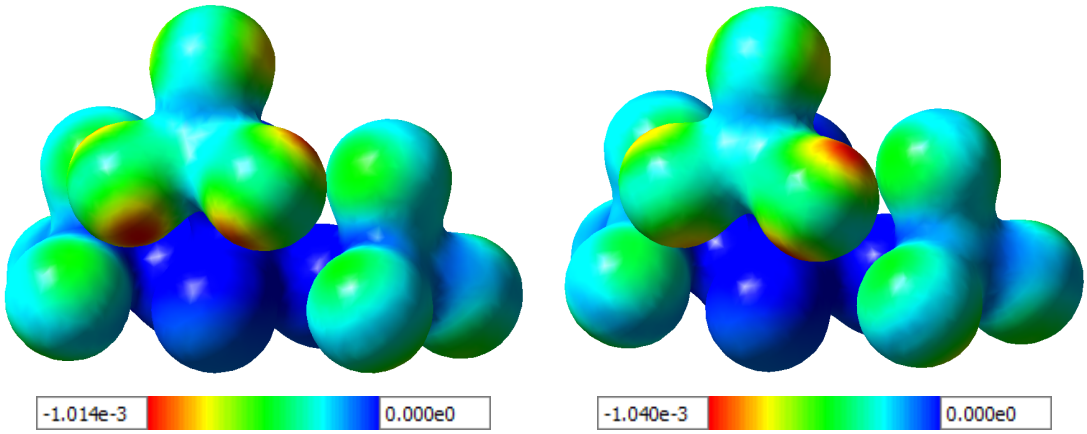
$[Al_4Cl_{13}]^-$ $[Ga_4Cl_{13}]^-$

Figure 5.18: Linear $[M_4Cl_{13}]^- \rightarrow M_4Cl_{13}$ Fukui functions projected onto the linear $[M_4Cl_{13}]^-$ total density at an isovalue of 0.008

The Fukui function of the linear $[M_4Cl_{13}]^-$ anions are consistent with the trend that the terminal chloride ligands on the terminal metals loose most of the electron density from the 3p orbitals. The relative loss of electron density from the terminal chlorides 3p orbitals is greater in the chloroaluminate system than it is in the chlorogallate system.

The nucleophilic sites of the linear $[M_4Cl_{13}]^-$, described by the Fukui functions describe different nucleophilic sites than the MEPs. the MEPs indicate that a cation will form the most stable IPs when interacting with the side of the anion opposite to the bridging chlorides while the Fukui functions indicate that an interaction with the terminal chloride ligands on the terminal metals will lead to the lowest energy structures.

Fukui function of the branched $[M_4Cl_{13}]^-$ species



$[Al_4Cl_{13}]^-$ $[Ga_4Cl_{13}]^-$

Figure 5.19: Branched $[M_4Cl_{13}]^- \rightarrow M_4Cl_{13}$ Fukui functions projected onto the branched $[M_4Cl_{13}]^-$ total density at an isovalue of 0.008

The projected Fukui functions of the branched $[Al_4Cl_{13}]^-$ and $[Ga_4Cl_{13}]^-$ species are shown on the left and right side of figure 5.19, respectively. The magnitude of electron density lost at the sites where most electron density is lost is similar to the charge loss shown in the Fukui functions of the linear $[M_4Cl_{13}]^-$ species.

The Fukui function of the branched $[M_4Cl_{13}]^-$ shows that the most nucleophilic sites are on the terminal chloride ligands which are part of the branched MCl_3 moiety. The Fukui functions contrast with the MEPs which indicate the most nucleophilic region of the anion to between the branched and linear portion of the anion adjacent to the largest concentration of terminal chloride ligands. The IP analyses will give insight into which of these analyses is more defining of the interaction profiles.

5.1.4 Liquid phase anion structures charge distribution, MEPs and Fukui function – Key Takeaways

The NACs showed that the species of the chloroaluminate systems have M-Cl bonds which have a more covalent character. The M-Cl bonding becomes progressively more ionic when moving down group 13. The chlorogallates have more ionic M-Cl bonding than the chloroaluminates and the M-Cl bonding in the chloroindate system is the most ionic of the chlorometallate systems evaluated.

The saturation of the indium in the chloroindate complexes with additional chlorides causes the difference in NACs between the metals and chloride ligands to become bigger. The difference in charges of metals and chlorides becomes smaller upon oligomerization in the chloroaluminate and chlorogallate systems. The different environments of both the chloride ligands and metals diversify as the structures get larger. In the multimetallic structures of the chloroaluminate and chlorogallate systems the magnitude of NACs of different chloride environments is ordered; bridging chlorides < terminal chloride attached to a bridging metals < Terminal chlorides attached to a terminal metals.

The MEPs coincide with the NAC assignments with respect to where charge is localized. Additionally, the MEPs revealed that there are sigma holes present in all of the monometallic species as extensions of the M-Cl bonds. The MEPs showed that there are localized pockets of highest electrostatic potential wedged between chlorides in all chlorometallate species. There are usually multiple sites on each anion which feature the strongest negative potential indicating a broad range of interactions which should lead to a high number of stable IP conformations. There are regions of relatively weak negative potential wedged between the chlorides at the terminal ends of the oligomerized species.

The Fukui functions revealed that the loss of electron density occurs on selected 3p orbitals of the chlorides in all species. For the oligomerized $[M_2Cl_7]^-$, $[M_3Cl_{10}]^-$ and $[M_4Cl_{13}]^-$ species only the 3p orbitals of the chlorides located on the terminals of the structure loose electron density with the largest loss of electron density occurring at the chlorides which were furthest from the bridging chloride ligands. Since the two descriptions of the most nucleophilic sites on the anions via the MEP and the Fukui functions are different it must be determined which approach gives more valuable insight into what kind of IP structures will form.

5.2 Liquid phase cation electronic structure evaluation

The electronic structure of the stable cation conformers was also evaluated through the NACs, MEPs and Fukui functions to predict IP interactions. The different approaches to determine electronic structure were undertaken to determine which of the methods used to evaluate the electronic structure are the most useful in describing the formation of IPs.

5.2.1 1-ethyl-3-methyl-imidazolium electronic structure

1-ethyl-3-methyl-imidazolium electronic structure

The NACs were assigned using the same schemes as for the anions, NPA, ChelpG and ADCH. Each charge distribution scheme is shown without subdividing the atoms into different environments as the differences in the NACs assigned by the different methods is more than just the magnitude of the charges.

Figure 5.20 shows the atomic numbering of the two $[C_2C_1Im]^+$ conformers. Figures 5.21 and 5.22 show the assigned NACs of the in and out of plane $[C_2C_1Im]^+$ conformers, respectively. There are large differences between the NACs assigned by the different methods.

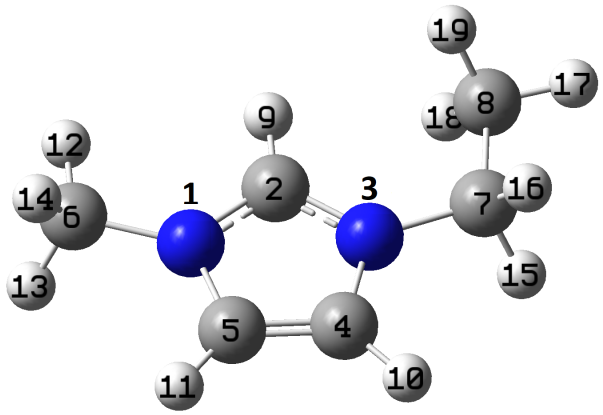


Figure 5.20: $[C_2C_1Im]^+$ atomic numbering

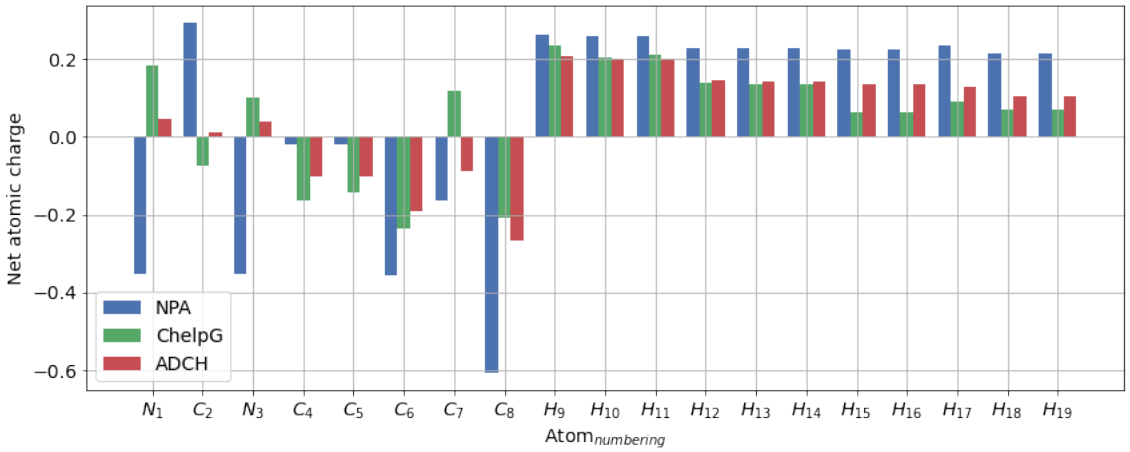


Figure 5.21: $[C_2C_1Im]^+$ in plane net atomic charges computed in NPA, ChelpG and ADCH

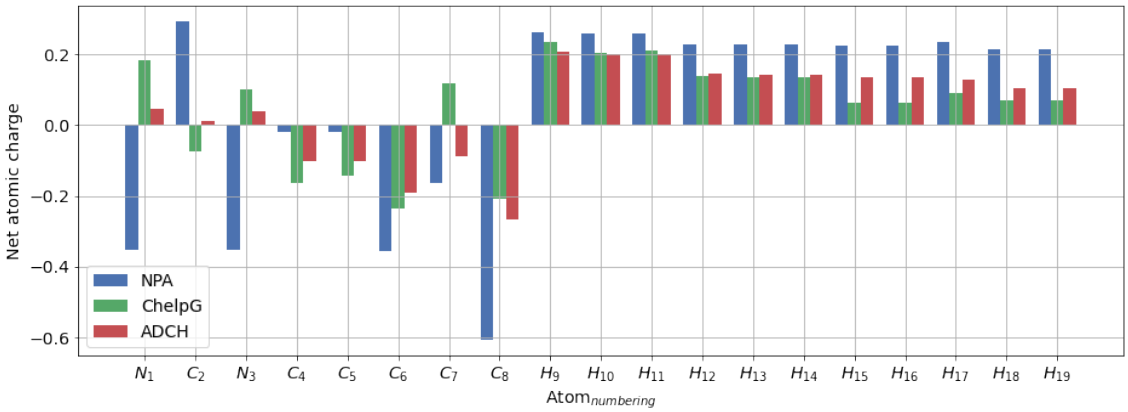


Figure 5.22: $[C_2C_1Im]^+$ out of plane net atomic charges computed in NPA, ChelpG and ADCH

The magnitude of NACs assigned is different from one method to another. Additionally, the nature of the assigned charges varies for some atoms with respect to the NAC assignment scheme. According to one NAC assignment method a positive partial charge is assigned to an atom and according to another a negative partial charge is assigned. In both conformers the C_2, N_1, C_7 and N_3 atoms are assigned positive or negative NACs by different NAC assignment methods. The NPA method is the only method which assigns a negative charge to the N_1 nitrogen atoms in both structures and the N_3 nitrogen in the in plane structure. The ChelpG method assigns the contradicting charge to the C_2 and C_7 carbons in both conformers and the N_3 nitrogen in the out of plane conformer. The difference in NAC assignment is most evident in the C_2 carbon and both nitrogen atoms in both conformers. The C_2 carbon in both conformers has the highest concentration of positive charge according to the NPA method while the ADCH method and ChelpG assigned a small positive and negative partial charges, respectively. Both nitrogen atoms, N_1 and N_3 are prescribed strong negative charges by the NPA method while the other methods only assign weak positive or negative charges in both conformers.

The NPA method assigns the C_2 carbon with the most positive NAC followed by the hydrogen atoms which are attached to the imidazolium ring carbon atoms. The hydrogen atoms of the methyl and ethyl moieties also have a positive NAC of > 0.2. The localization of positive charge in the C_2 carbon and the different hydrogen environments by the NPA method is consistent in both conformers. The nitrogen atoms and remaining carbon atoms all have a negative NACs. The two nitrogen atoms and the two terminal carbon atoms of the ethyl and methyl moieties have relatively strong negative partial charges of $<$ -0.35 in both conformers. The terminal carbon on the ethyl appendage must most negative charge according to the NPA method at about -0.6 in both conformers. The NACs assigned by the NPA method have a higher magnitude than those assigned by the other two methods.

the ChelpG method assigns recognizably different charges to the individual atoms in both conformers. In the in-plane conformer the ChelpG method assigns the hydrogen atoms of the imidazolium ring the most positive NACs species followed by the nitrogen adjacent to the methyl arm. In the out of plane conformer the charges of the ring hydrogen atoms and the N_1 nitrogen are more degenerate in the magnitude of positive charge. In the in plane conformer the methyl arms hydrogen atoms feature the next largest positive NAC followed by the C_7 carbon. In the out of plane structure C_7 carbon is more positively charged than the methyl moieties hydrogen atoms. The N_3 and the remainder of the hydrogen atoms of both conformers carry the smallest positive charge but the small positive charges are far smaller in magnitude in the out of plane structure than in the in plane structure. According to the ChelpG method, the carbon of the methyl moiety has the most negative NAC in both conformers and is approximately the same. In the in plane conformer the terminal C_8 carbon of the ethyl arm also carries a strong negative charge while in the out of plane structure it is marginal. The carbon atoms in the imidazolium ring carry the third and fourth strongest negative charge in the in-plane conformer and the second and third strongest negative charge in the out of plane conformer. The N_1 nitrogen carries the lowest and fourth lowest negative charge in the in and out of plane conformers, respectively.

The difference between the NAC assignments of the two conformers determined by the ChelpG NAC assignment method shows that the grid-based method is far more effected by changes in conformation than the NPA method. The largest difference in NACs assigned occur on the side of the imidazolium where the ethyl arm is rotated. The discrepancy between the NAC assignments likely arises due to the grid points of the rotated ethyl arms atoms overlapping with atoms in close proximity to the N_3 nitrogen.

The ADCH NAC method assigned the same nature of charges as the NPA method to all atoms except for the nitrogen atoms. The NACs assigned by the ADCH method always have a lower magnitude than those assigned by the NPA method. According to the ADCH method the hydrogen atoms of the imidazolium ring carry the most positive charge. In the out of plane structure the H_{11} is the most positively charged atom while in the in plane structure it is the H_9 hydrogen. The remainder of the hydrogen atoms on the methyl and ethyl moieties which are α to the nitrogen atoms are carry the next highest charge and are very similar in charge magnitude. The hydrogen at the terminal end of the ethyl moiety has the lowest positive charge of all hydrogen atoms in both conformers. The N_1, C_2 and N_3 carry the smallest positive charge in the in plane structure while the N_3 does not carry a positive charge in the out of plane structure. The most negative charge according to the ADCH method is located on the C_8 carbon at the terminal end of the ethyl arm in both conformers. The second strongest magnitude in negative charge is located on the terminal C_6 methyl carbon. The back two carbons of the imidazolium ring, C_5 and C_4 have the next largest negative charge. The C_7 carbon of the in plane structure has a similar magnitude in negative charge while the magnitude in

charge is smaller in the out of plane structure.

All NAC assignment methods concur that the positive charge throughout the $[C_2C_1Im]^+$ cation is predominantly localized on the hydrogen atoms in both conformers. In all the NAC assignment methods there is a hierarchy of hydrogen electrophilicity based on the environment of the hydrogen atoms. The hydrogen atoms which are directly attached to the imidazolium ring carry the most positive charge of any hydrogen environment according to every NAC assignment method. The aliphatic hydrogens do not carry as much positive charge as the ring hydrogens but are all net positive. The order of magnitude of positive charge carried by the aliphatic hydrogen atoms varies based on charge method. In the NPA and ADCH methods the aliphatic hydrogens α to the nitrogen atoms carry the second highest positive charge while the hydrogens on the ethyl arm, which are β to the nitrogen atoms carry the lowest positive charge of all the hydrogen atoms. In the ChelpG Branched $[M_4Cl_{13}]^-$ method the distinction between the aliphatic hydrogen environments is stronger based on whether the hydrogen atoms are part of the methyl or ethyl moiety. The ChelpG method shows that hydrogen atoms of the methyl moiety are more positively charged than those of the ethyl moiety. The terminal hydrogen atoms of the ethyl moiety, which are the hydrogen atoms β to the nitrogen, carry more positive charge than the α hydrogen atoms in the in-plane structure according to the ChelpG method. The NPA method assigns the C_2 carbon the most positive partial charge. The most stable IP interactions will likely maximize the interactions between the anions nucleophilic sites with the hydrogen atoms around the $[C_2C_1Im]^+$ cation. Interactions with the C_2 carbon are also favorable according to the NPA method.

Figure 5.23 shows the MEP maps of both $[C_2C_1Im]^+$ conformers. The MEP of the in-plane conformer is depicted on the left and the MEP of the out of plane conformer is depicted on the right. The magnitude of the strongest positive potential is the same in both conformers while the lowest positive potential is slightly larger in the in-plane conformer.

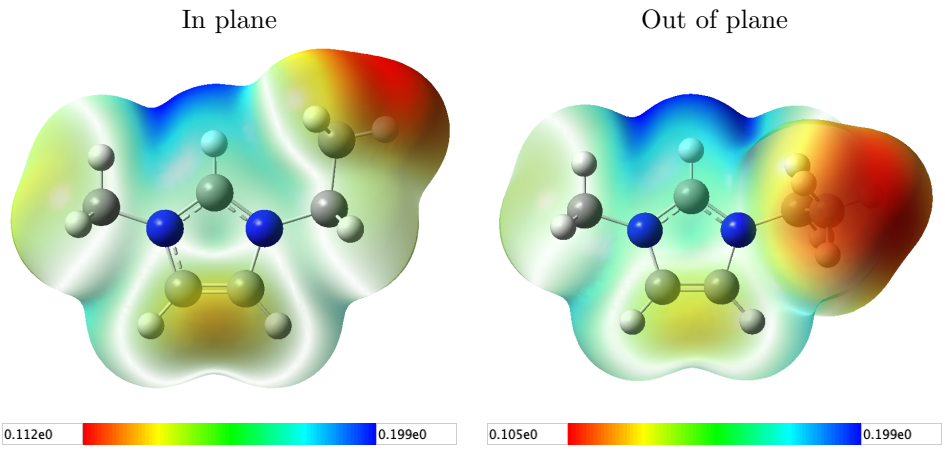


Figure 5.23: $[C_2C_1Im]^+$ molecular electrostatic potential projected onto the $[C_2C_1Im]^+$ total density at an isovalue of 0.0008

The MEPs of both the in plane and out of plane $[C_2C_1Im]^+$ conformers are the same around the methyl moiety and the imidazolium ring and different around the ethyl moiety. The strongest positive potential is located in the plane of the imidazolium ring, adjacent to the hydrogen of the C_2 carbon in front of the ring. In the in-plane structure the C_2 hydrogen is less accessible and is blocked by the ethyl arm. The ethyl arm has the least positive potential making the interaction relatively less attractive. The regions adjacent to the other two hydrogen atoms of the imidazolium ring, at the back of the ring, also feature a relatively strong positive potential. The potential is stronger in the out of plane structure. Hence it is likely that the out of plane structure will be favoured to interact with by the anions. The region above and below the C_2 carbon are also feature a more positive potential than the remainder of the structure.

The MEPs indicate that the most stable interactions with anions will feature the anions interacting with the front side of the imidazolium ring. Other stable conformers may feature the anions at the back of the ring. The larger trimetallic and tetrametallic anions of the chloroaluminate and chlorogallate system could wrap around the ring and feature secondary interactions with the ethyl arm.

The Fukui functions of the cation, f_+ were used predict the most electrophilic sites on the cation. The Fukui functions, projected onto the total electron density of the $[Cation]^+$. The isovalues are different from cation to cation to highlight the regions where electron density gain occurs for clarity. Consequentially the magnitude of electron loss at different points cannot be precisely compared from the figures where the isovalues are not the same. The projected Fukui functions of the in plane and out of plane conformers are shown in figures 5.24 and 5.25, respectively. The localization in the gain of electron density is marginally

more concentrated in the out of plane structure.

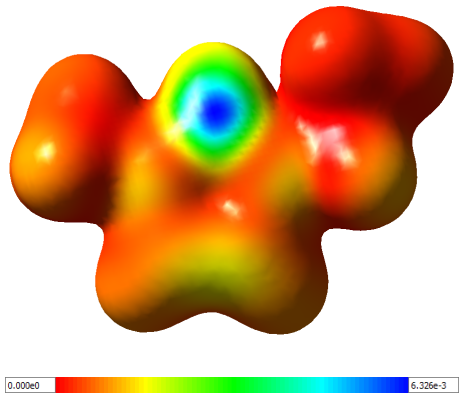


Figure 5.24: In plane $[C_2C_1Im]^+ \rightarrow C_2C_1Im$ Fukui function projected onto the $[C_2C_1Im]^+$ total density at an isovalue of 0.0004

In the in-plane conformer the most electrophilic sites are above and below the C_2 carbon as show by the blue dot above the region. The sites above and below the ring show an equal loss in electron density which makes both sites equally favourable to interact with. The electron density is predominantly gained in the p orbital of the C_2 carbon.

The Fukui function of the out of plane structure also shows the most electrophilic site above and below the C_2 carbon but there is a difference in the magnitude of electron density gained from one side to the other. The site on the opposite site of the ethyl arm features a larger gain in electrons than the other as seen on the right-hand side of figure 5.25. The difference in electron density gained indicates that the side opposite of the ethyl arm in the out of plane conformation is more favourable to interact with.

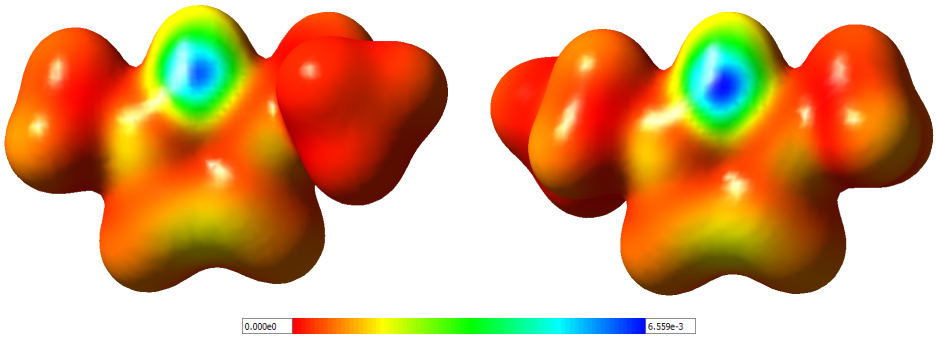


Figure 5.25: Out of plane $[C_2C_1Im]^+ \rightarrow C_2C_1Im$ Fukui function projected onto the $[C_2C_1Im]^+$ total density at an isovalue of 0.0004

The evaluation of the charge distribution and electrophilic sites of the $[C_2C_1Im]^+$ cations conformers via NACs, MEPs and Fukui functions reveal different sites of preferential interactions. The NPA NAC assignments indicate the C_2 carbon to be the most attractive site to interact with while the other NAC assignment methods feature the imidazolium rings hydrogens as the sites which will be most favourable to interact with for an anion. The MEPs indicates that the hydrogen at the front of the imidazolium ring, adjacent to the C_2 carbon is the most favourable site to interact with. The Fukui function indicates that an interaction profile incorporating an anion interacting with the C_2 carbon, above or below the imidazolium ring, will lead to the most stable IP structures. The IP structures will give insights into which techniques of analysing the electronic structure and sites of electrophilicity are best suited at predicting the most stable interactions between the ions.

5.2.2 $[Choline]^+$, $[N_{2110}]^+$ and $[N_{2111}]^+$ cations electronic structure

The electronic structure of the stable conformers of the three stable cations is shown through the MEPs and the projected Fukui functions to convey information as succinctly as possible. The NACs are helpful in determining the charge distribution but the information gained from the NAC assignments is similar to the information from the MEPs to add valuable insight for the ammonium based cations. The NAC assignments are only referenced in the discussion and all the NAC assignments can be found in the appendix.

Figures 5.26 and 5.27 show the MEPs of the three cations in all stable conformations. Figure 5.26 shows the MEPs of the gauche and trans conformers of the $[Choline]^+$ cation. The magnitude of the strongest positive potential is analogous in both conformers while the magnitude of the weakest positive potential is greater in the gauche conformer.

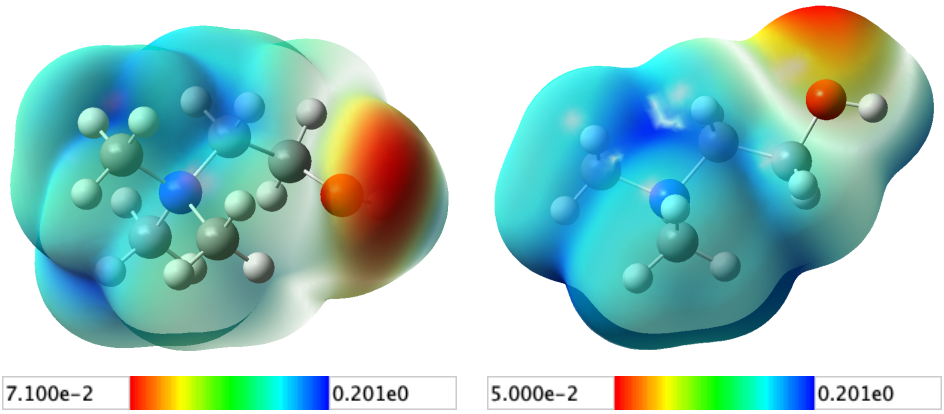


Figure 5.26: $[Choline]^+$ molecular electrostatic potential projected onto the $[Choline]^+$ total density at an isovalue of 0.0008

The MEPs of the $[Choline]^+$ cations conformers show that the sites with the strongest positive potential are located between the methyl arms of both the gauche and trans structures. The oxygen atom of the hydroxyl group has the weakest positive potential in both conformers. According to the MEP the regions between the methyl groups hydrogens are the most attractive sites to interact with while the oxygen is the least attractive site to interact with for the anions.

In the MEPs the hydrogen of the hydroxyl group is not the most electropositive site which contrasts with all the NAC assignment methods in which the most electropositive site is always the hydroxyl hydrogen. According to the NAC assignment methods the OH hydrogen carries between two to three times as much positive charge as the remaining hydrogen atoms in both conformers. According to the NAC assignment methods the hydroxyl hydrogen is the most appealing site for the anions to interact with. Every methyl group contains three hydrogen atoms adjacent to one another which could likely interact with the anions, compensating for an interaction with the hydroxyl hydrogen not occurring. The interactions with three methyl hydrogens could likely result in a more or equally stabilizing interaction with the anions.

Figure 5.28 shows the MEPs of the $[N_{2110}]^+$ and $[N_{2111}]^+$ cations on the left and right, respectively. The magnitude of the most positive potential of the $[N_{2110}]^+$ cation is higher and the $[N_{2111}]^+$ cation is slightly lower than the $[Choline]^+$ cation. The magnitude of the weakest positive potentials is larger than in both $[Choline]^+$ conformers and about equal in the $[N_{2110}]^+$ and $[N_{2111}]^+$ cations.

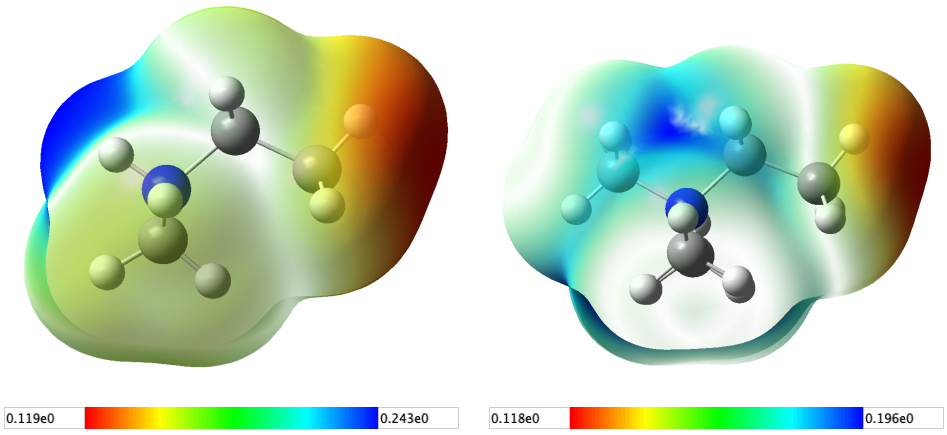
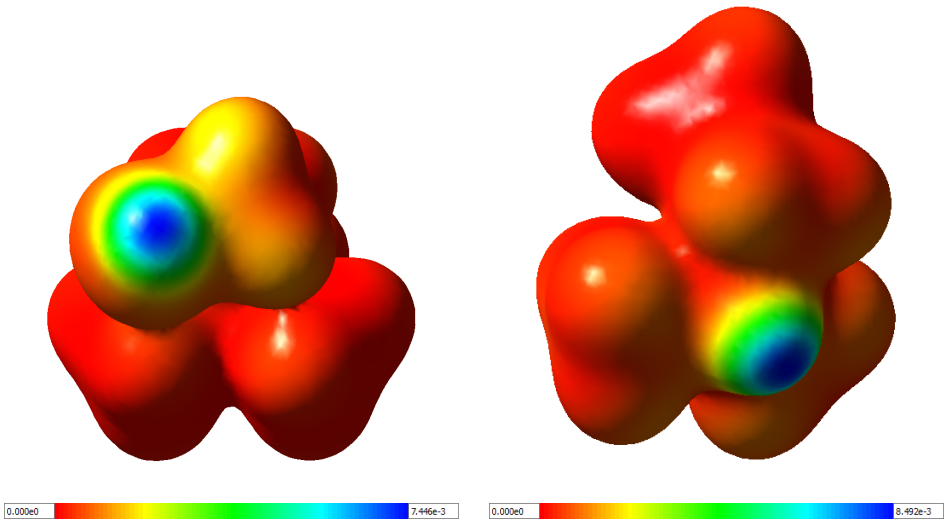


Figure 5.27: $[N_{2110}]^+$ and $[N_{2111}]^+$ molecular electrostatic potentials projected onto the $[N_{2110}]^+$ and $[N_{2111}]^+$ total densities at an isovalue of 0.0008

The MEPs of the $[N_{2110}]^+$ and $[N_{2111}]^+$ cations show that the terminal methyl group of the ethyl arms are is always the regions with the least negative potential. The hydrogen atoms which are α to the nitrogen always have a slightly stronger positive potential compared to the terminal hydrogens on the ethyl arm. In the $[N_{2111}]^+$ cation the regions of the most positive charge are located analogously to the $[choline]^+$ cation, between the methyl hydrogen atoms. In the $[N_{2110}]^+$ cation the hydrogen atom attached to the nitrogen has the most positive potential surrounding it.

According to the MEPs shown in figures 5.26 and 5.27 the hydrogen adjacent to the nitrogen of $[N_{2111}]^+$ has a stronger positive potential than the hydroxyl hydrogen in both $[Choline]^+$ conformers. The ChelpG and ADCH NAC assignment methods assign the $[choline]^+$ cations hydroxyl hydrogen a higher positive partial charge than the N-H hydrogen of the $[N_{2110}]^+$ cation while the NPA NAC method assigns them the same positive partial charge.

Figures 5.27 and 5.28 show the Fukui functions of the ammonium based cations. The Fukui function of the gauche and trans $[Choline]^+$ structures reveal analogous information so the trans Fukui function is omitted but can be found in the appendix. Figure 5.28 shows the projected Fukui functions of $[Choline]^+$ and $[N_{2110}]^+$. The projected Fukui functions show that the magnitude of electron density lost is larger for the $[N_{2110}]^+$ than the $[Choline]^+$ at the point where most density is lost.



$[Choline]^+$ $[N_{2110}]^+$

Figure 5.28: Gauche $[Choline]^+ \rightarrow$ Choline and $[\mathrm{N}_{2110}]^+ \rightarrow \mathrm{N}_{2110}$ Fukui functions projected onto the $[Choline]^+$ and $[\mathrm{N}_{2110}]^+$ total densities at an isovalue of 0.01

The Fukui functions of both of the $[Choline]^+$ and $[N_{2110}]^+$ cations show that the hydroxyl and N-H hydrogen are the most electrophilic sites, respectively. According to the Fukui functions the N-H hydrogen of the $[N_{2110}]^+$ cation loses more electrons than the OH hydrogen of the $[Choline]^+$ cation which coincides with the ESPs but is in contrast to the ADCH and ChelpG NAC methods.

Figure 5.29 shows the projected Fukui function of the $[N_{2111}]^+$ cation. The magnitude of charge lost at the sites with the greatest loss of charge is much smaller in the $[N_{2111}]^+$ cation when compared with the $[Choline]^+$ and $[N_{2110}]^+$ cations. The projected Fukui function of $[N_{2111}]^+$ shows that the loss of charge occurs at multiple sites. The gained electron density is evenly spread out in the $[N_{2111}]^+$ cation across all the methyl hydrogen atoms. The gain in charge density is slightly stronger in the methyl than the ethyl hydrogen atoms. The Fukui function coincides with the MEP showing that the α hydrogen atoms are more electrophilic than the β hydrogen atoms of the ethyl arm. In contrast to the MEP the most attractive points are at the extensions of various C-H bonds which are alpha to the nitrogen and not the regions between the methyl hydrogen atoms.

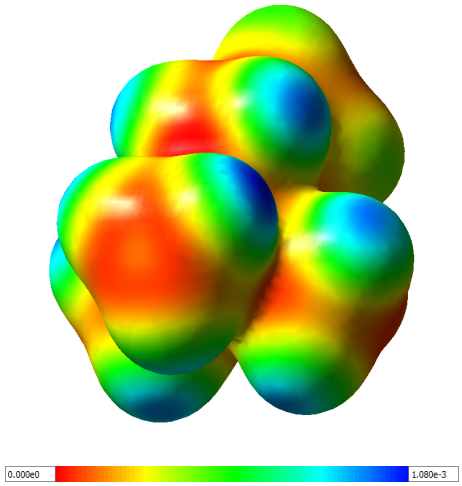


Figure 5.29: $[N_{2111}]^+ \rightarrow N_{2111}$ Fukui function projected onto the N_{2111} total density at an isovalue of 0.01

The different methods of evaluating the electronic structure of each of the ammonium based cations revealed contradicting results for the $[Choline]^+$ cation. The evaluations of the $[N_{2110}]^+$ and $[N_{2111}]^+$ cations electronic structure are in agreement with one another. In the $[Choline]^+$ cation the most electrophilic site is located either on the hydroxyl hydrogen or between the methyl hydrogen atoms. In the $[N_{2110}]^+$ cation all evaluation techniques show that the N-H hydrogen is by far the most electrophilic site and in the $[N_{2111}]^+$ cation all the methyl hydrogens are equally electrophilic.

Bibliography

[1] Tian LU and Fei-Wu CHEN. Comparison of computational methods for atomic charges. *Acta Physico-Chimica Sinica*, 28(1):1–18, 2012.

[2] Curt M Breneman and Kenneth B Wiberg. Determining atom-centered monopoles from molecular electrostatic potentials. the need for high sampling density in formamide conformational analysis. *Journal of Computational Chemistry*, 11(3):361–373, 1990.

[3] Alan E Reed, Robert B Weinstock, and Frank Weinhold. Natural population analysis. *The Journal of Chemical Physics*, 83(2):735–746, 1985.

[4] Tian Lu and Feiwu Chen. Atomic dipole moment corrected hirshfeld population method. *Journal of Theoretical and Computational Chemistry*, 11(01):163–183, 2012.

[5] Yan Li and Jeremy NS Evans. The fukui function: a key concept linking frontier molecular orbital theory and the hard-soft-acid-base principle. *Journal of the American Chemical Society*, 117(29):7756–7759, 1995.

Chapter 6

Ion Pair Interaction Profiles

This chapter discusses the IP interactions between the $[C_2C_1Im]^+$, $[Choline]^+$, $[N_{2111}]^+$ and $[N_{2111}]^+$ and the chlorometallate anions which were found to be stable. The chapter discusses the IPs featuring $[C_2C_1Im]^+$ in detail while the IPs featuring the other cations are discussed more sparingly due to running out of time for further investigation. The IP structures shown in this chapter are named according to the IP nomenclature described in section 3.2.8.

6.1 $[C_2C_1Im]Cl\text{-}MCl_3$ ion pair evaluation in the gas phase and liquid phase

This section displays selected IP structures from the $[C_2C_1Im]Cl\text{-}AlCl_3$,$[C_2C_1Im]Cl\text{-}GaCl_3$ and $[C_2C_1Im]Cl\text{-}InCl_3$ systems in the GP and LP. The most stable IP structures constituting of the chlorometallate anions and the $[C_2C_1Im]^+$ cation are shown to highlight the most stable IP interactions. Additionally, selected IP structures are shown to give insight into the variety of interactions which can lead to stable IP structures. The IP interactions are evaluated and the effect of the interactions on the chemical properties of the chlorometallate ILs at different x_{MCl_3} are discussed.

6.1.1 Gas phase ion pair evaluation

This subsection discusses the stable IP structures which were found in the GP. The interactions between the anions and cations are predicated upon two factors; the conformers the constituent ions are in and the position and orientation the ions have with relative to one another. The conformers the ions can assume are dependent on the flexibility of the whole structure and the moieties of the structures. The position and orientation ions have with respect to one another is based on the stabilizing interactions which occur between the nucleophilic sites of the anions and the electrophilic sites of the cations.

Due to some ions having more flexibility and a higher number of nucleophilic sites, some IPs have a higher number of structures and a broader range in relative stability of the IP structures. Hence a diverse range of stabilizing interactions is evident by the number of unique stable IP conformers and their range of relative stability. For each IP, table 6.1 shows the total number IP structures on the right column and the IP structures grouped by relative Gibbs free energy. The stable structures are grouped by 10 kJ mol^{-1} increments of relative Gibbs free energy up to < 50. For example, in the GP, 10 IP structures were found for the $[C_2C_1Im][AlCl_4]$ IP as listed on the column on the right side of table 6.1. 9 of the $[C_2C_1Im][AlCl_4]$ IP structures are within 10 kJ mol^{-1} of the lowest energy structure and 1 IP structure is between 10 and

20 kJ mol^{-1} less stable than the lowest energy structure. Table 6.1 also shows in which table in the appendix in section 9.2.1 depictions of each IP structure can be found.

Table 6.1: Number of IP structures grouped by relative Gibbs free energy with respect to the lowest energy structure of each IP in the ranges of ≤ 10, $10 \leq 20$, $20 \leq 30$, $30 \leq 40$, $40 \leq 50$ and $50 <$ kJ mol^{-1} of each $[C_2C_1Im][M_xCl_y]^{z-}$ IP in the gas phase and the appendix table where the structures can be found

Anion	≤ 10	$10 \leq 20$	$20 \leq 30$	$30 \leq 40$	$40 \leq 50$	$50 <$	Total	Appendix Table
$[AlCl_4]^-$	9	1	0	0	0	0	10	93
$[Al_2Cl_7]^-$	16	3	3	0	0	0	22	94
$[Al_3Cl_{10}]^-$	5	7	2	3	2	0	20	95
Branched $[Al_4Cl_{13}]^-$	3	6	9	0	1	0	19	96
Linear $[Al_4Cl_{13}]^-$	2	7	0	5	2	0	16	97
$[GaCl_4]^-$	5	0	0	0	0	0	5	98
$[Ga_2Cl_7]^-$	15	4	2	0	0	0	19	99
$[Ga_3Cl_{10}]^-$	7	6	5	1	2	1	22	100
Branched $[Ga_4Cl_{13}]^-$	3	2	2	10	3	0	20	101
Linear $[Ga_4Cl_{13}]^-$	5	3	3	4	2	0	17	102
$[InCl_4]^-$	7	0	0	0	0	0	7	103
$[InCl_5]^{2-}$	10	2	0	0	0	0	12	104
$[InCl_6]^{3-}$	1	0	0	1	0	0	2	105

The grouping of structures by their relative Gibbs free energy shows that there is a correlation between the range of relative stability of IPs states and the size of the constituent anion. All monometallic anions except for the $[InCl_6]^{3-}$ anion only have relative Gibbs free energy as high as 20 kJ mol^{-1}. All IPs featuring trimetallic and tetrametallic anions have numerous structures which are 20 - 50 kJ mol^{-1} less stable than the lowest energy IP structures. The broader the range in the relative Gibbs free energy of the IP structures of the IPs containing the larger anions indicates a larger diversity in interactions which can lead to stable structures. The broader variety in interaction profiles is likely a result of the increased number of nucleophilic sites on the larger anions.

The number of IP structures found for each IP, listed on the right-hand side of table 6.1, underline the diversity of interactions between the cations and the multi metallic anions. The IPs featuring monometallic anions have an average of 7.2 stable structures while the IPs featuring multimetallic anions feature on average 19.4 stable structures.

The flexibility of $[M_3Cl_{10}]^-$ and linear $[M_4Cl_{13}]^-$ complexes of the chloroaluminate and chlorogallate should also allow for much more versatile interactions with the cation which in turn result in larger range of interactions with smaller relative Gibbs free energies. The comparison of the number of structures in different groups of relative Gibbs free energy of linear trimetllic and tetrametallic structures to the more ridged branched structure shows that the flexibility does not result in larger difference in relative Gibbs free energy. 43% of the IPs featuring the $[M_3Cl_{10}]^-$ and linear $[M_4Cl_{13}]^-$ structures are > 20 kJ mol^{-1} while 64% of the branched $[M_4Cl_{13}]^-$ structures are > 20 kJ mol^{-1}. The results imply that the flexibility likely results in more stable IP arrangements.

To understand how the differences in stability of IP structures arise the interaction profiles of the lowest energy structures and other selected structures are shown and discussed. The remainder of this section is dedicated to the evaluation of the molecular structure of the IPs with respect to their Gibbs free energy. Later sections will evaluate the electronic structure of the interaction profiles.

Gas phase $[C_2C_1Im][MCl_{4-6}]^{0-2-}$ structures interaction profile evaluation

Figure 6.1 depicts all the lowest energy structural configurations of the $[C_2C_1Im]^+$ cation with the monometallic anions in the GP. The position of the anion relative to the cation and the interaction profiles of the lowest energy structures are similar across all metal systems for the smaller anions.

In the GP, all of the most stable IP structures featuring the monometallic anions include an interaction between a chloride atom of the anions and the C_2 carbon on the cation. The distances from the metal centres to the C_2 carbon are all between 3.7 and 3.8 Åin all the structures shown in figure 6.1 apart from the $[C_2C_1Im][InCl_6]^{2-}$ IP structure where the distance is 4 Ådue to the steric hindrance. The steric hindrance effects the interaction due it the saturated coordination sphere of $[InCl_6]^{3-}$. All GP IP structures containing monometallic or dimetallic anions found here feature an interaction between a chloride and the C_2 carbon. The interaction is also featured in the lowest energy structures between $[C_2C_1Im]^+$ and the trimetallic and tetrametallic species of the chloroaluminate and chlorogallate systems.

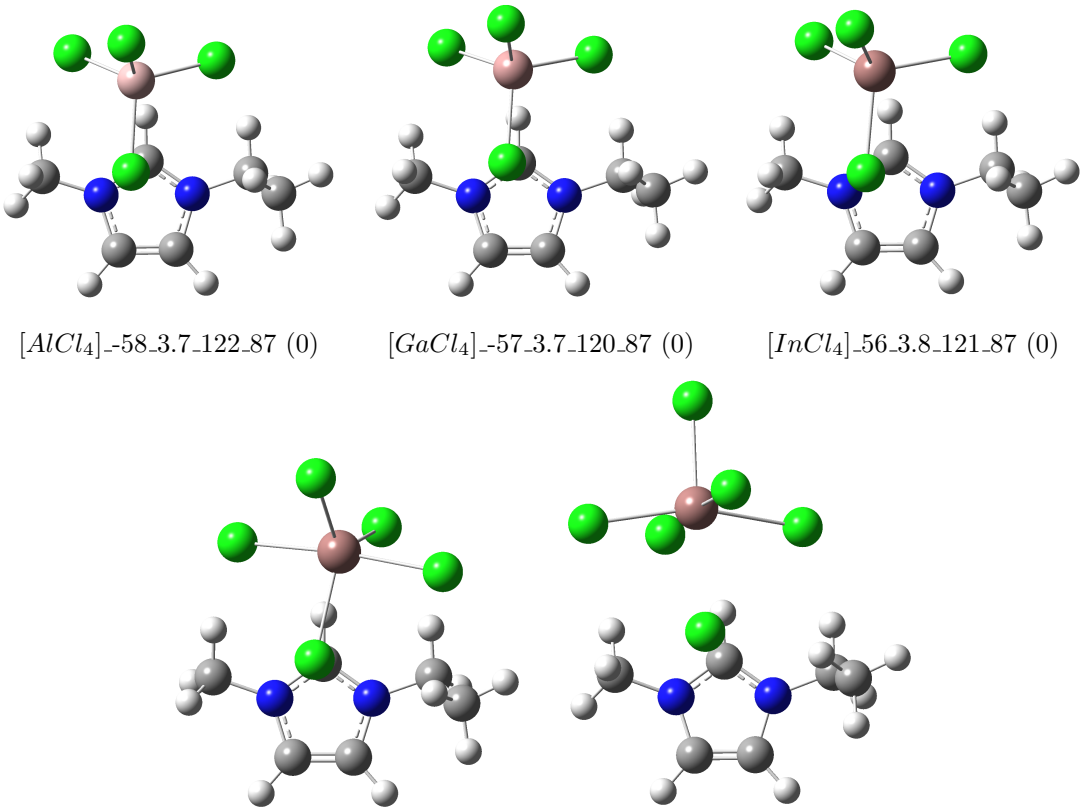


Figure 6.1: $[C_2C_1Im][MCl_4]$, $[C_2C_1Im][InCl_5]^-$ and $[C_2C_1Im][InCl_6]^{2-}$ lowest energy gas phase structures

Out of the methods evaluating the electronic structure as well as the nucleophilicity and electrophilicity of the constituent ions of the IPs, the NPA NAC assignment scheme and the Fukui functions best describe the interaction between the chloride and the C_2 carbon as the most stabilizing interaction. As the Fukui functions and NPA scheme are the best indicators of the most stabilizing interaction in all GP IP structures the interaction is likely based on in phase MO overlapping. The localized interaction based on the orbitals is characterized as the stereoelectric effect which is characteristic of soft interactions, in the context of HSAB theory.

The IP structures in figure 6.1 show that all the interactions leading to the lowest energy $[C_2C_1Im][MCl_4]$ structures are analogous across all chlorometallate systems in the GP. The dihedral angle of the ethyl arm in the lowest energy IPs featuring $[MCl_4]^-$ anions is indistinguishable between systems with respect to the error margin being between 56° and 58° in all three IP structures.

Figure 6.2 depicts the interaction profile between $[AlCl_4]^-$ and $[C_2C_1Im]^+$, highlighting various interaction

between the chloride ligands and various sites on the cation which are shorter than 4.0 Åin dashed lines. The interactions between the metal and the C_2 carbon and C_2 hydrogen are excluded in figure 6.2 for clarity.

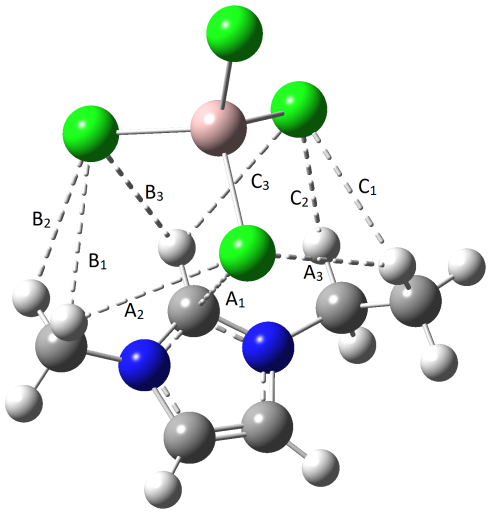


Figure 6.2: $[C_2C_1Im][AlCl_4]$_-58_3.7_122_87 (0) interaction profile

There are additional commonalities in the interaction profiles between the $[MCl_4]^-$ anions and $[C_2C_1Im]^+$. The interaction profile shown in figure 6.2 is analogous in the chlorogallate and chloroindate systems. Table 6.2 lists the distance corresponding to each interaction depicted in figure 6.2 as well as the analogous interactions of the $[C_2C_1Im]^+$ cation with the $[GaCl_4]^-$ and $[InCl_4]^-$ anions, shown in figure 6.1. Additionally to the interactions shown in figure 6.2 the distance between the metal centre and the C_2 hydrogen atom is listed.

The distances of the intermolecular interactions in each of the lowest energy structures of the chloroaluminate and chlorogallate systems are analogous while the chloroindate anion has slightly larger distances in specific interactions. The larger interaction distances in the chloroindate system are due to the larger dimensions of the $[InCl_4]^-$ anion. The interaction profiles of the $[C_2C_1Im]^+$ cation interacting with the $[MCl_4]^-$ species of each system in the GP reveal that the lowest energy structures are primarily stabilized through the chloride - C_2 carbon interaction. Secondly, the system maximizes the interactions between the chlorine atoms of the anion and the hydrogen atoms of the cation.

Table 6.2: $[C_2C_1Im][MCl_4]$ lowest energy structures interactions distances in Å

Interaction	M = Al	M = Ga	M = In
A_1 (C_2-Carbon)	3.2	3.2	3.2
A_2 (Methyl-Hydrogen1)	3.1	3.1	3.1
A_3 (Ethyl-Hydrogen1)	3.1	3.1	3.2
B_1 (Methyl-Hydrogen1)	3.1	3.1	3.3
B_2 (Methyl-Hydrogen2)	2.9	2.9	2.8
B_3 (C_2-Hydrogen)	2.8	2.8	2.8
C_1 (Ethyl-Hydrogen1)	2.7	2.7	2.7
C_2 (Ethyl-Hydrogen2)	3.0	3.0	3.0
C_3 (C_2-Hydrogen)	3.0	3.0	3.2
M-C_2-Hydrogen	3.2	3.2	3.3

The secondary interactions between the chloride ligands and the hydrogen atoms in the IPs additionally stabilize the IP structures. The maximization of the number of interactions between the chlorine ligands of the anion and the hydrogen atoms of the $[C_2C_1Im]^+$ cation are paramount to lowering an IP structures energy. Additionally, there is a hierarchy to the electrophilicity of the hydrogen atoms of the $[C_2C_1Im]^+$ cation which in turn make interactions with particular hydrogen atoms more favourable than with others. The electrophilic hierarchy of the hydrogen atoms of the $[C_2C_1Im]^+$ cation are evaluated by considering alternative stable $[C_2C_1Im][AlCl_4]$ IP structures.

The orientation of anion towards the cation has an effect on the stability by determining the number of Cl-H interactions the IP structure can engage in. The effect of the orientation of the anion towards the cation is shown through the relative energy of the $[C_2C_1Im][AlCl_4]$ IP structure -112_4_113_82, shown in figure 6.3. The structure in figure 6.3 is 16 kJ mol^{-1} less stable than the lowest energy structure, in Gibbs free energy. The distance of the metal centre from the C_2 carbon is 0.3 Ålonger than in the lowest energy structure due to the different orientation of the anion. The position of the anion relative to the cation in both structures is relatively similar as shown through the angle and dihedral angles outlined in the methodology being 122° and 87° in the lowest energy structure and 113° and 82° in the structure in figure 6.3.

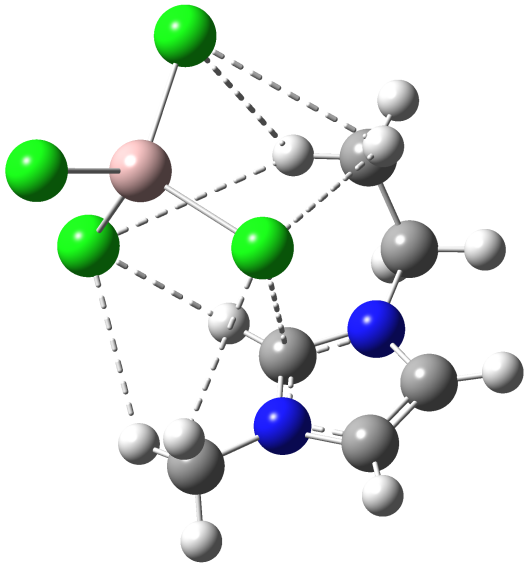
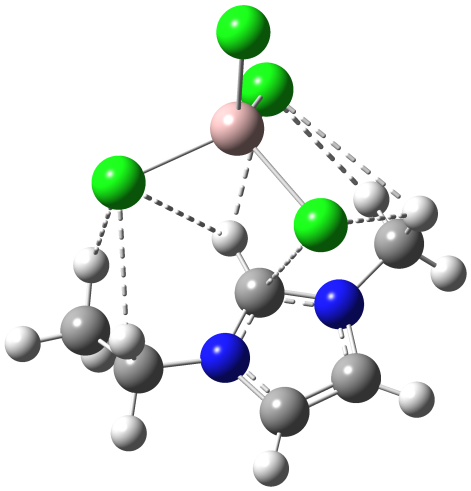


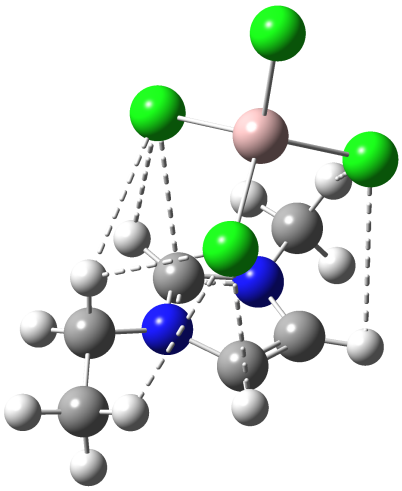
Figure 6.3: $[C_2C_1Im][AlCl_4]$_-112_4_113_82 (16) [1] interaction profile (showing interactions shorter than 3.4 Å) in the gas phase

The difference in orientation of the anion between the lowest energy structure and -112_4_113_82 has the consequence that the chloride ligands interact with less electrophilic hydrogen atoms. The lowest energy structure features six interactions between chloride ligands and hydrogen atoms which are α to the nitrogen atoms and two interactions with hydrogen atoms β to the nitrogen atoms. The -112_4_113_82 structure features three interactions with α-hydrogen atoms and four interactions with β-hydrogen atoms. Additionally, the lowest energy structure features two interactions with the C_2 hydrogen atom while the -112_4_113_82 structure only features one. In consequence the lower number of interactions between the chloride ligands and the more electrophilic hydrogen atoms causes the IP structure to be less stable.

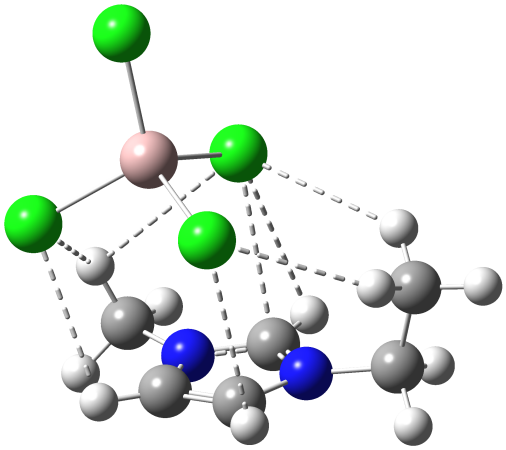
Figure 6.4 depicts three additional $[C_2C_1Im][AlCl_4]$ IP structures which show IP interactions which have nuanced differences from the lowest energy structure. The position of the anion relative to the cation and the rotation of the ethyl arm cause the structures to be slightly less stable than the lowest energy structure.



-148_3.7_115_-87 (10) [Low 1]



-28_4_77_-94 (7)



-78_4.3_64_81 (8)

Figure 6.4: $[C_2C_1Im][AlCl_4]$ interaction profiles (showing interactions shorter than 3.4 Å) in the gas phase

Structure -148_3.7_115_-87 features the anion in a similar position as the lowest energy structure with two chloride ligands interacting with the C_2 carbon while one chloride ligand is located below the ring. The difference to the lowest energy structure is the rotation of the ethyl arm. Due to the larger dihedral angle of the ethyl arm the structure features one fewer interactions with a β-hydrogen which causes the energy of the structure to be 10 kJ mol^{-1} less stable than the lowest energy structure.

Structure -28_4_77_-94 features the anion located further back with respect to the imidazolium ring, towards the C_4- and C_5-carbons. Due to the position of the anion relative to the cation the stabilizing interactions

with the C_2-hydrogen atom of the cation is substituted by the interactions with the interactions with the C_4- and C_5-hydrogen atoms of the imidazolium ring. The structure features one less interaction with a β-hydrogen and one less interaction with the C_2-hydrogen but the stabilization from interacting with the C_4- and C_5 α-hydrogen atoms compensate so the structure is 7 kJ mol^{-1} higher in energy than the lowest energy structure.

In structure -78_4.3_64_81 the anion is located in a similar position to structure -28_4_77_-94 but the ethyl arm rotation causes the structure to have one fewer interaction with an α-hydrogen of the ethyl arm. The interaction is replaced by a β-hydrogen interaction which causes the energy to be 8 kJ mol^{-1} higher than the lowest energy structure and 1 kJ mol^{-1} higher than the -28_4_77_-94 structure which makes the two effectively degenerate.

The interaction profiles of the $[C_2C_1Im][AlCl_4]$ IPs and their relative Gibbs free energies show that higher energy structures have less idealized secondary interactions between chlorides and hydrogen atom. One chloride ligand interacting with the C_2 carbon is consistent throughout all structures but the remainder of the IP structures have different numbers of Cl-H interactions and the Cl-H interactions are with different hydrogen atoms. The $[C_2C_1Im][AlCl_4]$ IP structures confirm the hierarchy of hydrogen atom electrophilicity of the $[C_2C_1Im]^+$ cation established by the NPA and ADCH schemes. The interaction of chloride ligands with the C_2 hydrogen atom which is α to two nitrogen atoms is most stabilizing. The second most stabilizing hydrogen bonds are with the other alpha hydrogen atoms of the imidazolium ring. the third most stabilizing hydrogen bonds are with the α hydrogen atoms of the methyl and ethyl arm. The least stabilizing interactions are between the β hydrogen atoms of the ethyl moiety and the chlorine ligands. The hierarchy of electrophilicity of the hydrogen atoms described for the $[C_2C_1Im][AlCl_4]$ IP are analogous in all IPs evaluated.

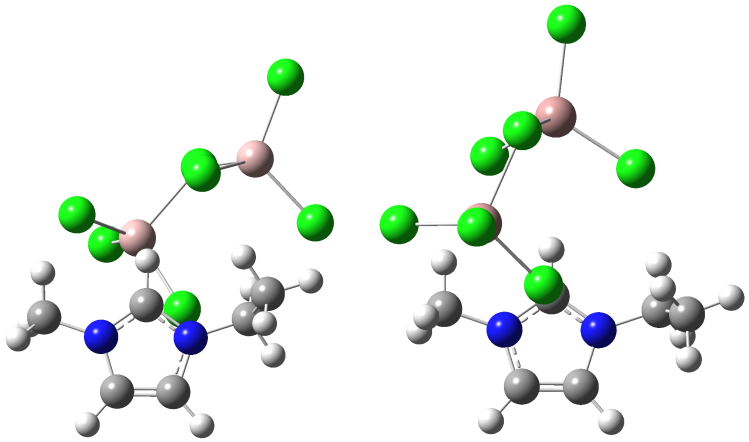
Additionally, none of the IP structures featuring monometallic anions have interactions in which the linear extension of a metal-chloride bond is pointed directly towards an electrophilic site of the $[C_2C_1Im]^+$. The σ-holes shown in the MEPs of the anions predicted that an interaction along the extension of the M-Cl bonds would be less stabilizing. The interaction with the faces of the anions may also be more favourable due to it allowing for the interaction with three chlorides instead of one or two.

Gas phase $[C_2C_1Im][M_2Cl_7]$ structures interaction profile evaluation

The $[C_2C_1Im][M_2Cl_7]$ IPs of the chloroaluminate and chlorogallate systems were evaluated next to determine how the increase in anion size and in turn larger diversity of chloride environments effects the interaction

profiles. The $[M_2Cl_7]^-$ anions has two different chloride environments; bridging and terminal chlorides. The difference in charge localization between the terminal a bridging chlorides should have an effect on interaction with the $[C_2C_1Im]^+$ cation.

The interaction profiles of the dimetallic chloroaluminate and chlorogallate complexes with the $[C_2C_1Im]^+$ cation are very similar and hence the interaction profiles are described using only the chloroaluminate IP structures. The differences between the highest energy and the lowest energy structures are highlighted as the structural differences between the structures which have relatively similar Gibbs free energy are based on the hierarchy of electrophilicity of the $[C_2C_1Im]^+$ cations which was described for the IP structures featuring the monometallic anions. The two lowest energy structures of the $[C_2C_1Im][Al_2Cl_7]$ and $[C_2C_1Im][Ga_2Cl_7]$ IPs are shown in figure 6.5.



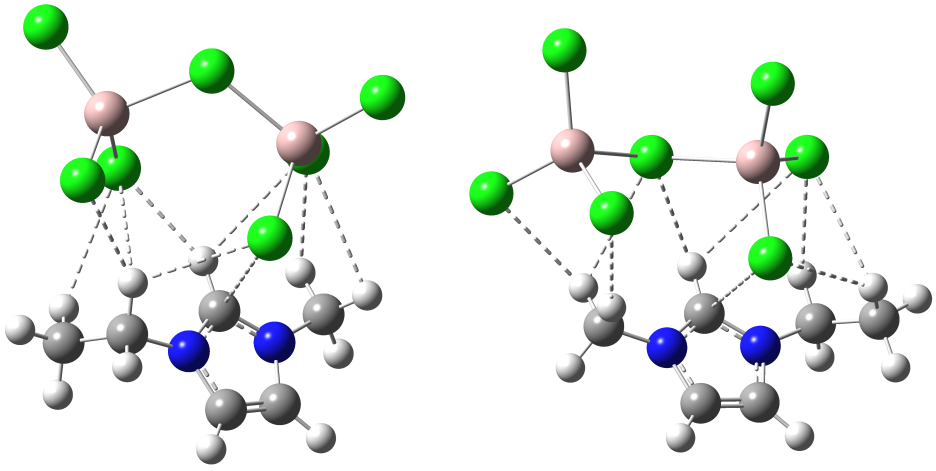
$[Al_2Cl_7]$_-104_5.3_135_-107 (0) $[Ga_2Cl_7]$_-67_5.3_127_80 (0)

Figure 6.5: $[C_2C_1Im][M_2Cl_7]$ lowest energy gas phase structures

In the lowest energy $[C_2C_1Im][Al_2Cl_7]$ and $[C_2C_1Im][Ga_2Cl_7]$ structures the positions of the anions with respect to the cation are similar in that one MCl_3 moiety is located above or below the imidazolium ring plane and the other is located in front of the ring. The difference between the lowest energy structures of the chloroaluminate and chlorogallate systems is that the chlorogallate anion is located on the side of the imidazolium ring where the ethyl arm is. In contrast, the $[Al_2Cl_7]^-$ anion is closer to the methyl arm. The positions of the dimetallic anions of the lowest energy structures of the chloroaluminate and chlorogallate systems maximize the most stabilizing interactions described for the $[C_2C_1Im][AlCl_4]$ IPs.

Additional nuance to the interaction profiles of the dimetallic anions with the $[C_2C_1Im]^+$ arises when considering the orientation of the dimetallic anions towards the cation. Figure 6.6 shows two interaction

profiles in which the $[Al_2Cl_7]^-$ anion is in relatively similar positions above the front part of the $[C_2C_1Im]^+$ cation. The core difference between the two IP structures in figure 6.6 is that the anion is oriented differently towards the cation.



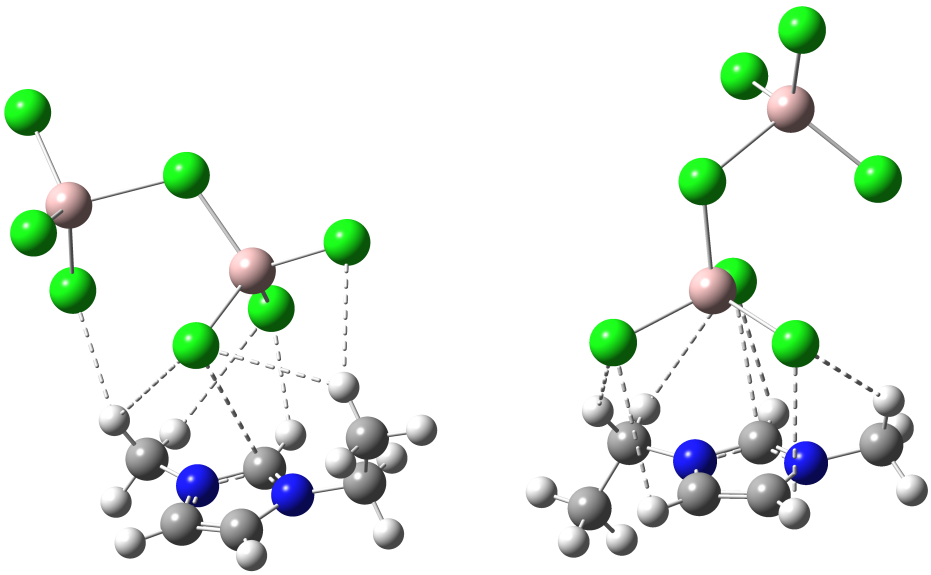
-104_5.3_135_-107 (0)

-53_3.6_134_55 (23) [1]

Figure 6.6: $[C_2C_1Im][Al_2Cl_7]$ interaction profiles (showing interactions shorter than 3.4 Å) in the gas phase

Although the position relative to the cation in both -104_5.3_135_-107 and -53_3.6_134_55 are relatively similar due to the orientation of the anion one the 53_3.6_134_55 structure is 23 kJ mol^{-1} higher in energy. Both structures have the same number of interactions with α and β hydrogen atoms but the nucleophilicity of the chlorine atoms interacting with the hydrogen atoms is different. In structure -104_5.3_135_-107 the side of the anion opposite to the bridging chlorine ligand is interacting with the cation. The orientation of the -104_5.3_135_-107 structure allows the interaction profile to maximize the number of interactions with the more nucleophilic terminal chloride ligands. Structure -53_3.6_134_55 features the anion interacting with the bridging chloride ligand which is less nucleophilic and hence causes the interaction to be less stabilizing. The interaction with the side of the anion opposite of the bridging chloride ligand is preferable and is predicted by all NAC assignment schemes, the ESPs and the Fukui functions.

Other relatively high energy IP structure featuring dimetallic anions feature the anion oriented in a way that result in fewer chloride ligands interacting with the cations electrophilic hydrogen atoms. Figure 6.7 depicts two structures with where the anion is oriented towards the cation in a way that generates fewer chloride-hydrogen interactions with the cation.



-64_5.9_110_74 (23) [1]

-68_6_83_-93 (20)

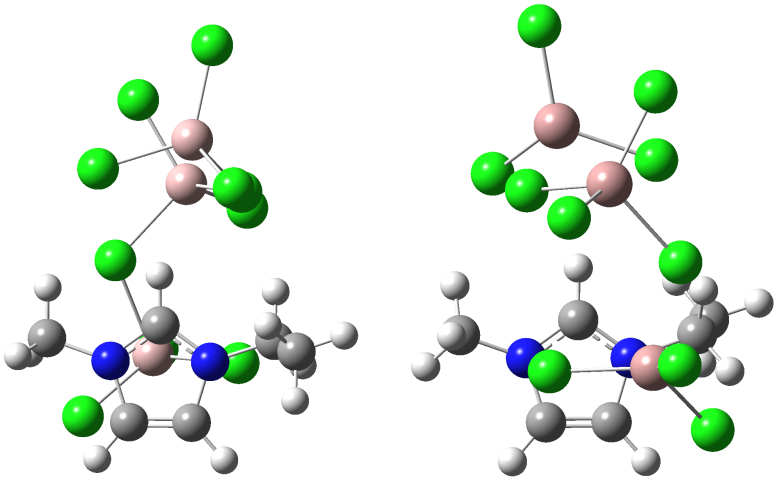
Figure 6.7: $[C_2C_1Im][Al_2Cl_7]$ interaction profiles (showing interactions shorter than 3.4 Å) in the gas phase

Structures -64_5.9_110_74 and -68_6_83_-93 both feature one MCl_3 segment of the $[Al_2Cl_7]^-$ anion predominantly interacting with the anion. In structure -64_5.9_110_74 one additional interaction between the methyl arm and a chloride of the other MCl_3 segment occurs. Both structures are at least 20 kJ mol^{-1} less stable than the lowest energy structure because of the reduced number of interactions with the cation. The anions orientation towards the cations results in a less stabilizing interaction due to the reduction of the number of interactions. Structure -64_5.9_110_74 only features four interactions with α hydrogen atoms and two with β hydrogen atoms. Structure -68_6_83_-93 features six interactions with α hydrogen atoms and none with β hydrogen atoms. The two interactions in figure 6.7 highlight the dependence on the IP structures stability on the maximization of the interactions with the anion. The ability to maximize the interactions between the chloride ligands and the hydrogen atoms depends on the structure and orientation of the anions.

Gas phase $[C_2C_1Im][M_3Cl_{10}]$ structures interaction profile evaluation

The IP structures featuring trimetallic anions introduce further complexity. Additional differentiation between chloride environments, the flexibility of the $[M_3Cl_{10}]^-$ anions add more diversity to the interaction profiles. The terminal chloride ligands attached to terminal metals versus terminal chloride ligands attached to bridging metals were shown to have different magnitudes of nucleophilicity. Additionally the

higher degree of flexibility of the $[M_3Cl_{10}]^-$ anions allows them to contort to maximize the interactions with the cation more effectively. Figure 6.8 shows the lowest energy structures of the $[C_2C_1Im][Al_3Cl_{10}]$ and $[C_2C_1Im][Ga_3Cl_{10}]$ IPs in the GP.

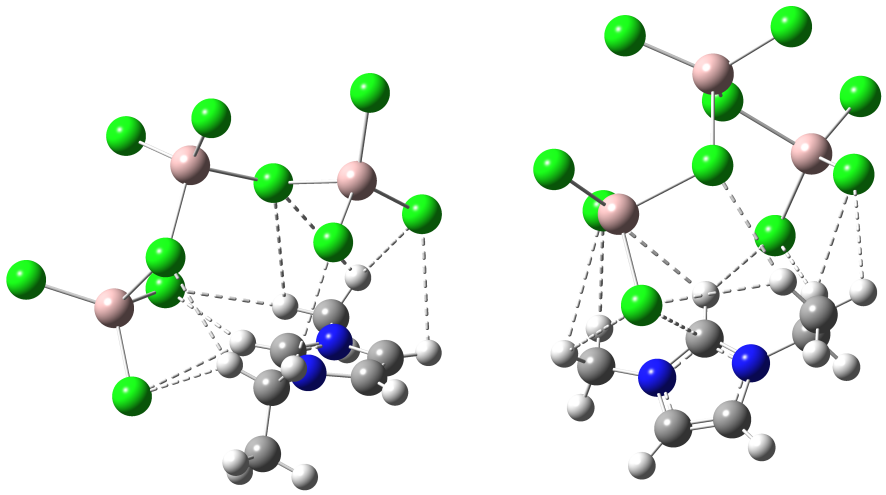


$[Al_3Cl_{10}]$_-78_4.8_124_-90 (0) $[Ga_3Cl_{10}]$_96_4.8_124_92 (0) [fnc]

Figure 6.8: $[C_2C_1Im][M_3Cl_{10}]$ lowest energy gas phase structures

The lowest energy IP structures of the chloroaluminate and chlorogallate systems featuring the $[M_3Cl_{10}]^-$ anions are the most stable due to the same principles described for the lowest energy IPs featuring monometallic and dimetallic anions. In the lowest energy structures of both systems a segment of the cation is located above the imidazolium ring and the remainder is wrapping around the front of the imidazolium ring. The terminal chlorides are localized to maximize the number of interactions with the hydrogen atoms of the imidazolium ring, the ethyl and methyl arm. One key difference between the lowest energy structure of the $[C_2C_1Im][Al_3Cl_{10}]$ IP to the previously observed lowest energy structures is that there is no direct interaction between a chloride ligand and the C_2 carbon although a portion of the anion is localized below the ring as depicted in figure 6.9.

The structural factors effecting the stability of the IP structures are analogous in the chloroaluminate and chlorogallate systems. Hence the evaluation of the interaction profiles of the IPs featuring trimetallic anions will also be shown exclusively through examples from the chloroaluminate system. Figure 6.9 shows the interaction profiles of two selected $[C_2C_1Im][Al_3Cl_{10}]$ IP structures.



-78_4.8_124_-90 (0)

-68_5.9_138_111 (5.5)

Figure 6.9: $[C_2C_1Im][Al_3Cl_{10}]$ interaction profiles (showing interactions shorter than 3.4 Å) in the gas phase

Figure 6.9 shows the interaction profiles of the two lowest energy structures of the $[C_2C_1Im][Al_3Cl_{10}]$ IP. Structure -78_4.8_124_-90 does not feature a direct interaction between a terminal chloride ligand and the C_2 carbon but there is still an anion-π interaction. There are also seven interactions between terminal chlorides and α hydrogen atoms and three interactions between bridging chloride ligands and α hydrogen atoms. The -68_5.9_138_111 structure features a direct interaction between a terminal chloride ligand and the C_2 carbon but only has six interactions between terminal chloride ligands and α hydrogen atoms, two between terminal chloride ligands and β hydrogen atoms and one between a bridging ligand and a β hydrogen. The high quantity and quality of the secondary interactions in structure -78_4.8_124_-90 is more stabilizing than the direct interaction between a chloride ligand with the C_2 carbon in structure -68_5.9_138_111.

The lowest energy structure of the $[C_2C_1Im][Al_3Cl_{10}]$ IP shows that the chloride - C_2 carbon interaction is no longer a requirement for a structure to be stable. The larger the anions become the more chloride - hydrogen interactions it engages in. The multitude of chloride - hydrogen interactions can result in a more stabilizing interaction which compensates for an IP structure stability when it does not feature a chloride - C_2 carbon interaction. The primary interaction between the C_2 carbon and a terminal chloride is additionally compensated for by alternative anion-π interactions.

Four interaction profiles of higher energy $[C_2C_1Im][Al_3Cl_{10}]$ IP structures are depicted in figure 6.10 which highlight how the orientation of the trimetallic anion effects the stability of the structure.

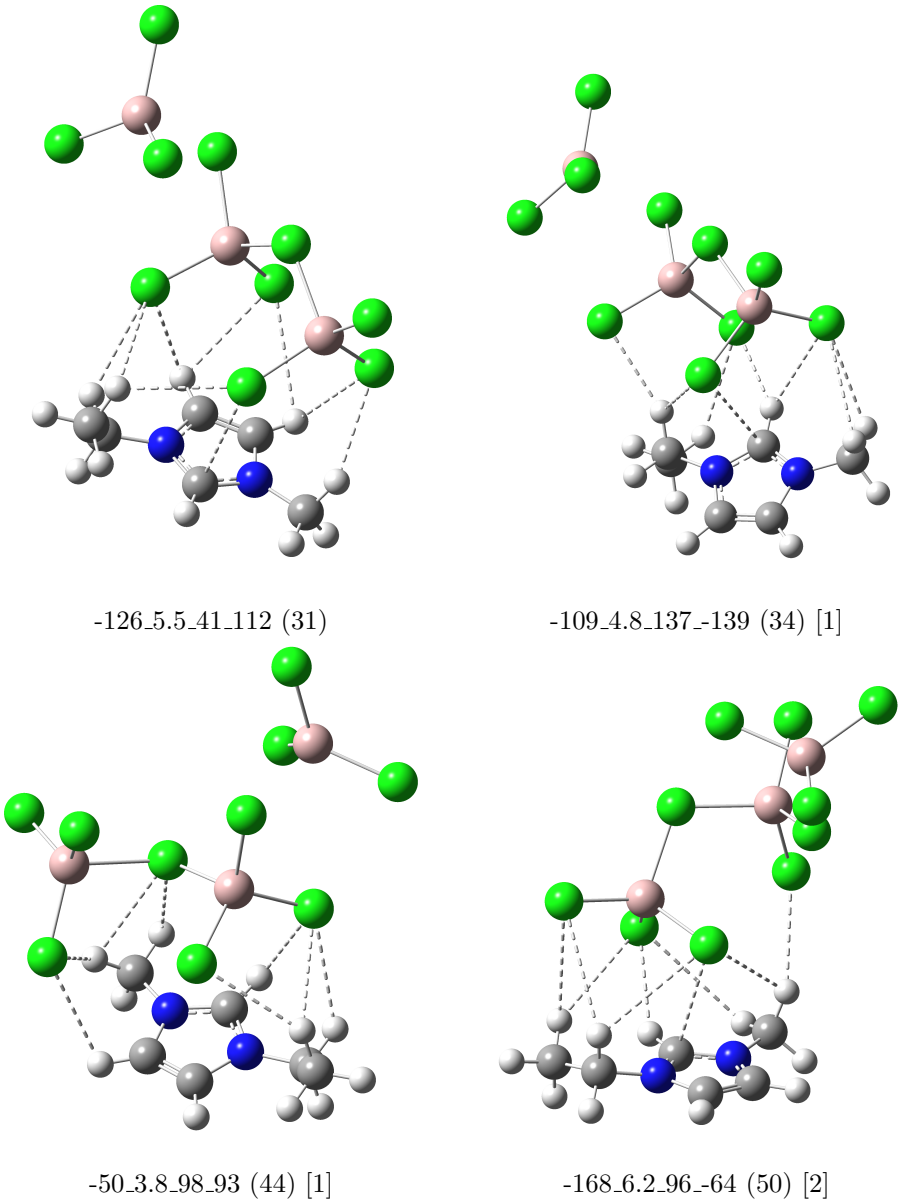


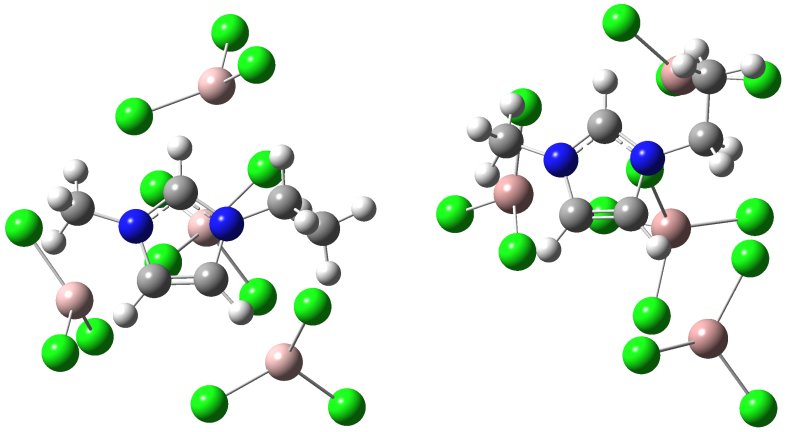
Figure 6.10: $[C_2C_1Im][Al_3Cl_{10}]$ interaction profiles (showing interactions shorter than 3.4 Å) in the gas phase

The four interaction profiles depicted in figure 6.10 demonstrate how the principles determined from the interaction profiles of the monometallic and dimetallic anions with the $[C_2C_1Im]^+$ cation translate to the interaction profiles of the trimetallic anion with the $[C_2C_1Im]^+$ cation. The $[C_2C_1Im][Al_3Cl_{10}]$ IPs have additional nuance due to the higher diversity of interaction sites and the flexibility of the anion. The structures -126_5.5_41_112 and -109_4.8_137_-139 interact with the with the top and front of the cation, respectively. Both structures feature four chloride ligands located on the side of the anion opposite to the bridging chloride interacting with the cation; two of the interacting chloride ligands are part of a terminal

MCl_3 segment and the other two are part of the bridging MCl_3 segment. The anion in structure -50_3.8_98_93 is in a similar position to the anion in structure -109_4.8_137_-139 but the anion is tilted and interacts with the cation with three terminal chlorides and one bridging chloride. Structure -168_6.2_96_-64 is interacting with the cation analogously to -64_5.9_110_74 structure. These progressively less favourable interaction profiles show that the principles established for the monometallic and dimetallic interaction profiles with the cation are transferable to the larger trimetallic anions. The results show that applicability of the ADHC NAC assignment scheme to predict the interaction profiles is effective as the relative stability of the structures reflects hierarchy of nucleophilicity and electrophilicity established for the chemical environments of chlorides ligands and hydrogen atoms in the anions and cations, respectively.

Gas phase $[C_2C_1Im][M_4Cl_{13}]$ structures featuring the branched $[M_4Cl_{13}]^-$ species interaction profile evaluation

The lowest energy IPs structures composed of the branched $[Al_4Cl_{13}]^-$ and $[Ga_4Cl_{13}]^-$ anions with the $[C_2C_1Im]^+$ cation are shown in figure 6.11.

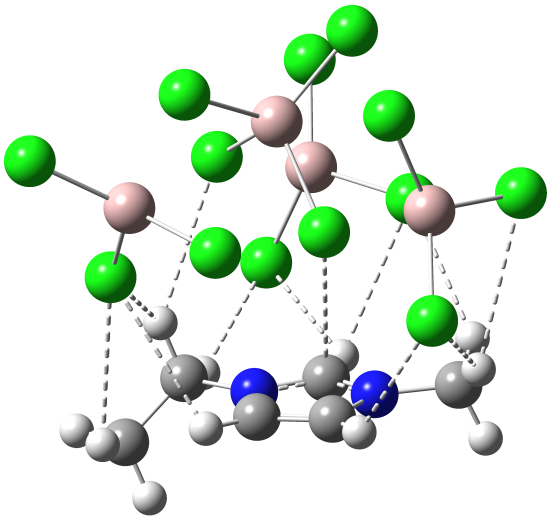


$[Al_4Cl_{13}]$_-44_4.8_87_-96 (0) $[Ga_4Cl_{13}]$_-164_5.4_68_-90 (0) [fnc]

Figure 6.11: branched $[C_2C_1Im][M_4Cl_{13}]$ lowest energy gas phase structures

The relative stability of the IP structures featuring the branched $[M_4Cl_{13}]^-$ anions is based on the principles described for the interaction profiles of the IPs featuring the monometallic, dimetallic and trimetallic anions. The interactions between the chloride ligands of the anion with the C_2 carbon and hydrogen atoms of the imidazolium cation and the maximization of these interactions also lead to the most stable $[C_2C_1Im][Al_4Cl_{13}]$ IP structures. The principles leading to the lowest energy IP structures can be observed by evaluating the

interaction profile of the lowest energy structure of the $[C_2C_1Im][Al_4Cl_{13}]$ IP, which are shown in figure 6.12. The branched tetrametallic chloroaluminate and chlorogallate complexes have similar interaction profiles so only the chloroaluminate system is shown here.



-44_4.8_87_-96 (0)

Figure 6.12: Branched $[C_2C_1Im][Al_4Cl_{13}]$ lowest energy gas phase structure interaction profiles (showing interactions shorter than 3.4 Å)

The interaction profile of the most stable $[C_2C_1Im][Al_4Cl_{13}]$ IP structure featuring the branched $[Al_4Cl_{13}]^-$ anion features a chloride - C_2 carbon interaction while maximizing the number of chloride - hydrogen interactions with the cation. The large dimensions of the anion allow it to engage with most hydrogen atoms around the ring simultaneously. Less stable IP structures feature fewer of interactions due to the orientation and position of the anion relative to the cation, leading to one or two MCl_3 segments not interacting with the cation.

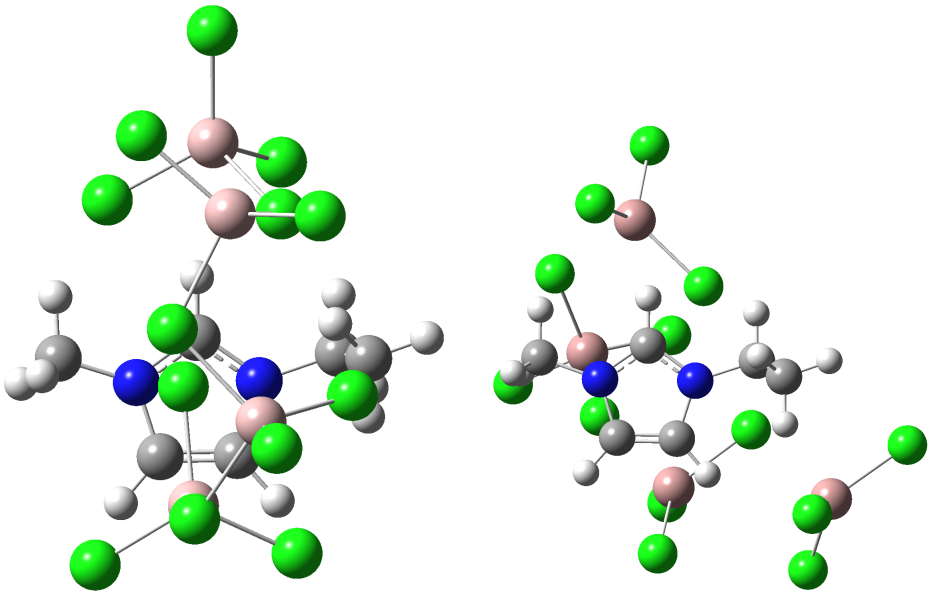
The Fukui functions and NAC assignment schemes revealed that the terminal chlorides are far more nucleophilic than the bridging chlorides of the branched $[Al_4Cl_{13}]^-$ anion. In the interaction profile of the lowest energy structure feature a maximization of the number of terminal chlorides interacting with various hydrogen atoms so the difference in nucleophilic hierarchy of the chlorides is shown in the interaction profiles. The MEPs of the branched $[Al_4Cl_{13}]^-$ anion showed that most of the negative potential is localized in a wedge between the two bridging chlorides of the linear portion of the anion and between the terminal chlorides of the terminal $AlCl_3$ segments. the anion in the lowest energy structures is interacting with the opposite side of where the strongest negative potential is located so the MEPs are not an ideal

indicator of the interaction profiles between the branched anion and the imidazolium cation. The MEPs may not be good at describing the interaction due to the contortion the anion undergoes when interacting with the cation which may change where the strongest negative potential is localized.

The structure of the branched $[Al_4Cl_{13}]^-$ anion contorts to maximize the interactions with the cation. The contortion is stronger than in any scans undertaken for the branched species indicating a high degree of flexibility when exposed to the cation in the GP. The IP structures show that the branched anions can readily adjust their structure to accommodate additional interactions.

Gas phase $[C_2C_1Im][M_4Cl_{13}]$ structures featuring the linear $[M_4Cl_{13}]^-$ species interaction profile evaluation

The interaction profiles of the IP structures composed of the linear $[M_4Cl_{13}]^-$ anion and the $[C_2C_1Im]^+$ cation have additional nuances, which occur as a result of a greater diversity of chloride environments. The most stable $[C_2C_1Im][M_4Cl_{13}]$ IP structures the chloroaluminate and chlorogallate systems are shown in figure 6.13.

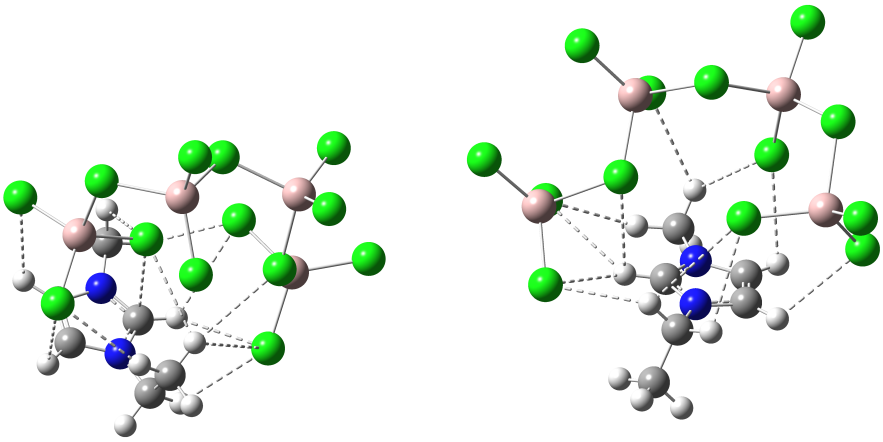


$[Al_4Cl_{13}]$_-82_6.4_97_84 (0) $[Ga_4Cl_{13}]$_-69_3.9_63_-67 (0)

Figure 6.13: Linear $[C_2C_1Im][M_4Cl_{13}]$ lowest energy gas phase structures

In the interaction profiles of the most stable $[C_2C_1Im][M_4Cl_{13}]$ IP structures the ions interact on the same principles as described for the previous IPs. However, in the lowest energy $[C_2C_1Im][Al_4Cl_{13}]$ IP structure

the linear $[Al_4Cl_{13}]$ anion predominantly interacts with the terminal $AlCl_3$ segments. Figure 6.14 shows two of the interaction profiles of the most stable $[C_2C_1Im][Al_4Cl_{13}]$ IP structures, where the lowest energy structure on the left and what one might expect to be the lowest energy structure on the right.



-82_6.4_97_84 (0)

-100_5.8_86_-85 (5)

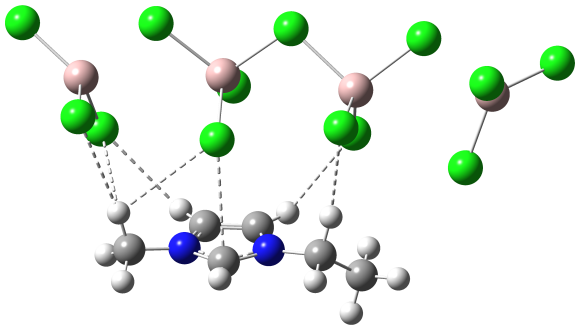
Figure 6.14: Linear $[C_2C_1Im][Al_4Cl_{13}]$ lowest energy structures interaction profiles (showing interactions shorter than 3.4 Å)

In the lowest energy structure, -82_6.4_97_84, the anion exclusively interacts with the hydrogen atoms and C_2 carbon with the terminal chloride ligands of the terminal $AlCl_3$ segments. In contrast, the second lowest energy structure, -100_5.8_86_-85, the anion interacts with the cation with a larger variety of chloride ligands across the whole cation. The lowest energy structure has seven interactions with α hydrogen atoms, four with β hydrogen atoms and a direct interaction with the C_2 carbon. The -100_5.8_86_-85 structure has 11 interactions with α hydrogen atoms.

The difference in relative Gibbs free energy and the interactions both IP structures engage in highlights the difference in nucleophilicity of the terminal and bridging segments of the linear$[Al_4Cl_{13}]^-$ anion. Although structure -100_5.8_86_-85 features an equivalent number of interactions to -82_6.4_97_84 with more electrophilic hydrogen atoms of the $[C_2C_1Im]^+$ cation, the lower nucleophilicity of bridging chlorides does not compensate for the elevated nucleophilicity of the terminal $AlCl_3$ segments. The Fukui functions and the ADCH NAC assignment scheme highlighted the large difference in nucleophilicity between the different chloride environments and predict the stabilizing effect on the interactions of the IP structures well.

Contortion of the anion also contributes largely to the stabilization of the IP structures of the $[C_2C_1Im][M_4Cl_{13}]$ IP. Some of the IP structures featuring linear $[M_4Cl_{13}]^-$ anions featured the anions in its

linear non-contorted conformation as shown in figure 6.15.



-47_6.2_65_-106 (43) [1]

Figure 6.15: Linear $[C_2C_1Im][Al_4Cl_{13}]$ highest energy gas phase structure interaction profile (showing interactions shorter than 3.4 Å)

The lack of contortion of the anion in structure -47_6.2_65_-106 results in far fewer stabilizing interactions. Additionally the relative instability of anion conformation contributes to a less stable IP structure as shown by the contortion scan of the isolated $[Al_4Cl_{13}]^-$ anion. In consequence the structure is 43 kJ mol^{-1} less stable than the lowest energy structure. The contortion of the anions lowers the energy of the anionic structure by approximately 20 kJ mol^{-1} and allows for more stabilizing interactions with the cation. Hence the contortion of the anion stabilizes the anion and allows for more stabilizing interactions with the cation.

Gas phase IP structures interaction profile evaluation summery

The evaluation of the interaction profiles showed that there is a clear hierarchy to the preference for selected interactions between the $[C_2C_1Im]^+$ cation and the chlorometallate anions. The hierarchy of attractiveness of the cations sites are; the C_2 carbon, the C_2 hydrogen, the C_4 and C_5 hydrogen atoms, the α hydrogen atoms of the ethyl and methyl arm and the β hydrogen atoms of the ethyl arm. Additionally even if there is no direct interaction (>3.4 Å) with the C_2 carbon there is always a MCl_3 segment of the anion no further than 3.8 Åfrom the C_2 carbon located above the remainder of the imidazolium ring. No stable structure was found in the GP where the anion was not partially or fully above or below in imidazolium ring. The preferences for interaction sites are most accurately predicted by a combination of the Fukui function and the ADCH charge scheme for the primary interactions and the MEPs for secondary interactions.

As the anions become larger there is more diversity in the nucleophilic chloride ligand environments. In

the bimetallic $[M_2Cl_7]^-$ anions there is a clear preference for interactions with the terminal chloride ligands over the bridging one. This principle holds true for all trimetallic and tetrametallic structures as well. The terminal chloride ligands are more nucleophilic than the bridging ones and the terminal chloride ligands attached to terminal metals are more nucleophilic than the terminal chloride ligands attached to bridging metals in the trimetallic and tetrametallic species. The interaction preferences are most amply described by the Fukui functions and the ADCH assignment scheme for all stable anions. Due to this difference in nucleophilicity there is a preference for interactions on the side opposite to the bridging ligands. The preference of the cation to interact with the $[M_3Cl_{10}]^-$ and $[M_4Cl_{13}]^-$ anions on the side opposite to the bridging chloride ligands is described by the MEP of the anionic species.

The hierarchy of nucleophilicity of the chloride ligands of the anions and the hierarchy of electrophilicity of the carbon and hydrogen atoms of the $[C_2C_1Im]^+$ cation described by the Fukui functions and the ADCH NAC assignment scheme are the most reliable methods for predicting the interaction profiles of the IPs. The IP structures found show a hierarchy in the sites which are most preferential to interact with. In the IP structures found featuring the monometallic and dimetallic structures the interaction between a chloride ligand and the C_2 carbon were essential for the structures to stabilize. In the IP structures featuring the trimetallic and tetrametallic anions the interactions were not required as the multitude of nucleophilic sites on the anion could compensate by interacting with alternative electrophilic sites. In consequence the maximization of the number of interactions between highly nucleophilic chloride ligands and electrophilic hydrogen atom around the cation is a key component of the interaction profiles as the anions become larger. The larger the anions become the more the interaction profile is dominated by the nucleophilicity of the chloride sites while when the anions are small the electrophilicity of the cationic sites dominates the interaction profile.

Dissociated chloroindate complexes in the gas phase chloroindate IP structures

Additionally to the interaction profiles, the dissociation of the $[InCl_6]^{3-}$ anions occurred during the optimization of the IP structures in the GP. The $[InCl_6]^{3-}$ structure readily dissociates into $[InCl_5]^{2-} + Cl^-$ as shown in the four structures depicted in figure 6.16.

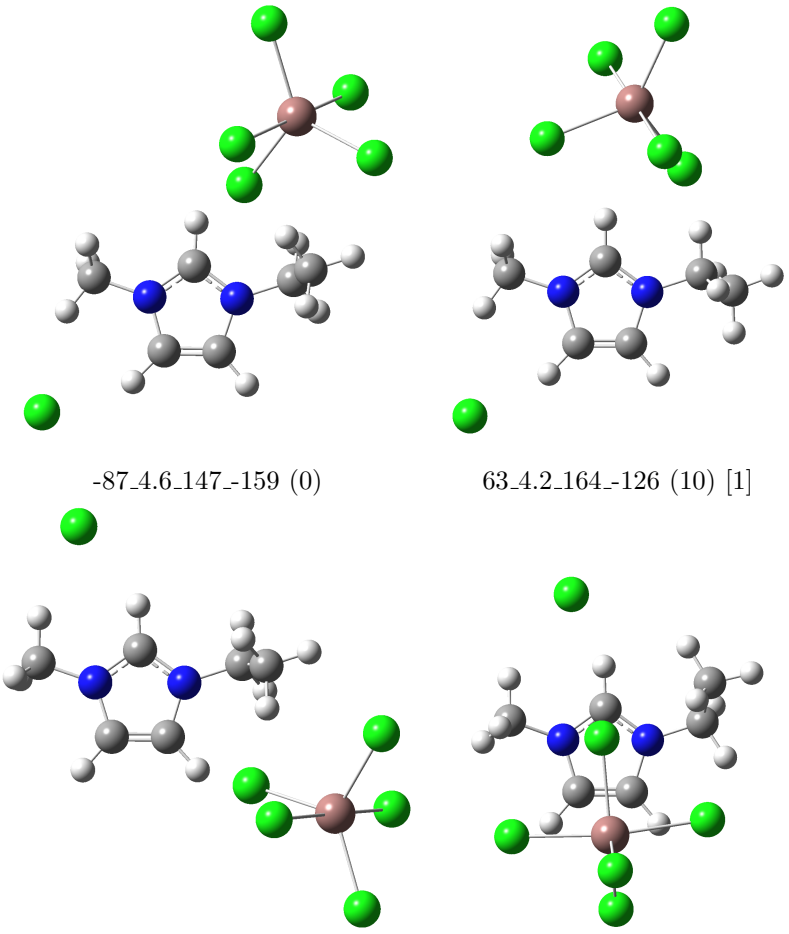


Figure 6.16: Dissociated $[C_2C_1Im][InCl_6]^{2-}$ gas phase ion pair structures

The lowest energy dissociated structure is 163 kJ mol^{-1} more stable than the non-dissociated structure and on average the non-dissociated structures are 165 kJ mol^{-1} less stable than the dissociated structures. Based on the relative stability of the isolated anions the dissociation of $[InCl_6]^{3-}$ into $[InCl_5]^{2-} + Cl^-$ is favourable by 483 kJ mol^{-1}. Hence the $[C_2C_1Im]^+$ cation has an average stabilizing effect of 318 kJ mol^{-1} on the $[InCl_6]^{3-}$ anion.

Changes to the structure of the anions upon interacting with the cation

None of the multimetallic chloroaluminate or chlorogallate anions featured dissociation upon interacting with the cation. The structure of the larger anions only changes by contorting as described by the scans in chapter 4 to maximize the interactions with the cation. Among the multimetallic chlorogallate anions the $[Ga_2Cl_7]^-$

anion and both the branched and linear $[Ga_4Cl_{13}]^-$ anions experience an elongation in gallium - chlorine bonds upon interaction when only one $GaCl_3$ moiety interacts with the cation. The gallium chloride bond from the $GaCl_3$ moiety to the bridging chlorine is elongated by 0.1 Å. In the tetrametallic species elongations of the bonds between bridging chlorine atoms and terminal gallium atoms is 0.1 and 0.13 for the branched and linear species, respectively. The structural changes are not very large but potentially indicate the bonds which will fragment during MS GP speciation.

6.1.2 Liquid phase ion pair evaluation

This section discusses the evaluation of the interaction profiles of the IPs in the LP. Due to the combination of the D3BJ dispersion and the SMD solvation model not a single LP IP structure converged in the frequency analysis. However, all structures which are considered stable were found to have negligible force values which implies that they are at a minimum on a particularly flat PES and can be considered representative of stable lowest energy states. Since none of the structures converged in the LP the [fnc] label, denoting a non-converged frequency calculation, is omitted. All the interaction preferences described for the GP IPs hold true in the LP so the LP interaction profiles will be discussed more sparingly and the nuanced differences between the GP and LP will be highlighted by presenting and discussing selected structures.

The interaction preferences determined for the GP IPs hold true in the LP without exception. The stabilizing effects from the SMD continuum solvation model induce two changes in the interaction profiles. There is more versatility in the interaction profiles between the anions and the $[C_2C_1Im]^+$ cation and the differences in energy between all the stable structures is smaller due to the implicit solvation model stabilizing IPs which were previously unfeasible. Table 6.3 shows the number of stable IP structures in different ranges of Gibbs free energy relative to the lowest energy structure of each IP in increments of 10 kJ mol^{-1}. Table 6.3 also shows in which table in the appendix in section 9.2.2 depictions of each IP structure can be found.

Table 6.3: Number of IP structures divided into relative Gibbs free energy with respect to the lowest energy structure of each IP in the ranges of ≤ 10, $10 \leq 20$, $20 \leq 30$ and $30 \leq 40$ in kJ mol^{-1} of each $[C_2C_1Im][M_xCl_{3y}]^{z-}$ IP in the liquid phase and the appendix table where the structures can be found

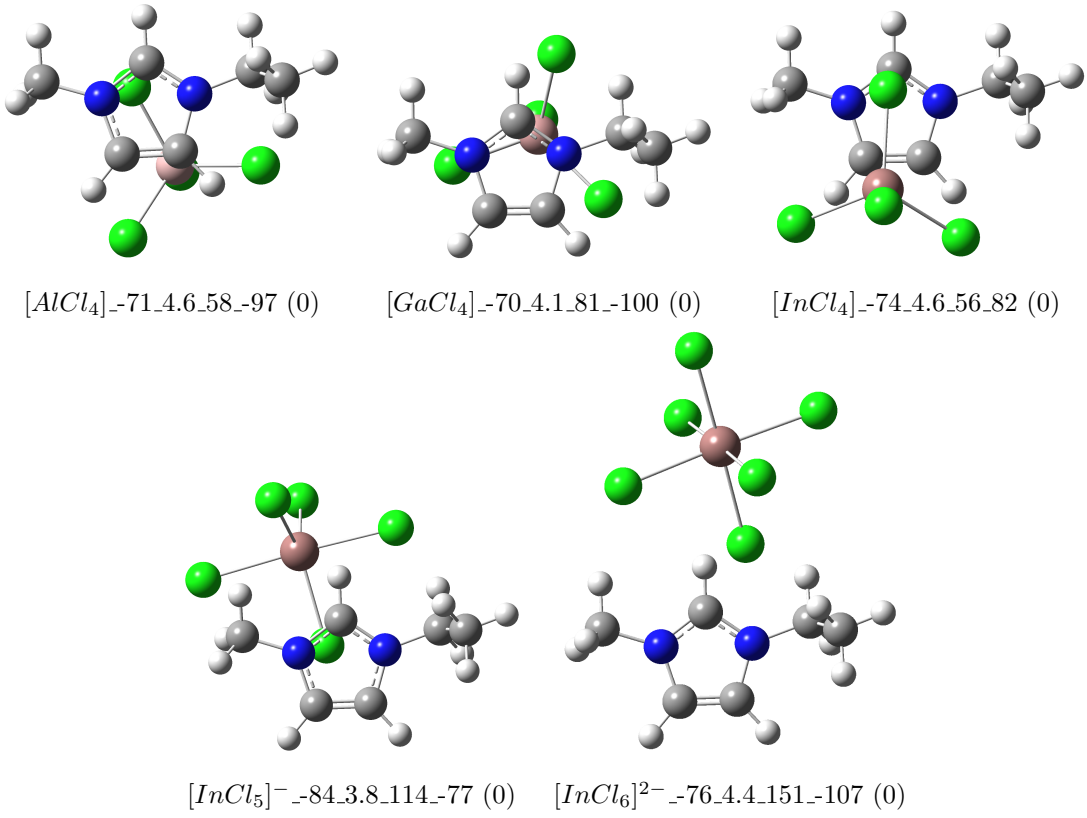
Anion	≤ 10	$10 \leq 20$	$20 \leq 30$	$30 \leq 40$	Total	Appendix Table
$[AlCl_4]^-$	11	16	0	0	27	106
$[Al_2Cl_7]^-$	15	4	0	0	19	107
$[Al_3Cl_{10}]^-$	13	6	0	0	19	108
Branched $[Al_4Cl_{13}]^-$	4	7	0	0	11	109
Linear $[Al_4Cl_{13}]^-$	15	0	0	0	15	110
$[GaCl_4]^-$	13	3	0	0	16	111
$[Ga_2Cl_7]^-$	9	4	1	0	14	112
$[Ga_3Cl_{10}]^-$	1	9	3	2	15	113
Branched $[Ga_4Cl_{13}]^-$	3	2	3	1	9	114
Linear $[Ga_4Cl_{13}]^-$	10	5	0	0	15	115
$[InCl_4]^-$	7	7	1	0	15	116
$[InCl_5]^{2-}$	18	6	3	0	27	117
$[InCl_6]^{3-}$	9	7	0	1	17	118

The relative Gibbs free energies of the stable IP structures are smaller than in the GP. No structure exceeds a relative energy of 40 kJ mol^{-1} but there is a larger variety of different interaction profiles in the LP which will be shown via selected IP structures. Additionally, the lowest energy structures of each IP are shown to highlight the most stabilizing interactions. When stable structures are analogous to the GP the nuanced differences between the GP and LP are discussed. The total range of stable LP structures can be found in the $[C_2C_1Im][M_xCl_y]$ liquid Ion pair structures appendix section.

Liquid phase $[C_2C_1Im][MCl_{4-6}]^{0-2-}$ structures interaction profile evaluation

The number of stable structures is much larger for each IPs which features monometallic anions. The higher number of stable structures is due to anions being stabilized in positions relative to the cation where they were previously not found to be stable in the GP. The IPs containing monometallic anions have an average of 13 more unique structures in every system which is indicative of how much more diverse the interaction profiles of the monometallic species with the cation are in the LP. Figure 6.17 features all the lowest energy

structures of the IPs containing monometallic anions in the LP.



$[AlCl_4]$_-71_4.6_58_-97 (0) $[GaCl_4]$_-70_4.1_81_-100 (0) $[InCl_4]$_-74_4.6_56_82 (0)

$[InCl_5]^-$_-84_3.8_114_-77 (0) $[InCl_6]^{2-}$_-76_4.4_151_-107 (0)

Figure 6.17: $[C_2C_1Im][MCl_4]$, $[C_2C_1Im][InCl_5]^-$ and $[C_2C_1Im][InCl_6]^{2-}$ lowest energy liquid phase structures

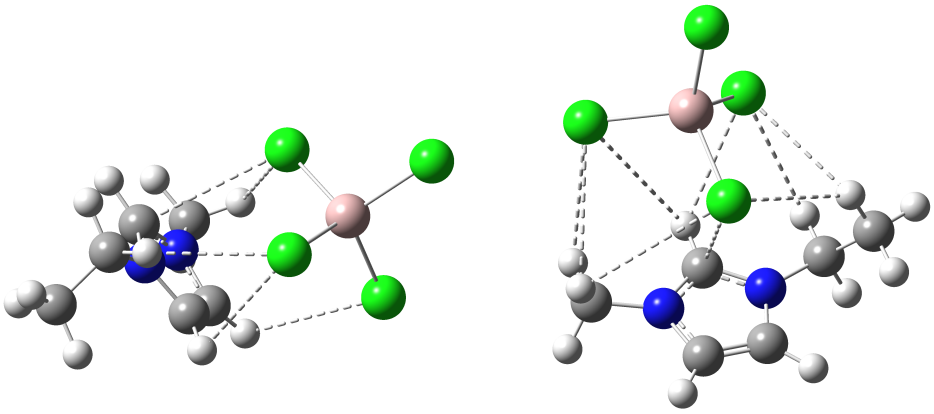
The interaction between a chloride ligand and the C_2 carbon is also prevalent in all of the lowest energy IP structures in the LP. The anions in the lowest energy structures featuring the $[MCl_4]^-$ anions are shifted further towards the back of the imidazolium ring when compared to the lowest energy GP structures indicating a lower preference to interact with the front hydrogen atoms on the C_2 carbon, methyl arm and ethyl arm. The preference of the anions to interact with the back of the imidazolium ring is not a result of a stabilizing interaction between the anion and cation in the chloroaluminate and chlorogallate systems but comes from the entropy contribution of the structures. Table 6.4 shows the thermodynamics of the lowest energy IP structures of the $[C_2C_1Im][MCl_4]$ IPs in the GP and LP.

Table 6.4: $[C_2C_1Im][MCl_4]$ gas phase and liquid Phase lowest energy structures thermodynamics

IP Structure	ΔH	$T\Delta S$ at 298.15K	ΔG
		Gas Phase	
$[AlCl_4]$_-58_3.7_122_87	0	9.3	0
$[GaCl_4]$_-57_3.7_120_87	0	9	0
$[InCl_4]$_56_3.8_121_87	1.1	4.3	0
		Liquid Phase	
$[AlCl_4]$_-71_4.6_58_-97_LP	1.4	12.2	0
$[GaCl_4]$_-70_4.1_81_-100_LP	0.4	7.3	0
$[InCl_4]$_-74_4.6_56_82_LP	0	4.3	0

The hierarchy of attractiveness of the nucleophilic sites on the anion and electrophilic sites on the cation are analogous in the GP and LP. However, the higher entropy contribution in the LP stabilizes structures which do not exhibit the most stabilizing interaction profiles. The $[InCl_4]^-$ anion is the exception due to the larger dimensions of the anion allowing it to interact with the C_2 carbon and the C_4 and C_5 hydrogen atoms simultaneously. The position closer to the back of the cation in conjunction with the larger distance results in the most stabilizing interaction of the $[C_2C_1Im][InCl_4]$ IP in the LP.

On the left side of figure 6.18 the interaction profiles of the lowest energy structure of the $[C_2C_1Im][AlCl_4]$ IP in the LP is depicted. The structure shown on the right of figure 6.18 is the stable LP structure which most closely resembles the lowest energy structure of the $[C_2C_1Im][AlCl_4]$ IP in the GP. Structure -60_3.9_109_86 is the most stable structure with respect to enthalpy but due to the entropy contribution the structure -71_4.6_58_-97 is more stable.



-71_4.6_58_-97 (0) -60_3.9_109_86 (11)

Figure 6.18: Selected $[C_2C_1Im][AlCl_4]$ ion pair structure interaction profiles in the liquid phase

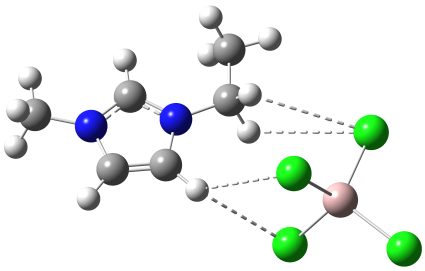
When comparing the interactions of the most stable GP structure and the corresponding LP structure there are some significant differences in the interactions because the distance between the anion and cation is larger in all LP structures. The distance between the anion and cation and the stabilization from the continuum likely impacts the entropic contribution to the Gibbs free energy. Table 6.5 shows the distances of each interaction of the most stable GP structure and the LP structure which is most like it.

Table 6.5: The most stable $[C_2C_1Im][AlCl_4]$ gas phase structure and corresponding liquid phase structure interaction distances and differences in Å

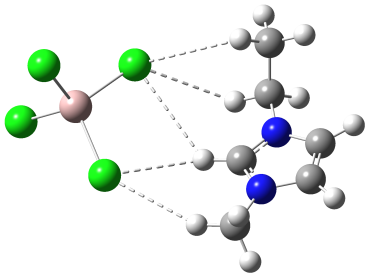
Interaction	Gas Phase	Liquid Phase	Δ_{GP-LP}
A_1 (C_2-Carbon)	3.2	3.5	0.3
A_2 (Methyl-Hydrogen1)	3.1	3.7	0.6
A_3 (Ethyl-Hydrogen1)	3.1	3.2	0.1
B_1 (Methyl-Hydrogen1)	3.1	3.3	0.2
B_2 (Methyl-Hydrogen2)	2.9	3.3	0.4
B_3 (C_2-Hydrogen)	2.8	3.8	1.0
C_1 (Ethyl-Hydrogen1)	2.7	3.1	0.4
C_2 (Ethyl-Hydrogen2)	3.0	3.1	0.1
C_3 (C_2-Hydrogen)	3.0	3.2	0.2
M-C_2-Hydrogen	3.2	3.9	0.7
Average	3.0	3.4	0.4

The distances of individual interaction between the anion and the cation are on average 0.4 Ålonger in the LP structure compared to the corresponding GP structure. The distance of the anion - cation interactions is elongated by 0.4 Åthroughout all IP structures when comparing GP to LP IP structures of all chlorometallate systems. Due to the change in interaction distances the interaction profiles have nuanced changes due to the dimensions of the species. The larger distance between the ions prevents the same optimized interactions observed in the GP and the IP structures have alternative structural configurations to idealize the interactions described for the GP.

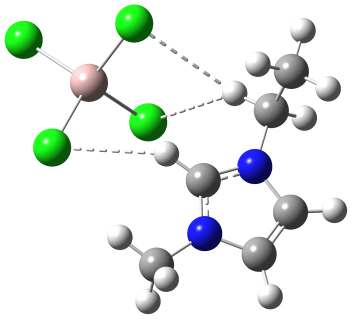
The anion-π interaction is still the most stabilizing interaction as it is found in all of the lower energy structures. However due to the stabilizing effect of the solvation environment there is more versatility of the interaction profiles. There are stable IP structures which feature the anion in positions around the cation in which the anion is not interacting with the π-system. Figure 6.19 shows three $[C_2C_1Im][AlCl_4]$ IP structures in the LP where the anion located in front or the side in the plane of the imidazolium ring, interacting with the aromatic and aliphatic hydrogen atoms.



178_6.1_55_-180 (19)



-75_4.8_161_109 (15)



-87_4.2_149_-121 (11)

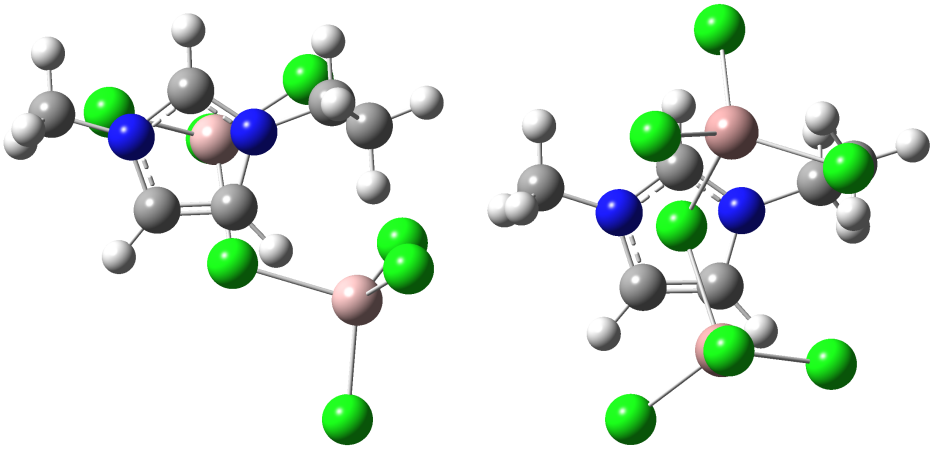
Figure 6.19: $[C_2C_1Im][AlCl_4]$ ion pair structure interaction profiles (showing interactions shorter than 4.0 Å) in the liquid phase

The three structures depicted in figure 6.19 are all less stable than the lowest energy structure by $>$ 10 kJ mol^{-1} indicating an interaction with the π-system is favourable in the LP. In structures -75_4.8_161_109 and -87_4.2_149_-121 the anion is in front of the imidazolium ring in different orientations interacting with two and three chlorides with four and two hydrogen atoms, respectively. In structure 178_6.1_55_-180 the anion is in plane of the imidazolium ring at the back on the side of the ethyl arm side of the imidazolium ring and features three chloride ligands interacting with three hydrogen atoms. The position at the back is less favoured than the position in the front by 6 kJ mol^{-1} on average. Analogously to the interactions in a GP the interaction with the face of the anion is more favourable than with the edge and the corner of the tetrahedral structure as the anion can engage in more interactions with the cations nucleophilic sites.

Liquid phase $[C_2C_1Im][M_2Cl_7]$ structures interaction profile evaluation

In the LP the IP structures featuring the $[M_2Cl_7]^-$ anions have a preference for interacting with the π-system of the imidazolium ring. All of the structures which are within $<$ 10 kJ mol^{-1} of the lowest energy structure feature an anion-π interaction. Analogously to the IPs featuring monometallic anions in the LP, the anion-π interaction is not a requirement for the IP structure to be stable in the LP.

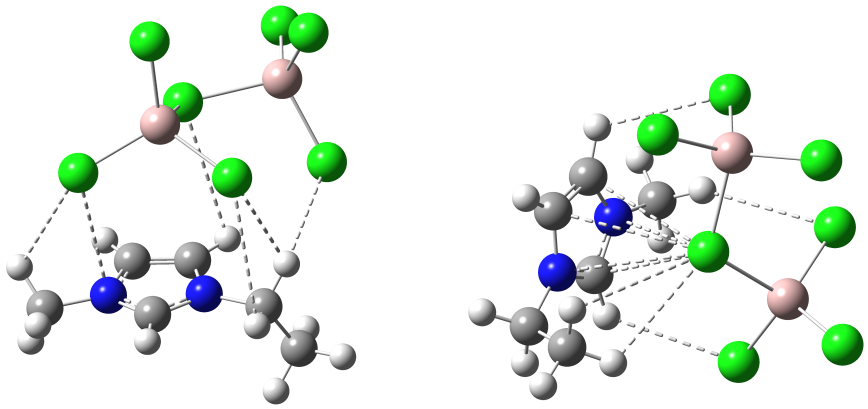
The most stable IP structures of the chloroaluminate and chlorogallate $[C_2C_1Im][M_2Cl_7]$ IPs in the LP are depicted in figure 6.20. In the LP the $[M_2Cl_7]^-$ anions have a different preferred orientation towards the cation when interacting with the cation. The $[Al_2Cl_7]^-$ and $[Ga_2Cl_7]^-$ are oriented towards the cation to allow for interactions between the bridging chloride and terminal chlorides with the electrophilic sites of the cation.



$[Al_2Cl_7]$_-69_4.9_44_-100 (0) $[Ga_2Cl_7]$_-95_3.4_73_84 (0)

Figure 6.20: $[C_2C_1Im][M_2Cl_7]$ lowest energy liquid phase structures

The lowest energy $[C_2C_1Im][M_2Cl_7]$ structures of both systems feature an interaction in which the anion is oriented towards the cation via the side of the anion. In the lowest energy structure of the $[C_2C_1Im][Al_2Cl_7]$ IP one $AlCl_3$ segment interacts with the cation via two terminal chloride ligands while the other $AlCl_3$ segment only interacts with one terminal chlorine ligand. The lowest energy structures of both systems feature a high entropy contribution, so they are not representative of the strongest interactions between the ions. The structures which do feature the strongest interaction profiles based on the enthalpy are also oriented towards the cation in the same way as exhibited in the structures in figure 6.21. Figure 6.21 shows the interaction profiles of the most stable $[C_2C_1Im][Al_2Cl_7]$ IP structures according to Gibbs free energy and enthalpy.

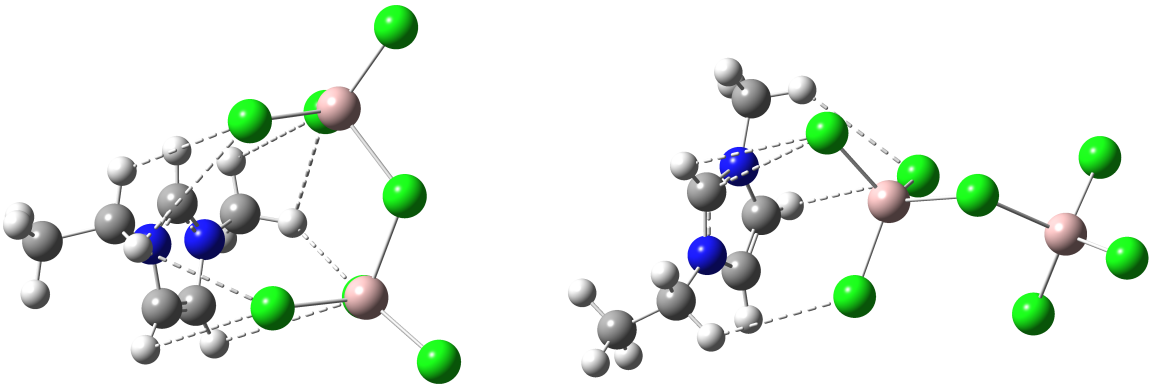


-69_4.9_44_-100 (0)

-79_3.4_73_87 (1)

Figure 6.21: $[C_2C_1Im][Al_2Cl_7]$ interaction profiles (showing interactions shorter than 3.6 Å) in the liquid phase

The two lowest energy structures of the $[C_2C_1Im][Al_2Cl_7]$ both feature the anion interacting with the $[C_2C_1Im]^+$ via the side. However, when compared to alternative interaction profiles, as those depicted in figure 6.22, and looking at the relative energy of 3 and 5 kJ mol^{-1} the key feature of the interaction profiles is not the orientation of the anion but the partial or full positioning of the anion above or below the imidazolium ring.



-67_5.5_92_-92 (5)

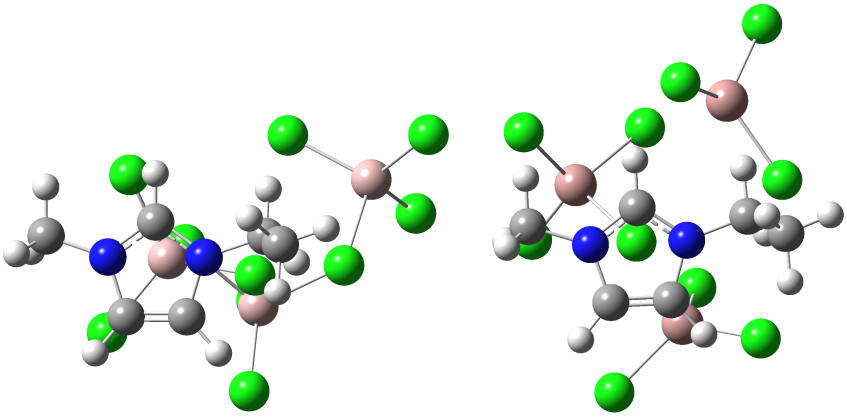
-73_6.3_83_-84 (3)

Figure 6.22: $[C_2C_1Im][Al_2Cl_7]$ interaction profiles (showing interactions shorter than 3.6 Å) in the liquid phase

The LP environment stabilizes the IP regardless of the orientation of the anion, even when only one of the MCl_3 segments is interacting with the imidazolium. All structures which have a higher relative Gibbs free energy of $>$ 10 kJ mol^{-1} feature the anion located in the plane of the ring, not engaging in an anion-π interaction. In the $[C_2C_1Im][Al_2Cl_7]$ structures the primary factor effecting the energy of the systems is the location of the anion with respect to the cation which determines whether an anion-π interaction is possible or not. The $[C_2C_1Im][Ga_2Cl_7]$ IP is stabilized analogously to the $[C_2C_1Im][Al_2Cl_7]$ IP but the relative energies are slightly larger as some structures which are interacting with the π systems are up to 11 kJ mol^{-1} less stable than the lowest energy structure.

Liquid phase $[C_2C_1Im][Al_3Cl_{10}]$ structures interaction profile evaluation

The Interaction profiles of the $[C_2C_1Im][M_3Cl_{10}]$ IPs can be described by an amalgamation of the principles described for the $[C_2C_1Im][Al_3Cl_{10}]$ IPs in the GP and the $[C_2C_1Im][M_2Cl_7]$ IPs in the LP. The most stable $[C_2C_1Im][M_3Cl_{10}]$ IP structures feature anion-π interactions. The maximization of the number of interactions between the electrophilic sites of the cation and the nucleophilic sites on the anion occurs in the most stable IP structures. The contortion of the anion contributes to the maximization of the number of interactions between the imidazolium cation and the trimetallic anions. The two lowest energy structures of the $[C_2C_1Im][M_3Cl_{10}]$ IPs of the chloroaluminate and chlorogallate systems are shown in figure 6.23.



$[Al_3Cl_{10}]$_-78_7.6_72_-98 (0)　　$[Ga_3Cl_{10}]$_-67_4.8_94_-77 (0)

Figure 6.23: $[C_2C_1Im][M_3Cl_{10}]$ lowest energy liquid phase structures

In the lowest energy structure of the $[C_2C_1Im][Ga_3Cl_{10}]$ IP the $[Ga_3Cl_{10}]^-$ anion exhibits a high amount of intramolecular interactions which is highlighted in figure 6.24. The self-interaction of the $[Ga_3Cl_{10}]^-$ is between the chloride ligands in close proximity to one another ($3.7 > 3.9$ Å). The self-interaction is stabilizing with respect to the enthalpy and the entropy of the system meaning that the more compact the ion is the better it can interact and move more freely. There are no additional novelties in the $[C_2C_1Im][M_3Cl_{10}]$ IPs. The interaction profiles of the $[C_2C_1Im][M_4Cl_{13}]$ IPs containing the branched $[M_4Cl_{13}]^-$ anions follow analogous principles to the trimetallic system so the interaction profiles are not elaborated upon.

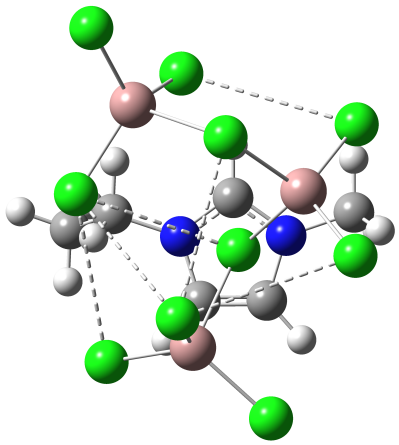
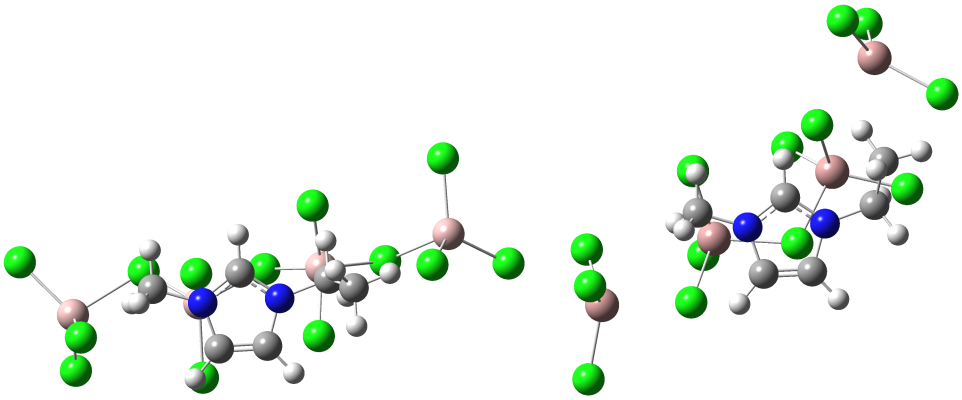


Figure 6.24: $[C_2C_1Im][Ga_3Cl_{10}]$ self interactions between 3.7 and 3.9 Åin length

Liquid phase $[C_2C_1Im][M_4Cl_{13}]$ structures featuring the linear $[M_4Cl_{13}]^-$ species interaction profile evaluation

The LP $[C_2C_1Im][M_4Cl_{13}]$ IPs featuring the linear $[M_4Cl_{13}]^-$ anion are different from the GP IPs. Most of the IP structures feature the linear $[M_4Cl_{13}]^-$ anion in a fully elongated, non-contorted conformation. The $[M_4Cl_{13}]^-$ anions do not contort in the LP IP structures due to the stabilizing effect of the solvation environment. Figure 6.25 shows the most stable structures from the $[C_2C_1Im][M_4Cl_{13}]$ IPs of the chloroaluminate and chlorogallate systems.



$[Al_4Cl_{13}]$_-77_6.2_83_-101 (0) $[Ga_4Cl_{13}]$_-146_4_65_-101 (0)

Figure 6.25: Linear $[C_2C_1Im][M_4Cl_{13}]$ lowest energy liquid phase structures

The hierarchy of electrophilic and nucleophilic sites on the cation and anion are the same as in the GP. The lowest energy structures feature the $[M_4Cl_{13}]^-$ anion above the imidazolium ring due to the preferential interaction with the π system while maximizing the number of chloride - hydrogen interactions. The LP $[C_2C_1Im][M_4Cl_{13}]$ IP structures do not show a preference for the cation to interact with the terminal chloride ligands of the terminal MCl_3 segments as in the GP. The lack of contortion was also observed for the IPs featuring the branched $[M_4Cl_{13}]^-$ species in the LP.

Dissociated chloroindate complexes in the liquid phase chloroindate IP structures

In the LP one structure featured a $[InCl_6]^{3-}$ anion dissociated into $[InCl_5]^{2-}$ + Cl^-. Figure 6.26 depicted the dissociated structure which is 15 kJ mol^{-1} more stable than the lowest energy structure of the $[C_2C_1Im][InCl_6]^{2-}$ IP and on average 25 kJ mol^{-1} $[C_2C_1Im][InCl_6]^{2-}$ IP structures where the $[InCl_6]^{3-}$ species does not dissociate.

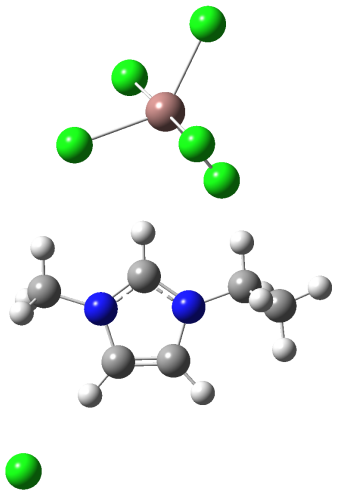


Figure 6.26: $[C_2C_1Im][InCl_6]^{2-}$_56_4.3_156_-108 (-15) Ion pair structure

The dissociation energy of $[InCl_6]^{3-}$ dissociating into $[InCl_5]^{2-}$ + Cl^- is reduced from 54 kJ mol^{-1} from the isolated species to 25 kJ mol^{-1} in the IP structures. The $[InCl_6]^{3-}$ complex is stabilized by 29 kJ mol^{-1} through the explicit interaction with one counter ion in the LP, relative to the computations of the isolated anions. The addition of more counter cations will likely stabilize the 3- charged anion further and this will be discussed in chapter 7.

Liquid phase ion pair structures interaction profile evaluation summery

The interaction profiles of the LP IP structures follow analogous principles to the GP interaction profiles. The hierarchy of the electrophilic sites on the cation and nucleophilic sites on the anions are analogous and are best described by the ADCH NAC assignment scheme and the Fukui functions. The most stable interactions in the LP involve the anions interacting with the π-system of the imidazolium ring. The solvation environment stabilizes anions in alternative positions around the cation.

Due to the increased distances between the ions the interactions themselves differ as optimal positions to generate the interactions change for some IPs. Entropy plays a larger role in the LP causing structures which have the strongest interactions not to be the most stable structures. The entropy causes the orientation of the anions towards the cations to be less significant in the LP compared to the GP.

One key difference between the GP and LP IP structures arises due to the stabilization of the anion segments which are not interacting with the cation. IP structures in which anions are partially interacting with the

cations are relatively stable in the LP for IPs which feature multimetallic anions. In many stable structures one or more of the MCl_3 segments are not or only partially interacting the cation as the stabilization of the implicit solvation model allows for the structures to be stabilized without interacting. Additionally, many anion structures which were shown to be more stable in the contorted state are found more commonly in a fully elongated state due to the stabilization of the solvation environment.

6.1.3 $[C_2C_1Im]Cl$-MCl_3 ion pair interaction profile evaluation in the gas phase and liquid phase summery

The relative stability and interaction profiles of the GP IP structures showed that there is a strict hierarchy of electrophilic sites and nucleophilic sites on the anion and the cation, respectively. The most attractive sites on both anions and cations are described best by the Fukui functions and the ADCH NAC assignments of the isolated species. The hierarchy of attractiveness of the sites is also applicable to the LP structures but is not as clearly exhibited due to the stabilizing effects of the solvation environment and entropy contributions resulting in alternative stable interaction profiles.

The hierarchy of electrophilicity of the cations sites are as follows; The C_2 carbon, the C_2 hydrogen, the C_4 and C_5 hydrogen atoms, the ethyl and methyl α hydrogen atoms and lastly the ethyl β hydrogen atoms. The anions interact with the cation to maximize the interaction with the electrophilic sites. In the case of the monometallic anions that means that the anion is located above or below the cation and a face of the tetrahedral, trigonal bipyramidal or octahedral structure is oriented towards the cation. The larger anions have more complexity in their interactions as the nucleophilicity of the terminal chloride ligands on terminal metal interacting with the most electrophilic sites on the cation result in the most stable IP structures.

In the LP the anions are further away from the cation and do not interact with the cation analogously to the GP. The interactions with the terminal chlorides on terminal metals of the trimetallic and tetrametallic anions are not as stabilizing as they were in the GP. The three factors which effect the stability of the LP IP structures are the interaction with the π-system, the amount of MCl_3 moieties interacting with the cation and the entropy exhibited by the IP. The $[M_3Cl_{10}]^-$ and the linear $[M_4Cl_{13}]^-$ anions exhibit self-interaction stabilize the structure which may also in turn stabilize the interaction with the cation.

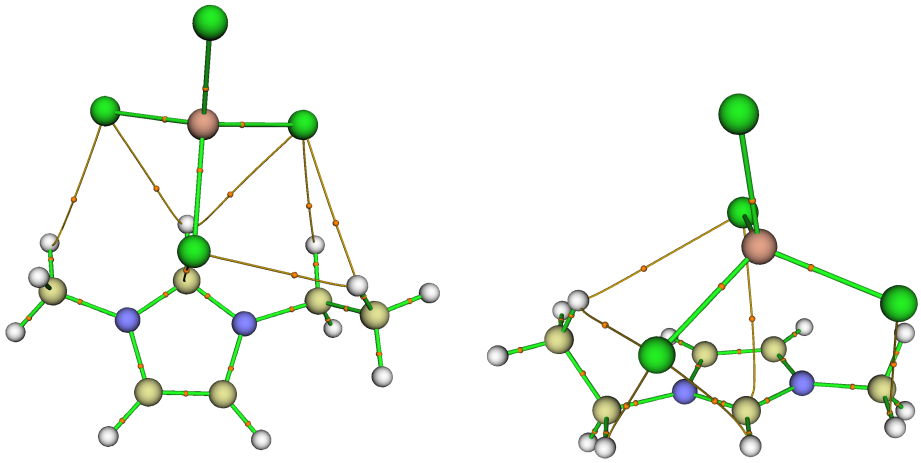
6.1.4 $[C_2C_1Im]Cl\text{-}MCl_3$ ion pair Gas phase and liquid phase ion pair electronic structure evaluation

To understand how the electronic structure of the IP structures determines the relative stability in different interaction profiles four techniques were used to evaluate the stable IP structures for additional insight. The MOs of the IPs were evaluated to see how much the stabilization of interactions were based on in phase orbital overlaps between the MOs of the anions and the cation, but no conclusive results could be determined and hence they are not shown here but the MOs can be found in the appendix. AIM analysis was used to determine the critical points between the interacting sites of the anions and cations in the IP structures. The NCIplot and IRI analyses were both used to visualize the interaction regions between the IP structures and show where interactions are strongest. NCIplot and IRI analysis are modelled from the reduced density gradient. NCIplot is a more established technique while IRI is more novel but has a broader range of interactions it highlights. Hence both techniques were carried out but the visualizations from the NCIplot were used to confirm the results from the IRI and IRI plots are shown here. A full set of visualizations of the MOs and AIM analyses can be found in the appendix sections 9.2.3 and 9.2.4.

Atoms in molecules analysis of ion pairs

AIM analysis was used to understand where the interactions between the anions and cations are localized via the topology of the electron density of the IP structure. The results of the AIM analysis were compared to the evaluation of the IP structures to determine whether the interaction profiles described for the IPs in each phase by the structural evaluation are indicative of the most stabilizing interactions. AIM analysis was used to understand the differences in interaction profiles between the GP and LP as the interaction profiles between the $[C_2C_1Im]^+$ cation and the anions are relatively similar in both phases with complexity increasing with the size of the anions due to the greater variety in nucleophilic sites. The evaluation of the $[C_2C_1Im][AlCl_4]$ IP structures is presented here as the insights are similar for each IP across all chlorometallate systems.

The two most stable $[C_2C_1Im][AlCl_4]$ IP structures from each phase were compared and two IP structures which most resemble the most stable structure in the other phase to see how the interactions are different in both phases. Figure 6.27 visualizes the bond critical points (BCPs) of the inter molecular interactions of the lowest energy structure of the GP, -58_3.7_122_87, on the left and the corresponding structure of the LP, -60_3.9_109_86_LP on the right.



-58_3.7_122_87 (0)

-60_3.9_109_86_LP (11)

Figure 6.27: $[C_2C_1Im][AlCl_4]$ gas phase and liquid phase AIM topology

The BCPs show that the evaluation based on the proximity of the chloride ligands of the anion to the electrophilic sites of the cation provides a reasonable approximation of which interactions occur in the IPs. In the LP there is one fewer interaction between one of the chloride ligands and the C_2 hydrogen. Both structures do not feature an interaction between the chloride ligand situated above the C_2 carbon and the methyl arm which shows that proximity is a good first indicator of intermolecular interactions. There may still be an interaction between the two points which is not visualized as there is no bond critical point as the minimum of the electron densities topology is found in the adjacent BCP. Tables 6.6 and 6.7 shows the electron density in $e\ a_0^{-3}$ and the strength of the H-Cl bonds computed according to a method devised by Tian lu and co workers.[1,2] from the electron density at the BCPs.

Table 6.6: $[C_2C_1Im][AlCl_4]$_-58_3.7_122_87 (0) BCP electron density and interaction strength

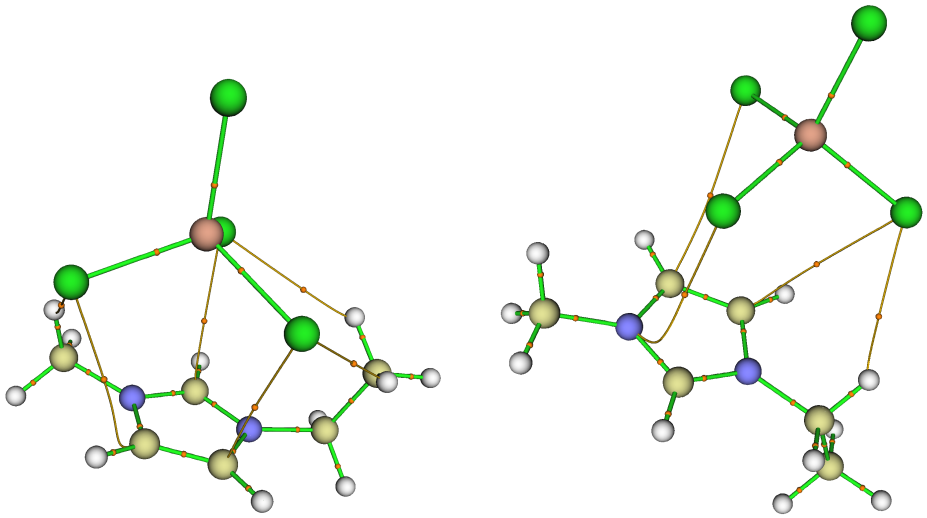
type	ea_0^{-3}	H-Bond strength contribution (kJ mol^{-1})
Cl - C_2 hydrogen	8.3E-03	-5
Cl - C_2 hydrogen	6.1E-03	-3
Cl - C_2 Carbon	1.0E-02	N/a
Cl - methyl α-hydrogen	8.2E-03	-5
Cl - ethyl α-hydrogen	1.0E-02	-6
Cl - ethyl β-hydrogen	6.5E-03	-3
Cl - ethyl β-hydrogen	4.9E-03	-2
Total interaction	5.4E-02	-22

Table 6.7: $[C_2C_1Im][AlCl_4]$_-60_3.9_109_86_LP (11) BCP electron density and interaction strength

type	ea_0^{-3}	H-Bond strength contribution (kJ mol^{-1})
Cl - C_2 Carbon	6.1E-03	N/a
Cl - C_2 hydrogen	5.6E-03	-2
Cl - methyl α-hydrogen	4.3E-03	-1
Cl - ethyl α-hydrogen	4.7E-03	-1
Cl - ethyl β-hydrogen	4.5E-03	-1
Cl - ethyl β-hydrogen	5.4E-03	-2
Total interaction	3.1E-02	-7

The electron density at BCPs can be used to predict the interaction strength of hydrogen bonds [1]. hence the interaction strength of intermolecular forces which are not hydrogen bonds cannot be determined through this method and are omitted. The values of electron density at each BCP indicate that the H-bond interactions are far stronger in the GP due to the proximity of the chloride ligands to the hydrogen atoms. The largest value of electron density for both species is the BCP which interacts with the C_2 carbon which indicates that this is by far the strongest interaction as predicted through the structural analysis. The AIM analysis confirms that due to the larger distance between the ions that the chloride ligands can no longer interact with the anion as strongly as in the GP. All H-bonds in the LP only stabilize the system by 1-2 kJ mol^{-1} while in the GP some of the individual interactions stabilize the structure by up to 6 kJ mol^{-1}. The same evaluation was undertaken for the lowest energy structure of LP and the corresponding GP structure shown

in figure 6.28 and tables 6.8 and 6.9.



-78_4.3_64_81 (8) -71_4.6_58_-97_LP (0)

Figure 6.28: $[C_2C_1Im][AlCl_4]$ gas phase and liquid phase AIM topology

The topology of the lowest energy structure of the LP, -71_4.6_58_-97_LP, shows that there is only one direct interaction with a hydrogen atom and that the remainder of the electron density is localized between the anion and the π-system. The corresponding GP structure, -78_4.3_64_81 has slightly different interactions but also interacts with three points on the imidazolium ring. In the GP structure there is an additional interaction with the ethyl arm in the which are not prevalent in the LP.

Table 6.8: $[C_2C_1Im][AlCl_4]$_-78_4.3_64_81 (8) BCP electron density and interaction strength

type	ea_0^{-3}	H-Bond strength contribution ($kJ\ mol^{-1}$)
Cl - C_2-Carbon	1.1E-02	N/a
Cl - C_4-Carbon	7.7E-03	N/a
Cl - C_5-Carbon	8.2E-03	N/a
Cl - ethyl β-hydrogen	6.9E-03	-3
Cl - ethyl β-hydrogen	7.7E-03	-4
Cl - methyl α-hydrogen	9.7E-03	-6
Total interaction	5.2E-02	-13

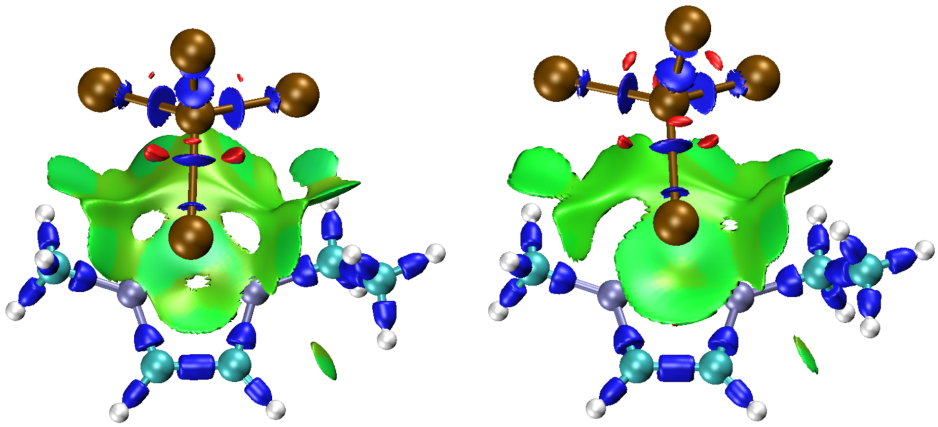
Table 6.9: $[C_2C_1Im][AlCl_4]$_-71_4.6_58_-97_LP (0) BCP electron density and interaction strength

type	ea_0^{-3}	H-Bond strength contribution ($kJ\ mol^{-1}$)
Cl - N_3 Nitrogen	7.1E-03	N/a
Cl - C_4 Carbon	4.6E-03	N/a
Cl - C_5 Carbon	5.0E-03	N/a
Cl - ethyl α-hydrogen	6.8E-03	-3
Total interaction	2.3E-02	-3

The total electron density of the BCPs of both GP structures indicate a stronger interaction in the IP structures which are not the lowest energy structure which confirms that the structure does not derive its stability from the strong interaction but rather from the entropy.

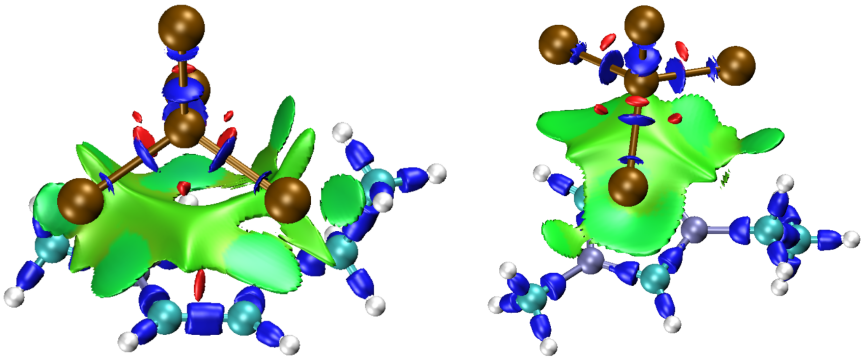
Interaction region indicator analysis of ion pairs

The IRI and a NCI plot analysis were used to visualize the interaction regions between the anion and the cation, The IRIs are shown here and the NCiplot is omitted as the information both visualizations convey is analogous. The blue regions are strong interactions which are located between bonds. the red regions are repulsive interactions, and the green regions are weak intermolecular interactions. There are regions of weak interaction between the anion and cation with single interaction points which coincide with the BCPs exhibited in AIM showing slightly stronger interactions where the green colour is more turquoise.



-58_3.7_122_87 (0) -60_3.9_109_86_LP (11)

Figure 6.29: $[C_2C_1Im][AlCl_4]$ gas phase and liquid phase IRIs



-78_4.3_64_81 (8) -71_4.6_58_-97_LP (0)

Figure 6.30: $[C_2C_1Im][AlCl_4]$ gas phase and liquid phase IRIs

6.2 [Choline][$AlCl_4$], [N_{2110}][$AlCl_4$] and [N_{2111}][$AlCl_4$] ion pair interaction profiles evaluation

This section evaluates the interaction profiles of the tetrahedral monometallic species, $[MCl_4]^-$ with the three ammonium based cations in the GP. The LP interaction profiles are similar and the principles described for the interaction profiles in the $[C_2C_1Im]Cl$ - MCl_3 systems hold true as the size of the anion increases. The interaction profiles with the larger anions are omitted as changing the anion only prompts similar changes to the interaction profiles as those which were observed for the IPs featuring the $[C_2C_1Im]^+$ cation. When the chloroaluminate and chlorogallate anions oligomerize the principle that interactions with the primary site in combination with a maximization of interactions with secondary sites result in the most stable IP structures holds true for the ammonium-based cations.

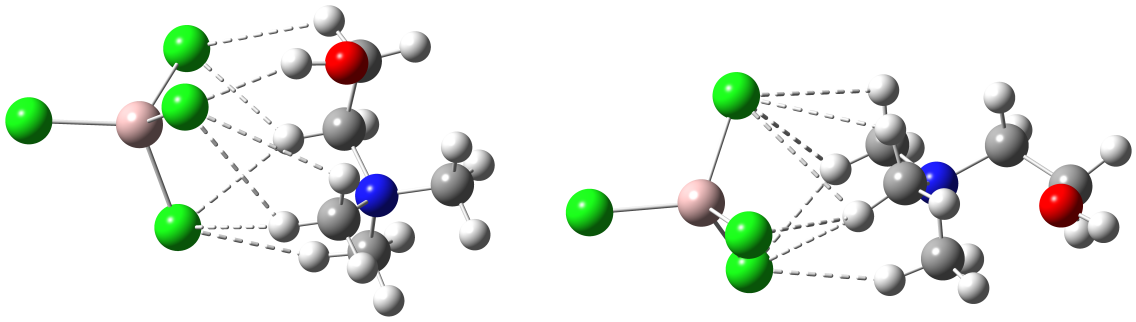
6.2.1 [Choline][$AlCl_4$], [N_{2110}][$AlCl_4$] and [N_{2111}][$AlCl_4$] ion pair interaction profiles

The evaluation of the IPs of the $[C_2C_1Im]Cl$ - MCl_3 systems showed that the interaction profiles of the IPs are based on analogous principles in the GP and LP. Consequentially this section only focuses on the interaction profiles of the GP IPs structures. The interaction profiles between the ammonium based cations and the halometallate anions are exclusively described via the interactions exhibited by the [Cation][$AlCl_4$] IPs. In the GP the pentacoordinate and hexacoordinate indium complexes commonly dissociate for the

$[Choline]^+$ and $[N_{2110}]^+$ complexes whereas only the hexacoordinate complex dissociates in the IPs featuring the $[N_{2111}]^+$ cation. The full range of all IP structures featuring the ammonium-based cations along with a tabulation of the number of structures in different energy ranges can be found in the appendix section 9.2.8-10.

Two factors primarily contribute to the stability of the IPs featuring the $[Choline]^+$ cation and are described via four examples. The gauche conformation of the $[Choline]^+$ cation is far more stable than the trans conformer and hence IP structures featuring the gauche are generally more stable. IP structures featuring interactions of the anions with the hydroxyl hydrogen are more stable. The maximization of the number of interactions with the remaining hydrogen atoms which are α to the nitrogen and oxygen also contribute to lowering the energy.

Figure 6.31 shows two $[Choline][AlCl_4]$ IP structures with the $[Choline]^+$ in a gauche conformation.



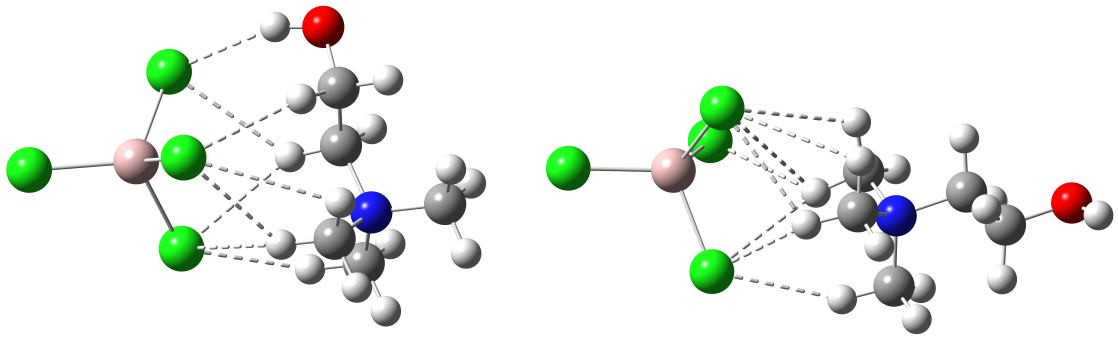
-52_4.7_50_111 (0)

-62_4.6_152_125 (25)

Figure 6.31: Gauche $[Choline][AlCl_4]$ interaction profiles (showing interactions shorter than 3.4 Å) in the gas phase

The two structures in figure 6.31, -52_4.7_50_111 and -62_4.6_152_125 are the lowest and highest energy structures featuring the gauche $[Choline]^+$ conformers. The difference of 25 $kJ\ mol^{-1}$ arises due to the position of the anion relative to the cation. Both structures feature 8 interactions via the terminal chlorine atoms with the cation but structure -52_4.7_50_111 interacts with the hydroxyl hydrogen which makes the IP far more stable.

Figure 6.32 shows the lowest and highest energy IP structures of the $[Choline][AlCl_4]$ IP featuring the trans $[Choline]^+$ conformers.



168_4.7_57_92 (10)

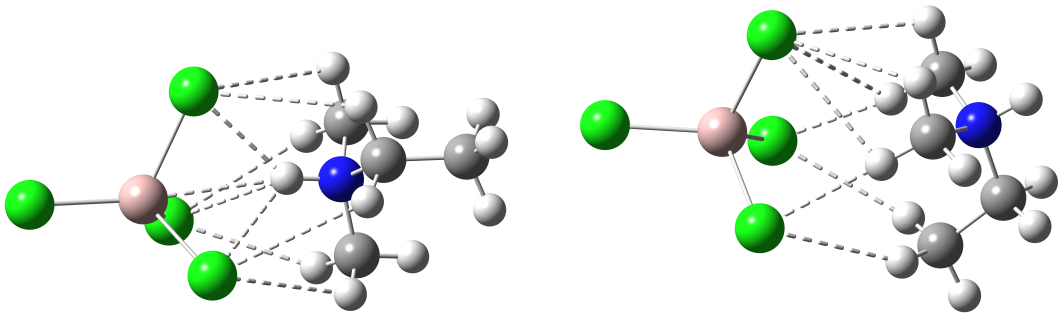
170_4.6_150_134 (30)

Figure 6.32: Trans [Choline][$AlCl_4$] Interaction profiles (showing interactions shorter than 3.4 Å(in the gas phase

The relative stability of the IP structures featuring the trans $[Choline]^+$ conformer highlight the stability of the gauche conformer as the gauche conformers lead to lower energy IP structures. Specifically the comparison between structure -62_4.6_152_125 and 170_4.6_150_134 which feature the anion interacting with the $[Choline]^+$ analogously show that there is a 5 $kJ\ mol^{-1}$ differences between the two conformations. The difference in energy between the lowest energy trans and gauche structures is even larger as the gauche conformation allows for a better interaction with the hydroxyl hydrogen and the remainder of the hydrogen atoms on the cation.

The lowest energy trans conformer also features a rotation of the hydrogen to the side. The rotation of the hydrogen allows for a more stabilizing interaction with the anion which is required. In all the IP structures which were found the hydroxyl hydrogen atom is only oriented the way it is structure 170_4.6_150_134 when the anion is not interacting with the hydroxyl hydrogen. The hydroxyl hydrogen is too far away from the remainder of the hydrogen atoms and hence a rotation of the O-H bond with respect to the remainder of the structure requires stabilizing interactions to occur with the remainder of the cation.

Figure 6.33 shows the interaction profiles of the [N_{2110}][$AlCl_4$] IP. Due to the rigidity of the cations structure the contortion of the cation does not factor into the stability of the IP structures as for the $[choline]^+$ cation.

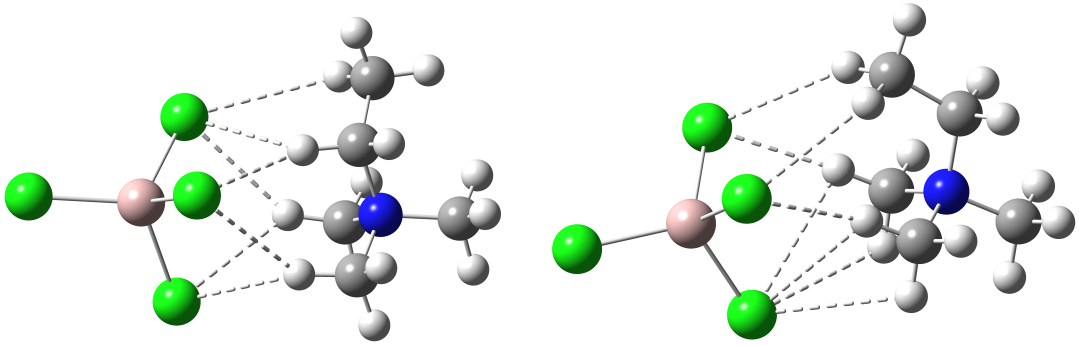


3.7_112_176 (0) 4.7_103_0 (54)

Figure 6.33: $[N_{2110}][AlCl_4]$ Interaction profiles (showing interactions shorter than 3.4 Å) in the gas phase

The two interaction profiles show that the interaction with the N-H hydrogen is by far the most stabilizing interaction. The structure of the left of figure 6.33 is the most stable $[N_{2110}][AlCl_4]$ IP structure while the structure on the right is the most stable IP structure which does not feature an interaction with the NH hydrogen. The relative stability of the two IP structures is 54 kJ mol^{-1} which indicates that an interaction with the NH nitrogen is required. The stability generated through the interaction between the anion and the NH hydrogen of the $[N_{2110}]^+$ cation is larger than the stability the interactions with the OH of the $[choline]^+$ provides. The N-H hydrogen of $[N_{2110}]^+$ being more electrophilic than the hydroxyl hydrogen of $[choline]^+$ was best described by the Fukui functions of the respective species.

The differences in energy of the $[N_{2111}]^+$ are not very large as all the sites around the cation do not have the same disparity in electropositivity as the hydrogen environments are much more similar around the cation. Figure 6.34 shows the most and least stable structures of the $[N_{2111}][AlCl_4]$ IP.



4.5_69_-44 (0) 4.7_102_0 (9)

Figure 6.34: $[N_{2111}][AlCl_4]$ Interaction profiles (showing interactions shorter than 3.4 Å) in the gas phase

The difference in stability between the lowest and highest energy structures is < 10 kJ mol^{-1}, which is small compared to the IPs featuring $[\text{Choline}]^+$ and $[\text{N}_{2110}]^+$ as there is no site with which an interaction causes the IPs to stabilize more. The hydrogen atoms which are α to the nitrogen are slightly more electrophilic which results in the differences in energy between the IP structures.

Bibliography

[1] Yunchang Fan, Hongwei Wu, Dongxu Cai, Tuojie Yang, and Lei Yang. Effective extraction of harmine by menthol/anise alcohol-based natural deep eutectic solvents. *Separation and Purification Technology*, 250:117211, 2020.

[2] Saeedreza Emamian, Tian Lu, Holger Kruse, and Hamidreza Emamian. Exploring nature and predicting strength of hydrogen bonds: A correlation analysis between atoms-in-molecules descriptors, binding energies, and energy components of symmetry-adapted perturbation theory. *Journal of computational chemistry*, 40(32):2868–2881, 2019.

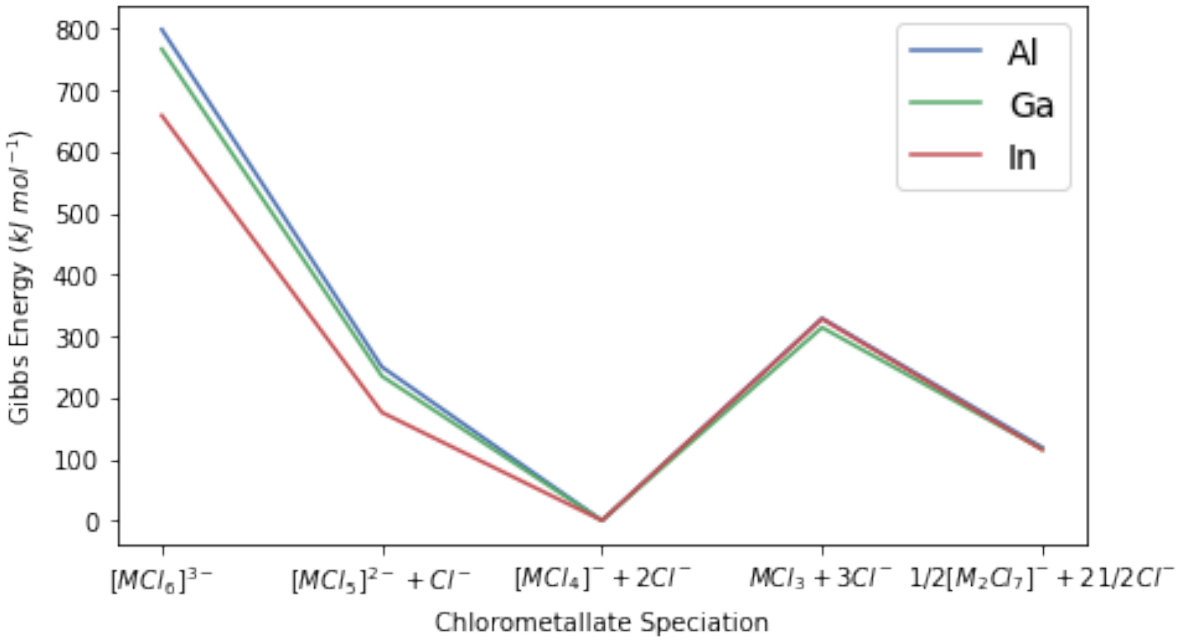
Chapter 7

Anionic speciation

7.1 Chlorometallate gas phase speciation through thermodynamic comparisons from isolated anions

This subsection describes the relative difference in Gibbs free energy between combinations of species representative of a particular x_{MCl_3} as outlined in section 3.2.4. The comparisons were carried out at x_{MCl_3} = 0.25, 0.33, 0.5, 0.67, 0.75 and 0.8 to determine the likely GP anionic speciation. For the sake of clarity the largest differences in Gibbs free energy shown are below 1000 kJ mol^{-1} and additional comparisons encompassing all combinations of GP species can be found in the appendix section 9.1.2.

7.1.1 Gas phase chlorometallate speciation at x_{MCl_3} = 0.25, 0.33 and 0.5



Metal	$[MCl_6]^{3-}$	$[MCl_5]^{2-} + Cl^-$	$[MCl_4]^- + 2Cl^-$	$MCl_3 + 3Cl^-$	$\frac{1}{2}[M_2Cl_7]^- + 2\frac{1}{2}Cl^-$
Al	799	250	0	329	119
Ga	767	235	0	314	116
In	659	176	0	328	115

Figure 7.1: Gibbs free energy differences in kJ mol^{-1} of possible anionic speciations at $x_{MCl_3} = 0.25$ in the gas phase

Figure 7.1 shows the relative Gibbs free energy of selected combinations of species at $x_{MCl_3} = 0.25$ in the GP. The anionic speciation in the GP at $x_{MCl_3} = 0.33$ and $x_{MCl_3} = 0.5$ can also be interpreted from figure 7.1. To evaluate the speciation at $x_{MCl_3} = 0.33$ one chloride is subtracted and the speciation at $x_{MCl_3} = 0.5$ can be evaluated by subtracting two chlorides. As the energy of chlorides is consistent the relative Gibbs free energy does not change. For $x_{MCl_3} = 0.33$, $[MCl_6]^{3-}$ is ignored and the remainder of structures are the same with one less free chloride. For $x_{MCl_3} = 0.5$, $[MCl_6]^{3-}$ and $[MCl_5]^{2-} + Cl^-$ are ignored and the remainder of the structures can be viewed with two less chlorides. The comparison to alternative speciations can be found in the appendix section 9.1.2 in tables 9.32 and 9.33.

At $x_{MCl_3} = 0.25$, 0.33 and 0.5, $[MCl_4]^- + 2Cl^-$ is most favourable speciation in the GP for all chlorometallate systems. The pentacooridnate with one free chloride ($[MCl_5]^{2-} + Cl^-$) and hexacoodinate ($[MCl_6]^{3-}$) structures are significantly less stable than the tetracoordinate with two free chlorides ($[MCl_4]^- + 2Cl^-$) in the GP at > 175 kJ and > 650 kJ mol^{-1}, respectively. The highly charged 2- and 3- anions are highly unstable in the GP. The comparison of the Gibbs free energy of complexes of different charge is not reliable as the energy is dominated by the instability of the most highly charged species.

There is a higher energy penalty in the case of the chloroalluminate and chlorogallate systems versus the chloroindate system between the tetracoordinate complex with two free chlorides and the pentacoordinate complex with one free chloride. For $[MCl_5]^{2-} + Cl^-$ the energy penalty is approximately 66.5 kJ mol^{-1} higher for the chloroaluminate and chlorogallate versus the chloroindate system. The difference between the chloroaluminate and chlorogallate versus the chloroindate system is even larger when comparing the tetracoordinate complex with two free chlorides to the hexacoordinate complex at approximately 124 kJ mol^{-1}. The larger difference is likely a result of the coordination chemistry of the metals. Aluminium[1] and gallium[2] are known to form penta- and hexacoordinate complexes with fluoride and water molecules, forming pentacoordinate and hexacoordinate aluminium complexes. However, the chloride ions incur steric hindrance in the smaller coordination spheres of aluminium and gallium which in turn results in higher energy penalties.

In the aluminium- and gallium-based systems the large energy penalty to form the pentacoordinate and hexacoordinate complexes is expected and coincides with MS GP speciation of both systems stated in literature.[3–6] There are no published MS GP speciation results for the chloroindate system. In a review on halometallate ionic liquids the author states that unpublished MS results of chloroindate systems showed the formation of dimetallic $[In_2Cl_7]^-$ in the GP, which does not occur in the LP.[7] The review does not discuss further discrepancies between the GP and LP speciation of the chloroindate system. In the LP $[InCl_5]^{2-}$ and $[InCl_6]^{3-}$ are known to be the predominant speciation at $x_{MCl_3} = 0.33$ and $x_{MCl_3} = 0.25$, respectively.

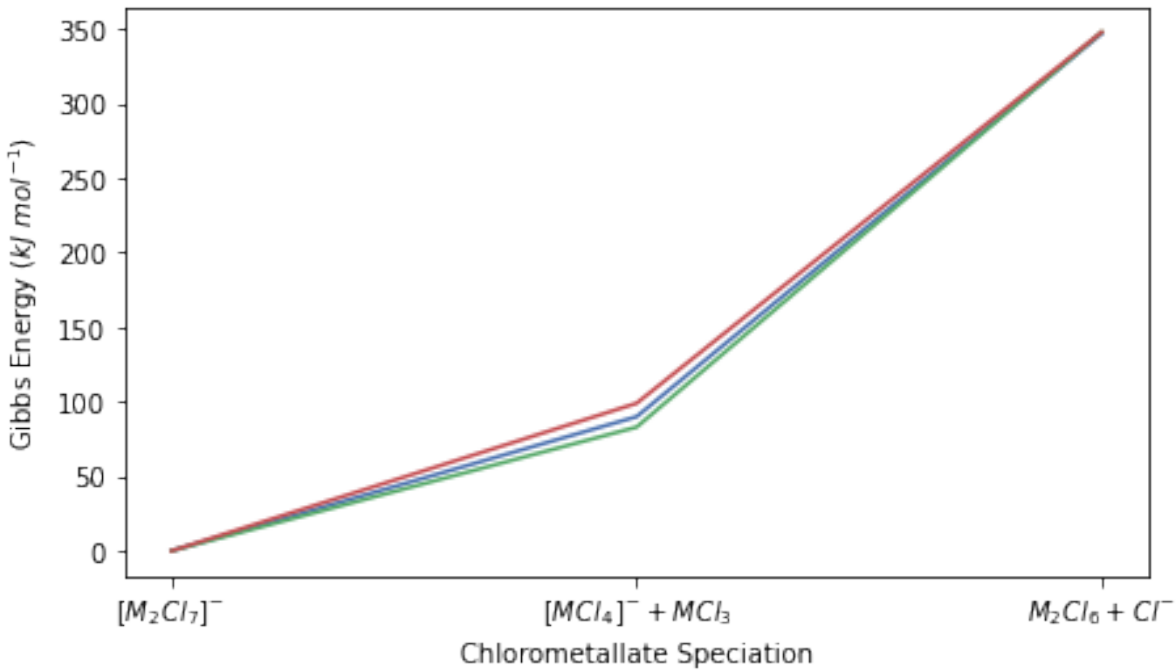
According to the relative stability determined here the 5 and 6 coordinate chloroindate complexes will not be part of the GP speciation under normal conditions at $x_{MCl_3} < 0.5$. The discrepancy between the LP speciation determined experimentally and the GP speciation determined here is likely due to the lack of a stabilizing solvation environment for the more highly charged 5 and 6 coordinate chloroindate complexes.

Additionally to the comparison between the monometallic speciations the relative Gibbs free energy of $MCl_3 + 3Cl^-$ and $\frac{1}{2}[M_2Cl_7]^- + 2\frac{1}{2}Cl^-$ is shown in figure 7.1. The relative Gibbs free energy can be used to interpret the ability of the system to form dimetallic complexes at $x_{MCl_3} = 0.5$ when two chlorides are subtracted from each molecular formula. The relative Gibbs free energy shows that the formation of $[MCl_4]^-$ is favoured when MCl_3 is introduced to the system with free chlorides. The average energy penalty of 117 kJ mol^{-1} for the formation of $\frac{1}{2}[M_2Cl_7]^- + \frac{1}{2}Cl^-$ over $[MCl_4]^-$, indicates a preference for the formation of $2[MCl_4]^-$ over $[M_2Cl_7]^- + Cl^-$ for all metals in the GP at $x_{MCl_3} = 0.5$. The preference for $[MCl_4]^-$ coincides with previously determined GP speciation at $x_{MCl_3} = 0.5$ in the chloroaluminate and chlorogallate systems.[3–6]

7.1.2 Gas phase chlorometallate speciation at $x_{MCl_3} = 0.67$

Figure 7.2 shows the relative Gibbs free energies of anionic speciations at $x_{MCl_3} = 0.67$. $[M_2Cl_3]^{3+} + 4Cl^-$, $[M_2Cl_4]^{2+} + 3Cl^-$, $[M_2Cl_5]^+ + 2Cl^-$ are omitted for clarity as the Gibbs free energy of each combination mentioned relative to $[M_2Cl_7]^-$ is > 1100 kJ mol^{-1}. The $2MCl_3 + Cl^-$ speciation has been omitted as the relative Gibbs free energy of $2MCl_3 + Cl^-$ to $[MCl_4]^- + MCl_3$ is analogous to the ΔG between $MCl_3 + Cl^-$ and $[MCl_4]^-$ shown in figure 7.1. The complete set of Gibbs free energy comparisons at $x_{MCl_3} = 0.67$ can be found in tables 9.23 and 9.24 of appendix section 9.1.2.

The relative Gibbs free energy of the structures shows that at $x_{MCl_3} = 0.67$ the $[M_2Cl_7]^-$ structure is the most stable chlorometallate structure in all three systems in the GP. To split $[M_2Cl_7]^-$ into $[MCl_4]^-$ and MCl_3, there is an average energy penalty of 91 kJ mol^{-1} which will not be overcome under normal conditions. $M_2Cl_6 + Cl^-$ is less favoured than the split into $[MCl_4]^- + MCl_3$, and is hence unlikely to occur in the GP at $x_{MCl_3} = 0.67$ for all chlorometallate systems. Hence $[M_2Cl_7]^-$ is the preferred speciation at $x_{MCl_3} = 0.67$ in the GP for all group 13 chlorometallates. Thermodynamically the speciation of the oligomerized complexes is expected in the GP as the charge is more dispersed the more the species oligomerize.



Metal	$[M_2Cl_7]^-$	$[MCl_4]^- + MCl_3$	$M_2Cl_6 + 1Cl^-$
Al	0	90	347
Ga	0	83	348
In	0	99	348

Figure 7.2: Gibbs free energy differences in kJ mol^{-1} of possible anionic speciations at $x_{MCl_3} = 0.67$ in the gas phase

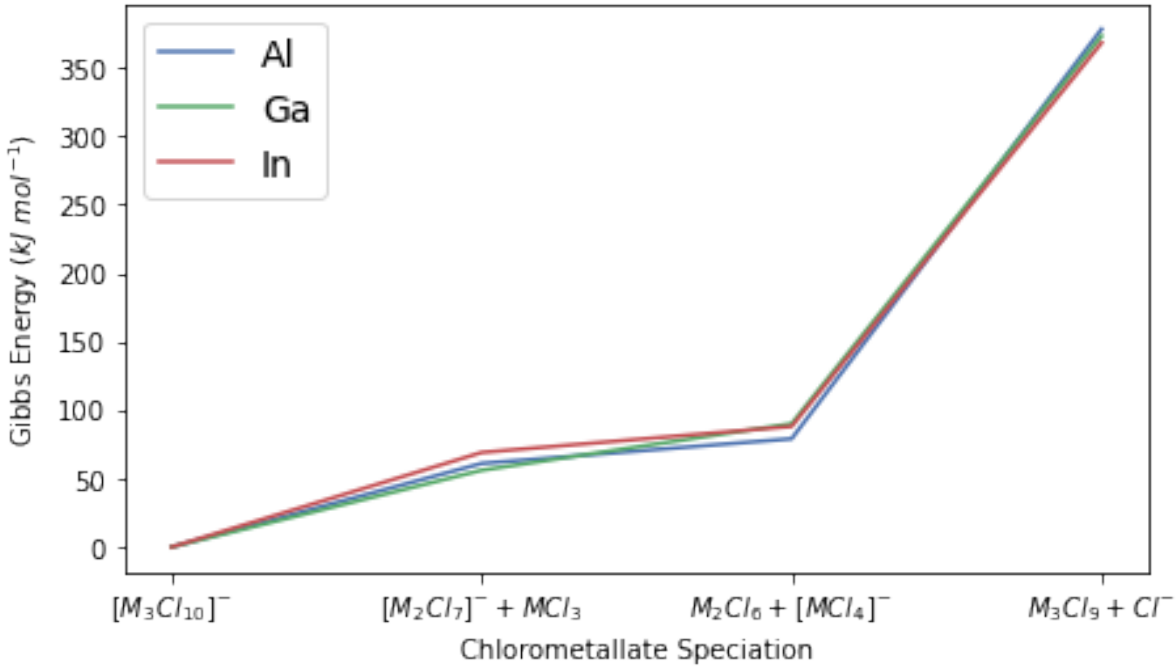
The $[Al_2Cl_7]^-$ and $[Ga_2Cl_7]^-$ species have been detected by MS investigations in the GP at $x_{MCl_3} = 0.67$.[3–6] MS investigations of the chloroaluminate and chlorogallate systems at $x_{MCl_3} = 0.67$ showed that small amounts of $[M_2Cl_7]^-$ are present in each system in the GP. Proportionally to the LP the $[M_2Cl_7]^-$ species were only found in small amounts. The thermodynamic preference for the dimetallic structures determined here does not align with the speciation determined through MS. The discrepancy between the MS results and the thermodynamic preference for the $[M_2Cl_7]^-$ determined here indicates that the chloroaluminate and chlorogallate systems is perturbed going from the LP to the GP. The ionization process of the MS perturbs the speciation of the the Al and Ga based systems.

The relative stability of the $[In_2Cl_7]^-$ complex in the GP found here is in agreement with unpublished results from Swadźba-Kwaśny and coworkers in which $[In_2Cl_7]^-$ was found while determining the anionic speciation the chloroindate system via FAB-MS and ESI-MS at $0.5 < x_{InCl_3}$.[7] However, the exact speciation profile

was not revealed via the unpublished results. The thermodynamic preference established computationally indicates $[In_2Cl_7]^-$ is the dominant species at $x_{InCl_3} = 0.67$ while the unpublished results only allude to the presence of $[In_2Cl_7]^-$. Both the unpublished results and the thermodynamic evaluation undertaken here support the discrepancy between the chloroindate speciation in the GP and LP.

7.1.3 Gas phase chlorometallate speciation at $x_{MCl_3} = 0.75$

The relative Gibbs free energy of selected speciations at $x_{MCl_3} = 0.75$ in the GP are shown in figure 7.3. A full range of comparisons of all possible speciations at $x_{MCl_3} = 0.75$ can be found in tables 9.19 and 9.20 in the appendix section 9.1.2. The two $[M_3Cl_{10}]^-$ conformers showed evidence of a high degree of structural flexibility but scans were not carried out for GP structures so there may be lower energy conformers.



Metal	$[M_3Cl_{10}]^-$	$[M_2Cl_7]^- + MCl_3$	$M_2Cl_6 + [MCl_4]^-$	$M_3Cl_9 + Cl^-$
Al	0	61	79	378
Ga	0	56	90	373
In	0	69	88	368

Figure 7.3: Gibbs free energy differences in kJ mol^{-1} of possible anionic speciations at $x_{MCl_3} = 0.75$ in the gas phase

The comparison of the Gibbs free energy of different combinations of structures in the GP at $x_{MCl_3} = 0.75$ show that the $[M_3Cl_{10}]^-$ structure is the most stable for all group 13 chlorometallate systems. The $[M_3Cl_{10}]^-$ speciation is on average 59 kJ mol^{-1} more stable than the second most stable speciation, $[M_2Cl_7]^- + MCl_3$ and 86 kJ mol^{-1} more stable than $[MCl_4]^- + M_2Cl_6$. The dissociation of $[M_3Cl_{10}]^-$ into $M_3Cl_9 + Cl^-$ requires an average of 373 kJ mol^{-1}. The relative stability of the $[M_3Cl_{10}]^-$ species is due to spreading out the negative charge over a larger molecular volume, thus stabilizing the charge in the GP. The dispersion of charge is evidenced by the partial charges outlined in chapter 5. The magnitude of the NACs on the constitute atoms of the chlorometallate species become smaller as the species become larger.

MS speciation of the chloroaluminate and chloroindate systems has not been carried out at $x_{MCl_3} = 0.75$, so comparisons with experimental results can be made for these systems. $[Ga_3Cl_{10}]^-$ was not found to be part of the speciation profile at $x_{GaCl_3} = 0.74$ by MS speciation studies.[4] However, MS peaks could be assigned to $[Ga_3Cl_9]^-$ which is in sharp contrast with the finding here, considering the relative stability of $Ga_3Cl_9 + Cl^-$ at +373 kJ mol^{-1} versus $[Ga_3Cl_{10}]^-$. The discrepancy between the results here and the MS studies show that the perturbations to the anionic speciation could be exacerbated at higher x_{GaCl_3}. This is most likely due to the susceptibility of oligomerized species to fragmentation during the ionization process.

The lower energy penalties for the dissociation of $[M_3Cl_{10}]^-$ $x_{MCl_3} = 0.75$ as compared to the dissociation of $[M_2Cl_7]^-$ at $x_{MCl_3} = 0.67$ shows a trend that the oligomerisation of the halometallate complexes becomes progressively less favourable as x_{MCl_3} is increases. Each subsequent oligomerization becoming less favourable coincides with LP speciation determined for the chloroaluminate and chlorogallate systems.

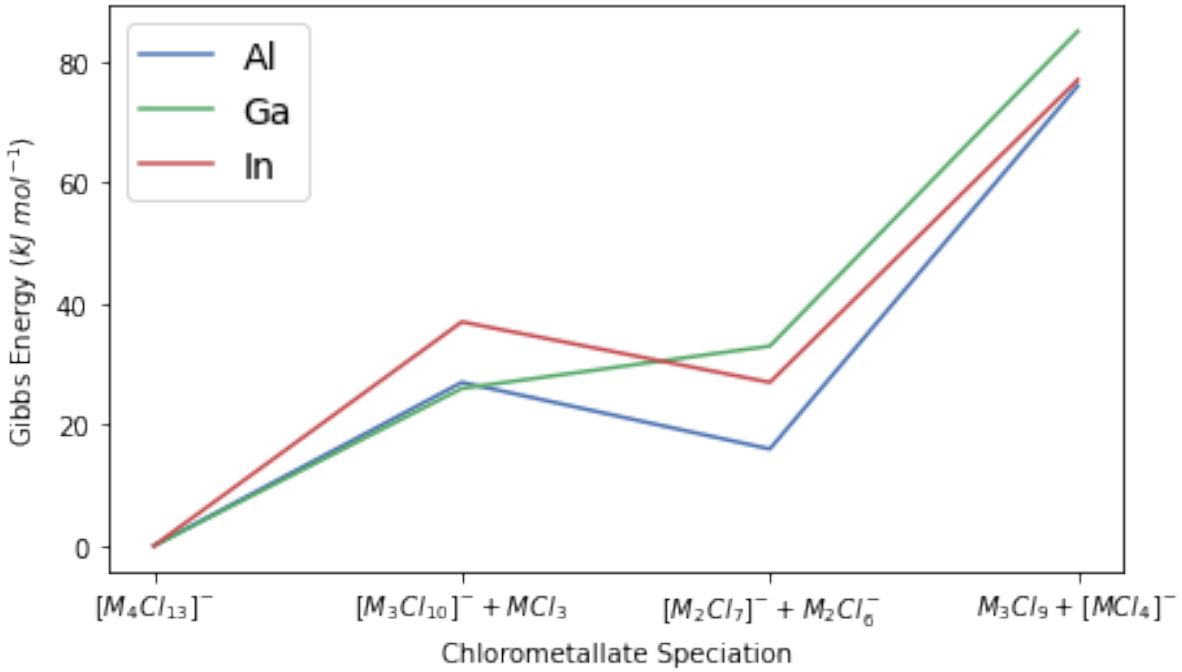
The difference in energy between the speciation of $[M_2Cl_7]^- + MCl_3$ versus $[MCl_4]^- + M_2Cl_6$ is approximatly 24 kJ mol^{-1}. The formation of M_2Cl_6 becomes more competitive the more the chlorometallates oligomerize, which is in agreement with LP speciation results.[7]

The preference for the oligomeric complexes found here is well documented in the LP of the chloroaluminate and chlorogallate systems. In contrast, $[In_3Cl_{10}]^-$ has never been observed, in either GP or LP. The $[In_3Cl_{10}]^-$ complex may be experimentally infeasible to obtain because the required amount of indium chloride dissolved in the LP is impossible to achieve due to precipitation of $InCl_3$ beyond $x_{InCl_3} = 0.5$.

7.1.4 Gas phase chlorometallate speciation at $x_{MCl_3} = 0.8$

Figure 7.4 shows the comparisons of the Gibbs free energy of selected speciations for all chlorometallate systems at $x_{MCl_3} = 0.8$ in the GP. A full set of comparisons of speciations relative Gibbs free energies

at $x_{MCl_3} = 0.8$ can be found in tables 9.12-14 in the appendix section 9.1.2. The linear and branched $[M_4Cl_{13}]^-$ structures have not been scanned for additional conformers. There may be alternative lower energy conformations which are not considered here. The speciations and respective relative Gibbs free energies are are still representative as the additional conformers will only have a marginal impact on the relative Gibbs free energy.



Metal	$[M_4Cl_{13}]^-$	$[M_3Cl_{10}]^- + MCl_3$	$[M_2Cl_7]^- + M_2Cl_6$	$M_3Cl_9 + [MCl_4]^-$
Al	0	27	16	76
Ga	0	26	33	85
In	0	37	27	77

Figure 7.4: Gibbs free energy differences in kJ mol^{-1} of possible anionic speciations at $x_{MCl_3} = 0.8$ in the gas phase

At $x_{MCl_3} = 0.8$ in the GP, $[M_4Cl_{13}]^-$ speciation is favoured. $[M_4Cl_{13}]^-$ is more stable than $[M_3Cl_{10}]^- + MCl_3$, $[M_2Cl_7]^- + M_2Cl_6$ and $M_3Cl_9 + [MCl_4]^-$ by 30, 25 and 79 kJ mol^{-1} on average, respectively. There is no comparable MS based GP speciation data at $x_{MCl_3} = 0.8$ for any of the three chlorometallate systems.

The continued oligomerisation into $[M_4Cl_{13}]^-$ is less favourable than the oligomerisations into $[M_2Cl_7]^-$ and $[M_3Cl_{10}]^-$ at $x_{MCl_3} = 0.67$ and 0.75, respectively. Speciations which are 25 and 35 kJ mol^{-1} higher in energy are feasibly accessible under normal conditions meaning the dissociations may occur. The lower

energy penalty for the dissociation coincides with the trend that oligomerisation of halometallates becomes progressively less favourable as the x_{MCl_3} increases.

The dissociation into $[M_2Cl_7]^-$ and M_2Cl_6 is competitive with the dissociation into $[M_3Cl_{10}]^-$ and MCl_3, incurring a similar energy penalty. In the chloroaluminate and chloroindate systems the dissociation into $[M_2Cl_7]^-$ and M_2Cl_6 is more favourable than the dissociation into $[M_3Cl_{10}]^-$ and MCl_3. If the relative energy of the different dissociation pathways of the tetrametallic species hold true in the LP the amount of metal dissolved is inherently regulated by precipitating Al_2Cl_6. The relative stability could be indicative of a pathway shown in equation 7.1.1

$$[M_3Cl_{10}]^- + MCl_3 \rightleftharpoons [M_4Cl_{13}]^- \rightarrow [M_2Cl_7]^- + M_2Cl_6 \downarrow \tag{7.1.1}$$

7.1.5 Gas phase chlorometallate speciation summery

In summary, in the GP the results for the all systems shows large discrepancies to the speciation determined through MS. Thus our computational results indicate that MS experiments perturb speciation in all systems. The discrepancies between MS and LP speciation techniques is well documented.[8] Evidence that speciation changes from the LP into the GP during the MS experiment has not been shown for the chloroaluminate and chlorogallate systems but the relative stabilities found here indicate that these systems are also strongly effected by the perturbations occuring during the MS speciation experiments.[7]

Novel branched $[M_4Cl_{13}]^-$ structures were found to be stable. The relative stability of the $[M_3Cl_{10}]^-$ and $[M_4Cl_{13}]^-$ speciations at $x_{MCl_3} = 0.75$ and 0.8 indicate they could form in the GP. $[Ga_3Cl_{10}]^-$ complexes have not be found to be stable by MS investigations for the chlorogallate systems at $x_{GaCl_3} = 0.74$ and investigations at higher x_{MCl_3} have not been carried out in other systems. Consequentially the trimetallic and tetrametallic structures have never been found by MS speciation experiments.

The speciations determined computationally at x_{MCl_3} where MS speciation has been carried out favour oligomerized complexes like $[M_2Cl_7]^-$ at $x_{MCl_3} = 0.67$. In the MS speciation experiments the low abundance of dimetallic complexes at $x_{MCl_3} = 0.67$ indicate that the speciation of oligomerized chlorometallates is disfavoured in the MS experiments. Hence it is likely that trimetallic and tetrametallic species can not be speciated by MS studies as the perturbations the oligomerized chlorometallates experience during ionization result in their fragmentation and consequentially in the inability of MS to correctly determine the speciation of chlorometallates. The discrepancies determined underline the necessity to study chlorometallate speciation

in the phase of interest and be aware of the perturbations to anionic speciation which can occur during MS experiments. The discrpeancies in speciation between MS GP speciation and LP speciation have been accredited to unpredictable perturbation effects as a result of the ionization process.[8] Our results indicate that the perturbations effect the chloroaluminate and chlorogallate systems, which have been said to be unaffected by the perturbations.[7]

7.2 Chlorometallate liquid phase speciation through thermodynamic comparisons from isolated anions

In this subsection the general LP speciation is determined by comparing the Gibbs free energy of the isolated LP structures as outlined in section 3.2.4. The comparisons between different anionic speciations representing the molecular compositions at x_{MCl_3} =0.25, 0.33, 0.5, 0.67, 0.75 and 0.8 are are shown. This section presents the comparison of selected speciations for the sake of clarity. A full set of thermodynamic comparisons of all possible speciations can be found in the appendix, section 9.1.5 in tables 9.58-79.

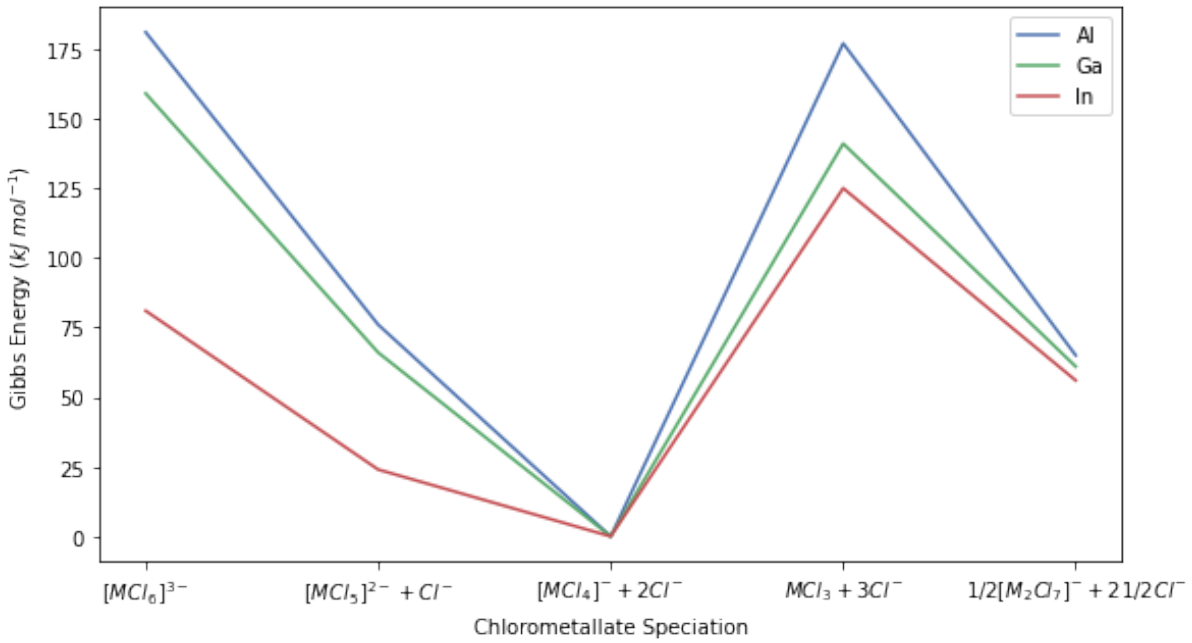
7.2.1 Liquid phase chlorometallate speciation at x_{MCl_3} = 0.25, 0.33 and 0.5

Figure 7.5 shows the relative Gibbs free energy of selected speciations at $x_{MCl_3} = 0.25$ in the LP. The anionic speciation at $x_{MCl_3} = 0.33$ and $x_{MCl_3} = 0.5$ can also evaluated from the relative Gibbs free energy of the anionic speciations presented in figure 7.5 by subtracting one or two free chloride ions, respectively. The comparison to additional speciations can be found in the appendix section 9.1.5 in tables 9.78 and 9.79 but are omitted here due to their larger relative Gibbs free energy.

The trend in the stability of monometallic species in the LP, shown in figure 7.5, is the same for the trend observed in the GP in figure 7.1 at $x_{MCl_3} = 0.25$, 0.33 and 0.5. $[MCl_4]^-$ + $2Cl^-$, $[MCl_4]^-$ + Cl^- and $[MCl_4]^-$ are the most stable states in the LP for all three chlorometallate systems at $x_{MCl_3} = 0.25$, 0.33 and 0.5, respectively.

It requires less energy to form $[MCl_5]^{2-}$ + Cl^- and $[MCl_6]^{3-}$ from $[MCl_4]^-$ + $2Cl^-$ in the LP when compared to the GP in all chlorometallate systems. The highly charged pentacoodinate and hexacoordinate structures are more stabilized in the LP relative to the singly charged tetrahedral species. Thereby the stabilization of 3- and 2- species by the continuum solvation model is stronger than that of the singly charged tetrahedral species.

In the chloroaluminate and chlorogallates systems the relative stability of different speciations are similar. The $[MCl_5]^{2-}$ + Cl^- and $[MCl_6]^{3-}$ speciations are on average 71 and 168 kJ mol^{-1} less stable than the $[MCl_4]^-$ + $2Cl^-$ speciation in the $AlCl_3$-Cl and $GaCl_3$-Cl systems. The formation of $\frac{1}{2}[M_2Cl_7]^-$ +2 $\frac{1}{2}Cl^-$ at x_{MCl_3} = 0.5 requires 62 kJ mol^{-1} in the chloroaluminate and chlorogallate systems. The relative Gibbs free energies computed here show that, under normal conditions, $[MCl_4]^-$ is the only chlorometallate species which will speciate up to x_{MCl_3} = 0.5 in the chloroaluminate and chlorogallate systems in the LP. The stability of each composition at x_{MCl_3} = 0.25, 0.33 and 0.5 concurs with LP speciation stated in literature. LP speciation studies have determined that $[MCl_4]^-$ is the only chlorometallate species that forms up to x_{MCl_3} = 0.5 in the chloroaluminate and chlorogallate systems.[7]



Metal	$[MCl_6]^{3-}$	$[MCl_5]^{2-} + Cl^-$	$[MCl_4]^- + 2Cl^-$	$MCl_3 + 3Cl^-$	$\frac{1}{2}[M_2Cl_7]^- + 2\frac{1}{2}Cl^-$
Al	181	76	0	177	65
Ga	159	66	0	141	61
In	81	24	0	125	56

Figure 7.5: Gibbs free energy differences in kJ mol^{-1} of possible anionic speciations at $x_{MCl_3} = 0.25$ in the liquid phase

Relative to $[InCl_4]^-$ + $2Cl^-$, The $[InCl_6]^{3-}$ and $[InCl_5]^{2-}$ + Cl^- speciations are much more stable compared to the same speciations in the chloroaluminate and chlorogallate systems in the LP. The formation of $[InCl_5]^{2-}$ + Cl^- and $[InCl_6]^{3-}$ require 24 and 81 kJ mol^{-1} of Gibbs free energy in the LP,

respectively. The pentachloroindate and hexachloroindate complexes are likely more stable in the chloroindate system due to the coordination chemistry described in the analysis of the thermodynamics of GP species. The larger coordination sphere of the Indium can accommodate more chloride ligands without incurring significant energy pentalties through steric hindrance.

The hexachloroindate and pentachloroindate are known to be the predominant species present in the LP at $x_{MCl_3} = 0.25$ and 0.33, respectively.[9] The results here indicate that there is a preference for the formation of $[InCl_4]^- + 2Cl^-$ over both $[InCl_5]^{2-} + Cl^-$ and $[InCl_6]^{3-}$.

The discrepancy between known chloroindate speciation at $x_{MCl_3} = 0.25$ and 0.33 between the results here and those stated in literature may occur due to multiple reasons. The implicit solvation model may not account for explicit ion-ion interactions which are necessary to stabilize $[InCl_5]^{2-}$ and $[InCl_6]^{3-}$ leading to erroneous solvation energies of each species. The solvation energy of species with a higher charge may be too small in the SMD solvation model leading to discrepancies in the solvation energies. The discrepancy likely occurs as only two of the six SMD continuum solvation model parameters are changed between systems and species. Ideally all the parameters should be changed to reflect the change in solvation environment according to changes in the anionic speciation which occurs. An analysis of the solvation energies and scans of the dissociation of the hexacoordinate and pentacoordinate indium structures in section 7.4 will be used to evaluate whether the solvation model does not correctly describe the solvation of more highly charged species.

7.2.2 Liquid phase chlorometallate speciation at $x_{MCl_3} = 0.67$

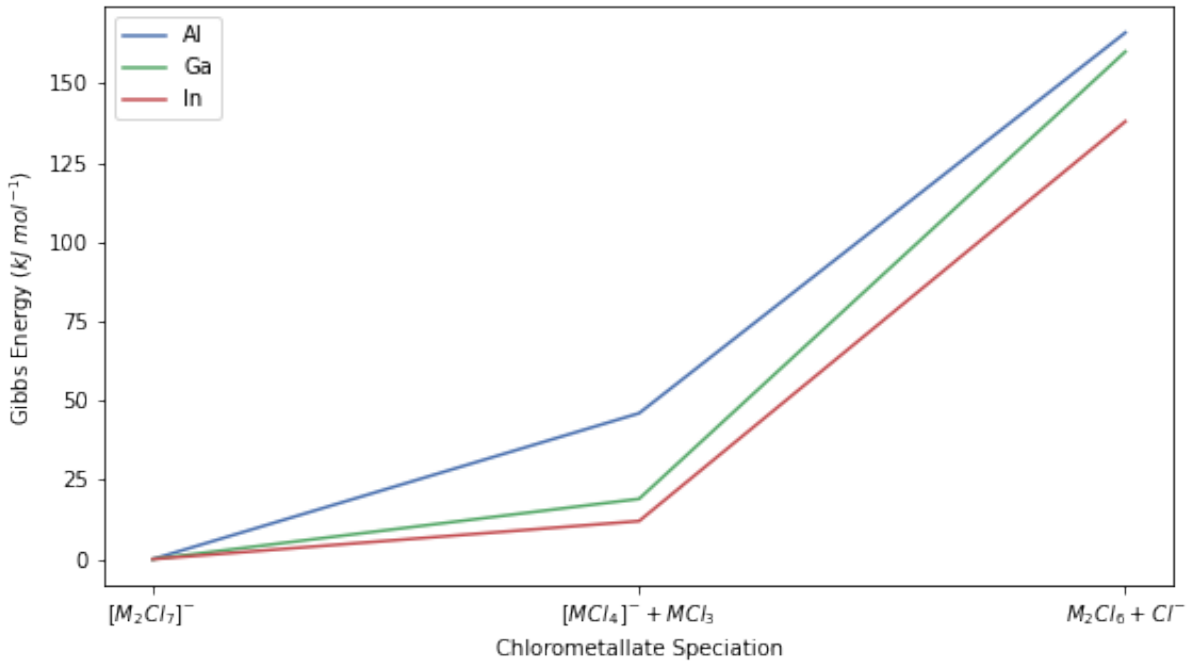
Figure 7.6 shows the relative Gibbs free energy of different speciations of the chlorometallate systems at $x_{MCl_3} = 0.67$. The comparison of the full range of possible speciations can be found in tables 9.73 and 9.74 in the appendix section 9.1.5.

At $x_{MCl_3} = 0.67$ the dimetallic $[M_2Cl_7]^-$ is the most stable state in all three chlorometallate systems in the LP. The split into the constituent M_2Cl_6 and Cl^- is not favoured in any chlorometallate system as the energy required for the dissociation ilies at 153 kJ mol^{-1} on average. The dissociation into $[MCl_4]^- + MCl_3$ is highly disfavoured in the chloroaluminate system at 46 kJ mol^{-1} and slightly disfavoured in the chlorogallate and chloroindate systems at 19 at 12 kJ mol^{-1}, respectively.

The formation of $[M_2Cl_7]^-$ in the chloroaluminate and chlorogallate systems is in agreement with other LP speciation studies. Studies have found that $[Al_2Cl_7]^-$ and $[Ga_2Cl_7]^-$ are the dominant species in the chloroaluminate and chlorogallate systems at $x_{MCl_3} = 0.67$, respectively.[7] $[In_2Cl_7]^-$ as the LP speciation of

the chloroindate system does not agree with previous LP speciation studies. $InCl_3$ is known to precipitate out of the LP to form $[InCl_4]^- + InCl_3 \downarrow$ at $x_{InCl_3} \geq 0.5$.[9]

The relatively low energy of 49 and 21 kJ mol^{-1}, required to dissociated the $[M_2Cl_7]^-$ species indicates a low stability of the oligomerized structure than in the GP. According to the relative stability stated here the chloroaluminate system will less readily dissociate $[Al_2Cl_7]^-$ under normal conditions. In contrast the $[Ga_2Cl_7]^-$ is in equilibrium with $[GaCl_4]^- + GaCl_3$ according to the relative stabilities of the speciations. The results indicate that between $x_{GaCl_3} = 0.5$ and $x_{GaCl_3} = 0.67$ there is an equilibrium.



Metal	$[M_2Cl_7]^-$	$[MCl_4]^- + MCl_3$	$M_2Cl_6 + Cl^-$
Al	0	46	167
Ga	0	19	160
In	0	12	138

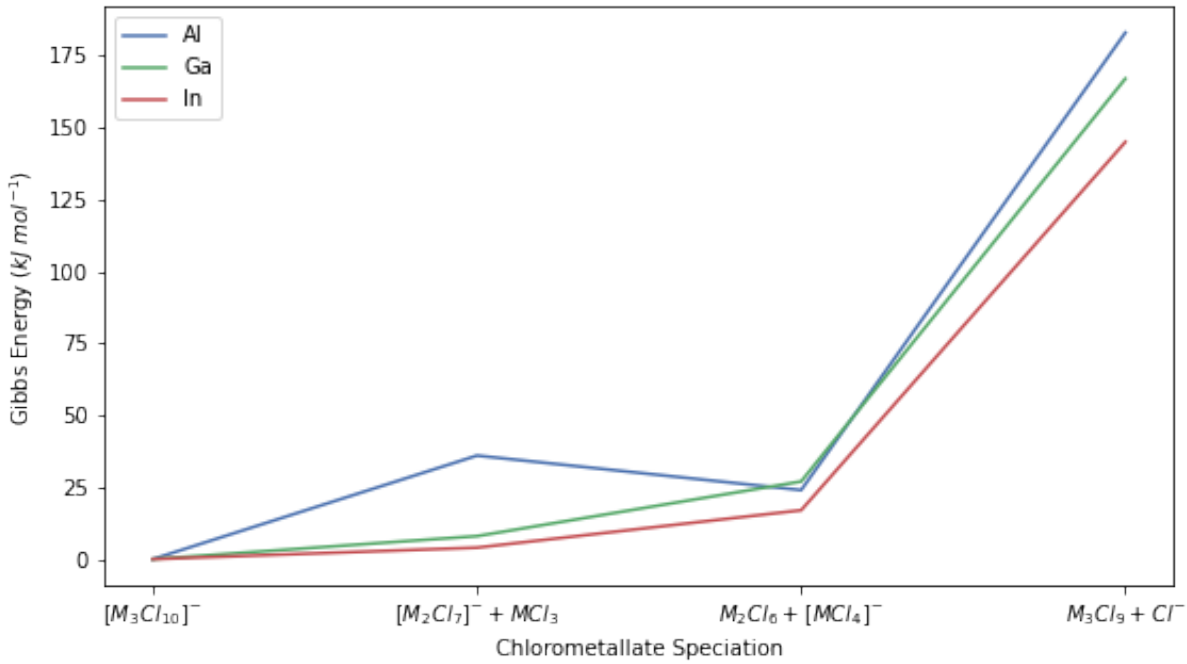
Figure 7.6: Gibbs free energy differences in kJ mol^{-1} of possible anionic speciations at $x_{MCl_3} = 0.67$ in the liquid phase

The x_{MCl_3} is purely controlled by the amount of metal chloride introduced into the system as the precipitation of M_2Cl_6 will not occur based on the relative stability of the dissociation into $M_2Cl_6 + Cl^-$ in the chloroaluminate and the chlorogallate systems in the LP. This coincides with literature studies of the chloroaluminate and chlorogallate systems which have been found to precipitate Al_2Cl_6 and Ga_2Cl_6 at

$x_{AlCl_3} \geq 0.67$ and $x_{GaCl_3} \geq 0.75$.

7.2.3 Liquid phase chlorometallate speciation at $x_{MCl_3} = 0.75$

Figure 7.7 shows the relative Gibbs free energy of selected speciations at $x_{MCl_3} = 0.75$ in the LP. A comparison of the full range of speciations at $x_{MCl_3} = 0.75$ in the LP with respect to Gibbs free energy can be found in tables 9.65 and 9.66 in the appendix, section 9.1.5.



Metal	$[M_3Cl_{10}]^-$	$[M_2Cl_7]^- + MCl_3$	$M_2Cl_6 + [MCl_4]^-$	$M_3Cl_9 + Cl^-$
Al	0	34	24	183
Ga	0	8	27	167
In	0	4	17	145

Figure 7.7: Gibbs free energy differences in kJ mol^{-1} of possible anionic speciations at $x_{MCl_3} = 0.75$ in the liqud phase

$[M_3Cl_{10}]^-$ is the most favourable speciation in the LP in all chlorometallate systems at $x_{MCl_3} = 0.75$. The dissociation into $[M_2Cl_7]^-$ + MCl_3 as well as M_2Cl_6 + $[MCl_4]^-$ is viable according to the relative stability of each combination in all chlorometallate systems. The relative stability of the structures align with the speciation determined for the chloroaluminate and chlorogallate systems in literature while the chloroindate

speciation determined here is divergent from what has been determined.[7,9]

Speciation studies of the chloroaluminate system have shown that the system remains homogeneously liquid until $x_{AlCl_3} = 0.67$, at which point Al_2Cl_6 precipitates out of the LP. Studies have also shown that $[Al_3Cl_{10}]^-$ starts forming at $x_{MCl_3} \geq 0.67$.[7] The relative stability of $[Al_2Cl_7]^-$ + $AlCl_3$ and Al_2Cl_6 + $[AlCl_4]^-$ to $[Al_3Cl_{10}]^-$, found here, are indicative of why the precipitation of Al_2Cl_6 readily occurs at $x_{MCl_3} = 0.67$. Upon the formation of $[Al_3Cl_{10}]^-$ the structure more favourably dissociates into Al_2Cl_6 + $[AlCl_4]^-$ over $[Al_2Cl_7]^-$ + $AlCl_3$ by 11 kJ mol^{-1}. As a consequence of this thermodynamic preference the equilibrium will self regulate the amount of metal chloride dissolved by precipitating excess metal chloride in the form Al_2Cl_6 as defined by the relationship in equation 7.1.2.

$$[Al_2Cl_7]^- + AlCl_3 \rightleftharpoons [Al_3Cl_{10}]^- \rightarrow [AlCl_4]^- + Al_2Cl_6 \downarrow \tag{7.2.1}$$

Speciation studies of chlorogallate systems have shown that the mixtures of chlorogallates remain in the liquid phase up to $x_{GaCl_3} = 0.75$, at which point Ga_2Cl_6 precipitates.[7] The precipitation of Ga_2Cl_6 likely coincides with the formation of $[Ga_4Cl_{13}]^-$ which will be shown in the analysis of relative stability at $x_{GaCl_3} = 0.8$.[7] The Gibbs free energy required to dissociate $[Ga_3Cl_{10}]^-$ into $[Ga_2Cl_7]^-$ + $GaCl_3$ is 19 kJ mol^{-1} lower than the energy required for the dissociation into Ga_2Cl_6 + $[GaCl_4]^-$. The difference in relative stability of different combinations of species between the chloroaluminate and chlorogallate systems give insight into why the precipitation of M_2Cl_6 only occurs at higher x_{MCl_3} in the cholorgallate systems. The findings here coincide with the behavior stated in literature regarding the precipitation at different x_{MCl_3}.

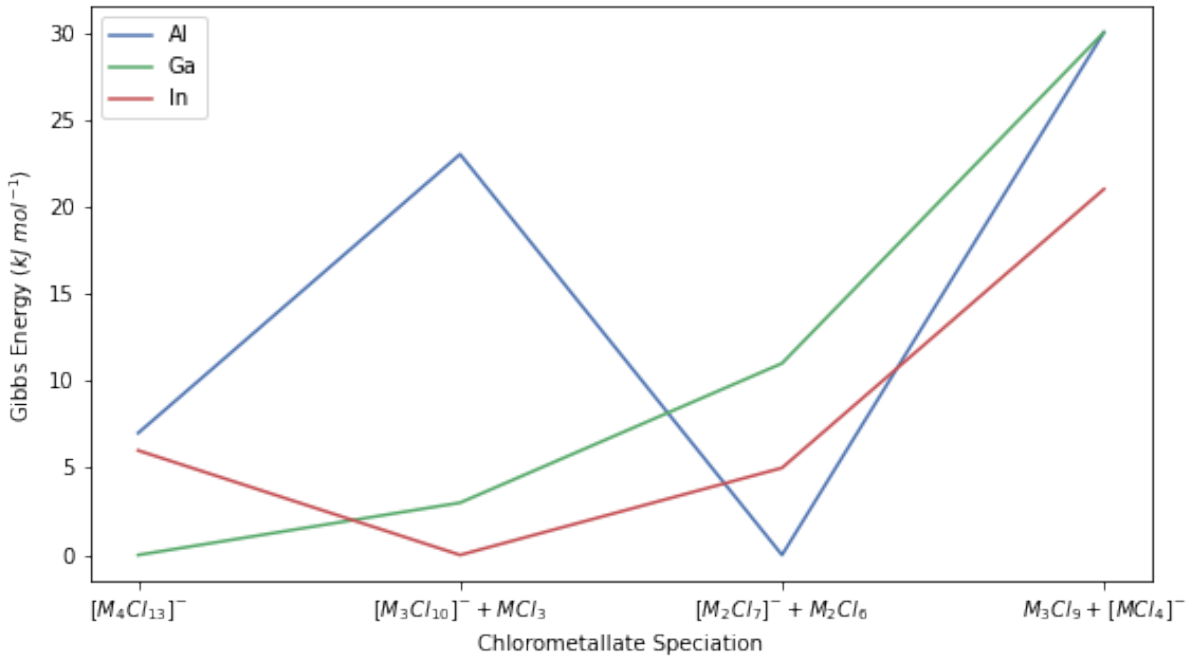
There is a difference between the relative stability of dissociation into $[M_2Cl_7]^-$ + MCl_3 and M_2Cl_6 + $[MCl_4]^-$ between the chloroaluminate and chlorogallate systems. However, the energy required for the dissociation into Ga_2Cl_6 + $[GaCl_4]^-$ should make it thermodynamically accessible. The $[Ga_3Cl_{10}]^-$ configuration is approximately 1400 times more likely than the Ga_2Cl_6 + $[GaCl_4]^-$ configuration when computing a Boltzmann distribution at 298K in the LP so some precipitation should occur upon the formation of $[Ga_3Cl_{10}]^-$, at lower x_{GaCl_3}, according to our results here.

The dissociation into Ga_2Cl_6 + $[GaCl_4]^-$ could be kinetically disfavoured. There could be conformers of the $[Ga_3Cl_{10}]^-$ structure which are more stable than those considered here and the energy required for dissociation into Ga_2Cl_6 + $[GaCl_4]^-$ could become too large to surmount under normal conditions. There could be a stabilizing effect upon explicit interactions with cations which stabilize the dissociation into $[Ga_2Cl_7]^-$ + $GaCl_3$ and/or destabilize the dissociation into Ga_2Cl_6 + $[GaCl_4]^-$ preventing the precipitation of Ga_2Cl_6. Perhaps the precipitation of Ga_2Cl_6 below $x_{GaCl_3} = 0.75$ is so miniscule that it can not be

observed but it may be of interest to see if precipitate forms at the bottom of old chlorogallate ILs which were prepared between $x_{GaCl_3} = 0.67$ and 0.75 to evaluate the hypothesis.

7.2.4 Liquid phase chlorometallate speciation at $x_{MCl_3} = 0.8$

Figure 7.8 shows the comparison of anionic speciations at $x_{MCl_3} = 0.8$ in the LP with respect to Gibbs free energy. The comparisons of the relative stabilities of the remaining speciations can be found in tables 9.58-60 in appendix section 9.1.5.



Metal	$[M_4Cl_{13}]^-$	$[M_3Cl_{10}]^- + MCl_3$	$[M_2Cl_7]^- + M_2Cl_6$	$M_3Cl_9 + [MCl_4]^-$
Al	7	23	0	30
Ga	0	3	11	30
In	6	0	5	21

Figure 7.8: Gibbs free energy differences in kJ mol^{-1} of possible anionic speciations at $x_{MCl_3} = 0.8$ in the liquid phase

There are differences in the anionic speciation in the LP between all chlorometallate systems at $x_{MCl_3} = 0.8$. $[Al_2Cl_7]^- + Al_2Cl_6$ is the preferred speciation in the chloroaluminate system. The $[Ga_4Cl_{13}]^-$ species is more stable than $[Ga_2Cl_7]^- + Ga_2Cl_6$ in the chlorogallate system in the LP. The dissociation into $[In_3Cl_{10}]^- + InCl_3$ is favoured in the chloroindate system. The dissociation into $M_3Cl_9 + [MCl_4]^-$ is least favoured in

all systems but could occur in the LP. $[M_4Cl_{13}]^-$ complexes are known to form in both the chloroaluminate and chlorogallate systems at $x_{MCl_3} > 0.75$.

The relative stability determined here suggests that the $[M_4Cl_{13}]^-$ structures are accessible but are susceptible to dissociation leading to the accelerated precipitation of M_2Cl_6 in all three both systems. In the chloroaluminate system the lowest energy $[Al_4Cl_{13}]^-$ structure is favoured to form from the constituent $[Al_3Cl_{10}]^-$ and $AlCl_3$. However, the dissociation from the $[Al_4Cl_{13}]^-$ into $[Al_2Cl_7]^-$ + Al_2Cl_6 is favoured by 7 kJ mol^{-1}. Consequentially the relative stability indicated that $[Al_4Cl_{13}]^-$ functions as an intermediate between $[Al_3Cl_{10}]^-$ + $AlCl_3$ and $[Al_2Cl_7]^-$ + Al_2Cl_6 as follows:

$$[Al_3Cl_{10}]^- + AlCl_3 \rightleftharpoons [Al_4Cl_{13}]^- \rightarrow [Al_2Cl_7]^- + M_2Cl_6 \downarrow \tag{7.2.2}$$

In the chlorogallate system the most stable $[Ga_4Cl_{13}]^-$ conformer is more stable than $[Ga_3Cl_{10}]^-$ + $GaCl_3$. The tetrametallic chlorogallate structure is likely going to form in reasonable amounts before dissociating into either $[Ga_3Cl_{10}]^-$ + $GaCl_3$ or $[Ga_2Cl_7]^-$ + Ga_2Cl_6. The precipitation of Ga_2Cl_6 is not readily facilitated as in the chlorogallate system as the dissociation into $[Ga_3Cl_{10}]^-$ + $GaCl_3$ is more favourable than the dissociation into $[Ga_2Cl_7]^-$ + Ga_2Cl_6

The relative stability of the chloroaluminate and chlorogallate structures at $x_{MCl_3} = 0.8$ correlates with literature. However, the magnitude of instability of the $[M_4Cl_{13}]^-$ structures in both systems is too large. Likely the lowest energy $[M_4Cl_{13}]^-$ isomers/conformers have not been identified and this will be evaluated in the scan section. The formation of $[In_4Cl_{13}]^-$ is possible according to the relative stabilities of the structures so there must be additional factors which prevent the multimetallic chloroindate complexes from speciating.

7.3 Speciation evaluation from isolated anions summary

Different speciations at $x_{MCl_3} = 0.25$, 0.33, 0.5, 0.67, 0.75 and 0.8 have been evaluated in the GP and LP for each chlorometallate system with respect to the Gibbs free energy. Tables 7.1 and 7.2 summarize the predominant speciation in the GP according to the comparisons carried out. Tables 7.3 and 7.4 summarize the predominant speciation in the LP according to the comparisons carried out here. The tables and discussions have been split into $x_{MCl_3} = 0.25$, 0.33 and 0.5 and $x_{MCl_3} = 0.67$, 0.75 and 0.8 as the the systems become more complex at higher x_{MCl_3}.

Table 7.1 summerizes the predominant species for all chlorometallate systems in the GP at $x_{MCl_3} \leq 0.5$.

The predominant species determined for all chlorometallate systems in the GP at $x_{MCl_3} \leq 0.5$ is always $[MCl_4]^-$. For the chloroaluminate and chlorogallate systems the $[MCl_4]^-$ being the predominant chlorometallate speciation is in alignment with MS studies reflecting GP speciation.[4] There are no published MS studies of the chloroindate systems and an adequate comparison could not be made.

Table 7.1: Dominant specation in the gas phase speciation in the group 13 chlorometallate ionic liquids with at $x_{MCl_3} = 0.25$, 0.33 and 0.5

0.25	0.33	0.5
$[AlCl_4]^- + 2Cl^-$	$[AlCl_4]^- + Cl^-$	$[AlCl_4]^-$
$[GaCl_4]^- + 2Cl^-$	$[GaCl_4]^- + Cl^-$	$[GaCl_4]^-$
$[InCl_4]^- + 2Cl^-$	$[InCl_4]^- + Cl^-$	$[InCl_4]^-$

Table 7.2 summarizes the predominant species for all chlorometallate systems in the GP at $x_{MCl_3} > 0.5$. The predominant species determined via the Gibbs free energy of each structure at different x_{MCl_3} in every chlorometallate system in the GP is always the anion reflecting the ratio of chlorides to metals. $[M_2Cl_7]^-$, $[M_3Cl_{10}]^-$ and $[M_4Cl_{13}]^-$ are the predominant species in each system at $x_{MCl_3} = 0.67$, 0.75 and 0.8, respectively. The chloroaluminate system also forms Al_2Cl_6 at $x_{AlCl_3} = 0.8$

Table 7.2: Dominant specation in the gas phase speciation in the group 13 chlorometallate ionic liquids with at $x_{MCl_3} = 0.67$, 0.75 and 0.8

0.667	0.75	0.8
$[Al_2Cl_7]^-$	$[Al_3Cl_{10}]^-$	$[Al_4Cl_{13}]^-$, Al_2Cl_6
$[Ga_2Cl_7]^-$	$[Ga_3Cl_{10}]^-$	$[Ga_4Cl_{13}]^-$
$[In_2Cl_7]^-$	$[In_3Cl_{10}]^-$	$[In_4Cl_{13}]^-$

For the chloroaluminate and chlorogallate systems the GP speciation determined via MS does not reflect the GP speciation determined through the relative Gibbs free energies at $x_{MCl_3} = 0.67$ or 0.75. No MS studies were carried out at $x_{MCl_3} = 0.8$ for either system so no comparison could be made. At $x_{MCl_3} = 0.67$ or 0.75 in both systems, MS studies found $[MCl_4]^-$ to be the predominant species and $[Ga_3Cl_{10}]^-$ could not be identified at $x_{GaCl_3} = 0.74$. The relatively low amount of $[M_2Cl_7]^-$ found in the GP by MS also contradict the relative stability of structures found here. The perturbations which effect the speciation of HMILs which have been determined for other MS studies evaluating speciation likely effect the chloroaluminate and

chlorogallate systems as well.

In the chloroindate system the relative stability of $[In_2Cl_7]^-$ at $x_{InCl_3} = 0.67$ is in alignment with the unpublished results of MS studies of the chloroindate system.[7] However, the amount of $[In_2Cl_7]^-$ which has been determined remains unclear. Furthermore, the multimetallic $[In_3Cl_{10}]^-$ and $[In_4Cl_{13}]^-$ have not been identified in the GP. It should be determined whether $[In_3Cl_{10}]^-$ and $[In_4Cl_{13}]^-$ form in the GP when x_{MCl_3} is high enough. If $[In_3Cl_{10}]^-$ and $[In_4Cl_{13}]^-$ form as predicted the perturbations from the LP to the GP should be identified. The trimetallic and tetrametallic chloroindate complexes will likely not form due to fragmentation which has been observed in the chloroaluminate and chlorogallate systems.

The predominant speciation for all chlorometallate systems in the LP at $x_{MCl_3} \leq 0.5$ are summerized in table 7.3. The predominant species determined for all chlorometallate systems in the LP is analogous to the GP speciations at $x_{MCl_3} \leq 0.5$. $[MCl_4]^-$ is the preferred speciation in the LP for All systems at $x_{MCl_3} =$ 0.25, 0.33 and 0.5.

Table 7.3: Dominant specation in the liquid phase speciation in the group 13 chlorometallate ionic liquids with at $x_{MCl_3} = 0.25$, 0.33 and 0.5

0.25	0.33	0.5
$[AlCl_4]^- + 2Cl^-$	$[AlCl_4]^- + Cl^-$	$[AlCl_4]^-$
$[GaCl_4]^- + 2Cl^-$	$[GaCl_4]^- + Cl^-$	$[GaCl_4]^-$
$[InCl_4]^- + 2Cl^-$	$[InCl_4]^- + Cl^-$	$[InCl_4]^-$

Speciation studies of the LP at $x_{MCl_3} \leq 0.5$ in the chloroaluminate and chlorogallate systems agree with $[MCl_4]^-$ being the only chlorometallate species which forms.[7] The speciation predicted for the chloroindate systems here is in contrast with the speciation determined by other speciation studies. $[InCl_5]^{2-}$ and $[InCl_6]^{3-}$ are known to be the predominant speciation at $x_{InCl_3} = 0.33$ and 0.25, respectively.[9]

The predominant species for all chlorometallate systems in the LP at $x_{MCl_3} = 0.67$, 0.75 and 0.8 are shown in table 7.4. $[Al_2Cl_7]^-$ and $[Al_3Cl_{10}]^-$ are the predominant species in the chloroaluminate system at x_{AlCl_3} = 0.67 and 0.75 respectively. The $[Al_4Cl_{13}]^-$ species forms at $x_{AlCl_3} = 0.8$ but dissociates into $[Al_2Cl_7]^-$ and the Al_2Cl_6 precipitate. The chloroaluminate system also forms Al_2Cl_6 at $x_{AlCl_3} = 0.75$ but the dissociation shown in eq. 7.2.2 and 7.2.3 leading to precipitation is less favoured at $x_{AlCl_3} = 0.75$ while it is favourable $x_{AlCl_3} = 0.8$. The relative stability of the different combinations of structures at each $x_{ACl_3} > 0.5$ determined here coincide with the speciation stated in literature.

Table 7.4: Dominant specation in the liquid phase speciation in the group 13 chlorometallate ionic liquids with at x_{MCl_3} = 0.67, 0.75 and 0.8

0.67	0.75	0.8
$[Al_2Cl_7]^-$	$[Al_3Cl_{10}]^-$, $Al_2Cl_6 \downarrow$	$[Al_3Cl_{10}]^-$, $Al_2Cl_6 \downarrow$
$[Ga_2Cl_7]^-$	$[Ga_3Cl_{10}]^-$, $Ga_2Cl_6 \downarrow$	$[Ga_4Cl_{13}]^-$, $Ga_2Cl_6 \downarrow$
$[In_2Cl_7]^-$	$[In_3Cl_{10}]^-$, $InCl_3 \downarrow$	$[In_3Cl_{10}]^-$, $InCl_3 \downarrow$

The most stable species in the chlorogallate system are $[Ga_2Cl_7]^-$, $[Ga_3Cl_{10}]^-$, $[Ga_4Cl_{13}]^-$ at x_{GaCl_3} = 0.67, 0.75 and 0.8, respectively. Ga_2Cl_6 precipitates at 0.75 and 0.8 but is unfavourable at both x_{GaCl_3}. The relative stability of the different combinations of structures at each x_{GaCl_3} = 0.67, 0.75 and 0.8 determined here coincide with the speciation stated in literature. The precipitation of Ga_2Cl_6 at higher x_{GaCl_3} agrees with the literature.

The speciation determined for the chloroindate system in the LP does not agree with other LP speciation studies. According to the relative stability of the speciations at x_{InCl_3} = 0.67, 0.75 and 0.8 determined here, oligomeric chloroindate complexes should form. $[In_2Cl_7]^-$, $[In_3Cl_{10}]^-$, $[In_4Cl_{13}]^-$ should be possible speciations at x_{InCl_3} = 0.67, 0.75 and 0.8 in the LP, respectively. There must factors outside of the stability of the isolated anions which prevent the oligomerization of the multimetallic indium complexes. Either there is a critical error in previous experimental speciation of the chloroindate system or the solvation of the chloroindate complexes is missing a critical variable. Potentially the parameterization of the SMD model or the inability of the model to account for stabilizing explicit interactions may be the issue.

Additionally to the speciation determined, two novelties were found in both the chloroaluminate and chlorogallate systems in both the LP and all systems in the GP. The branched $[M_4Cl_{13}]^-$ structures which occurs when $x_{MCl_3} > 0.75$ have not previously been identified and are accessible according to the relative stability. Two and three of stable conformers of the linear $[M_3Cl_{10}]^-$ were found in the GP and LP, respectively. The linear $[M_4Cl_{13}]^-$ anions can likely also assume different conformations which have not been determined yet. The high degree of flexibility of these structures indicates that there are further degrees of freedom leading to the lowest energy states in the chloroaluminate and chlorogallate systems at high x_{MCl_3}. The chloroaluminate and chlorogallate systems at $x_{MCl_3} \geq 0.67$ are known to have complex equilibria featuring various species and the flexibility of the individual structures adds another dimension of complexity to the system which has to be evaluated.

The issue with the speciation in the chloroindate system is most likely a consequence of the

over-generalization of the parameterization of the solvation environment. Alternatively, the solvation environment can not describe explicit anion-anion or cation-anion interactions which stabilize the $[InCl_6]^{3-}$ and $[InCl_5]^{2-}$ structures. Both issues will be addressed. The discrepancies between the LP speciation of the chloroindate system determined here and the LP speciation determined through other studies will be addressed by evaluating the solvation energies and dissociation scans of the indium complexes. Additionally, the speciation will be reevaluated based on optimized IP structures to deterine whether explicit interactions play a key role in the stablization of the pentacoodinate and hexacoodinate complexes.

The discrepancies of the chlorogallate system will be addressed analogously by evaluating the relative stability of $[Ga_3Cl_{10}]^-$ and $[Ga_4Cl_{13}]^-$ when the structures are interacting with a counter ion. All stable IP conformers featuring the $[Ga_3Cl_{10}]^-$ and $[Ga_4Cl_{13}]^-$ isomers will be determined in the GP and LP to determine if the speciation determined in these sections holds true.

7.3.1 Monometallic chlorometallate system speciation discrepancies

The magnitude of error generated by the SMD model for highly charged species was determined by scanning the dissociation of $[MCl_4]^-$ into MCl_3 + Cl^- $[InCl_5]^{2-}$ into $[InCl_4]^-$ + Cl^- and $[InCl_6]^{3-}$ into $[InCl_5]^{2-}$ + Cl^-. The scan coordinates used are distances between 1 of the Cl^- and the metal center as illustrated in figure 7.9. All dissociation scans were carried out in the LP where the discrepancies in chloroindate speciation were observed.

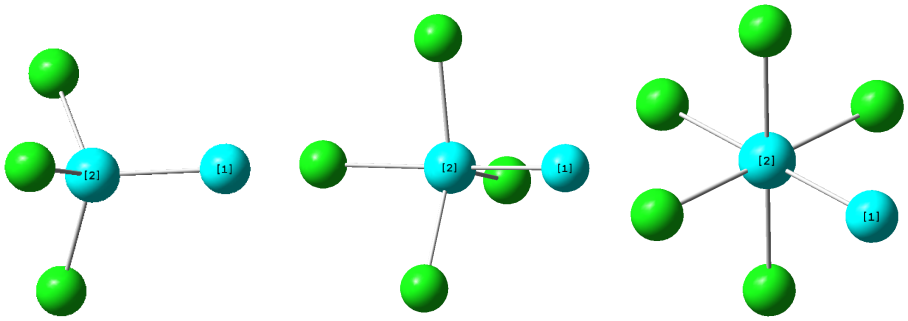


Figure 7.9: $[MCl_4]^-$, $[InCl_5]^{2-}$ and $[InCl_6]^{3-}$ dissociation scan coordinates - M(2)-Cl(1) distance where M=Al, Ga or In

The scans of the dissociation of $[AlCl_4]^-$ $[GaCl_4]^-$ $[InCl_4]^-$, $[InCl_5]^{2-}$ and $[InCl_6]^{3-}$ anions give outputs in SCF energy with respect to the metal chloride distance. The full scans can be found in the appendix section 9.1.7. As the BDEs computed from scans are SCF energies and the BDE computed from the isolated

species is in Gibbs free energy they could not be compared. Table 7.5 summerizes the Gibbs free energy and SCF energy of dissociation of the isolated ions as well as the SCF energy of dissociaiton from the scans. Additionally, table 7.5 includes the difference between the SCF BDE computed from the isolated species and the scans.

Table 7.5: Monometallic species dissociation $\Delta G_{dissociation}$, $\Delta SCF_{dissociation}$, $\Delta SCF^{Scan}_{dissociation}$ and difference between the two computed SCF energies in kJ mol^{-1}

Reaction	ΔG	ΔSCF	ΔSCF_{scan}	$\delta SCF^{isolated}_{scan}$
$[AlCl_4]^- \rightarrow AlCl_3 + Cl^-$	177	212	200	-12
$[GaCl_4]^- \rightarrow GaCl_3 + Cl^-$	141	176	175	-1
$[InCl_4]^- \rightarrow InCl_3 + Cl^-$	125	160	157	3
$[InCl_5]^{2-} \rightarrow [InCl_4]^- + Cl^-$	-25	10	27	17
$[InCl_6]^{3-} \rightarrow [InCl_5]^{2-} + Cl^-$	-53	-19	10	29

In the dissociation scans the remaining structure reconfigured. During the dissociation of $[MCl_4]^-$, the remaining MCl_3 structure reconfigured into a trigonal planar structure as the chloride moved further away. As the $[InCl_5]^{2-}$ dissociated into $[InCl_4]^- + Cl^-$, the remaining $[InCl_4]^-$ reconfigured into a tetrahedral structure. The dissociation of $[InCl_6]^{3-}$ into $[InCl_5]^{2-} + Cl^-$ resulting in the remaining chloroindate species being a trigonal bipyramidal structure.

The SCF-BDEs of the $[MCl_4]^-$ species computed from the isolated species agree with the SCF-BDEs from the scans but there is a minor discrepancy for the dissociation of $[AlCl_4]^-$. The $[AlCl_4]^-$ BDE, is larger in the isolated calculation versus the scans. The scan of the $[AlCl_4]^-$ terminated early and could not be completed before the dissociated structures could stabilize leading to the discrepancy. Hence the the results for the $[AlCl_4]^-$ may not be absolutely reliable.

The SCF-BDEs from the scans indicate that the dissociation of $[InCl_5]^{2-}$ and $[InCl_6]^{3-}$ is not correct when computed from the isolated species. The discrepancies in the SCF-BDE become more significant relative to the charge of the species. The larger discrepancies relative to charge indicate that the more highly charged species with will have a greater error when being treated by the SMD model.

The source of the error is most likely the result of how the SMD solvation model functions or using imperfect input parameters for the SMD model. The implicit solvation environment does not change sufficiently as the speciation changes and hence over-stabilizes lower charged dissociated species over the more highly charged ones. Alternatively, the system over-stabilizes the lower charged species because the electrostatic component

of the implicit solvation model interacts with the anions based on a the solvent accessible surface area which stays constant regardless of charge. Reduced species have a more electrons which in turn enlarge the ionic radius of the constituent atoms. The surface accessible area which is being treated by the model does not account for the enlargement of the ionic radius of the constituent atoms which could lead to discrepancies. Lastly the error could lie within the DFT method itself which is not ideal for determining the thermodynamics of homolytic dissociation due to it being a single reference method.

The determined LP speciation of the chloroindate system is partially corrected by the results from the scans. The discrepancies show that if the SMD model would describe the solvation of different species accurately the determined speciation would coincide with the literature speciation. The system at $x_{InCl_3} = 0.25$, 0.33 and 0.5 can only be correctly described by including three, two or one counter ion(s), respectively. The counter ions will balance out the charge and in turn provide additional stability to the $[InCl_5]^{2-}$ and $[InCl_6]^{3-}$ complexes. The explicit solvation of the complexes should further stabilize the more highly charged anions by directly interacting with them. The chloroindate speciation determined by other studies will likely agree with the computational speciation when the system is modeled more holistically. The evaluation shows the necessity of modeling these systems with one or more counter ions present.

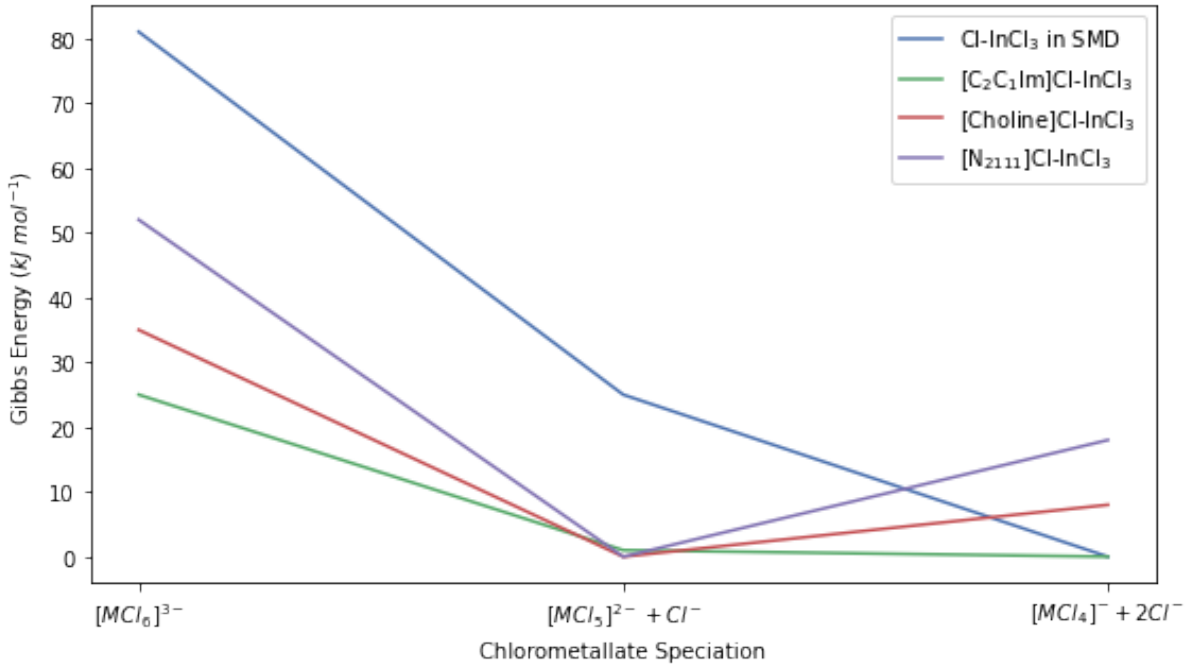
7.4 Chlorometallate liquid phase speciation through thermodynamic comparisons of ion pair structures

The discrepancy observed in the speciation of the chloroindate system within the LP, compared to experimental studies, strongly suggests that explicit solvation of chloroindate complexes via the cations is required to stabilize the more highly charged anions. Addressing the chloroindate discrepancy requires reevaluating speciation based on optimized IP structures to discern the role of explicit interactions in stabilizing complexes. Similarly, discrepancies in the chlorogallate system will be resolved by assessing the relative stability of IP structures.

Additionally, the evaluation of the of the speciation with respect to the changing the cation is evaluated and discussed to determine the effect of cations on the speciation. Consequently an additional evaluation of the speciation by explicitly solvating the anions with $[C_2C_1Im]^+$, $[Choline]^+$, and $[N_{2111}]^+$ is shown in this section. This expanded analysis aims to account for potential variations in solvation environments and their impact on speciation outcomes. By explicitly incorporating the cations into the evaluation process the relative stability of the IP structures should provide a deeper understanding of the cations effect on speciation.

Only the pertinent speciations at the different x_{MCl_3} are shown as comparisons between structures which are in ion pairs compared to those would likely increase the delta between structures in IPs vs those which are isolated. At x_{MCl_3} = 0.25, 0.33 and 0.5 only the chloroindate speciations are are compared while at x_{MCl_3} = 0.67, 0.75 and 0.8 only chloroaluminate and chlorogallate speciations are discussed.

7.4.1 Liquid phase chloroindate speciation at x_{MCl_3} = 0.25, 0.33 and 0.5 with explicit solvations



System	$[InCl_6]^{3-}$	$[InCl_5]^{2-} + Cl^-$	$[InCl_4]^- + 2Cl^-$	$InCl_3 + 3Cl^-$	$\frac{1}{2}[M_2Cl_7]^- + 2\frac{1}{2}Cl^-$
$Cl - InCl_{3 implicit SMD}$	81	25	0	125	56
$[C_2C_1Im]Cl - InCl_3$	25	1	0	122	54
$[Choline]Cl - InCl_3$	35	0	8	119	51
$[N_{2111}]Cl - InCl_3$	52	0	18	116	48

Figure 7.10: Gibbs free energy differences in kJ mol^{-1} of possible anionic speciations at $x_{InCl_3} = 0.25$ in the liquid phase

The Gibbs free energy of the IP underscore the significance of explicit solvation in addressing the initial discrepancies in the chloroindate system. The addition of one counter ion, even in cases where there would usually be two or three shows a clear effect on the stabilization of the more highly charged $[InCl_6]^{3-}$ and

$[InCl_5]^{2-}$ compared to $[InCl_4]^-$. This underscores the pivotal role of evaluating speciation with explicit solvation. By elucidating how the addition of a single counter ion can significantly enhance the stability of more highly charged complexes, these results underscore the importance of considering solvation effects in understanding speciation accurately.

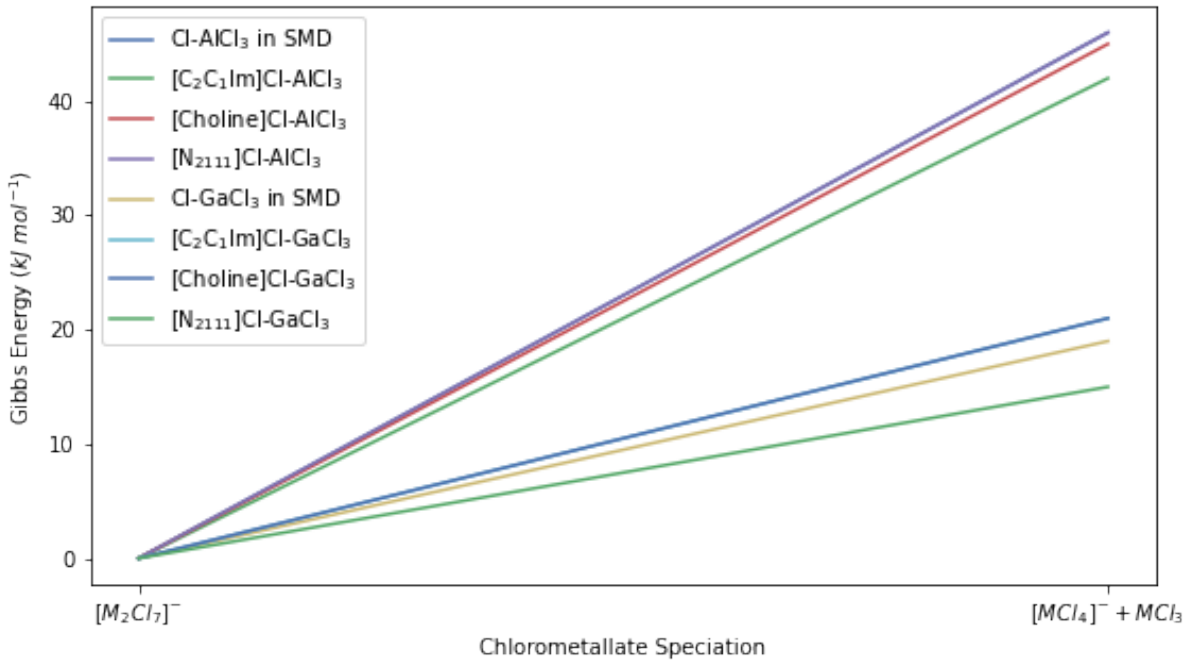
The $[N_{2111}]^+$ cation stabilizes the $[InCl_5]^{2-}$ anion the most followed by the $[Choline]^+$ and the least stabilization is exhibited by $[C_2C_1Im]^+$. curiously this trend is reversed in the stabilization of the $[InCl_6]^{3-}$ anion where the $[C_2C_1Im]^+$ cation is most stabilizing and the $[N_{2111}]^+$ is least stabilizing. The results indicate that $[InCl_6]^{3-}$ more stabilized by cations with the possibility for H-Bonding while the $[InCl_5]^{2-}$ species is more stabilized the overall interaction with the multitude of hydrogen atoms.

Overall the results are conclusive about the requirements over explicit solvation in evaluating the speciation of the chloroindate system, particularly in circumstances when more highly charged complexes are present. to ideally determine the speciation the same computations should be carried out with two and three counter ions to ascertain the exact speciation at every x_{InCl_3}. However the stability of the multimetallic chloroindate complexes is still not adressed by this evaluation.

7.4.2 Liquid phase chloroaluminate and chlorogallate speciation at $x_{MCl_3} = 0.67$ with explicit solvations

The assessment of the speciation of the chloroaluminate and chlorogllate systems at $x_{MCl_3} = 0.67$ reveals that the implicit solvation environment effectively models the chloroaluminate and chlorogallate systems at these amounts of metal halide introduced capturing their behavior with reasonable accuracy. This is evidenced by the consistency of the trends of the thermodynamic stability of the $[M_2Cl_7]^-$ speciation compared to the $[MCl_4]^-$ + MCl_3 speciation as described from the isolated anions and the IPs. The differences in all systems between the specition determined through the isolated anions an the IPs is 4 kJ mol^{-1} in the chloroaluminate system and 6 kJ mol^{-1} in the chlorogallate system. This indicates that the stabilizing effects of the IP interactions are equivalent for the $[MCl_4]^-$ and $[M_2Cl_7]^-$ species.

The findings suggest that the overall speciation determined from the isolated anions hold true even without explicitly solvating the singly charged anions. These results indicate that while explicit solvation may introduce refinements, particularly in more complex scenarios or under different conditions but its significance in determining speciation at $x_{MCl_3} = 0.67$ is comparatively less pronounced. Hence, the implicit solvation model appears sufficient for capturing the essential speciation dynamics in the chloroaluminate and chlorogallate systems at $x_{MCl_3} = 0.67$.



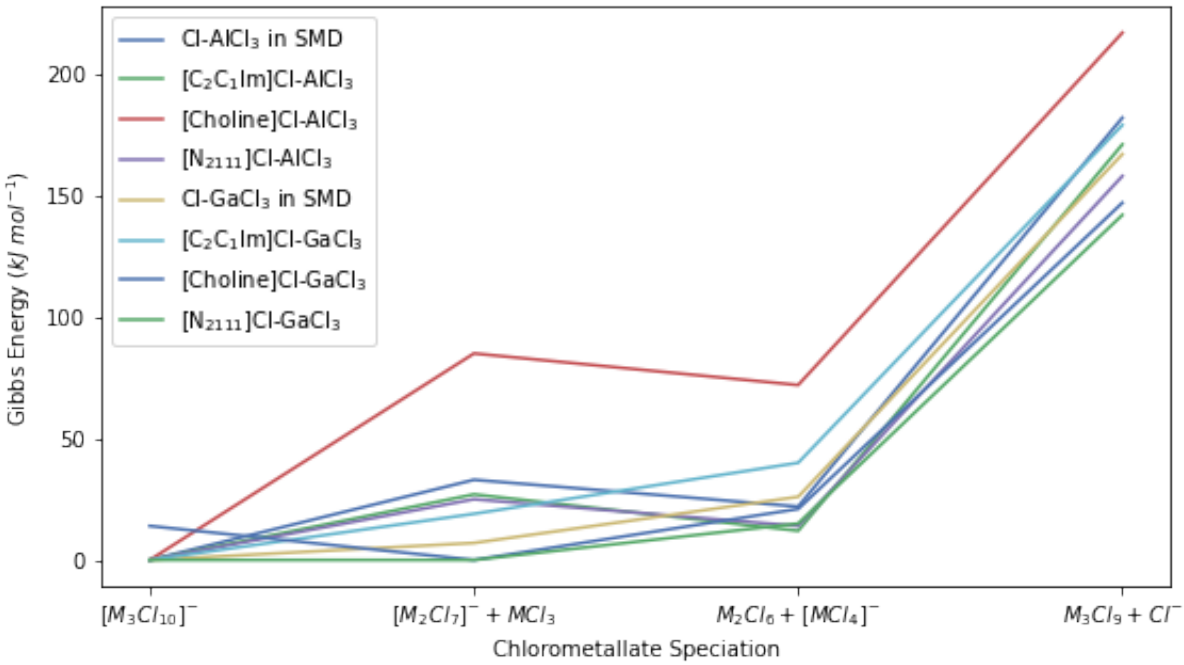
System	$[M_2Cl_7]^-$	$[MCl_4]^- + MCl_3$
$Cl - AlCl_{3implicitSMD}$	0	46
$[C_2C_1Im]Cl - AlCl_3$	0	42
$[Choline]Cl - AlCl_3$	0	45
$[N_{2111}]Cl - AlCl_3$	0	46
$Cl - GaCl_{3implicitSMD}$	0	19
$[C_2C_1Im]Cl - GaCl_3$	0	21
$[Choline]Cl - GaCl_3$	0	21
$[N_{2111}]Cl - GaCl_3$	0	15

Figure 7.11: Gibbs free energy differences in kJ mol^{-1} of possible anionic speciations at x_{AlCl_3} and x$_{GaCl_3}$ = 0.67 in the liquid phase

7.4.3 Liquid phase chloroaluminate and chlorogallate speciation at x$_{MCl_3}$ = 0.75 with explicit solvations

Similarly, the evaluation of speciation at x$MCl3 = 0.75$ suggests that the implicit solvation model continues to effectively characterize the behavior of the chloroaluminate systems. This is evident from the consistency observed in the thermodynamic stability trends of the $[Al_3Cl_{10}]^-$ species compared to the $[Al_2Cl_7]^-$ + $AlCl_3$ and Al_2Cl_6 + $[AlCl_4]^-$ speciations, as described from both isolated anions and IPs. The only significant

outlier is the system featuring the choline cation which stabilizes the $[Al_3Cl_{10}]^-$ anion more than any other cation or the implicit solvation by approximatly 60 kJ mol^{-1}.



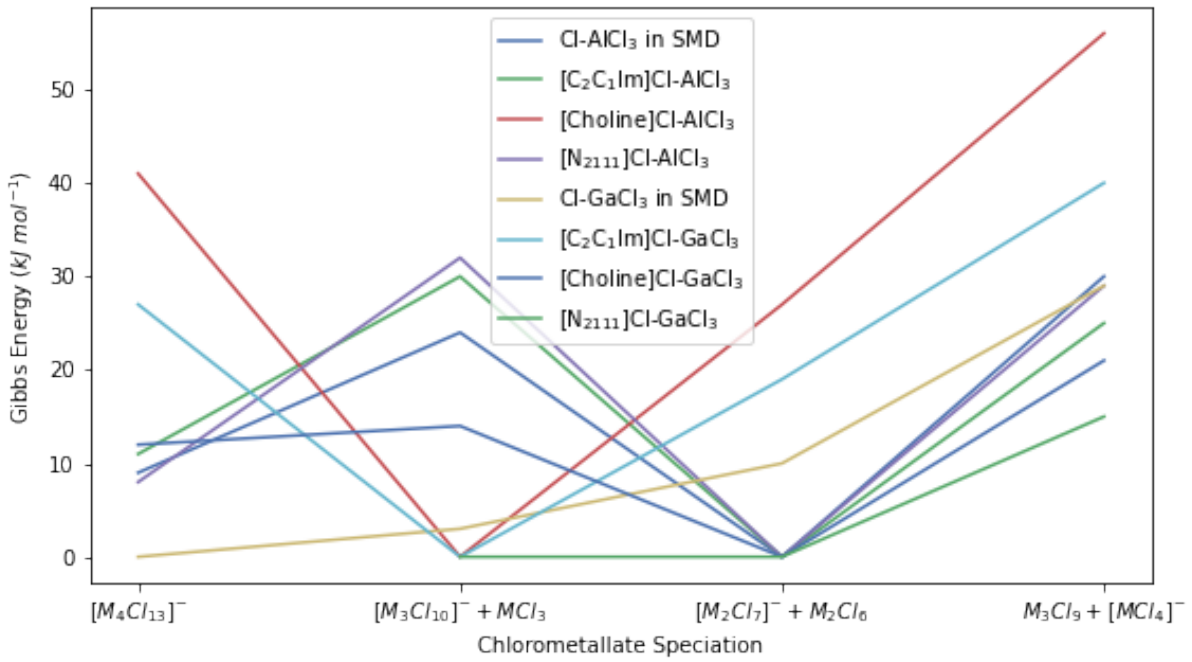
System	$[M_3Cl_{10}]^-$	$[M_2Cl_7]^- + MCl_3$	$M_2Cl_6 + [MCl_4]^-$	$M_3Cl_9 + Cl^-$
$Cl - AlCl_{3implicitSMD}$	0	33	22	182
$[C_2C_1Im]Cl - AlCl_3$	0	27	12	171
$[Choline]Cl - AlCl_3$	0	85	72	217
$[N_{2111}]Cl - AlCl_3$	0	25	14	158
$Cl - GaCl_{3implicitSMD}$	0	7	26	167
$[C_2C_1Im]Cl - GaCl_3$	0	19	40	179
$[Choline]Cl - GaCl_3$	14	0	21	147
$[N_{2111}]Cl - GaCl_3$	0	0	15	142

Figure 7.12: Gibbs free energy differences in kJ mol^{-1} of possible anionic speciations at x_{AlCl_3} and x_{GaCl_3} = 0.75 in the liquid phase

The results from the thermodynamic comparisons of the chlorogallate system indicate that the trends described by the implicit solvation model are slighly strengthend through the explicit solvation with of the $[C_2C_1Im]^+$ cation. However for the ammonium based cations the trends in stability are impacted. In the choline system the $[Ga_2Cl_7]^-$ + $GaCl_3$ speciation is 14 kJ mol^{-1} more stable than the $[Ga_3Cl_{10}]^-$ speciation. In the $[N_{2111}]^+$ cation the $[Ga_3Cl_{10}]^-$ and $[Ga_2Cl_7]^-$ + $GaCl_3$ speciations are equal in energy.

The results indicate that the aromatic ring or another feature of the imidazolium cation is particularly stabilizing for the $[Ga_3Cl_{10}]^-$ complex. The lack of stability of the $[Ga_3Cl_{10}]^-$ speciation in the $[Choline]^+$ and $[N_{2111}]^+$ cations at $x_{GaCl_3} = 0.75$ are curious and should be experimentally explored.

7.4.4 Liquid phase chloroaluminate and chlorogallate speciation at $x_{MCl_3} = 0.8$ with explicit solvations



System	$[M_4Cl_{13}]^-$	$[M_3Cl_{10}]^- + MCl_3$	$[M_2Cl_7]^- + M_2Cl_6$	$M_3Cl_9 + [MCl_4]^-$
$Cl - AlCl_{3 implicit SMD}$	9	24	0	30
$[C_2C_1Im]Cl - AlCl_3$	11	30	0	25
$[Choline]Cl - AlCl_3$	41	0	27	56
$[N_{2111}]Cl - AlCl_3$	8	32	0	29
$Cl - GaCl_{3 implicit SMD}$	0	3	10	29
$[C_2C_1Im]Cl - GaCl_3$	27	0	19	40
$[Choline]Cl - GaCl_3$	12	14	0	21
$[N_{2111}]Cl - GaCl_3$	N/a	0	0	15

Figure 7.13: Gibbs free energy differences in kJ mol^{-1} of possible anionic speciations at x_{AlCl_3} and x_{GaCl_3} = 0.8 in the liquid phase

The evaluation of speciation at $x_{MCl_3} = 0.8$ further affirms the utility of the implicit solvation model in capturing the speciation in the chloroaluminate systems. The trends in speciation of the IPs featuring $[C_2C_1Im]^+$ and $[N_{2111}]^+$. Deviations from expected patterns are observed with in the $[Choline]^+$ system indicating that specific interactions may influence the stability of certain species. The $[Al_3Cl_{10}]^-$ anion could also be vastly over-stabilized as indicated from the relative stability at $x_{MCl_3} = 0.75$.

In the chlorogallte system the thermodynamic comparisons imply that the overall trends revealed by using solely the implicit solvation model are sufficient at higher x_{MCl_3}. The explicit solvation only introduce nuanced interactions but with respect to the stability of the different speciations the direct exposure to a counter ion instead of a continuum has highlighted the change in behavior of the chlorogallate systems with respect to the prevalent cation.the nature of the cation plays a significant role in the stability of different speciations inducing a shift in stability trends highlighting the need to to study the chlorogallate system with explicit solvation at $x_{MCl_3} = 0.75$ and beyond. In particular, systems featuring ammonium based cations exhibit unexpected stability orders with the $[M_2Cl_7]^-$ + M_2Cl_6 the most stable speciation in both systems. However, the $[Ga_4Cl_{13}]^-$ species did not stabilize in conjunction with the $[N_{2111}]^+$ cation so there may be an unfound minimum which could shift the trend in favor of the one observed in the implicit solvation model.

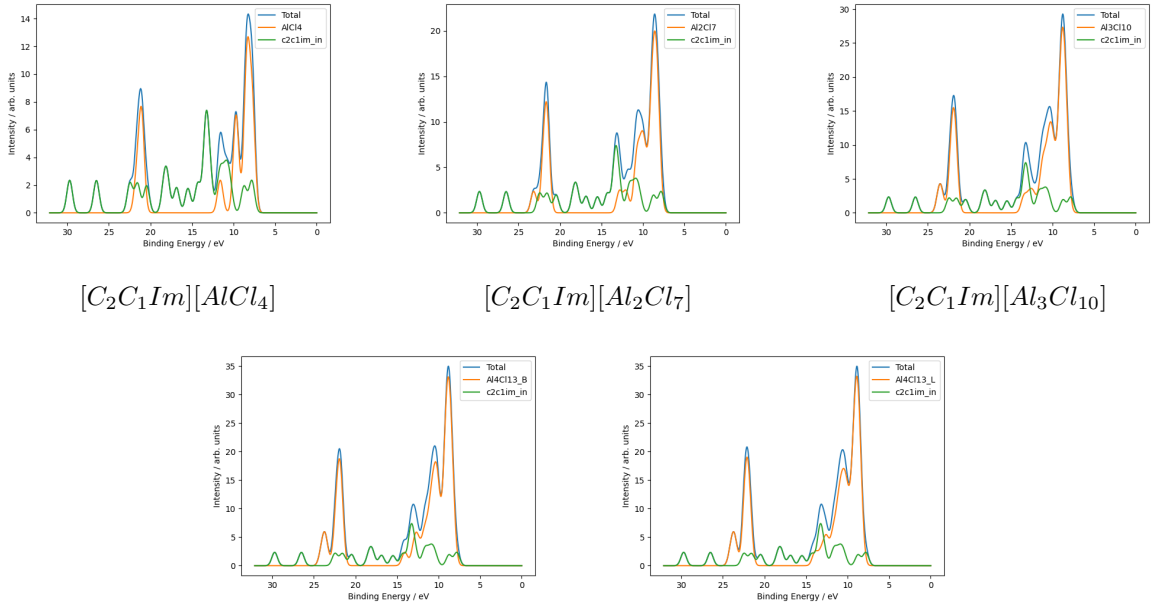
7.4.5 Liquid phase ion pair speciation summery

The discrepancies in chloroindate highlight the crucial role of explicit solvation in stabilizing more highly charged anions, such as $[InCl_6]^{3-}$ and $[InCl_5]^{2-}$, compared to $[InCl_4]^-$, a factor inadequately captured by the implicit solvation model alone. The gap necessitates a reevaluation of speciation based on optimized IPs structures, to accurately discern the influence of explicit cation-anion interactions. The effect of $[C_2C1Im]^+$, $[Choline]^+$, and $[N2111]^+$ on the chloroindate speciations at $x_{MCl_3} = 0.25$, 0.33 and 0.5 is evident and highlights the necessity of studying systems with more highly charged species with the appropriate counter ions present in order to determine their stability.

The evaluation also demonstrates the effectiveness of the implicit solvation model at certain concentrations ($x_{MCl_3} = 0.67$ and beyond), particularly in chloroaluminate system, where it captures the speciation dynamics with reasonable accuracy. However, explicit solvation becomes increasingly important for understanding speciation at higher concentrations, revealing nuanced interactions that are missed by the implicit model. The observed discrepancies and the stabilization trends among various cations, especially in systems featuring ammonium-based cations, highlight the need for further experimental and computational studies to fully elucidate the speciation mechanisms in these complex solvation environments.

7.5 XPS spectra

Based on the methods developed by Richard Fogarty and employed by Kevin Lovelock the XPS spectra of various IPs to predict the XPS output from minimum energy structures was used. The method allows for the prediction of XPS outputs and lets the contribution from different species be determined. A full set of XPS spectra can be found in the appendix while only the subset of the $[C_2C_1Im]Cl$-$AlCl_3$ XPS spectra are shown here in figure 7.14.



$[C_2C_1Im][AlCl_4]$ $[C_2C_1Im][Al_2Cl_7]$ $[C_2C_1Im][Al_3Cl_{10}]$

$[C_2C_1Im][Al_4Cl_{13}]_{Bra}$ $[C_2C_1Im][Al_4Cl_{13}]_{Lin}$

Figure 7.14: $[C_2C_1Im][Al_xCl_y]$ IP Simulated XPS Spectra

The spectra are are reasonable based on known binding energies of similar species. However, out of the group 13 chlorometallate systems only the chloroindate system has been studied with XPS. Specifcally the $[C_8C_1Im]Cl$-$InCl_3$ at a $x_{InCl_3} = 0.5$ with a speciation of $[C_8C_1Im][InCl_4]$. Figure 7.15 shows the experimentally and computationally generated XPS specta of $[InCl_4]^-$.

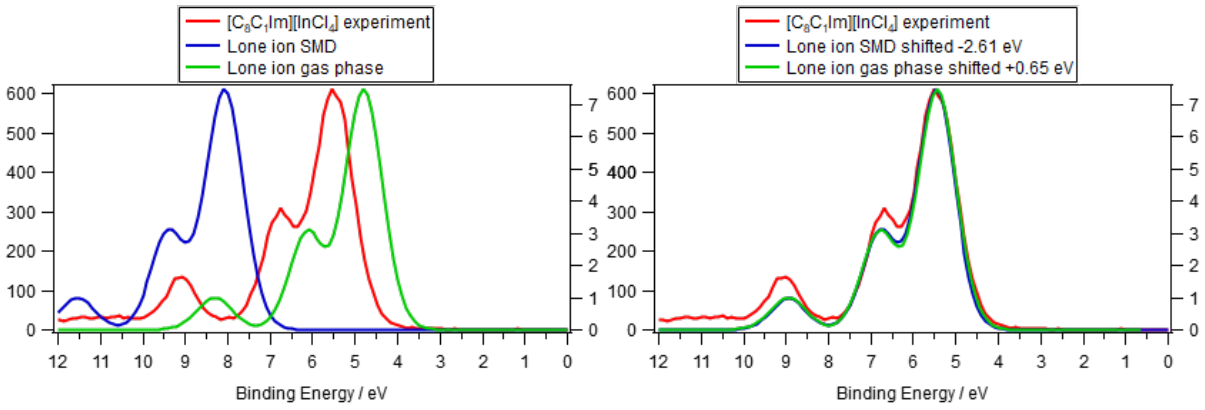


Figure 7.15: Simulated $[InCl_4]^-$ XPS Spectra vs experimental $[InCl_4]^-$ XPS spectra[10]

With respect to shape the spectra show good match as seen on the left of figure 7.15 although spectrum must be shifted to the right in the LP and to the left for the GP structures. The LP indicates that the system overbinds by 2.61 eV and the GP underbinds by 0.65 eV. The spectra must be adjusted accordingly in order to generate a better match between the experimental and computational XPS outputs. When accounting for the discrepancy in binding energy the computational and experimental spectra match well as shown on the right of figure 7.15.

7.6 Speciation summery

The speciation of chlorometallate species of the chloroaluminate, chlorogallate and chloroindate systems has been determined at x_{MCl_3} = 0.25, 0.33, 0.5, 0.67, 0.75 and 0.8 have been determined in the GP and LP according to the species Gibbs free energy. The speciations are summerized in the key take aways sections. The GP speciation determined here concurs with known MS speciation studies below x_{MCl_3} = 0.5 for the chloroaluminate and chlorogallate systems. Above x_{MCl_3} = 0.5 the MS speciation is different to the GP speciation determined here. The oligomerized chlorometallate species which were shown to be thermodynamically stable have only been found sparingly or not at all in the GP. There is not published MS results below x_{InCl_3} = 0.5 so no adequate comparison could be made but above x_{MCl_3} = 0.5 the speciation of the dimetallic $[In_2Cl_7]^-$ species was shown to concur with the speciation described in unpublished results in the HMIL revisted review.[7]

The LP speciation of the chloroaluminate and chlorogallate systems concurs with the speciation determined in other studies. The LP speciation determined for the chloroindate system does not agree with the chloroindate

speciation determined in other studies. The $[InCl_4]^-$ species is the dominant speciation at $x_{MCl_3} = 0.25$ and 0.33 although it is known that $[InCl_6]^{3-}$ and $[InCl_5]^{2-}$ are known to be the predominant speciation. The multimetallic chloroindate species have also been shown to be thermodynamically stable at $x_{InCl_3} = 0.67$, 0.75 and 0.8. The discrepancies between the chloroindate speciation determined here and in other speciation studies were addressed through scans and evaluating the solvation energy. The evaluations showed that the discrepancies at x_{InCl_3} below 0.5 are not necessarily a result of the solvation environment and $[InCl_5]^{2-}$ and $[InCl_6]^{3-}$ are stabilized through the explicit interactions with the surrounding cations which were not extensively evaluated here. The speciation of the oligomerized chloroindate complexes in the LP also has to be addressed.

The generated XPS spectra show that the chlorometallate speciation determined by the Gibbs free energy of each species can be tested. Additionally, it provides reference data which XPS data can be compared to.

Bibliography

[1] JC Bailey. Formation of cryolite and other aluminofluorides: a petrologic review. *Bulletin of the Geological Society of Denmark*, 29:1–45, 1980.

[2] R Chen, B Sun, and Q Zhang. Far ft-ir spectra of gallium hexafluoride ions. *Guang pu xue yu Guang pu fen xi= Guang pu*, 17(1):62–64, 1997.

[3] Bradley L Ackermann, Anthony Tsarbopoulos, and John Allison. Fast atom bombardment mass spectrometric studies of the aluminum chloride/n-butylpyridinium chloride molten salt. *Analytical chemistry*, 57(8):1766–1768, 1985.

[4] Steven P Wicelinski, Robert J Gale, Krishna M Pamidimukkala, and Roger A Laine. Fast atom bombardment mass spectrometry of low temperature chloroaluminate and chlorogallate melts. *Analytical Chemistry*, 60(20):2228–2232, 1988.

[5] Ala'a K Abdul-Sada, Anthony M Greenway, Kenneth R Seddon, and Thomas Welton. A fast atom bombardment mass spectrometric study of room-temperature 1-ethyl-3-methylimidazolium chloroaluminate (iii) ionic liquids. evidence for the existence of the decachlorotrialuminate (iii) anion. *Organic mass spectrometry*, 28(7):759–765, 1993.

[6] Ala'a K Abdul-Sada, Anthony M Greenway, Kenneth R Seddon, and Thomas Welton. Upon the existence of [al3cl10]- in room temperature chloroaluminate ionic liquids. *Organic mass spectrometry*, 24(10):917–918, 1989.

[7] J Estager, JD Holbrey, and Malgorzata Swadźba-Kwaśny. Halometallate ionic liquids–revisited. *Chemical Society Reviews*, 43(3):847–886, 2014.

[8] Valerio B Di Marco, Luca Raveane, Annalisa Dean, and Pietro Traldi. Perturbations produced by electrospray ionization mass spectrometry in the speciation of aluminium (iii)/1, 6-dimethyl-4-hydroxy-3-pyridinecarboxylate aqueous solutions. *Rapid Communications in Mass Spectrometry: An International Journal Devoted to the Rapid Dissemination of Up-to-the-Minute Research in Mass Spectrometry*, 24(7):868–874, 2010.

[9] David C Apperley, Christopher Hardacre, Peter Licence, Richard W Murphy, Natalia V Plechkova, Kenneth R Seddon, Geetha Srinivasan, Małgorzata Swadźba-Kwaśny, and Ignacio J Villar-Garcia. Speciation of chloroindate (iii) ionic liquids. *Dalton Transactions*, 39(37):8679–8687, 2010.

[10] Kevin R. J. Lovelock. Collaboration with kevin r. j. lovelock. 2021.

Chapter 8

Conclusion

In summary, the group 13 chlorometallate ionic liquids were studied by hierarchally building up the complexity of the systems. Initially a structure search of isolated chlorometallate species and a conformer search of the cations was conducted in the GP and LP. The electronic structure of the most stable structures were evaluated before IPs were evaluated with a focus on the interaction between chlorometallate species and the cations. Lastly the speciation of the chlorometallate species was determined based on the Gibbs free energy of the chlorometallate species

The IP interactions involve a hierarchy of nucleophilic and electrophilic sites on the anions and cations, respectively. The prediction of this hierarchy is best achieved through a combination of Fukui functions, the ADCH NAC assginement method and the MEPs. Both GP and LP IP structures exhibit analogous attractiveness hierarchies for the sites on ions. In LP structures, entropy plays a more prominent role in determining stability. For anions interacting with the $[C_2C_1Im]^+$ cation, the preferred interaction sites are in the following order: C_2 carbon, C_2 hydrogen, C_4 and C_5 hydrogen atoms, ethyl and methyl α hydrogen atoms, and finally the ethyl β hydrogen atoms. Similarly, in ammonium-based cations which feature a more nucelophilic site such as $[Choline]^+$ and $[N_{2110}]^+$, interactions with the hydroxyl and N-H hydrogen atoms result in the most stabilizing interactions, followed by the alpha and beta hydrogen atoms around the structures. Maximizing the number of interactions leads to the most stabilizing ion pair interactions. The stability of IP structures is based on three factors: the interaction with the π-system, the number of MCl_3 moieties interacting with the cation, and the entropy of the ion pair. Additionally, self-interactions in anions like $[M_3Cl_{10}]^-$ and linear $[M_4Cl_{13}]^-$ can stabilize the structure simoultaneously enhancing the interaction with the cation.

The results indicate that there are large discrepancies between MS speciation and the GP speciation determined here. Either the thermodynamics does not drive the speciation of GP complexes, as indicated by studies conducted through MS in other systems or there may be alternative kinetic effects which were not considered. The speciation determined by MS studies and the relative stability of isolated species in the GP show some similarities in certain regions of x_{MCl_3}, but generally diverge from each other. The thermodynamic favorability of multimetallic chloroindate complexes, particularly trimetallic and tetrametallic complexes, above $x_{MCl_3} = 0.5$, has not been previously determined. The absence of pentacoordinate and hexacoordinate chloroindate species at $x_{InCl_3} = 0.33$ and 0.25 in the GP could be possible but there arent any published MS speciation studies and as such there is a lack of reference data. In the chloroaluminate and chlorogallate systems, the speciation agrees with MS speciation below $x_{MCl_3} = 0.67$, but diverges as x_{MCl_3} increases. This divergence may be attributed to the increased susceptibility of oligomerized species to fragmentation, and the thermodynamic stability of the complexes may not withstand the ionization process in MS.

In the LP speciation of the chloroaluminate and chlorogallate systems, there is generally agreement with previous studies. However, a thermodynamically stable branched $[M_4Cl_{13}]^-$ species, which could have been previously overlooked, was discovered to be stable. The LP speciation of the chloroindate system differs significantly from known LP speciation, except at $x_{InCl_3} = 0.5$. At $x_{InCl_3} = 0.25$ and 0.33, the speciation is dominated by $[InCl_4]^-$ although $[InCl_5]^{2-}$ and $[InCl_6]^{3-}$ are known to be present. Above x_{InCl_3} the oligomerized chloroindate chomplexes were shown to be stable although they are known not to speciate due to the precipitation of $InCl_3$.

Future investigations should focus on trying to solve the issue of modeling the LP speciation of the chloroindate system. Ideally the speciation should be studied with an adequate amount of cations to balance the system to evaluate speciation more comprehensively. Alternatively the a specialized implicit solvation model coud be devised which can account for such extreme circumstances as three counter cations. Experimentalists should use the XPS data provided to idealize the understanding of speciation at different x_{MCl_3} in each system. A particular focus should be on trying to identify the branched $[M_4Cl_{13}]^-$ species in the chloroalumiante and chlorogallate sytems with the reference data provided.

Appendix A

appendix

A.1 Anion Structure Data

A.1.1 Optimized Gas Phase Anion Structures

Table A.1: Evaluated monometallic chlorometallate species

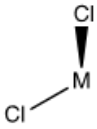
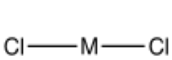
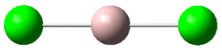
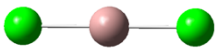
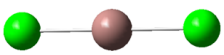
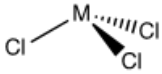
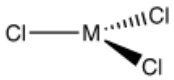
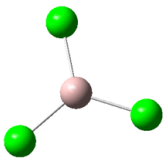
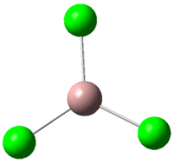
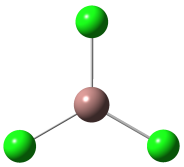
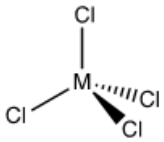
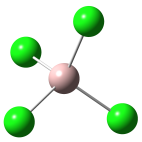
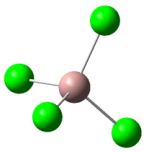
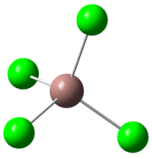
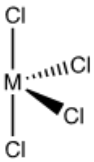
Starting structure	$AlCl_3 - Cl$	$GaCl_3 - Cl$	$InCl_3 - Cl$
			
(01)$[MCl]^{2+}$	$[AlCl]^{2+}$	$[GaCl]^{2+}$	$[InCl]^{2+}$
	Converged to (3)	Converged to (3)	Converged to (3)
(02)$[MCl_2]^{+}$			
			
(03)$[MCl_2]^{+}$	$[AlCl_2]^{+}$	$[GaCl_2]^{+}$	$[InCl_2]^{+}$
	Converged to (5)	Converged to (5)	Converged to (5)
(04)MCl_3			
			
(05)MCl_3	$AlCl_3$	$GaCl_3$	$InCl_3$
			
(06)$[MCl_4]^{-}$	$[AlCl_4]^{-}$	$[GaCl_4]^{-}$	$[InCl_4]^{-}$
	TS structure [1]	TS structure [1]	TS structure [1]
(07)$[MCl_4]^{-}$			
	converged to (6)	converged to (6)	converged to (6)
(65)$[MCl_4]^{-}$			

Table A.2: Evaluated monometallic chlorometallate species continued

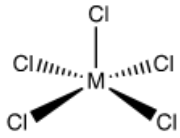
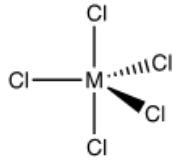
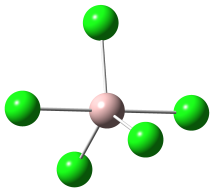
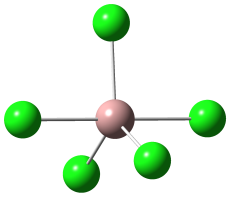
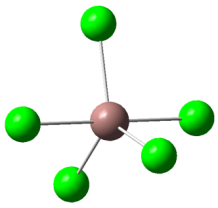
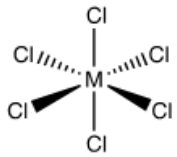
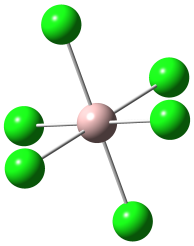
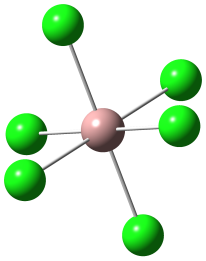
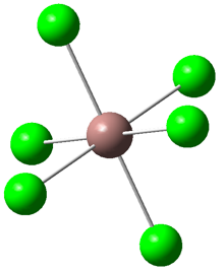
	TS structure [1]	TS structure [1]	Converged to (9)
$(08)[MCl_5]^{2-}$			
			
$(09)[MCl_5]^{2-}$	$[AlCl_5]^{2-}$	$[GaCl_5]^{2-}$	$[InCl_5]^{2-}$
			
$(10)[MCl_6]^{3-}$	$[AlCl_6]^{3-}$	$[GaCl_6]^{3-}$	$[InCl_6]^{3-}$

Table A.3: Evaluated dimetallic chlorometallate species

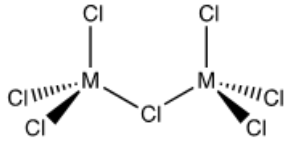
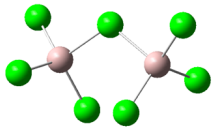
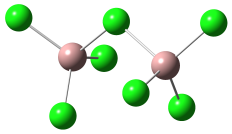
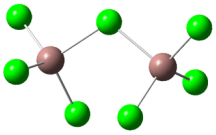
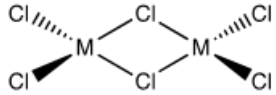
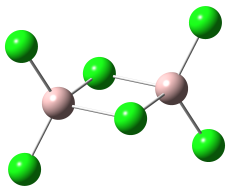
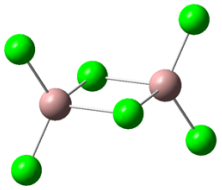
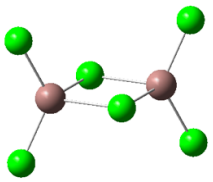
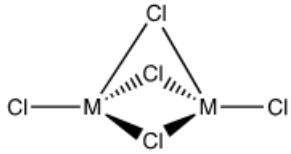
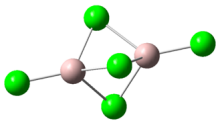
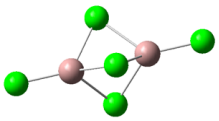
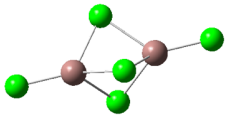
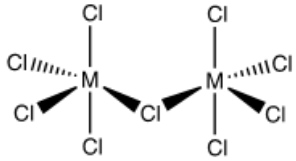
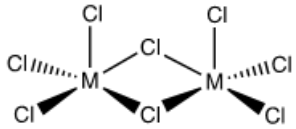
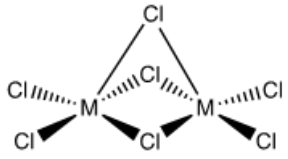
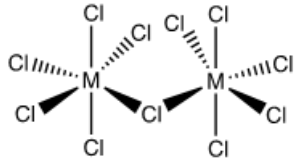
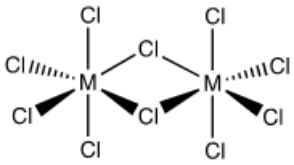
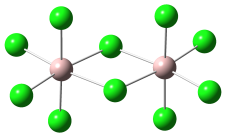
Starting structure	$AlCl_3 - Cl$	$GaCl_3 - Cl$	$InCl_3 - Cl$
			
(11)$[M_2Cl_7]^-$	$[Al_2Cl_7]^-$ {16}	$[Ga_2Cl_7]^-$	$[In_2Cl_7]^-$
			
(12)M_2Cl_6	Al_2Cl_6 {49}	Ga_2Cl_6 {52}	In_2Cl_6 {41}
			
(13)$[M_2Cl_5]^+$	$[Al_2Cl_5]^+$ (0)	$[Ga_2Cl_5]^+$ {37} (1.8)	$[In_2Cl_5]^+$ (0)
	Structure dissociates	Structure dissociates	TS structure [2]
(14)$[M_2Cl_9]^{3-}$			
	Structure dissociates	Structure dissociates	TS structure [1]
(15)$[M_2Cl_8]^{2-}$			
	represented in (11)	converged to (11)	converged to (11)
(16)$[M_2Cl_7]^-$	$[Al_2Cl_7]^-$		
	Structure dissociates	Structure dissociates	Structure dissociates
(17)$[M_2Cl_{11}]^{5-}$			

Table A.4: Evaluated dimetallic chlorometallate species continued I

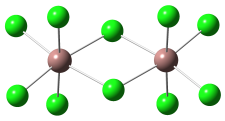


(18)$[M_2Cl_{10}]^{4-}$

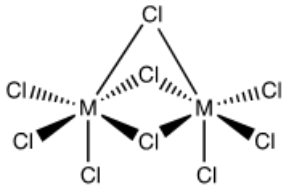


$[Al_2Cl_{10}]^{4-}$

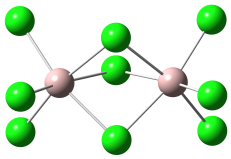
Structure dissociates



$[In_2Cl_{10}]^{4-}$

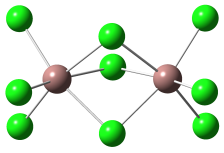


(19)$[M_2Cl_9]^{3-}$

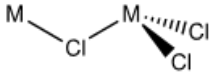


$[Al_2Cl_9]^{3-}$

Structure dissociates



$[In_2Cl_9]^{3-}$

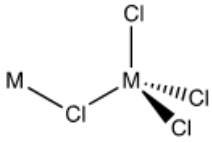


(31)$[M_2Cl_3]^{3+}$

Structure dissociates

Structure dissociates

Structure dissociates

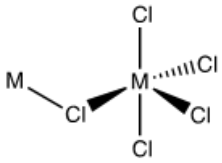


(32)$[M_2Cl_4]^{2+}$

Structure dissociates

Structure dissociates

Structure dissociates

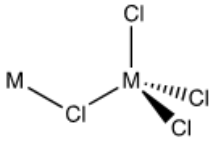


(33)$[M_2Cl_5]^{+}$

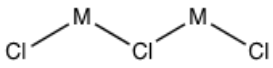
Converges to (12)

Converges to (12)

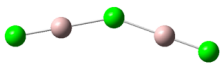
Converges to (12)



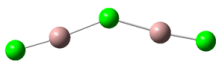
(34)M_2Cl_6



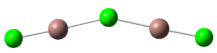
(35)$[M_2Cl_3]^{3+}$



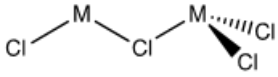
$[Al_2Cl_3]^{3+}$ (0)



$[Ga_2Cl_3]^{3+}$ (0)



$[In_2Cl_3]^{3+}$ (0)



(36)$[M_2Cl_4]^{2+}$

Converges to (50)

Structure dissociates

Structure dissociates

Table A.5: Evaluated dimetallic chlorometallate species continued II

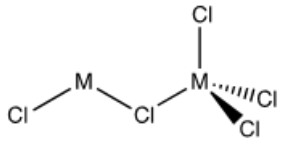
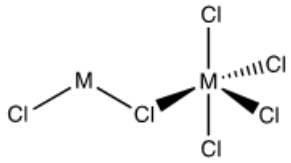
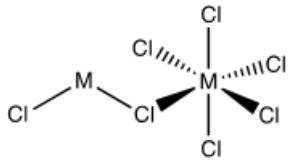
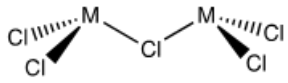
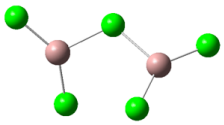
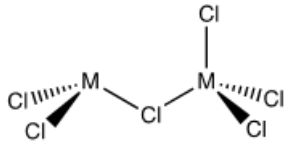
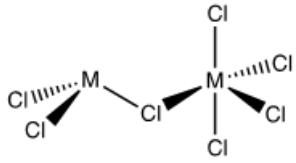
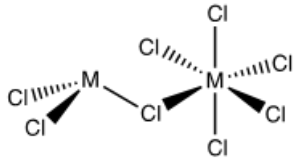
 (37)$[M_2Cl_5]^+$	Converges to (13)	represented in (13) $[Ga_2Cl_5]^+$	Converges to (13)
 (38)M_2Cl_6	Converges to (12)	Converges to (12)	Converges to (12)
 (39)$[M_2Cl_7]^-$	Converges to (11)	Converges to (11)	Converges to (11)
 (40)$[M_2Cl_5]^+$	Converges to (51)	 $[Ga_2Cl_5]^+$ {59} (0.1)	Converges to (13)
 (41)M_2Cl_6	converges to (12)	Converges to (12)	represented in (12) In_2Cl_6
 (42)$[M_2Cl_7]^-$	Converged to (11)	Converges to (11)	Converges to (11)
 (43)$[M_2Cl_8]^{2-}$	Structure dissociates	Structure dissociates	Structure dissociates

Table A.6: Evaluated dimetallic chlorometallate species continued III

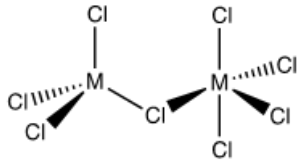
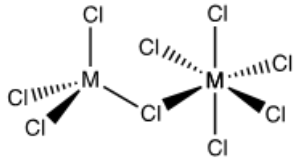
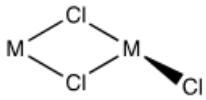
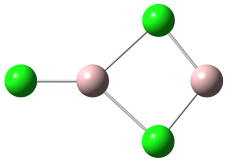
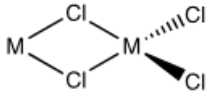
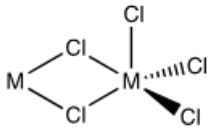
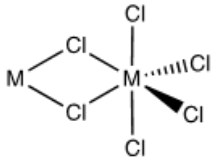
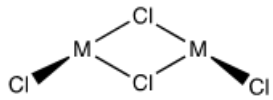
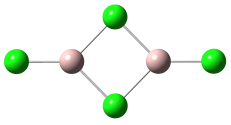
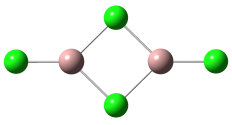
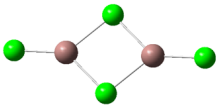
	Structure dissociates	Structure dissociates	Structure dissociates
(44)$[M_2Cl_8]^{2-}$			
	Structure dissociates	Structure dissociates	Structure dissociates
(45)$[M_2Cl_9]^{3-}$			
		TS structure [1]	TS structure [1]
(46)$[M_2Cl_3]^{3+}$	$[Al_2Cl_3]^{3+}$ (100.43)		
	Structure dissociates	Structure dissociates	Structure dissociates
(47)$[M_2Cl_4]^{2+}$			
	Structure dissociates	Converges to (51)	Converges to (13)
(48)$[M_2Cl_5]^{+}$			
	represented in (12)	converged to (12)	converged to (12)
(49)M_2Cl_6	Al_2Cl_6		
			
(50)$[M_2Cl_4]^{2+}$	$[Al_2Cl_4]^{2+}$	$[Ga_2Cl_4]^{2+}$	$[In_2Cl_4]^{2+}$

Table A.7: Evaluated dimetallic chlorometallate species continued IV

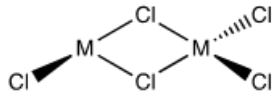
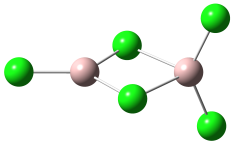
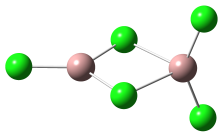
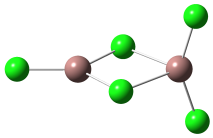
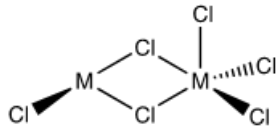
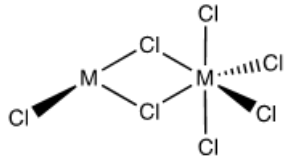
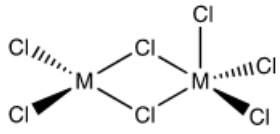
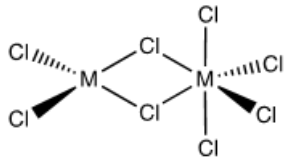
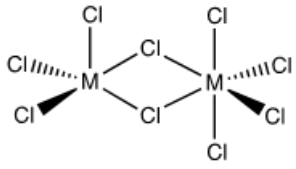
			
(51)$[M_2Cl_5]^+$	$[Al_2Cl_5]^+$ (20.7)	$[Ga_2Cl_5]^+$ (0)	$[In_2Cl_5]^+$ (16.2)
	Converges to (12)	represented in (12)	converged to (12)
(52)M_2Cl_6		Ga_2Cl_6	
	Converges to (11)	Converges to (11)	Converges to (11)
(53)$[M_2Cl_7]^-$			
	Converges to (11)	Converges to (11)	Converges to (11)
(54)$[M_2Cl_7]^-$			
	Structure dissociates	Structure dissociates	Structure dissociates
(55)$[M_2Cl_8]^{2-}$			
	Structure dissociates	Structure dissociates	Structure dissociates
(56)$[M_2Cl_9]^{3-}$			

Table A.8: Evaluated dimetallic chlorometallate species continued V

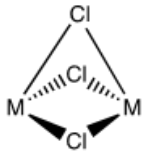
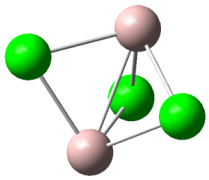
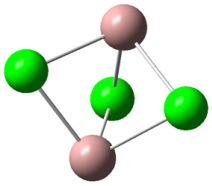
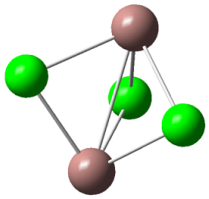
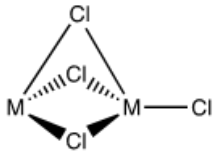
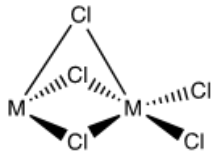
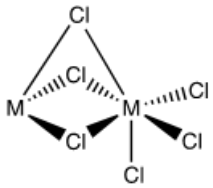
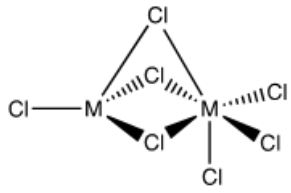
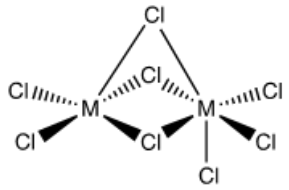
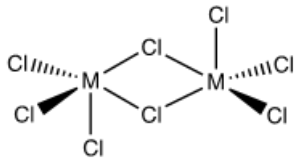
			
(57)$[M_2Cl_3]^{3+}$	$[Al_2Cl_3]^{3+}$ (173.8)	$[Ga_2Cl_3]^{3+}$ (252.7)	$[In_2Cl_3]^{3+}$ (200.7)
	Structure dissociates	Structure dissociates	Structure dissociates
(58)$[M_2Cl_4]^{2+}$			
	Structure dissociates	Represented in (40)	Converges to (13)
(59)$[M_2Cl_5]^{+}$		$[Ga_2Cl_5]^{+}$	
	converged to (12)	converged (12)	Converges to (12)
(60)M_2Cl_6			
	converged to (12)	Converges to (12)	converged (41)
(61)M_2Cl_6			
	converged to (11)	converged to (11)	Converges to (11)
(62)$[M_2Cl_7]^{-}$			

Table A.9: Evaluated dimetallic chlorometallate species continued VI



Structure dissociates | Structure dissociates | Structure dissociates

(63)$[M_2Cl_8]^{2-}$



Structure dissociates | Structure dissociates | Structure dissociates

(64)$[M_2Cl_8]^{2-}$

Table A.10: Evaluated trimetallic chlorometallate species

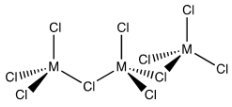
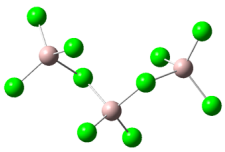
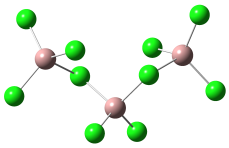
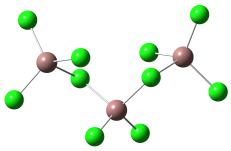
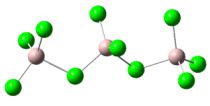
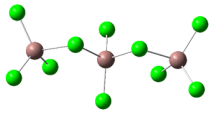
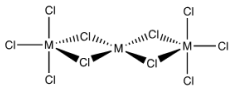
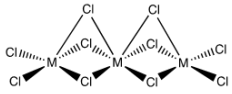
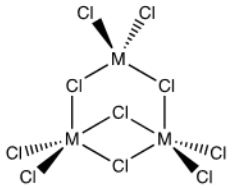
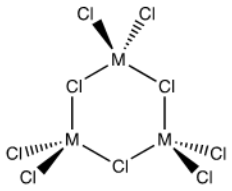
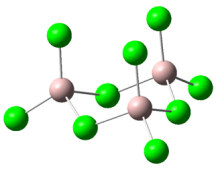
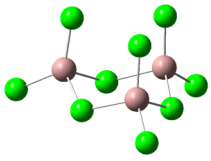
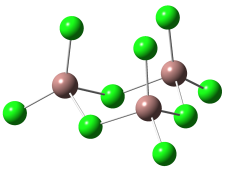
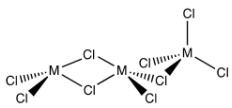
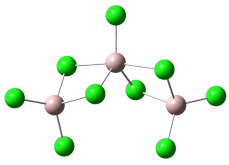
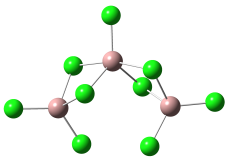
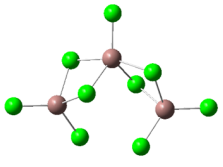
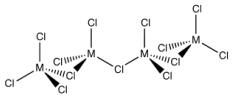
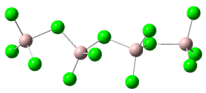
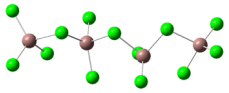
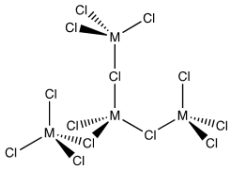
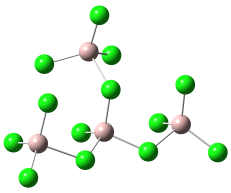
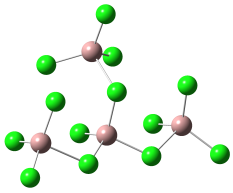
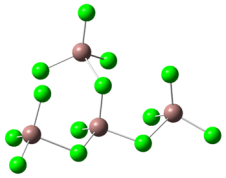
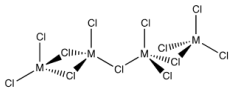
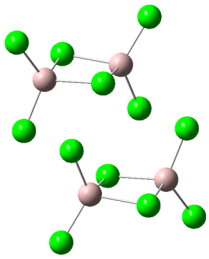
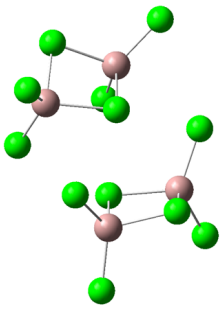
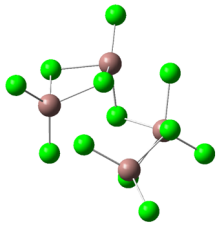
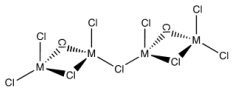
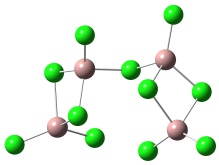
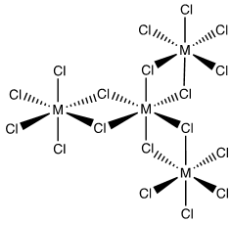
Starting structure	$AlCl_3 - Cl$	$GaCl_3 - Cl$	$InCl_3 - Cl$
	Converged to (20)	Converged to (20)	Converged to (20)
			
(20)$[M_3Cl_{10}]^-$	$[Al_3Cl_{10}]^-$ {21} (0)	$[Ga_3Cl_{10}]^-$ {21} (0)	$[In_3Cl_{10}]^-$ {21} (0)
			
	$[Al_3Cl_{10}]^-$ {22} (7.2)	$[Ga_3Cl_{10}]^-$ {22} (7.4)	$[In_3Cl_{10}]^-$ {22} (12)
	Represented in (20)	Represented in (20)	Represented in (20)
(21)$[M_3Cl_{10}]^-$			
	Represented in (20)	Represented in (20)	Represented in (20)
(22)$[M_3Cl_{10}]^-$			
	TS Structure [2]	Converges to (20)	TS Structure [2]
(23)$[M_3Cl_{10}]^-$			
			
(24)M_3Cl_9	Al_3Cl_9 (0)	Ga_3Cl_9 (0)	In_3Cl_9 (0)
			
(25)M_3Cl_9	Al_3Cl_9 (13.7)	Ga_3Cl_9 (24.7)	In_3Cl_9 (2.2)

Table A.11: Evaluated tetrametallic chlorometallate species

Starting structure	$AlCl_3 - Cl$	$GaCl_3 - Cl$	$InCl_3 - Cl$
			
(26)$[M_4Cl_{13}]^-$	$[Al_4Cl_{13}]^-$ [Low 2] (0)	$[Ga_4Cl_{13}]^-$ [Low 2] (0)	$[In_4Cl_{13}]^-$ [Low 2] (0)
			
(27)$[M_4Cl_{13}]^-$	$[Al_4Cl_{13}]^-$ (6.2)	$[Ga_4Cl_{13}]^-$ (2.2)	$[In_4Cl_{13}]^-$ (16.6)
			
(28)M_4Cl_{12}	Al_4Cl_{12}	Ga_4Cl_{12}	In_4Cl_{12}
	TS structure [2]		TS structure [2]
(29)$[M_4Cl_{11}]^-$		$[Ga_4Cl_{11}]^-$	
	Structure dissociates	Structure dissociates	Structure dissociates
(30)$[M_4Cl_{18}]^{6-}$			

A.1.2 Gas Phase structure Gibbs Free Energy Comparisons

Table A.12: $[M_4Cl_{13}]^-$ comparison I

Metal	$[M_4Cl_{13}]^-$	$M_4Cl_{12} + Cl^-$	$[M_4Cl_{11}]^+ + 2Cl^-$	$[M_3Cl_{10}]^- + MCl_3$	$[M_2Cl_7]^- + 2MCl_3$
Al	0.0	375.8	-	27.2	88.1
Ga	0.0	374.2	1095.1	25.6	81.2
In	0.0	342.5	-	37.3	105.8

Table A.13: $[M_4Cl_{13}]^-$ comparison II

Metal	$[MCl_4]^- + 3MCl_3$	$M_3Cl_9 + [MCl_4]^-$	$[M_2Cl_7]^- + M_2Cl_6$	$[M_2Cl_8]^{2-} + [M_2Cl_5]^+$
Al	178.3	76.2	16.2	-
Ga	163.8	84.7	32.7	-
In	204.5	76.8	27.0	866.6

Table A.14: $[M_4Cl_{13}]^-$ comparison III

Metal	$[M_2Cl_9]^{3-} + [M_2Cl_4]^{2+}$	$[M_2Cl_{10}]^{4-} + [M_2Cl_3]^{3+}$
Al	2705.2	-
Ga	-	-
In	2404.1	4895.5

Table A.15: M_4Cl_{12} comparison I

Metal	M_4Cl_{12}	$[M_4Cl_{11}]^+ + Cl^-$	$M_3Cl_9 + MCl_3$	$[M_3Cl_{10}]^- + [MCl_2]^+$	$2M_2Cl_6$
Al	12.6	-	41.6	584.6	0.0
Ga	0.0	720.8	24.3	539.2	6.5
In	0.0	-	62.3	535.2	32.3

Table A.16: M_4Cl_{12} comparison II

Metal	$[M_2Cl_7]^- + [M_2Cl_5]^+$	$[M_2Cl_8]^{2-} + [M_2Cl_4]^{2+}$	$[M_2Cl_9]^{3-} + [M_2Cl_3]^{3+}$
Al	475.3	-	4391.2
Ga	470.6	-	-
In	-	1722.2	3946.2

Table A.17: M_4Cl_{11} comparison I

Metal	$[M_4Cl_{11}]^+$	$M_3Cl_9 + [MCl_2]^+$	$[M_3Cl_{10}]^- + MCl_3$	$2M_2Cl_6 + [M_2Cl_5]^+$
Al	-	140.0	1467.0	0.0
Ga	0.0	191.3	1490.1	97.8
In	-	78.1	1262.4	0.0

Table A.18: M_4Cl_{11} comparison II

Metal	$[M_2Cl_7]^- + [M_2Cl_4]^{2+}$	$[M_2Cl_8]^{2-} + [M_2Cl_3]^{3+}$
Al	953.5	-
Ga	1005.5	-
In	850.2	2782.2

Table A.19: M_3Cl_{10} comparison I

Metal	$[M_3Cl_{10}]^-$	$M_3Cl_9 + Cl^-$	$[M_2Cl_{10}]^{4-} + M^{3+}$	$[M_2Cl_9]^{2-} + [MCl]^{2+}$	$[M_2Cl_8]^{2-} + [MCl_2]^+$
Al	0.0	377.6	-	3252.4	-
Ga	0.0	372.9	-	-	-
In	0.0	367.5	5882.7	2847.6	956.3

Table A.20: M_3Cl_{10} comparison II

Metal	$[M_2Cl_7]^- + MCl_3$	$M_2Cl_6 + [MCl_4]^-$	$[M_2Cl_5]^+ + [MCl_5]^{2-}$	$[M_2Cl_4]^{2+} + [MCl_6]^{3-}$
Al	60.9	79.2	1151.8	3001.0
Ga	55.5	89.7	1137.0	2924.5
In	68.5	88.4	1056.2	2737.7

Table A.21: M_3Cl_9 comparison I

Metal	M_3Cl_9	$[M_2Cl_9]^{3-} + M^{3+}$	$[M_2Cl_8]^{2-} + [MCl]^{2+}$	$[M_2Cl_7]^{-} + [MCl_2]^{+}$
Al	0.0	5627.9	-	603.9
Ga	0.0	-	-	570.4
In	0.0	4908.3	2140.6	541.4

Table A.22: M_3Cl_9 comparison II

Metal	$M_2Cl_6 + MCl_3$	$[M_2Cl_5]^{+} + [MCl_4]^{-}$	$[M_2Cl_4]^{2+} + [MCl_5]^{2-}$	$[M_2Cl_3]^{3+} + [MCl_6]^{3-}$
Al	30.2	523.8	2074.6	4672.6
Ga	30.7	529.0	2019.8	4604.4
In	48.9	513.1	1886.7	4254.7

Table A.23: M_2Cl_{10} comparison I

Metal	$[M_2Cl_{10}]^{4-}$	$[M_2Cl_9]^{3-} + Cl^{-}$	$[M_2Cl_8]^{2-} + 2Cl^{-}$	$[M_2Cl_7]^{-} + 3Cl^{-}$	$M_2Cl_6 + 4Cl^{-}$
Al	-	566.3	-	0.0	346.9
Ga	-	-	-	0.0	348.0
In	993.6	386.8	47.4	0.0	347.9

Table A.24: M_2Cl_{10} comparison II

Metal	$[M_2Cl_5]^{+} + 5Cl^{-}$	$[M_2Cl_4]^{2+} + 6Cl^{-}$	$[M_2Cl_3]^{3+} + 7Cl^{-}$	$2[MCl_5]^{2-}$	$[MCl_6]^{3-} + [MCl_4]^{-}$
Al	1169.2	2469.6	4518.7	262.3	560.7
Ga	1160.2	2415.9	4468.7	239.1	535.8
In	1140.1	2338.2	4222.8	121.7	429.7

Table A.25: M_2Cl_9 comparison

Metal	$[M_2Cl_9]^{3-}$	$[MCl_5]^{2-} + [MCl_4]^{-}$	$[MCl_6]^{3-} + MCl_3$
Al	554.4	0.0	877.4
Ga	-	0.0	845.6
In	440.6	0.0	811.4

Table A.26: M_2Cl_8 comparison

Metal	$[M_2Cl_8]^{2-}$	$2[MCl_4]^-$	$[MCl_5]^{2-} + MCl_3$	$[MCl_6]^{3-} + [MCl_2]^+$
Al	-	0.0	579.0	2048.3
Ga	-	0.0	549.0	1968.6
In	276.6	0.0	503.4	1827.3

Table A.27: M_2Cl_7 comparison

Metal	$[M_2Cl_7]^-$	$[MCl_4]^- + MCl_3$	$[MCl_5]^{2-} + [MCl_2]^+$	$[MCl_6]^{3-} + [MCl]^{2+}$
Al	0.0	90.2	1261.1	3514.5
Ga	0.0	82.7	1205.6	3409.2
In	0.0	98.7	1114.6	3149.9

Table A.28: M_2Cl_6 comparison

Metal	M_2Cl_6	$2MCl_3$	$[MCl_4]^- + [MCl_2]^+$	$[MCl_5]^{2-} + [MCl]^{2+}$	$[MCl_6]^{3-} + M^{3+}$
Al	0.0	71.9	663.8	2618.8	5940.7
Ga	0.0	48.5	622.4	2529.3	5784.5
In	0.0	78.8	591.3	2318.6	5230.3

Table A.29: M_2Cl_5 comparison

Metal	$[M_2Cl_5]^+$	$MCl_3 + [MCl_2]^+$	$[MCl_4]^- + [MCl]^{2+}$	$[MCl_5]^{2-} + M^{3+}$
Al	0.0	170.2	1546.2	4569.7
Ga	0.0	124.1	1482.1	4440.6
In	0.0	127.0	1350.8	3954.6

Table A.30: M_2Cl_4 comparison

Metal	$[M_2Cl_4]^{2+}$	$2[MCl_2]^+$	$MCl_3 + [MCl]^{2+}$	$[MCl_4]^- + M^{3+}$
Al	209.7	0.0	784.1	3228.6
Ga	243.8	0.0	748.0	3193.5
In	230.7	0.0	711.4	2811.8

Table A.31: M_2Cl_3 comparison

Metal	$[M_2Cl_3]^{3+}$	$[MCl_2]^+ + [MCl]^{2+}$	$MCl_3 + M^{3+}$
Al	554.4	0.0	1852.6
Ga	624.9	0.0	1845.6
In	563.5	0.0	1587.9

Table A.32: MCl_6 comparison I

Metal	$[MCl_6]^{3-}$	$[MCl_5]^{2-} + Cl^-$	$[MCl_4]^- + 2Cl^-$	$MCl_3 + 3Cl^-$
Al	799.1	250.4	0.0	328.6
Ga	766.9	235.1	0.0	313.8
In	658.9	175.5	0.0	328.0

Table A.33: MCl_6 comparison II

Metal	$[MCl_2]^+ + 4Cl^-$	$[MCl]^{2+} + 5Cl^-$	$M^{3+} + 6Cl^-$
Al	1249.2	2953.8	5727.0
Ga	1201.6	2873.4	5596.8
In	1168.4	2720.2	5148.5

A.1.3 selected Gas Phase Structures Structural Data

Table A.34: $[AlCl_4]^-$ Gas Phase Distances and Angles

Al-Cl distance	2.17
Cl-Al-Cl Angles	109.5

Table A.35: $[GaCl_4]^-$ Gas Phase Distances and Angles

Ga-Cl distances	2.22
Cl-Ga-Cl Angles	109.5

Table A.36: $[InCl_4]^-$ Gas Phase Distances and Angles

In-Cl distance	2.37
Cl-In-Cl Angles	109.5

Table A.37: $[InCl_5]^{2-}$ Gas Phase Distances and Angles

In-Cl distance (axial)	2.55
In-Cl distance (equitorial)	2.47
Cl-In-Cl Ax-Eq Angle	90
Cl-In-Cl Eq-Eq Angle	120

Table A.38: $[InCl_6]^{3-}$ Gas Phase Distances and Angles

In-Cl distance	2.62
Cl-In-Cl Angles	90

Table A.39: $[Al_2Cl_7]^-$ Gas Phase Distances and Angles

Measurement	1	2	3	4	5	6	Average
Al-Cl(T) distance	2.14	2.12	2.13	2.13	2.14	2.12	2.13
Al-Cl(B) distance	2.3	2.3					2.30
Cl(T)-Al-Cl(T) Angle	112.6	115	113.8	112.6	115	113.8	113.8
Cl(B)-Al-Cl(T) Angle	101.9	106	106.1	101.9	106	106.1	104.7
Al-Cl-Al Angle	113.5						113.5
Cl(T)-Al-Al_Cl(T) dihedral 1	60.3						60.3
Cl(T)-Al-Al_Cl(T) dihedral 2	-73.3						-73.3
Cl(T)-Al-Al_Cl(T) dihedral 3	173						173.0

Table A.40: $[Ga_2Cl_7]^-$ Gas Phase Distances and Angles

Measurement	1	2	3	4	5	6	Average
Ga-Cl(T) distance	2.18	2.19	2.18	2.18	2.19	2.18	2.18
Ga-Cl(B) Distance	2.38	2.38					2.38
Cl(T)-Ga-Cl(T) Angle	113	115.4	114.3	113	114.3	115.4	114.2
Cl(B)-Ga-Cl(T) Angle	102	105.1	105.3	102	105.1	105.3	104.1
Ga-Cl-Ga Angle	111.5						111.5
Cl(T)-Ga-Ga-Cl(T) dihedral 1	-62.6						-62.6
Cl(T)-Ga-Ga-Cl(T) dihedral 2	71.7						71.7
Cl(T)-Ga-Ga-Cl(T) dihedral 3	-174.2						-174.2

Table A.41: $[Al_3Cl_{10}]^-$ Gas Phase Distances and Angles

Measurement	1	2	3	4	5	6	Average
Al (T) - Cl (T) distance	2.12	2.13	2.12	2.12	2.13	2.12	2.12
Al (T) - Cl (B) distance	2.34	2.34					2.34
Al (B) - Cl (B) distance	2.24	2.24					2.24
Al (B) - Cl (TB) distance	2.1	2.1					2.10
Cl (T) - Al (T) - Cl (T) Angle	114	115.4	115.1	114	115.4	115.1	114.8
Cl (T) - Al (T) - Cl (B) Angle	104.9	103.8	101.4	104.9	103.8	101.4	103.4
Al (T) - Cl (B) - Al (B) Angle	111.2	111.2					111.2
Cl (B) - Al (B) - Cl (B) Angle	104						104.0
Cl (B) - Al (B) - Cl (TB) Angle	110	107.1	110	107.1			108.6
Cl (TB) - Al (B) - Cl (TB) Angle	117.9						117.9

Table A.42: $[Ga_3Cl_{10}]^-$ Gas Phase Distances and Angles

Measurement	1	2	3	4	5	6	Average
Ga (T) - Cl (T) distance	2.17	2.17	2.18	2.17	2.17	2.18	2.17
Ga (T) - Cl (B) distance	2.43	2.43					2.43
Ga (B) - Cl (B) distance	2.3	2.3					2.30
Ga (B) - Cl (TB) distance	2.16	2.16					2.16
Cl (T) - Ga (T) - Cl (T) Angle	104	102.6	101.2	104	102.6	101.2	102.6
Cl (T) - Ga (T) - Cl (B) Angle	114.5	115.8	115.8	114.5	115.8	115.8	115.4
Ga (T) - Cl (B) - Ga (B) Angle	109.6	109.6					109.6
Cl (B) - Ga (B) - Cl (B) Angle	103.1						103.1
Cl (B) - Ga (B) - Cl (TB) Angle	109.3	107.5	109.3	107.5			108.4
Cl (TB) - Ga (B) - Cl (TB) Angle	119.1						119.1

Table A.43: Branched $[Al_4Cl_{13}]^-$ Gas Phase Distances and Angles

Measurement	1	2	3	4	5	6	Average
Al (TLin) - Cl (TLin) distance	2.11	2.11	2.12	2.11	2.11	2.12	2.11
Al (TLin) - Cl (BLin) distance	2.41	2.41					2.41
Al (Tbra) - Cl (Tbra) distance	2.11	2.11	2.12				2.11
Al (Tbra) - Cl (Bbra) distance	2.41						2.41
Al (B) - Cl (Tbra) distance	2.22	2.22					2.22
Al (B) - Cl (Bbra) distance	2.19						2.19
Al (B) - Cl (TB) distance	2.07						2.07
Cl (T) - Al (TLin) - Cl (B) Angle	98.9	102.9	102.7	98.9	102.9	102.7	101.5
Cl (T) - Al (TLin) - Cl (T) Angle	116.6	116	115.7	116.6	116	115.7	116.1
Cl (Tbra) - Al (Tbra) - Cl (Bbra) Angle	102.1	99.5	102.1				101.2
Cl (Tbra) - Al (Tbra) - Cl (Tbra) Angle	116.1	116.6	116.1				116.3
Al (TLin) - Cl (B) - Al (B) angle	112.9	112.9					112.9
Al (Tbra) - Cl (B) - Al (B) angle	110.6						110.6
Cl (B) - Al (B) - Cl (B) Angle	99.3						99.3
Cl (B) - Al (B) - Cl (BBra) Angle	105.3	105.3					105.3
Cl (B) - Al (B) - Cl (TB) Angle	113.9	113.9					113.9
Cl (Bbra) - Al (B) - Cl (TB) Angle	117.2						117.2

Table A.44: Branched $[Ga_4Cl_{13}]^-$ Gas Phase Distances and Angles

Measurement	1	2	3	4	5	6	Average
Ga (TLin) - Cl (T) distance	2.17	2.16	2.16	2.17	2.16	2.16	2.16
Ga (TLin) - Cl (B) distance	2.52	2.52					2.52
Ga (Tbra) - Cl (Tbra) distance	2.17	2.16	2.16				2.16
Ga (Tbra) - Cl (Bbra) distance	2.51						2.51
Ga (B) - Cl (Tbra) distance	2.26	2.26					2.26
Ga (B) - Cl (Bbra) distance	2.24						2.24
Ga (B) - Cl (TB) distance	2.13						2.13
Cl (T) - Ga (TLin) - Cl (B) Angle	98.4	101.3	101.5	98.4	101.3	101.5	100.4
Cl (T) - Ga (TLin) - Cl (T) Angle	117.5	116.3	116.7	117.5	116.3	116.7	116.8
Cl (Tbra) - Ga (Tbra) - Cl (Bbra) Angle	100.7	100.7	99.3				100.2
Cl (Tbra) - Ga (Tbra) - Cl (Tbra) Angle	116.8	116.8	117.2				116.9
Ga (TLin) - Cl (B) - Ga (B) Angle	110.6	110.6					110.6
Ga (Tbra) - Cl (B) - Ga (B) Angle	108.6						108.6
Cl (B) - Ga (B) - Cl (B) Angle	101.3						101.3
Cl (B) - Ga (B) - Cl (BBra) Angle	104.7	104.7					104.7
Cl (B) - Ga (B) - Cl (TB) Angle	114	114					114.0
Cl (Bbra) - Ga (B) - Cl (TB) Angle	116.5						116.5

Table A.45: Linear $[Al_4Cl_{13}]^-$ Gas Phase Distances and Angles

Measurement	1	2	3	4	5	6	Average
Al (T) - Cl (T) distance	2.12	2.12	2.12	2.12	2.12	2.12	2.12
Al (T) - Cl (B) Distance	2.36	2.36					2.36
Al (B) - Cl (TB) distance	2.1	2.09	2.1	2.09			2.10
Al (B) - Cl (B) distance	2.24	2.24					2.24
Al (B) - Cl (BB) Distance	2.3	2.3					2.30
Cl (T) - Al (T) - Cl (B) angle	101.6	101.8	104.1	101.6	101.8	104.1	102.5
Cl (T) - Al (T) - Cl (T) angle	114.8	115.7	115.7	114.8	115.7	115.7	115.4
Al (T) - Cl (B) - Al (B) Angle	107.9	108					108.0
Cl (B) - Al (B) - Cl (BB) Angle	95.4	95.4					95.4
Al (B) - Cl (BB) - Al (B) Angle	107.7						107.7
Cl (B) - Al (B) - Cl (TB) Angle	110.4	111.1	110.4	111.1			110.8
Cl (BB) - Al (B) - Cl (TB) Angle	107.5	106	107.5	106			106.8
Cl (TB) - Al (B) - Cl (TB) Angle	122.7	122.7					122.7

Table A.46: Linear $[Ga_4Cl_{13}]^-$ Gas Phase Distances and Angles

Measurement	1	2	3	4	5	6	Average
Ga (T) - Cl (T) distance	2.17	2.17	2.17	2.17	2.17	2.17	2.17
Ga (T) - Cl (B) Distance	2.45	2.45					2.45
Ga (B) - Cl (TB) distance	2.14	2.15	2.14	2.15			2.15
Ga (B) - Cl (B) distance	2.3	2.3					2.30
Ga (B) - Cl (BB) Distance	2.36	2.36					2.36
Cl (T) - Ga (T) - Cl (B) angle	103.2	101.7	99.8	103.2	101.7	99.8	101.6
Cl (T) - Ga (T) - Cl (T) angle	116.1	116.5	115.6	116.1	116.5	115.6	116.1
Ga (T) - Cl (B) - Ga (B) Angle	106.3	106.3					106.3
Cl (B) - Ga (B) - Cl (BB) Angle	95.5	95.5					95.5
Ga (B) - Cl (BB) - Ga (B) Angle	106.3						106.3
Cl (B) - Ga (B) - Cl (TB) Angle	110.2	111.2	110.1	111.2			110.7
Cl (BB) - Ga (B) - Cl (TB) Angle	107.2	104.9	107.2	104.9			106.1
Cl (TB) - Ga (B) - Cl (TB) Angle	123.8	123.8					123.8

A.1.4 Optimized Liquid Phase Anion Structures

Table A.47: Evaluated monometallic chlorometallate species in solution

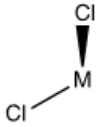
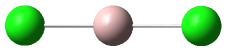
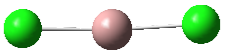
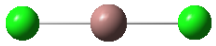
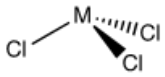
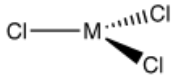
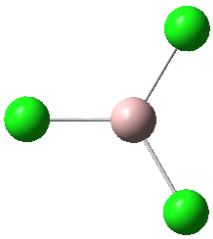
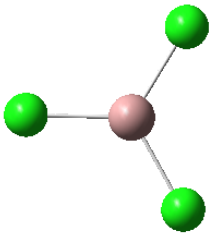
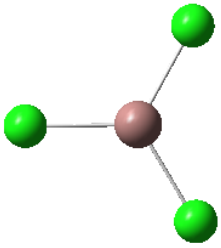
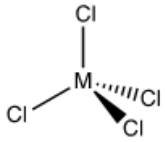
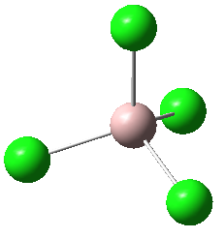
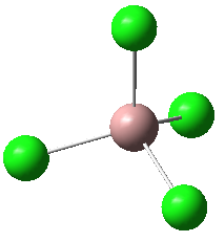
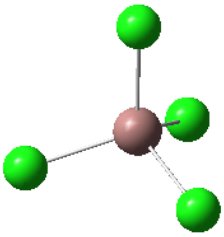
Starting structure	$AlCl_3 - Cl$	$GaCl_3 - Cl$	$InCl_3 - Cl$
Cl—M			
(01)$[MCl]^{2+}$	$[AlCl]^{2+}$	$[GaCl]^{2+}$	$[InCl]^{2+}$
	Converged to (3)	Represented in (3)	Converges to (3)
(02)$[MCl_2]^{+}$		$[GaCl_2]^{+}$	
Cl—M—Cl			
(03)$[MCl_2]^{+}$	$[AlCl_2]^{+}$	$[GaCl_2]^{+}$	$[InCl_2]^{+}$
	Converged to (05)	Converged to (05)	Converged to (05)
(04)MCl_3			
			
(05)MCl_3	$AlCl_3$	$GaCl_3$	$InCl_3$
			
(06)$[MCl_4]^{-}$	$[AlCl_4]^{-}$ {65}	$[GaCl_4]^{-}$	$[InCl_4]^{-}$ {65}
	TS structure [2]	TS structure [2]	TS structure [2]
(07)$[MCl_4]^{-}$			

Table A.48: Evaluated monometallic chlorometallate species in solution continued

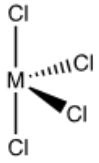
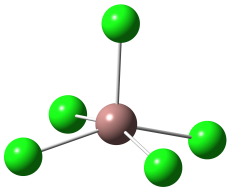
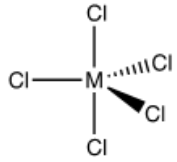
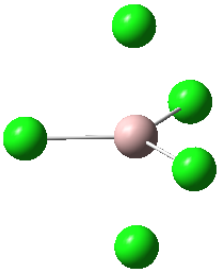
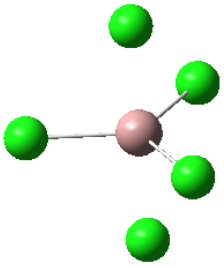
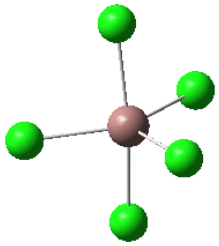
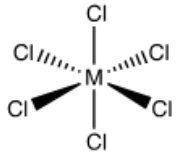
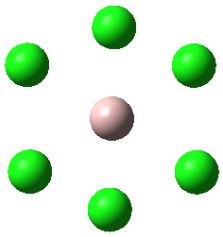
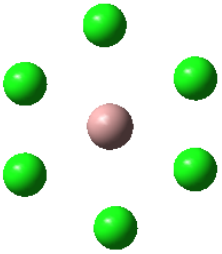
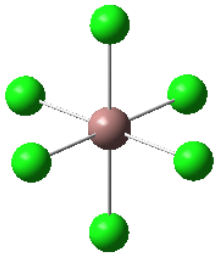
	Represented in (06)	Converged to (6)	Represented in (06)
(65)$[MCl_4]^-$	$[AlCl_4]^-$		$[InCl_4]^-$
	TS structure [1]	TS structure [1]	
(08)$[MCl_5]^{2-}$			$[InCl_5]^{2-}$ (3)
			
(09)$[MCl_5]^{2-}$	$[AlCl_5]^{2-}$	$[GaCl_5]^{2-}$	$[InCl_5]^{2-}$
			
(10)$[MCl_6]^{3-}$	$[AlCl_6]^{3-}$	$[GaCl_6]^{3-}$	$[InCl_6]^{3-}$

Table A.49: Evaluated dimetallic chlorometallate species in solution

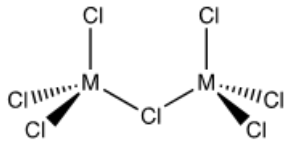
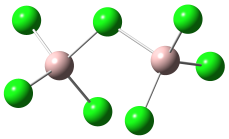
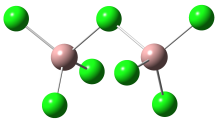
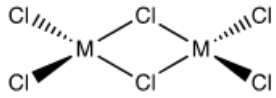
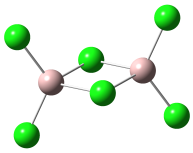
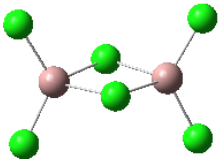
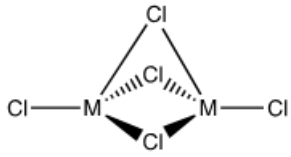
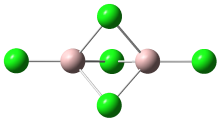
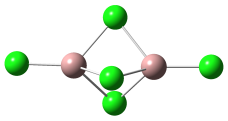
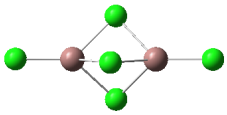
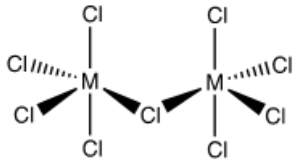
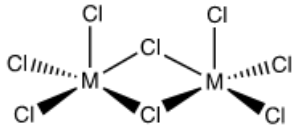
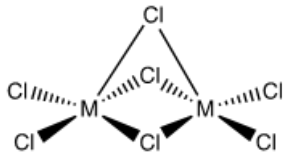
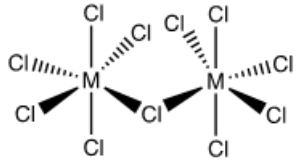
Starting structure	$AlCl_3 - Cl$	$GaCl_3 - Cl$	$InCl_3 - Cl$
			TS structure [3]
(11)$[M_2Cl_7]^-$	$[Al_2Cl_7]^-$ {42}	$[Ga_2Cl_7]^-$	
			TS structure [1]
(12)M_2Cl_6	Al_2Cl_6 {49} (0)	Ga_2Cl_6	
			
(13)$[M_2Cl_5]^+$	$[Al_2Cl_5]^+$ (203.8)	$[Ga_2Cl_5]^+$ (21.9)	$[In_2Cl_5]^+$ (9.2)
	Structure dissociates	Structure dissociates	Structure dissociates
(14)$[M_2Cl_9]^{3-}$			
	Converges to (64)	Structure dissociates	Converges to (64)
(15)$[M_2Cl_8]^{2-}$			
	Converges to (11)	Converges to (11)	Converges to (11)
(16)$[M_2Cl_7]^-$			
	Structure dissociates	Structure dissociates	Structure dissociates
(17)$[M_2Cl_{11}]^{5-}$			

Table A.50: Evaluated dimetallic chlorometallate species in solution continued I

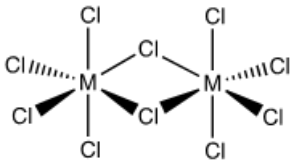
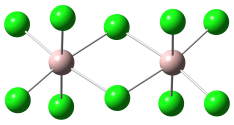
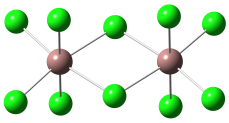
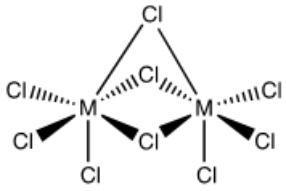
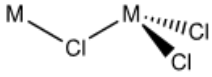
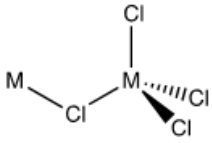
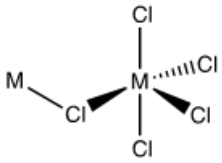
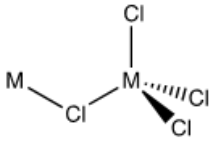
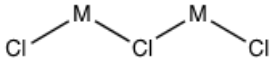
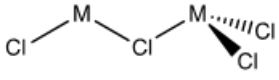
		Structure dissociates	
(18)$[M_2Cl_{10}]^{4-}$	$[Al_2Cl_{10}]^{4-}$		$[In_2Cl_{10}]^{4-}$
	Structure dissociates	Structure dissociates	Structure dissociates
(19)$[M_2Cl_9]^{3-}$			
	Structure dissociates	Structure dissociates	Structure dissociates
(31)$[M_2Cl_3]^{3+}$			
	Structure dissociates	Structure dissociates	Structure dissociates
(32)$[M_2Cl_4]^{2+}$			
	Converges to (51)	Structure dissociates	Structure dissociates
(33)$[M_2Cl_5]^{+}$			
	Converges to (12)	Converges to (12)	Converges to (12)
(34)M_2Cl_6			
	TS structure [1]	Structure dissociates	TS structure [1]
(35)$[M_2Cl_3]^{3+}$			
	Structure dissociates	Structure dissociates	Structure dissociates
(36)$[M_2Cl_4]^{2+}$			

Table A.51: Evaluated dimetallic chlorometallate species in solution continued II

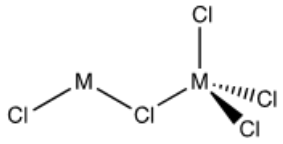
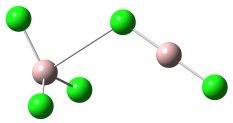
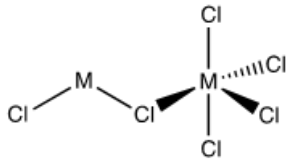
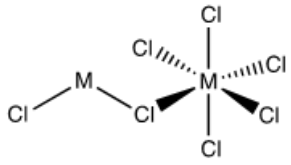
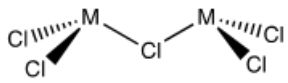
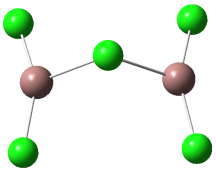
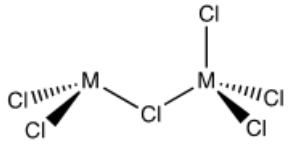
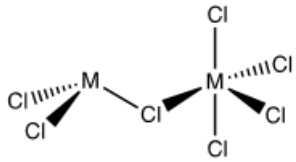
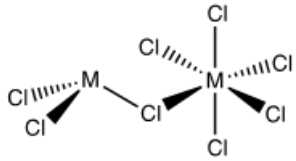
 (37)$[M_2Cl_5]^+$	 $[Al_2Cl_5]^+$ [Low 1] (109)	Structure dissociates	Structure dissociates
 (38)M_2Cl_6	Structure dissociates	Structure dissociates	Structure dissociates
 (39)$[M_2Cl_7]^-$	Converges to (11)	Converges to (11)	Converges to (11)
 (40)$[M_2Cl_5]^+$	TS structure [3]	TS structure [3]	 $[In_2Cl_5]^+$ (8.6)
 (41)M_2Cl_6	Structure dissociates	TS structure [2]	TS structure [3]
 (42)$[M_2Cl_7]^-$	represented in (11) $[Al_2Cl_7]^-$	Converged to (11)	Converges to (11)
 (43)$[M_2Cl_8]^{2-}$	Structure dissociates	Structure dissociates	Structure dissociates

Table A.52: Evaluated dimetallic chlorometallate species in solution continued III

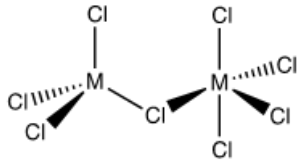
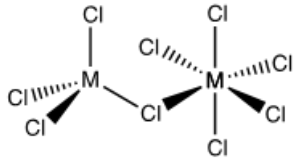
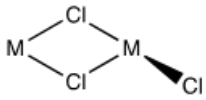
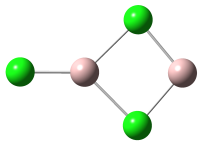
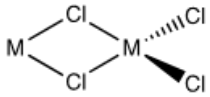
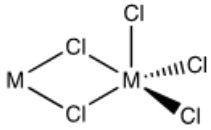
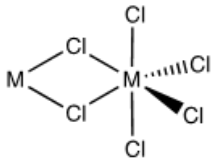
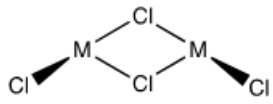
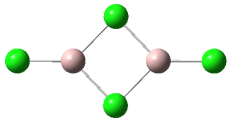
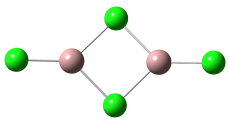
	Structure dissociates	Structure dissociates	Structure dissociates
(44)$[M_2Cl_8]^{2-}$			
	Structure dissociates	Structure dissociates	Converges to (64)
(45)$[M_2Cl_9]^{3-}$			
		Structure dissociates	Structure dissociates
(46)$[M_2Cl_3]^{3+}$	$[Al_2Cl_3]^{3+}$ (0)		
	Structure dissociates	Structure dissociates	Structure dissociates
(47)$[M_2Cl_4]^{2+}$			
	Converges to (40)	Converges to (51)	Structure dissociates
(48)$[M_2Cl_5]^{+}$			
	Converged to (12)	Converges to (12)	Converges to (12)
(49)M_2Cl_6			
			TS structure [2]
(50)$[M_2Cl_4]^{2+}$	$[Al_2Cl_4]^{2+}$	$[Ga_2Cl_4]^{2+}$	

Table A.53: Evaluated dimetallic chlorometallate species in solution continued IV

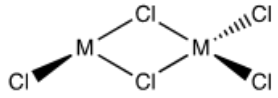
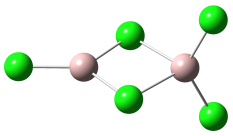
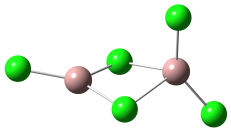
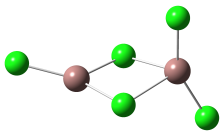
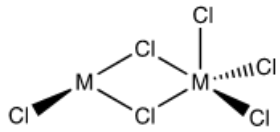
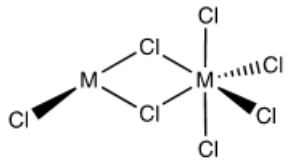
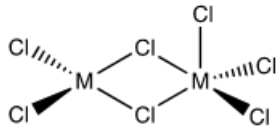
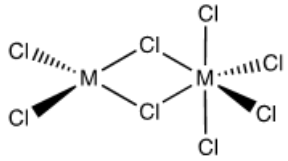
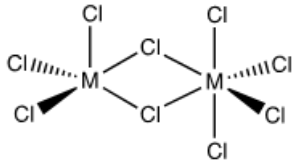
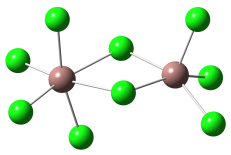
 (51)$[M_2Cl_5]^+$	 $[Al_2Cl_5]^+$ (0)	 $[Ga_2Cl_5]^+$ {59} (0)	 $[In_2Cl_5]^+$ {59} (0)
 (52)M_2Cl_6	Converges to (12)	Converges to (12)	Structure dissociates
 (53)$[M_2Cl_7]^-$	Converges to (12)	Converges to (11)	Converges to (11) [Low 1]
 (54)$[M_2Cl_7]^-$	Converges to (11)	Converges to (11)	Converges to (11)
 (55)$[M_2Cl_8]^{2-}$	Structure dissociates	Structure dissociates	Structure dissociates
 (56)$[M_2Cl_9]^{3-}$	Converges to (64)	Structure dissociates	 $[In_2Cl_9]^{3-}$

Table A.54: Evaluated dimetallic chlorometallate species in solution continued V

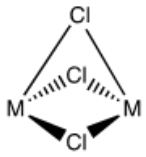
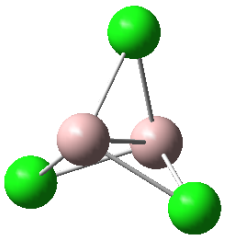
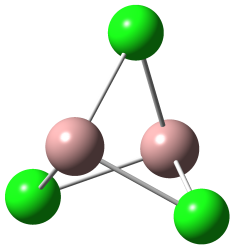
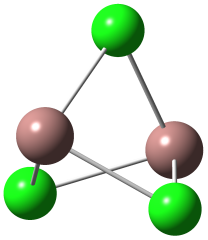
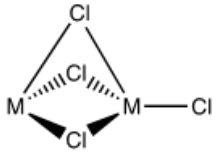
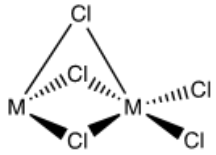
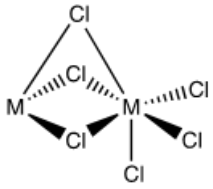
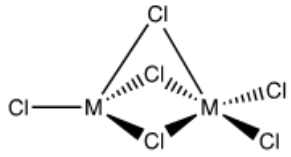
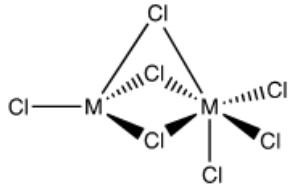
			
(57)$[M_2Cl_3]^{3+}$	$[Al_2Cl_3]^{3+}$ (68.9)	$[Ga_2Cl_3]^{3+}$ (0)	$[In_2Cl_3]^{3+}$ [Low 1]
	TS structure [1]	Structure dissociates	Structure dissociates
(58)$[M_2Cl_4]^{2+}$			
	Converges to (51)	Represented in (51)	Represented in (51)
(59)$[M_2Cl_5]^{+}$		$[Ga_2Cl_5]^{+}$	$[In_2Cl_5]^{+}$
	Structure dissociates	Structure dissociates	Structure dissociates
(60)M_2Cl_6			
	Structure dissociates	Structure dissociates	TS structure [1]
(61)M_2Cl_6			
	Converges to (11)	Converges to (11)	Converges to (11)
(62)$[M_2Cl_7]^{-}$			

Table A.55: Evaluated dimetallic chlorometallate species in solution continued VI

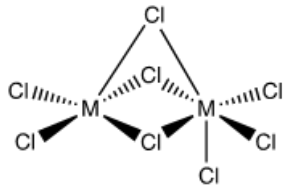
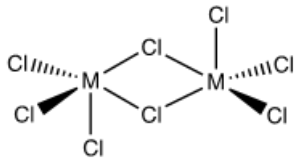
 (63)$[M_2Cl_8]^{2-}$	Structure dissociates	Structure dissociates	Structure dissociates
 (64)$[M_2Cl_8]^{2-}$	TS structure [3]	TS structure [2]	TS structure [3]

Table A.56: Evaluated trimetallic chlorometallate species in solution

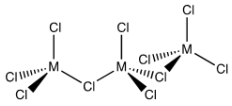
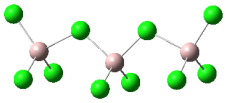
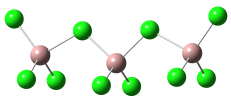
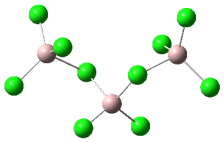
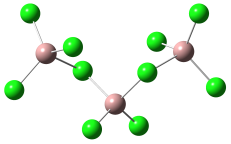
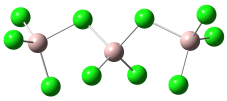
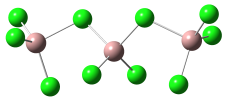
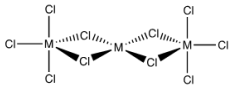
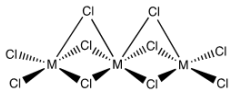
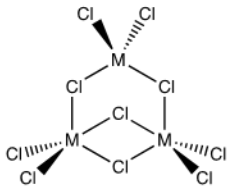
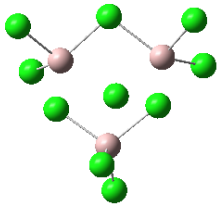
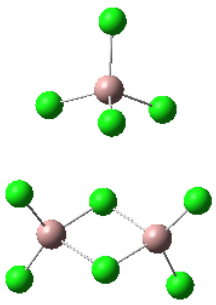
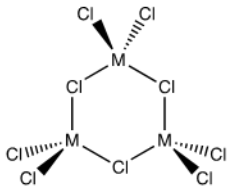
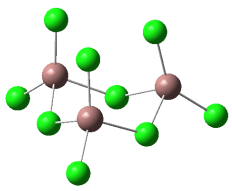
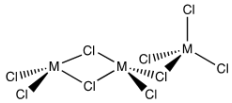
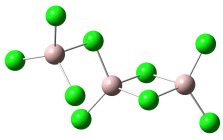
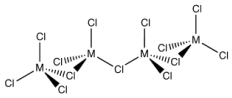
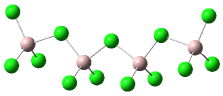
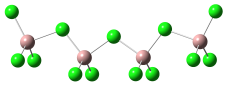
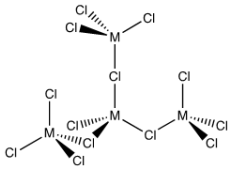
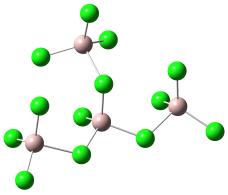
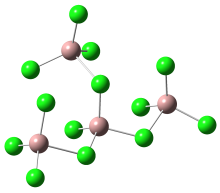
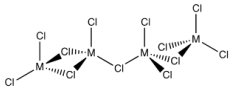
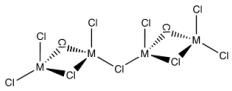
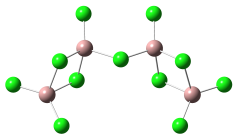
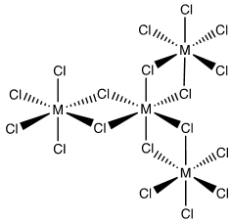
Starting structure	$AlCl_3 - Cl$	$GaCl_3 - Cl$	$InCl_3 - Cl$
			TS structure [4]
(20)$[M_3Cl_{10}]^-$	$[Al_3Cl_{10}]^-$ [Low 2] (22.4)	$[Ga_3Cl_{10}]^-$ (11.4)	
			
	$[Al_3Cl_{10}]^-$ {21} (0)	$[Ga_3Cl_{10}]^-$ [Low 1] {21} (0)	
			
	$[Al_3Cl_{10}]^-$ {22} (3.8)	$[Ga_3Cl_{10}]^-$ {22} (4.6)	
	Represented in (20)	Represented in (20)	TS structure [2]
(21)$[M_3Cl_{10}]^-$			
	Represented in (20)	Represented in (20)	Structure dissociates
(22)$[M_3Cl_{10}]^-$			
			Structure dissociates
(23)$[M_3Cl_{10}]^-$	$[Al_3Cl_{10}]^-$ [Low 1]	$[Ga_3Cl_{10}]^-$	
	Structure dissociates	Structure dissociates	
(24)M_3Cl_9			In_3Cl_9
		Structure dissociates	Structure dissociates
(25)M_3Cl_9	Al_3Cl_9		

Table A.57: Evaluated Tetrametallic chlorometallate species in solution

Starting structure	$AlCl_3 - Cl$	$GaCl_3 - Cl$	$InCl_3 - Cl$
			TS structure [7]
(26)$[M_4Cl_{13}]^-$	$[Al_4Cl_{13}]^-$ [Low 2] (20.2)	$[Ga_4Cl_{13}]^-$ [Low 5] (21.3)	
			TS structure [3]
(27)$[M_4Cl_{13}]^-$	$[Al_4Cl_{13}]^-$ (0)	$[Ga_4Cl_{13}]^-$ [Low 2] (0)	
	Structure dissociates	Structure dissociates	Structure dissociates
(28)M_4Cl_{12}			
	TS structure [1]		TS structure [2]
(29)$[M_4Cl_{11}]^-$		$[Ga_4Cl_{11}]^+$ [Low 1]	
	Structure dissociates	Structure dissociates	Structure dissociates
(30)$[M_4Cl_{18}]^{6-}$			

A.1.5 Gas Phase structure Gibbs Free Energy Comparisons

Table A.58: $[M_4Cl_{13}]^-$ comparison I

Metal	$[M_4Cl_{13}]^-$	$M_4Cl_{12} + Cl^-$	$[M_4Cl_{11}]^+ + 2Cl^-$	$[M_3Cl_{10}]^- + MCl_3$	$[M_2Cl_7]^- + 2MCl_3$
Al	6.8	212.0	456.3	22.8	57.1
Ga	0.0	N/A	439.5	2.9	11.2
In	5.5	188.0	356.8	0.0	3.4

Table A.59: $[M_4Cl_{13}]^-$ comparison II

Metal	$[MCl_4]^- + 3MCl_3$	$M_3Cl_9 + [MCl_4]^-$	$[M_2Cl_7]^- + M_2Cl_6$	$[M_2Cl_8]^{2-} + [M_2Cl_5]^+$
Al	103.4	29.6	0.0	396.9
Ga	30.0	29.5	11.2	N/A
In	15.6	20.5	5.3	162.7

Table A.60: $[M_4Cl_{13}]^-$ comparison III

Metal	$[M_2Cl_9]^{3-} + [M_2Cl_4]^{2+}$	$[M_2Cl_{10}]^{4-} + [M_2Cl_3]^{3+}$
Al	865.8	1608.3
Ga	660.2	1222.1
In	474.8	924.9

Table A.61: M_4Cl_{12} comparison I

Metal	M_4Cl_{12}	$[M_4Cl_{11}]^+ + Cl^-$	$M_3Cl_9 + MCl_3$	$[M_3Cl_{10}]^- + [MCl_2]^+$	$2M_2Cl_6$
Al	46.1	290.4	40.3	213.8	0.0
Ga	N/A	269.3	0.0	92.3	0.5
In	45.5	214.3	2.2	66.9	0.0

Table A.62: M_4Cl_{12} comparison II

Metal	$[M_2Cl_7]^- + [M_2Cl_5]^+$	$[M_2Cl_8]^{2-} + [M_2Cl_4]^{2+}$	$[M_2Cl_9]^{3-} + [M_2Cl_3]^{3+}$
Al	168.9	663.9	1331.9
Ga	112.5	N/A	924.2
In	82.1	297.6	708.2

Table A.63: M_4Cl_{11} comparison I

Metal	$[M_4Cl_{11}]^+$	$M_3Cl_9 + [MCl_2]^+$	$[M_3Cl_{10}]^- + MCl_3$	$2M_2Cl_6 + [M_2Cl_5]^+$
Al	0.0	106.9	582.6	44.5
Ga	9.6	0.0	309.8	12.5
In	2.2	0.0	216.1	7.8

Table A.64: M_4Cl_{11} comparison II

Metal	$[M_2Cl_7]^- + [M_2Cl_4]^{2+}$	$[M_2Cl_8]^{2-} + [M_2Cl_3]^{3+}$
Al	311.6	1005.5
Ga	198.0	N/A
In	147.9	461.9

Table A.65: M_3Cl_{10} comparison I

Metal	$[M_3Cl_{10}]^-$	$M_3Cl_9 + Cl^-$	$[M_2Cl_{10}]^{4-} + M^{3+}$	$[M_2Cl_9]^{2-} + [MCl]^{2+}$	$[M_2Cl_8]^{2-} + [MCl_2]^+$
Al	0.0	183.4	2270.9	1148.3	453.2
Ga	0.0	167.3	1532.2	777.2	N/A
In	0.0	145.2	1076.9	546.9	151.4

Table A.66: M_3Cl_{10} comparison II

Metal	$[M_2Cl_7]^- + MCl_3$	$M_2Cl_6 + [MCl_4]^-$	$[M_2Cl_5]^+ + [MCl_5]^{2-}$	$[M_2Cl_4]^{2+} + [MCl_6]^{3-}$	$[MCl_4]^- + 2MCl_3$
Al	34.3	23.5	434.4	972.1	80.6
Ga	8.2	27.1	364.2	802.8	27.1
In	3.9	17.0	261.1	595.5	15.6

Table A.67: M_3Cl_9 comparison I

Metal	M_3Cl_9	$[M_2Cl_9]^{3-} + M^{3+}$	$[M_2Cl_8]^{2-} + [MCl]^{2+}$	$[M_2Cl_7]^- + [MCl_2]^+$
Al	0.0	1977.0	928.9	207.8
Ga	0.0	1237.2	N/A	100.5
In	0.0	861.6	371.1	72.2

Table A.68: M_3Cl_9 comparison II

Metal	$M_2Cl_6 + MCl_3$	$[M_2Cl_5]^+ + [MCl_4]^-$	$[M_2Cl_4]^{2+} + [MCl_5]^{2-}$	$[M_2Cl_3]^{3+} + [MCl_6]^{3-}$
Al	16.8	175.0	684.0	1420.6
Ga	0.5	131.3	542.1	1069.8
In	0.0	95.2	397.3	830.3

Table A.69: M_2Cl_{10} comparison I

Metal	$[M_2Cl_{10}]^{4-}$	$[M_2Cl_9]^{3-} + Cl^-$	$[M_2Cl_8]^{2-} + 2Cl^-$	$[M_2Cl_7]^- + 3Cl^-$	$M_2Cl_6 + 4Cl^-$
Al	208.4	98.0	62.0	0.0	165.9
Ga	159.8	32.2	N/A	0.0	159.7
In	109.9	36.3	2.1	64.5	202.2

Table A.70: M_2Cl_{10} comparison II

Metal	$[M_2Cl_5]^+ + 5Cl^-$	$[M_2Cl_4]^{2+} + 6Cl^-$	$[M_2Cl_3]^{3+} + 7Cl^-$	$2[MCl_5]^{2-}$	$[MCl_6]^{3-} + [MCl_4]^-$
Al	500.8	933.8	1565.8	21.7	50.3
Ga	431.2	776.4	1210.8	9.2	37.0
In	422.1	700.0	1076.3	0.0	32.3

Table A.71: M_2Cl_9 comparison

Metal	$[M_2Cl_9]^{3-}$	$[MCl_5]^{2-} + [MCl_4]^-$	$[MCl_6]^{3-} + MCl_3$
Al	152.3	0.0	281.4
Ga	88.6	0.0	234.2
In	60.5	0.0	181.2

Table A.72: M_2Cl_8 comparison

Metal	$[M_2Cl_8]^{2-}$	$2[MCl_4]^-$	$[MCl_5]^{2-} + MCl_3$	$[MCl_6]^{3-} + [MCl_2]^+$
Al	192.3	0.0	252.7	714.3
Ga	-	0.0	206.4	559.4
In	50.5	0.0	148.9	415.4

Table A.73: M_2Cl_7 comparison

Metal	$[M_2Cl_7]^-$	$[MCl_4]^- + MCl_3$	$[MCl_5]^{2-} + [MCl_2]^+$	$[MCl_6]^{3-} + [MCl]^{2+}$
Al	0.0	46.4	479.3	1243.1
Ga	0.0	18.8	344.0	914.6
In	0.0	11.7	246.6	663.7

Table A.74: M_2Cl_6 comparison

Metal	M_2Cl_6	$2MCl_3$	$[MCl_4]^- + [MCl_2]^+$	$[MCl_5]^{2-} + [MCl]^{2+}$	$[MCl_6]^{3-} + M^{3+}$
Al	0.0	57.1	237.3	972.5	2089.3
Ga	0.0	0.0	118.8	661.5	1382.3
In	1.4	0.0	85.3	470.8	983.7

Table A.75: M_2Cl_5 comparison

Metal	$[M_2Cl_5]^+$	$MCl_3 + [MCl_2]^+$	$[MCl_4]^- + [MCl]^{2+}$	$[MCl_5]^{2-} + M^{3+}$
Al	0.0	79.2	561.6	1649.8
Ga	12.0	0.0	336.4	1029.3
In	11.4	0.0	236.6	717.9

Table A.76: M_2Cl_4 comparison

Metal	$[M_2Cl_4]^{2+}$	$2[MCl_2]^+$	$MCl_3 + [MCl]^{2+}$	$[MCl_4]^- + M^{3+}$
Al	0.0	3.1	305.3	1140.7
Ga	97.6	0.0	217.5	704.1
In	79.3	0.0	151.4	483.0

Table A.77: M_2Cl_3 comparison

Metal	$[M_2Cl_3]^{3+}$	$[MCl_2]^+ + [MCl]^{2+}$	$MCl_3 + M^{3+}$
Al	0.0	30.3	685.5
Ga	54.8	0.0	367.7
In	94.4	0.0	246.4

Table A.78: M_3Cl_9 comparison I

Metal	$[MCl_6]^{3-}$	$[MCl_5]^{2-} + Cl^-$	$[MCl_4]^- + 2Cl^-$	$MCl_3 + 3Cl^-$
Al	180.7	76.0	0.0	176.7
Ga	159.0	65.6	0.0	140.8
In	80.8	24.2	0.0	124.7

Table A.79: M_3Cl_9 comparison II

Metal	$[MCl_2]^+ + 4Cl^-$	$[MCl]^{2+} + 5Cl^-$	$M^{3+} + 6Cl^-$
Al	533.6	1192.8	2204.9
Ga	400.4	877.5	1504.9
In	334.6	695.9	1152.2

A.1.6 selected Liquid Phase Structures Structural Data

Table A.80: $[AlCl_4]^-$ Liquid Phase Distances and Angles

Al-Cl distance	2.16
Cl-Al-Cl Angles	109.4

Table A.81: $[GaCl_4]^-$ Liquid Phase Distances and Angles

Ga-Cl distance	2.22
Cl-Ga-Cl Angles	109.5

Table A.82: $[InCl_4]^-$ Liquid Phase Distances and Angles

In-Cl distance	2.38
Cl-In-Cl Angles	109.5

Table A.83: $[InCl_5]^{2-}$ Liquid Phase Distances and Angles

In-Cl distance (axial)	2.52
In-Cl distance (equitorial)	2.47
In-Cl-distance (eq2)	2.43
Cl-In-Cl Eq-Eq Angle	109
Cl-In-Cl Eq-Eq Angle 2	142
Cl-In-Cl Ax-Eq Angle	88.2
Cl-In-Cl Ax-Eq Angle 2	95.6
Cl-In-Cl Ax-Ax Angle	168.8

Table A.84: $[InCl_6]^{3-}$ Liquid Phase Distances and Angles

In-Cl distance	2.56
Cl-In-Cl Angles	90

Table A.85: $[Al_2Cl_7]^-$ Liquid Phase Distances and Angles

Measurement	1	2	3	4	5	6	Average
Al-Cl(T) distance	2.13	2.13	2.13	2.13	2.13	2.13	2.13
Al-Cl(B) distance	2.3	2.3					2.30
Cl(T)-Al-Cl(T) Angle	113.1	113.8	114.4	113.1	113.8	114.4	113.8
Cl(B)-Al-Cl(T) Angle	105.9	105.9	102.3	105.9	105.9	102.3	104.7
Al-Cl-Al Angle	112						112.0
Cl(T)-Al-Al-Cl(T) dihedral 1	60.4						60.4
Cl(T)-Al-Al-Cl(T) dihedral 2	-74.2						-74.2
Cl(T)-Al-Al-Cl(T) dihedral 3	172.6						172.6

Table A.86: $[Ga_2Cl_7]^-$ Liquid Phase Distances and Angles

Measurement	1	2	3	4	5	6	Average
Ga-Cl(T) distance	2.19	2.18	2.18	2.19	2.18	2.18	2.18
Ga-Cl(B) Distance	2.38	2.38					2.38
Cl(T)-Ga-Cl(T) Angle	115	113.9	114.8	115	113.9	114.8	114.6
Cl(B)-Ga-Cl(T) Angle	104.8	104.3	102.1	104.8	104.3	102.1	103.7
Ga-Cl-Ga Angle	110.9						110.9
Cl(T)-Ga-Ga-Cl(T) dihedral 1	-60.5						-60.5
Cl(T)-Ga-Ga-Cl(T) dihedral 2	73.9						73.9
Cl(T)-Ga-Ga-Cl(T) dihedral 3	-172.4						-172.4

Table A.87: $[Al_3Cl_{10}]^-$ Liquid Phase Distances and Angles

Measurement	1	2	3	4	5	6	Average
Al (T) - Cl (T) distance	2.12	2.12	2.13	2.12	2.12	2.13	2.12
Al (T) - Cl (B) distance	2.33	2.33					2.33
Al (B) - Cl (B) distance	2.24	2.24					2.24
Al (B) - Cl (TB) distance	2.11	2.11					2.11
Cl (T) - Al (T) - Cl (T) Angle	114.8	114.8	114.3	114.8	114.8	114.3	114.6
Cl (T) - Al (T) - Cl (B) Angle	104.2	105	101.4	104.2	105	101.4	103.5
Al (T) - Cl (B) - Al (B) Angle	111.3	111.3					111.3
Cl (B) - Al (B) - Cl (B) Angle	104.1						104.1
Cl (B) - Al (B) - Cl (TB) Angle	109.7	106.9	109.7	106.9			108.3
Cl (TB) - Al (B) - Cl (TB) Angle	118.6						118.6

Table A.88: $[Ga_3Cl_{10}]^-$ Liquid Phase Distances and Angles

Measurement	1	2	3	4	5	6	Average
Ga (T) - Cl (T) distance	2.18	2.18	2.18	2.18	2.18	2.18	2.18
Ga (T) - Cl (B) distance	2.43	2.43					2.43
Ga (B) - Cl (B) distance	2.31	2.31					2.31
Ga (B) - Cl (TB) distance	2.16	2.16					2.16
Cl (T) - Ga (T) - Cl (T) Angle	115.4	116.7	115.2	115.4	116.7	115.2	115.8
Cl (T) - Ga (T) - Cl (B) Angle	103.4	102.4	100.3	103.4	102.4	100.3	102.0
Ga (T) - Cl (B) - Ga (B) Angle	110.7	110.7					110.7
Cl (B) - Ga (B) - Cl (B) Angle	101.6						101.6
Cl (B) - Ga (B) - Cl (TB) Angle	109.4	106.5	109.4	106.5			108.0
Cl (TB) - Ga (B) - Cl (TB) Angle	121.5						121.5

Table A.89: Branched $[Al_4Cl_{13}]^-$ Liquid Phase Distances and Angles

Measurement	1	2	3	4	5	6	Average
Al (TLin) - Cl (T) distance	2.11	2.11	2.12	2.11	2.11	2.12	2.11
Al (TLin) - Cl (B) distance	2.39	2.39					2.39
Al (Tbra) - Cl (Tbra) distance	2.12	2.12	2.12				2.12
Al (Tbra) - Cl (Bbra) distance	2.37						2.37
Al (B) - Cl (Tbra) distance	2.21	2.21					2.21
Al (B) - Cl (Bbra) distance	2.2						2.20
Al (B) - Cl (TB) distance	2.08						2.08
Cl (T) - Al (TLin) - Cl (B) Angle	103.3	103.2	99.3	103.3	103.2	99.3	101.9
Cl (T) - Al (TLin) - Cl (T) Angle	115.5	116.2	115.7	115.5	116.2	115.7	115.8
Cl (Tbra) - Al (Tbra) - Cl (Bbra) Angle	103.3	103.3	99.6				102.1
Cl (Tbra) - Al (Tbra) - Cl (Tbra) Angle	115.6	115.6	116.1				115.8
Al (TLin) - Cl (B) - Al (B) angle	113.6	113.6					113.6
Al (Tbra) - Cl (B) - Al (B) angle	111.5						111.5
Cl (B) - Al (B) - Cl (B) Angle	100.4						100.4
Cl (B) - Al (B) - Cl (BBra) Angle	105.4	105.4					105.4
Cl (B) - Al (B) - Cl (TB) Angle	114.2	114.2					114.2
Cl (Bbra) - Al (B) - Cl (TB) Angle	115.7						115.7

Table A.90: Branched $[Ga_4Cl_{13}]^-$ Liquid Phase Distances and Angles

Measurement	1	2	3	4	5	6	Average
Ga (TLin) - Cl (T) distance	2.16	2.17	2.17	2.16	2.17	2.17	2.17
Ga (TLin) - Cl (B) distance	2.52	2.52					2.52
Ga (Tbra) - Cl (Tbra) distance	2.17	2.17	2.17				2.17
Ga (Tbra) - Cl (Bbra) distance	2.49						2.49
Ga (B) - Cl (Tbra) distance	2.26	2.26					2.26
Ga (B) - Cl (Bbra) distance	2.26						2.26
Ga (B) - Cl (TB) distance	2.14						2.14
Cl (T) - Ga (TLin) - Cl (B) Angle	101.4	101.7	97.1	101.4	101.7	97.1	100.1
Cl (T) - Ga (TLin) - Cl (T) Angle	116.7	116.6	117.7	116.7	116.6	117.7	117.0
Cl (Tbra) - Ga (Tbra) - Cl (Bbra) Angle	101.5	101.5	98				100.3
Cl (Tbra) - Ga (Tbra) - Cl (Tbra) Angle	116.9	116.9	116.8				116.9
Ga (TLin) - Cl (B) - Ga (B) Angle	111.2	111.2					111.2
Ga (Tbra) - Cl (B) - Ga (B) Angle	110.6						110.6
Cl (B) - Ga (B) - Cl (B) Angle	102.7						102.7
Cl (B) - Ga (B) - Cl (BBra) Angle	104.8	104.8					104.8
Cl (B) - Ga (B) - Cl (TB) Angle	113.7	113.7					113.7
Cl (Bbra) - Ga (B) - Cl (TB) Angle	115.8						115.8

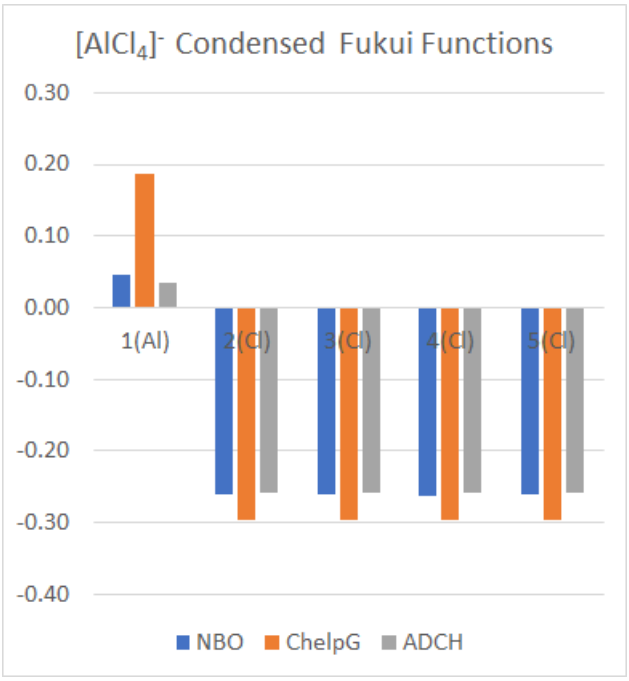
Table A.91: Linear $[Al_4Cl_{13}]^-$ Liquid Phase Distances and Angles

Measurement	1	2	3	4	5	6	Average
Al (T) - Cl (T) distance	2.12	2.12	2.12	2.12	2.12	2.12	2.12
Al (T) - Cl (B) Distance	2.36	2.36					2.36
Al (B) - Cl (TB) distance	2.1	2.1	2.1	2.1			2.10
Al (B) - Cl (B) distance	2.24	2.24					2.24
Al (B) - Cl (BB) Distance	2.28	2.28					2.28
Cl (T) - Al (T) - Cl (B) angle	99.9	104.5	104.5	99.9	104.5	104.5	103.0
Cl (T) - Al (T) - Cl (T) angle	115.3	115.3	114.9	115.3	115.3	114.9	115.2
Al (T) - Cl (B) - Al (B) Angle	113.9	113.9					113.9
Cl (B) - Al (B) - Cl (BB) Angle	96.1	96.1					96.1
Al (B) - Cl (BB) - Al (B) Angle	110.5						110.5
Cl (B) - Al (B) - Cl (TB) Angle	111.1	111.1	111.1	111.1			111.1
Cl (BB) - Al (B) - Cl (TB) Angle	108.3	108.3	108.3	108.3			108.3
Cl (TB) - Al (B) - Cl (TB) Angle	119.3	119.3					119.3

Table A.92: Linear $[Ga_4Cl_{13}]^-$ Liquid Phase Distances and Angles

Measurement	1	2	3	4	5	6	Average
Ga (T) - Cl (T) distance	2.17	2.17	2.17	2.17	2.17	2.17	2.17
Ga (T) - Cl (B) Distance	2.47	2.47					2.47
Ga (B) - Cl (TB) distance	2.15	2.15	2.15	2.15			2.15
Ga (B) - Cl (B) distance	2.29	2.29					2.29
Ga (B) - Cl (BB) Distance	2.37	2.37					2.37
Cl (T) - Ga (T) - Cl (B) angle	99.9	102.3	102.3	99.9	102.3	102.3	101.5
Cl (T) - Ga (T) - Cl (T) angle	115.9	116.2	116.2	115.9	116.2	116.2	116.1
Ga (T) - Cl (B) - Ga (B) Angle	110.3	110.3					110.3
Cl (B) - Ga (B) - Cl (BB) Angle	95.1	95.1					95.1
Ga (B) - Cl (BB) - Ga (B) Angle	112						112.0
Cl (B) - Ga (B) - Cl (TB) Angle	111.3	111.3	111.3	111.3			111.3
Cl (BB) - Ga (B) - Cl (TB) Angle	106.8	106.8	106.8	106.8			106.8
Cl (TB) - Ga (B) - Cl (TB) Angle	121.9	121.9					121.9

A.1.7 Condensed Fukui Functions



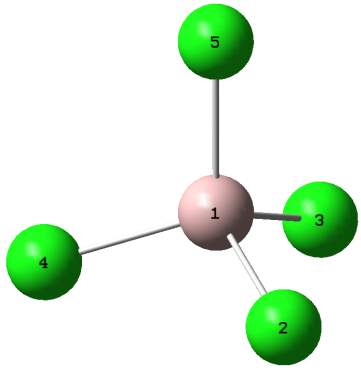
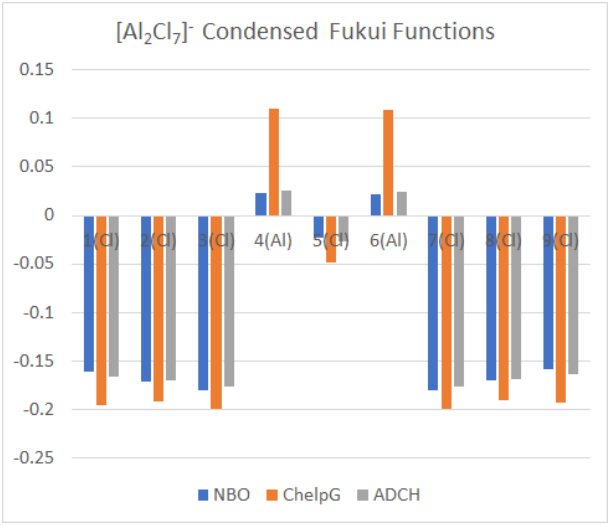


Figure A.1: $[AlCl_4]^-$ Condensed Fukui functions



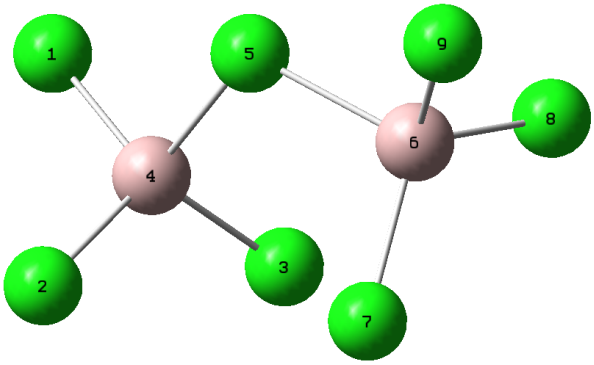


Figure A.2: $[Al_2Cl_7]^-$ Condensed Fukui functions

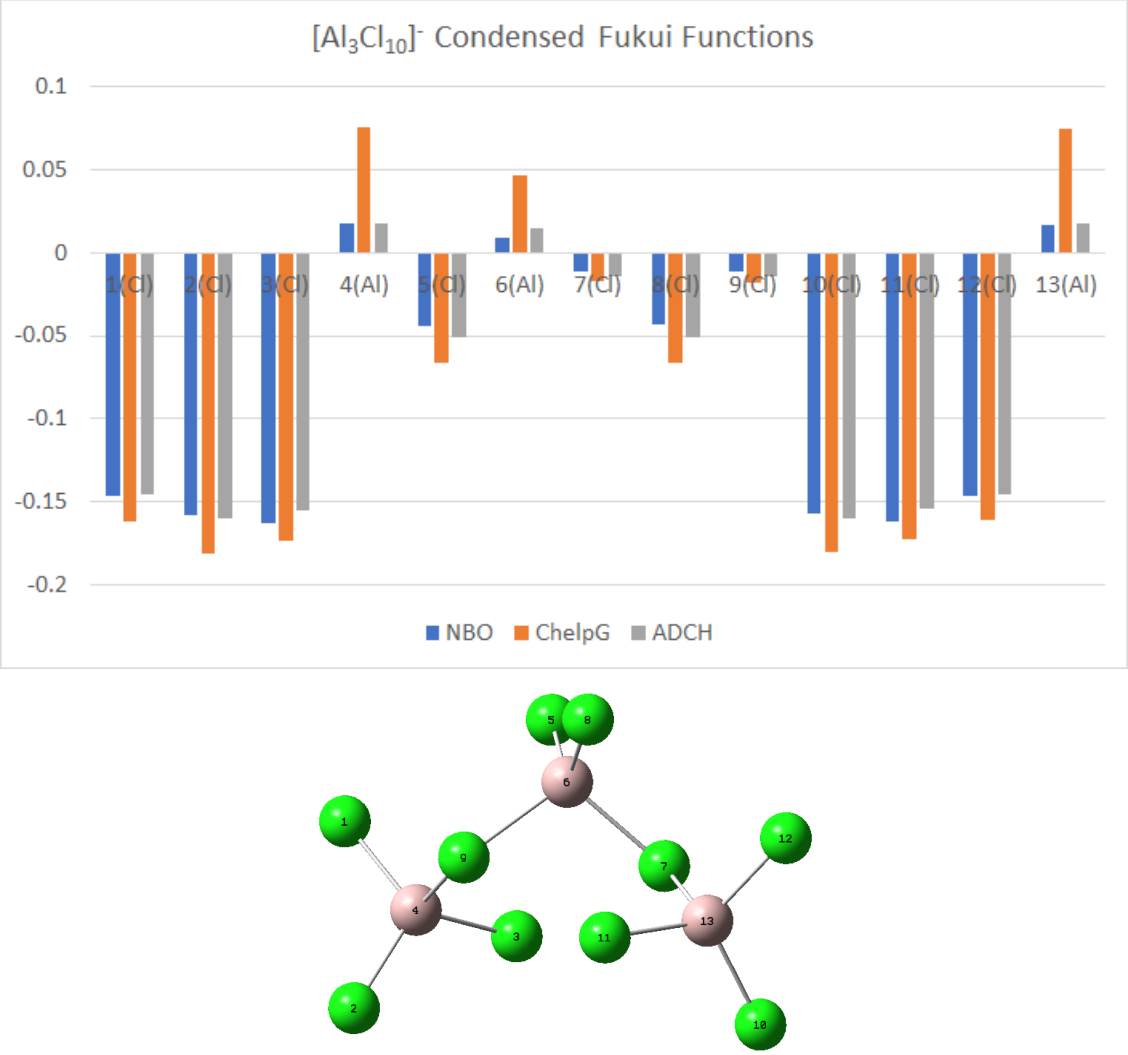


Figure A.3: $[Al_3Cl_{10}]^-$ Condensed Fukui functions

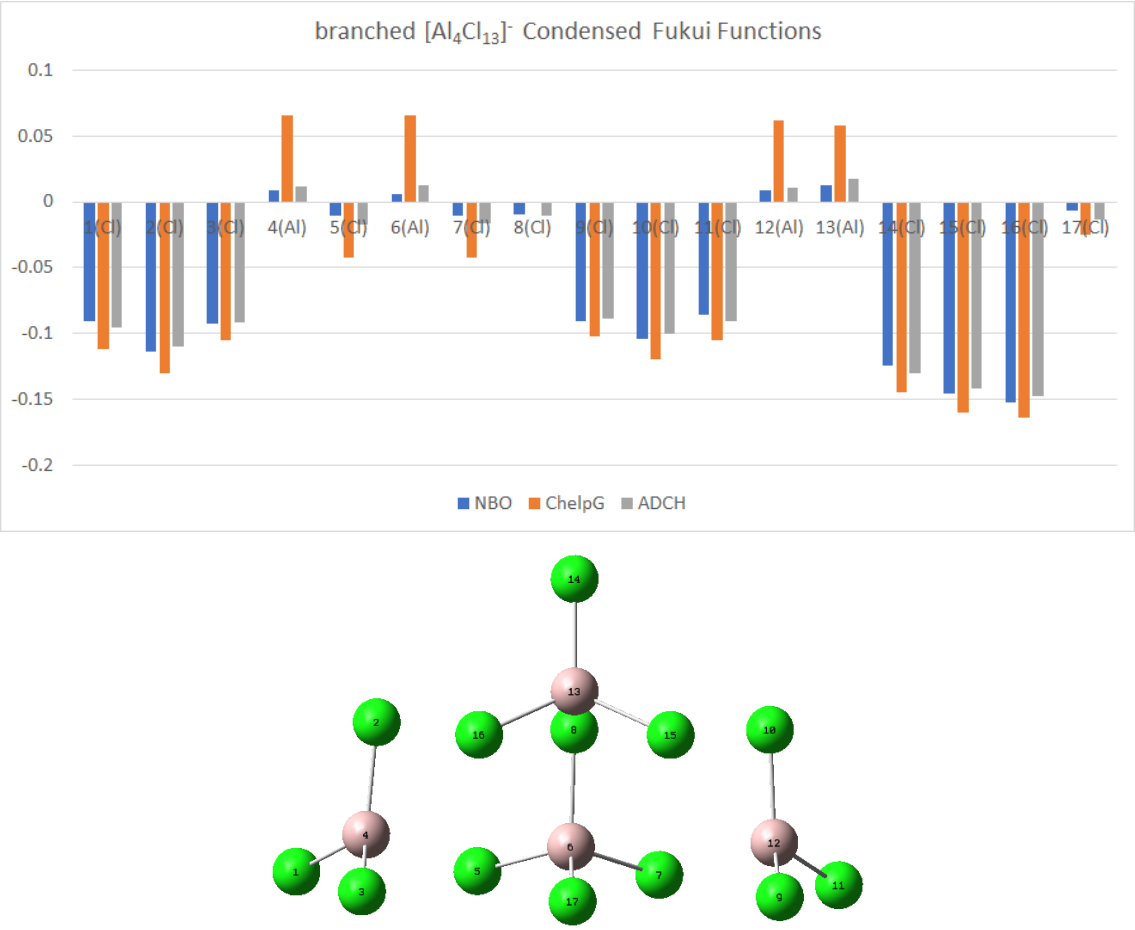


Figure A.4: Branched $[Al_4Cl_{13}]^-$ Condensed Fukui functions

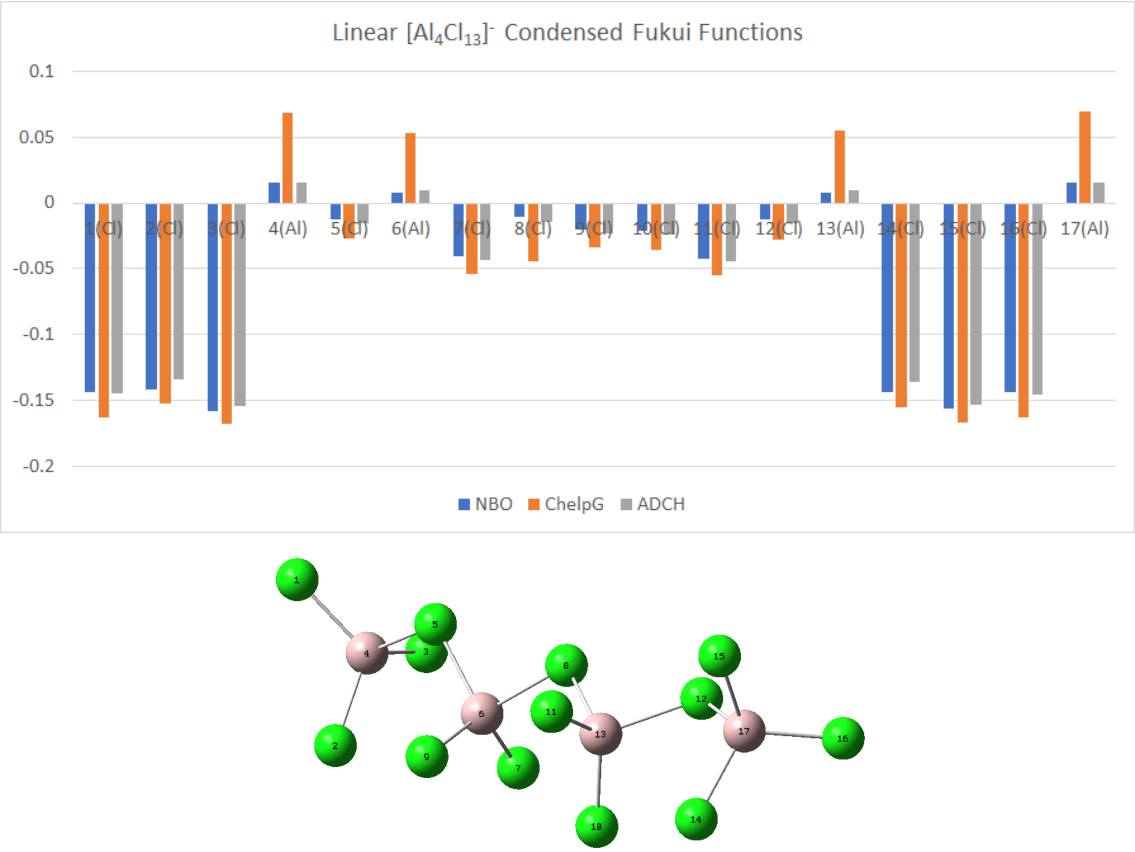


Figure A.5: Linear $[Al_4Cl_{13}]^-$ Condensed Fukui functions

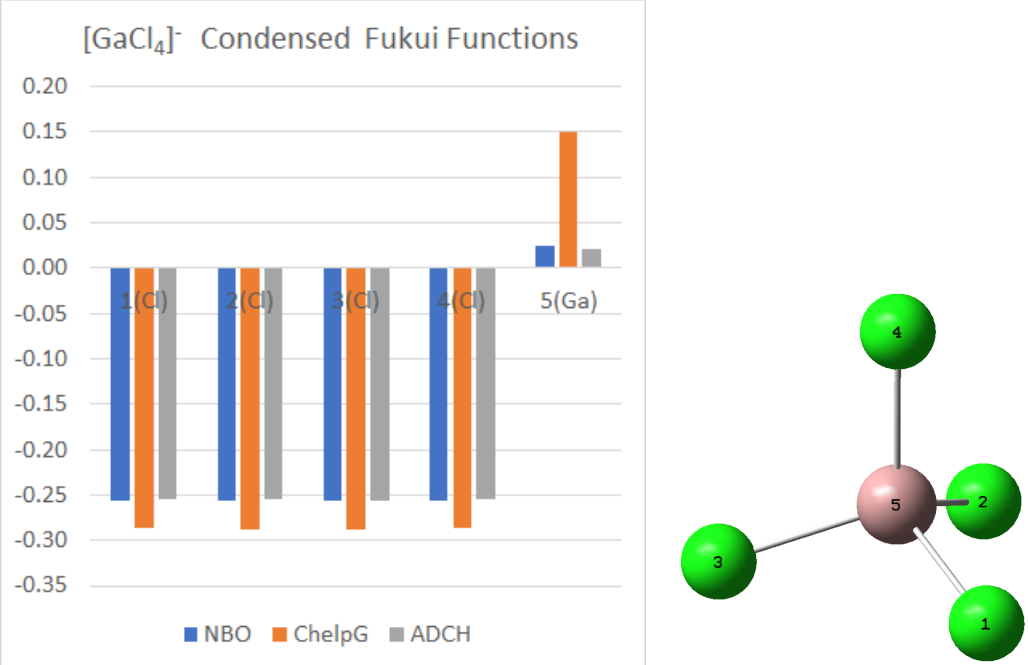


Figure A.6: $[GaCl_4]^-$ Condensed Fukui functions

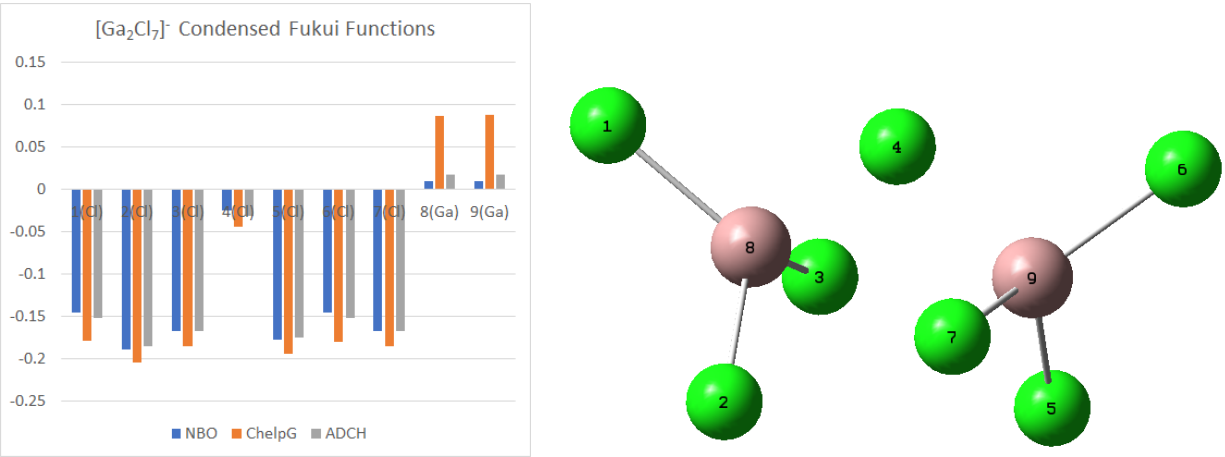


Figure A.7: $[Ga_2Cl_7]^-$ Condensed Fukui functions

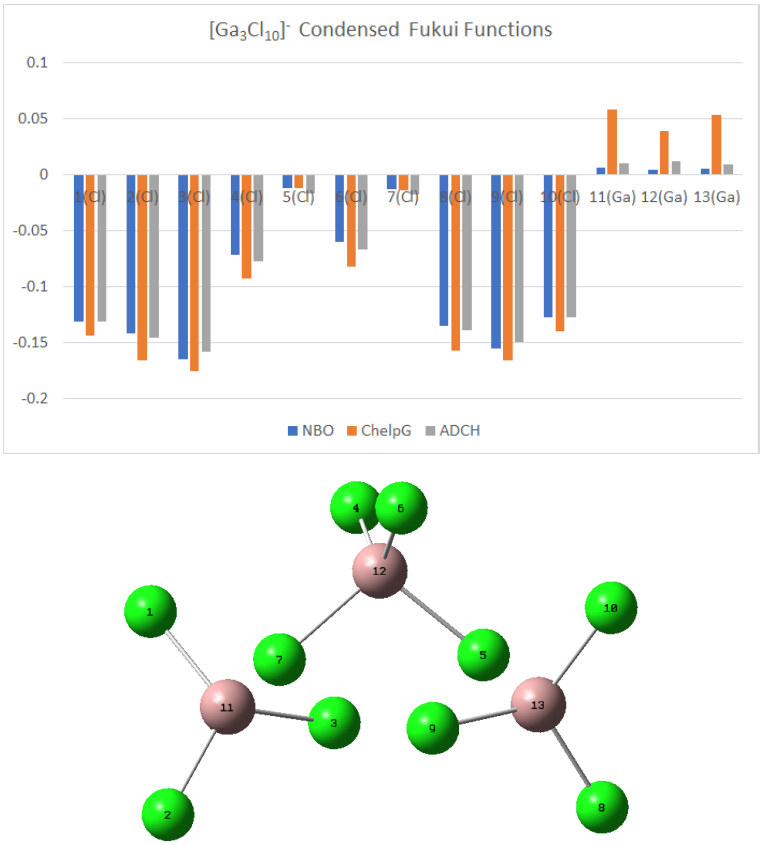


Figure A.8: $[Ga_3Cl_{10}]^-$ Condensed Fukui functions

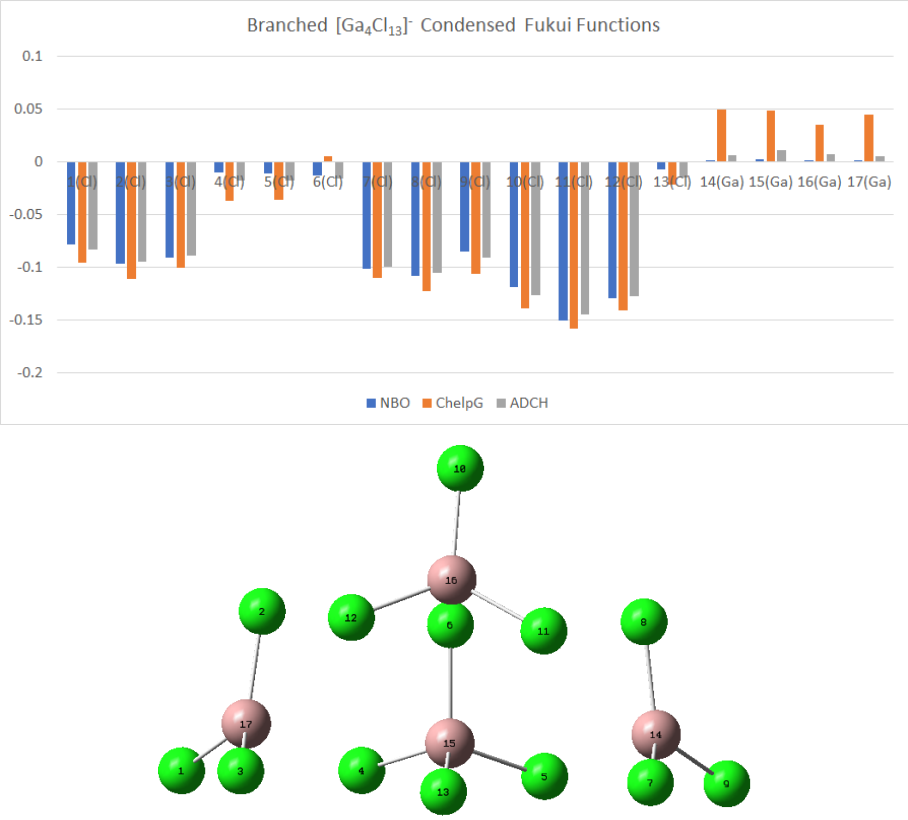


Figure A.9: Branched $[Ga_4Cl_{13}]^-$ Condensed Fukui functions

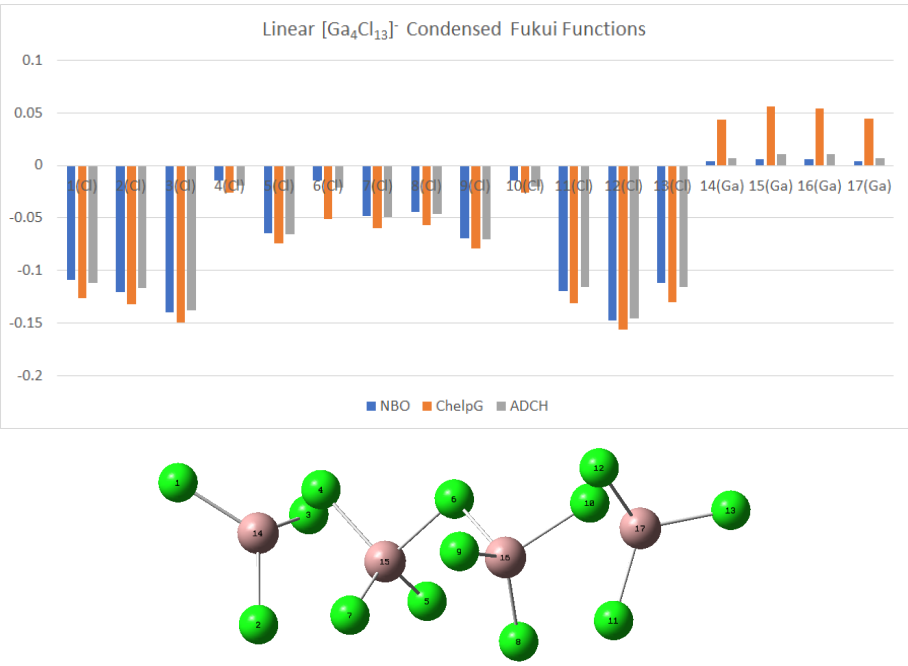


Figure A.10: Linear $[Ga_4Cl_{13}]^-$ Condensed Fukui functions

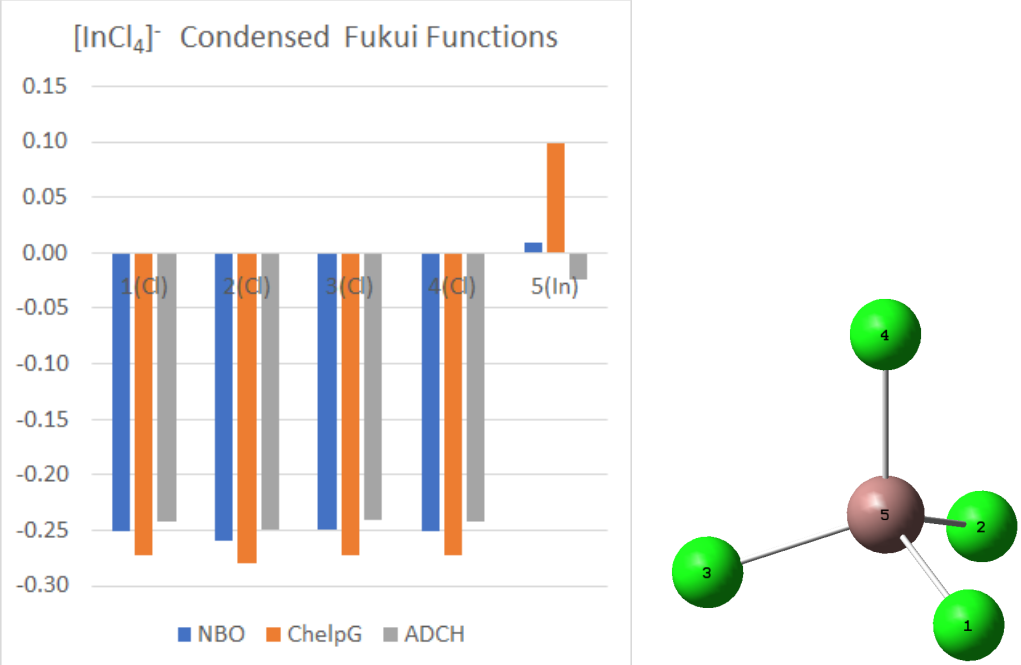


Figure A.11: $[InCl_4]^-$ Condensed Fukui functions

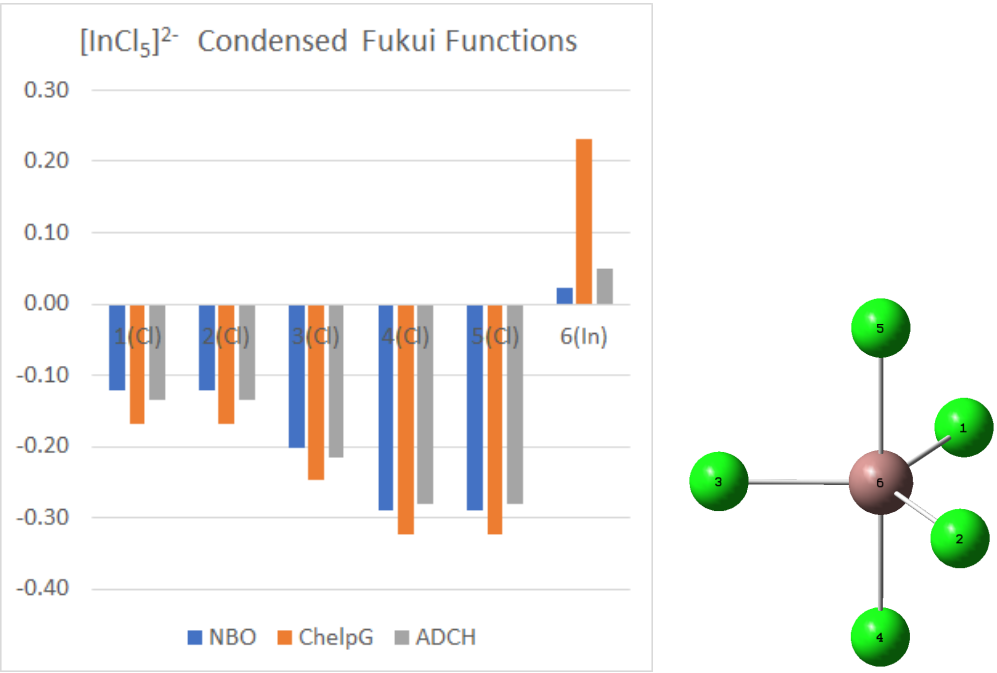


Figure A.12: $[InCl_5]^{2-}$ Condensed Fukui functions

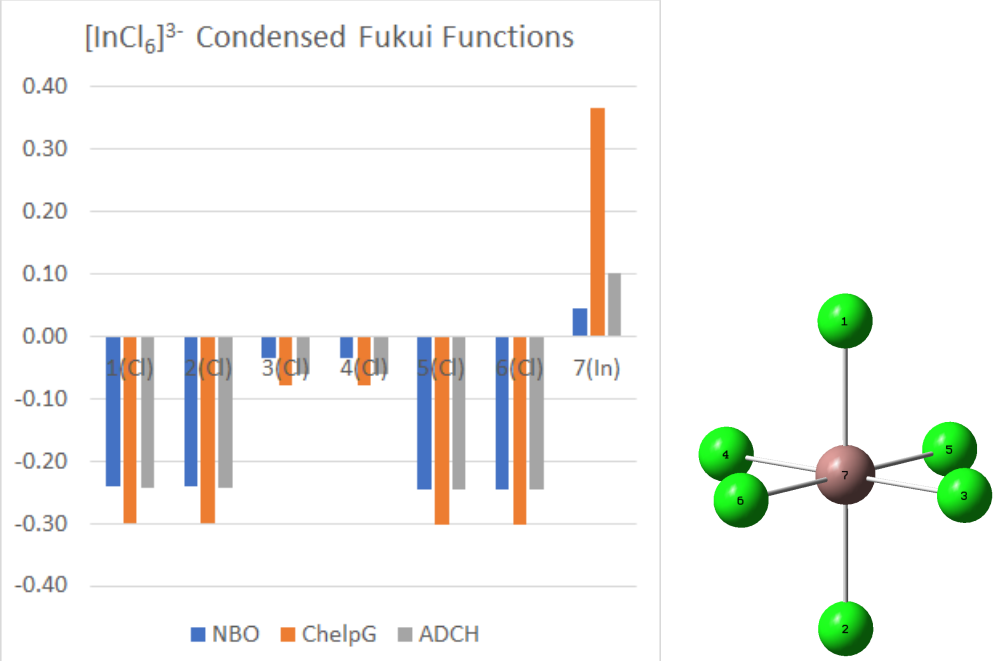


Figure A.13: $[InCl_6]^{3-}$ Condensed Fukui functions

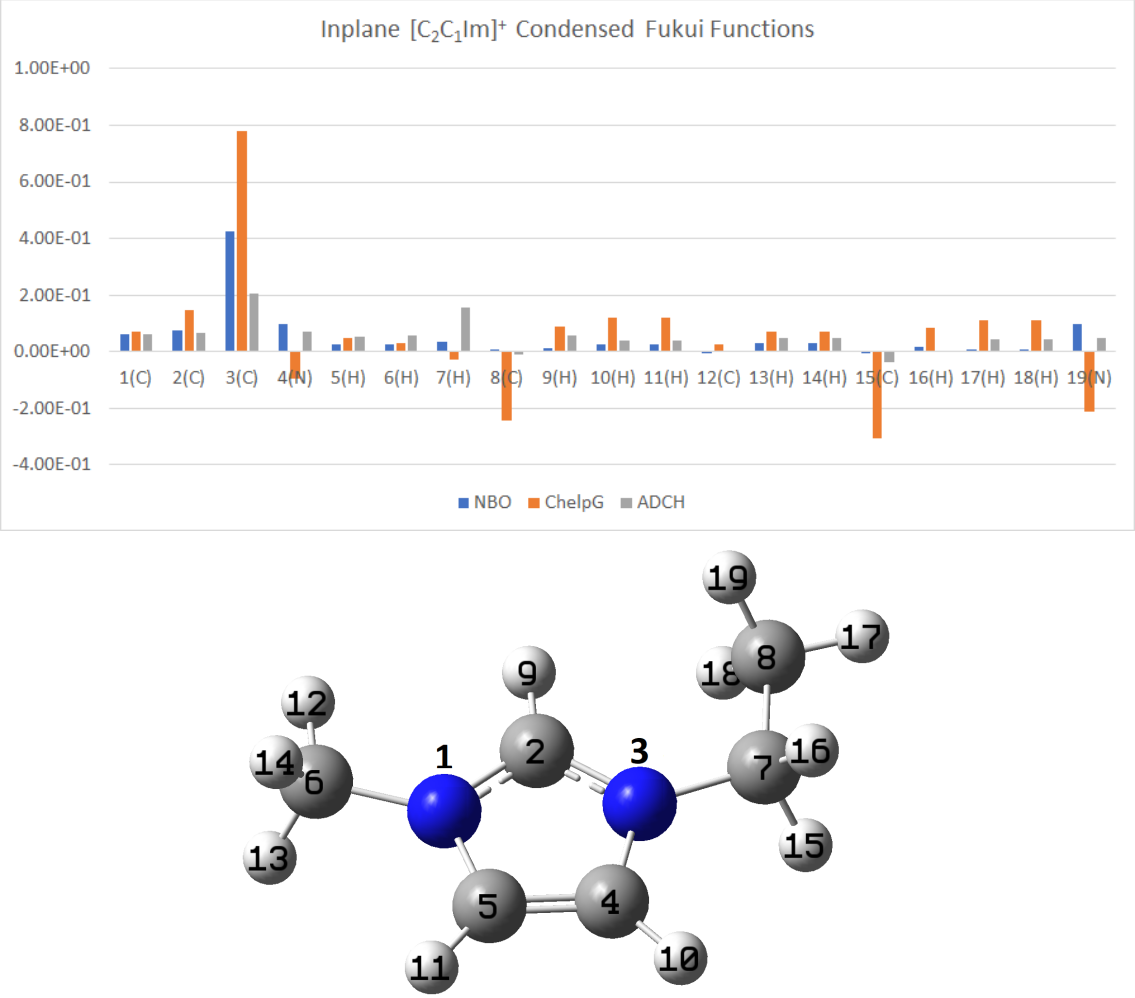


Figure A.14: $Inplane[c_2c_1Im]^+$ Condensed Fukui functions

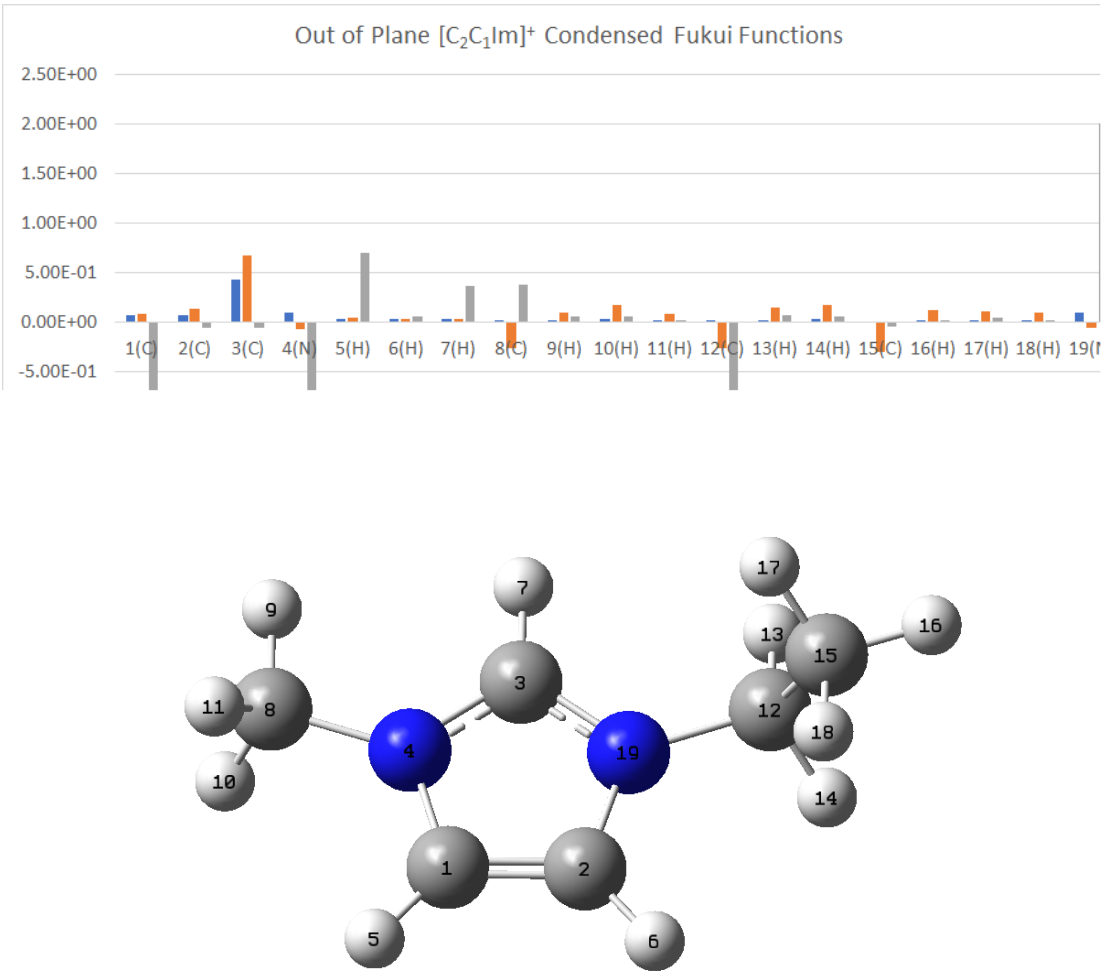


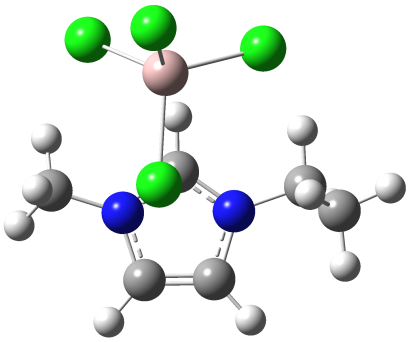
Figure A.15: Out of Plane $[c_2c_1Im]^+$ Condensed Fukui functions

A.2 $[C_2C_1Im][M_xCl_y]$ Ion pair Data

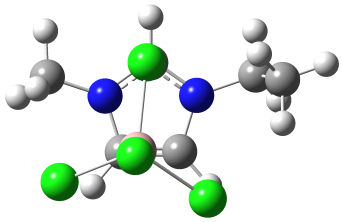
A.2.1 $[C_2C_1Im][M_xCl_y]$ Gas Ion pair structures

Table A.93: $[C_2C_1Im][AlCl_4]$ Gas Phase Ion Pair Structures

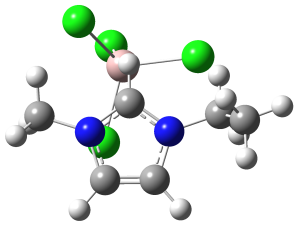
-58_3.7_122_87 (0)



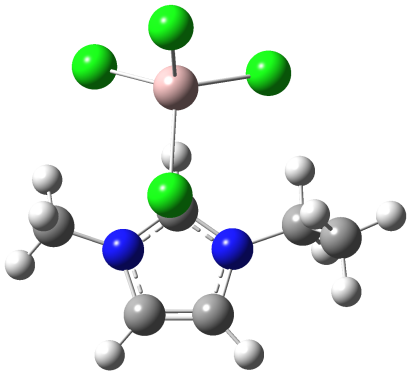
-78_4.3_64_81 (8)



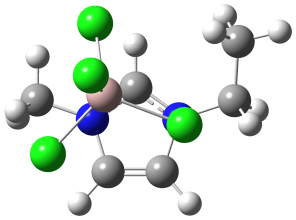
-69_3.7_112_-87 (1)



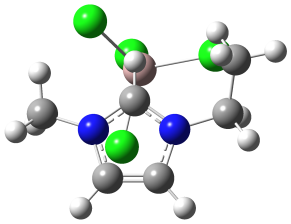
-58_3.7_122_87 (1)



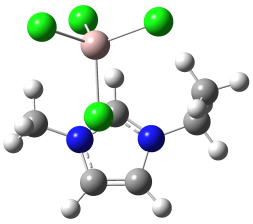
-161_3.9_83_85 (4)



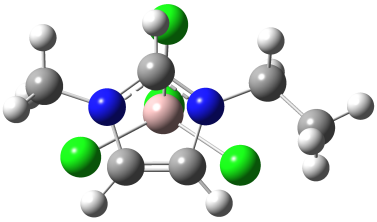
-148_3.7_115_-87 (10) [1]



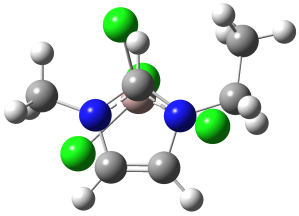
-112_4_113_82 (16) [1]



-28_4_77_-94 (7)



161_3.9_83_-85 (5)



-70_4_79_-97 (2) [fnc]

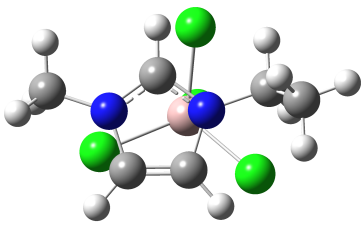
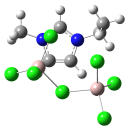


Table A.94: $[C_2C_1Im][Al_2Cl_7]$ Gas Phase Ion Pair Structures

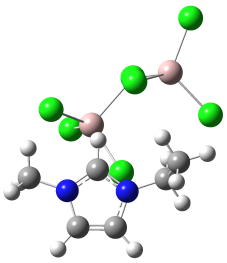
-68_6_83_-93 (20)



-108_4.9_38_98 (12)



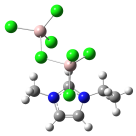
-104_5.3_135_-107 (0)



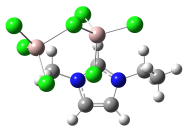
-52_3.8_102_59 (7)



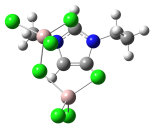
-57_4_119_54 (5)



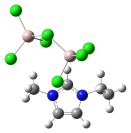
-64_5.9_110_74 (23) [1]



-63_4.5_53_59 (11)



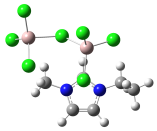
-62_5.3_133_74 (2)



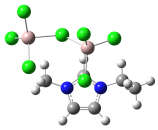
-35_5.2_132_98 (9) [1]



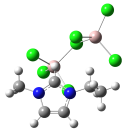
-54_3.6_135_58 (23) [1]



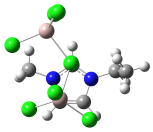
-53_3.6_134_55 (23) [1]



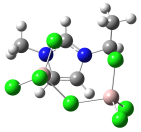
-62_5.3_126_-105 (2)



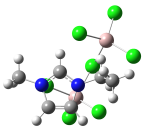
-72_3.3_85_88 (5)



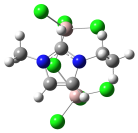
-155_4.7_43_101 (10)



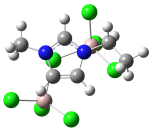
-69_5.4_97_-110 (8)



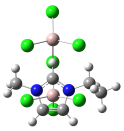
-64_3.5_73_-76 (3)



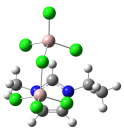
-18_3.6_72_-72 (10)



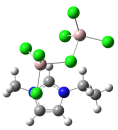
-58_5.1_98_-90 (3)



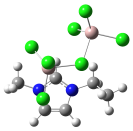
-51_5.2_96_83 (8)



-52_3.7_112_117 (2)



-52_3.7_112_116 (1)



-63_4.1_119_55 (1)

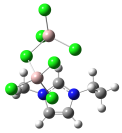
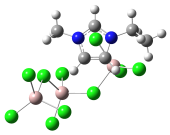
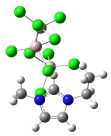


Table A.95: $[C_2C_1Im][Al_3Cl_{10}]$ Gas Phase Ion Pair Structures

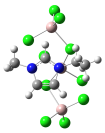
-42_6.1_51_-60 (15)



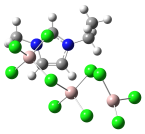
-148_4.9_157_-57 (5)



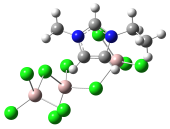
-66_5_86_-102 (11) [1]



-126_5.5_41_112 (31)



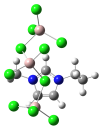
-42_6.1_51_-60 (16)



-50_3.8_98_93 (44) [1]



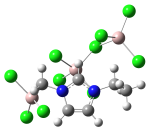
-61_4.8_97_76 (10) [1]



-113_6.1_51_119 (12)



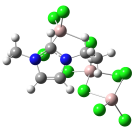
-66_4_99_-86 (13) [fnc]



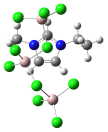
-68_6.3_96_-123 (12)



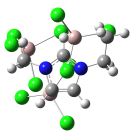
-67_5.9_74_-122 (9)



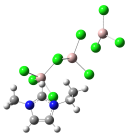
-57_5.1_61_71 (6) [fnc]



-168_6.2_96_-64 (50) [2,fnc]



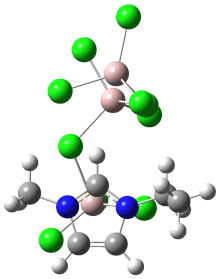
-109_4.8_137_-139 (34) [1]



-139_4.6_98_-75 (14) [1]



-78_4.8_124_-90 (0)



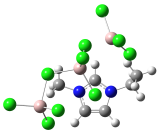
-61_3.9_145_76 (37) [1]



-68_5.9_138_111 (6)



-102_4_98_94 (27)



-64_6.9_80_98 (24)

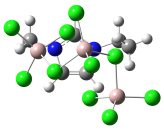
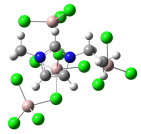
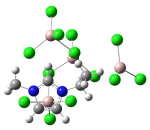


Table A.96: $[C_2C_1Im][Al_4Cl_{13}]_Bra$ Gas Phase Ion Pair Structures

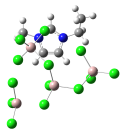
-48_5.4_66_-94 (3) [1]



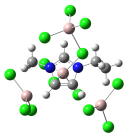
-117_5.8_105_-109 (15) [1]



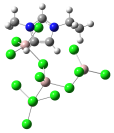
-136_6.3_33_97 (28)



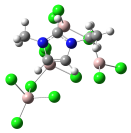
69_5.1_85_-89 (8)



-53_3.4_31_-96 (24)



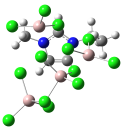
-79_5.3_71_-83 (27)



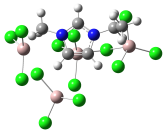
-73_5.8_51_-113 (18) [1]



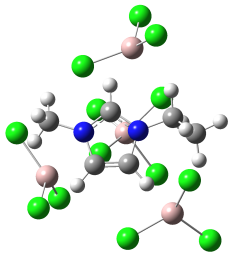
-70_5.8_61_88 (26)



-78_5.2_75_-86 (22)



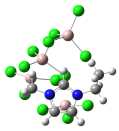
-44_4.8_87_-96 (0)



-55_5_89_-88 (18)



-134_5.3_113_-66 (21)



-133_4.9_94_-88 (19)



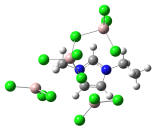
-74_4.3_100_-93 (27) [1]



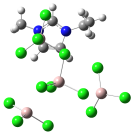
-96_5_109_-107 (28) [1]



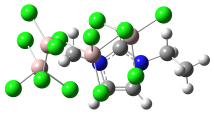
-40_4.7_91_67 (19)



-90_5.9_33_101 (21)



-37_6.9_86_76 (45) [1]



-56_5_92_83 (20)

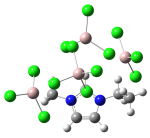
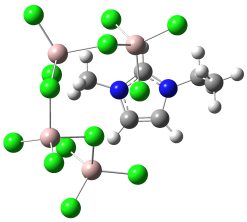
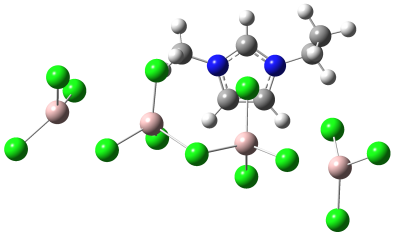


Table A.97: $[C_2C_1Im][Al_4Cl_{13}]_Lin$ Gas Phase Ion Pair Structures

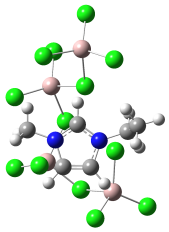
-67_8.1_85_60 (12)



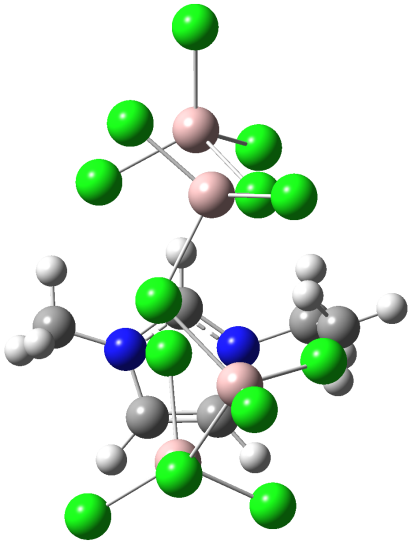
-124_6.3_61_69 (36)



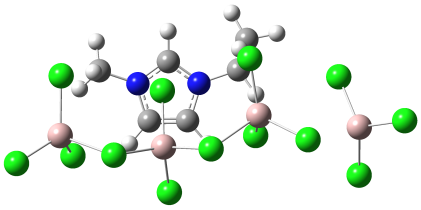
-100_5.8_86_-85 (4)



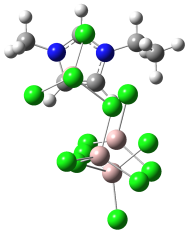
-82_6.4_97_84 (0)



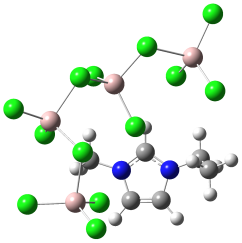
-135_6.4_64_101 (34)



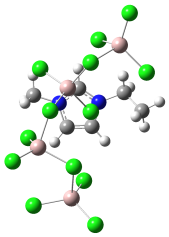
-60_5.9_14_79 (13)



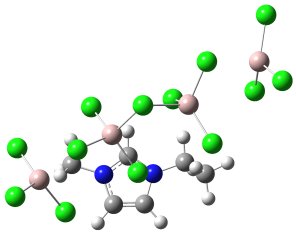
-61_6.1_124_69 (12)



-29_6.1_85_74 (13)



-55_5.7_111_93 (37) [1,fnc]



-55_5.7_109_93 (41) [1,fnc]

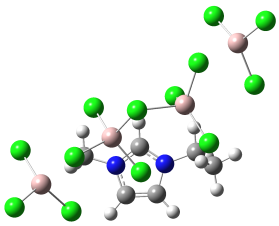
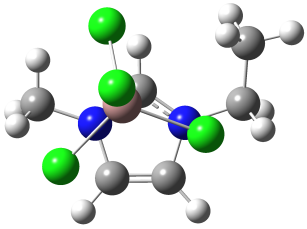
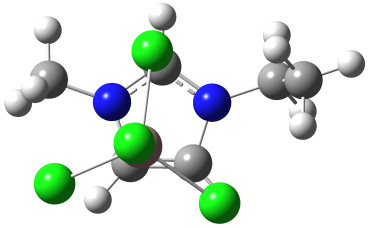


Table A.98: $[C_2C_1Im][GaCl_4]$ Gas Phase Ion Pair Structures

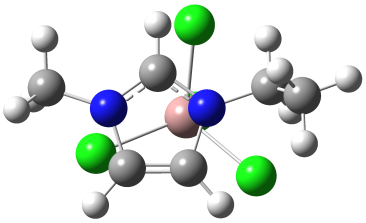
-162_3.9_85_83 (3) [fnc]



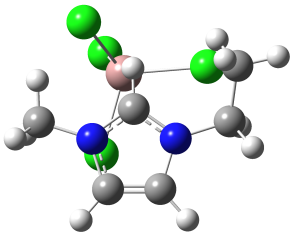
-78_4.3_64_80 (6)



-71_4_79_-97 (1)



-156_3.7_111_-87 (9) [1]



-57_3.7_120_87 (0)

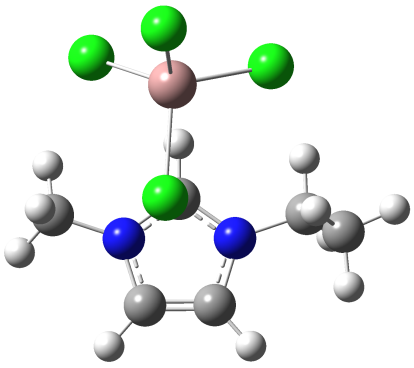
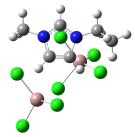
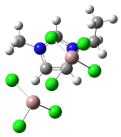


Table A.99: $[C_2C_1Im][Ga_2Cl_7]$ Gas Phase Ion Pair Structures

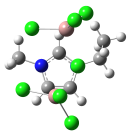
-45_6_53_-89 (8)



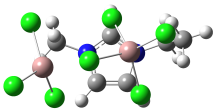
-141_6_59_87 (9) [fnc]



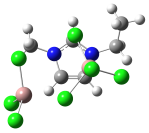
138_3.5_73_105 (2)



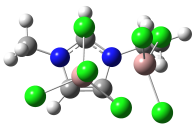
-76_6.1_72_73 (12)



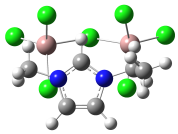
-147_4.7_43_76 (7) [fnc]



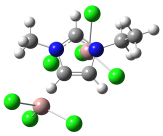
-78_6.3_72_85 (25)



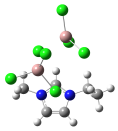
-75_5.3_105_-91 (4) [fnc]



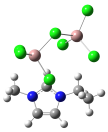
-81_3.5_75_-74 (0)



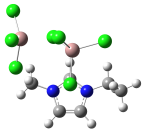
-53_3.5_130_60 (1)



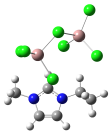
-49_5.4_137_102 (2)



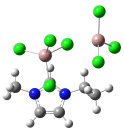
-50_5.8_109_80 (20)



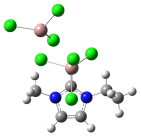
-50_5.4_138_103 (2)



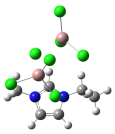
-52_3.5_137_121 (12)



-57_3.9_118_53 (2)



-53_3.5_130_60 (1)



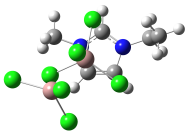
-58_5.9_110_90 (19)



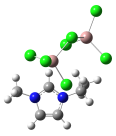
-49_5.4_137_102 (3)



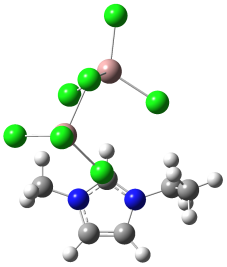
-76_6.4_72_82 (29)



105_5.4_134_107 (8) [1]



-67_5.3_127_80 (0)



57_3.6_73_107 (2)

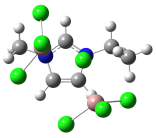
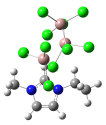


Table A.100: $[C_2C_1Im][Ga_3Cl_{10}]$ Gas Phase Ion Pair Structures

-54_4.9_156_133 (4)



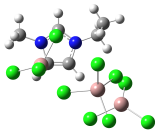
-59_4_113_100 (27)



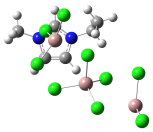
-53_4.7_97_-76 (5)



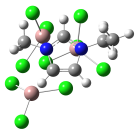
-111_6_50_120 (12)



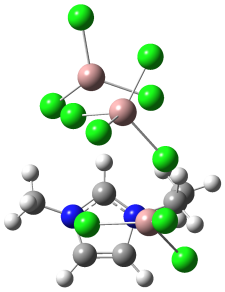
-105_5.5_46_121 (43)



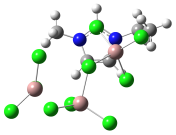
-80_9.1_72_-76 (55) [2]



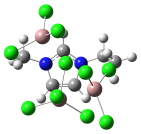
96_4.8_124_92 (0) [fnc]



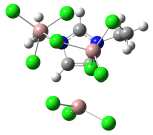
-75_7.2_45_71 (22)



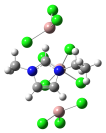
-69_4.6_55_82 (22)



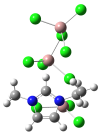
-74_6_68_105 (18)



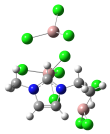
-61_4.9_91_-102 (9) [1]



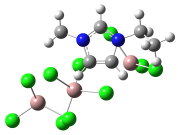
-89_4.4_127_-88 (5)



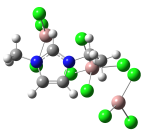
-49_4.1_99_-88 (15) [1]



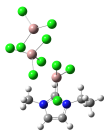
-44_6.1_50_-59 (16)



-61_5.4_80_-118 (17) [1]



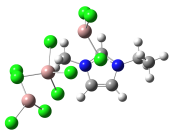
-54_4.6_141_43 (40) [1]



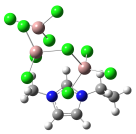
-59_5_61_71 (6)



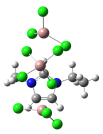
-64_6.1_75_53 (13)



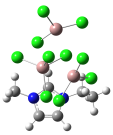
-51_5.8_111_64 (21) [1]



-60_4.8_96_76 (8) [1]



-56_3.8_105_83 (31) [1]



-42_7_126_100 (26)

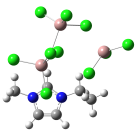
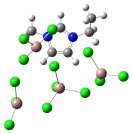
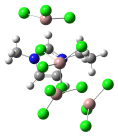


Table A.101: $[C_2C_1Im][Ga_4Cl_{13}]_Bra$ Gas Phase Ion Pair Structures

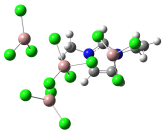
-134_6.4_32_97 (36)



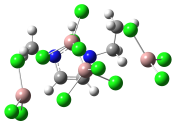
-56_5_68_100 (34)



-86_6.2_72_58 (34) [fnc]



-145_4.6_60_102 (40)



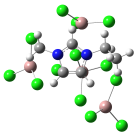
-77_5.6_105_-118 (26)



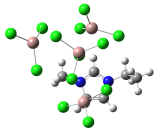
-159_6.4_31_84 (37)



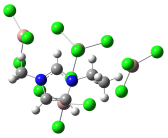
-47_5.4_66_-90 (6) [1]



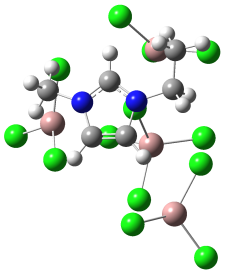
-62_5.5_98_75 (12) [fnc]



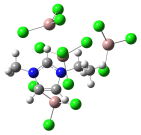
-55_5.2_110_-108 (36)



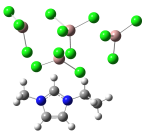
-164_5.4_68_-90 (0) [fnc]



-61_5.4_103_-104 (7)



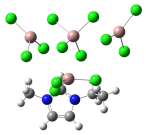
-42_5.1_163_150 (46) [1]



37_5_88_93 (27)



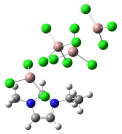
-62_5.1_133_103 (34)



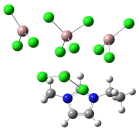
57_4.4_93_98 (16)



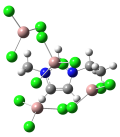
-66_5.9_129_103 (37)



-55_5_146_66 (33)



-53_5.2_83_84 (41) [1]



-59_6.5_90_110 (48)

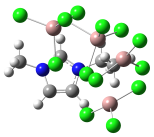
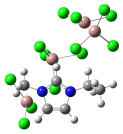


Table A.102: $[C_2C_1Im][Ga_4Cl_{13}]_Lin$ Gas Phase Ion Pair Structures

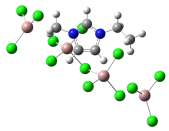
-69_4.3_121_-127 (6)



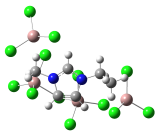
-142_8.1_87_-117 (15)



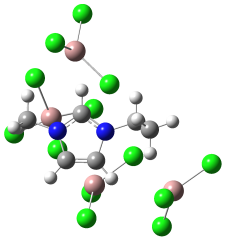
-32_6.1_55_-89 (36) [fnc]



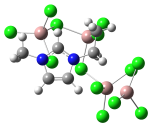
-63_6.5_61_-83 (10)



-69_3.9_63_-67 (0)



-166_6.4_81_-106 (9)



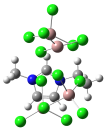
-168_6.2_76_77 (35)



-53_3.3_78_85 (5)



-57_8.1_94_97 (18) [1]

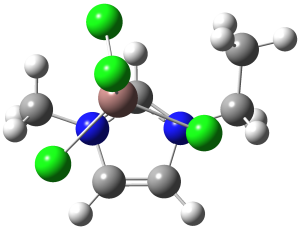


-64_8.1_87_-119 (11) [fnc]

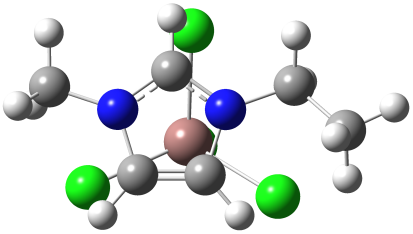


Table A.103: $[C_2C_1Im][InCl_4]$ Gas Phase Ion Pair Structures

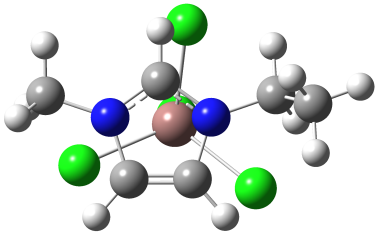
-160_4_83_83 (3) [fnc]



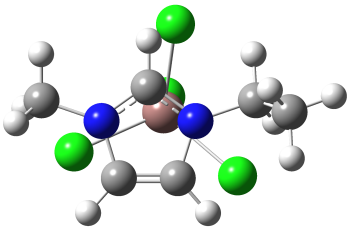
-31_4.1_73_-94 (4)



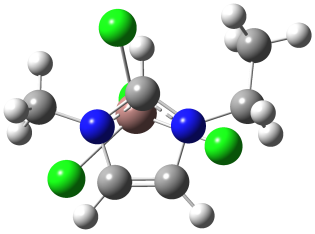
-74_4.1_78_-97 (0)



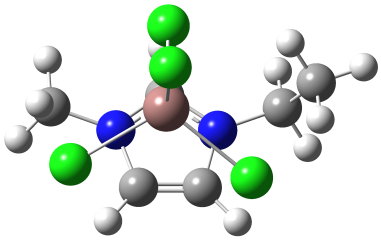
-75_4_79_-98 (1)



160_4_83_-83 (3)



-77_4.4_63_81 (5) [fnc]



56_3.8_121_87 (0)

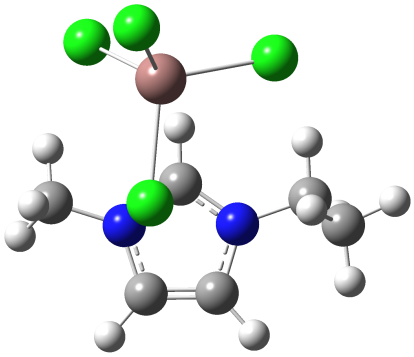
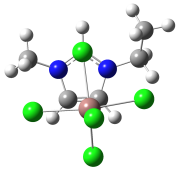
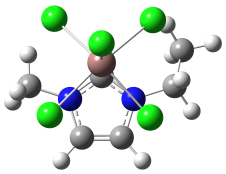


Table A.104: $[C_2C_1Im][InCl_5]^-$ Gas Phase Ion Pair Structures

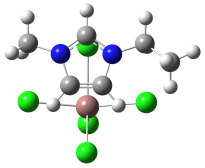
-140_4.2_43_89 (9)



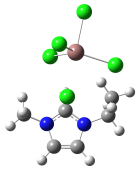
149_3.5_93_89 (5)



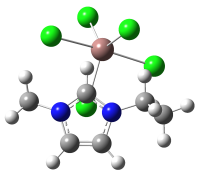
-43_4.3_52_91 (8)



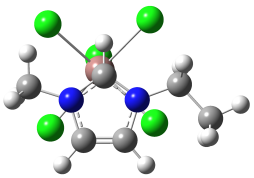
143_4.1_137_96 (14)



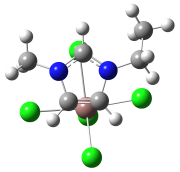
62_3.8_124_-96 (1)



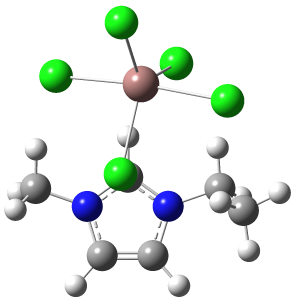
-3_3.5_95_-88 (6)



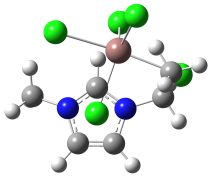
140_4.2_53_-89 (9)



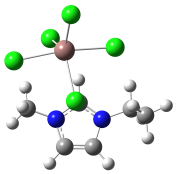
-49_3.7_129_100 (0)



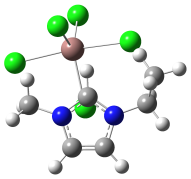
-121_3.6_118_-98 (4)



-56_3.7_124_75 (0)



-142_3.7_121_-78 (1)



-63_4.1_144_90 (12)

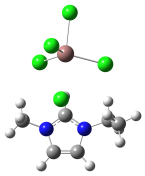
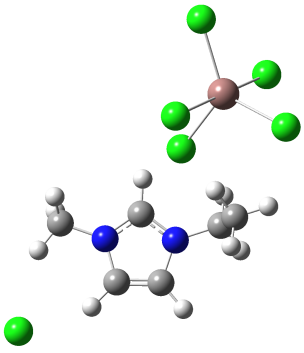
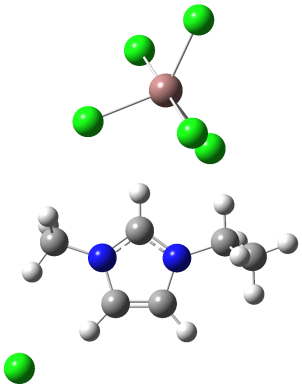


Table A.105: $[C_2C_1Im][InCl_6]^{2-}$ Gas Phase Ion Pair Structures

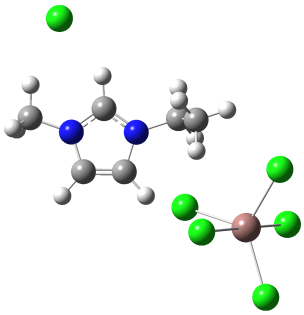
-87_4.6_147_-159 (0)



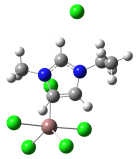
63_4.2_164_-126 (10) [1]



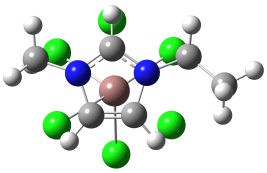
-73_6.2_52_-162 (16)



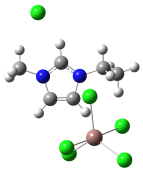
74_5.2_42_-70 (21) [1]



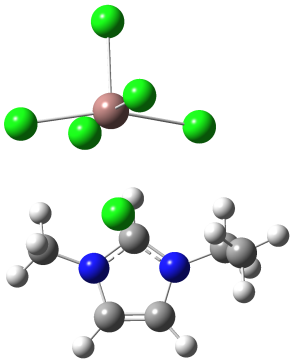
-38_4.6_74_-91 (193) [fnc]



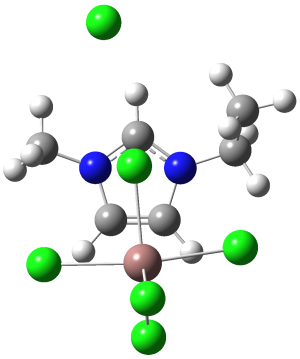
67_5.5_38_122 (19) [1]



-66_4_145_78 (163)



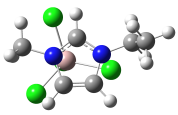
-126_4.5_56_91 (12) [fnc]



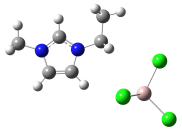
A.2.2 $[C_2C_1Im][M_xCl_y]$ liquid phase Ion pair structures

Table A.106: $[C_2C_1Im][AlCl_4]$ Liquid Phase Ion pair structures

-77_4.1_82_-82 (7)



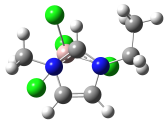
178_6.1_55_-180 (19)



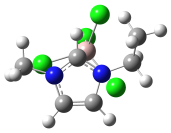
-73_4.5_61_-84 (5)



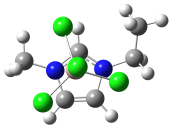
163_4.1_83_-82 (12)



-150_4.1_85_-99 (12)



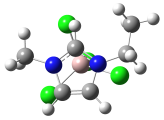
-161_4.1_82_83 (13)



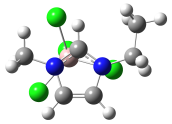
-74_4.5_63_80 (6)



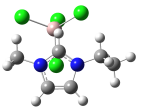
161_4.1_82_-83 (12)



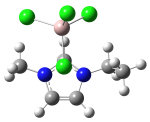
164_4.1_82_-83 (12)



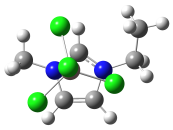
61_3.9_111_-86 (10)



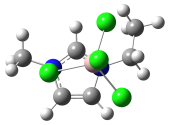
-60_3.9_109_86 (11)



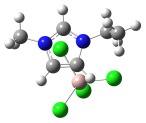
-158_4.1_81_84 (12)



150_4.1_85_99 (12)



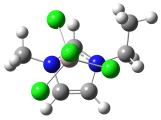
-69_4.6_57_-98 (7)



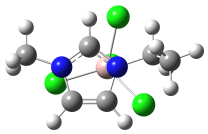
-71_4.5_62_80 (5)



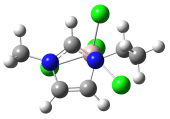
-165_4.1_82_83 (11)



-69_4.1_81_-99 (6)



-70_4.1_82_-101 (8)



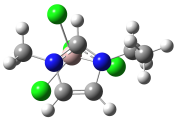
-125_4.6_57_97 (11)



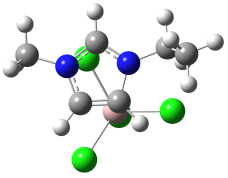
-78_4.1_81_-82 (9)



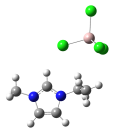
-76_4.1_82_-81 (9)



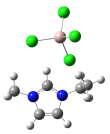
-71_4.6_58_-97 (0)



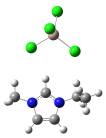
-75_5.3_134_155 (13)



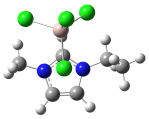
-87_4.2_149_-121 (11)



-75_4.8_161_109 (15)



-61_3.9_111_85 (8)



-61_4.2_107_96 (12)

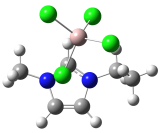
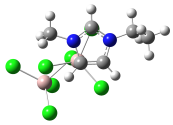


Table A.107: $[C_2C_1Im][Al_2Cl_7]$ Liquid Phase Ion pair structures

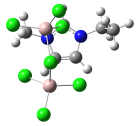
-72_4.5_47_-80 (7)



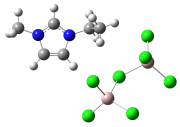
-73_6.5_68_-87 (3)



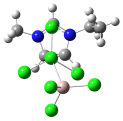
-73_6.4_68_75 (7)



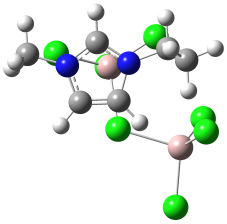
-82_5.8_52_178 (19) [1]



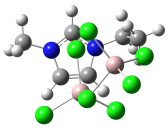
-75_6.6_67_84 (5)



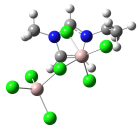
-69_4.9_44_-100 (0)



-81_6.6_65_87 (5)



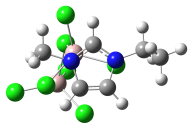
-75_6.5_65_80 (6)



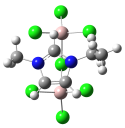
-70_3.4_76_-89 (3)



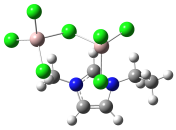
-73_6.3_83_-84 (3)



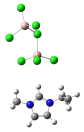
-67_5.5_92_-92 (5)



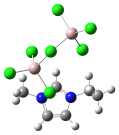
-60_3.9_122_55 (10)



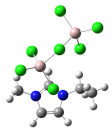
-77_6.7_173_-121 (13)



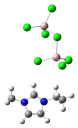
-61_5.8_113_91 (9)



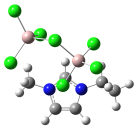
-62_5.8_114_92 (9)



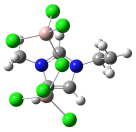
-72_7_156_169 (16)



-52_5.7_115_80 (7)



-79_3.4_73_87 (1)



-68_5.7_110_87 (7)

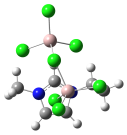
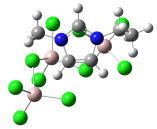
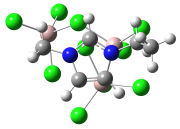


Table A.108: $[C_2C_1Im][Al_3Cl_{10}]$ Liquid Phase Ion pair structures

-69_6.8_72_-75 (2)



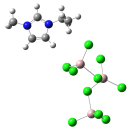
-72_7_85_-101 (4)



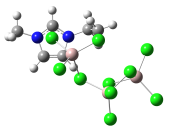
-81_6.4_46_175 (15)



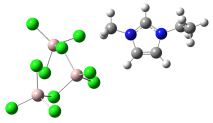
-70_9.5_47_-149 (15)



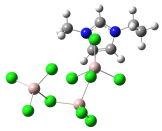
-79_7_48_130 (4)



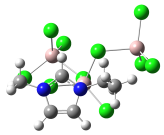
-73_6.1_55_3 (19)



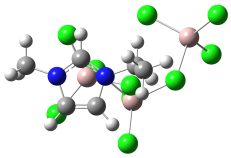
-74_8.2_58_76 (11) [1]



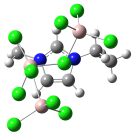
-76_4.4_78_-108 (5)



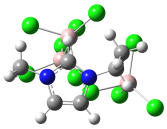
-78_7.6_72_-98 (0)



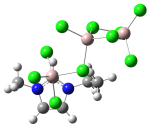
-51_4.6_76_66 (4)



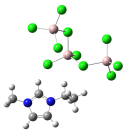
-122_7.1_88_-84 (12)



-85_6.5_119_107 (2)



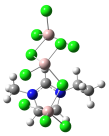
-65_5_132_140 (14)



-41_4.6_75_68 (5)



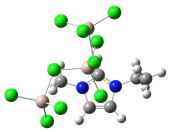
-65_5.4_111_87 (6)



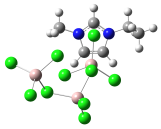
-77_6.4_72_53 (5)



-78_4_97_78 (9)



-70_8.2_57_76 (5)



-85_6.6_119_107 (5)

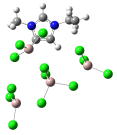


Table A.109: $[C_2C_1Im][Al_4Cl_{13}]_Bra$ Liquid Phase Ion pair structures

-154_4.8_59_89 (12)



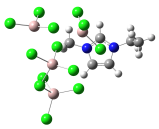
-92_6.7_37_95 (8)



-45_6.6_33_-99 (11)



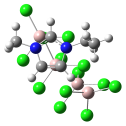
-75_7_72_56 (10)



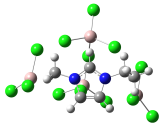
-76_4.5_75_-82 (0)



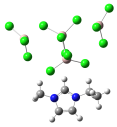
-78_7.3_70_-91 (6)



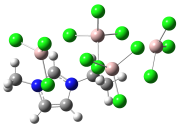
-64_5.5_78_-84 (5)



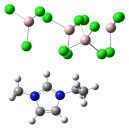
-60_5.4_175_84 (19) [1]



-50_5.5_110_125 (14)



149_5.7_-135_-72 (16)



-71_8.3_56_84 (12) [1]

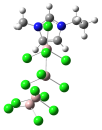
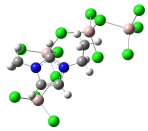


Table A.110: $[C_2C_1Im][Al_4Cl_{13}]_Lin$ Liquid Phase Ion pair structures

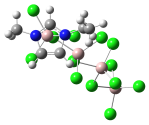
-141_3.7_125_-103 (1)



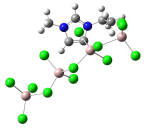
-96_5_52_45 (8)



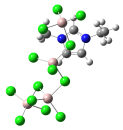
-78_9.3_74_-93 (8)



-81_6.4_52_78 (5)



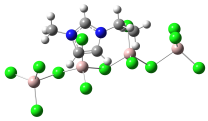
-85_5.4_31_80 (1)



-68_9.1_82_74 (9) [1]



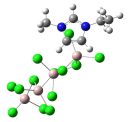
-52_6.5_62_-109 (8)



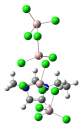
-37_4.5_60_-128 (7)



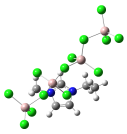
-70_9.3_73_-79 (6)



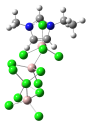
-62_5.8_104_92 (4)



-68_6_101_88 (1)



-68_9.9_63_81 (5)



-64_6_86_-102 (3)



-77_6.2_83_-101 (0)



-71_9.3_76_-94 (5)

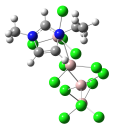
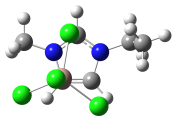
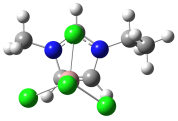


Table A.111: $[C_2C_1Im][GaCl_4]$ Liquid Phase Ion pair structures

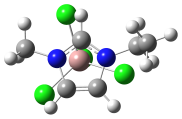
-76_4.5_62_79 (1)



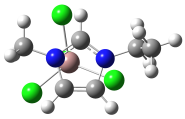
-71_4.5_64_79 (3)



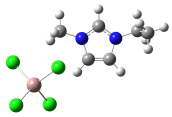
-82_4.1_82_-83 (2)



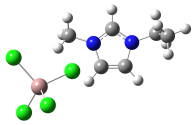
-78_4.1_80_-83 (1)



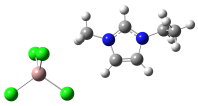
-72_5.9_50_21 (18) [1]



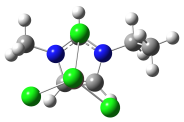
-73_5.7_57_-31 (15) [1]



-74_6.3_64_1 (18) [1]



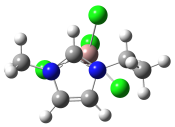
-68_4.5_62_80 (3)



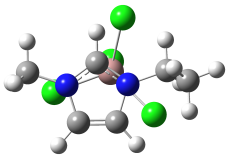
-66_4.1_77_-96 (3)



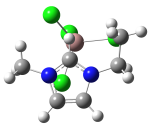
-68_4.1_81_-101 (1)



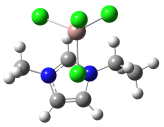
-70_4.1_81_-100 (0)



-163_3.9_105_-90 (8)



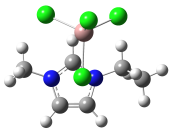
-55_3.9_110_89 (4)



-57_3.9_112_90 (7)



-54_3.9_111_90 (7)



-77_4.1_104_73 (4)

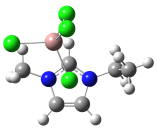
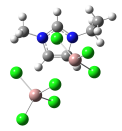
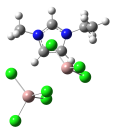


Table A.112: $[C_2C_1Im][Ga_2Cl_7]$ Liquid Phase Ion pair structures

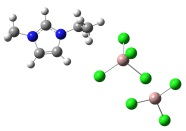
-112_6.3_50_84 (6)



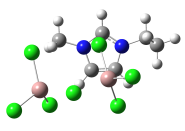
-95_6.3_50_80 (8) [1]



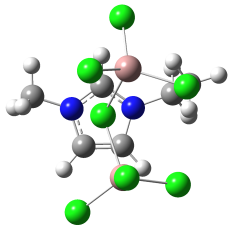
-72_8.7_58_-175 (22)



-70_6.3_66_73 (5)



-95_3.4_73_84 (0)



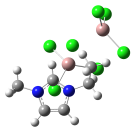
-67_3.7_69_-83 (1)



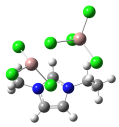
-76_6.2_93_-84 (5)



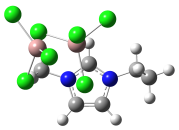
-144_3.6_126_-116 (7)



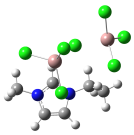
-63_5.9_110_90 (11)



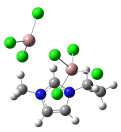
-64_6.1_105_88 (11)



-55_3.6_125_116 (5)



-55_5.9_111_86 (11)



-70_5.9_87_-74 (11)



-71_6.5_72_81 (10)

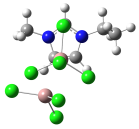
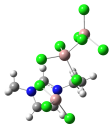
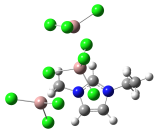


Table A.113: $[C_2C_1Im][Ga_3Cl_{10}]$ Liquid Phase Ion pair structures

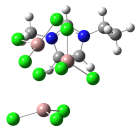
-76_6.2_103_105 (12)



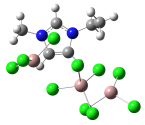
-79_3.9_99_75 (27) [1]



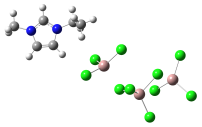
-67_4.3_64_88 (15)



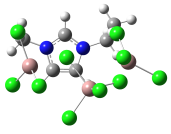
-85_6.7_47_106 (17)



-69_10.3_49_168 (39)



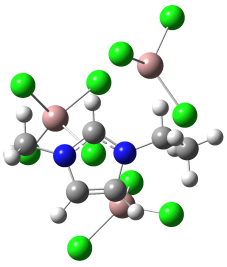
-128_4.8_52_108 (28) [2]



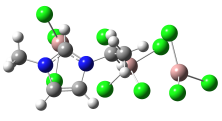
-81_6.4_70_52 (15)



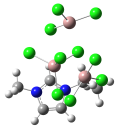
-67_4.8_94_-77 (0)



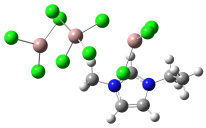
-77_5.9_83_-127 (11)



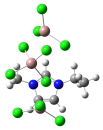
-56_3.9_104_85 (19)



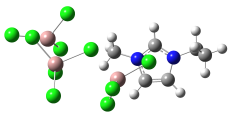
-60_6.3_102_56 (25)



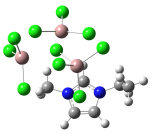
-62_4.8_97_72 (14)



-74_6.8_87_32 (16)



-71_4.2_100_88 (16)

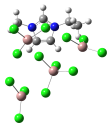


-91_7.9_98_83 (35) [1]

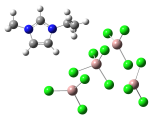


Table A.114: $[C_2C_1Im][Ga_4Cl_{13}]_Bra$ Liquid Phase Ion pair structures

-69_6.8_47_93 (6)



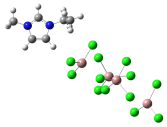
-75_6.6_52_164 (21)



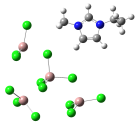
-87_6.6_46_106 (0)



-76_9.9_50_-175 (33)



-70_7.1_36_-1 (21)



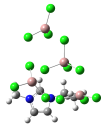
-66_5.3_105_-105 (6) [1]



-57_7.8_164_103 (26)



-60_6_116_107 (12)



-68_6.7_109_-94 (11)

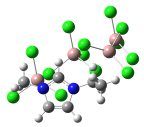
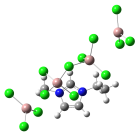
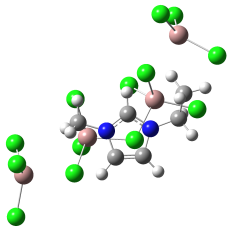


Table A.115: $[C_2C_1Im][Ga_4Cl_{13}]_Lin$ Liquid Phase Ion pair structures

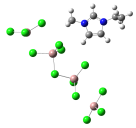
-62_6_101_91 (4)



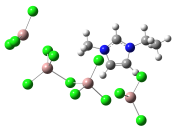
-146_4_65_-101 (0)



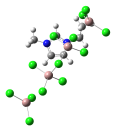
-74_8_39_8 (18)



-69_5.6_55_19 (11)



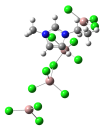
-138_6.2_56_86 (8)



-78_9_81_103 (7)



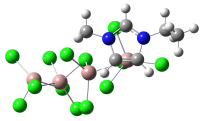
-58_6.6_61_-99 (8)



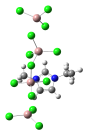
-157_4.3_60_123 (3)



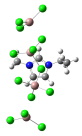
-70_9.3_76_-76 (18) [1]



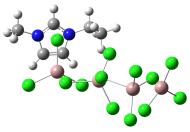
-77_6.1_94_77 (9)



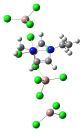
-66_3.7_66_97 (1)



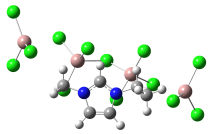
-80_9_82_102 (12)



-81_6.5_66_-88 (6)



-65_5.9_97_-88 (6)



-74_9.5_71_-91 (13)

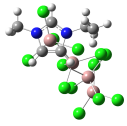
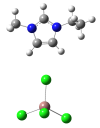
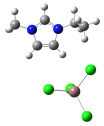


Table A.116: $[C_2C_1Im][InCl_4]$ Liquid Phase Ion pair structures

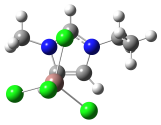
-72_7.8_5_-71 (21) [1]



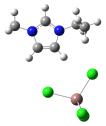
-68_6.5_23_-154 (12)



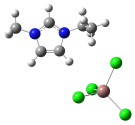
-71_4.6_58_79 (1)



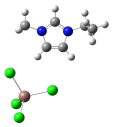
-71_6.7_20_175 (20) [1]



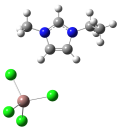
-73_6.5_38_-163 (13)



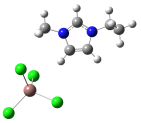
-74_6.7_22_-9 (17)



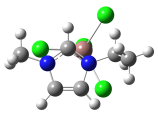
-73_6.7_24_-5 (15)



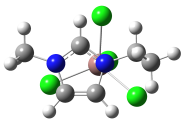
-72_6.3_38_0 (16)



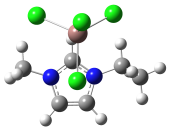
-72_4.1_88_-104 (5)



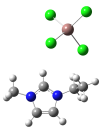
-66_4.2_75_-97 (2)



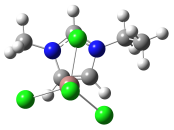
-58_3.9_112_88 (4)



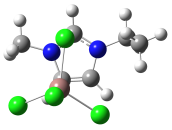
-80_5.1_154_-175 (11)



-70_4.6_57_78 (1)



-71_4.5_60_79 (1)



-74_4.6_56_82 (0)

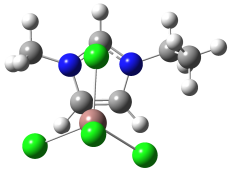
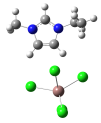
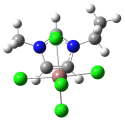


Table A.117: $[C_2C_1Im][InCl_5]^-$ Liquid Phase Ion pair structures

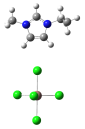
-71_6.3_11_144 (12)



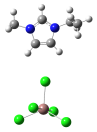
-125_4.4_50_87 (5)



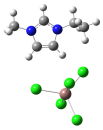
-73_8_3_60 (23)



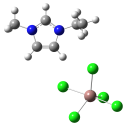
-73_7.9_4_67 (28) [1]



-67_6.4_15_-157 (12)



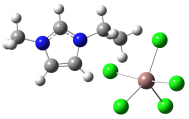
-84_7_31_-174 (15)



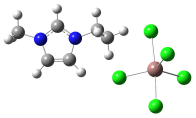
-66_4.3_57_-89 (6)



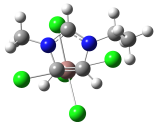
-60_6_55_-168 (24) [1]



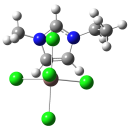
-60_6.6_64_-170 (19)



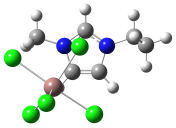
-70_4.3_58_-88 (3)



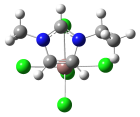
-84_5_55_76 (10)



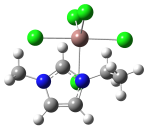
-69_4.7_59_68 (6)



-66_4.4_50_-90 (1)



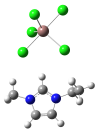
-73_3.8_114_-106 (0)



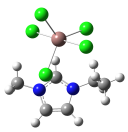
-70_3.8_110_-109 (1)



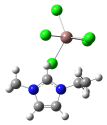
-81_4.9_176_146 (11)



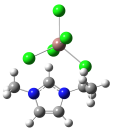
-63_4_121_97 (2)



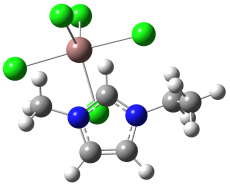
-84_4.4_140_-124 (7) [1]



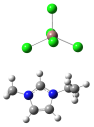
-82_4.3_123_-103 (5)



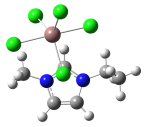
-84_3.8_114_-77 (0)



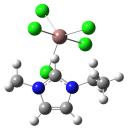
-80_4.5_163_167 (11)



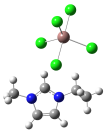
-62_3.8_119_75 (1)



-79_4.1_121_-96 (2) [1]



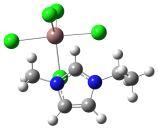
-65_4.6_155_144 (2)



-63_3.9_117_96 (2)



-75_3.8_114_-74 (1)



-63_3.9_120_74 (2)

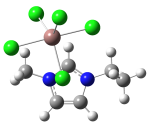
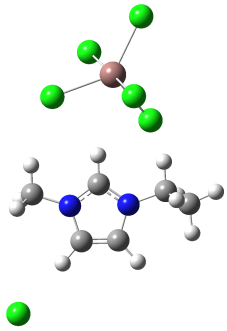
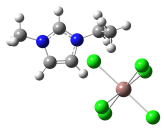


Table A.118: $[C_2C_1Im][InCl_6]^{2-}$ Liquid Phase Ion pair structures

56_4.3_156_-108 (-15)



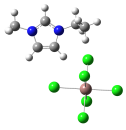
-82_6.3_49_-149 (15)



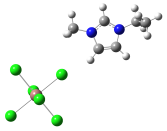
-80_6.4_35_-150 (14)



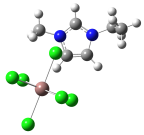
-73_6.5_30_-163 (17)



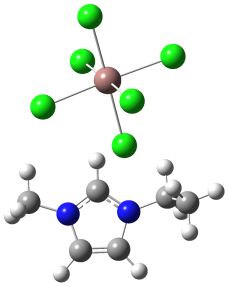
-74_7.8_49_-3 (34)



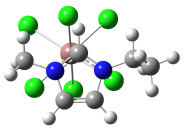
-76_5.9_45_52 (16)



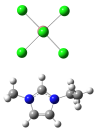
-76_4.4_151_-107 (0)



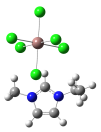
-71_4.7_86_-86 (14)



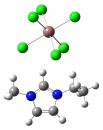
-79_5_179_127 (6)



-77_4.3_144_85 (5)



-68_4.5_170_147 (4)



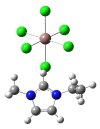
-76_4.3_144_86 (2)



-88_4.6_145_-119 (2)



-86_4.4_149_-99 (0)



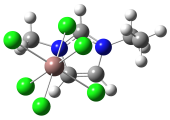
-64_4.4_165_124 (0)



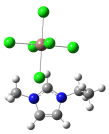
-69_5.2_92_65 (15)



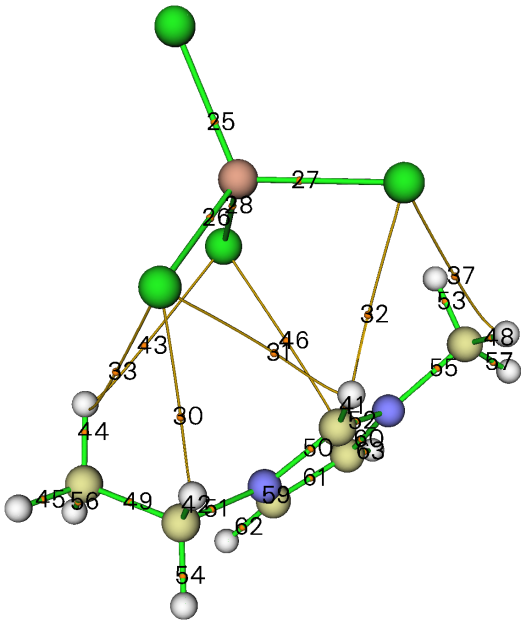
-74_5.1_73_78 (18)



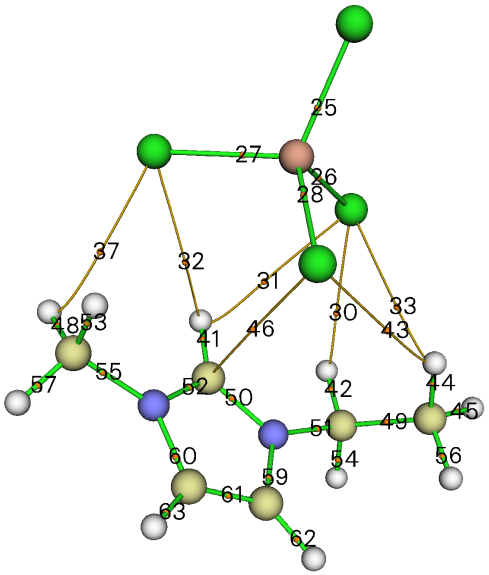
-70_4.5_140_78 (5)



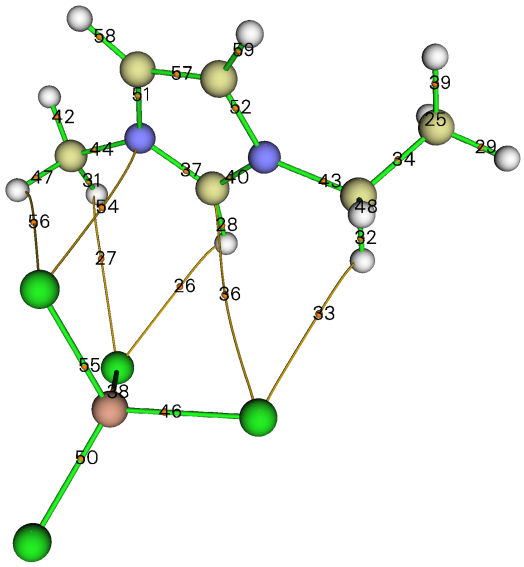
A.2.3 $[C_2C_1Im][M_xCl_y]$ AIM analysis



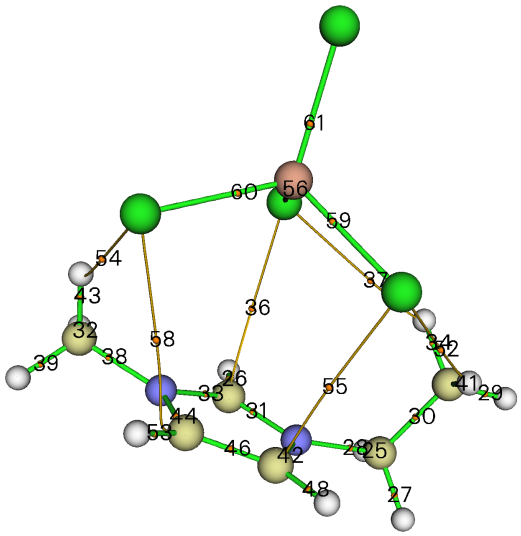
-58_3.7_122_87



-58_3.7_122_87

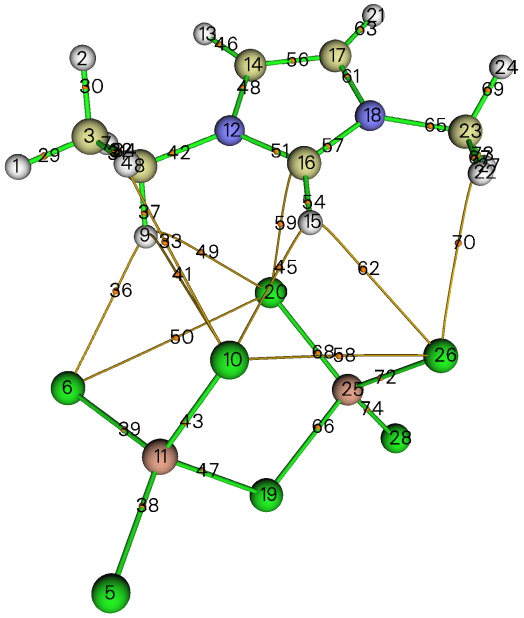


-69_3.7_112_-87

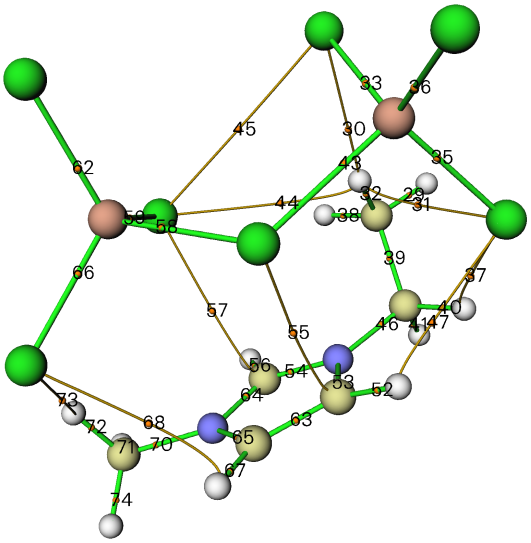


-78_4.3_64_81

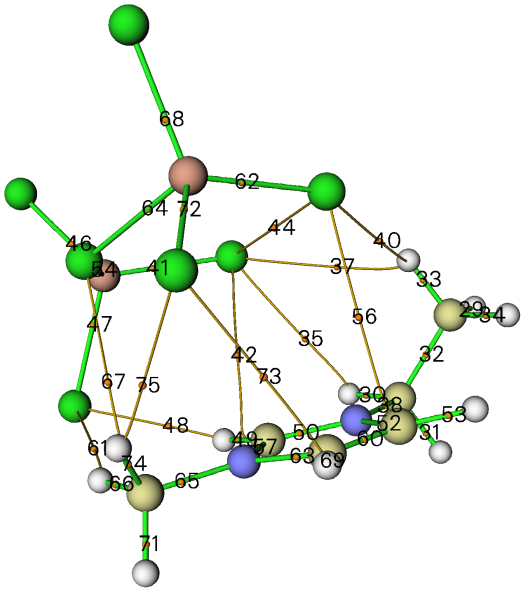
Figure A.16: $[C_2C_1Im][AlCl_4]$ IP AIM Critical points



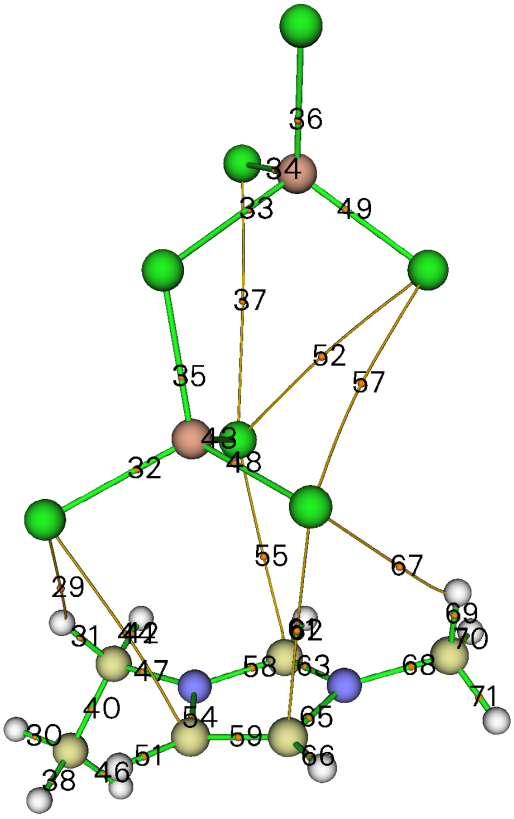
-104_5.3_135_-107



-108_4.9_38_98

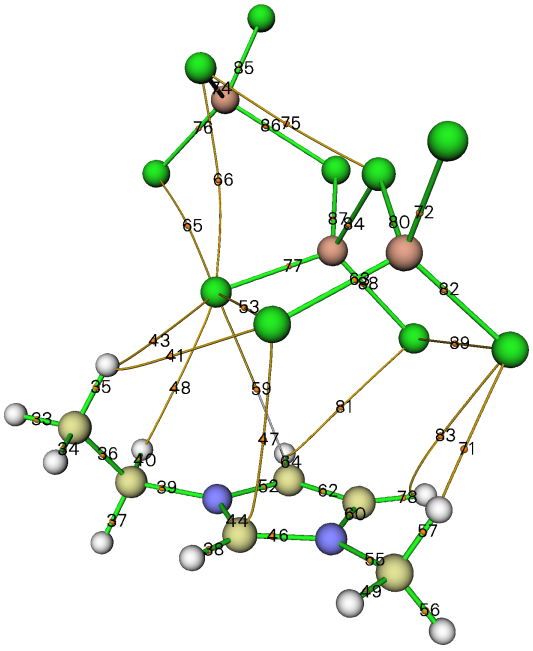


-52_3.8_102_59

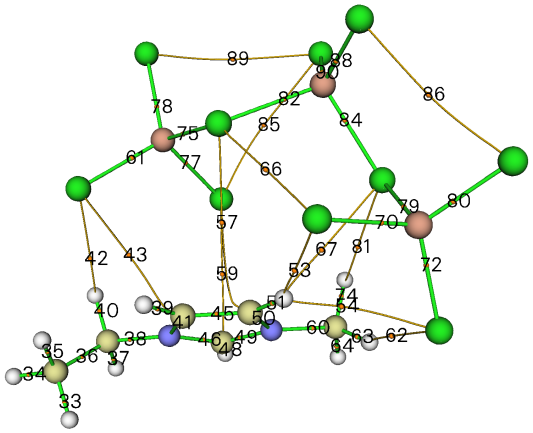


-68_6_83_-93

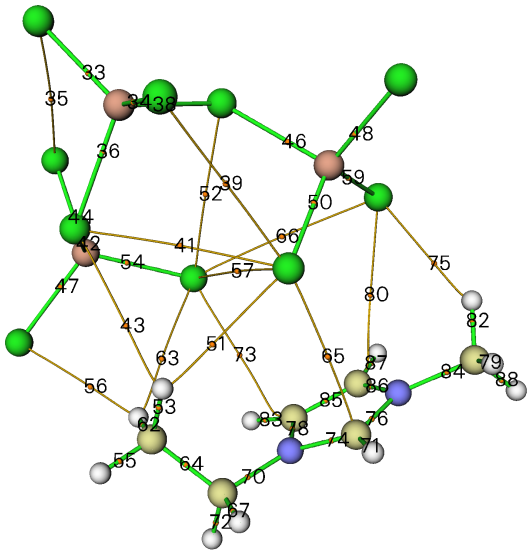
Figure A.17: $[C_2C_1Im][Al_2Cl_7]$ IP AIM Critical points



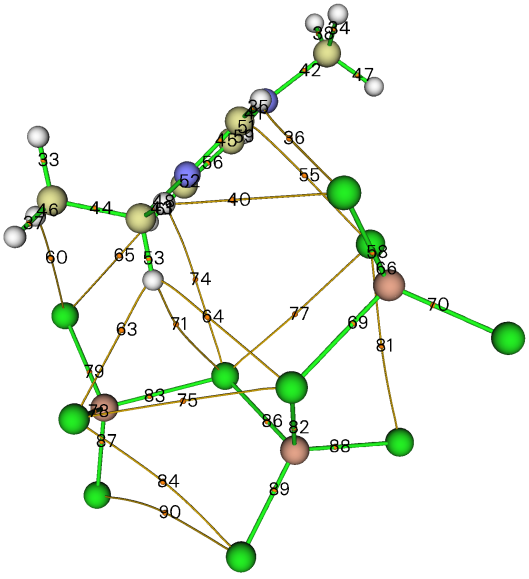
-126_5.5_41_112



-42_6.1_51_-60



-64_6.9_80_98



-67_5.9_74_-122

Figure A.18: $[C_2C_1Im][Al_3Cl_{10}]$ IP AIM Critical points

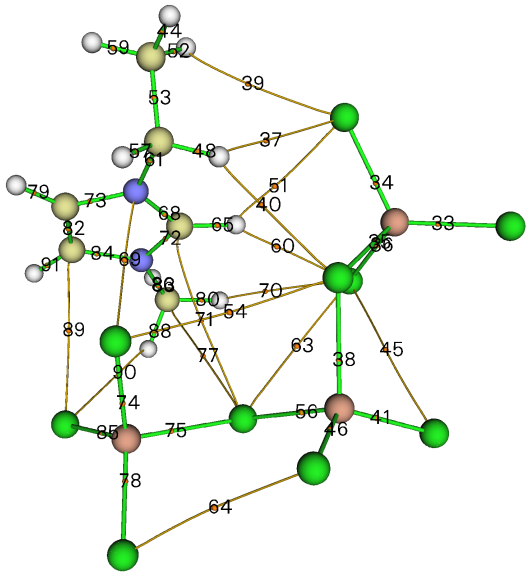
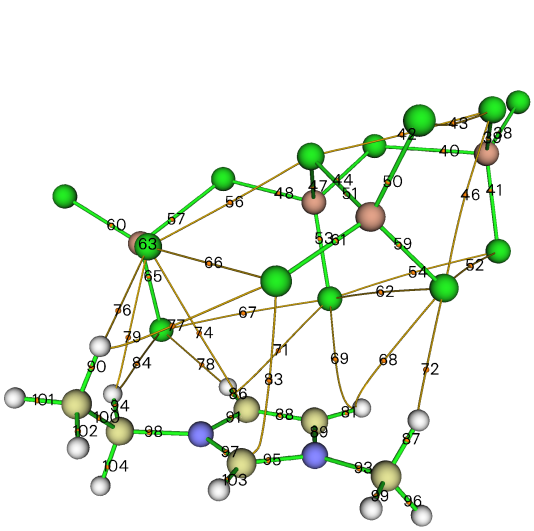
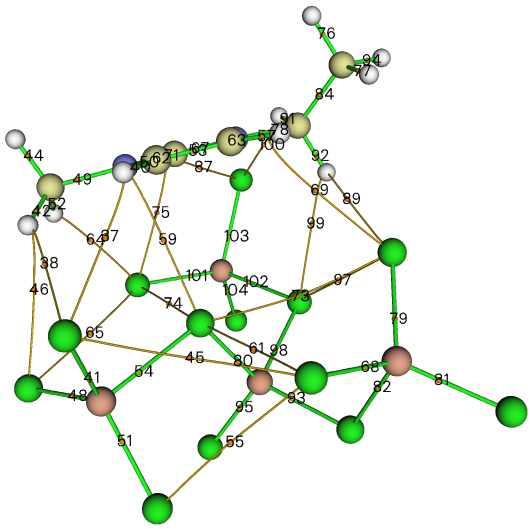


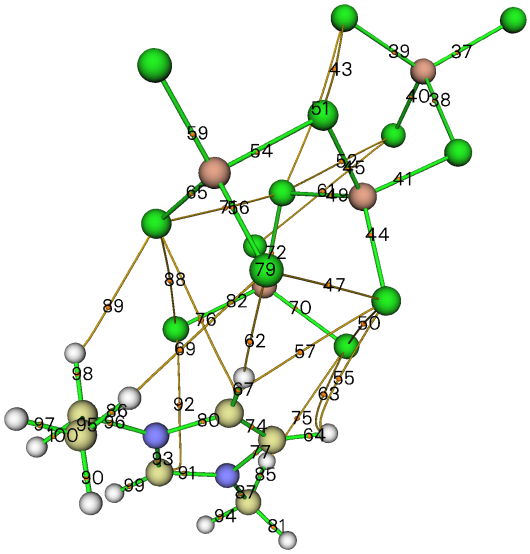
Figure A.19: $[C_2C_1Im][Al_3Cl_{10}]$ IP AIM Critical points continued



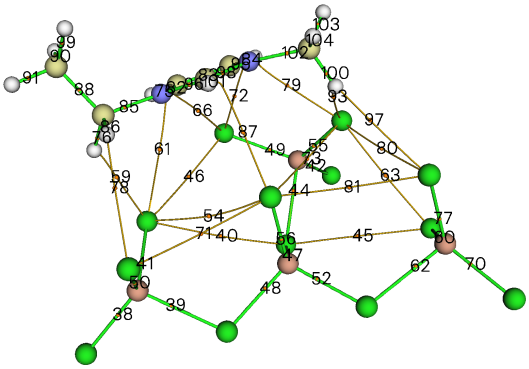
-136_6.3_33_97



-44_4.8_87_-96

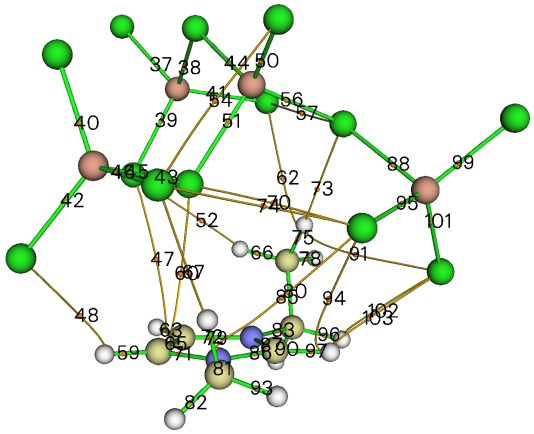


-53_3.4_31_-96



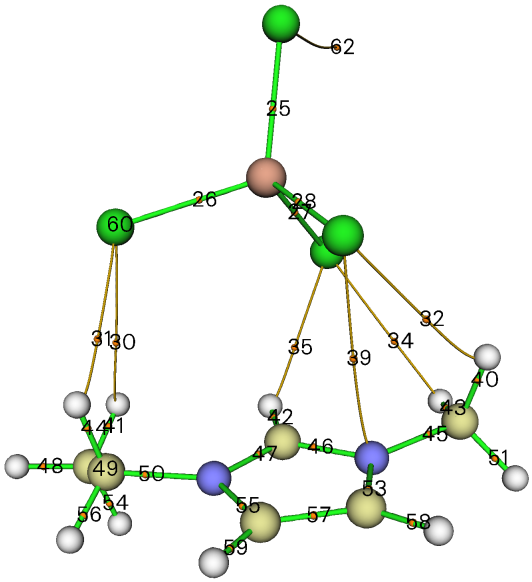
-78_5.2_75_-86

Figure A.20: $[C_2C_1Im][Al_4Cl_{13}]_Bra$ IP AIM Critical points

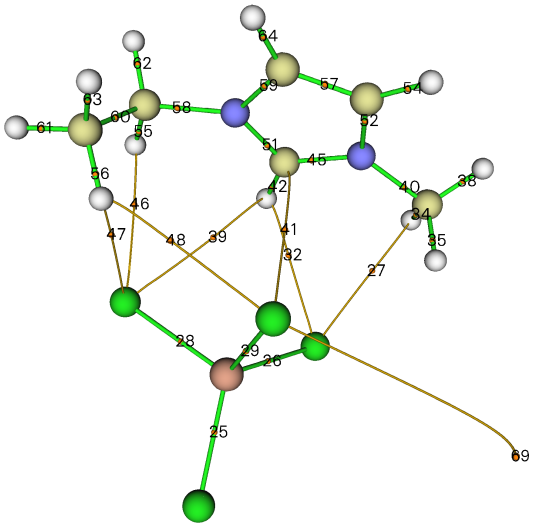


69_5.1_85_-89

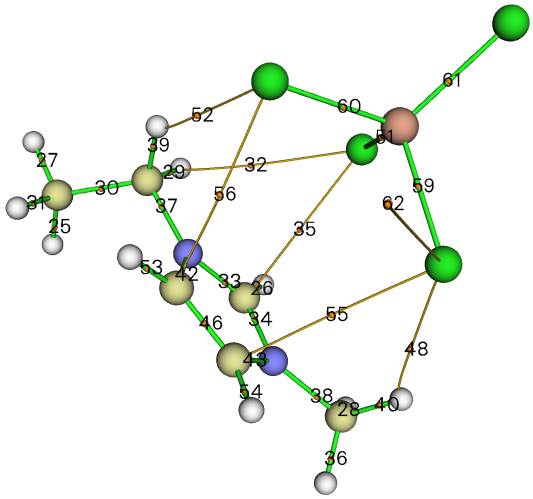
Figure A.21: $[C_2C_1Im][Al_4Cl_{13}]_Bra$ IP AIM Critical points continued



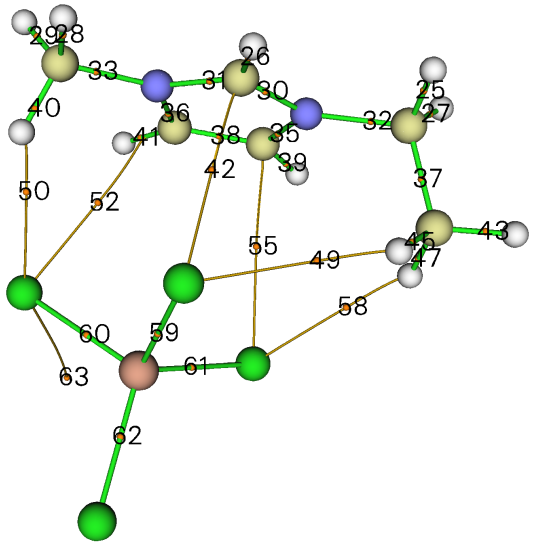
-156_3.7_111_-87



-57_3.7_120_87

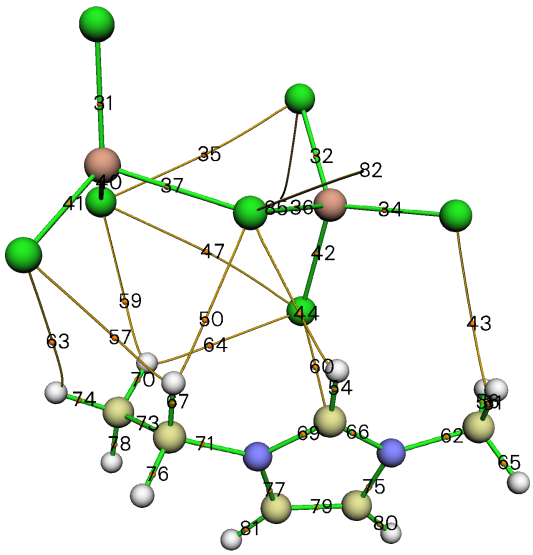


-71_4_79_-97

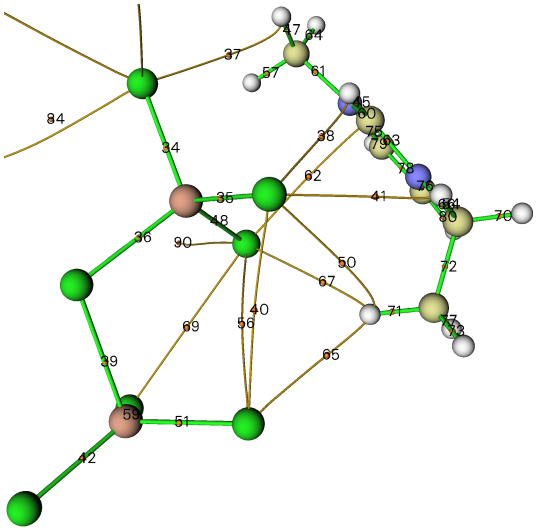


-78_4.3_64_80

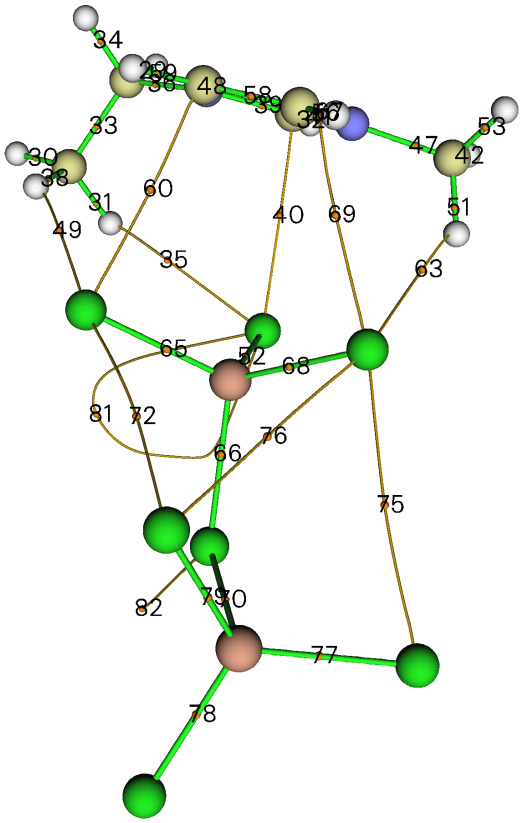
Figure A.22: $[C_2C_1Im][GaCl_4]$ IP AIM Critical points



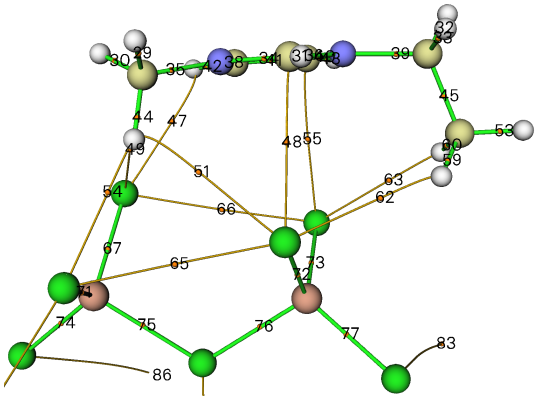
-52_3.5_137_121



-58_5.9_110_90

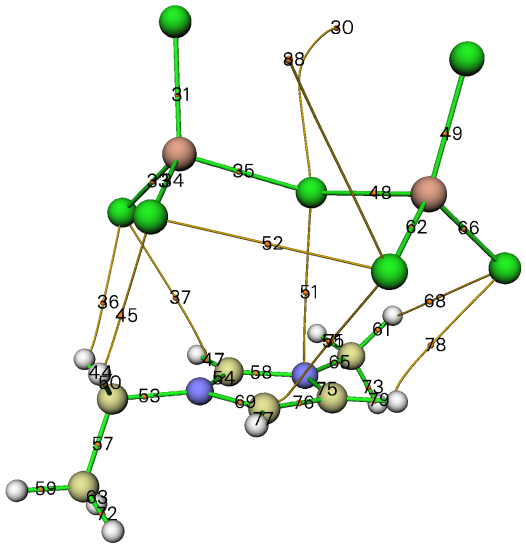


-76_6.4_72_82



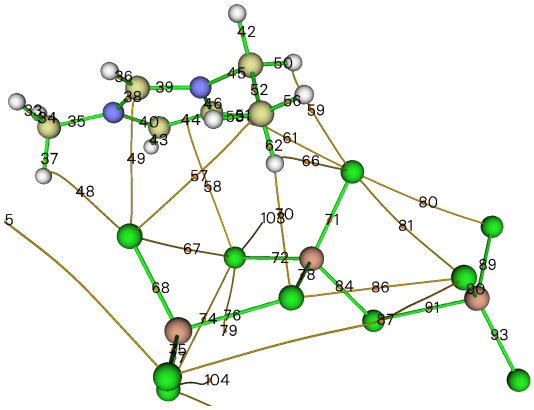
-76_6.1_72_73

Figure A.23: $[C_2C_1Im][Ga_2Cl_7]$ IP AIM Critical points

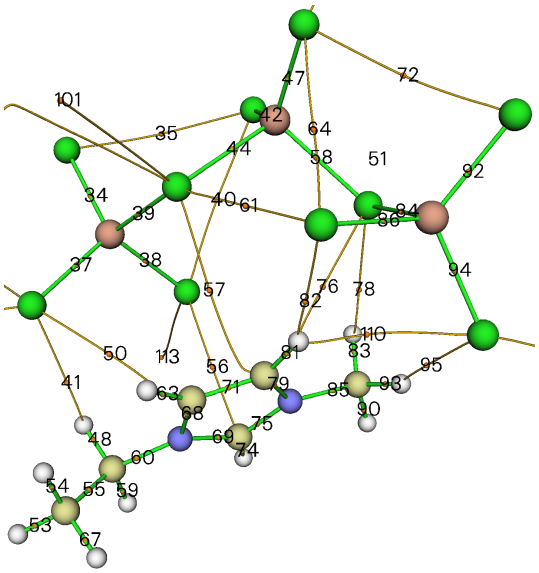


-81_3.5_75_-74

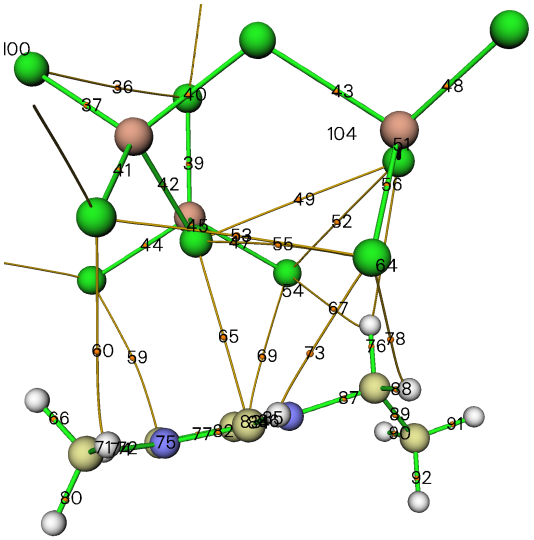
Figure A.24: $[C_2C_1Im][Ga_2Cl_7]$ IP AIM Critical points continued



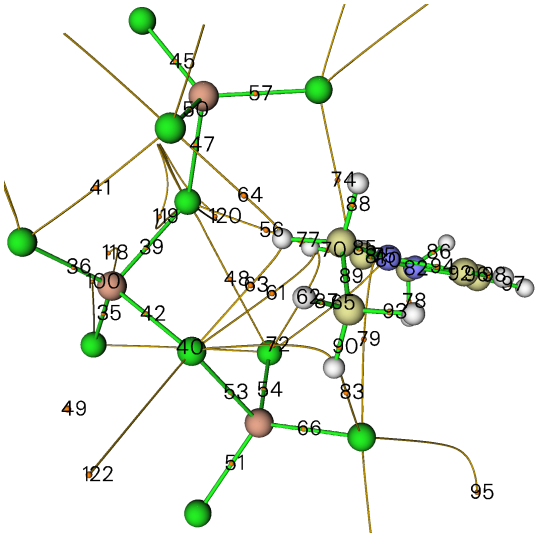
-105_5.5_46_121



-44_6.1_50_-59

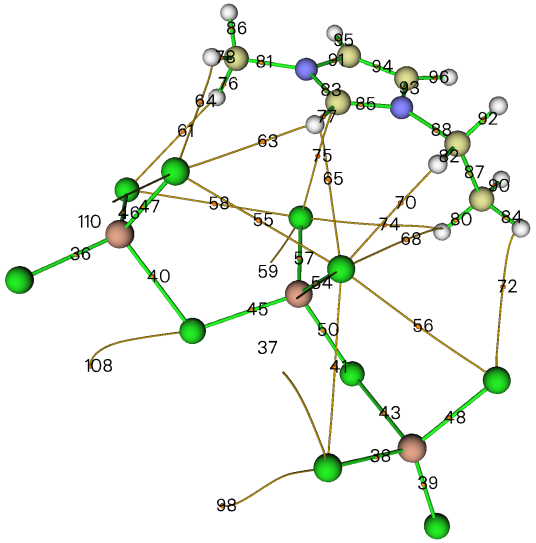


-53_4.7_97_-76



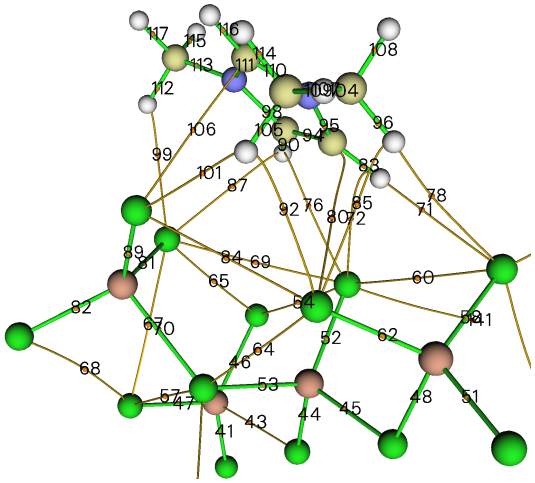
-54_4.9_156_133

Figure A.25: $[C_2C_1Im][Ga_3Cl_{10}]$ IP AIM Critical points

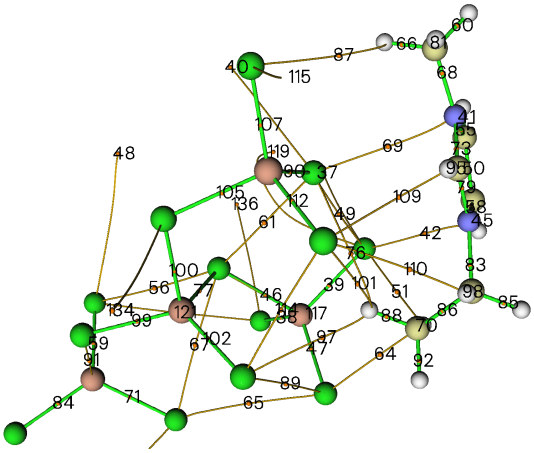


-59_4_113_100

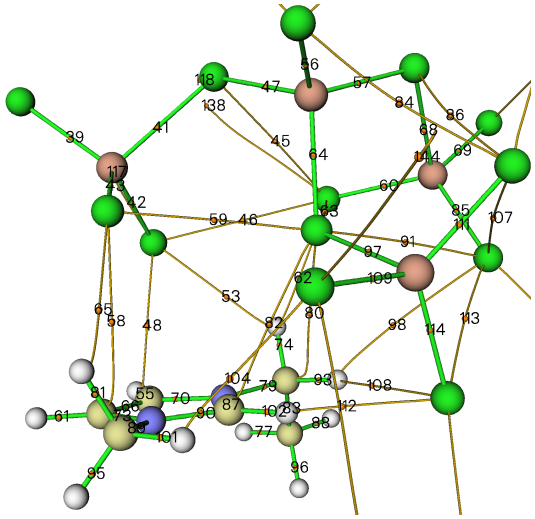
Figure A.26: $[C_2C_1Im][Ga_3Cl_{10}]$ IP AIM Critical points continued



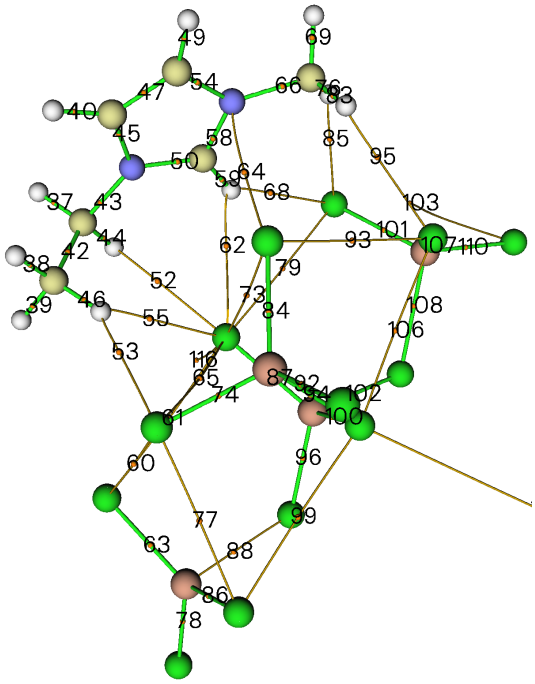
-134_6.4_32_97



-59_6.5_90_110



-61_5.4_103_-104



-62_5.1_133_103

Figure A.27: $[C_2C_1Im][Ga_4Cl_{13}]_Bra$ IP AIM Critical points

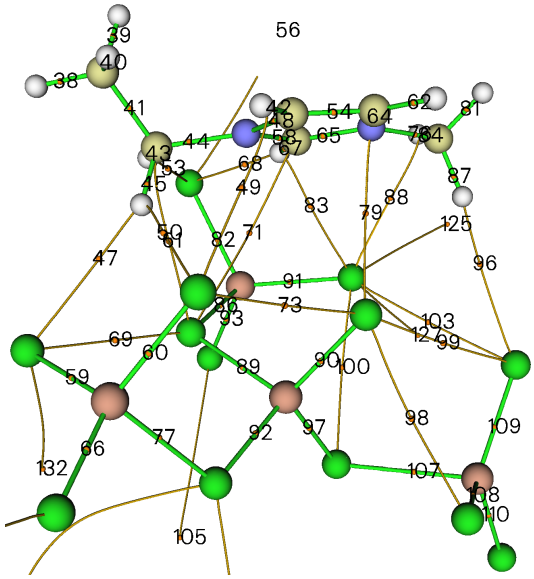
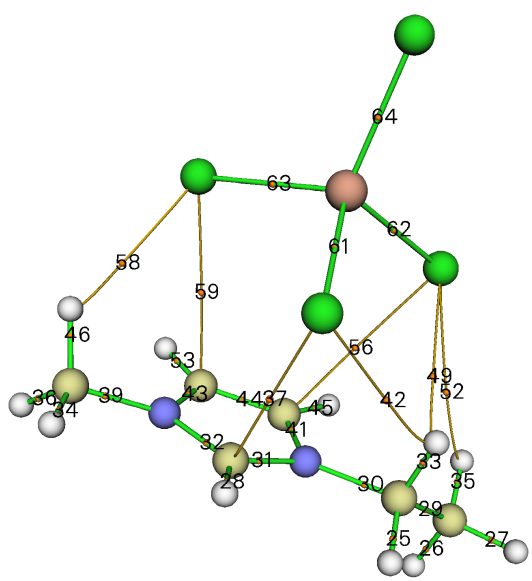
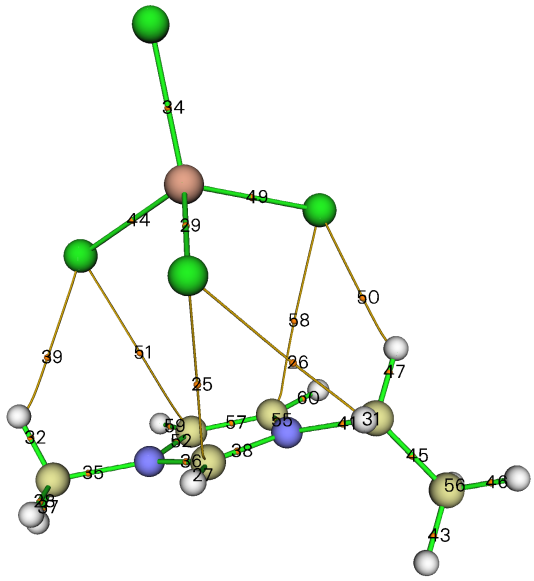


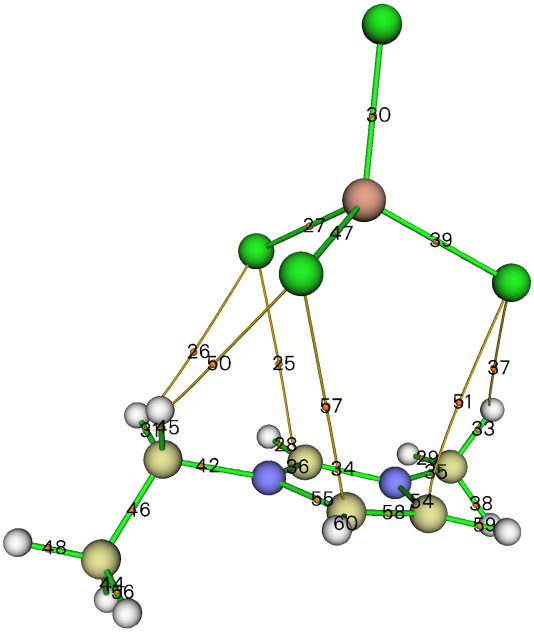
Figure A.28: $[C_2C_1Im][Ga_4Cl_{13}]_Bra$ IP AIM Critical points continued



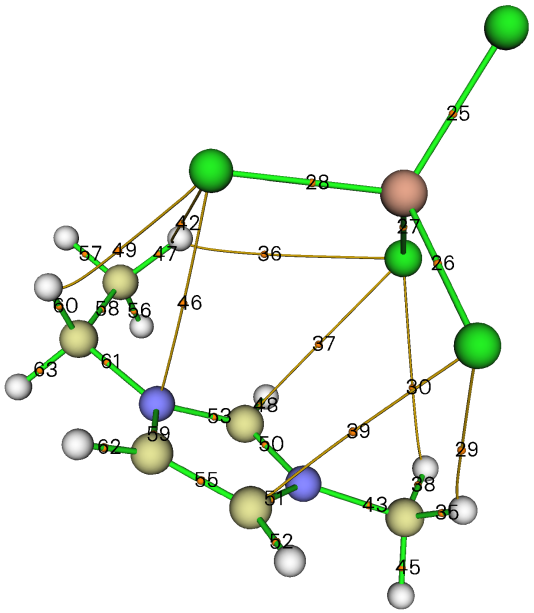
-31_4.1_73_-94



-74_4.1_78_-97

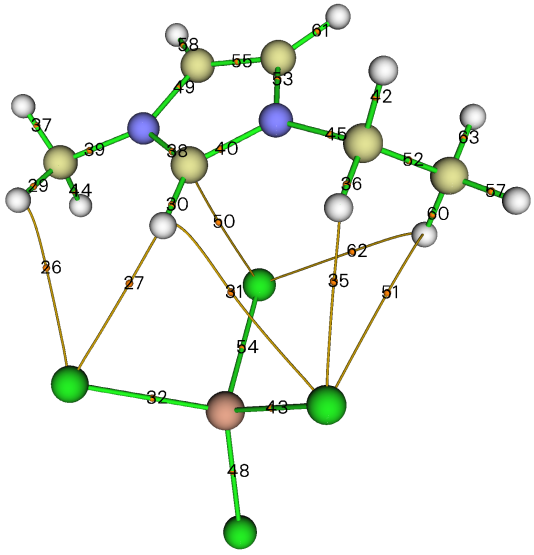


-75_4_79_-98

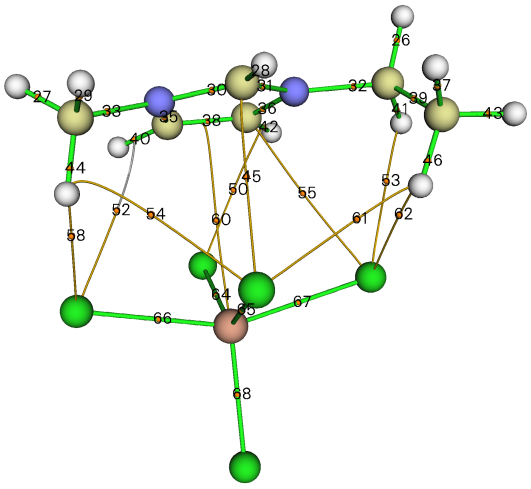


160_4_83_-83

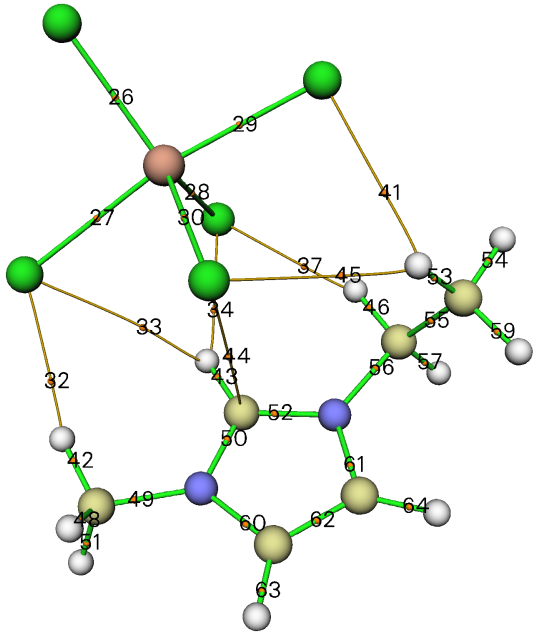
Figure A.29: $[C_2C_1Im][InCl_4]$ IP AIM Critical points



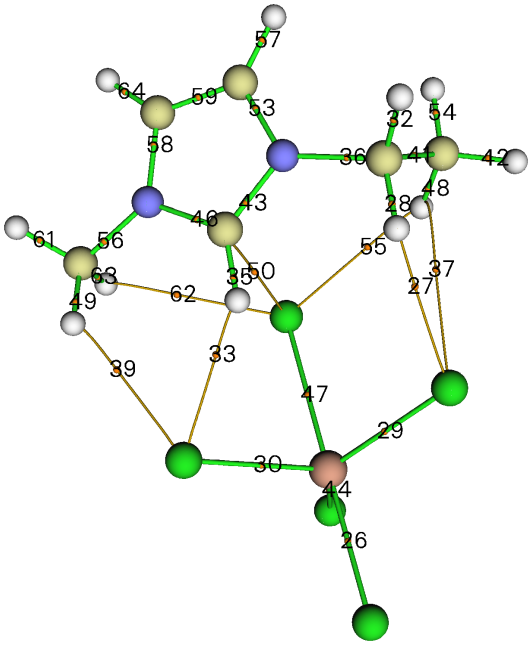
-56_3.7_124_75



140_4.2_53_-89

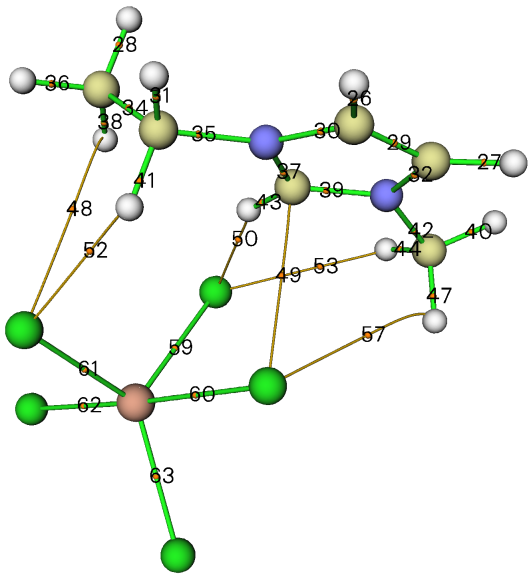


-49_3.7_129_100

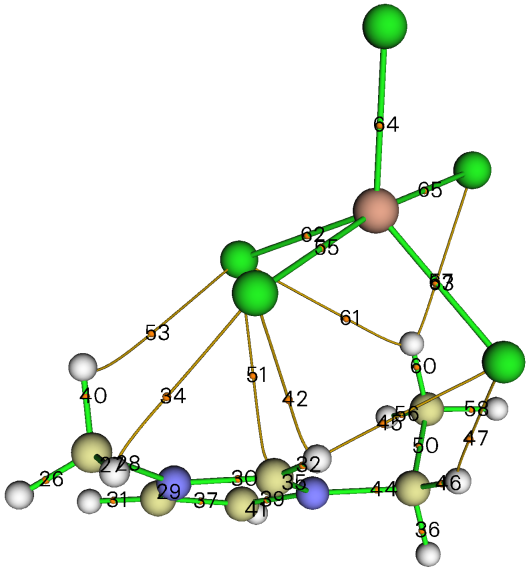


-63_4.1_144_90

Figure A.30: $[C_2C_1Im][InCl_5]^-$ IP AIM Critical points

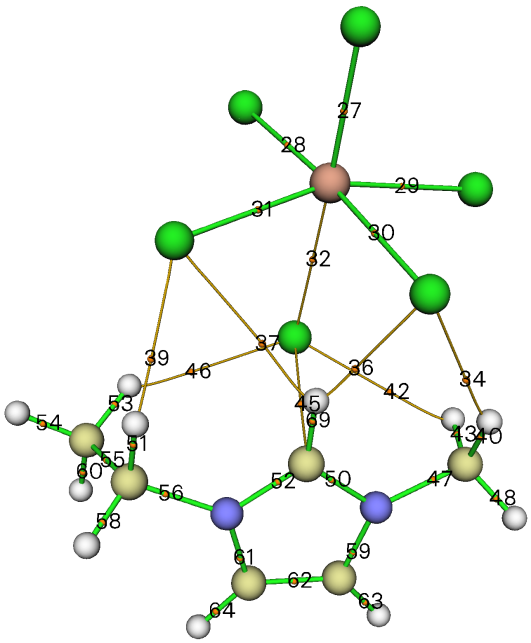


143_4.1_137_96

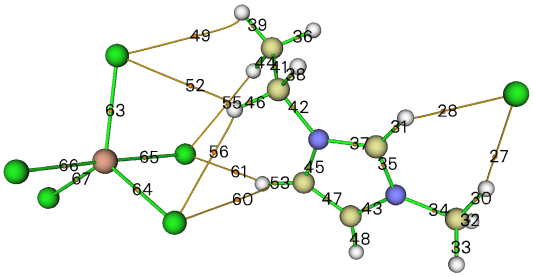


62_3.8_124_-96

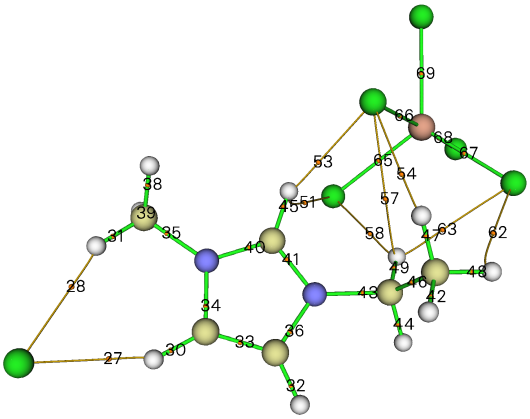
Figure A.31: $[C_2C_1Im][InCl_5]^-$ IP AIM Critical points continued



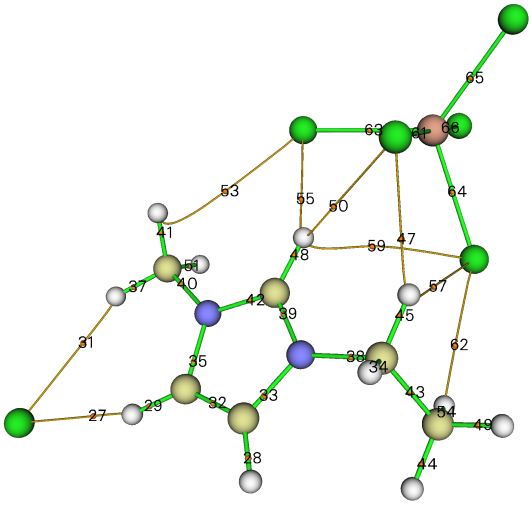
-66_4_145_78



-73_6.2_52_-162

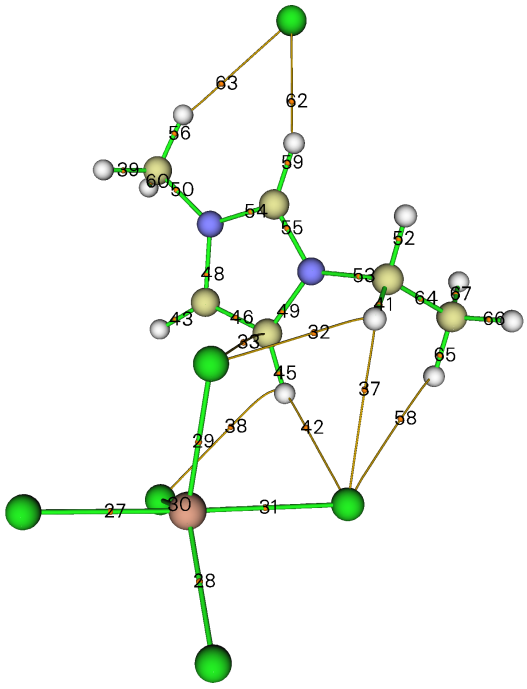


-87_4.6_147_-159



63_4.2_164_-126

Figure A.32: $[C_2C_1Im][InCl_6]^{2-}$ IP AIM Critical points



67_5.5_38_122

Figure A.33: $[C_2C_1Im][InCl_6]^{2-}$ IP AIM Critical points continued

A.2.4 $[C_2C_1Im][AlCl_4]$ Molecular orbitals

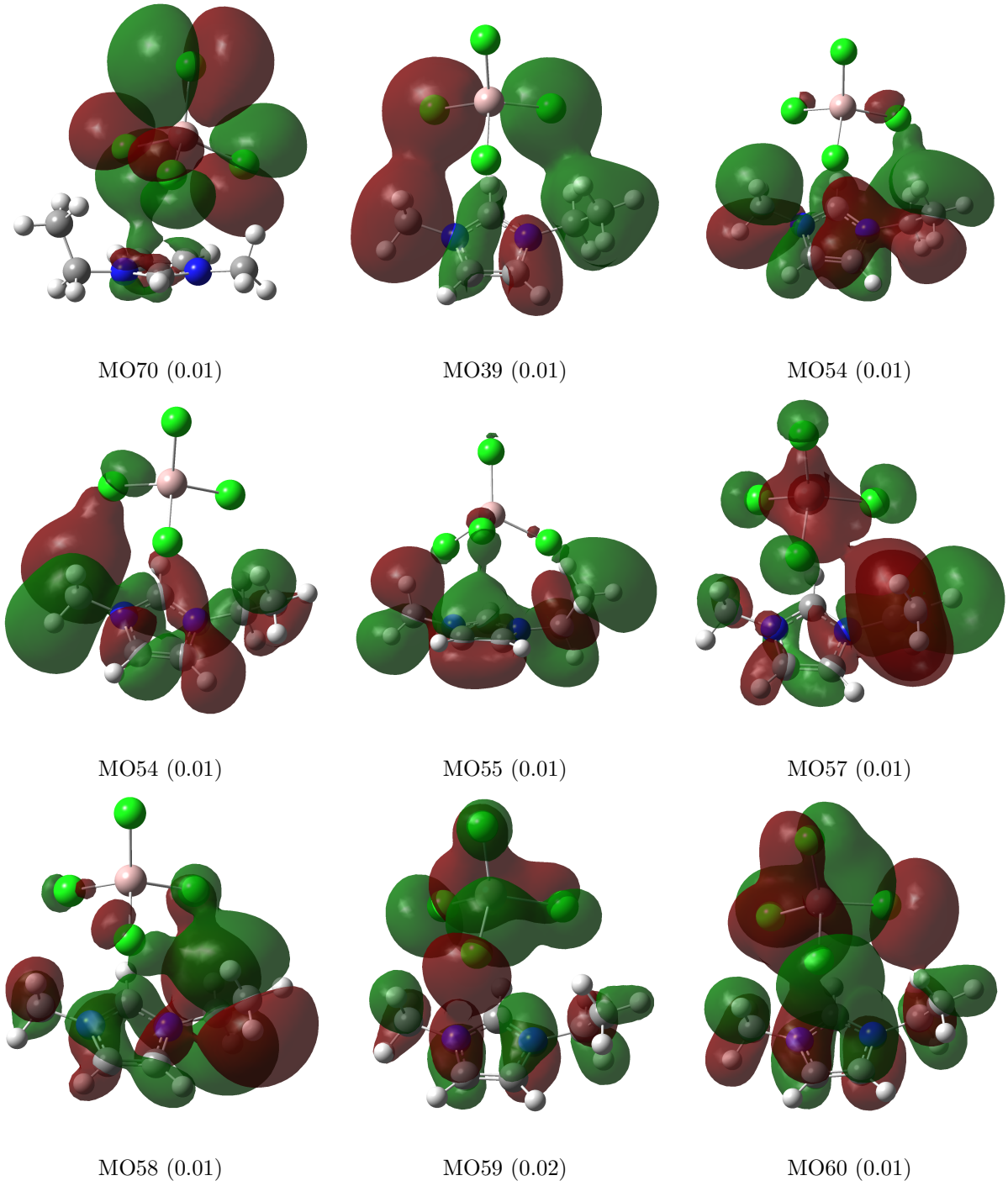
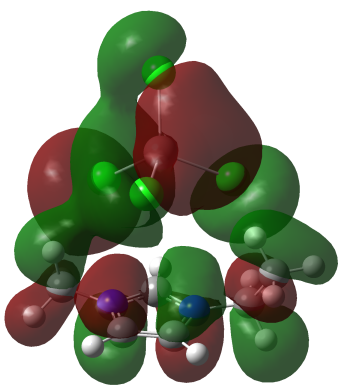
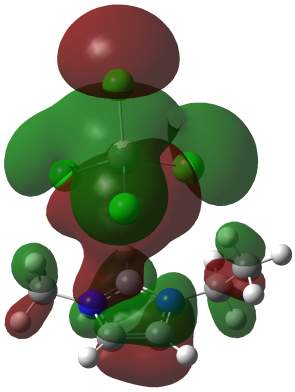


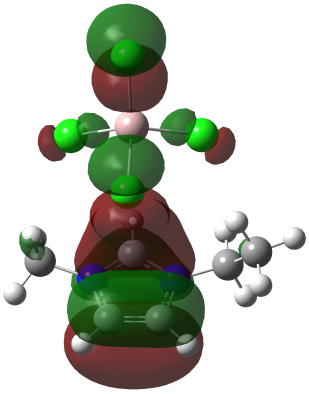
Figure A.34: $[C_2C_1Im][AlCl_4]$_ – 58_3.7_122_87 IP MOs I



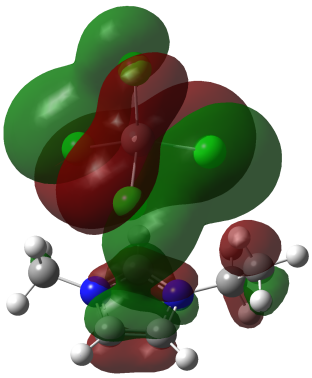
MO61 (0.01)



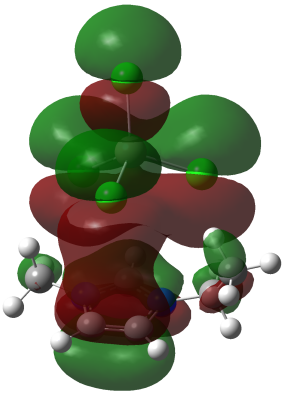
MO62 (0.01)



MO63 (0.02)

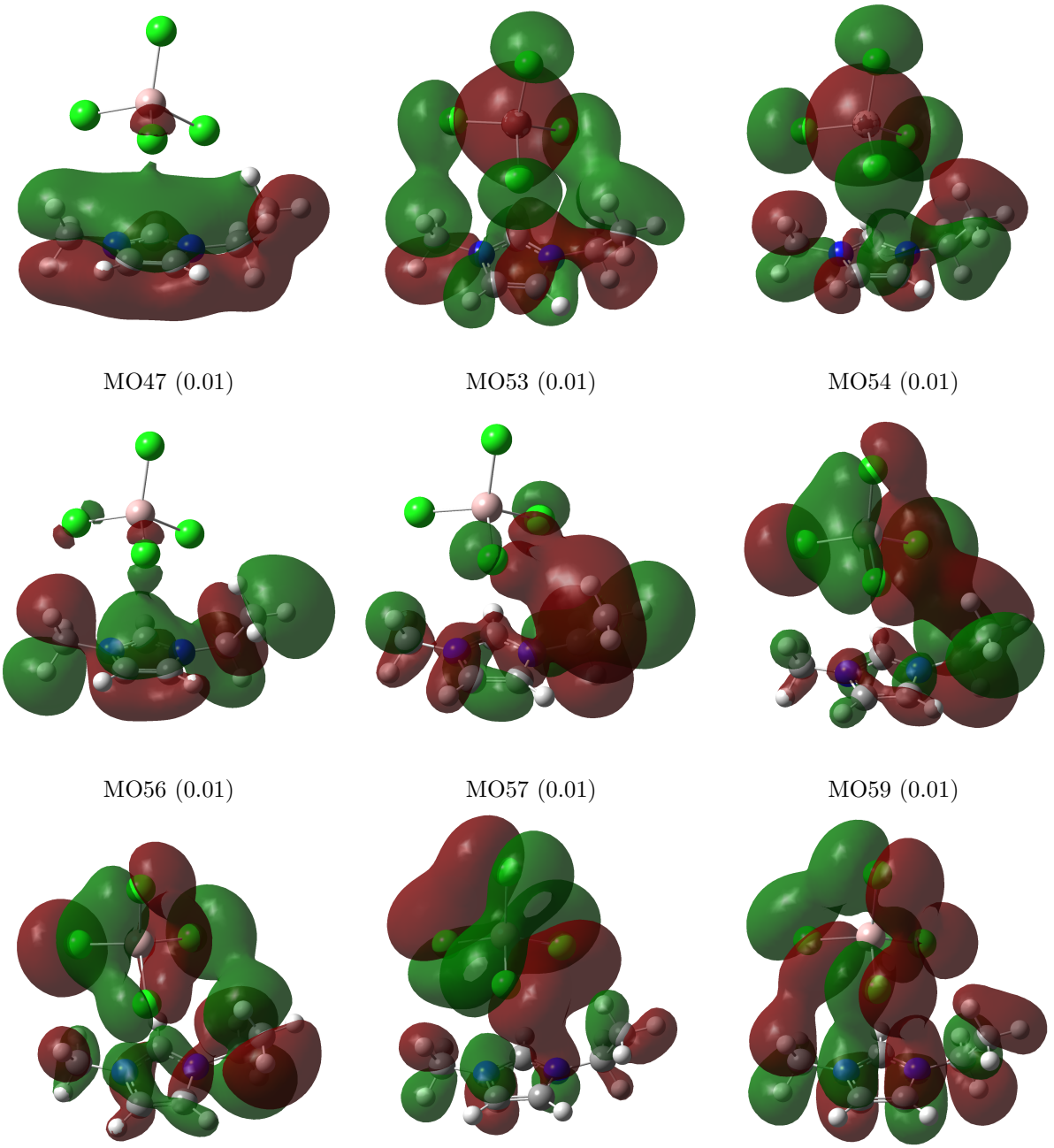


MO65 (0.01)



MO66 (0.01)

Figure A.35: $[C_2C_1Im][AlCl_4]_- - 58_3.7_122_87$ IP MOs II

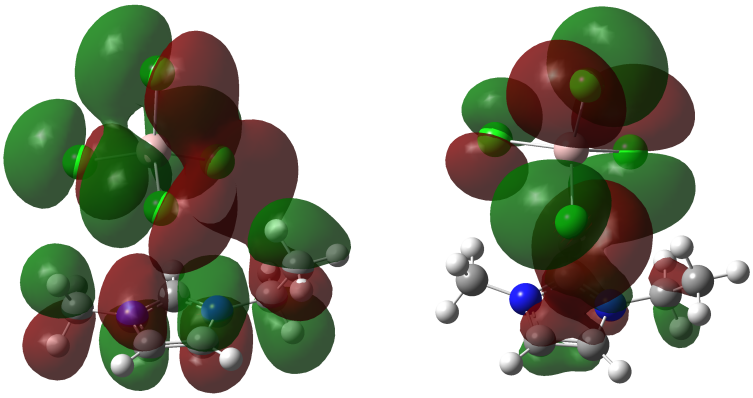


MO47 (0.01) MO53 (0.01) MO54 (0.01)

MO56 (0.01) MO57 (0.01) MO59 (0.01)

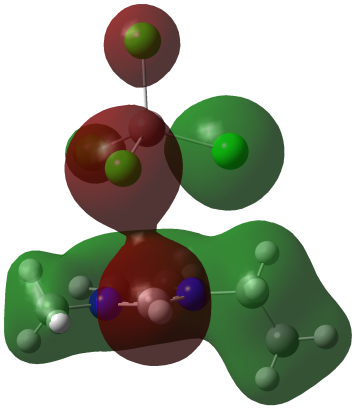
MO61 (0.01) MO63 (0.01) MO64 (0.01)

Figure A.36: $[C_2C_1Im][AlCl_4]_ - 60_3.9_109_86_LP$ IP MOs I

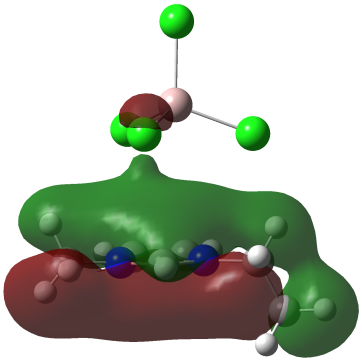


MO67 (0.01) MO68 (0.01)

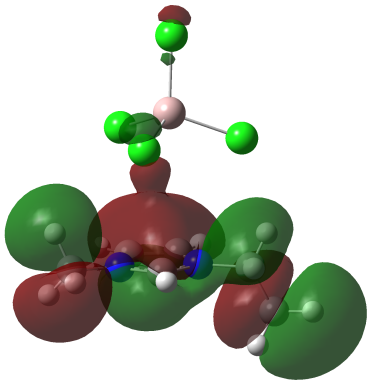
Figure A.37: $[C_2C_1Im][AlCl_4]_ - 60_3.9_109_86_LP$ IP MOs II



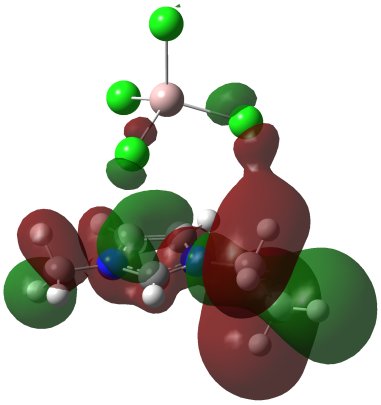
MO38 (0.01)



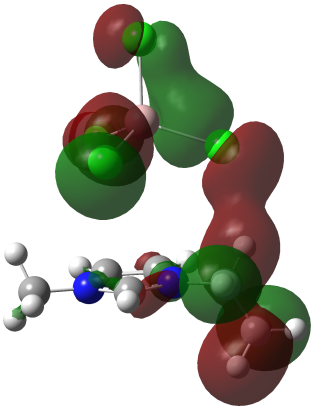
MO47 (0.01)



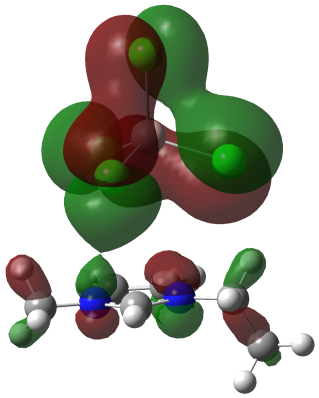
MO55 (0.01)



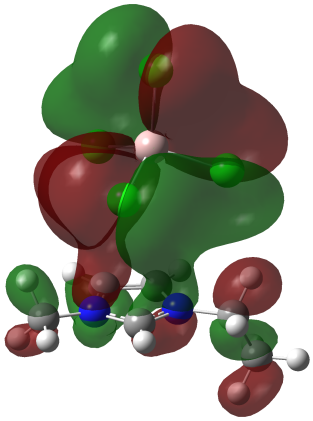
MO57 (0.01)



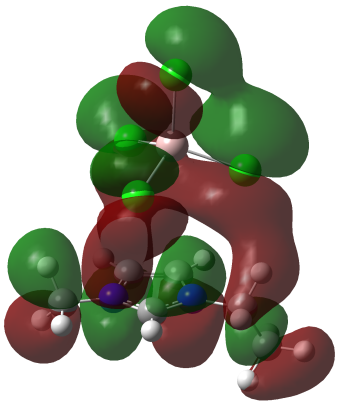
MO58 (0.02)



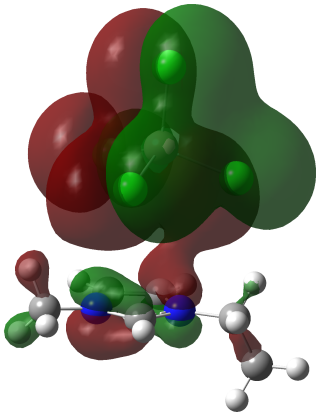
MO62 (0.02)



MO63 (0.01)

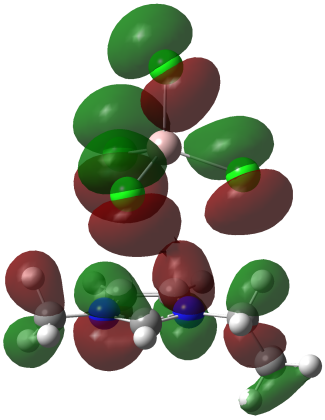


MO64 (0.01)

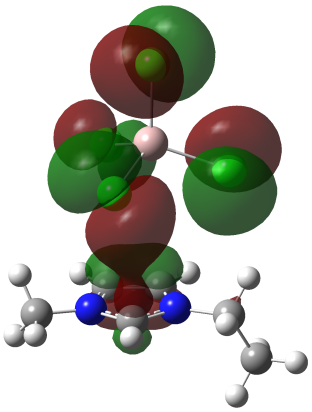


MO65 (0.01)

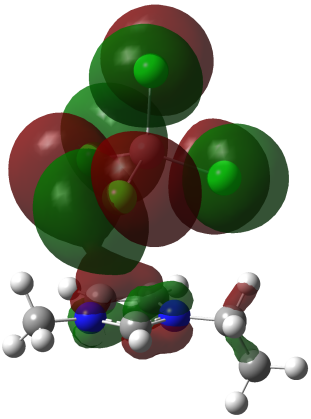
Figure A.38: $[C_2C_1Im][AlCl_4]_- - 71_4.6_58_- - 97_LP$ IP MOs I



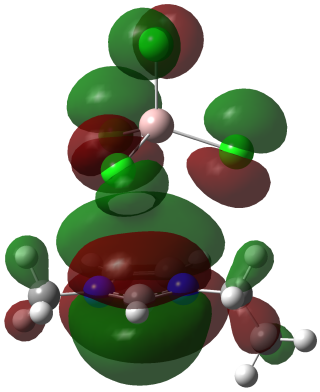
MO67 (0.02)



MO68 (0.02)

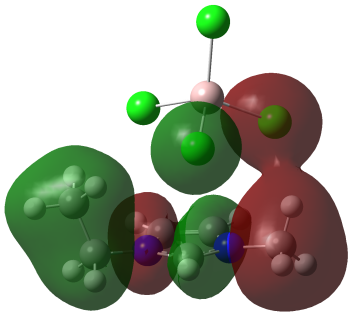


MO69 (0.01)

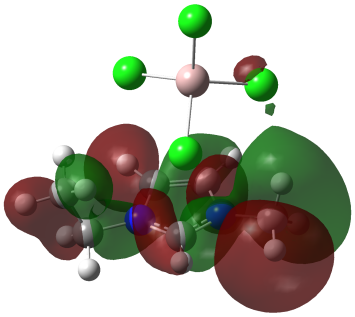


MO71 (0.01)

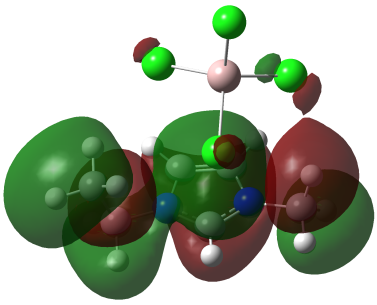
Figure A.39: $[C_2C_1Im][AlCl_4]_- - 71_4.6_58_- - 97_LP$ IP MOs II



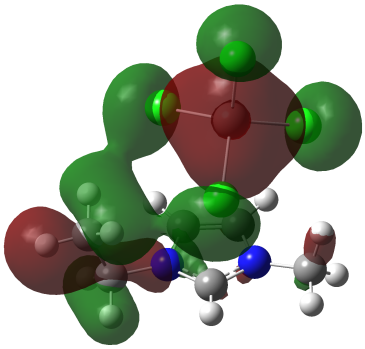
MO39 (0.01)



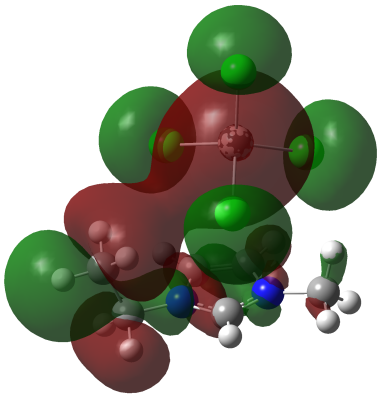
MO54 (0.01)



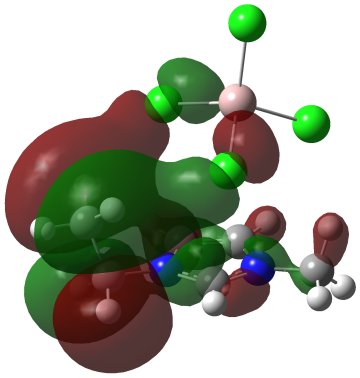
MO55 (0.01)



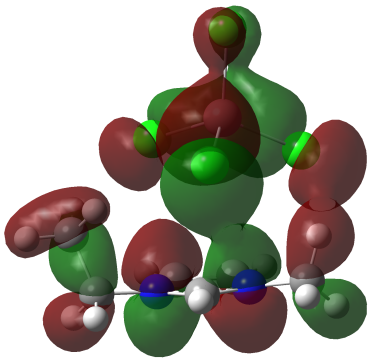
MO56 (0.02)



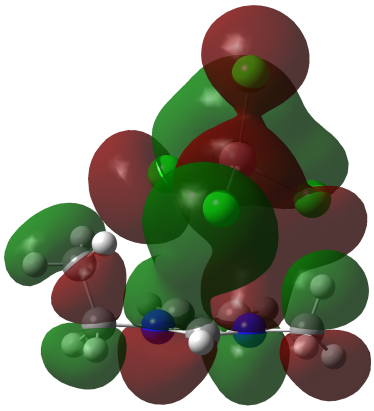
MO57 (0.01)



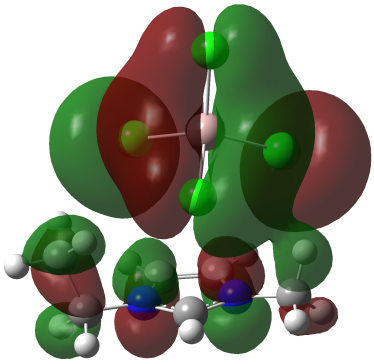
MO58 (0.01)



MO59 (0.02)

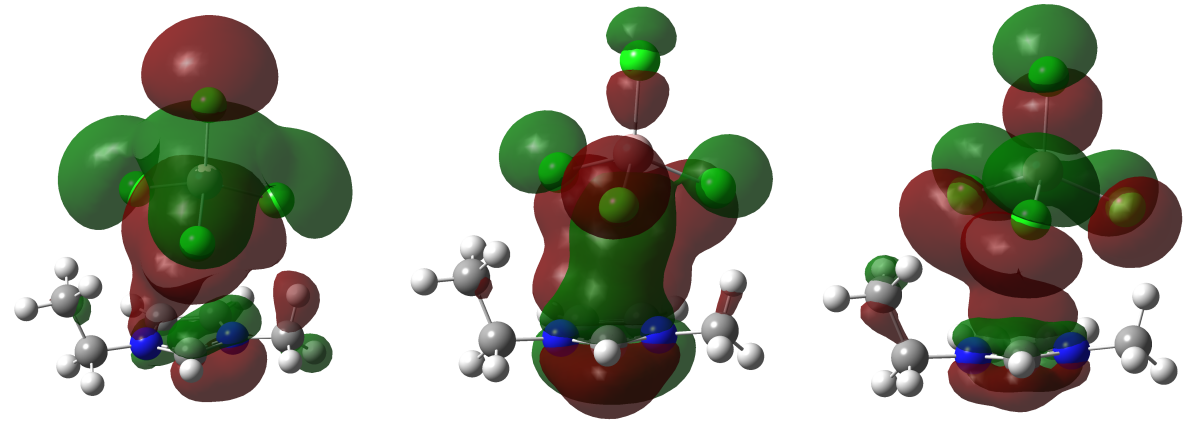


MO60 (0.01)

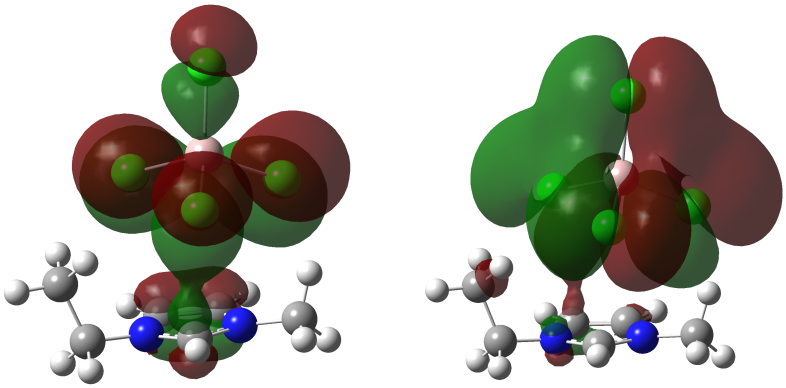


MO61 (0.01)

Figure A.40: $[C_2C_1Im][AlCl_4]$_ – 78_4.3_64_81 IP MOs I



MO62 (0.01) MO63 (0.02) MO65 (0.02)

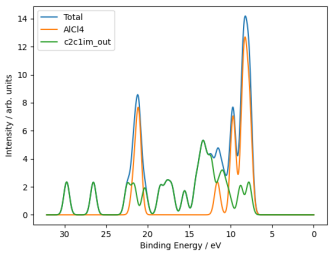


MO66 (0.02) MO67 (0.01)

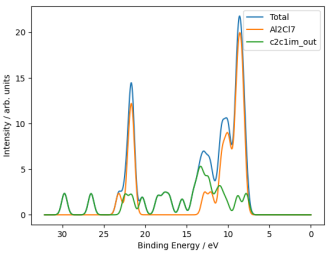
Figure A.41: $[C_2C_1Im][AlCl_4]_- - 78_4.3_64_81$ IP MOs II

A.2.5 Ion Pair XPS spectra

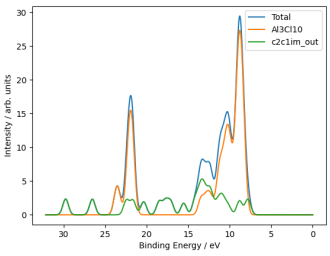
Table A.119: $[C_2C_1Im][M_xCl_y]$ IP Simulated XPS Spectra



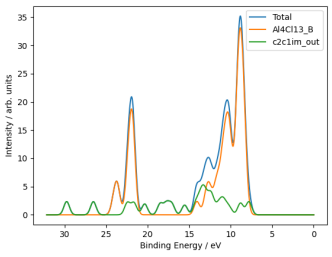
$[C_2C_1Im][AlCl_4]$



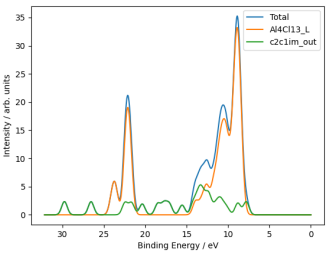
$[C_2C_1Im][Al_2Cl_7]$



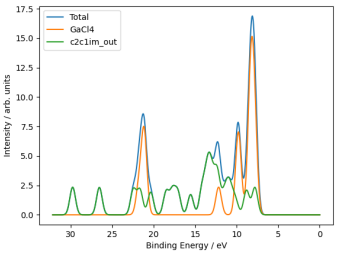
$[C_2C_1Im][Al_3Cl_{10}]$



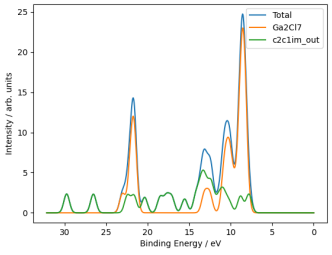
$[C_2C_1Im][Al_4Cl_{13}]_{Bra}$



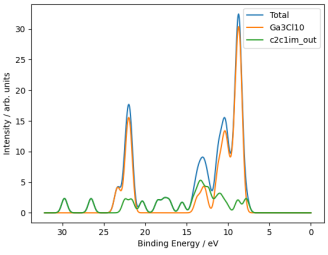
$[C_2C_1Im][Al_4Cl_{13}]_{Lin}$



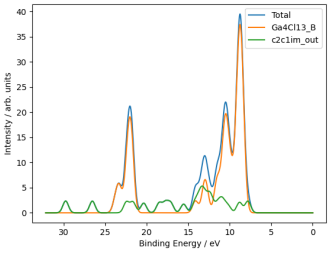
$[C_2C_1Im][GaCl_4]$



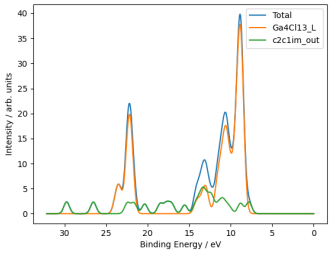
$[C_2C_1Im][Ga_2Cl_7]$



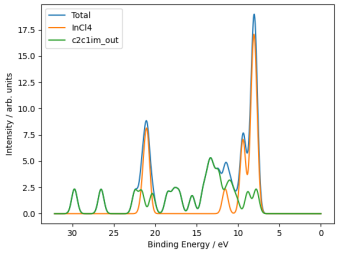
$[C_2C_1Im][Ga_3Cl_{10}]$



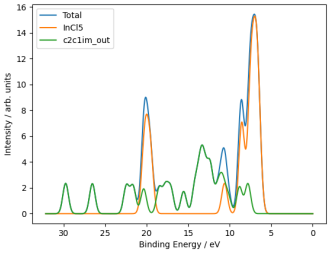
$[C_2C_1Im][Ga_4Cl_{13}]_{Bra}$



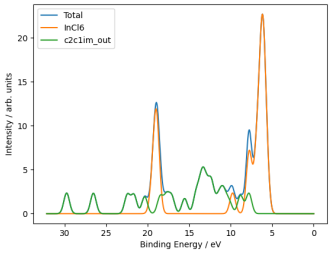
$[C_2C_1Im][Ga_4Cl_{13}]_{Lin}$



$[C_2C_1Im][InCl_4]$

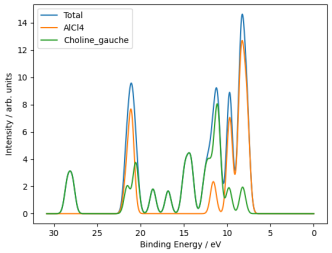


$[C_2C_1Im][InCl_5]^-$

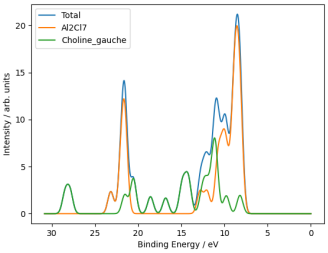


$[C_2C_1Im][InCl_6]^{2-}$

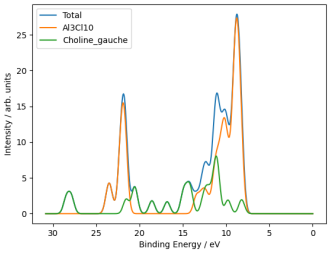
Table A.120: $[Choline][M_xCl_y]$ IP Simulated XPS Spectra



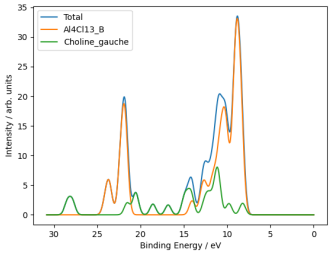
$[Choline][AlCl_4]$



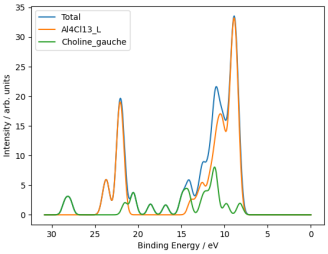
$[Choline][Al_2Cl_7]$



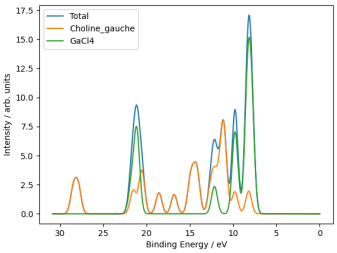
$[Choline][Al_3Cl_{10}]$



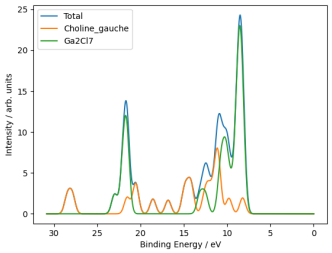
$[Choline][Al_4Cl_{13}]_{Bra}$



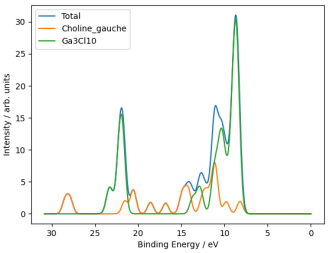
$[Choline][Al_4Cl_{13}]_{Lin}$



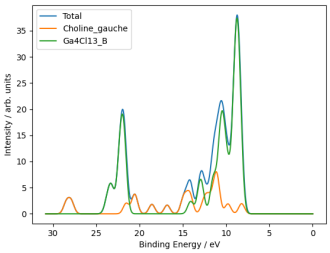
$[Choline][GaCl_4]$



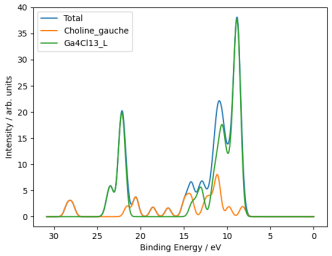
$[Choline][Ga_2Cl_7]$



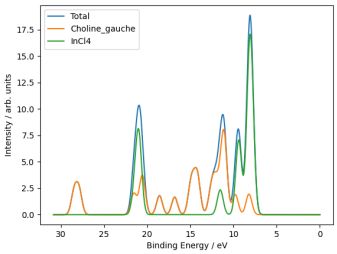
$[Choline][Ga_3Cl_{10}]$



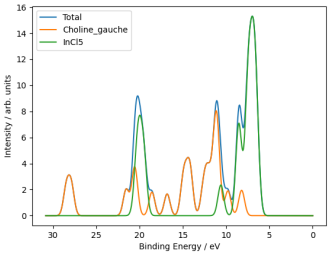
$[Choline][Ga_4Cl_{13}]_{Bra}$



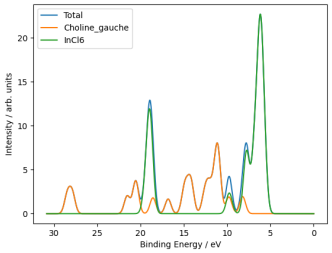
$[Choline][Ga_4Cl_{13}]_{Lin}$



$[Choline][InCl_4]$

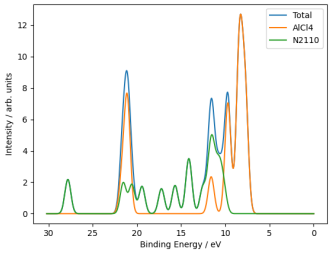


$[Choline][InCl_5]^-$

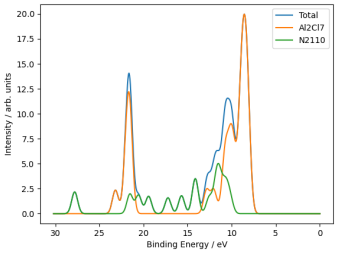


$[Choline][InCl_6]^{2-}$

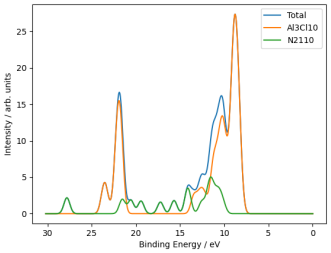
Table A.121: $[N_{2110}][M_xCl_y]$ IP Simulated XPS Spectra



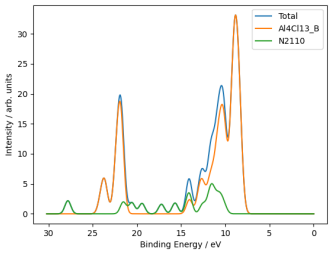
$[N_{2110}][AlCl_4]$



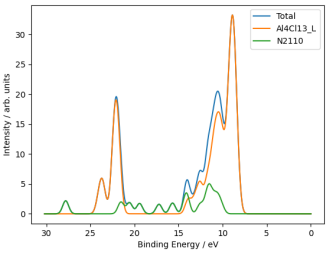
$[N_{2110}][Al_2Cl_7]$



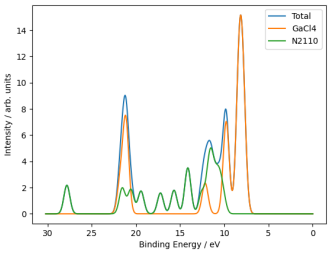
$[N_{2110}][Al_3Cl_{10}]$



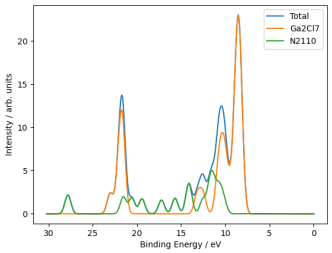
$[N_{2110}][Al_4Cl_{13}]_Bra$



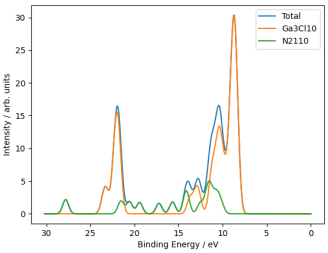
$[N_{2110}][Al_4Cl_{13}]_Lin$



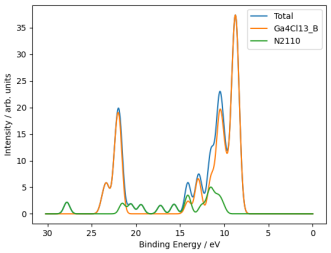
$[N_{2110}][GaCl_4]$



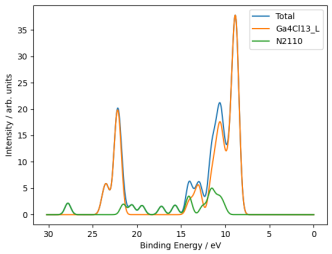
$[N_{2110}][Ga_2Cl_7]$



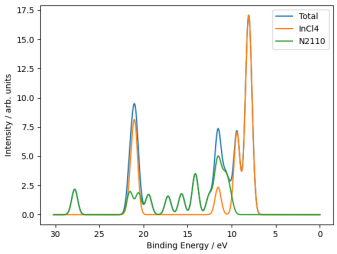
$[N_{2110}][Ga_3Cl_{10}]$



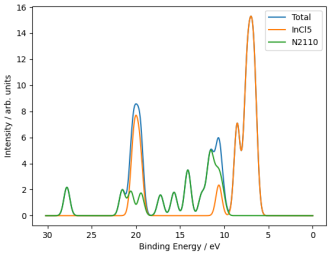
$[N_{2110}][Ga_4Cl_{13}]_Bra$



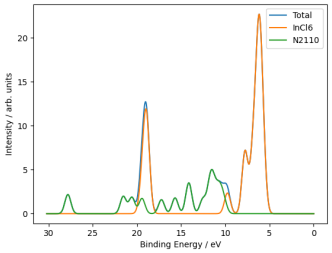
$[N_{2110}][Ga_4Cl_{13}]_Lin$



$[N_{2110}][InCl_4]$

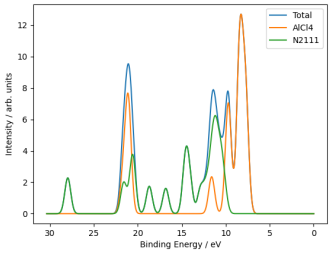


$[N_{2110}][InCl_5]^-$

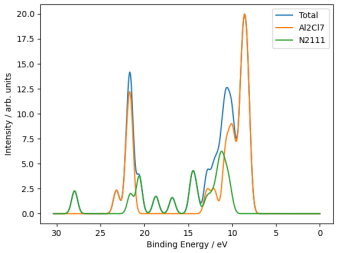


$[N_{2110}][InCl_6]^{2-}$

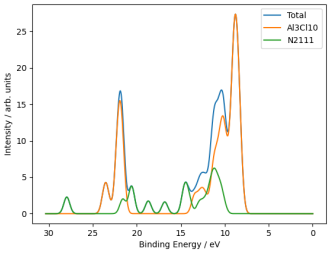
Table A.122: $[N_{2111}][M_xCl_y]$ IP Simulated XPS Spectra



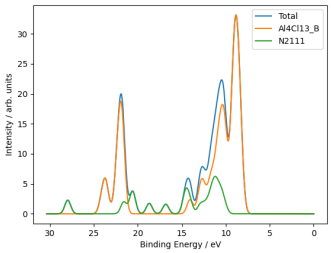
$[N_{2111}][AlCl_4]$



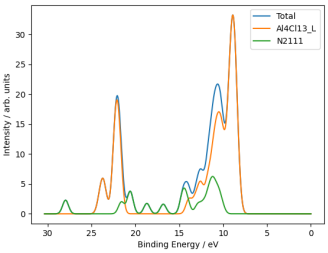
$[N_{2111}][Al_2Cl_7]$



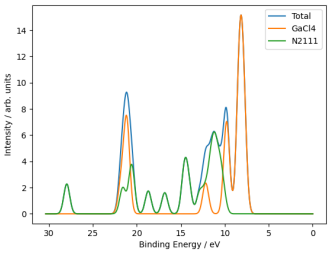
$[N_{2111}][Al_3Cl_{10}]$



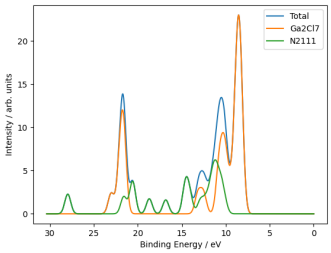
$[N_{2111}][Al_4Cl_{13}]_Bra$



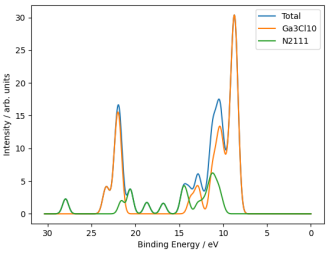
$[N_{2111}][Al_4Cl_{13}]_Lin$



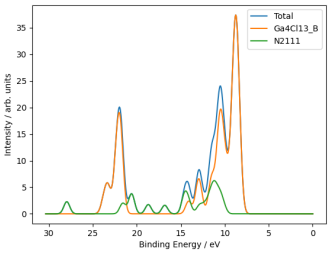
$[N_{2111}][GaCl_4]$



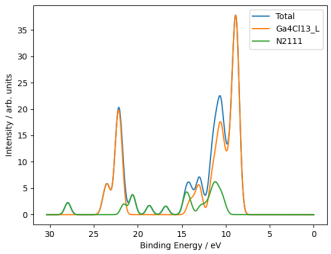
$[N_{2111}][Ga_2Cl_7]$



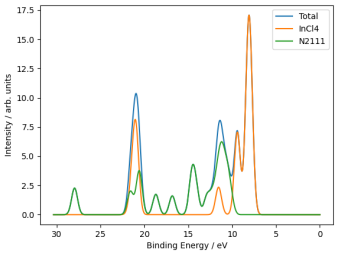
$[N_{2111}][Ga_3Cl_{10}]$



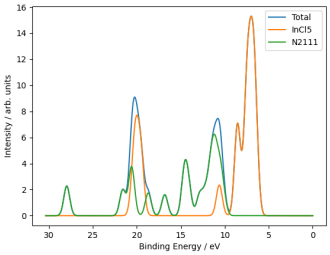
$[N_{2111}][Ga_4Cl_{13}]_Bra$



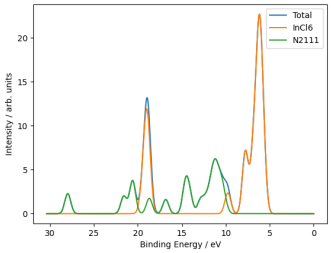
$[N_{2111}][Ga_4Cl_{13}]_Lin$



$[N_{2111}][InCl_4]$



$[N_{2111}][InCl_5]^-$



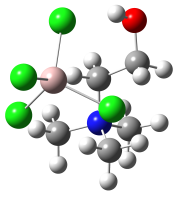
$[N_{2111}][InCl_6]^{2-}$

A.2.6 $[Choline][M_xCl_y]$ Gas Ion pair structures

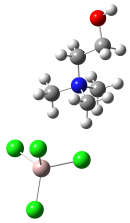
Table A.123: Number of IP structures divided into relative Gibbs free energy with respect to the lowest energy structure of each IP in the ranges of ≤ 10, $10 \leq 20$, $20 \leq 30$, $30 \leq 40$, $40 \leq 50$ and $50 <$ in $kJ\ mol^{-1}$ of each $[Choline][M_xCl_{3y}]^{z-}$ IP in the Gas Phase

Anion	≤ 10	$10 \leq 20$	$20 \leq 30$	$30 \leq 40$	$40 \leq 50$	$50 <$	Total
$[AlCl_4]^-$	6	6	6	1	0	0	19
$[Al_2Cl_7]^-$	1	5	7	0	1	1	15
$[Al_3Cl_{10}]^-$	4	4	2	2	0	2	14
Branched $[Al_4Cl_{13}]^-$	2	3	4	2	0	0	13
Linear $[Al_4Cl_{13}]^-$	5	3	1	0	3	1	13
$[GaCl_4]^-$	6	6	5	1	0	0	18
$[Ga_2Cl_7]^-$	9	1	0	0	0	0	10
$[Ga_3Cl_{10}]^-$	3	0	3	3	0	2	11
Branched $[Ga_4Cl_{13}]^-$	3	3	3	0	0	2	11
Linear $[Ga_4Cl_{13}]^-$	3	4	4	0	1	1	13
$[InCl_4]^-$	5	3	7	1	0	0	16
$[InCl_5]^{2-}$	6	2	0	4	2	0	14
$[InCl_6]^{3-}$	1	0	0	0	0	0	1

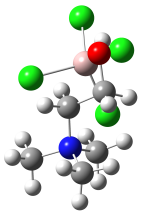
Table A.124: $[Choline][AlCl_4]$ Gas Phase Ion Pair Structures



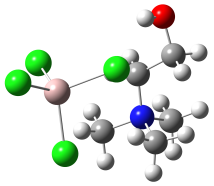
168_4.7_57_92 (10)



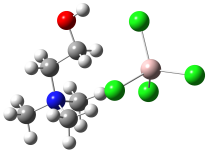
170_4.6_150_134 (30)



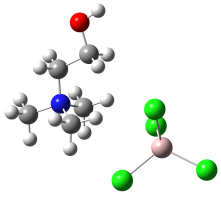
173_4.7_68_-101 (13)



-177_4.6_63_110 (12)



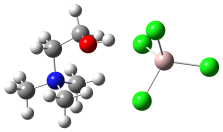
178_5.1_76_12 (24)



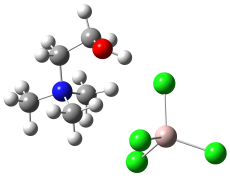
-180_4.7_118_-13 (24)



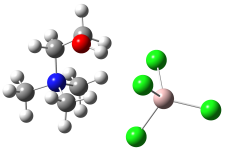
180_4.5_180_1 (23)



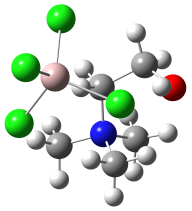
-72_5.1_84_-12 (8)



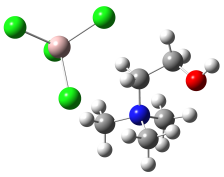
-73_4.7_112_14 (11)



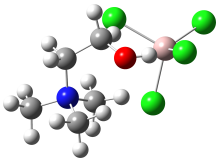
-81_4.8_98_-13 (8)



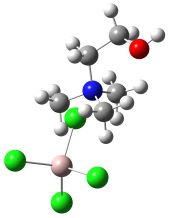
-52_4.7_50_111 (0)



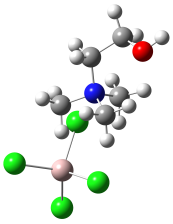
-55_4.6_45_170 (10)



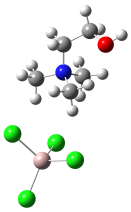
-56_5_84_-39 (13)



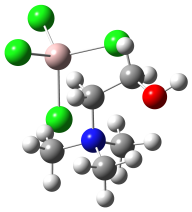
-62_4.6_143_-124 (21)



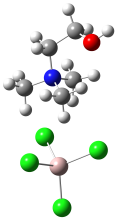
-62_4.6_144_-124 (22)



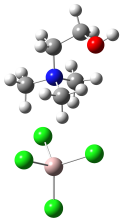
-62_4.6_152_125 (25)



-63_4.5_69_-104 (3)



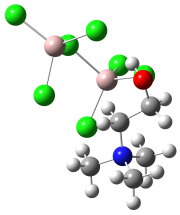
-64_4.5_176_-132 (20)



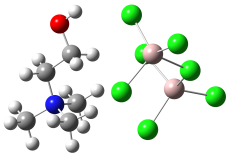
-64_4.5_176_-134 (20)

Table A.125: $[Choline][Al_2Cl_7]$ Gas Phase Ion Pair Structures

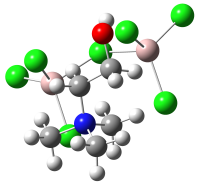
−163_6.1_57_ − 120 (13)



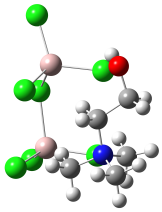
171_6.4_86_ − 5 (21)



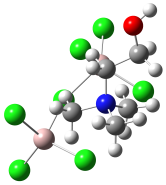
175_5.9_81_ − 103 (15)



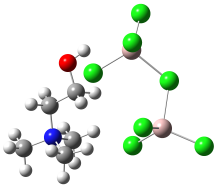
177_6_76_ − 114 (24)



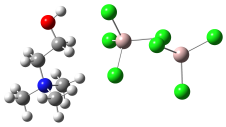
−164_6_105_ − 107 (24)



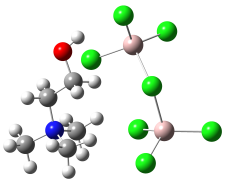
179_6.4_77_ − 47 (18)



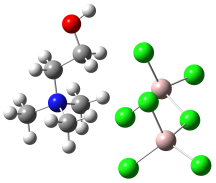
−177_7.1_83_ − 11 (49)



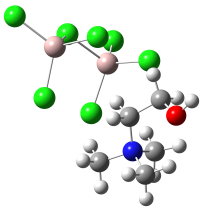
177_4.7_79_ − 33 (22)



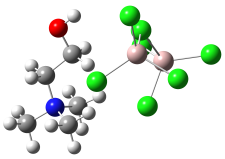
−180_6_108_ − 26 (20)



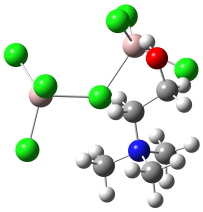
−67_6_51_ − 124 (0)



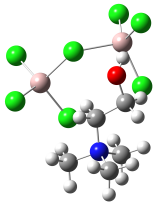
−170_5.5_61_11 (29)



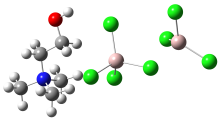
−167_4.1_72_ − 114 (19)



−165_4.8_36_ − 118 (15)



177_7.1_83_10 (51)



179_4.5_125_ − 16 (21)

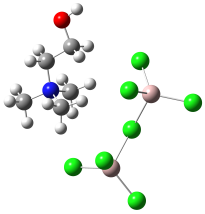
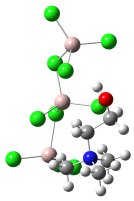
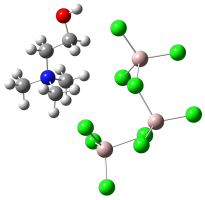


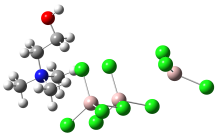
Table A.126: $[Choline][Al_3Cl_{10}]$ Gas Phase Ion Pair Structures



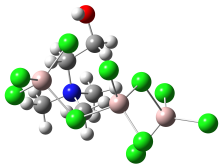
−155_4.9_62_ − 109 (15)



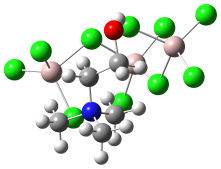
−179_7.5_102_20 (24)



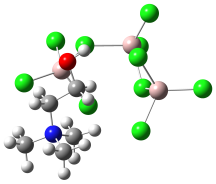
−180_5_113_5 (31)



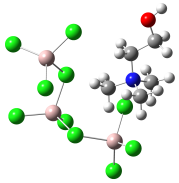
176_6.2_81_61 (0)



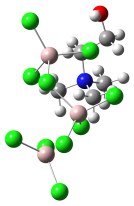
173_6.6_90_ − 94 (6)



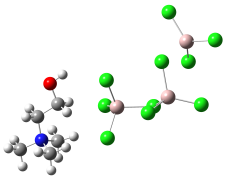
−176_6.2_63_ − 49 (15)



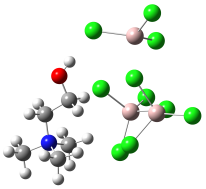
−164_6.2_115_ − 148 (23)



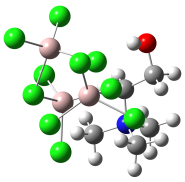
−172_6.6_89_85 (13)



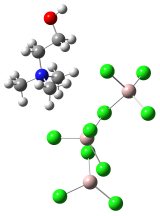
−176_8.5_77_3 (67)



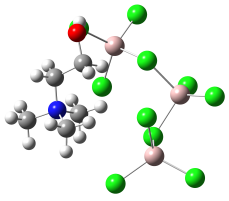
−172_5.7_82_ − 15 (19)



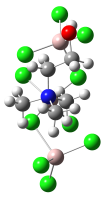
−178_7.8_50_99 (56)



180_4.7_151_6 (34)

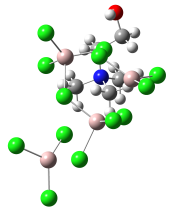


176_6.1_93_ − 41 (2)

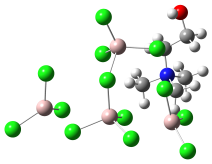


173_5.9_106_ − 109 (1)

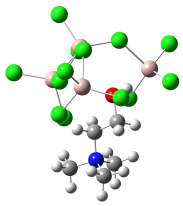
Table A.127: $[Choline][Al_4Cl_{13}]$ Branched Gas Phase Ion Pair Structures



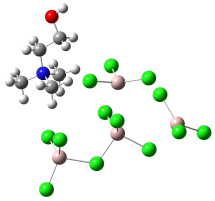
−172_6_97_83 (25)



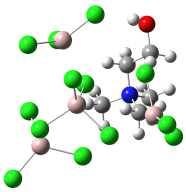
−175_5.9_96_108 (23)



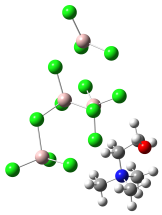
175_6_9_ − 146 (25)



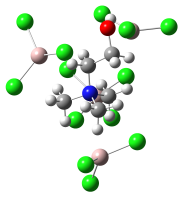
179_5.8_135_1 (17)



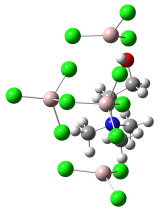
169_5.7_79_87 (0)



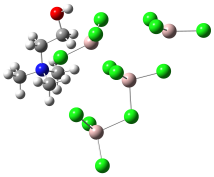
−73_5.9_28_174 (13)



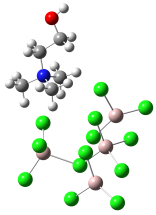
174_5.6_108_ − 108 (8)



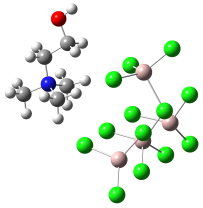
176_6_62_86 (20)



−176_5.9_92_20 (20)

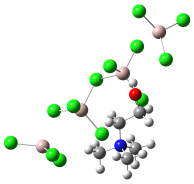


−175_5.8_149_ − 7 (39)

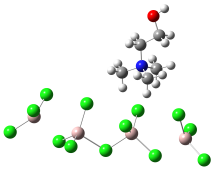


178_5.9_126_4 (39)

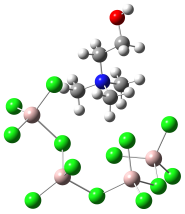
Table A.128: $[Choline][Al_4Cl_{13}]$ Linear Gas Phase Ion Pair Structures



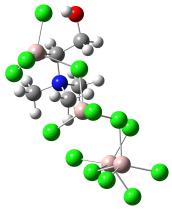
−161_6.2_60_ − 112 (45)



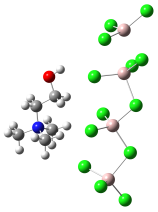
−178_6.7_154_ − 178 (50)



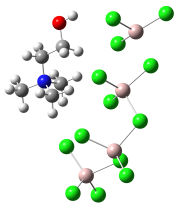
167_6.5_144_81 (13)



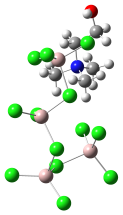
174_5.2_102_41 (1)



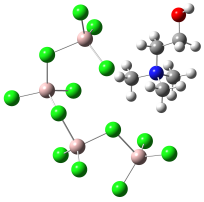
178_7.2_78_2 (46)



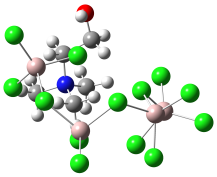
165_6.8_107_12 (20)



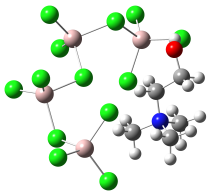
−172_6.9_119_100 (12)



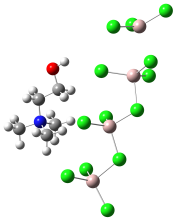
164_6.6_102_124 (8)



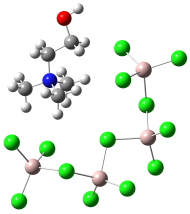
−173_6.9_80_63 (0)



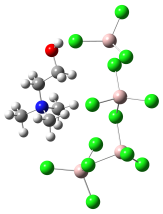
178_4.3_54_175 (4)



178_7.1_80_12 (48)

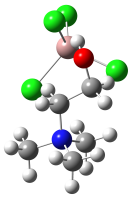


−179_4.6_138_6 (7)

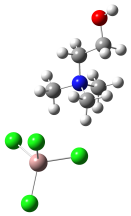


167_4.7_104_ − 5 (26)

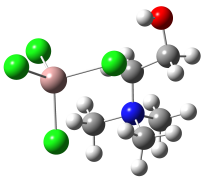
Table A.129: $[Choline][GaCl_4]$ Gas Phase Ion Pair Structures



-167_4.8_56_-92 (10)



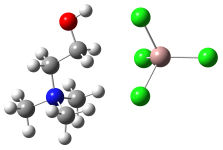
169_4.6_148_134 (31)



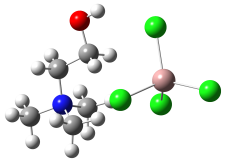
-177_4.6_63_111 (12)



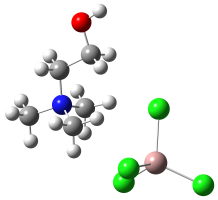
-180_4.5_179_0 (24)



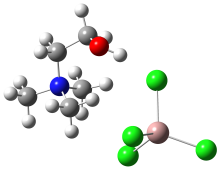
-179_5.2_75_-9 (30)



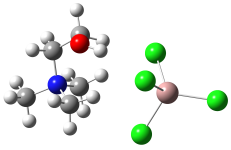
177_5.1_76_12 (24)



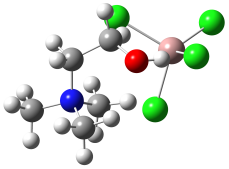
179_4.7_119_13 (24)



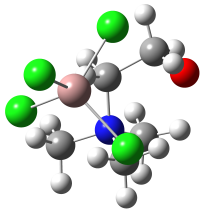
-73_4.7_113_14 (13)



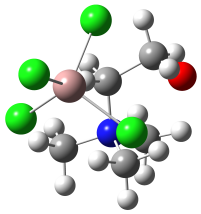
-81_4.8_99_-13 (10)



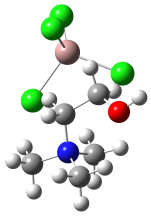
-56_5_83_-40 (15)



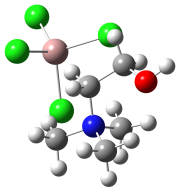
-57_4.8_61_102 (3)



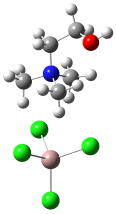
-58_4.8_57_103 (9)



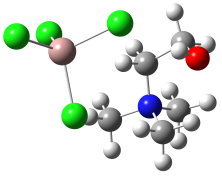
-61_4.8_57_-86 (5)



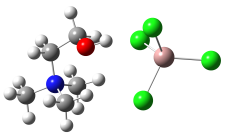
-63_4.6_69_-104 (4)



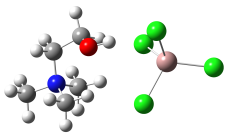
-64_4.6_176_-132 (22)



-66_4.7_52_126 (0)

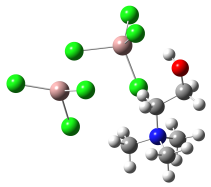


-71_5.1_84_-12 (10)

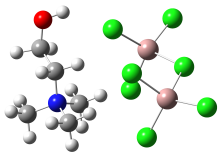


-72_5.1_84_-12 (10)

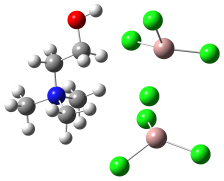
Table A.130: $[Choline][Ga_2Cl_7]$ Gas Phase Ion Pair Structures



−163_6.2_57_ − 134 (2)



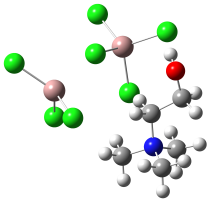
−174_6_82_102 (2)



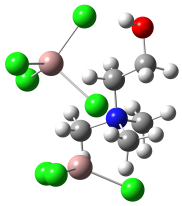
170_4.2_92_ − 13 (3)



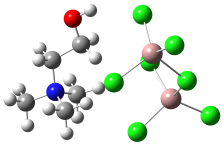
169_4.4_144_122 (12)



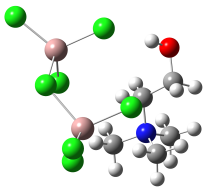
−166_4.7_34_ − 154 (1)



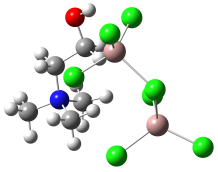
166_4.4_68_73 (3)



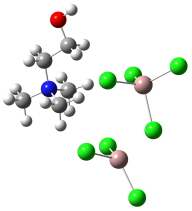
−166_6.4_85_16 (8)



162_6.2_56_121 (0)

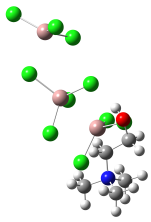


−180_6.5_78_47 (4)

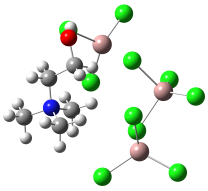


179_6.1_111_18 (6)

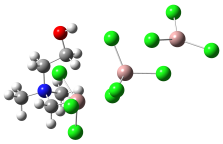
Table A.131: $[Choline][Ga_3Cl_{10}]$ Gas Phase Ion Pair Structures



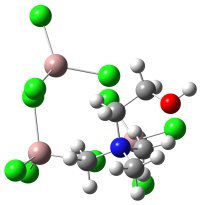
−163_5.5_40_ − 140 (30)



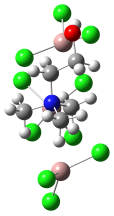
177_6.1_94_ − 42 (1)



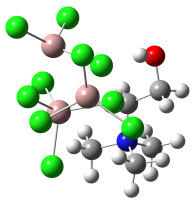
−175_5.6_73_22 (34)



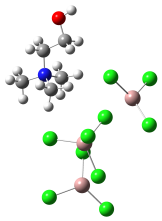
−60_5.5_102_ − 117 (2)



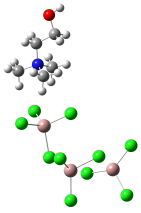
173_5.8_107_ − 110 (0)



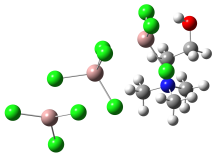
−177_7.7_48_99 (61)



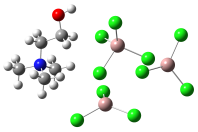
179_4.7_151_6 (34)



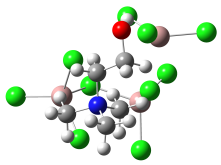
−180_7.8_161_33 (67)



164_5_72_128 (26)

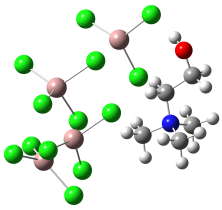


−177_5.2_74_ − 19 (33)

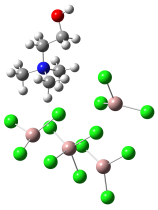


174_6.6_105_ − 98 (24)

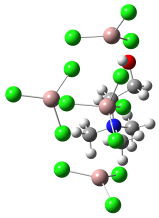
Table A.132: $[Choline][Ga_4Cl_{13}]$ Branched Gas Phase Ion Pair Structures



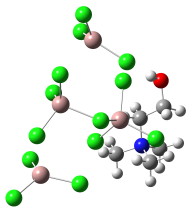
−165_5.7_67_ − 173 (6)



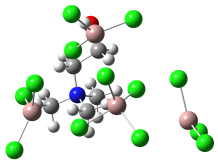
176_5.4_157_28 (11)



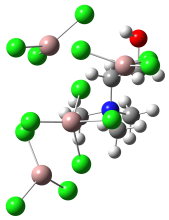
175_6.1_62_85 (23)



165_7.9_59_109 (56)



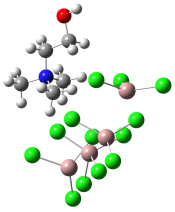
177_5.6_83_62 (22)



169_5.6_81_80 (0)



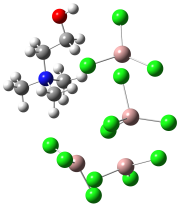
175_4.9_103_ − 109 (22)



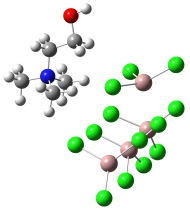
176_5.9_122_43 (13)



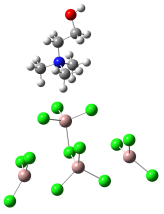
−172_5.5_89_66 (5)



−176_5.3_114_12 (14)

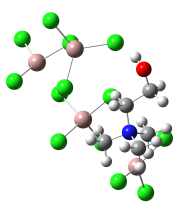


180_6_126_0 (33)

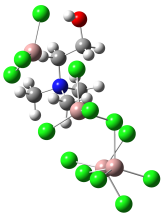


178_7.7_161_53 (57)

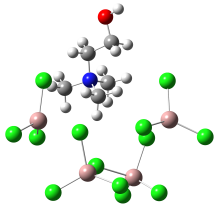
Table A.133: $[Choline][Ga_4Cl_{13}]$ Linear Gas Phase Ion Pair Structures



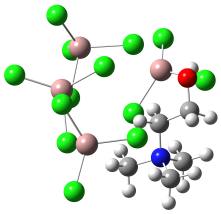
−162_7.2_84_ − 124 (16)



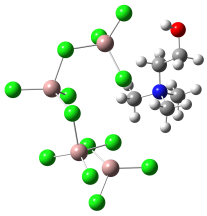
173_5.1_101_40 (0)



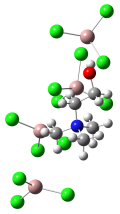
173_4.8_149_72 (15)



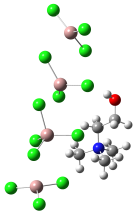
169_4.7_61_ − 176 (9)



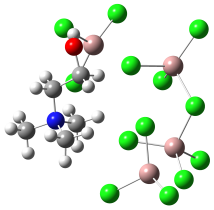
172_6.7_88_100 (15)



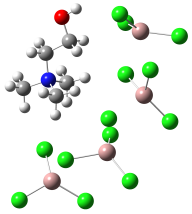
180_6.5_92_ − 118 (44)



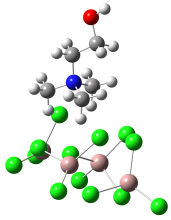
160_6.5_50_117 (52)



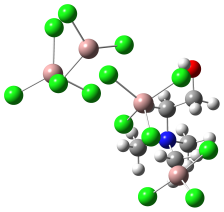
−177_6.8_94_ − 35 (4)



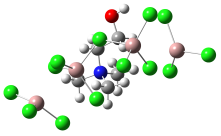
−177_5.1_106_36 (24)



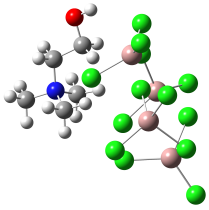
174_6.6_161_ − 11 (27)



169_7.2_49_95 (19)

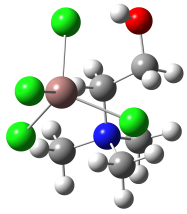


178_4.9_48_69 (20)



−175_6.8_111_14 (22)

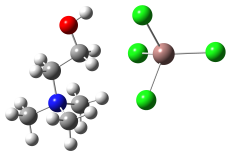
Table A.134: $[Choline][InCl_4]$ Gas Phase Ion Pair Structures



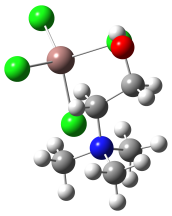
165_4.9_57_91 (10)



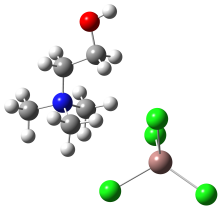
-168_4.7_145_-97 (31)



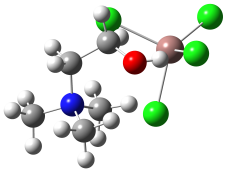
-176_5.2_76_-12 (23)



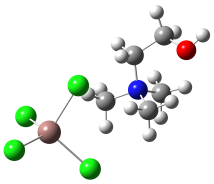
177_4.7_64_-112 (13)



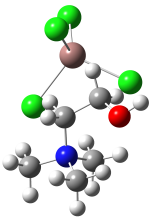
-179_4.7_121_-13 (24)



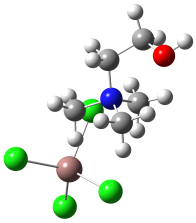
-55_5.1_83_-42 (14)



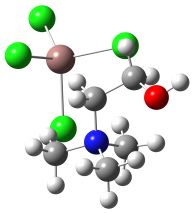
-57_4.7_98_152 (26)



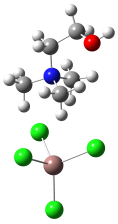
-61_4.9_57_-86 (5)



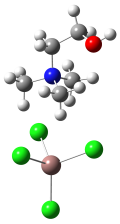
-62_4.7_137_-122 (21)



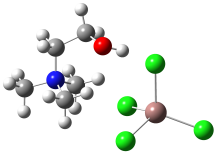
-63_4.7_70_-104 (6)



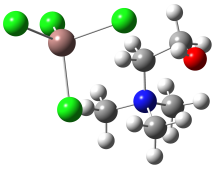
-64_4.6_176_-131 (23)



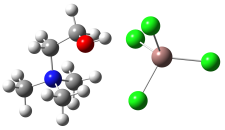
-64_4.6_177_-130 (23)



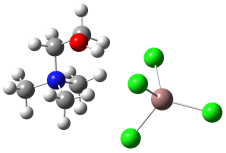
-64_4.9_111_-10 (21)



-66_4.8_51_128 (0)

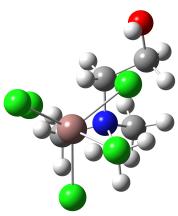


-71_5.2_84_-12 (10)

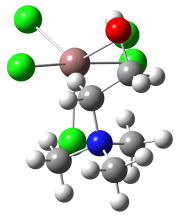


-82_4.8_99_-14 (10)

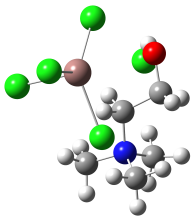
Table A.135: $[Choline][InCl_5]^-$ Gas Phase Ion Pair Structures



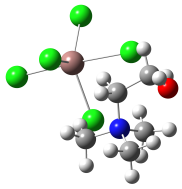
−167_5_74_100 (10)



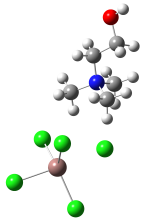
168_4.7_74_ − 105 (9)



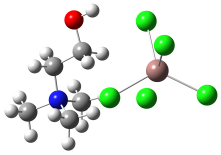
167_4.8_70_ − 115 (8)



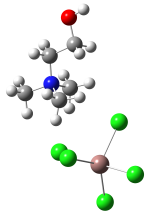
−68_4.8_71_ − 115 (16)



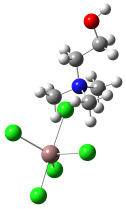
169_4.9_146_140 (42)



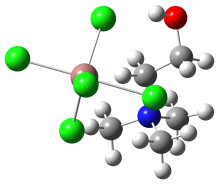
174_5.5_74_14 (32)



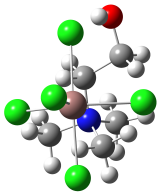
177_4.9_144_20 (34)



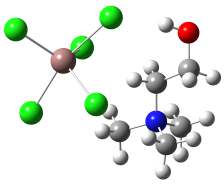
−168_4.9_145_ − 141 (49)



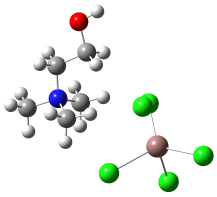
166_5_55_105 (8)



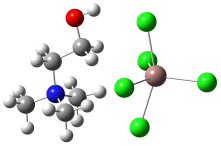
176_4.5_66_90 (0)



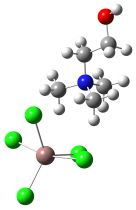
165_4.5_54_144 (4)



−178_4.9_120_ − 15 (31)

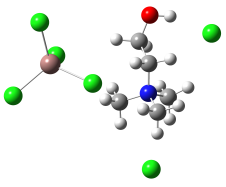


−176_4.7_82_3 (16)

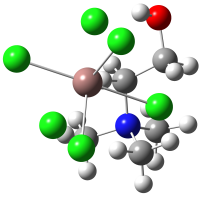


165_4.4_135_112 (35)

Table A.136: $[Choline][InCl_6]^{2-}$ Gas Phase Ion Pair Structures



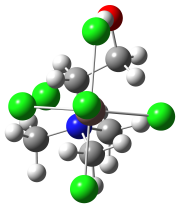
−159_5.5_68_ − 91 (0)



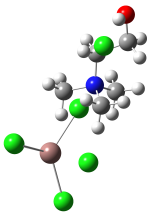
165_5.2_57_96 (220)



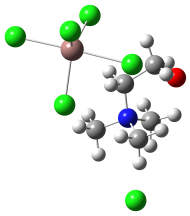
169_5_60_91 (31)



−175_4.8_69_77 (33)



−168_5_144_ − 132 (27)



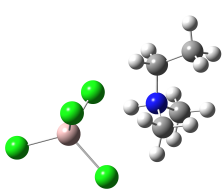
−60_5.2_38_130 (31)

A.2.7 $[N_{2110}][M_xCl_y]$ Gas Ion pair structures

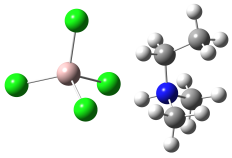
Table A.137: Number of IP structures divided into relative Gibbs free energy with respect to the lowest energy structure of each IP in the ranges of ≤ 10, $10 \leq 20$, $20 \leq 30$, $30 \leq 40$, $40 \leq 50$ and $50 <$ in $kJ\ mol^{-1}$ of each $[N_{2110}][M_xCl_{3y}]^{z-}$ IP in the Gas Phase

Anion	≤ 10	$10 \leq 20$	$20 \leq 30$	$30 \leq 40$	$40 \leq 50$	$50 <$	Total
$[AlCl_4]^-$	1	2	0	0	0	3	6
$[Al_2Cl_7]^-$	3	0	1	1	1	4	10
$[Al_3Cl_{10}]^-$	4	3	2	2	1	2	14
Branched $[Al_4Cl_{13}]^-$	5	3	0	0	0	4	12
Linear $[Al_4Cl_{13}]^-$	4	4	2	3	0	3	16
$[GaCl_4]^-$	1	0	0	0	0	3	4
$[Ga_2Cl_7]^-$	6	1	0	0	2	2	11
$[Ga_3Cl_{10}]^-$	7	3	1	1	1	1	14
Branched $[Ga_4Cl_{13}]^-$	1	0	8	0	1	3	13
Linear $[Ga_4Cl_{13}]^-$	6	4	1	1	1	2	15
$[InCl_4]^-$	2	0	0	0	1	2	5
$[InCl_5]^{2-}$	2	0	0	0	0	5	7
$[InCl_6]^{3-}$	1	0	0	0	0	1	2

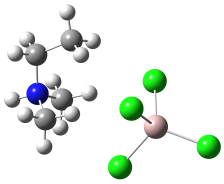
Table A.138: $[N_{2110}][AlCl_4]$ Gas Phase Ion Pair Structures



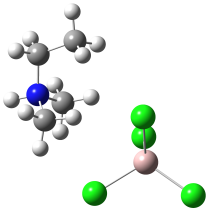
3.7_112_176 (0)



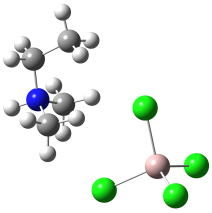
3.9_80_ − 180 (13)



4.7_103_0 (54)

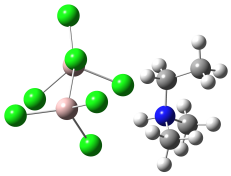


4.6_122_ − 14 (55)

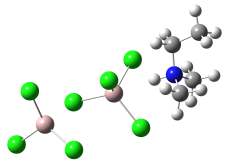


4.9_123_0 (70)

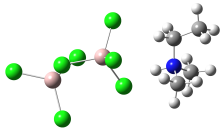
Table A.139: $[N_{2110}][Al_2Cl_7]$ Gas Phase Ion Pair Structures



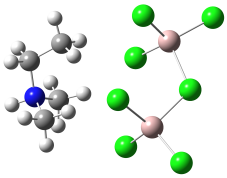
4.2_61_174 (6)



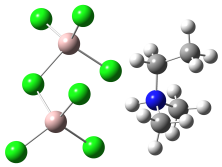
5.9_107_ – 168 (35)



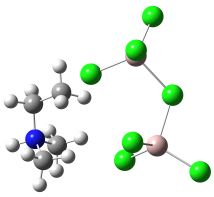
5.9_90_169 (29)



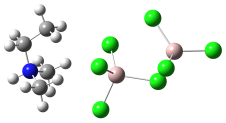
6.3_92_ – 1 (53)



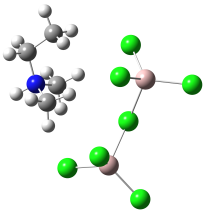
5.1_88_175 (0)



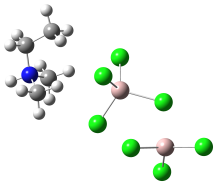
6.3_81_ – 50 (52)



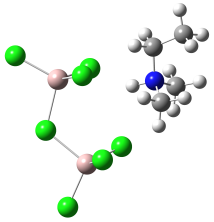
6.8_104_0 (73)



4.5_127_ – 15 (48)

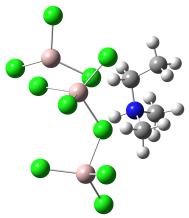


6.8_106_1 (73)

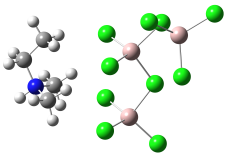


5.2_112_161 (1)

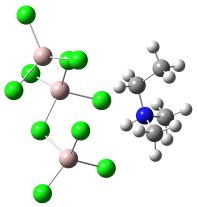
Table A.140: $[N_{2110}][Al_3Cl_{10}]$ Gas Phase Ion Pair Structures



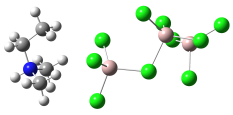
4.1_87_ – 142 (34)



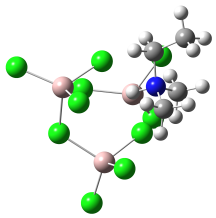
5.2_93_ – 12 (66)



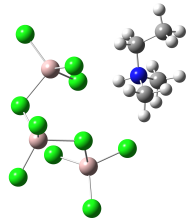
4.7_72_ – 161 (18)



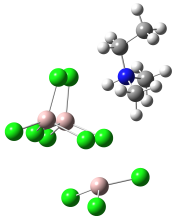
8_91_ – 7 (82)



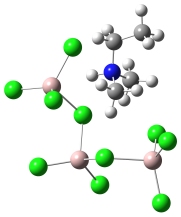
4.8_141_ – 156 (18)



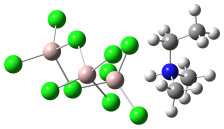
6_110_139 (9)



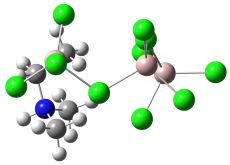
4.8_99_138 (17)



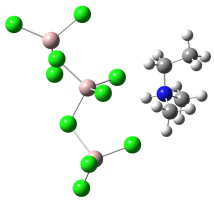
5.4_155_ – 140 (9)



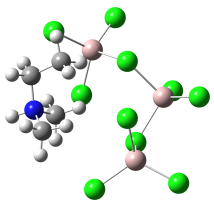
6.2_86_ – 178 (5)



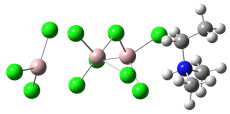
6.2_73_31 (43)



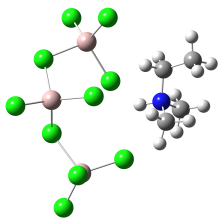
4.1_88_176 (25)



6.1_96_ – 41 (37)

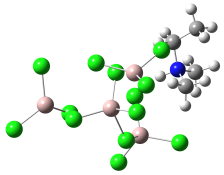


4.8_74_158 (30)

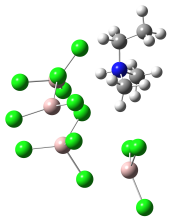


5_91_155 (0)

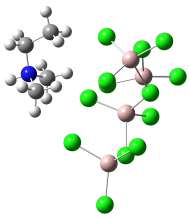
Table A.141: $[N_{2110}][Al_4Cl_{13}]$ Branched Gas Phase Ion Pair Structures



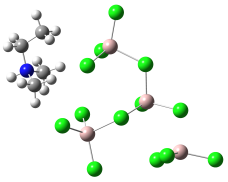
4.5_100_133 (13)



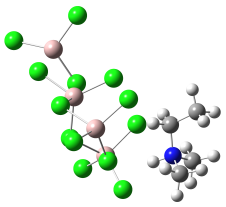
5_144_164 (0)



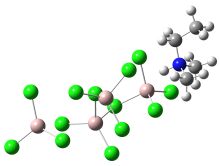
6.2_122_ – 42 (52)



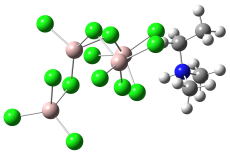
7.3_113_2 (53)



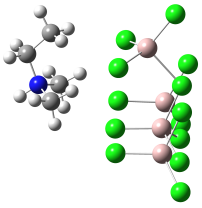
5.5_56_176 (3)



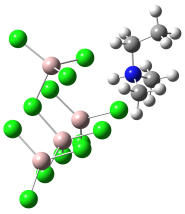
6.5_118_ – 179 (14)



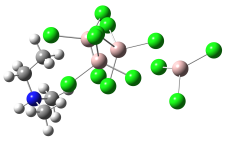
5.7_71_158 (10)



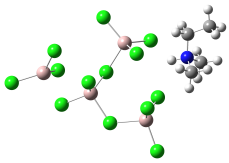
5.9_128_ – 4 (53)



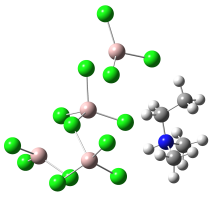
5.1_133_180 (9)



5.4_79_ – 14 (51)

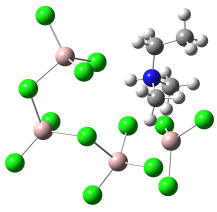


6.5_112_165 (10)

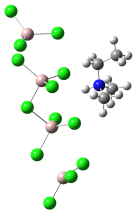


5.1_71_ – 156 (4)

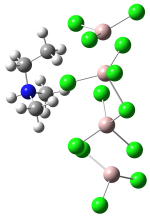
Table A.142: $[N_{2110}][Al_4Cl_{13}]$ Linear Gas Phase Ion Pair Structures



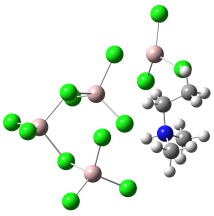
4.1_138_167 (17)



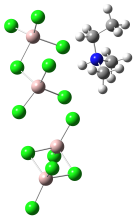
5.5_107_ – 180 (33)



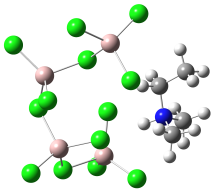
6.7_95_30 (74)



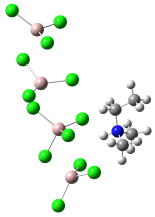
5.4_68_ – 173 (8)



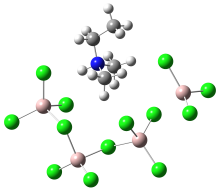
6_111_147 (27)



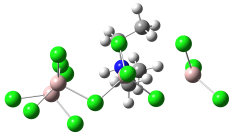
5.9_78_166 (0)



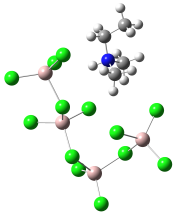
5.9_72_ – 180 (33)



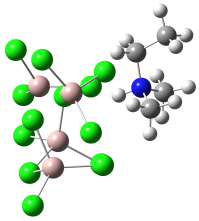
4.9_168_89 (13)



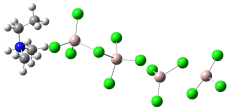
5.2_94_100 (15)



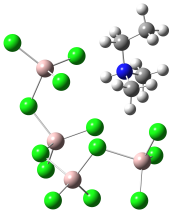
6.3_147_135 (8)



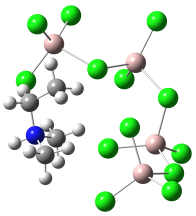
5.9_114_144 (15)



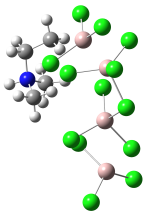
9.9_96_0 (103)



5.9_126_146 (3)



6.6_91_ – 47 (33)

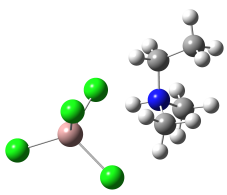


6.7_95_32 (75)

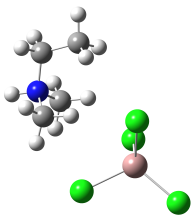


4.8_79_51 (25)

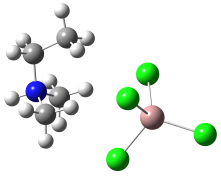
Table A.143: $[N_{2110}][GaCl_4]$ Gas Phase Ion Pair Structures



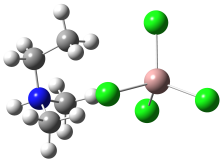
3.7_113_176 (0)



4.6_122_ – 14 (55)

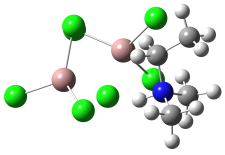


4.7_104_0 (53)

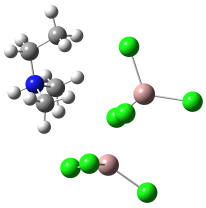


5.1_82_12 (63)

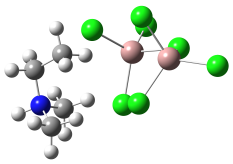
Table A.144: $[N_{2110}][Ga_2Cl_7]$ Gas Phase Ion Pair Structures



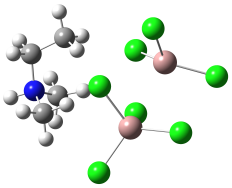
3.4_100_ – 143 (10)



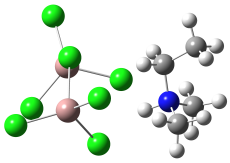
4.2_114_ – 3 (47)



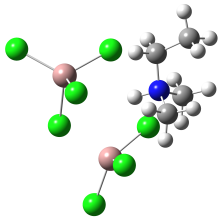
6.3_83_ – 46 (51)



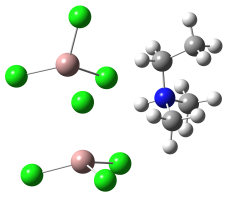
4.2_104_5 (53)



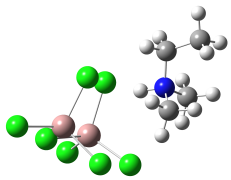
4.2_59_173 (5)



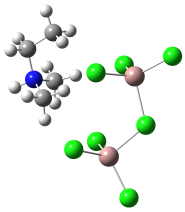
5.2_111_ – 162 (2)



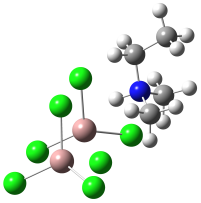
3.4_84_148 (6)



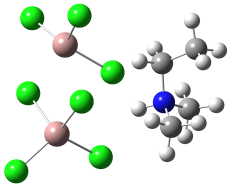
5.2_117_164 (2)



6.1_113_18 (46)

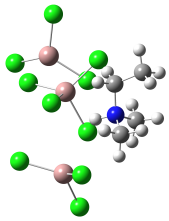


3.4_144_ – 180 (6)

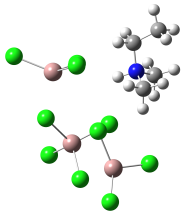


5.2_87_174 (0)

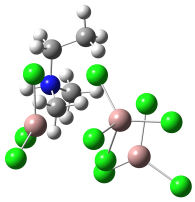
Table A.145: $[N_{2110}][Ga_3Cl_{10}]$ Gas Phase Ion Pair Structures



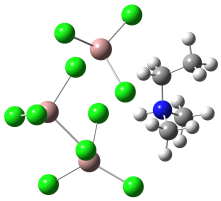
4.1_86_ – 140 (32)



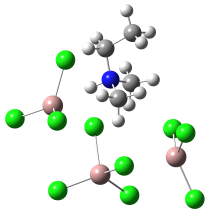
5_134_167 (11)



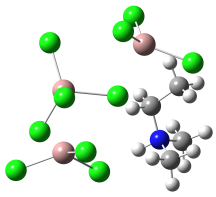
5.6_91_54 (47)



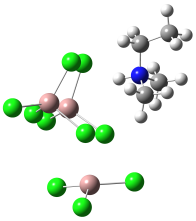
5.2_85_146 (2)



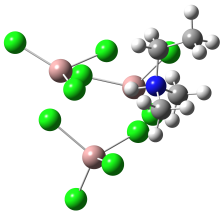
5.4_156_ – 137 (6)



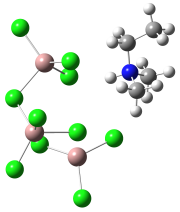
5.3_67_ – 149 (0)



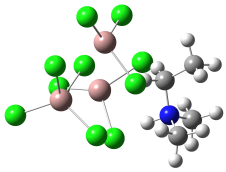
4.8_100_138 (15)



4.8_140_ – 154 (15)



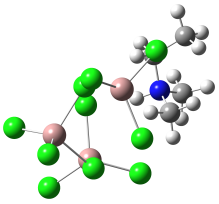
6.1_107_137 (6)



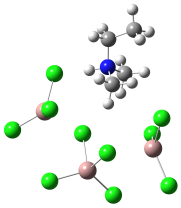
4.6_73_154 (4)



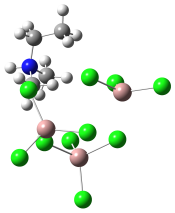
4.8_73_158 (24)



5.3_93_140 (2)

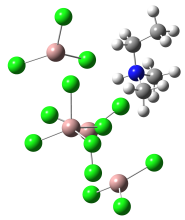


5.5_162_109 (9)

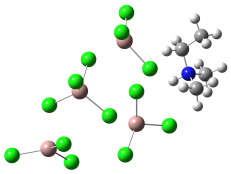


5.4_133_26 (56)

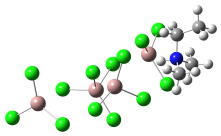
Table A.146: $[N_{2110}][Ga_4Cl_{13}]$ Branched Gas Phase Ion Pair Structures



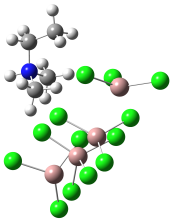
4.3_119_146 (24)



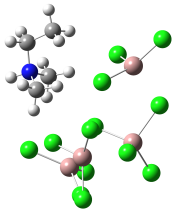
6.5_88_171 (25)



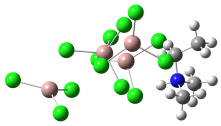
6.5_117_ – 164 (26)



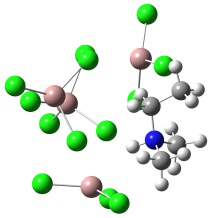
6_123_43 (59)



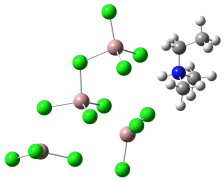
6.3_125_3 (43)



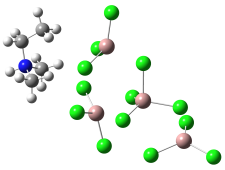
4.5_62_160 (23)



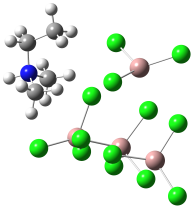
5.5_80_ – 143 (0)



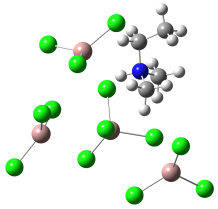
6.3_111_ – 179 (27)



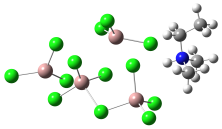
7.3_112_ – 1 (69)



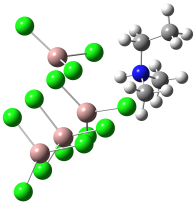
5.7_132_ – 15 (60)



4.5_142_ – 141 (26)

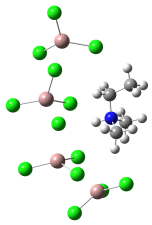


6.5_98_167 (28)

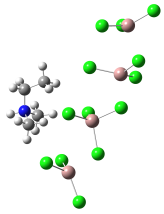


5.1_133_ – 180 (24)

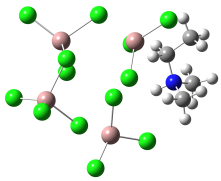
Table A.147: $[N_{2110}][Ga_4Cl_{13}]$ Linear Gas Phase Ion Pair Structures



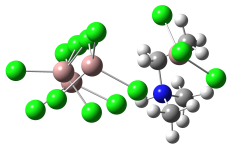
3.5_87_146 (27)



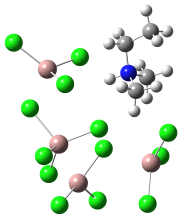
7.2_83_8 (78)



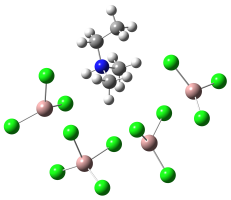
5.6_68_ – 173 (5)



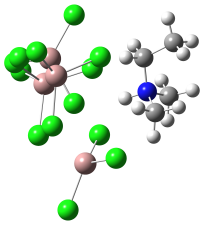
4.8_45_146 (16)



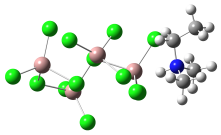
5.9_125_145 (3)



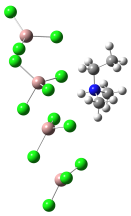
4.5_173_102 (10)



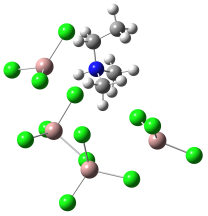
5.9_76_ – 179 (11)



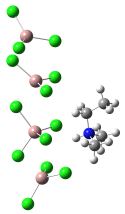
8.6_94_ – 171 (9)



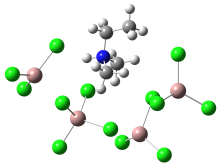
5.5_106_ – 179 (35)



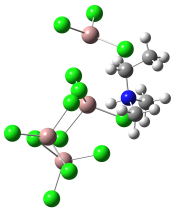
6.5_151_ – 123 (4)



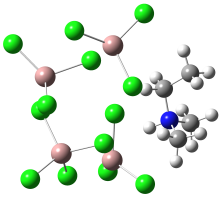
5.6_65_179 (42)



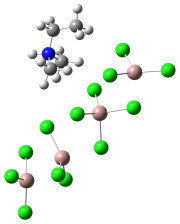
4.6_167_ – 36 (14)



5.9_117_ – 150 (11)

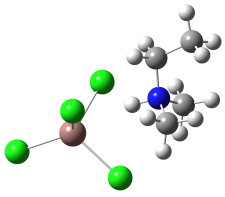


5.9_77_168 (0)

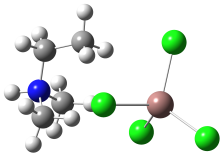


7.1_141_ – 32 (82)

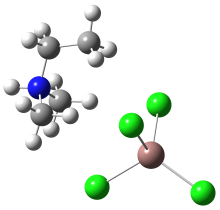
Table A.148: $[N_{2110}][InCl_4]$ Gas Phase Ion Pair Structures



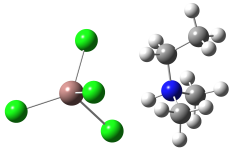
3.8_113_ – 171 (0)



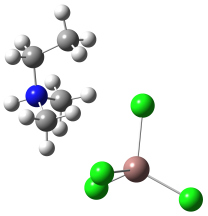
5.1_81_12 (59)



4.7_104_0 (50)

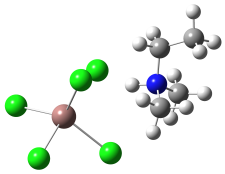


4_84_170 (0)

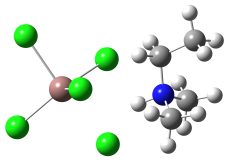


4.7_124_15 (50)

Table A.149: $[N_{2110}][InCl_5]^-$ Gas Phase Ion Pair Structures



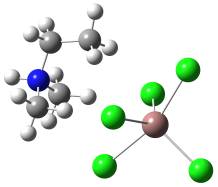
3.9_114_160 (60)



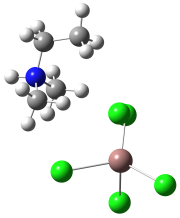
3.9_87_ – 180 (60)



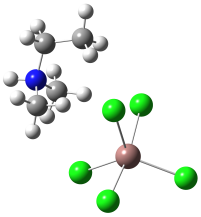
5_79_ – 62 (0)



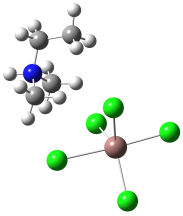
4.7_89_0 (153)



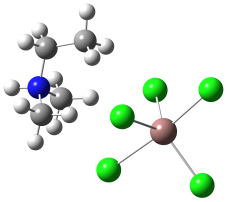
4.9_123_ – 15 (150)



4.8_109_14 (150)

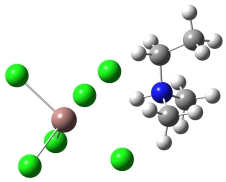


4.9_122_ – 20 (154)

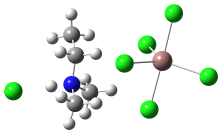


4.9_95_0 (154)

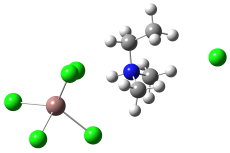
Table A.150: $[N_{2110}][InCl_6]^{2-}$ Gas Phase Ion Pair Structures



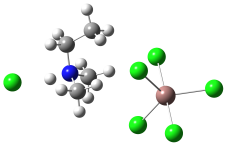
4.1_106_ – 180 (145)



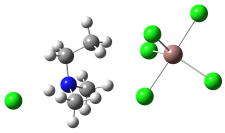
4.8_64_117 (0)



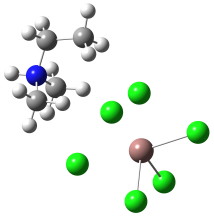
4.1_108_145 (11)



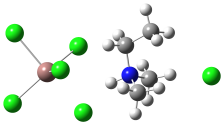
5_104_7 (10)



5.5_78_ – 9 (13)



5.1_106_0 (262)



4.1_83_176 (8)

A.2.8 $[N_{2111}][M_xCl_y]$ Gas Ion pair structures

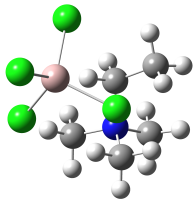
Table A.151: Number of IP structures divided into relative Gibbs free energy with respect to the lowest energy structure of each IP in the ranges of ≤ 10, $10 \leq 20$, $20 \leq 30$, $30 \leq 40$, $40 \leq 50$ and $50 <$ in $kJ\ mol^{-1}$ of each $[N_{2111}][M_xCl_{3y}]^{z-}$ IP in the Gas Phase

Anion	≤ 10	$10 \leq 20$	$20 \leq 30$	$30 \leq 40$	$40 \leq 50$	$50 <$	Total
$[AlCl_4]^-$	7	0	0	0	0	0	7
$[Al_2Cl_7]^-$	6	1	0	1	0	0	8
$[Al_3Cl_{10}]^-$	3	1	1	2	0	1	8
Branched $[Al_4Cl_{13}]^-$	1	3	2	3	2	1	12
Linear $[Al_4Cl_{13}]^-$	8	1	0	1	4	0	14
$[GaCl_4]^-$	4	1	0	0	0	0	5
$[Ga_2Cl_7]^-$	3	0	1	0	0	0	4
$[Ga_3Cl_{10}]^-$	2	2	1	1	2	1	9
Branched $[Ga_4Cl_{13}]^-$	2	5	5	1	0	1	14
Linear $[Ga_4Cl_{13}]^-$	1	0	0	0	0	0	1
$[InCl_4]^-$	7	1	0	0	0	0	8
$[InCl_5]^{2-}$	3	3	0	0	0	0	6
$[InCl_6]^{3-}$	1	0	1	0	0	0	2

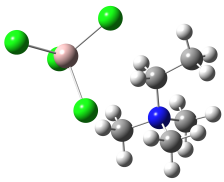
Table A.152: $[N_{2111}][AlCl_4]$ Gas Phase Ion Pair Structures



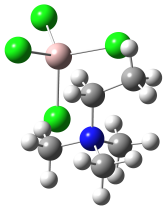
1_0.8_167 (3)



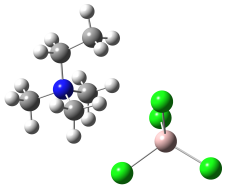
4.7_55_99 (2)



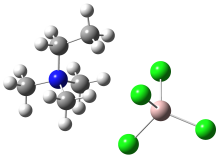
4.8_49_151 (3)



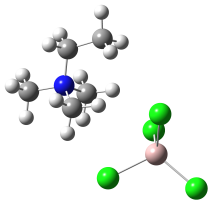
4.5_69_ – 44 (0)



4.7_122_ – 15 (7)

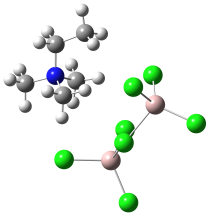


4.7_102_0 (9)

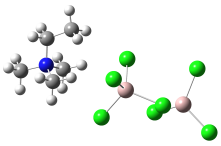


4.7_122_ – 13 (7)

Table A.153: $[N_{2111}][Al_2Cl_7]$ Gas Phase Ion Pair Structures



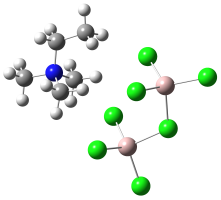
4.5_127_15 (8)



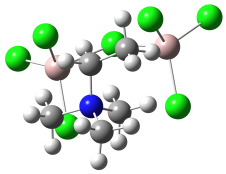
6.8_104_ – 1 (33)



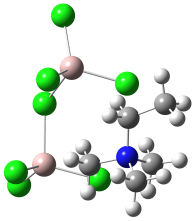
5.9_153_ – 69 (4)



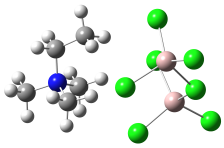
6.1_113_ – 18 (7)



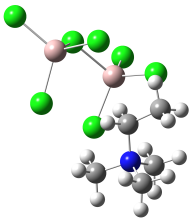
5.9_84_ – 103 (2)



5.9_85_ – 131 (2)

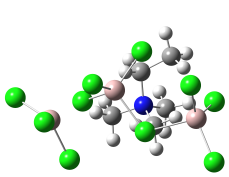


6.3_91_1 (16)

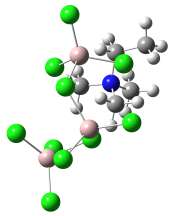


5.9_49_ – 133 (0)

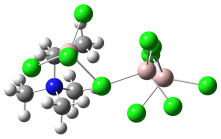
Table A.154: $[N_{2111}][Al_3Cl_{10}]$ Gas Phase Ion Pair Structures



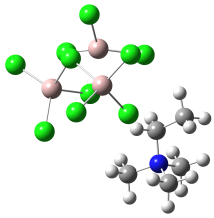
4.8_64_100 (36)



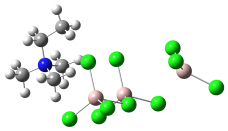
6.6_92_86 (19)



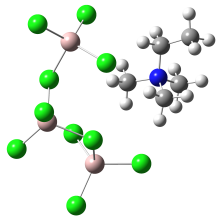
6.2_71_34 (8)



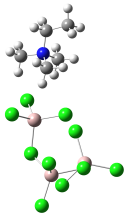
7.4_72_ – 150 (55)



4.9_115_6 (30)

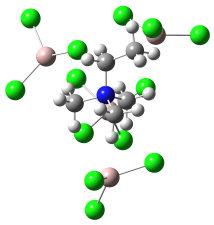


5.8_107_133 (0)

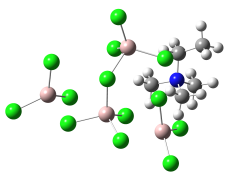


7.8_164_29 (37)

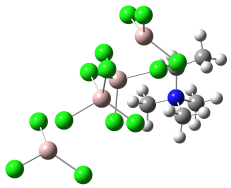
Table A.155: $[N_{2111}][Al_4Cl_{13}]$ Branched Gas Phase Ion Pair Structures



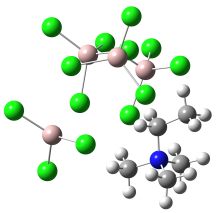
5.6_112_ – 107 (15)



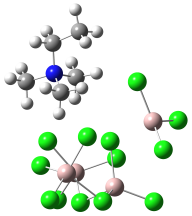
5.8_100_112 (34)



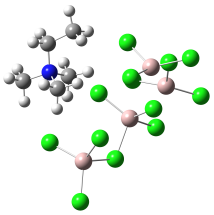
7.7_77_98 (64)



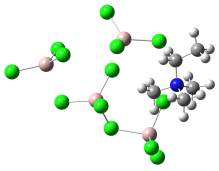
5.7_37_ – 167 (16)



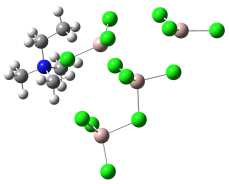
6.2_151_10 (0)



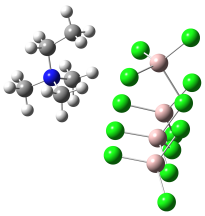
5.9_125_ – 47 (34)



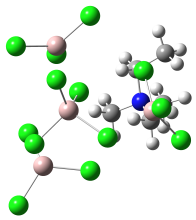
5.8_105_ – 160 (25)



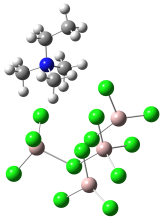
5.8_98_17 (35)



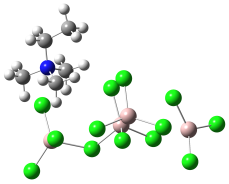
5.9_127_ – 5 (40)



5.7_76_118 (19)

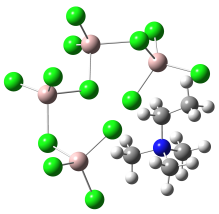


5.8_150_ – 9 (45)

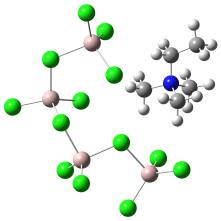


5.8_135_ – 41 (26)

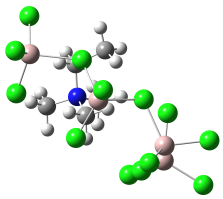
Table A.156: $[N_{2111}][Al_4Cl_{13}]$ Linear Gas Phase Ion Pair Structures



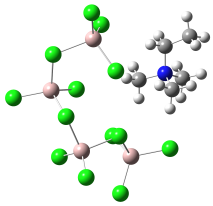
4.3_53_173 (9)



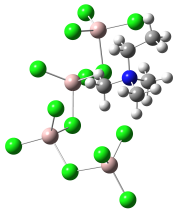
6.6_100_139 (0)



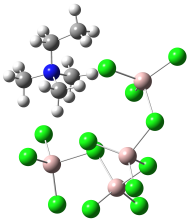
5.2_80_45 (9)



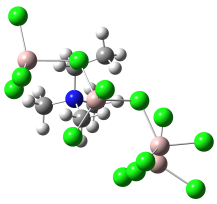
6.5_103_132 (9)



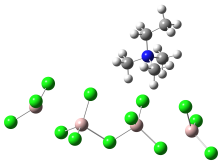
6.7_124_ – 134 (7)



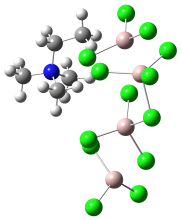
6.7_128_16 (2)



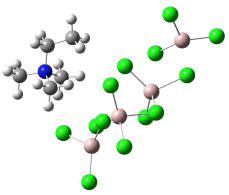
5.1_77_44 (2)



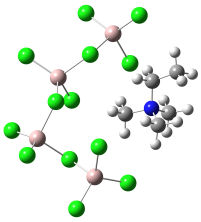
6.7_153_180 (47)



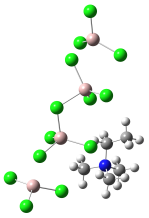
6.8_95_32 (49)



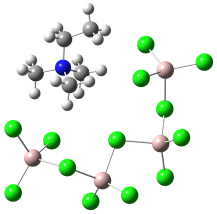
6.7_103_2 (49)



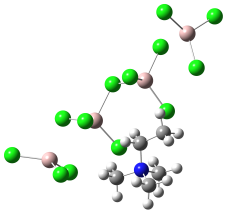
5.2_85_154 (10)



6.7_46_117 (43)

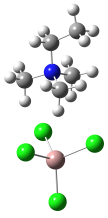


4.6_138_8 (6)

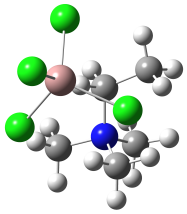


6.1_52_ – 124 (37)

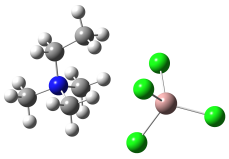
Table A.157: $[N_{2111}][GaCl_4]$ Gas Phase Ion Pair Structures



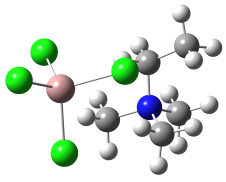
4.5_180_177 (3)



4.7_54_100 (2)

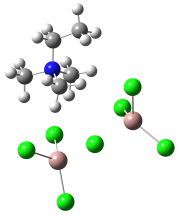


4.7_102_0 (8)

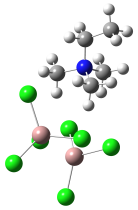


4.5_69_113 (0)

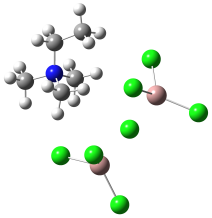
Table A.158: $[N_{2111}][Ga_2Cl_7]$ Gas Phase Ion Pair Structures



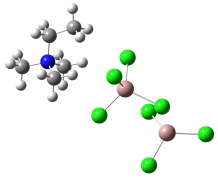
4.9_120_ – 47 (5)



6.9_172_129 (0)

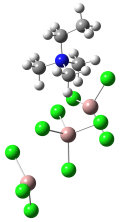


7.1_103_ – 7 (0)

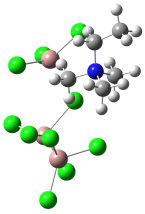


6.8_117_ – 32 (29)

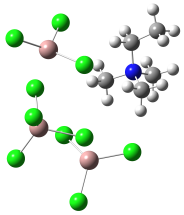
Table A.159: $[N_{2111}][Ga_3Cl_{10}]$ Gas Phase Ion Pair Structures



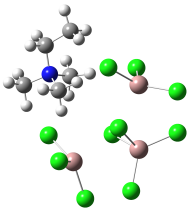
4.6_177_ – 68 (45)



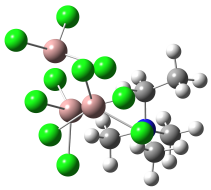
5.8_135_ – 147 (2)



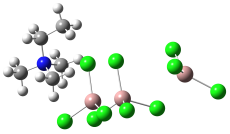
5.8_107_133 (0)



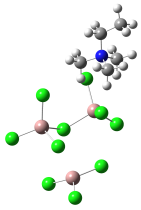
5.9_135_7 (16)



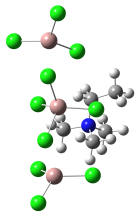
7.8_53_103 (61)



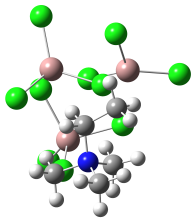
4.9_117_4 (33)



6.3_139_173 (42)

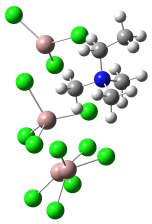


4.8_65_102 (19)

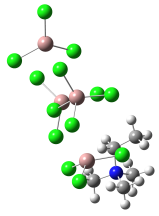


5.9_98_ – 106 (30)

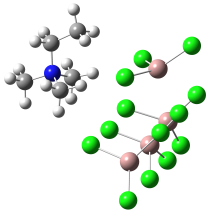
Table A.160: $[N_{2111}][Ga_4Cl_{13}]$ Branched Gas Phase Ion Pair Structures



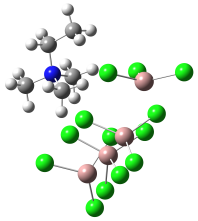
5.1_123_ – 148 (16)



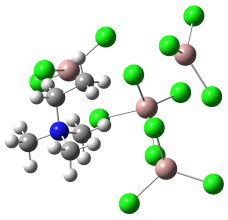
6.3_28_123 (22)



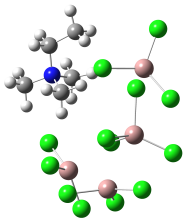
6_126_0 (39)



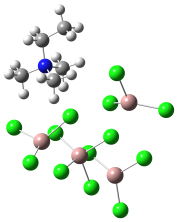
5.9_124_45 (17)



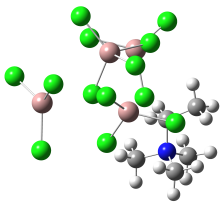
5.4_95_ – 62 (5)



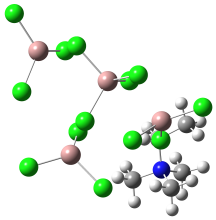
5.1_125_16 (20)



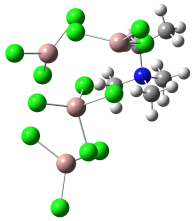
5.4_159_33 (14)



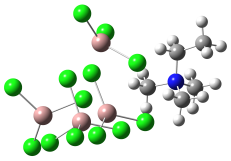
5.3_30_177 (0)



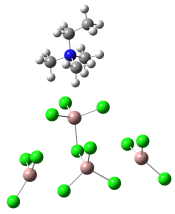
6.2_31_126 (23)



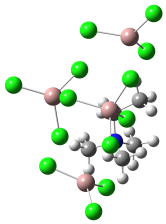
6.1_88_116 (11)



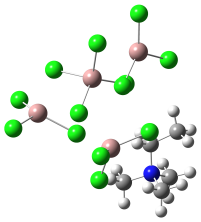
5.8_104_125 (22)



7.7_163_60 (59)

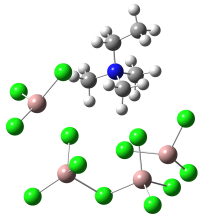


6.1_58_88 (23)



6.1_29_152 (21)

Table A.161: $[N_{2111}][Ga_4Cl_{13}]$ Linear Gas Phase Ion Pair Structures

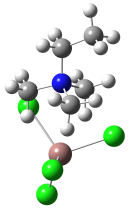


6.6_145_90 (0)

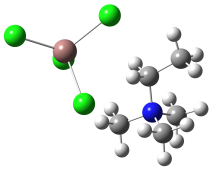
Table A.162: $[N_{2111}][InCl_4]$ Gas Phase Ion Pair Structures



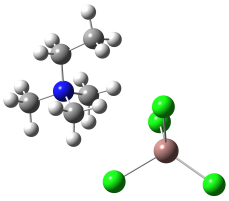
4.6_180_172 (3)



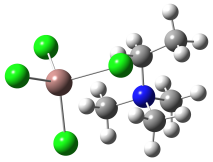
4.7_145_ – 107 (7)



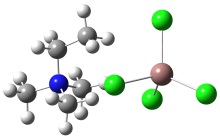
4.7_47_157 (3)



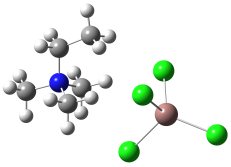
4.7_125_ – 15 (5)



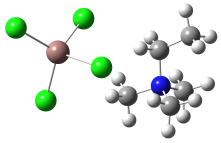
4.6_69_114 (0)



5.2_80_11 (17)

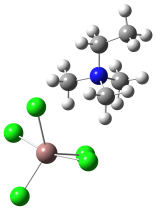


4.8_103_0 (7)

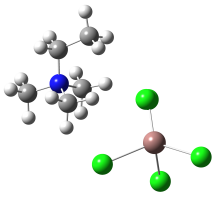


4.7_67_151 (4)

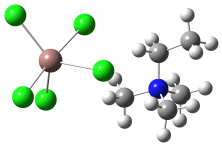
Table A.163: $[N_{2111}][InCl_5]^-$ Gas Phase Ion Pair Structures



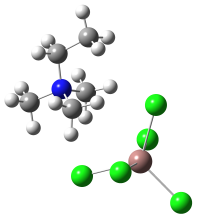
4.4_134_121 (4)



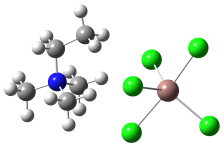
4.9_125_ – 17 (12)



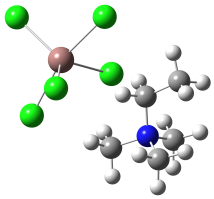
4.9_72_146 (15)



4.4_138_0 (1)

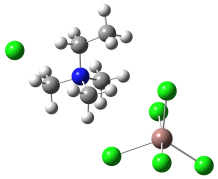


5_94_0 (19)

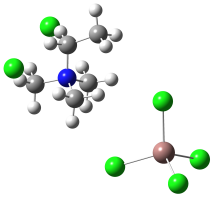


4.4_54_ – 169 (0)

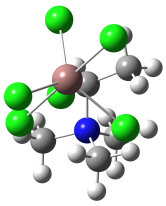
Table A.164: $[N_{2111}][InCl_6]^{2-}$ Gas Phase Ion Pair Structures



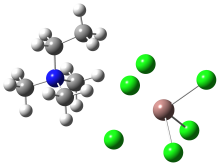
4.8_130_ – 14 (44)



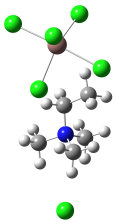
5.4_124_0 (10)



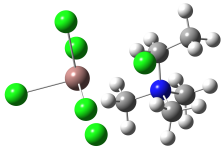
5.2_55_84 (49)



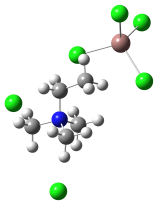
5.2_105_0 (259)



5.1_44_ – 117 (46)



5_71_113 (243)



5.5_54_ – 64 (0)